Transactions of the ASME®

Journal of Heat Transfer

Published Bimonthly by The American Society of Mechanical Engineers

VOLUME 125 • NUMBER 6 • DECEMBER 2003

TECHNICAL PAPERS

This journal is printed on acid-free paper, which exceeds the ANSI Z39.48-1992 specification for permanence of paper and library materials. ⊗™
☺ 85% recycled content, including 10% post-consumer fibers.

ANNOUNCEMENTS

The ASME Journal of Heat Transfer is abstracted and indexed in the following:

Applied Science and Technology Index, AMR Abstracts Database, Chemical Abstracts, Chemical Engineering and Biotechnology Abstracts (Electronic equivalent of Process and Chemical Engineering), Civil Engineering Abstracts, Compendex (The electronic equivalent of Engineering Index), Corrosion Abstracts, Current Contents, E & P Health, Safety, and Environment, Ei EncompassLit, Engineered Materials Abstracts, Engineering Index, Enviroline (The electronic equivalent of Environment Abstracts), Environment Abstracts, Environmental Engineering Abstracts, Environmental Science and Pollution Management, Fluidex, Fuel and Energy Abstracts, Index to Scientific Reviews, INSPEC, International Building Services Abstracts, Mechanical & Transportation Engineering Abstracts, Mechanical Engineering Abstracts, METADEX (The electronic equivalent of Metals Abstracts and Alloys Index), Petroleum Abstracts, Process and Chemical Engineering, Referativnyi Zhurnal, Science Citation Index, SciSearch (The electronic equivalent of Science Citation Index), Theoretical Chemical Engineering

Thermal Processing of Materials: From Basic Research to Engineering

Yogesh Jaluria

Fellow ASME,
Board of Governors Professor,
Department of Mechanical and Aerospace
Engineering,
Rutgers, The State University of New Jersey,
New Brunswick, NJ 08903

This paper reviews the active and growing field of thermal processing of materials, with a particular emphasis on the linking of basic research with engineering aspects. In order to meet the challenges posed by new applications arising in electronics, telecommunications, aerospace, transportation, and other areas, extensive work has been done on the development of new materials and processing techniques in recent years. Among the materials that have seen intense interest and research activity over the last two decades are semiconductor and optical materials, composites, ceramics, biomaterials, advanced polymers, and specialized alloys. New processing techniques have been developed to improve product quality, reduce cost, and control material properties. However, it is necessary to couple research efforts directed at the fundamental mechanisms that govern materials processing with engineering issues that arise in the process, such as system design and optimization, process feasibility, and selection of operating conditions to achieve desired product characteristics. Many traditional and emerging materials processing applications involve thermal transport, which plays a critical role in the determination of the quality and characteristics of the final product and in the operation, control, and design of the system. This review is directed at the heat and mass transfer phenomena underlying a wide variety of materials processing operations, such as optical fiber manufacture, casting, thin film manufacture, and polymer processing, and at the engineering aspects that arise in actual practical systems. The review outlines the basic and applied considerations in thermal materials processing, available solution techniques, and the effect of the transport on the process, the product and the system. The complexities that are inherent in materials processing, such as large material property changes, complicated and multiple regions, combined heat and mass transfer mechanisms, and complex boundary conditions, are discussed. The governing equations for typical processes, along with important parameters, common simplifications and specialized methods employed to study these processes are outlined. The field of thermal materials processing is quite extensive and only a few important techniques employed for materials processing are considered in detail. The effect of heat and mass transfer on the final product, the nature of the basic problems involved, solution strategies, and engineering issues involved in the area are brought out. The current status and future trends are discussed, along with critical research needs in the area. The coupling between the research on the basic aspects of materials processing and the engineering concerns in practical processes and systems is discussed in detail. [DOI: 10.1115/1.1621889]

Introduction

Materials processing is one of the most important and active areas of research in heat transfer today. With growing international competition, it is has become crucial to improve the present processing techniques and the quality of the final product. New materials and processing methods are needed to meet the growing demand for special material properties in new and emerging applications related to diverse fields such as environment, energy, bioengineering, transportation, communications, and computers. It is also critical to use the fundamental understanding of materials processing in the design and optimization of the relevant systems.

Heat transfer is extremely important in a wide range of materials processing techniques such as crystal growing, casting, glass fiber drawing, chemical vapor deposition, spray coating, soldering, welding, polymer extrusion, injection molding, and composite materials fabrication. The flows that arise in the molten mate-

rial in crystal growing due to temperature and concentration differences, for instance, can affect the quality of the crystal and, thus, of the semiconductors fabricated from the crystal. Therefore, it is important to understand these flows and develop methods to minimize or control their effects. Similarly, the profile of the neck-down region in an optical fiber drawing process is largely governed by the viscous flow of molten glass, which is in turn determined by the thermal field in the glass. The buoyancy-driven flows generated in the liquid melt in casting processes strongly influence the microstructure of the casting and the shape, movement and other characteristics of the solid-liquid interface. In chemical vapor deposition, the heat and mass transfer processes determine the deposition rate and uniformity, and thus the quality of the thin film produced. The transport in furnaces and ovens used for heat treatment strongly influence the quality of the product.

As a consequence of the importance of heat and mass transfer in materials processing, extensive work is presently being directed at this area. But what is often lacking is the link between the basic mechanisms that govern diverse processing techniques and the thermal systems needed to achieve the given process. On the one

Table 1 Different types of thermal materials processing operations, along with examples of common techniques

1.	PROCESSES WITH PHASE CHANGE
	casting, continuous casting, crystal growing, drying
2.	HEAT TREATMENT
	annealing, hardening, tempering, surface treatment, curing, baking
3.	FORMING OPERATIONS
	hot rolling, wire drawing, metal forming, extrusion, forging
4.	CUTTING
	laser and gas cutting, fluid jet cutting, grinding, machining
5.	BONDING PROCESSES
	soldering, welding, explosive bonding, chemical bonding
6.	POLYMER PROCESSING
	extrusion, injection molding, thermoforming
7.	REACTIVE PROCESSING
	chemical vapor deposition, food processing
8.	POWDER PROCESSING
	powder metallurgy, sintering, sputtering, processing of nano-powders and ceramics
9.	GLASS PROCESSING
	optical fiber drawing, glass blowing, annealing
10.	COATING
	thermal spray coating, polymer coating
11.	OTHER PROCESSES
	composite materials processing, microgravity materials processing, rapid prototyping

transfer mechanisms. A few important materials processing techniques in which heat transfer plays a very important role are listed in Table 1.

This list contains both traditional processes and new or emerging methods. In the former category, we can include welding, metal forming, polymer extrusion, casting, heat treatment and drying. Similarly, in the latter category, we can include crystal growing, chemical vapor deposition and other thin film manufacturing techniques, thermal sprays, fabrication of composite materials, processing of nano-powders to fabricate system components, optical fiber drawing and coating, microgravity materials processing, laser machining and reactive extrusion. The choice of an appropriate material for a given application is an important consideration in the design and optimization of processes and systems [1].

A few thermal materials processing systems are also sketched in Fig. 1. These include the optical glass fiber drawing process in which a specially fabricated glass preform is heated and drawn into a fiber, thin film fabrication by chemical vapor deposition (CVD), Czochralski crystal growing in which molten material such as silicon is allowed to solidify across an interface as a seed crystal is withdrawn, and screw extrusion in which materials such as plastics are melted and forced through a die to obtain specific dimensions and shape. In all these processes, the quality and characteristics of the final product and the rate of fabrication are strong functions of the underlying thermal transport processes. Many books and review articles have discussed important practical considerations and the fundamental transport mechanisms in the area of manufacturing and materials processing [2–8].

Basic Research Versus Engineering

Research in thermal materials processing is largely directed at the basic processes and underlying mechanisms, physical understanding, effects of different transport mechanisms and physical parameters, general behavior and characteristics, and the thermal process undergone by the material. It is usually a long-term effort, which leads to a better quantitative understanding of the process under consideration. However, it can also provide inputs, which can be used for design and development.

Engineering studies in materials processing, on the other hand, are concerned with the design of the process and the relevant thermal system, optimization, product development, system control, choice of operating conditions, improving product quality, reduction in costs, process feasibility, enhanced productivity, repeatability, and dependability.

Figure 2 shows a schematic of the different steps that are typically involved in the design and optimization of a system. The iterative process to obtain an acceptable design by varying the design variables is indicated by the feedback loop connecting simulation, design evaluation and acceptable design. There is a feedback between simulation and modeling as well, in order to improve the model representation of the physical system on the basis of observed behavior and characteristics of the system, as obtained from simulation. Optimization of the system is undertaken after acceptable designs have been obtained.

Some of the important considerations that arise when dealing with the thermal transport in the processing of materials are given in Table 2. All these considerations make the mathematical and numerical modeling of the process and the associated system for materials processing very involved and challenging. Special procedures and techniques are generally needed to satisfactorily simulate the relevant boundary conditions and material property variations. The results from the simulation provide inputs for the design and optimization of the relevant system, as well as for the choice of the appropriate operating conditions. Experimental techniques and results are also closely linked with the mathematical modeling in order to simplify the experiments and obtain useful results in terms of important dimensionless parameters.

It is necessary for heat transfer researchers to thoroughly understand the concerns, intricacies and basic considerations that

hand, considerable effort has been directed at specific manufacturing systems, problems and circumstances in order to develop new products, reduce costs and optimize the process. Much of this effort has been based on expensive and time-consuming experimentation on practical systems. On the other hand, detailed research has been carried out to extract the main underlying features of the processes, develop new solution methods to simulate complex transport circumstances that arise, and to obtain a much better understanding of the governing mechanisms. However, quantitative information on the dependence of product quality, process control and optimization on the thermal transport is often unavailable The coupling between practical engineering systems and the basic transport mechanisms is a very important aspect that should be considered, so that the current and future research on thermal materials processing has a strong impact on the design, control and optimization of the relevant thermal systems. For instance, an understanding of the microscale mechanisms that determine material characteristics is important, but these must be linked with the boundary conditions that are usually imposed at the macroscale level in the system.

This review paper is directed at these important issues, focusing on the heat and mass transfer involved with materials processing and linking these with the characteristics of the product and with the system. However, it must be noted that the concerns, questions and considerations presented in this paper are not unique to the field of materials processing. Other traditional and emerging areas like those concerned with safety, cooling of electronic systems, automobile and aircraft systems, space, and energy also involve research on the basic transport processes and these need to be linked with engineering issues.

Thermal Processing of Materials

Thermal processing of materials refers to manufacturing and material fabrication techniques that are strongly dependent on the thermal transport mechanisms. With the substantial growth in new and advanced materials like composites, ceramics, different types of polymers and glass, coatings, specialized alloys and semiconductor materials, thermal processing has become particularly important since the properties and characteristics of the product, as well as the operation of the system, are largely determined by heat

Fig. 1 Sketches of a few common manufacturing processes that involve thermal transport in the material being processed: (a) optical fiber drawing; (b) chemical vapor deposition; (c) Czochralski crystal growing; and (d) plastic screw extrusion.

Fig. 2 Various steps involved in the design and optimization of a thermal system and in the implementation of the design

characterize materials processing in order to make a significant impact on the field and to play a leadership role. The dependence of the characteristics of the final product on the heat transfer must be properly understood and characterized so that analysis or experimentation can be used to design processes to achieve desired product characteristics and production rates.

Mathematical Modeling

Modeling is one of the most crucial elements in the design and optimization of thermal materials processing systems. Practical processes and systems are generally very complicated and must be simplified through idealizations and approximations to make the problem solvable. This process of simplifying a given problem so that it may be represented in terms of a system of equations, for analysis, or a physical arrangement, for experimentation, is termed modeling. Once a model is obtained, it is subjected to a variety of operating conditions and design variations. If the model is a good representation of the actual system under consideration, the outputs obtained from the model characterize the behavior of the given system. This information is used in the design process as

Table 2 Important considerations in thermal materials processing

1.	COUPLING OF TRANSPORT WITH MATERIAL CHARACTERISTICS
	different materials, properties, behavior, material structure
2.	VARIABLE MATERIAL PROPERTIES
	strong variation with temperature, pressure and concentration
3.	COMPLEX GEOMETRIES
	complicated domains, multiple regions
4.	COMPLICATED BOUNDARY CONDITIONS
	conjugate conditions, combined modes
5.	INTERACTION BETWEEN DIFFERENT MECHANISMS
	surface tension, heat and mass transfer, chemical reactions, phase change
6.	MICRO-MACRO COUPLING
	micro-structure changes, mechanisms operating at different length and time scales
7.	COMPLEX FLOWS
	non-Newtonian flows, free surface flows, powder and particle transport
8.	INVERSE PROBLEMS
	non-unique multiple solutions, iterative solution
9.	DIFFERENT ENERGY SOURCES
	laser, chemical, electrical, gas, fluid jet, heat
10.	SYSTEM OPTIMIZATION AND CONTROL
	link between heat transfer and manufacturing system

well as in obtaining and comparing alternative designs by predicting the performance of each design, ultimately leading to an optimal design.

A mathematical model is one that represents the performance and behavior of a given system in terms of mathematical equations. These models are the most important ones in the design of thermal systems, since they provide considerable flexibility and versatility in obtaining quantitative results that are needed as inputs for design. Mathematical models form the basis for simulation, so that the behavior and characteristics of the system may be investigated without actually fabricating a prototype. In addition, the simplifications and approximations that lead to a mathematical model also indicate the dominant variables in a problem. This helps in developing efficient physical or experimental models. Numerical models are based on the mathematical model and allow one to obtain, using a computer, quantitative results on the system behavior for different operating conditions and design parameters.

Governing Equations

General Equations. The governing equations for convective heat transfer in materials processing are derived from the basic conservation principles for mass, momentum and energy. For a pure viscous fluid, these equations may be written as

$$\frac{D\rho}{Dt} + \rho \nabla \cdot \bar{V} = 0 \tag{1}$$

$$\rho \frac{D\bar{V}}{Dt} = \bar{F} + \nabla \cdot \underline{\underline{\tau}} \tag{2}$$

$$\rho C_p \frac{DT}{Dt} = \nabla \cdot (k\nabla T) + \dot{Q} + \beta T \frac{Dp}{Dt} + \mu \Phi \tag{3}$$

Here, D/Dt is the substantial or particle derivative, given in terms of the local derivatives in the flow field by $D/Dt = \partial/\partial t + \bar{V} \cdot \nabla$. The other variables are defined in the Nomenclature.

For a solid, the energy equation is written as

$$\rho C_p \frac{DT}{Dt} = \frac{\partial T}{\partial t} + \bar{V} \cdot \nabla T = \nabla \cdot (k\nabla T) + \dot{Q} \tag{4}$$

where the specific heats at constant pressure and at constant volume are essentially the same for an incompressible fluid. If the solid is stationary, the convection term drops out and the particle derivative is replaced by the transient term $\partial/\partial t$, resulting in the conduction equation. In a deforming solid, as in wire drawing, extrusion or fiber drawing, the material is treated as a fluid, with an appropriate constitutive equation, and the additional terms due to pressure work and viscous heating are generally included. In

the preceding equations, the material is taken as isotropic, with the properties, which are taken as variable, assumed to be the same in all directions. For certain materials, such as composites, the nonisotropic behavior must be taken into account.

The stress tensor in Eq. (2) can be written in terms of the velocity $\bar{V}$ if the material characteristics are known. For instance, if μ is taken as constant for a Newtonian fluid, the relationships between the shear stresses and the shear rates, given by Stokes, are employed to yield

$$\rho \frac{D\bar{V}}{Dt} = \bar{F} - \nabla p + \mu \nabla^2 \bar{V} + \frac{\mu}{3} \nabla(\nabla \cdot \bar{V}) \qquad (5)$$

Here, the bulk viscosity $K = \lambda + (2/3)\mu$ is taken as zero. For an incompressible fluid, ρ is constant, which gives $\nabla \cdot \bar{V} = 0$ from Eq. (1). Then, the last term in Eq. (5) drops out.

Buoyancy Effects. The body force $\bar{F}$ is important in many manufacturing processes, such as crystal growing and casting where it gives rise to the thermal or solutal buoyancy term. The governing momentum equation is obtained from Eq. (5), when thermal buoyancy is included, as

$$\rho \frac{D\bar{V}}{Dt} = -\bar{e}g\rho\beta(T - T_a) - \nabla p_d + \mu \nabla^2 \bar{V} \qquad (6)$$

where p_d is the dynamic pressure, obtained after subtracting out the hydrostatic pressure p_a. Therefore, p_d is the component due to fluid motion, as discussed by Jaluria [9] and Gebhart et al. [10]. Boussinesq approximations, that neglect the effect of the density variation in the continuity equation and assume a linear variation of density with temperature, are employed here. However, in many practical cases, these approximations can not be used. The governing equations are coupled because of the buoyancy term in Eq. (6) and must be solved simultaneously [11].

Viscous Dissipation. The viscous dissipation term $\mu\Phi$ in Eq. (3) represents the irreversible part of the energy transfer due to the shear stress. Therefore, viscous dissipation gives rise to a thermal source in the flow and is always positive. For a Cartesian coordinate system, Φ is given by the expression

$$\Phi = 2\left[\left(\frac{\partial u}{\partial x}\right)^2 + \left(\frac{\partial v}{\partial y}\right)^2 + \left(\frac{\partial w}{\partial z}\right)^2\right] + \left(\frac{\partial v}{\partial x} + \frac{\partial u}{\partial y}\right)^2 + \left(\frac{\partial w}{\partial y} + \frac{\partial v}{\partial z}\right)^2$$
$$+ \left(\frac{\partial u}{\partial z} + \frac{\partial w}{\partial x}\right)^2 - \frac{2}{3}(\nabla \cdot \bar{V})^2 \qquad (7)$$

Similarly, expressions for other coordinate systems may be obtained. This term becomes important for very viscous fluids, such as glass, plastics and food, and at high speeds.

Processes With Phase Change. Many material processing techniques, such as crystal growing, casting, and welding, involve a phase change. Two main approaches have been used for the numerical simulation of these problems. The first one treats the two phases as separate, with their own properties and characteristics. The interface between the two phases must be determined so that conservation principles may be applied there [7,12]. This becomes fairly involved since the interface location and shape must be determined for each time step or iteration.

In the second approach, the conservation of energy is considered in terms of the enthalpy H, yielding the governing energy equation as

$$\rho \frac{DH}{Dt} = \rho \frac{\partial H}{\partial t} + \rho \bar{V} \cdot \nabla H = \nabla \cdot (k \nabla T) \qquad (8)$$

where each of the phase enthalpies H_i is defined as

$$H_i = \int_0^T C_i dT + H_i^o \qquad (9)$$

C_i being the corresponding specific heat and H_i^0 the enthalpy at $0K$. Then, the solid and liquid enthalpies are given by, respectively,

$$H_s = C_s T \quad H_l = C_l T + [(C_s - C_l)T_m + L_h] \qquad (10)$$

where L_h is the latent heat of fusion, and T_m the melting point. The continuum enthalpy and thermal conductivity are given, respectively, as

$$H = H_s + f_l(H_l - H_s) \quad k = k_s + f_l(k_l - k_s) \qquad (11)$$

where f_l is the liquid mass fraction, obtained from equilibrium thermodynamic considerations. The dynamic viscosity μ is expressed as the harmonic mean of the phase viscosities, employing the limit $\mu_s \to \infty$, i.e., $\mu = \mu_l/f_l$. This model smears out the discrete phase transition in a pure material. But the numerical modeling is much simpler since the same equations are employed over the entire computational domain and there is no need to keep track of the interface between the two phases [13–15]. In addition, impure materials, mixtures and alloys can be treated very easily by this approach.

Chemically Reactive Flows. Combined thermal and mass transport mechanisms are important in many materials processing circumstances, such as chemical vapor deposition and processing of food, reactive polymers, and several other materials with multiple species. Chemical reactions occurring in chemically reactive materials substantially alter the structure and characteristics of the product [16,17].

A simple approach to model the chemical conversion process in reactive materials, such as food, is based on the governing equation for chemical conversion, given as [18]

$$\frac{d}{dt}[(1 - \tilde{X})] = -K(1 - \tilde{X})^m \qquad (12)$$

where $\tilde{X}$ is the degree of conversion, defined as,

$$\tilde{X} = \frac{M_i - M_t}{M_i - M_f} \qquad (13)$$

here M is the amount of unconverted material, with subscripts i, f, and t referring to the amounts at the initial condition, final condition and at time t. The order of the reaction is m and K is the reaction rate, these generally being determined experimentally. Similarly, chemical kinetics play a critical role in the deposition of material from the gas phase in chemical vapor deposition systems [19,20].

Idealizations and Simplifications

In order to develop an appropriate mathematical model for a given materials processing system, several idealizations and simplifications are made to make the problem amenable to an analytical or numerical solution. A general procedure, which includes considerations of transient versus steady-state transport, number of spatial dimensions needed, neglecting of relatively small effects, idealizations such as isothermal or uniform heat flux conditions, and characterization of material properties, may be adopted to obtain the usual simplifications in analysis [1].

Boundary Conditions. Many of the boundary and initial conditions used in materials processing are the usual no-slip conditions for velocity and the appropriate thermal or mass transfer conditions at the boundaries. Similarly, the normal gradients are taken as zero at an axis or plane of symmetry, temperature and heat flux continuity is maintained in going from one homogeneous region to another, and initial conditions are often taken as zero flow at the ambient temperature, representing the situation before the onset of the process. For periodic processes, the initial conditions are arbitrary.
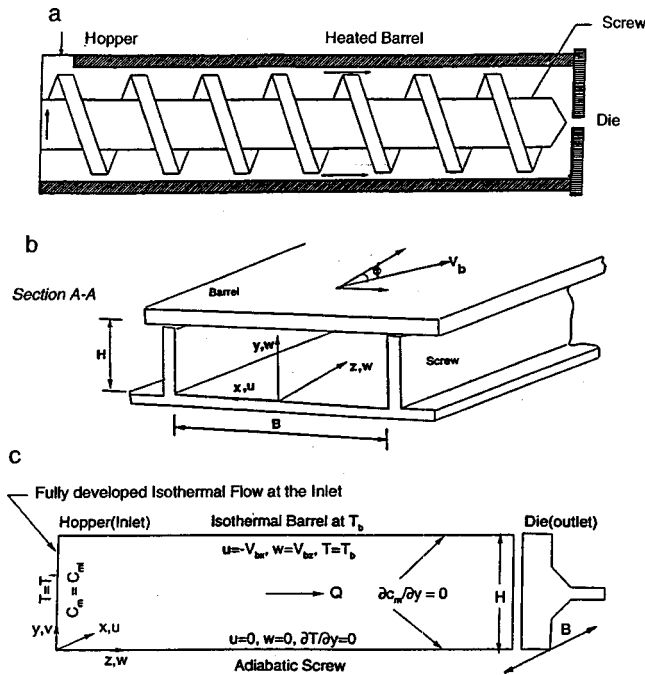
Fig. 3 Screw channel and simplified computational domain for a single-screw extruder

At a free surface, the shear stress is often specified as zero, yielding a Neumann condition of the form $\partial \bar{V}/\partial n = 0$, if negligible shear is applied on the surface. In general, a balance of all the forces acting at the surface is used to obtain the interface. As considered in detail by Roy Choudhury et al. [21] and as presented later, the free surface may be determined numerically by iterating from an initial profile and using the imbalance of the forces for correcting the profile at intermediate steps, finally yielding a converged profile. In a stationary ambient medium, far from the solid boundaries, the velocity and temperature may be given as $\bar{V} \to 0$, $T \to T_a$ as $n \to \infty$. However, frequently the condition $\partial \bar{V}/\partial n \to 0$ is used, instead, in order to allow for entrainment into the flow. The use of this gradient, or Neumann, condition generally allows the use of a much smaller computational domain, than that needed for a given value, or Dirichlet condition, imposed on the velocity $\bar{V}$ [22].

If a change of phase occurs at the boundary, the energy absorbed or released due to the change of phase must be taken into account. Thus, the boundary conditions at the moving interface between the two phases must be given if a two-zone model is being used. This is not needed in the enthalpy model mentioned earlier. For one-dimensional solidification, this boundary condition is given by the equation

$$k_s \frac{\partial T_s}{\partial y} - k_l \frac{\partial T_l}{\partial y} = \rho L_h \frac{d\delta}{dt} \qquad (14)$$

where $y = \delta$ is the location of the interface. This implies that the energy released due to solidification is conveyed by conduction in the two regions. Similarly, the boundary condition may be written for two or three-dimensional solidification [12]. For a stationary interface, as in crystal growing shown in Fig. 1(c) and for continuous casting, the appropriate boundary condition has been given by Siegel [23].

Other Simplifications. In the case of material flow in a moving cylindrical rod or a plate for extrusion or hot rolling, the temperature T is a function of time and location if a Lagrangian approach is used to follow a material element. However, by placing the coordinate system outside the moving material, a steady problem is obtained if the edge of the rod is far from the inlet and if the boundary conditions are steady. Transient problems arise for small lengths of the rod at short times following the onset of the process, and for boundary conditions varying with time [24]. Similarly, coordinate transformations are employed to convert transient problems to steady state ones in other circumstances.

In the case of a single-screw extruder, shown in Fig. 3, the coordinate system is generally fixed to the rotating screw and the channel straightened out mathematically, ignoring the effects of curvature. Then the complicated flow in the extruder is replaced by a simpler pressure and shear driven channel flow, with shear arising due to the barrel moving at the pitch angle over a stationary screw.

The basic nature of the underlying physical processes and the simplifications that may be obtained under various circumstances can be best understood in terms of dimensionless variables that arise when the governing equations and the boundary conditions are nondimensionalized. The commonly encountered governing dimensionless parameters are the Strouhal number Sr, the Reynolds number Re, the Grashof number Gr, the Prandtl number Pr and the Eckert number Ec. These are defined as

$$\mathrm{Sr} = \frac{L}{V_c t_c}, \quad \mathrm{Re} = \frac{V_c L}{\nu}, \quad \mathrm{Gr} = \frac{g\beta(T_s - T_a)L^3}{\nu^2}, \quad \mathrm{Pr} = \frac{\nu}{\alpha},$$

$$\mathrm{Ec} = \frac{V_c^2}{C_p(T_s - T_a)} \qquad (15)$$

where V_c is a characteristic speed, L a characteristic dimension, and t_c a characteristic time. The dimensionless equations may be used to determine the various regimes over which certain simplifications can be made, such as creeping flow at small Re and boundary layer at large Re.

Material Considerations

Variable Properties. The properties of the material undergoing thermal processing are very important in the modeling of the process, in the interpretation of experimental results and in the determination of the characteristics of the final product. The ranges of pressure, concentration and temperature are usually large enough to make it necessary to consider material property variations. Usually, the dependence of the properties on temperature T is the most important effect. This leads to nonlinearity in the governing equations and couples the flow with the energy transport. Thus the solution of the equations and the interpretation of experimental results become more involved than for constant property circumstances. Average constant property values at different reference conditions are frequently employed to simplify the solution [25,26]. However, most manufacturing processes require the solution of the full variable-property problem for accurate predictions of the resulting transport.

The variation of dynamic viscosity μ requires special consideration for materials such as plastics, polymers, food materials, several oils and rubber, that are of interest in a variety of manufacturing processes. Most of these materials are non-Newtonian in behavior, implying that the shear stress is not proportional to the shear rate. Thus, the viscosity μ is a function of the shear rate and, therefore, of the velocity field. The viscosity is independent of the shear rate for Newtonian fluids like air and water, but increases or decreases with the shear rate for shear thickening or thinning fluids, respectively. These are viscoinelastic (purely viscous) fluids, which may be time-independent or time-dependent, the shear rate being a function of both the magnitude and the duration of shear in the latter case.

Various models are employed to represent the viscous or rheological behavior of fluids of practical interest. Frequently, the fluid is treated as a Generalized Newtonian Fluid (GNF) with the non-Newtonian viscosity function given in terms of the shear rate which is related to the second invariant of the rate of strain tensor.

For instance, time-independent viscoinelastic fluids without a yield stress are often represented by the power-law model, given by [27]

$$\tau_{yx} = K_c \left| \frac{du}{dy} \right|^{n-1} \frac{du}{dy} \tag{16}$$

where K_c is the consistency index, and n the power law fluid index. Note that $n=1$ represents a Newtonian fluid. For $n<1$, the behavior is pseudoplastic (shear thinning) and for $n>1$, it is dilatant (shear thickening). Then the viscosity variation may be written as [27]

$$\mu = \mu_o \left(\frac{\dot{\gamma}}{\dot{\gamma}_o} \right)^{n-1} e^{-b(T-To)} \tag{17}$$

where

$$\dot{\gamma} = \left[\left(\frac{\partial u}{\partial y} \right)^2 + \left(\frac{\partial w}{\partial y} \right)^2 \right]^{1/2}, \quad \text{with } \tau_{yx} = \mu \frac{\partial u}{\partial y}, \quad \tau_{yz} = \mu \frac{\partial w}{\partial y} \tag{18}$$

for a two-dimensional flow, with u and w varying only with y. Similarly, expressions for other two- and three-dimensional flows may be written. Here $\dot{\gamma}$ is the shear strain rate, the subscript o denotes reference conditions and b is the temperature coefficient of viscosity. For food materials, the viscosity is also a strong function of the moisture concentration c_m. In addition, chemical changes, that typically occur at the microscale level in the material, affect the viscosity and other properties. Other models, besides the power-law model, are also employed to represent different materials [27–29].

Glass is another very important material. It is a supercooled liquid at room temperature. The viscosity varies almost exponentially with temperature. Even a change of a few degrees in temperature in the vicinity of the softening point, T_m, which is around 1600°C for fused silica, can cause substantial changes in viscosity and thus in the flow field and the transport [30]. An equation based on the curve fit of available data for kinematic viscosity ν is written for silica, in S.I. units, as

$$\nu = 4545.45 \exp \left[32 \left(\frac{T_m}{T} - 1 \right) \right] \tag{19}$$

indicating the strong, exponential, variation of ν with temperature. The heat transfer is further complicated by the fact that glass is a participating medium for thermal radiation. The absorption coefficient is a strong function of the wavelength λ and the radiation is absorbed and emitted over the volume of the material. A two-band spectral absorption model has been used extensively for studying the thermal transport in the neck-down region of a furnace-drawn optical fiber [31,32].

There are several other important considerations related to material properties, such as constraints on the temperature level in the material, as well as on the spatial and temporal gradients, for instance in the manufacturing of plastic-insulated wires [33]. Similarly, constraints arise due to thermal stresses in the material and are particularly critical for brittle materials such as glass and ceramics.

Link Between Transport Processes and Material Characteristics. Numerical and experimental investigation can lead to the prediction of the thermal history of the material as it undergoes a given thermal process. Similarly, the pressure, stress, mass transfer, and chemical reactions can be determined. The next and particularly critical step is to determine the changes in the structure or composition of the material as it goes through the system. But this requires a detailed information on material behavior and how structural or chemical changes occur in the material as a consequence of the temperature, pressure and other conditions to which it is subjected.

Nano, Micro, and Macro-Scale Coupling. The characteristics and quality of the material being processed are generally determined by the transport processes occurring at the micro or nanometer scale in the material, for instance at the solid-liquid interface in casting, over molecules involved in a chemical reaction in chemical vapor deposition and reactive extrusion, or at sites where defects are formed in an optical fiber. However, engineering aspects are generally concerned with the macroscale, involving practical dimensions, typical physical geometries and appropriate boundaries. It is crucial to link the two approaches so that the appropriate boundary conditions for a desired micro or nanostructure can be imposed in a physically realistic system. A considerable interest exists today in this aspect of materials processing. For instance, interest lies in understanding microscopic phenomena associated with solidification and intense current research work has been directed at this problem. The solidification front can be divided into various morphological forms such as planar, cellular and dendritic. Various models have been proposed and studied [34].

Similarly, detailed experimental work on the chemical conversion of starches has been carried out [18]. The order of the reaction m in Eq. (12) has been shown to be zero for starches and the rate of the reaction K given as a combination of thermal (T) and shear (S) driven conversion as

$$K = K_T + K_S \tag{20}$$

where

$$K_T = K_{To} \exp(-E_T/RT) \quad K_S = K_{So} \exp(-E_S/\tau\eta) \tag{21}$$

Here, τ is the shear stress, and η is a constant, which is obtained experimentally for the material, along with other constants in the equation. A simple approximation may be applied to model the degree of conversion defined in Eq. (13), as given by [35]

$$w \frac{d\tilde{X}}{dz} = K \tag{22}$$

Here, w is the velocity in the down-channel direction z in an extruder. Thus, numerical results on conversion in the channel are obtained by integrating this equation.

Another area in which the changes at the molecular level are considered is that of generation of defects in optical fiber drawing. The differential equation for the time dependence of the E' defect concentration was formulated by Hanafusa et al. [36] based on the theory of the thermodynamics of lattice vacancies in crystals. It was assumed that the E' defects are generated through breaking of the Si-O band, and, at the same time, some of the defects recombine to form Si-O again. If the concentration and activation energy of the E' defects are represented by n_d and E_d, and those of the precursors by n_p and E_p, the differential equation is given by

$$\frac{dn_d}{dt} = n_p \nu^* \exp \left(-\frac{E_p}{\tilde{k}T} \right) - n_d \nu^* \exp \left(-\frac{E_d}{\tilde{k}T} \right) \tag{23}$$

where, ν^* is the frequency factor for this reaction, and $\tilde{k}$ the Boltzmann constant. The first term on the right hand side of this equation expresses the generation of the defects while the second term expresses the recombination. Thus the distribution of these defects in the fiber may be calculated [37].

Inverse Problems. Material behavior can often be employed to determine the thermal cycle that a given material must undergo in order to achieve desired characteristics. Metallurgical considerations for steel, for instance, indicate the thermal process needed for annealing, which is an important process employed for relieving the stresses in the material and restoring the ductility. The thermal processing involves heating of the material to the annealing temperature of around 723°C for common sheet steel, maintaining the temperature at this value for a given time, known as

soaking period, so that this temperature level is attained everywhere in the material and the internal stresses are relieved, initial slow cooling to allow the microstructure to settle down, and final rapid cooling to reduce total time [38].

Since our interest lies in determining the conditions that would yield the desired temperature variation in the material, this is an inverse problem. Analysis only yields the outputs on system behavior for given inputs, rather than solve the inverse problem of yielding the inputs needed for a desired behavior. This latter problem is fairly difficult and has to be solved in order to select the design variables. The solution is not unique and efforts have to be made to narrow the domain over which design parameters and operating conditions are to be chosen. Iteration is generally necessary to obtain a satisfactory design. Optimization strategies may be used to obtain an essentially unique solution [39].

Solution Techniques and Simulation

Analytical. Due to the complexity of the governing equations and the boundary conditions, analytical methods can be used in very few practical circumstances and numerical approaches are generally needed to obtain the solution. However, analytical solutions are very valuable since they provide results that can be used for validating the numerical model, physical insight into the basic mechanisms and expected trends, and results for limiting or asymptotic conditions.

Consider, for example, the complex flow in a screw extruder, as shown in Fig. 1(d). This flow can be simplified and transformed to a shear and pressure driven flow in a channel, as discussed earlier and as shown in Fig. 3. If a fully developed flow, for which the velocity field remains unchanged downstream, is assumed, analytical solutions can be obtained for Newtonian fluids. If the pressure gradient is zero, the velocity profile is linear and the dimensionless flow rate, or throughput, q_v, which is the flow rate divided by the product of wall speed and cross-sectional area, is simply 0.5. For a favorable pressure gradient, i.e., pressure decreasing downstream, the throughput exceeds 0.5 and for an adverse pressure gradient it is smaller than 0.5. Similarly, for fully developed flow in a die, the relationship between the pressure drop Δp, across a cylindrical region of length L and radius R, and the mass flow rate $\dot{m}$ was obtained by Kwon et al. [40] for a power-law non-Newtonian fluid as

$$\Delta p = \frac{2L}{R} \hat{C}(T) \left[\frac{3n+1}{4n} \frac{4\dot{m}}{\rho \pi R^3} \right]^n \tag{24}$$

where $\mu = \hat{C}(T)(\dot{\gamma})^{1-n}$ and $\hat{C}(T)$ is a temperature dependent coefficient. This expression can be used for several common dies and it also applies for relatively long cylindrical regions in practical dies [41].

Numerical. The numerical solution of the governing equations is based on the extensive literature on computational heat transfer [11,42], with the most commonly employed technique being the SIMPLER algorithm, given by Patankar [43], and the several variations of this approach. This method employs the finite volume formulation with a staggered grid and solves for the primitive variables, such as velocity, pressure, concentration and temperature. For two-dimensional and axisymmetric problems, the governing equations are often cast in terms of the vorticity and streamfunction by eliminating the pressure from the two components of the momentum equation and by defining a streamfunction to take care of the continuity equation [11]. This reduces the number of equations by one and eliminates pressure as a variable, though it can be calculated after the solution is obtained. This approach is generally advantageous, as compared to the primitive variable approach, for two-dimensional and axisymmetric flows. The latter approach is more appropriate for three-dimensional circumstances.

In materials processing, both transient and steady-state solutions are of interest, depending on the process under consideration. In the former case, time marching is used with convergence at each time step to obtain the time-dependent variation of the transport. For steady problems also, time marching may be used to obtain steady-state results at large time. The problem can also be solved by iteration or by using false transients, with large time steps. Though central differences are desirable for all the approximations, numerical instability with the convection terms is often avoided by the use of upwind, exponential or power-law differencing schemes [43]. Because of the inaccuracy due to false diffusion, second-order upwind differencing and third-order QUICK schemes have become quite popular for discretizing the convection terms [44]. Under-relaxation is generally needed for convergence due to the strong nonlinearities that arise in these equations mainly due to property variations. Finite element and boundary element methods have also been used advantageously to simulate these systems.

Experimental. Experimental work is particularly important in a study of thermal processing of materials. This is needed for enhancing the basic understanding of the underlying transport processes, providing physical insight that can be used in the development of mathematical and numerical models, determining important aspects and variables, providing results for validation of mathematical and numerical models, and yielding quantitative results that can be used to characterize processes and components in the absence of accurate and dependable models. There are many complex transport processes where experimental results are needed to guide the development of the model and also generate quantitative data that can be used as empirical inputs if accurate modeling is not possible. Many important techniques have been developed in recent years on the measurement of flow, temperature and concentration distributions in a given system, and are being used in a variety of materials processing applications.

Typical Results From Numerical Simulation

The numerical results obtained for a few important processes are presented here to illustrate the basic characteristics of thermal processing of materials and some of the relevant considerations. Even though extensive results have been obtained in various studies, only a few typical results are presented.

Polymer Extrusion. This is an important manufacturing process, which has been mentioned earlier and is sketched in Figs. 1(d) and 3. Interest lies in the control and prediction of the heat transfer and flow in order to predict, improve and modify physical and chemical changes undergone by the material as it moves down the extruder channel. Figure 4 shows typical computed velocity and temperature fields in an extruder channel for a single-screw extruder. Large temperature differences arise across the channel height because of the relatively small thermal conductivity of plastics. There is little bulk mixing, due to the high viscosity, which is typically more than a million times that of water at room temperature. Reverse screw elements, sudden changes in the screw configuration and other such sharp changes in the channel are often used to disrupt the well-layered flow and promote mixing. The extruded material temperature rises beyond the imposed barrel temperature due to viscous dissipation. Additional results and trends are presented in several papers [27,28].

The residence time distribution (RTD) is an important consideration in the extrusion process. The residence time is the amount of time spent by a fluid particle in the extruder from the inlet to the die. An excessive residence time can lead to over-processing or degradation. Similarly, a short residence time can result in under-processing. The final product is, therefore, strongly affected by the residence time distribution since structural changes due to thermal processing and chemical reactions are usually time-dependent. The RTD is a function of the flow field and can be numerically simulated by particle tracking. Several results are
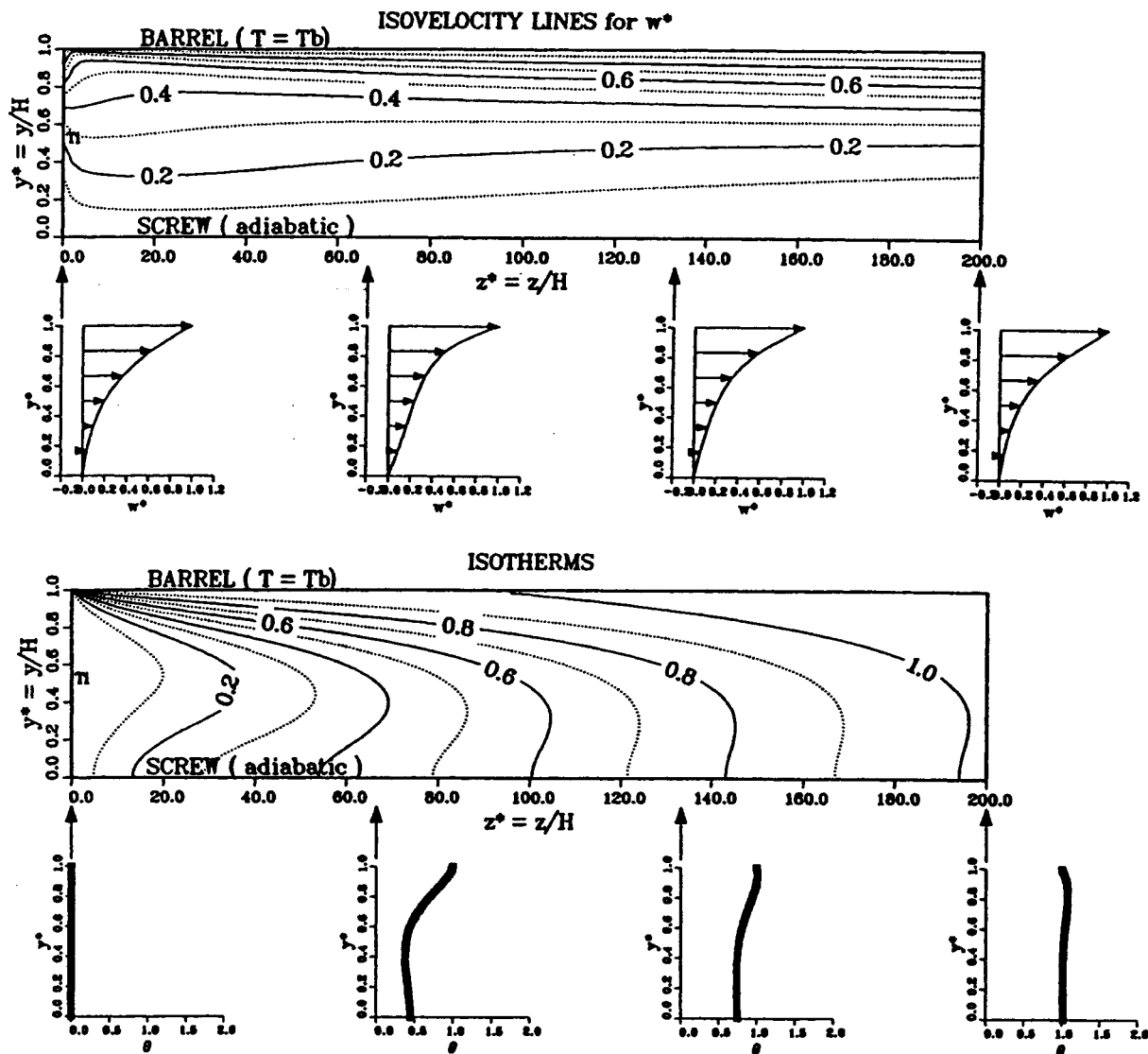
Fig. 4 Calculated velocity and temperature fields in the channel of a single screw extruder at $n=0.5$ and dimensionless throughput $q_v=0.3$, for typical operating conditions

given in the literature on RTD for different extruders [17,28,45]. It is experimentally obtained by releasing a fixed amount of color dye or tracer in the material at the inlet or hopper and measuring the flow rate of the dye material as it emerges from the extruder at the other end.

More recently, the use of twin-screw extruders for the processing of polymeric materials has increased substantially. The main advantages of twin-screw extruders, over single-screw extruders, are better stability, control and mixing characteristics. In twin screw extruders, two screws are positioned adjacent to each other in a barrel casing whose cross section is in a figure of eight pattern, see Fig. 5. Twin-screw extruders are of many types, such as, intermeshing, non-intermeshing, co-rotating, counter-rotating, to name a few.

The flow domain of a twin-screw extruder is a complicated one and the simulation of the entire region is very involved [46]. A major simplification in the numerical simulation is obtained by dividing the flow into two regions: the translation, or T region, and the mixing, or M region, as sketched in Fig. 5. This figure schematically shows sections taken normal to the screw axes of tangential twin screw extruders. Due to geometric similarity, the flow in the translation region is analyzed in a manner identical to that for a single screw extruder. The intermeshing, or mixing,

region is represented by the geometrically complex portion of the extruder between the two screws. A hypothetical boundary is used to numerically separate the two regions [47]. The finite-element method is particularly well suited for the modeling of the complex domain in a twin-screw extruder. Figure 6 shows the finite element mesh used and some typical results on the transport in the mixing or nip region of the extruder. Large gradients arise in pressure, velocity and shear rate in the nip region, resulting in substantial fluid mixing, unlike the small recirculation in single-screw extruders. Similarly, other approximations and results on twin-screw extruders have been presented in the literature [48].

Optical Fiber Drawing. The optical fiber drawing process has become critical for advancements in telecommunications and networking. In this process, as sketched in Fig. 1(a), a cylindrical rod, which is known as a preform and which is specially fabricated to obtain a desired refractive index variation, is heated in a furnace and drawn into a fiber. Its diameter changes substantially, from 2–10 cm to around 125 μm in a distance of only a few centimeters. The radiative transport within the glass, which is a participating medium, is determined using the optically thick medium approximation or improved models such as the zonal method [49]. Interest lies in obtaining high quality optical fibers,
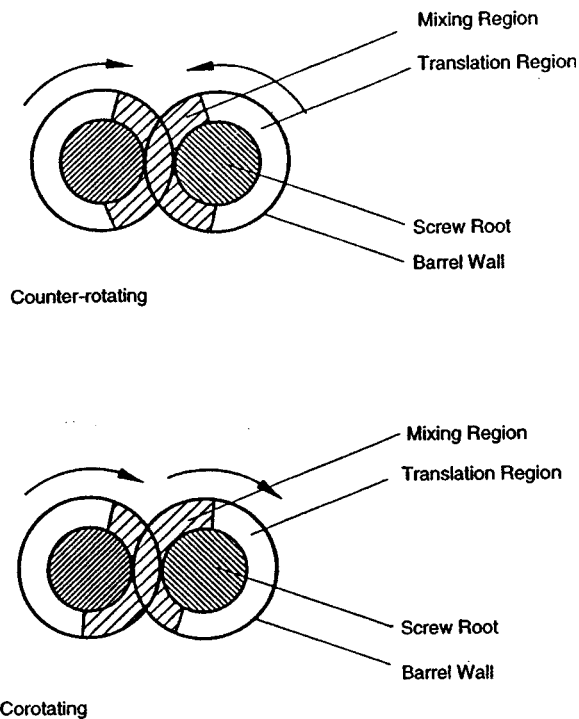
Fig. 5 Schematic diagram of the cross-section of a tangential twin screw extruder, showing the translation (T) and inter-meshing, or mixing (M), regions

as indicated by low concentration of process-induced defects, diameter uniformity, desired refractive index variation, low tension, strength, and other important measures, at high draw speeds.

Typical computed results in the neck-down region, for a specified profile, are shown in Fig. 7 in terms of the streamfunction, vorticity, viscous dissipation and temperature contours. The flow is seen to be smooth and well layered because of the high viscosity. Typical temperature differences of 50–100°C arise across the fiber for preform diameters of around 2.0 cm. Larger temperature differences arise for larger preform diameters [37]. Viscous dissipation, though relatively small, is mainly concentrated near the
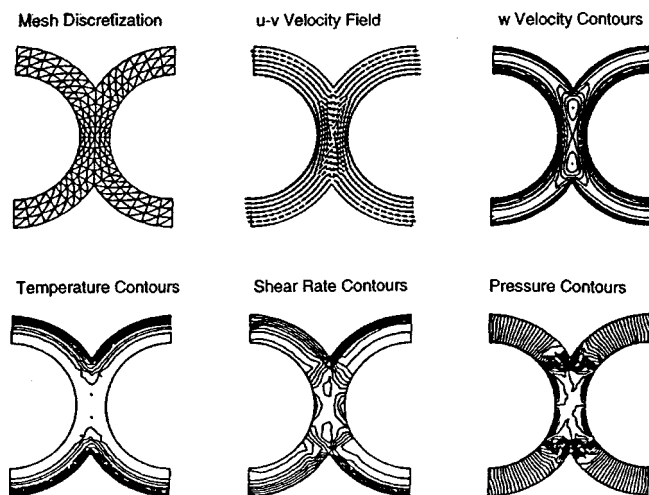
Fig. 6 Mesh discretization for the mixing region in a co-rotating tangential twin screw extruder, along with typical computed results for low density polyethylene (LDPE) at n=0.48, barrel temperature, T_b=320°C, inlet temperature, T_i=220°C, N=60 rpm, q_v=0.3

end of the neck-down, in the small diameter region, and plays an important role in maintaining the temperatures above the softening point [30].

The determination of the neck-down profile of the glass preform as it is drawn into a fiber is a particularly difficult problem. Relatively simple models had been employed in the past to study the flow in this region [50]. More recently, a combined analytical and numerical approach, based on the transport processes and the surface force balance, was developed for the calculation of the neck-down profile [21]. Axisymmetric, laminar flows were assumed in the glass and in the circulating inert gases. A correction scheme was obtained for the neck-down profile using the radially lumped axial velocity, the normal force balance and the vertical momentum equations. The profile was then determined numerically by iterating from an initial profile and using this scheme for correcting the profile at intermediate steps, finally yielding a converged profile.

A typical example of the numerical generation of neck-down profile with a cosinusoidal starting profile is shown in Fig. 8(a). It is seen that, for the first few iterations, the neck-down profile is quite unrealistic, with a flat region and an abrupt change in radius near the end of neck down. But after a few iterations, the shape becomes quite smooth and monotonically decreasing, eventually reaching a steady, converged, profile, as indicated by the invariance of the profile with further iterations. For convergent cases, perturbations to the initial profile and different starting shapes lead to the converged neck-down profile, as seen in Fig. 8(b), indicating the robustness of the numerical scheme and the stability of the drawing process. The force balance conditions were also closely satisfied if convergence was achieved. However, convergence does not occur in every case, leading to infeasible drawing conditions, as discussed later. It was found that viscous and gravitational forces are the dominant mechanisms in the determination of the profile. Surface tension effects are small. The external shear and inertial effects are small, as expected. Later papers obtained the profile at higher draw speeds and for larger preform diameters [37,51].

There are several other processes involved in a typical optical fiber manufacturing process, as shown in Fig. 1(a). The fiber is cooled as it moves away from the furnace and is then coated with a jacketing material for protection against abrasion, to reduce stress induced microbending losses, and for increased strength. The temperature of the fiber entering the coating section is limited by the properties of the coating material used, being around 150°C for commonly used curable acrylates. The wet coating is then cured by ultra-violet radiation as it passes through the curing station [52–55].

Casting. Casting is an important manufacturing process, which involves solidification and melting [15]. The buoyancy-driven flow due to temperature and concentration differences in the liquid or melt region is coupled with the conduction in the solid. For casting in an enclosed region, the interface between the liquid and the solid moves away from the cooled walls for solidification till the entire material is solidified. However, the time-dependent location of this interface is not known and must be obtained from the solution. A coordinate transformation, such as the Landau transformation, may be employed to simplify the computational domains [12,14]. In continuous casting and crystal growing, as shown in Fig. 1(c), the interface between the solid and the liquid is essentially stationary, but it is not known a priori and an iterative procedure may be adopted to determine its shape and location. Transformations and body fitted coordinates may be employed to approximate the irregular shaped computational domains. If the enthalpy model is employed, the entire region is treated as one, considerably simplifying the computational procedure [14,56]. From an engineering standpoint, interest lies in obtaining high quality castings, with few voids and defects, good grain structure and low stresses, at high production rates.

The coupled conduction in the walls of the mold is an important
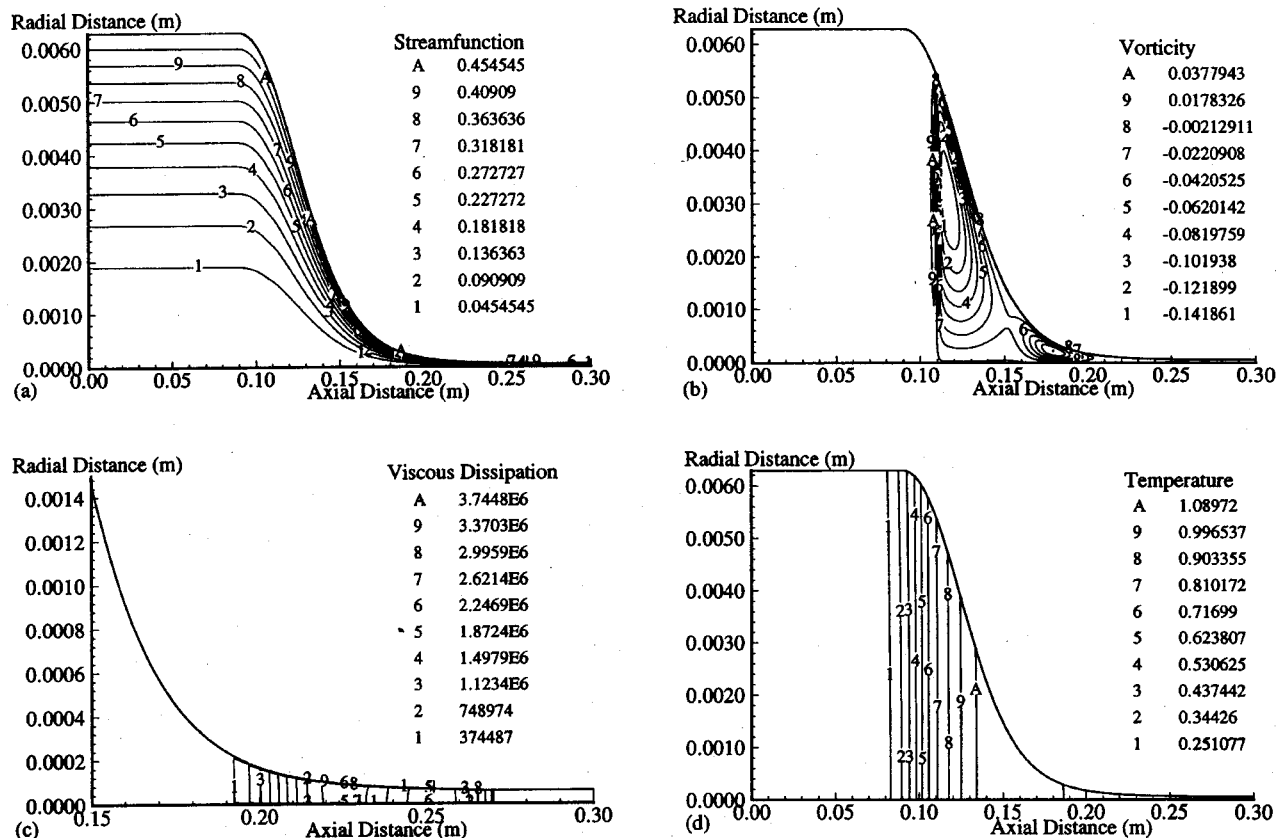
Fig. 7 Calculated (a) streamfunction, (b) vorticity, (c) viscous dissipation, and (d) temperature contours in the optical fiber drawing process for typical drawing conditions

consideration in these problems. The effect of the imposed conditions at the outer surface of the mold on the solidification process can be obtained by solving this conjugate problem, which yields the temperature distribution in the mold as well as that in the solid and the liquid. Banaszek et al. [57] carried out numerical simulations and appropriately designed experiments to demonstrate the importance of conduction in the wall, as shown in Fig. 9. Such numerical and experimental studies can be used to determine the movement of the solidification front with time and thus monitor the generation of voids and other defects in the casting. Experimental studies have been relatively few because of the complexity of the process. Detailed accurate experimental results are needed to critically evaluate the various models employed for simulation as well as to provide information on the characteristics of the interface for the development of microscale models.

Recent work on this problem has led to a much better understanding of the solidification process than before. The buoyancy-induced flow affects the heat and mass transfer processes, which in turn influence the characteristics of the melt-solid interface and the rate of melting/solidification. The transport also affects the quality of the product because of undesirable oscillations, generation of voids, and distribution of impurities. There has been a growing interest in the solidification of mixtures, particularly alloys, and polymers [58].

Continuous Processing. Continuously moving materials undergoing thermal processing are frequently encountered in manufacturing processes like hot rolling, wire drawing and extrusion. If the location of the moving surface is known, the continuous movement of the edge may be replaced by discrete steps and the numerical modeling carried out until results are obtained over a specified time or until the steady-state circumstance is obtained [22]. The corresponding initial and boundary conditions are obtained as:

$$t=0: \quad L(t)=0 \quad t>0: \quad \text{at } x=0, \quad T=T_o;$$

$$\text{at } x=L(t), \quad -k\frac{\partial T}{\partial x}=h_L(T-T_a) \tag{25}$$

where h_L is the heat transfer coefficient at the edge of the moving rod. The problem may be solved analytically [24] or numerically, the latter approach being more appropriate for two and three-dimensional problems and for practical circumstances. The length of the rod L increases with time and the temperature at the end decreases. At large time for steady ambient conditions, a steady temperature distribution arises over the rod and the temperature at the moving end reaches the ambient temperature.

In most practical circumstances, conjugate conditions arise at the surface and the convective transport in the fluid must be solved in conjunction with conduction in the moving solid. The region close to the point of emergence of the material usually has large axial gradients and requires the solution of the full equations. However, far downstream, the axial diffusion terms are small and boundary layer approximations may be made. Interest lies in controlling the local processing of the material in order to obtain uniformity, desired product characteristics and high productivity.

Figure 10 shows the typical calculated streamlines for a flat plate moving in a quiescent medium. The ambient fluid is drawn toward the moving surface because of large pressure gradients directed towards the origin. This effect decays downstream and
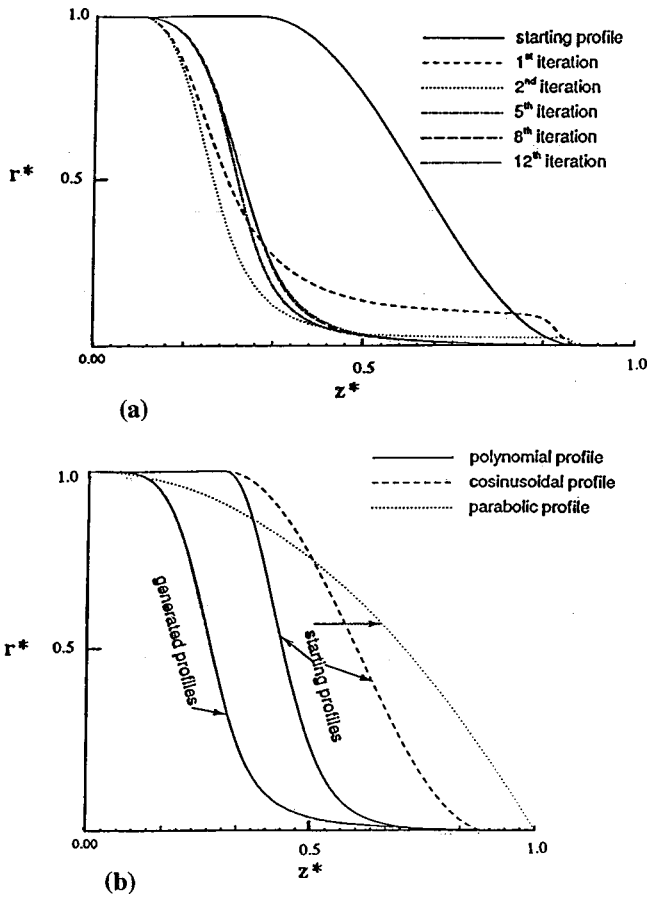
Fig. 8 **(a) Iterative convergence of the neck-down profile in optical fiber drawing; (b) results for different starting profiles. Here, $r^* = r/R$ and $z^* = z/L$, where R is the preform radius, and L the furnace length.**

the flow approaches the characteristics of a boundary-layer flow. The boundary-layer thickness increases in the direction of motion. If buoyancy effects due to the temperature differences are included, the maximum velocity in the flow is larger than the plate speed U_s, for an upward moving heated plate, as shown in the figure. This flow increases the heat transfer from the plate. Similarly, other orientations, the time-dependent flow at the initial stages of the process, and other important aspects have been investigated.

Chemical Vapor Deposition. Chemical vapor deposition involves the deposition of thin films from a gas phase on to a solid substrate by means of a chemical reaction that takes place during the deposition process. The activation energy needed for the chemical reactions is provided by an external heat source, see Fig. 1(b). The products of the reactions form a solid crystalline or an amorphous layer on the substrate. This technique has become quite important in materials processing and is used in a wide range of applications. The quality of the deposited film is characterized in terms of its purity, composition, thickness, adhesion, surface morphology and crystalline structure. The level of quality needed depends on the application, with electronic and optical materials imposing the most stringent demands. Much of the initial effort on this problem was directed at silicon deposition because of its importance in the semiconductor industry. However, recent efforts have been directed at the deposition of materials such as titanium nitride, silicon carbide, diamond, and metals like titanium, tungsten, aluminum, and copper.

Many different types of CVD reactors have been developed and applied for different applications. The quality, uniformity, and rate of deposition are dependent on the heat and mass transfer, and on the chemical reactions that are themselves strongly influenced by temperature and concentration levels [20,59]. The flow, heat transfer and chemical reactions in CVD reactors have been investigated by several researchers [59,60]. Some typical results obtained for silicon deposition are shown in Fig. 11, indicating a

TLC tracers

Temperature field

Evaluated velocity

Calculated velocity and temperature
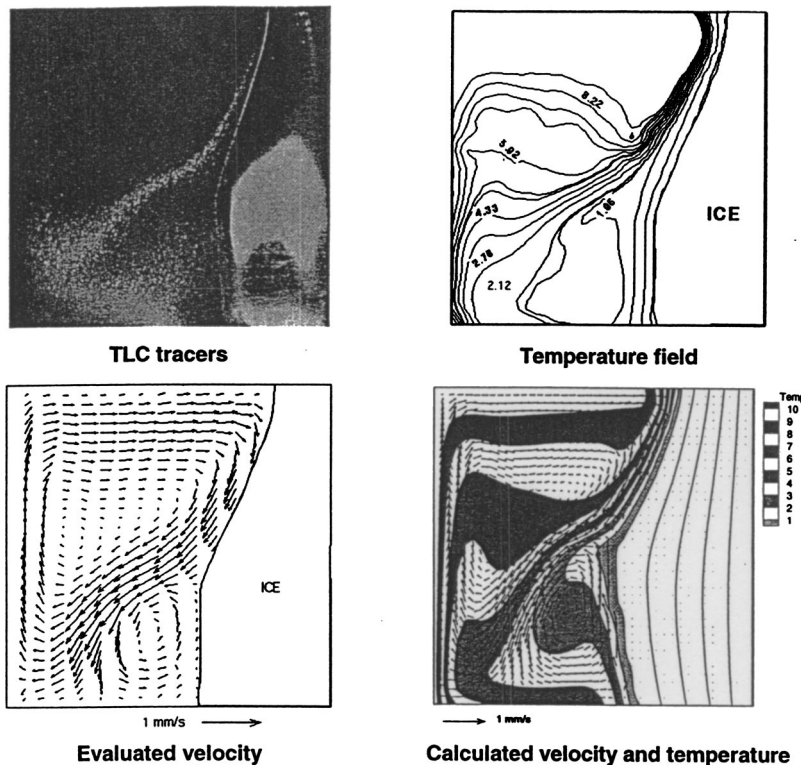
Fig. 9 Experimental and numerical results for water solidification driven by convection and conduction

STREAMLINES

(a)

(b)
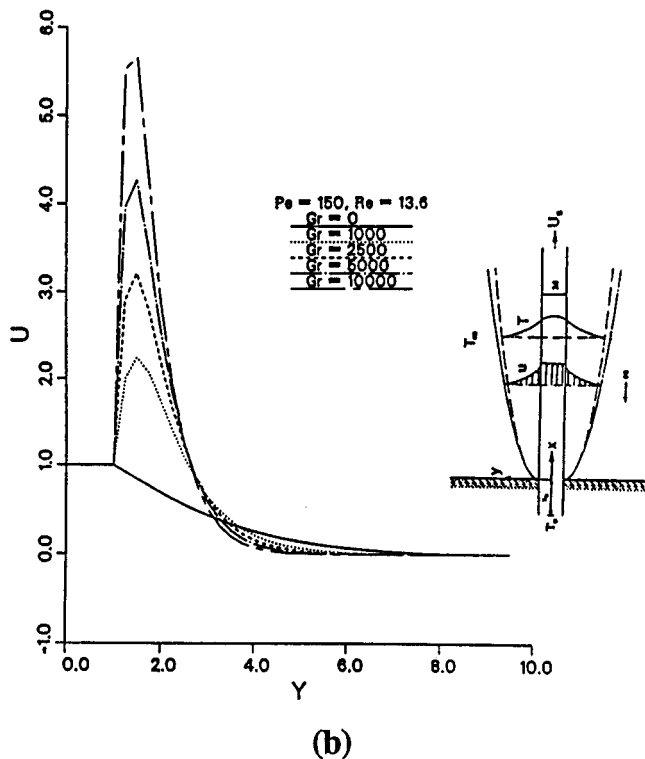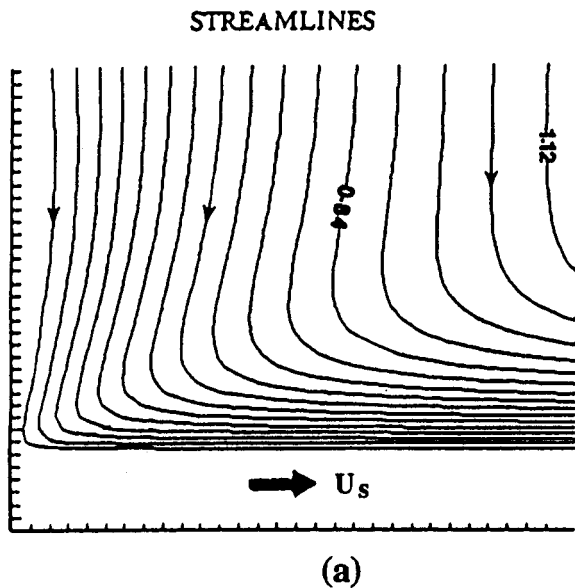
Fig. 10 (a) Flow in the ambient fluid due to a continuously moving material; (b) dimensionless velocity (u/U_s) distribution in the fluid due to a vertically moving heated plate with aiding buoyancy effects

Fig. 11 Comparisons between the numerical results on predicted film growth rate and the experimental data of [61]

comparison between numerical and experimental results from [61]. A fairly good agreement is observed, given the uncertainty with material property data and with the chemical kinetics. The two results from [60] refer to two different values of the diffusion coefficient, the one labeled as the reference case employing the same values as those in [62].

Conjugate transport at the heated surface is also an important consideration, since in actual practice thermal energy is supplied to the susceptor, often at a constant rate, and the temperature distribution at the surface depends on the transport processes that arise. An experimental and numerical study was carried out by

Chiu et al. [63] on the heat transfer in a horizontal channel with a finite heated region to approximate the susceptor. Figure 12 shows the typical results obtained, indicating good agreement between the experimental and numerical results. The characteristics of the flow, ranging from steady laminar to oscillatory and turbulent flow, were investigated and linked to the film uniformity.

Additional Processes.   Only a few thermal processing techniques have been presented in the preceding section. There are many other processes in which the thermal transport is of crucial importance and which have been of particular interest in recent years. Among these are crystal growing, microgravity materials processing and thermal sprays. The Czochralski method, shown in Fig. 1(c), has dominated the production of single crystals for microelectronics and has been the subject of considerable research interest over more than three decades [64,65]. Other crystal growth techniques, including Bridgman crystal growing in which the furnace has an upper zone at temperature above the melting point and a lower zone at temperature below the melting point, have also been investigated [64]. Microgravity conditions are obtained, for instance, in laboratories orbiting in space, where the processing of materials can be carried out with reduced effects of the terrestrial gravitational field. Gravity determines the buoyancy-driven flows in the melt of a crystal growing system and thus affects the quality and characteristics of the crystal. Thus, by controlling the gravitational force, the resulting transport processes and the final product can be improved [66]. Thermal sprays may be used for the manufacture of near-net shape structured materials. Sprays containing droplets of the desired deposition material are directed at a specified substrate and the material is deposited by rapid solidification. Due to the elimination of several traditional processing steps, the process is fast and rapid solidification eliminates macrosegregation, which weakens traditionally cast materials [67–69]. Superior properties, associated with fine-grained microstructures and non-equilibrium phases, are usually obtained.

Validation

A very important consideration in modeling and simulation is that of validation of the models. This is particularly critical in thermal materials processing because of lack of accurate material property data, combined mechanisms and other complexities in the process. Validation of the models is based on a consideration of the physical behavior of the results obtained, elimination of the effect of arbitrary parameters like grid and time step, and com-
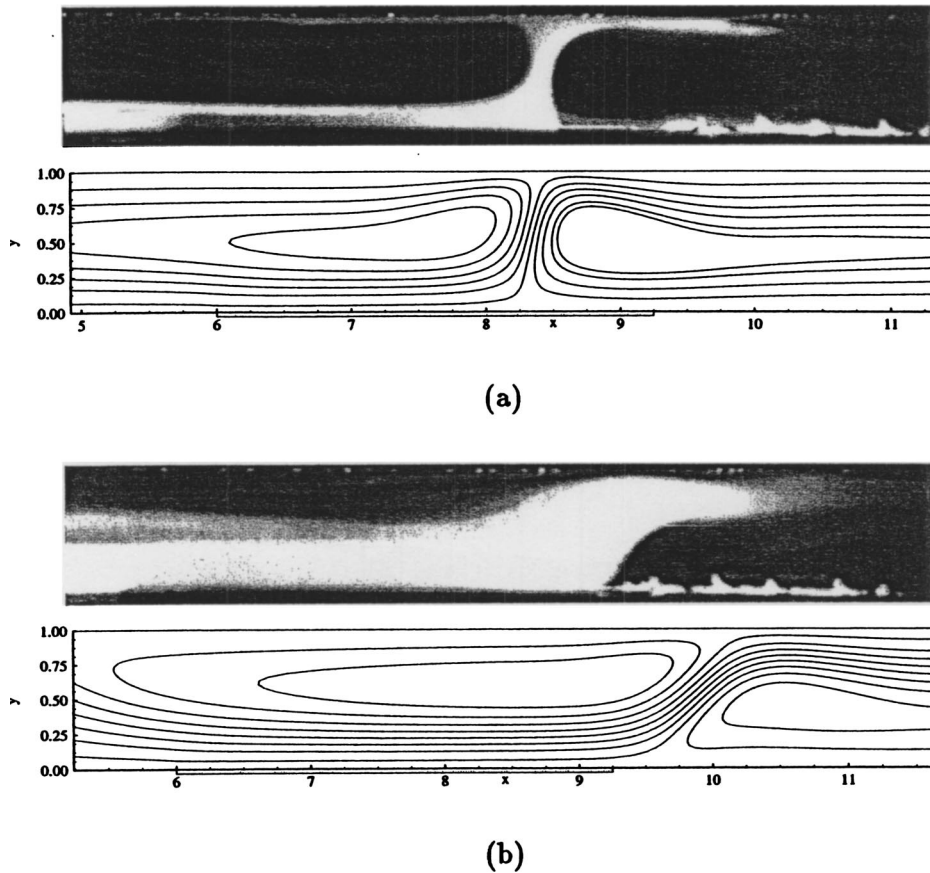
Fig. 12 Comparison between experimental observations and numerical predictions of streamlines at Re=9.48 and Re=29.7 for a ceramic susceptor

parisons with available analytical results for simpler configurations, with numerical results in the literature, and with experimental results on the process and on a prototype, if available [70,71]. A few examples are given here.

Polymer Extrusion. Measurements on the temperature and velocity distributions in an extruder channel are very complicated because of the complex domain, rotating screw and generally opaque nature of the typical materials. However, the overall characteristics of the extrusion process, in terms of pressure and temperature at the die, residence time distribution, total heat input, characteristics of the extrudate, total torque exerted on the screw, and flow rate, are available in the literature [16,27]. These can be used to validate the main predictions of the models for the polymer extrusion process. However, detailed temperature, velocity and pressure distributions are needed to determine the accuracy, validity and predictability of the local behavior. Esseghir and Sernas [72] have carried out innovative and well-designed experiments on single-screw extruders, using a cam-driven thermocouple which allowed the probe to travel in and out of the channel in a synchronized motion linked to the screw rotation.

A few experimental results for Viscasil-300M, which is a non-Newtonian fluid, are shown in Fig. 13, along with numerical results from two-dimensional finite volume and three-dimensional finite element calculations [29,73]. The effect of fluid recirculation in the screw channel is seen as the temperature near the screw root being closer to the barrel temperature, than that predicted by the two-dimensional model which does not consider this recirculation. A three-dimensional model is thus needed to simulate this recirculation and the results are seen to be close to the experimental data. Similarly, an experimental study was carried out to investigate the characteristics of the flow and the basic features of the

mixing process in the intermeshing, or mixing, region [74]. Experimentally and numerically obtained streamlines in the region between two rotating cylinders, approximating a twinscrew, were obtained and a good agreement between the two was observed.

Measurement of the velocity distribution in the channel is also very involved because of the complex geometry and rotating screws. Bakalis and Karwe [75] have carried out velocity measurements for heavy corn syrup, which is transparent. Employing a plexiglas window, a two-component Laser Doppler Anemometer (LDA) in the backscatter mode was used to measure the local velocities in the extruder, as shown in Fig. 14(a). The complicated, three-dimensional, flow field was studied and a comparison of the tangential velocity distribution in the translation region with the numerical predictions is shown in Fig. 14(b). A fairly good agreement is observed, lending support to the model. Similarly, different velocity components were measured in the intermeshing region and compared with numerical predictions, yielding good agreement.

Optical Fiber Drawing. Very little experimental work has been done on the thermal transport in the optical fiber drawing process because of the high temperatures encountered, high draw speeds, complex geometry, and difficult accessibility into the furnace [39,50]. Paek and Runk [76] experimentally determined the neck-down profile. Using the heat transfer coefficient values given by them and an appropriate parabolic furnace temperature distribution to obtain the experimental conditions, the neck-down profile was calculated in [21] and compared with the experimental results, as shown in Fig. 15(a). The analytical results obtained by Paek et al. [77] showed that the draw tension plotted on a
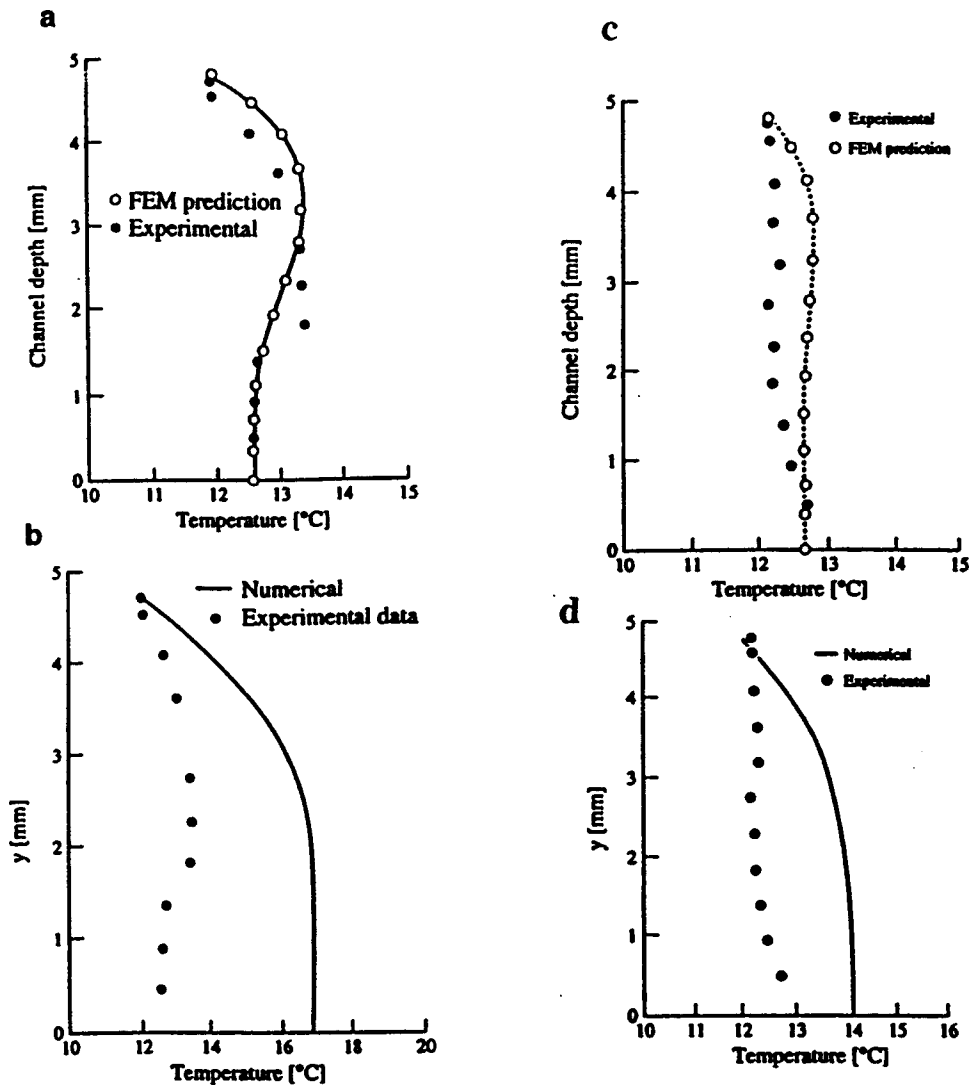
Fig. 13 Comparisons between numerical and experimental results on temperature profiles for Viscasil-300M, with (a) and (c) from the three-dimensional (FEM) model and (b) and (d) from the two-dimensional (FDM) model. For (a) and (b): T_i=20.3°C, T_b=12.2°C, N=20. For (c) and (d): T_i=18.8°C, T_b=22.3°C, N=35.

logarithmic scale varies linearly with the inverse of the furnace temperature. A comparison between the computed results and the experimental data show good agreement, as seen in Fig. 15(b).

Casting. Some numerical and experimental results were shown earlier for solidification of water, indicating good qualitative agreement. A benchmark problem, in which melting in a rectangular enclosed region is initiated by step changes in the temperatures at the left and right boundaries, the left being held at a temperature higher than the melting point and the right at a temperature lower than the melting point, has been used for validating the models. Figure 16 shows the experimental results and corresponding numerical predictions on the liquid-solid interface location, for melting of pure tin, using the enthalpy model [78,79]. Though these results are found to agree quite well, further detailed comparisons are needed to improve existing models.

System Simulation

In the preceding sections, we have discussed modeling and simulation of various processes and components that are of interest in the thermal processing of materials. However, there is another very important aspect that must be considered and that relates to the numerical simulation of the overall thermal system, which usually consists of several components, since the process undergone by the material results from the energy exchange with the various components of the system [1].

Consider, for instance, a typical electrical furnace, which consists of the heater, walls, insulation, enclosed gases and the material undergoing heat treatment. The transport mechanisms in all these components are coupled through the boundary conditions. Thus, the heater exchanges thermal energy with the walls, the gases and the material. Similarly, the material undergoing heat treatment is in energy exchange with the heater, the walls and the gases. The gas flow is driven by an externally imposed pressure difference, such as that due to a fan, by moving materials in continuous processing, and by buoyancy. Each individual component may first be mathematically modeled and numerically simulated as uncoupled from the others, by employing prescribed boundary conditions. Then, these individual simulations can be combined, employing the appropriate coupling through the boundary conditions. This procedure provides a systematic approach to the numerical simulation of the system, which may be a simple one or a complicated practical one [38]. Once the simulation of the system is achieved, with satisfactory experimental validation, the design and optimization of the process as well as of the system may be undertaken.
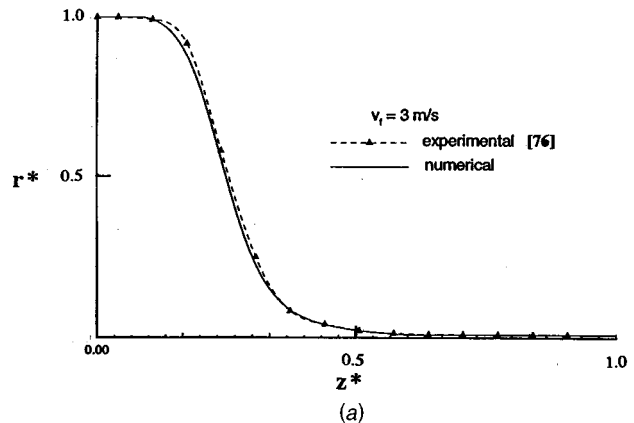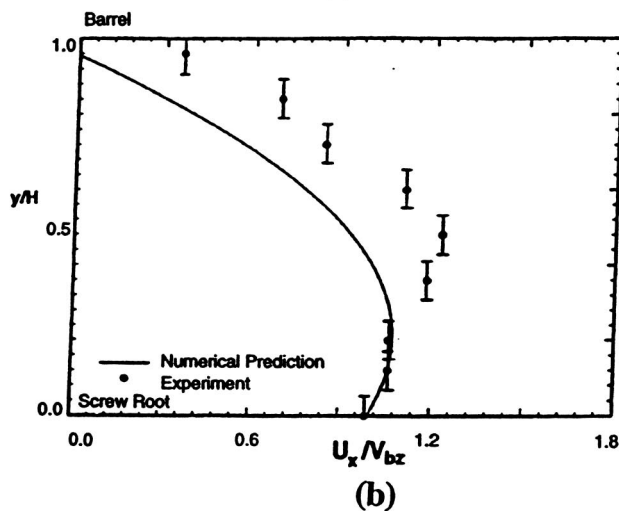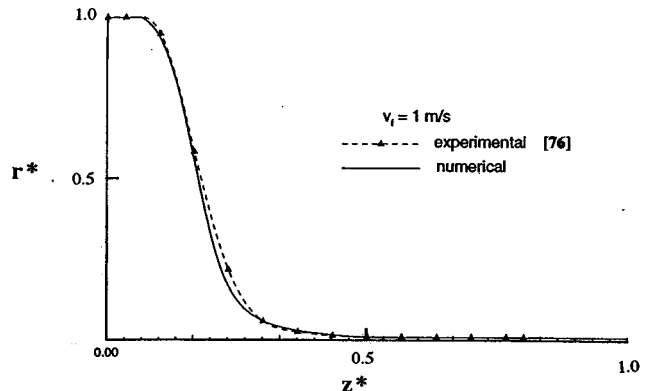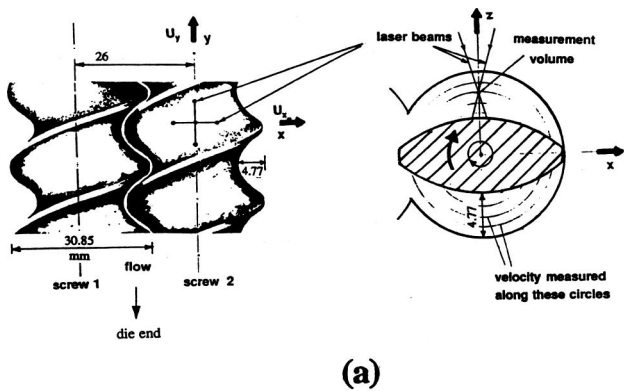
Fig. 14 (a) Experimental arrangement for velocity measurements in the flow of corn syrup in a twin-screw extruder; (b) comparison between calculated and measured tangential velocity U_x profiles for isothermal heavy corn syrup at 26.5°C, with mass flow rate of 6 kg/hr and screw speed of 30 rpm

Process Feasibility

An important consideration in the design of a system for materials processing is the feasibility of the process, since there is usually a fairly narrow domain of operating conditions in which the process is possible. Numerical simulation can play a significant role on this aspect since it can guide the selection of operating conditions and design parameters that can lead to successful thermal processing. A few studies in polymer extrusion and optical fiber drawing are discussed here as examples.

Polymer Extrusion. The feasibility of the process is determined largely by the flow and the pressure and temperature rise in the extruder. Using the modeling discussed earlier, the feasible domain for a self-wiping co-rotating twin-screw extruder is determined for the extrusion of Amioca, which is pure starch, as shown in Fig. 17. An upper limit is obtained for the mass flow rate. Beyond this limit, though the numerical scheme converges, the results are not physical acceptable. In actual practice, for a given screw rotational speed, each turn of the screw can move a specific maximum volume of material. Then the given mass flow rate can not exceed this limit given by the shear-driven flow. For higher mass flow rates, it is necessary to impose a favorable pressure gradient to push the material down the channel. Therefore, a negative pressure gradient along the axial direction will occur in the channel and that is not physically acceptable for an extruder [80]. For a specific screw speed, the simulation code also diverges for mass flow rates lower than the critical points shown in the figure because of flow instability and excessive pressures, temperatures
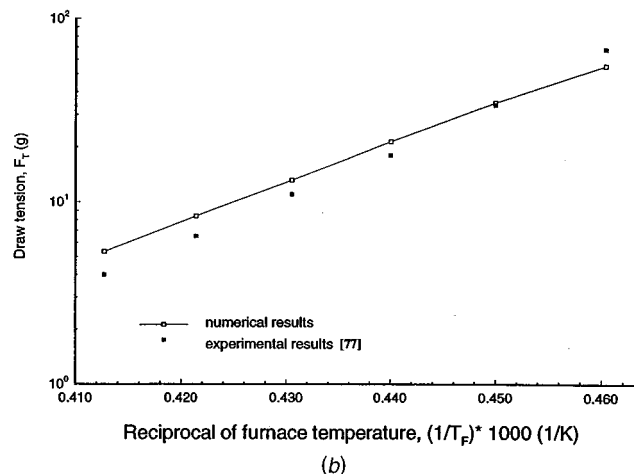
Fig. 15 Comparison of the numerical predictions of (a) the neck-down profile and (b) the draw tension with experimental results from [76,77]

and residence times. These results and trends show good agreement with the observations on practical systems that also yield a domain in which a stable reactive extrusion process can be created [81].

Optical Fiber Drawing. Using the mathematical and numerical models discussed earlier for optical fiber drawing, it has been shown that, for given fiber and preform diameters and for a given draw speed, it is not possible to draw the fiber at any arbitrary furnace wall temperature distribution [21,82,83]. If the furnace temperature is not high enough, it is found that the fiber breaks due to lack of material flow, a phenomenon that is known as viscous rupture [84]. This is first indicated by the divergence of
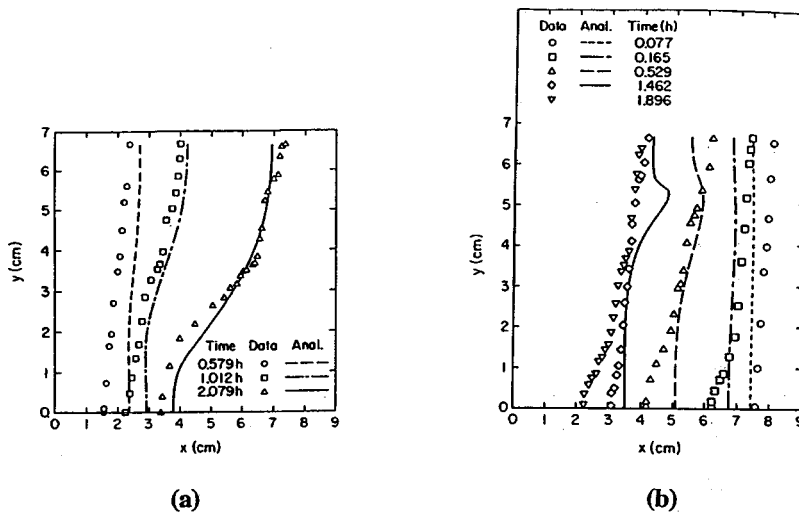
Fig. 16 Comparison between measured and predicted interface locations during (a) melting, and (b) solidification of pure tin from a vertical surface [78,79]

the numerical correction scheme for the profile and is then confirmed by excessive tension in the fiber. Similarly, it is determined that, for a given furnace temperature, there is a limit on the speed beyond which drawing is not possible, as this leads to rupture. Thus, as shown in Fig. 18(a), a region in which drawing is feasible can be identified. Beyond the boundaries of this region,

Fig. 17 Feasible domain for twin-screw extrusion of starch

drawing is not possible. For the domain in which the drawing process is feasible, the draw tension is calculated. The "isotension" contours are shown in Fig. 18(b). As expected, the draw tension is small at higher temperatures and lower speeds, which explains the positive slope of the iso-tension contours.

Similarly, different combinations of other physical and process variables, such as the inert gas flow velocity, furnace wall temperature distribution, furnace length and diameter, and preform and fiber diameters, may be considered to determine the feasibility of the process. Figure 18(c) shows the results when the furnace length and temperature are considered as the two main parameters. Again, the feasibility of the process is largely determined by viscous rupture, which is a direct result of high draw tension. It is seen that either a higher draw temperature or a longer residence time in the furnace, as regulated by its length, is needed to make fiber drawing possible at higher draw speeds. Using such results, the parameters in a fiber drawing system can be chosen to draw a fiber of desired diameter.

Additional Engineering Aspects

Several important considerations in the design and operation of practical thermal materials processing systems were discussed in the preceding sections. These included issues like rate of fabrication, quality of the product, and feasibility of the process. However, there are obviously many other aspects that need to be considered in the design and optimization of the system and for the selection of the operating conditions. Some of these are outlined here.

An important consideration in polymer extrusion is the mixing inside the screw channel since it determines the homogeneity of the processed material. The downstream motion of material particles may be considered for a better understanding of the mixing process. Similarly, the distributive mixing inside the channel may be considered in terms of mixing between two different types of materials, with each initially occupying one half of the channel. Several other measures of mixing have been considered in the literature. Substantial work has also been done on mixing in twin-screw extruders, including the use of chaos introduced by changes in the geometry and the boundary conditions [85]. Similarly, melting and solidification of the material, leakage across screw flights, instability in the flow, unfilled screw channels, and conjugate transport due to conduction in the barrel are other important engineering issues in polymer extrusion. Transient effects are also important, both for the start-up of the process and for changes in the operating conditions.
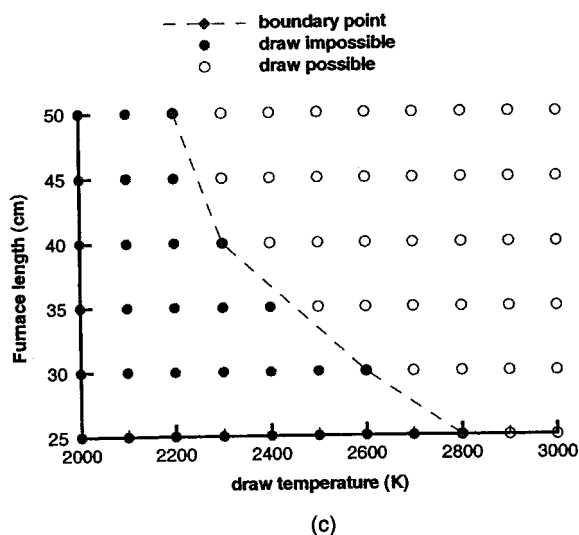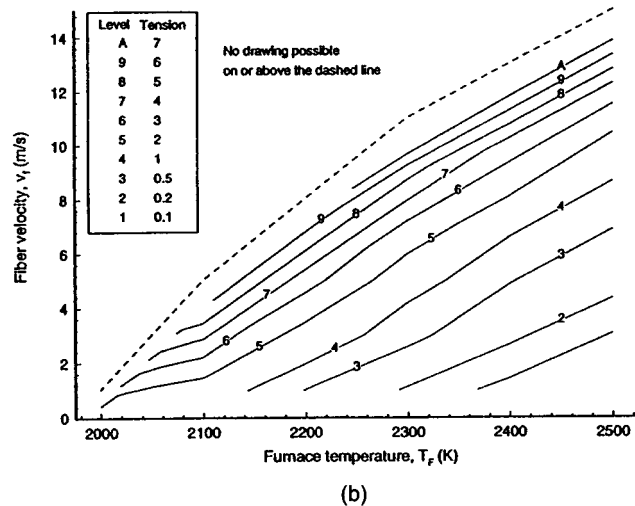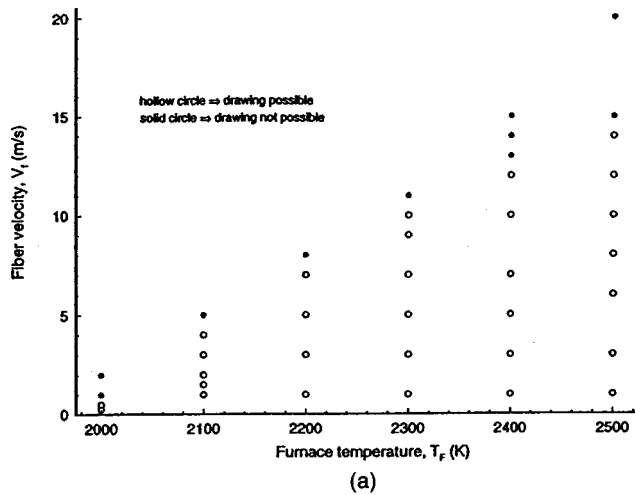
Fig. 18   Results obtained from a feasibility study of the optical fiber drawing process: (a) different cases studied, showing both feasible and infeasible combinations of parameters; (b) "iso-tension" contours for the feasible range of fiber drawing; (c) feasible domain at a draw speed of 15 m/s in terms of furnace length and temperature

Similarly, in other thermal materials processing systems, important aspects that are particularly relevant to the process under consideration arise and must be taken into account by the simulation and experimentation in order to provide the appropriate inputs for system design and optimization. These relate to engineering issues like durability, maintenance, availability of different materials and components, and the convenience and practical range of operating conditions.

Optimization

We have so far largely considered workable or acceptable design of a system. Such a design satisfies the requirements for the given application, without violating any imposed constraints. However, the design would generally not be the best or optimal design, as judged on the basis of cost, performance, efficiency, performance per unit cost, or other such measures, with acceptable environmental effects. The need to optimize is very important in the design of the materials processing systems and has become particularly crucial in the recent times due to growing global competition.

Any optimization process requires the specification of a quantity or function U, known as the objective function and which is to be minimized or maximized. The general mathematical formulation for the optimization of a system may be written as

$$U(x_1, x_2, x_3, \ldots, x_n) \rightarrow U_{\text{opt}} \qquad (26)$$

with,

$$G_i(x_1, x_2, x_3, \ldots, x_n) = 0, \quad \text{for } i = 1,2,3, \ldots, m \qquad (27)$$

and,

$$H_i(x_1, x_2, x_3, \ldots, x_n) \leq \text{or} \geq C_i, \quad \text{for } i = 1,2,3, \ldots, l \quad (28)$$

where x_i represent the design variables and operating conditions, G_i represent equality constraints, and H_i inequality constraints. If the number of equality constraints m is equal to the number of independent variables n, the constraint equations may simply be solved to obtain the variables and there is no optimization problem. If $m > n$, the problem is over constrained and a unique solution is not possible. Some constraints have to be discarded to make $m \leq n$. If $m < n$, an optimization problem is obtained.

For thermal materials processing, the objective function U could be taken as the number of items produced per unit cost, product quality, or the amount of material processed. The constraints are often given on the temperature and pressure due to material limitations. Conservation principles and equipment limitations restrict the flow rates, cutting speed, draw speed, and other variables. The second law of thermodynamics and entropy generation can also be used to optimize systems so that exergy, which is a measure of the availability of energy from a thermal system, can be maximized [86].

Search methods constitute the most important optimization strategy for thermal systems. The underlying idea is to generate a number of designs, which are also called trials or iterations, and to select the best among these. Effort is made to keep the number of trials small, often going to the next iteration only if necessary. The steepest ascent/descent method is an important search method for multivariable optimization and is widely used for a variety of applications including thermal systems. However, it does require the evaluation of gradients in order to determine the appropriate direction of movement, limiting the application of the method to problems where the gradients can be obtained accurately and easily. Several other such gradient-based methods have been developed for optimization and are used for a variety of thermal processes [1,87,88]. Genetic optimization algorithms, that are based on function evaluations instead, have also been developed, though these methods are often less efficient than gradient-based methods.

The objective function is among the most critical and difficult aspects to be decided in the optimization of thermal materials
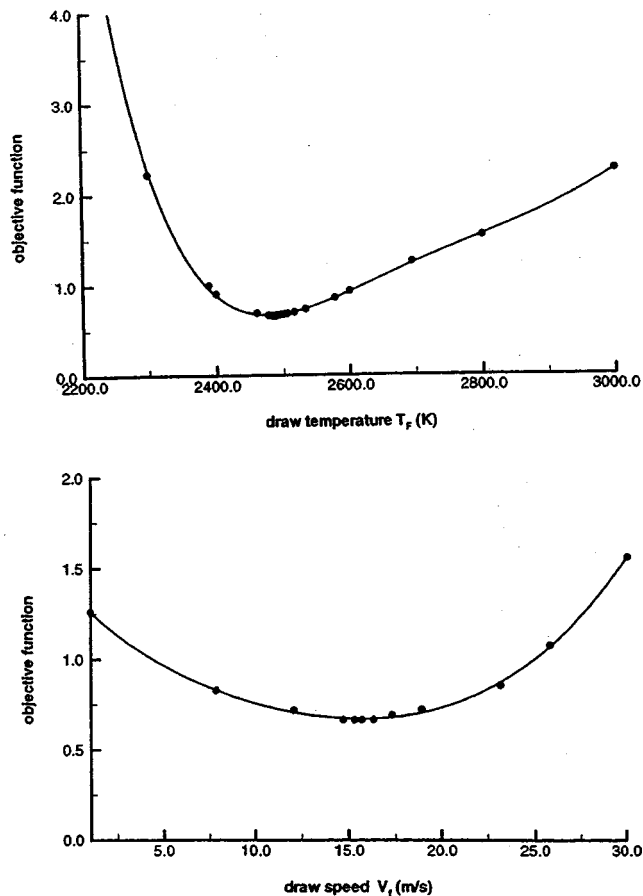
Fig. 19 Evaluation of optimal draw temperature at a draw speed of 15 m/s and the optimal draw speed at a draw temperature of 2489.78 K, obtained in the first part, by using the golden-section search method

processing systems, since the optimal design is a strong function of the chosen criterion for optimization. For illustration, let us consider a CVD system for deposition of TiN. As discussed in detail by Chiu et al. [88], the main qualities of interest include product quality, production rate, and operating cost. These three may be incorporated into one possible objective function U, which is to be minimized and is given by

$$U = \frac{(\text{Product Quality Deficiency}) \times (\text{Operating Cost})}{\text{Production Rate}} \quad (29)$$

Here, the product quality is defined in terms of uniformity of film thickness and other properties which quantify the desired attributes. Since the objective function is minimized, maximum production rate is achieved by placing it in the denominator. The objective function represents equal weighting for each design quality. Obviously, the objective function may assume many possible forms. Using the steepest ascent method, Chiu et al. [89] obtained the optimal design.

A similar study was carried out by Cheng [90] on the optical fiber drawing process, considering the numerical simulation of the draw furnace. The objective function could again be taken as the general form given by Eq. (29). Because of the complexity of the process and lack of information on operating costs, the effort was directed at the fiber quality, taking the tension, defect concentration and velocity difference across the fiber, all these being scaled to obtain similar ranges of variation, as the main considerations. The objective function U was taken as the square root of the sum of the squares of these three quantities and was minimized. Several search methods, such as golden-section for single variable

and univariate search for mutivariable cases, were employed. Figure 19 shows typical results from golden-section search for the optimal draw temperature and draw speed. The results from the first search are used in the second search, following the univariate search strategy, to obtain optimal design in terms of these two variables. Several other results were obtained on this complicated problem.

Knowledge Base

An important aspect in the design of systems for the thermal processing of materials is the use of the available knowledge base on the process to guide the design and operation of the system. The knowledge base typically includes relevant information on existing systems and processes, current practice, knowledge of an expert in the particular area, material property data, and empirical data on equipment and transport, such as heat transfer correlations. Some effort has been directed in recent years at streamlining the design process and improving the design methodology [91]. The basic concept behind knowledge-based systems is the storage and use of this knowledge to take logical decisions for selection, diagnostics and design [92]. Empirical data, heuristic arguments and rules for making decisions are all part of this knowledge-based methodology. The expert knowledge is obviously specific to a given application and represents the knowledge and experience acquired by the expert over a long period of work in the area of interest.

Knowledge-based design methodology is particularly useful in selecting an initial design for a given system. Two strategies may be used for generating an initial design. The first is based on a library of designs built using information from earlier design efforts and from existing systems. The design closest to the given problem may be selected by comparing the designs in the library with the desired specifications. The second approach uses the knowledge and experience of an expert to generate a design for the given requirements and constraints [93]. Of course, the user can always enter his/her own initial design if the output from the library or the expert rules is not satisfactory.

The knowledge base is also used in the redesign process to evaluate a given design and, if this is not satisfactory, to generate a new design. Expert rules establish the relationship between a design variable and the objective function. Several efficient strategies can be developed for selecting the design variables to go from one design to the next. The selection of design variables for the new design are guided by expert rules as well as by the results of the design process up to the given instant.

This approach may be applied to the casting of a material in an enclosed region. The need for design and optimization of the system arises because of the desire to reduce the solidification time and improve the product quality. A large number of design parameters arise in this problem, such as materials, initial melt pour temperature, cooling fluid and its flow rate, and dimensions. The quality of the casting is determined by grain size, composition, directional strength, concentration of defects, voids, thermal stresses, etc. It is necessary to carry out a thermal analysis of the solidification process, using modeling and simulation, to obtain inputs for design and to evaluate the nature of the casting.

Viswanath [94] and Viswanath and Jaluria [95] considered this problem, using knowledge-based methodolgy for design. Several models are available for the study of solidification, such as

1. *Steady conduction in solid model*: Melt is taken at freezing temperature, mold at fixed temperature and steady conduction in the solid is assumed.
2. *Chvorinov model*: Entire thermal resistance is assumed to be due to the mold
3. *Lumped mold model*: Temperature in the mold is assumed to be uniform and time-dependent, melt is taken at freezing temperature and steady conduction in the solid is assumed.
4. *One-dimensional conduction model*: Transient 1D temperature distributions are assumed in the mold, solid and melt.
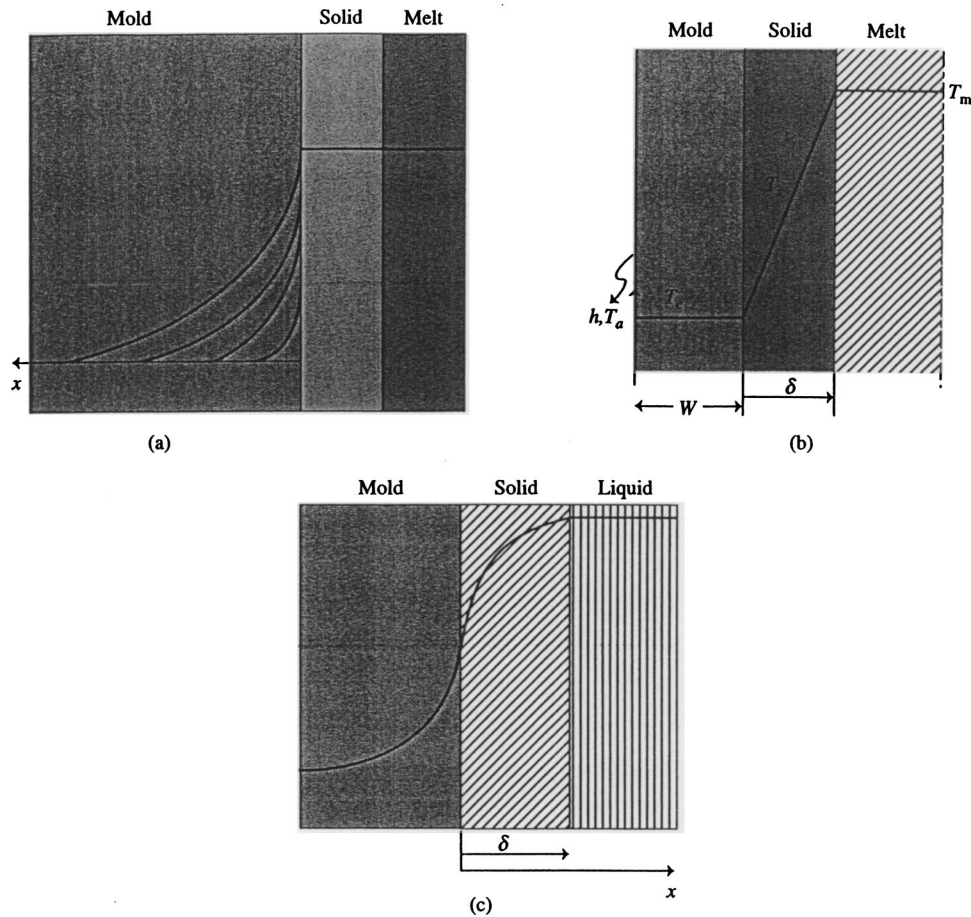
Fig. 20 Different mathematical models for ingot casting: (a) Chvorinov model; (b) lumped mold model; and (c) semi-infinite model

5. *Two and three-dimensional models*: Natural convection flow in the melt is included.
6. *More sophisticated models*: Needed for alloys, generation of voids, complicated geometries, etc.

Three models among these are sketched in Fig. 20. Each model has its own level of accuracy and validity. Different models may be chosen, depending on the application and materials involved. Expert knowledge plays a major role here. For instance, if an insulating material such as ceramic or sand is used for the mold,

Fig. 21 Results for design of an ingot casting system, showing solid-liquid interface movement with time and switching to a more complex model after many design trials

the Chvorinov model may yield good results since most of the thermal resistance is in the mold. One-dimensional models are adequate for solidification near the boundaries. Sophisticated models are needed for alloy solidification and for considering the microstructure in the casting.

The optimal design may be obtained with solidification time being chosen as the objective function and employing constraints from the expert knowledge to avoid unacceptable thermal stresses and defects in the casting. We may start with the simplest model and keep on moving to models with greater complexity till the results remain essentially unchanged from one model to the next. Thus, models may be automatically selected using decision-making based on accuracy considerations. In a typical design session, the cooling parameters are first varied to reduce the solidification time. If the solidification time does not reach the desired value, the pour temperature of the melt may be varied. If even this does not satisfy the requirements, the thickness of the mold wall may be changed. The material of the wall may also be varied, if needed. Thus, by first varying the operating conditions and then the dimensions and materials, the solidification time may be minimized or brought below a desired value. Figure 21 show some a typical run for the design of the given system, indicating model change as the design proceeds. Each successful design may be stored for help in future designs.

Conclusions and Future Research Needs

This paper presents a review of the current status of the important field of thermal processing of materials. It focuses on the link between basic research on the underlying transport mechanisms and the engineering aspects associated with the process and the

system. Several important processing techniques, such as optical fiber drawing, polymer extrusion and chemical vapor deposition, are discussed in particular detail to bring out the basic and applied issues in materials processing. These include modeling, validation, system simulation, process feasibility, and the design and optimization of the system. Important solution techniques, typical results in thermal materials processing and the implications for practical systems are discussed.

Our understanding of thermal processing of materials has grown significantly over the last three decades. Many new and improved techniques have been developed, along with new materials, new processing systems and better control on product quality and production costs. However, there are still many areas that need detailed further work. Among the most important ones are material properties and characteristics, experimental results, and coupling of micro or nano-scales, where materials processing occurs, and the macro-scale of interest in engineering. The measurement and availability of accurate material properties are crucial to a study in this area. Also, experimental results are strongly needed for validation of models and for providing inputs and insight for future model development.

In addition, work is needed on several other topics. Some of the main ones are transport in complex materials such as powders, particulates, and granules, characteristics of free surfaces and interfaces, accurate numerical modeling of combined mechanisms, multiple domains, and multiphase transport, and system instability. Experimental techniques are needed for practical materials which are often opaque and for measurements under high temperature and pressure. Similarly, numerical techniques are needed for large material property changes and for coupling the transport equations with the chemical kinetics which may involve several different reactions, with different reaction rates, activation energy, and other constants. Further development of new products, processes and systems on the basis of underlying thermal transport is needed. The design, control and optimization of the systems, as well as the selection of operating conditions, in order to achieve the desired processing needs further work.

Acknowledgments

Nomenclature

b = temperature coefficient of viscosity, Eq. (17)
C_p = specific heat at constant pressure
$\bar{e}$ = unit vector in the direction of gravitational force
E = activation energy
Ec = Eckert number, Eq. (15)
f_1 = liquid mass fraction
$\bar{F}$ = body force vector
g = magnitude of gravitational acceleration
Gr = Grashof number, Eq. (15)
h = convective heat transfer coefficient
H = enthalpy
H^{o} = enthalpy at 0 K
$\bar{i}$ = unit vector in x-direction
k = thermal conductivity,
K = bulk viscosity, reaction rate
K_c = consistency index for non-Newtonian fluid, Eq. (16)
L = characteristic length
L_h = latent heat of fusion

$\dot{m}$ = mass flow rate
n = power-law fluid index
N = speed in revolutions/min (rpm)
p = local pressure
Pr = Prandtl number, Eq. (15)
q = heat flux
q_v = dimensionless volume flow rate in a polymer extruder
$\dot{Q}$ = volumetric heat source
R = universal gas constant; radius
Re = Reynolds number, Eq. (15)
t = time
T = temperature
u, v, w = velocity components in x, y and z directions, respectively
U, U_s = speed of a moving solid or source
$\bar{V}$ = velocity vector
$\bar{x}$ = position vector
x, y, z = coordinate distances
X, Y, Z = dimensionless coordinate distances

Greek Symbols

α = thermal diffusivity
β = coefficient of thermal expansion
$\dot{\gamma}$ = strain rate
δ = location of interface between solid and liquid
ε = surface emissivity
λ = second viscosity coefficient
μ = dynamic viscosity of fluid
ν = kinematic viscosity
Φ = viscous dissipation function
ρ = density
θ = dimensionless temperature
τ = shear stress

References

[1] Jaluria, Y., 1998, *Design and Optimization of Thermal Systems*, McGraw-Hill, New York.
[2] Kalpakjian, S., 1989, *Manufacturing Engineering and Technology*, Addison-Wesley, Reading, MA.
[3] Szekely, J., 1979, *Fluid Flow Phenomena in Metals Processing*, Academic Press, New York.
[4] Fenner, R. T., 1979, *Principles of Polymer Processing*, Chemical Publishing, New York.
[5] Hughel, T. J., and Bolling, G. F., eds., 1971, *Solidification*, Amer. Soc. Metals, Metals Park, OH.
[6] Li, T., Ed., 1985, *Optical Fiber Communications, Vol. 1: Fiber Fabrication*, Academic Press, NY.
[7] Poulikakos, D., 1996, "Transport Phenomena in Materials Processing," Adv. Heat Transfer, **18**.
[8] Viskanta, R., 1988, "Heat Transfer During Melting and Solidification of Metals," ASME J. Heat Transfer, **110**, pp. 1205–1219.
[9] Jaluria, Y., 1980, *Natural Convection Heat and Mass Transfer*, Pergamon Press, Oxford, UK.
[10] Gebhart, B., Jaluria, Y., Mahajan, R. L., and Sammakia, B., 1988, *Buoyancy-Induced Flows and Transport*, Taylor and Francis, Philadelphia, PA.
[11] Jaluria, Y., and Torrance, K. E., 2003, *Computational Heat Transfer*, 2nd ed., Taylor and Francis, New York, NY.
[12] Ramachandran, N., Gupta, J. P., and Jaluria, Y., 1982, "Thermal and Fluid Flow Effects During Solidification in a Rectangular Enclosure," Int. J. Heat Mass Transfer, **25**, pp. 187–194.
[13] Bennon, W. D., and Incropera, F. P., 1988, "Developing Laminar Mixed Convection With Solidification in a Vertical Channel," ASME J. Heat Transfer, **110**, pp. 410–415.
[14] Viswanath, R., and Jaluria, Y., 1993, "A Comparison of Different Solution Methodologies for Melting and Solidification Problems in Enclosures," Numer. Heat Transfer, **24B**, pp. 77–105.
[15] Prescott, P. J., and Incropera, F. P., 1996, "Convection Heat and Mass Transfer in Alloy Solidification," Adv. Heat Transfer, **28**, pp. 231–338.
[16] Harper, J. M., 1981, *Extrusion of Foods: Volume I*, CRD Press, Boca Raton, FL.
[17] Kokini, J. L., Ho, C.-T., and Karwe, M. V., Eds., 1992, *Food Extrusion Science and Technology*, Marcel Dekker, New York.
[18] Wang, S. S., Chiang, C. C., Yeh, A. I., Zhao, B., and Kim, I. H., 1989, "Ki-

netics of Phase Transition of Waxy Corn Starch at Extrusion Temperatures and Moisture Contents,'' J. Food. Sci., **54**, pp. 1298–1301.

[19] Jensen, K. F., Einset, E. O., and Fotiadis, D. I., 1991, ''Flow Phenomena in Chemical Vapor Deposition of Thin Films,'' Annu. Rev. Fluid Mech., **23**, pp. 197–232.

[20] Mahajan, R. L., 1996, ''Transport Phenomena in Chemical Vapor-Deposition Systems,'' Adv. Heat Transfer, **28**, pp. 339–425.

[21] Roy Choudhury, S., Jaluria, Y., and Lee, S. H.-K., 1999, ''Generation of Neck-Down Profile for Furnace Drawing of Optical Fiber,'' Numer. Heat Transfer, **35**, pp. 1–24.

[22] Jaluria, Y., 1992, ''Transport From Continuously Moving Materials Undergoing Thermal Processing,'' Annu. Rev. Fluid Mech., **4**, pp. 187–245.

[23] Siegel, R., 1984, ''Two-Region Analysis of Interface Shape in Continuous Casting With Superheated Liquid,'' ASME J. Heat Transfer, **106**, pp. 506–511.

[24] Roy Choudhury, S., and Jaluria, Y., 1994, ''Analytical Solution for the Transient Temperature Distribution in a Moving Rod or Plate of Finite Length With Surface Heat Transfer,'' Int. J. Heat Mass Transfer, **37**, pp. 1193–1205.

[25] Chiu, W. K.-S., Jaluria, Y., and Glumac, N. C., 2000, ''Numerical Simulation of Chemical Vapor Deposition Processes Under Variable and Constant Property Approximations,'' Numer. Heat Transfer, **37**, pp. 113–132.

[26] Wang, Q., Yoo, H., and Jaluria, Y., 2003, ''Convection in a Horizontal Duct Under Constant and Variable Property Formulations,'' Int. J. Heat Mass Transfer, **46**, pp. 297–310.

[27] Tadmor, Z., and Gogos, C., 1979, *Principles of Polymer Processing*, Wiley, New York.

[28] Jaluria, Y., 1996, ''Heat and Mass Transfer in the Extrusion of Non-Newtonian Materials,'' Adv. Heat Transfer, **28**, pp. 145–230.

[29] Karwe, M. V., and Jaluria, Y., 1990, ''Numerical Simulation of Fluid Flow and Heat Transfer in a Single-Screw Extruder for Non-Newtonian Fluids,'' Numer. Heat Transfer, **17**, pp. 167–190.

[30] Lee, S. H.-K., and Jaluria, Y., 1996, ''Simulation of the Transport Processes in the Neck-Down Region of a Furnace Drawn Optical Fiber,'' Int. J. Heat Mass Transfer, **40**, pp. 843–856.

[31] Sayles, R., and Caswell, B., 1984, ''A Finite Element Analysis of the Upper Jet Region of a Fiber Drawing Flow Field,'' Int. J. Heat Mass Transfer, **27**, pp. 57–67.

[32] Myers, M. R., 1989, ''A Model for Unsteady Analysis of Preform Drawing,'' AIChE J., **35**, pp. 592–602.

[33] Jaluria, Y., 1976, ''Temperature Regulation of a Plastic-Insulated Wire in Radiant Heating,'' ASME J. Heat Transfer, **98**, pp. 678–680.

[34] Beckermann, C., and Wang, C. Y., 1995, ''Multiphase Scale Modeling of Alloy Solidification,'' Annu. Rev. Fluid Mech., **6**, pp. 115–198.

[35] Chiruvella, R. V., Jaluria, Y., and Karwe, M. V., 1996, ''Numerical Simulation of Extrusion Cooking of Starchy Materials,'' J. Food. Eng., **30**, pp. 449–467.

[36] Hanafusa, H., Hibino, Y., and Yamamoto, F., 1985, ''Formation Mechanism of Drawing-Induced E' Centers in Silica Optical Fibers,'' J. Appl. Phys., **58(3)**, pp. 1356–1361.

[37] Yin, Z., and Jaluria, Y., 2000, ''Neck Down and Thermally Induced Defects in High Speed Optical Fiber Drawing,'' ASME J. Heat Transfer, **122**, pp. 351–362.

[38] Jaluria, Y., 1984, ''Numerical Study of the Thermal Processes in a Furnace,'' Numer. Heat Transfer, **7**, pp. 211–224.

[39] Issa, J., Yin, Z., Polymeropoulos, C. E., and Jaluria, Y., 1996, ''Temperature Distribution in an Optical Fiber Draw Tower Furnace,'' J. Mater. Process. Manuf. Sci., **4**, pp. 221–232.

[40] Kwon, T. H., Shen, S. F., and Wang, K. K., 1986, ''Pressure Drop of Polymeric Melts in Conical Converging Flow: Experiments and Predictions,'' Polym. Eng. Sci., **28**, pp. 214–224.

[41] Lin, P., and Jaluria, Y., 1997, ''Conjugate Transport in Polymer Melt Flow Through Extrusion Dies,'' Polym. Eng. Sci., **37**, pp. 1582–1596.

[42] Minkowycz, W. J., and Sparrow, E. M., eds., 1997, *Advances in Numerical Heat Transfer*, **1**, Taylor & Francis, Philadelphia, PA.

[43] Patankar, S. V., 1980, *Numerical Heat Transfer and Fluid Flow*, Taylor & Francis, Philadelphia, PA.

[44] Leonard, B. P., 1997, ''Bounded Higher-Order Upwind Multidimensional Finite-Volume Convection-Diffusion Algorithms,'' in *Advances in Numerical Heat Transfer*, W. J. Minkowycz and E. M. Sparrow, eds., **1**, Taylor & Francis, Philadelphia, PA, pp. 1–57.

[45] Zhu, W., and Jaluria, Y., 2001, ''Residence Time and Conversion in the Extrusion of Chemically Reactive Materials,'' Polym. Eng. Sci., **41**, pp. 1280–1291.

[46] Wang, Y., and White, J. L., 1989, ''Non-Newtonian Flow Modeling in the Screw Region of an Intermeshing Co-Rotating Twin Screw Extruder,'' J. Non-Newtonian Fluid Mech., **32**, pp. 19–38.

[47] Sastrohartono, T., Jaluria, Y., and Karwe, M. V., 1994, ''Numerical Coupling of Multiple Region Simulations to Study Transport in a Twin Screw Extruder,'' Numer. Heat Transfer, **25**, pp. 541–557.

[48] Chiruvella, R. V., Jaluria, Y., Karwe, M. V., and Sernas, V., 1996, ''Transport in a Twin-Screw Extruder for the Processing of Polymers,'' Polym. Eng. Sci., **36**, pp. 1531–1540.

[49] Yin, Z., and Jaluria, Y., 1997, ''Zonal Method to Model Radiative Transport in an Optical Fiber Drawing Furnace,'' ASME J. Heat Transfer, **119**, pp. 597–603.

[50] Paek, U. C., 1999, ''Free Drawing and Polymer Coating of Silica Glass Optical Fibers,'' ASME J. Heat Transfer, **121**, pp. 775–788.

[51] Cheng, X., and Jaluria, Y., 2002, ''Effect of Draw Furnace Geometry on High-Speed Optical Fiber Manufacturing,'' Numer. Heat Transfer, **41**, pp. 757–781.

[52] Blyler, L. L., and DiMarcello, F. V., 1980, ''Fiber Drawing, Coating and Jacketing,'' Proc. IEEE, **68**, pp. 1194–1198.

[53] Paek, U. C., 1986, ''High Speed High Strength Fiber Coating,'' J. Lightwave Technol., **LT-4**, pp. 1048–1059.

[54] Ravinutala, S., Rattan, K., Polymeropoulos, C., and Jaluria, Y., 2000, ''Dynamic Menisci in a Pressurized Fiber Applicator,'' *Proc. 49th Int. Wire Cable Symp.*, Atlantic City, NJ, INCS, Inc., Eatontown, NJ.

[55] Vaskopulos, T., Polymeropoulos, C. E., and Zebib, A., 1995, ''Cooling of Optical Fibers in Aiding and Opposing Forced Gas Flow,'' Int. J. Heat Mass Transfer, **18**, pp. 1933–1944.

[56] Voller, V. R., 1997, ''An Overview of Numerical Methods for Solving Phase Change Problems,'' in *Advances in Numerical Heat Transfer*, W. J. Minkowycz and E. M. Sparrow, eds., **1**, Taylor & Francis, Philadelphia, PA, pp. 341–380.

[57] Banaszek, J., Jaluria, Y., Kowalewski, T. A., and Rebow, M., 1999, ''Semi-Implicit FEM Analysis of Natural Convection in Freezing Water,'' Numer. Heat Transfer, **36**, pp. 449–472.

[58] Lin, P., and Jaluria, Y., 1997, ''Heat Transfer and Solidification of Polymer Melt Flow in a Channel,'' Polym. Eng. Sci., **37**, pp. 1247–1258.

[59] Fotiadis, D. I., Boekholt, M., Jensen, K. F., and Richter, W., 1990, ''Flow and Heat Transfer in CVD Reactors: Comparison of Raman Temperature Measurements and Finite Element Model Predictions,'' J. Cryst. Growth, **100**, pp. 577–599.

[60] Yoo, H., and Jaluria, Y., 2002, ''Thermal Aspects in The Continuous Chemical Vapor Deposition of Silicon,'' ASME J. Heat Transfer, **124**, pp. 938–946.

[61] Eversteyn, F. C., Severin, P. J. W., Brekel, C. H. J., and Peek, H. L., 1970, ''A Stagnant Layer Model for the Epitaxial Growth of Silicon From Silane in a Horizontal Reactor,'' J. Electrochem. Soc., **117**, pp. 925–931.

[62] Mahajan, R. L., and Wei, C., 1991, ''Buoyancy, Soret, Dufour and Variable Property Effects in Silicon Epitaxy,'' ASME J. Heat Transfer, **113**, pp. 688–695.

[63] Chiu, W. K. S., Richards, C. J., and Jaluria, Y., 2001, ''Experimental and Numerical Study of Conjugate Heat Transfer in a Horizontal Channel Heated From Below,'' ASME J. Heat Transfer, **123**, pp. 688–697.

[64] Ostrach, S., 1983, ''Fluid Mechanics in Crystal Growth—The 1982 Freeman Scholar Lecture,'' J. Fluids Eng., **105**, pp. 5–20.

[65] Prasad, V., Zhang, H., and Anselmo, A. P., 1997, ''Transport Phenomena in Czochralski Crystal Growth Processes,'' Adv. Heat Transfer, **30**, pp. 313–435.

[66] Ostrach, S., 1982, ''Low-Gravity Fluid Flows,'' Annu. Rev. Fluid Mech., **14**, pp. 313–345.

[67] Wang, G. X., and Prasad, V., 2000, ''Rapid Solidification: Fundamentals and Modeling,'' Annu. Rev. Heat Transfer, **11**, pp. 207–297.

[68] Delplanque, J. P., and Rangel, R. H., 1998, ''A Comparison of Models, Numerical Simulation, and Experimental Results in Droplet Deposition Processes,'' Acta Mater., **46**, pp. 4925–4933.

[69] Pasandideh-Fard, M., Bhola, R., Chandra, S., and Mostaghimi, J., 1998, ''Deposition of Tin Droplets on a Steel Plate: Simulations and Experiments,'' Int. J. Heat Mass Transfer, **41**, pp. 2929–2945.

[70] Roache, P. J., 1998, *Verification and Validation in Computational Science and Engineering*, Hermosa Publishers, Albuquerque, New Mexico.

[71] De Vahl Davis, G., and Leonardi, E., eds., 2001, *Advances in Computational Heat Transfer II*, Begell House Pub., New York, NY.

[72] Esseghir, M., and Sernas, V., 1992, ''Experiments on a Single Screw Extruder With a Deep and Highly Curved Screw Channel,'' in *Food Extrusion Science and Technology*, J. L. Kokini, C. T. Ho, and M. V. Karwe, eds., Marcel Dekker, New York, pp. 21–40.

[73] Sastrohartono, T., Jaluria, Y., Esseghir, M., and Sernas, V., 1995, ''A Numerical and Experimental Study of Three-Dimensional Transport in the Channel of an Extruder for Polymeric Materials,'' Int. J. Heat Mass Transfer, **38**, pp. 1957–1973.

[74] Sastrohartono, T., Esseghir, M., Kwon, T. H., and Sernas, V., 1990, ''Numerical and Experimental Studies of the Flow in the Nip Region of a Partially Intermeshing Co-Rotating Twin Screw Extruder,'' Polym. Eng. Sci., **30**, pp. 1382–1398.

[75] Bakalis, S., and Karwe, M. V., 1997, ''Velocity Field in a Twin Screw Extruder,'' Int. J. Food Sci. Technol., **32**, pp. 241–253.

[76] Paek, U. C., and Runk, R. B., 1978, ''Physical Behavior of the Neck-Down Region During Furnace Drawing of Silica Fibers,'' J. Appl. Phys., **49**, pp. 4417–4422.

[77] Paek, U. C., Schroeder, C. M., and Kurkjian, C. R., 1988, ''Determination of the Viscosity of High Silica Glasses During Fibre Drawing,'' Glass Technol., **29(4)**, pp. 263–266.

[78] Wolff, F., and Viskanta, R., 1987, ''Melting of a Pure Metal From a Vertical Wall,'' Exp. Heat Transfer, **1**, pp. 17–30.

[79] Wolff, F., and Viskanta, R., 1988, ''Solidification of a Pure Metal at a Vertical Wall in the Presence of Liquid Superheat,'' Int. J. Heat Mass Transfer, **31**, pp. 1735–1744.

[80] Zhu, W., and Jaluria, Y., 2001, ''Transport Processes and Feasible Operating Domain in a Twin-Screw Polymer Extruder,'' Polym. Eng. Sci., **41**, pp. 107–117.

[81] Jongbloed, H. A., Kiewiet, J. A., Van Dijk, J. H., and Janssen, L. P. B. M., 1995, ''The Self-Wiping Co-Rotating Twin-Screw Extruder as a Polymerization Reactor for Methacrylates,'' Polym. Eng. Sci., **35**, pp. 1569–1579.

[82] Roy Choudhury, S., and Jaluria, Y., 1998, ''Practical Aspects in the Thermal Transport During Optical Fiber Drawing,'' J. Mater. Res., **13**, pp. 483–493.

[83] Cheng, X., and Jaluria, Y., 2003, ''Feasible Domain of High Speed Optical

Fiber Drawing,'' *Proc. ASME-JSME Thermal Engg. Jt. Conf.*, Hawaii, JSME, Tokyo, Japan.

[84] Dianov, E. M., Kashin, V. V., Perminov, S. M., Perminova, V. N., Rusanov, S. Y., and Sysoev, V. K., 1988, "The Effect of Different Conditions on the Drawing of Fibers From Preforms,'' Glass Technol., **29**(6), pp. 258–262.

[85] Ottino, J. M., 1997, *The Kinematics of Mixing: Stretching, Chaos, and Transport*, Cambridge University Press, Cambridge, England.

[86] Bejan, A., 1995, *Entropy Generation Minimization*, CRC Press, Boca Raton, FL.

[87] Arora, J. S., 1989, *Introduction to Optimum Design*, McGraw-Hill, New York.

[88] Stoecker, W. F., 1989, *Design of Thermal Systems*, 3rd ed., McGraw-Hill, New York.

[89] Chiu, W. K. S., Jaluria, Y., and Glumac, N. G., 2002, "Control of Thin Film Growth in Chemical Vapor Deposition Manufacturing Systems,'' ASME J. Manuf. Sci. Eng., **124**, pp. 715–724.

[90] Cheng, X., 2002, "Design and Optimization of the Draw Furnace for High Speed Optical Fiber Drawing,'' Ph.D. Thesis, Rutgers Univ., New Brunswick, NJ.

[91] Suh, N. P., 1990, *The Principles of Design*, Oxford Univ. Press, New York.

[92] Jaluria, Y., and Lombardi, D., 1991, "Use of Expert Systems in the Design of Thermal Equipment and Processes,'' Res. Eng. Des., **2**, pp. 239–253.

[93] Jamalabad, V. R., Langrana, N. A., and Jaluria, Y., 1994, "Rule-Based Design of a Materials Processing Component,'' Eng. Comput., **10**, pp. 81–94.

[94] Viswanath, R., 1993, "Modeling, Simulation and Design of Solidification Systems,'' Ph.D. Thesis, Rutgers Univ., New Brunswick, NJ.

[95] Viswanath, R., and Jaluria, Y., 1991, "Knowledge-Based System for the Computer Aided Design of Ingot Casting Processes,'' Eng. Comput., **7**, pp. 109–120.

Study on Optimization of Transverse Thermal Conductivities of Unidirectional Composites

Mingqing Zou

Boming Yu
e-mail: yu3838@public.wh.hb.cn

Duanming Zhang

Yongting Ma

Department of Physics and State Key Laboratory of Plastic Forming and Die & Mold Tech., Huazhong University of Science and Technology, Wuhan, 430074, P. R. China

Two models, E-S and R-S unit cell models, are presented based on the thermal-electrical analogy technique. The analytical expressions for transverse thermal conductivities of unidirectional composites are derived. The dimensionless effective transverse thermal conductivities k_e^+ are expressed as a function of the ratio (β) of thermal conductivities of filler to matrix, filler volume fraction (v_f) and the geometry ratio ($\rho = a/b$) of the filler. The optimization of transverse thermal conductivities of unidirectional composites is then analyzed under different filler volume fractions v_f, thermal conductivity ratios β and different geometric architectures. The present analysis allows for a fairly precise evaluation of configuration performance and comparisons of different arrangements. The results show that if a composite is designed for insulation material, we should choose $\rho < 1$, and if a composite is designed for heat dissipating purpose, we should choose $\rho > 1$.
[DOI: 10.1115/1.1621892]

Keywords: Composites, Conduction, Heat Transfer, Optimization, Thermophysical

1   Introduction

In the past decades, considerable attention has been given to optimization of geometries such as dimensions, spacings, shapes as well as distributions (allocations) of heat transfer in thermal engineering due to its application in electronic cooling, design of heat exchangers, reliability and economy. Some efforts were made to optimize the plate spacing [1–3] at different geometric configurations for maximizing the heat dissipation. Some investigations were focused on optimum design of finned surfaces such as finned tube [4–6], annular fin [7–9], and rectangular and triangular fins [10–12]. The objective of these researches was to optimize the fin dimension, thickness and height for maximizing the heat dissipation at the fin base. Ogiso [13] presented a method of assessing the overall cooling performance in the thermal design of electronics. This method is based on the entropy generation method [14]. In electronic equipment, the temperature of each component must be kept within an allowable upper limit for reliable operation performance.

Recently, Mawardi and Pitchumani [15] addressed the problem of determining the temperature and electrical current cycle, as well as the placement configuration of the conductive mats, for time-optimal curing of composites using embedded resistance heating elements. Vynnycky et al. [16] studied a transient inverse heat conduction problem on gas quenching of steel plates and ring. The objective was to calculate the transient convective heat transfer coefficient which would produce an optimized phase transformation cooling curve. Aung [17] and Bejan [18] developed the constructal-theory to design a network for conducting paths for cooling a heat generating volume. This theory provides a solution to the fundamental problem of how to correct and ''channel'' to one point the heat generated volumetrically in a low conductivity volume of given size. The solution is obtained as a sequence of optimization and organization steps. Optimized in each assembly are the shape of the assembly and the width of the newest high conductivity path. The results show that in the opti-

mal design, the high-conductivity material form a tree-like network. Neagu and Bejan [19] applied this theory to study the constructal placement of high-conductivity inserts in a slab. Their results were presented for the optimized architectures: spacings between inserts, penetration distances, taped inserts and constant-thickness inserts.

The results by Xia and Guo [20] indicated that for a given fraction of high-conductivity material in a composite, the longitudinal conductivity is higher than the transverse conductivity, in other words, the heat transfer (or heat dissipation) along the longitudinal direction is easier than the transverse direction. However, the direction of heat flow may often have to be designed to be perpendicular to the axis of filler in a composite. Therefore, the transverse thermal conductivity of unidirectional composites has been one of focuses of many investigators, including numerical solutions [21–23] and theoretical approaches [24–26] as well as experiments [27]. However, no general expression and optimization of the effective transverse thermal conductivity for unidirectional composites have been reported in the literature to the best of our knowledge.

The objectives of this work are to derive the general expressions for the effective transverse thermal conductivities of unidirectional composites and then to optimize the geometric shapes, sizes under the different volume fractions of filler materials and different ratios of component conductivities of the composites, based on maximizing thermal conductivities for heat dissipation and minimizing the thermal conductivities for heat insulation purposes. For convenience of analysis of optimization of transverse thermal conductivities of unidirectional composites, in this paper, the contact resistance between filler and matrix is not taken into account (i.e., assume the perfect contact). It is expected that this simplification does not affect the present analysis of optimization on thermal conductivities of composites. The analytically transverse thermal conductivities of unidirectional fiber composites with thermal barrier are given elsewhere [26]. In this paper, two geometry models, elliptical filament and square packing array unit cell model (E-S model) and rectangular filament and square pack-

Copyright © 2003 by ASME

(a)

(b)
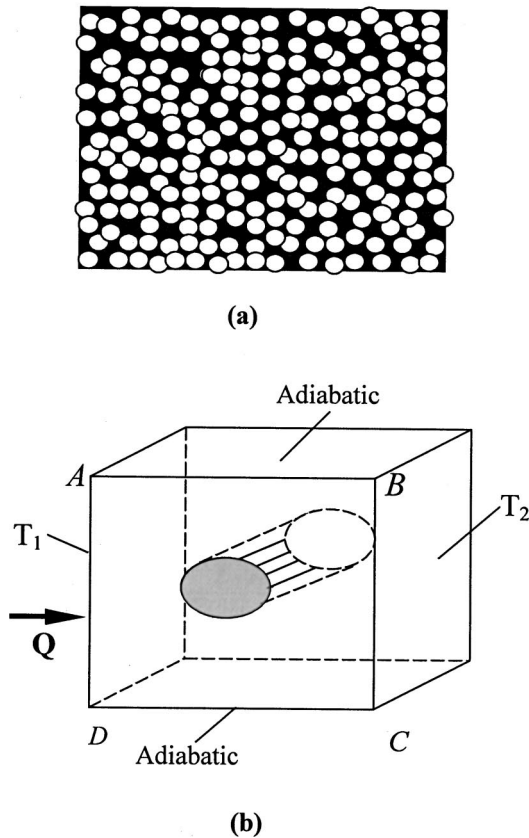
Fig. 1 (*a*) A cross-sectional view of a fiber reinforced unidirectional composite; and (*b*) a unit cell for the ellipsoidal filament and square array model for transverse heat conduction.

(a)

(b)

Fig. 2 (*a*) A simplified unit cell for the ellipsoidal filament-square packing array model; and (*b*) Schematic for calculation of the thermal resistances.

ing array unit cell model (R-S models), are presented and the optimization of thermal conductivities in unidirectional composites are systematically analyzed.

2 The Analysis of Transverse Thermal Conductivity

Figure 1(*a*) displays a cross sectional view of a fiber reinforced composite with unidirectional fibers (or aluminum wires, or brass wires as filler), and Fig. 1(*b*) is a generalized unit cell (or representative cell), the elliptical filament and square packing array unit cell model (E-S model). For simplicity, Fig. 1(*b*) is reduced to Fig. 2(*a*). The one-dimensional heat flow is assumed to be from the left to the right. Faces AB and DC in Fig. 2(*a*) are approximated to be adiabatic due to statistically symmetry, see Fig. 1(*a*). The boundaries AD and BC in Fig. 2(*a*) are held at constant temperatures T_1 and T_2, respectively. Zou et al. [26] used the cylinder filament and square packing array unit cell model (C-S model) to calculate the effective thermal conductivity with thermal barrier for unidirectional composites as shown in Fig. 1(*a*). In their model, they assumed that the one-dimensional heat flow is imposed on the C-S unit cell model with the same boundary conditions as those shown in Fig. 2(*a*). The only difference between the present E-S model and the C-S model is that in the E-S model the cross section of filler is elliptical, while in the C-S model the cross section of filler is circular. Their analytical results for the effective transverse thermal conductivities, based on the electric analogy technique and on the C-S model, have shown a better agreement with the existing experimental data [27], compared to those from the finite difference method [21] and the finite element method [23] for solution of a two-dimensional C-S model (with the same boundary conditions as our present E-S model) for the effective transverse thermal conductivities. This means that the one-dimensional heat flow assumption and the electrical analogy technique are valid for the
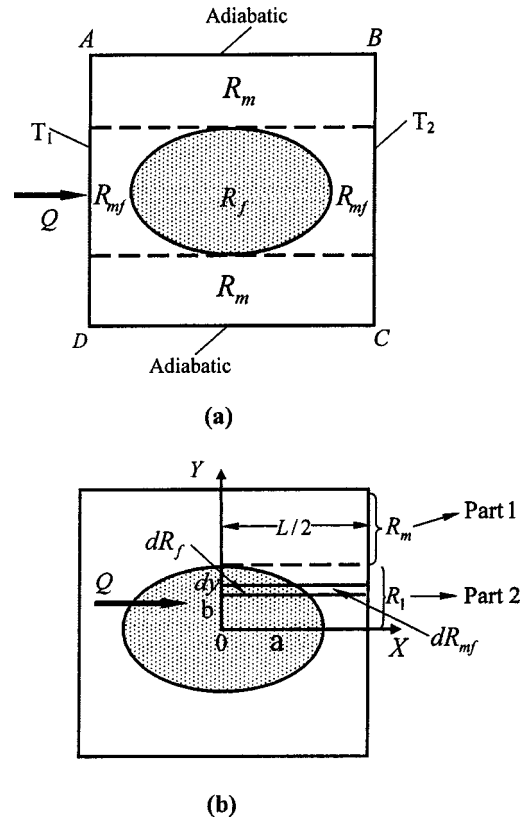
effective transverse thermal conductivities of unidirectional composites. For detailed comparison, readers may consult the paper by Zou et al. [26]. In the past, many models for the effective thermal conductivity were proposed based on the one-dimensional heat flow assumption. Zehnder and Schlunder [28] presented their correlation for the effective thermal conductivity based on the one-dimensional heat flow assumption for conduction through a packed bed of spherical particles. Hsu et al. [29] developed a lumped-parameter model, also based on the one-dimensional heat flow assumption, to determine the effective stagnant thermal conductivity of three-dimensional spatially periodic porous media with thermal resistance. Recently, Yu and Cheng [30] used the thermal-electrical analogy technique and also assumed one-dimensional heat flow model in a unit cell containing many random particles and pores for effective thermal conductivity of bi-dispersed porous media. One of their two models considered the effect of heat flow in the *y*-direction. However, their theoretical results show that the heat conduction in the *y*-direction has the negligible effect on effective thermal conductivity, and their theoretical results based on the assumption of one-dimensional heat flow are in good agreement with the experimental data.

Therefore, in this work we also assume the one-dimensional heat flow with the boundary conditions as shown in Fig. 2(*a*). Because of the symmetry of the problem, we further choose one quadrant of the unit cell as shown in Fig. 2(*b*) for the thermal-electric analogy analysis of the effective transverse thermal conductivity based on the present E-S model.

For determining the effective thermal conductivity, the quadrant in Fig. 2(*b*) is divided into two major parts, Parts 1 and 2, which are in parallel. The conductivities of Part 2 (matrix and filler) are considered as in series. The governing equations for thermal conductivities for each part are derived as follows.

Assume L, a, and b to be the side length of the square unit cell,

the axial lengths of the ellipse along the x-axis and y-axis respectively, and let the longitudinal length of the composite be unity.

Then, the thermal resistance of Part 1 in Fig. 2(b) is

$$R_m = \frac{L/2}{k_m(L/2-b)} \tag{1}$$

The lower part of the quadrant of the unit cell (Part 2) can be considered as series of R_f (thermal resistance of fiber) and R_{mf} (thermal resistance of matrix parallel to the fiber), and the perfect contact between fiber and matrix is assumed. The lower part is divided into many infinitesimal layers with each layer thickness of dy. Thus, in Part 2 the thermal resistances of each layer are

$$dR_f = \frac{x}{k_f dy} \tag{2}$$

and

$$dR_{mf} = \frac{L/2-x}{k_m dy} \tag{3}$$

Since dR_f and dR_{mf} are in series, the total thermal resistance of each layer, dR_s, is

$$dR_s = dR_f + dR_{mf} \tag{4}$$

However, since all infinitesimal layers with the thermal resistance dR_s are in parallel, the total thermal resistance of the lower part of the quadrant unit cell can be obtained by

$$\frac{1}{R_s} = \int \frac{1}{dR_s} \tag{5}$$

The total thermal resistance of the quadrant of the unit cell is considered to be the parallel of two parts (R_m and R_s), and it is

$$\frac{1}{R_t} = \frac{1}{R_s} + \frac{1}{R_m} \tag{6}$$

where R_t is the total thermal resistance. The total thermal flow through the quadrant unit cell is

$$Q = k_e \frac{\Delta T}{L/2} L/2 = \frac{\Delta T}{R_t} \tag{7}$$

Thus, the effective transverse thermal conductivity can be obtained by

$$k_e = \frac{1}{R_t} = \int_0^b \frac{k_f k_m dy}{k_m x + k_f(L/2-x)} + \frac{k_m(L/2-b)}{L/2} \tag{8}$$

Equation (8) is usually written as the dimensionless effective transverse thermal conductivity

$$k_e^+ = \frac{k_e}{k_m} = 1 - \frac{b}{L/2} + \int_0^b \frac{dy}{(1/\beta-1)x + L/2} \tag{9}$$

The ellipse equation is

$$(x/a)^2 + (y/b)^2 = 1 \tag{10}$$

Combining Eqs. (9) and (10) and integrating over y yield the dimensionless effective transverse thermal conductivity as

$$k_e^+ = 1 - \frac{1}{c} + \frac{\pi}{2d} - \frac{c}{d\sqrt{c^2-d^2}}\cos^{-1}\frac{d}{c} \quad \text{for } |c|>|d| \tag{11-1}$$

and

$$k_e^+ = 1 - \frac{1}{c} + \frac{\pi}{2d} - \frac{c}{d\sqrt{d^2-c^2}}\ln\left|\frac{d+\sqrt{d^2-c^2}}{c}\right| \quad \text{for } |c|<|d| \tag{11-2}$$

where v_f is the fiber volume fraction ($v_f = \pi ab/L^2$, to be valid, the constraint of $v_f \leq \pi/4$ must be satisfied for the E-S model), and β is the ratio of fiber conductivity to matrix conductivity ($\beta = k_f/k_m$), $\rho = a/b$, $c = \sqrt{\pi\rho/v_f}/2$, $d = \rho(1/\beta-1)$. Equation (11) is the general expression for dimensionless effective thermal conductivity of unidirectional composites. When $\rho=1$ (i.e., $a=b$),
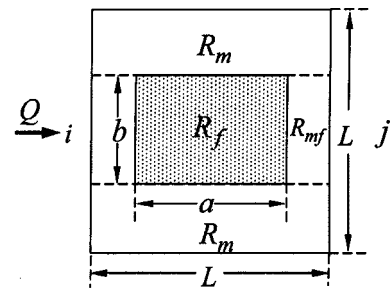
(a)
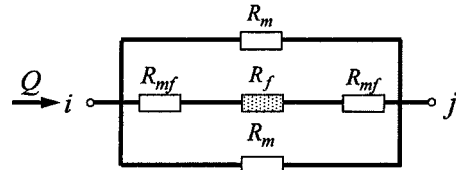
(b)

Fig. 3 (*a*) **A simplified unit cell for the rectangular filament and square packing array for transverse heat conduction; and** (*b*) **the thermal resistance network of** (*a*)**.**

the present model can be simplified as the cylindrical filament in square packing array unit cell model (C-S model), so the widely applied C-S model [21–26] is only the special case of $a=b$.

We here also derive the analytical solution for the rectangular filament and square packing array unit cell model (R-S model) as shown in Fig. 3. Applying the electrical analogue technique to Fig. 3(a), we have the thermal resistance networks as shown in Figs. 3(b) and similarly yield

$$R_m = \frac{L}{k_m(L-b)/2} \tag{12}$$

$$R_f = \frac{a}{k_f b} \tag{13}$$

$$R_{mf} = \frac{(L-a)/2}{k_m b} \tag{14}$$

The total thermal resistance of the unit cell can be obtained by

$$\frac{1}{R_t} = \frac{1}{R_m} + \frac{1}{R_{mf}+R_f+R_{mf}} + \frac{1}{R_m} = \frac{k_m\left(k_f - \frac{a}{L}(k_f-k_m)\left(1-\frac{b}{L}\right)\right)}{k_f - \frac{a}{L}(k_f-k_m)} \tag{15}$$

So, the effective transverse thermal conductivity is

$$k_e = \frac{1}{R_t} = \frac{k_m\left(k_f - \frac{a}{L}(k_f-k_m)\left(1-\frac{b}{L}\right)\right)}{k_f - \frac{a}{L}(k_f-k_m)} \tag{16}$$

The dimensionless effective transverse thermal conductivity can be written as

$$k_e^+ = \frac{k_e}{k_m} = 1 + \frac{v_f}{1 + \frac{1}{\beta-1} - \sqrt{\rho v_f}} \tag{17}$$

where $v_f = ab/L^2$, and to be valid, the constraint of $a \leq L$ and $b \leq L$ must be satisfied for the R-S model.

When the ratio $\rho = a/b = 1$, Eq. (17) can be simplified as the square filament and square packing array model (S-S model):

$$k_e^+ = \frac{k_e}{k_m} = 1 + \frac{v_f}{1 + \dfrac{1}{\beta - 1} - \sqrt{v_f}} \qquad (18)$$

Equation (18) reveals that $k_e^+ = 1$ ($k_e = k_m$) as $\beta = 1$ or $v_f = 0$, and $k_e^+ = \beta$ as $v_f = 1$, and these are expected and are consistent with the physical situations. It is seen that Eq. (17) is the general expression for transverse thermal conductivity of unidirectional composites, and Eq. (18) is only the special case of $a = b$. Equation (18) was obtained by Lu [31], who applied a boundary collocation scheme for calculation of the effective thermal conductivity of two-dimensional periodic arrays. The relevant boundary value problem for determination of the effective thermal conductivity is the steady-state heat conduction problem imposed with a linear ambient temperature field. This indirectly verifies the validity of the present R-S model.

Optimization of the Transverse Thermal Conductivities

In this section we put our emphases on the optimization of the transverse thermal conductivities. That is we want to get the maximum and minimum possible transverse thermal conductivities of the composites by choosing the different geometric shapes, sizes (various ρ) under the different volume fractions of filler materials and different ratios β of component conductivities.

To check the validity of the present model, we first assume $\rho = a/b = 1$ in the E-S model, i.e., Eq. (11) is thus simplified to the C-S mode. We then compare the present theoretical predictions from Eq. (11) at $\rho = 1$ with Pitchumani and Yao's fractal model [25]

$$k_e^+ = \left[1 - \left(1 + \frac{\pi}{2c} \right) \overline{v_f} \right] + \frac{2\overline{v_f}}{c\sqrt{1 - c^2}} \tan^{-1} \sqrt{\frac{1 + c}{1 - c}},$$
$$-1 < c < 1 \,\&\, c \neq 0 \qquad (19a)$$

$$= \left[1 - \left(1 + \frac{\pi}{2c} \right) \overline{v_f} \right] + \frac{\overline{v_f}}{c\sqrt{c^2 - 1}} \ln(-c + \sqrt{c^2 - 1}), \quad c < -1$$
$$(19b)$$

where $c = \left(\dfrac{\beta - 1}{\beta} \right) \left(\dfrac{4v_f}{\pi} \right)^{(1-\delta)/2}, \overline{v_f} = \left(\dfrac{4v_f}{\pi} \right)^{(1-\delta)/2},$

$$\delta = \frac{d_P - d_T}{d_P - 2d_P d_T + d_T} \qquad (19c)$$

In Eq. (19c), d_P and d_T are the local fractal dimensions of a composite cross section in the direction of heat flow and in the direction normal to heat flow, respectively. If $d_P = d_T$, Eq. (19) can be simplified as the C-S model with perfect contact between filament and matrix. The comparison is given in Fig. 4. Figure 4 indicates that the present analytical predictions from Eq. (11) ($\rho = 1$) present an excellent agreement with Pitchumani and Yao's fractal model Eq. (19) as $d_P = d_T$. This verifies the validity of the present analytical E-S model Eq. (11).

Figure 5 presents the dimensionless effective thermal conductivity k_e^+ versus ρ (as $\rho < 1$) at different volume fractions v_f up to the maximum volume fraction $v_f = \pi/4$ for a circular filler in a square. It can be seen that the dimensionless thermal conductivities (k_e^+) decrease with the decrease of ρ. The lower the values of ρ, the larger the thermal resistances and the lower the thermal conductivity. The lower the values of ρ, the father the deviations from the thermal conductivity values at $\rho = 1$. This is consistent with physical situation. It is also seen from Fig. 5 that all the thermal conductivity values are lower than both the upper limit values given by [21,32]

$$k_e^+ = \beta v_f + (1 - v_f) \qquad (20)$$
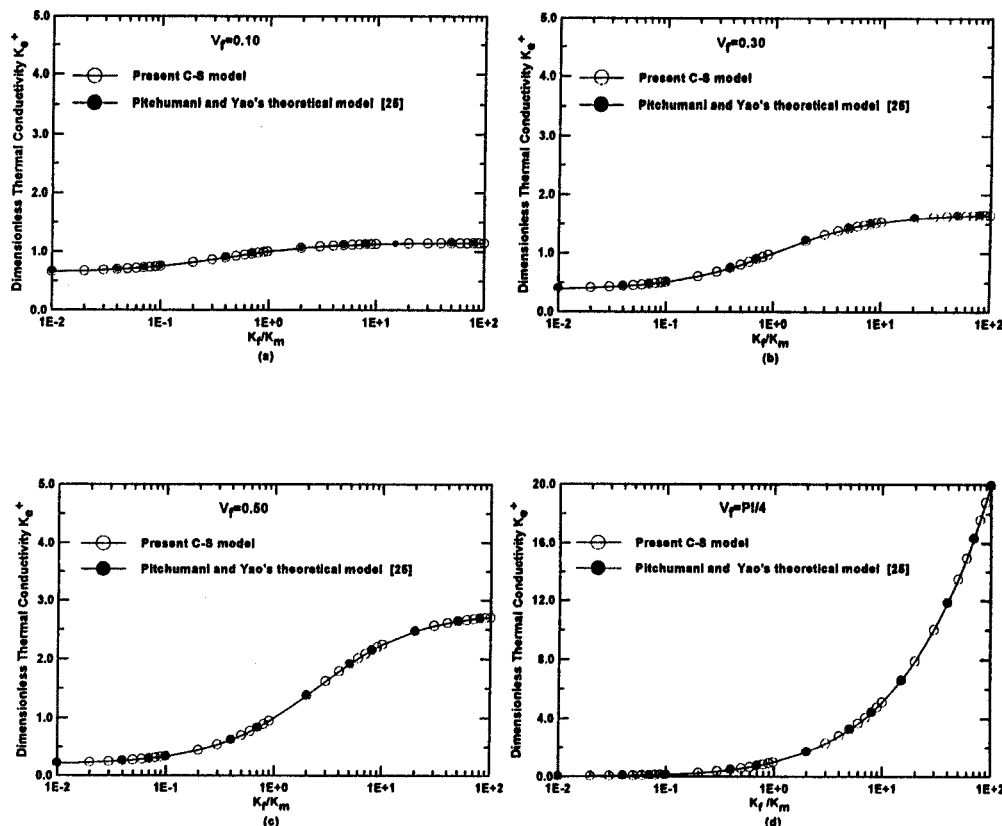
Fig. 4 A comparison on the thermal conductivities between the present Eq. (11) (as $\rho = 1$) and existing analytical solution Eq. (19) at $d_p = d_T$, here PI= π
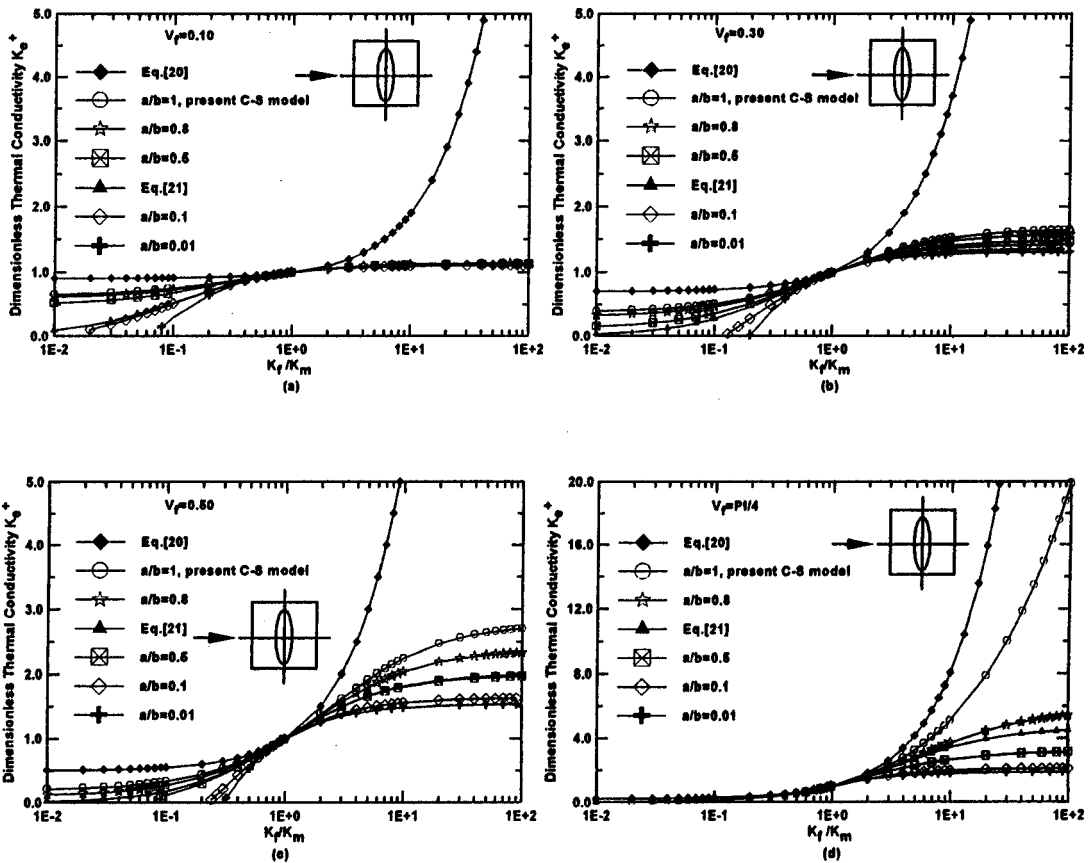
Fig. 5   Thermal conductivities when $\rho \leq 1$ for the E-S model, here PI=π
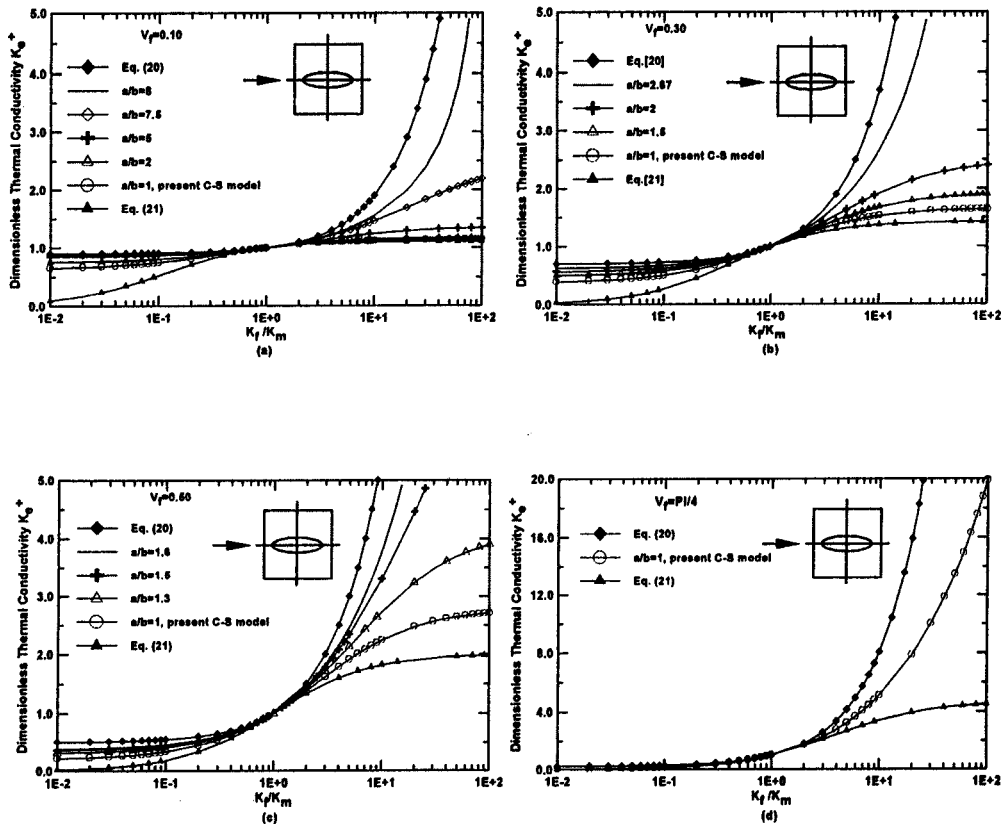
Fig. 6   Thermal conductivities when $\rho \geq 1$ for the E-S model, here PI=π
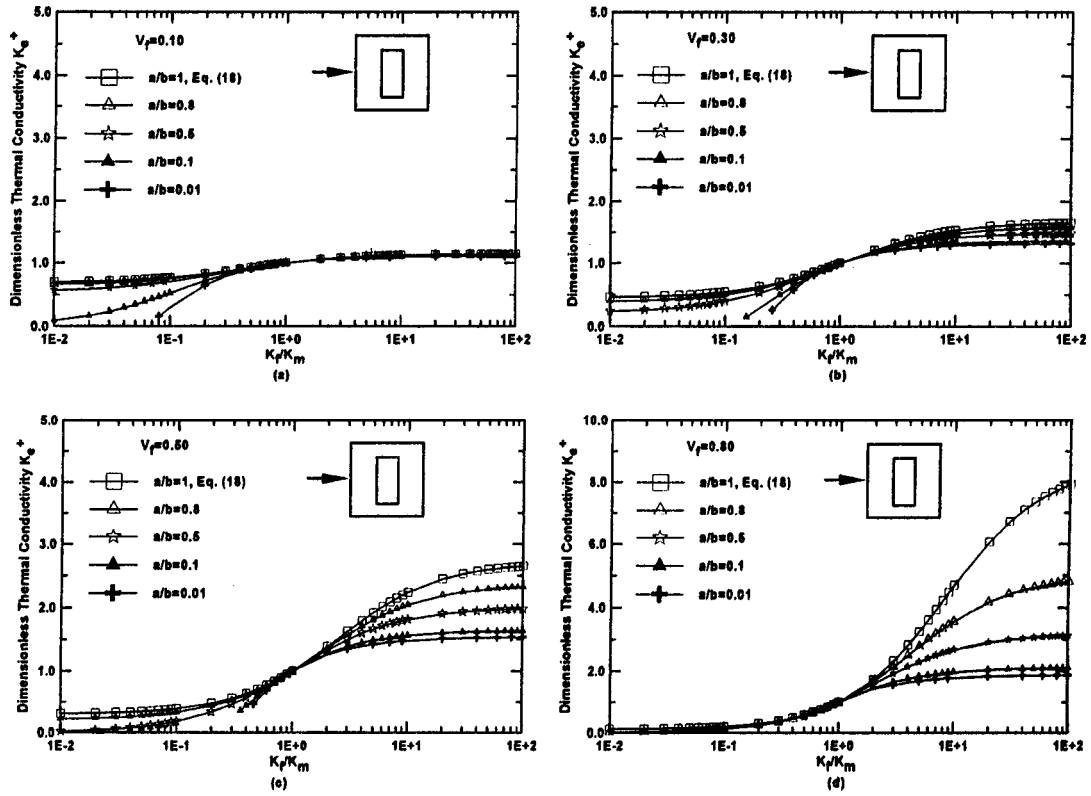
Fig. 7 Thermal conductivities when $\rho \leqslant 1$ for the R-S model
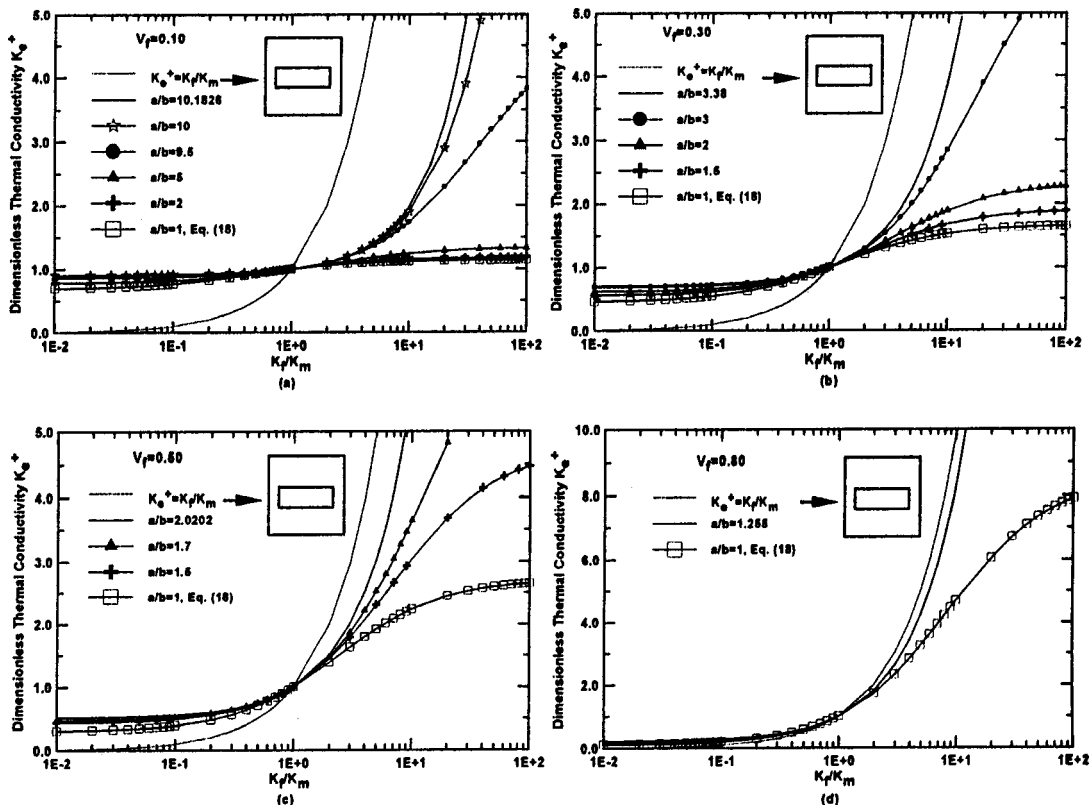
Fig. 8 Thermal conductivities when $\rho \geqslant 1$ for the R-S model
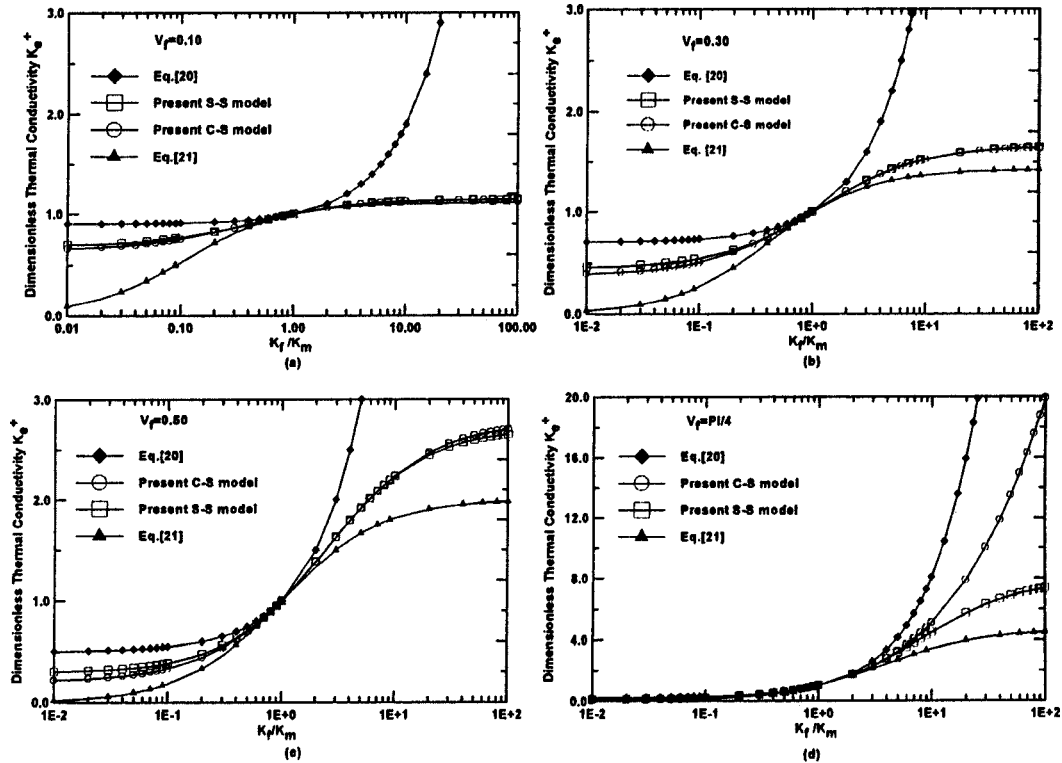
Fig. 9 A comparison on the results between the C-S model and the S-S model (i.e., at $\rho=1$)

and the values given by the present C-S model. In addition, an unusual phenomenon is observed that the values from Eq. (11) may be smaller than the lower bound given by [32]

$$\frac{1}{k_e^+} = \frac{v_f}{\beta} + (1-v_f) \tag{21}$$

when ρ is smaller than some certain value (such as $\rho \leq 0.1$ in Figs. 5(a)~(d) and $\rho \leq 0.5$ in Figs. 5(c)~(d)). We believe that this phenomenon is simply caused by the ratios of $\rho < 1$. However, this unusual thermal behavior of composite is impossible to appear in the C-S model, in which $\rho \equiv 1$.

From the above discussions, we can draw a conclusion that it is not an appropriate choice if a composite is designed for heat dissipating purpose as $\rho < 1$. In other words, if a composite is designed for insulation material, we should choose $\rho < 1$.

Figure 6 presents the dimensionless effective thermal conductivity k_e^+ versus ρ (as $\rho > 1$) at different volume fractions v_f up to the maximum volume fraction $\pi/4$ for a circular filler in a square. The figure shows that for a given $v_f(<\pi/4)$, the dimensionless thermal conductivities increase with ρ. The higher the values of ρ, the greater the deviations from the thermal conductivity values by the C-S model (i.e., $a/b=1$). In all situations, the curves are higher than that of the present C-S model (Eq. (11) as $\rho=1$). It was found in this work that when $v_f=0.1$ and $\rho>8$, the fluctuations were observed, i.e. some thermal conductivities may higher than the upper bond given by Eq. (20), this is unreasonable. Therefore, $\rho=8$ may be the maximum possible value for $v_f=0.1$. However, an interesting phenomenon is also found that when the filler volume v_f increases, the maximum possible value of ρ decreases. This is expected because the filler volume fraction is constrained by the maximum volume fraction $\pi/4$ and the length a is also constrained by the side length of square. In the limit situation of $v_f=\pi/4$, $\rho=1$, i.e., $a/b=1$ is the only feasible choice and any $\rho>1$ is inconsistent with the physical situation. See Fig. 6(d). Therefore, this analysis provides a new insight about the transverse thermal conductivity and probably enables engineers to motivate a new idea/design for cooling the electronic

component. Accordingly, the value of ρ should be chosen to be larger than 1 if a composite with a filler volume fraction $v_f < \pi/4$ is designed to be a heat dissipating material.

Figures 7 and 8 present the results by the present R-S model, and the similar results to those from E-S model are reported as follows:

1) When $\rho < 1$ (see Fig. 7), the values of k_e^+ decrease with the decrease of ρ. The lower the values of ρ, the larger the thermal resistance; the lower the values of ρ, the farther the deviations from the thermal conductivity values at $\rho=1$ (S-S model). When v_f is lower enough (such as 0.1) and $\beta>1$, $k_e^+ \to 1$. Obviously, as $\rho<1$, these configurations are suitable for composites used for insulation purpose.

2) When $\rho>1$ (see Fig. 8), the values of k_e^+ drastically increase with ρ. The higher the values of ρ, the larger the thermal conductivity; the greater the values of ρ, the farther the deviations from the thermal conductivity values by the S-S model. Fig. 8 also indicates that all the curves give the higher values than those by the present S-S model. These configurations may give the outstanding performance of heat dissipation in composites. Since in any situation the effective thermal conductivity should be constrained by the maximum possible value of $k_e^+ = \beta$ ($= k_f/k_m$) (i.e. in general, k_e^+ should be larger than β when $\beta<1$, and less than β when $\beta>1$). The maximum possible value of ρ is also constrained by the filler volume fraction v_f. In the limit situation of $v_f=1$, there is only one possible choice of $\rho=a/b=1$. This explains that the possible values of ρ decreases with the increase of v_f, see Fig. 8 again.

Further comparisons between the C-S model and the S-S model are given in Fig. 9. It can be seen from Fig. 9 that the S-S model and the C-S model give almost the same thermal conductivity when $v_f \leq 0.3$ (see Figs. 9(a) and (b)). However, the C-S model presents much higher conductivity than the S-S model when $v_f > 0.5$ (see Figs. 9(c) and (d)). This suggests that if desired, the

effect of v_f and a judicious choice of models should be considered when we choose the optimum model and optimum configuration as explained above.

4 Conclusions

The two models, the ellipsoidal filament and square packing array unit cell model, and the rectangular filament and square array unit cell model, have been derived for the thermal conductivities of unidirectional composites in this paper. The dimensionless effective transverse thermal conductivities k_e^+ are expressed as a function of β, v_f, and the geometry ratio ρ $(=a/b)$ of the filler. The present analysis allows for a fairly precise evaluation of configuration performance and comparisons of different arrangements. The results show that if a composite is designed for insulation material, we should choose $\rho<1$, and if a composite is designed for heat dissipating purpose, we should choose $\rho>1$.

The composite science is a multi-discipline, concerning with fatigue, failure, thermal and other subjects. This paper only presents an analysis of thermal conductivity and its optimization for unidirectional composites. The scheme may be easily extended to tackle other two-dimensional arrays, such as the rectangular array of infinitely long elliptic cylinders, the rectangular array of rectangular cylinders etc., which will be investigated in our next work.

Acknowledgment

Nomenclatures

a = the axis length along X axis of the ellipse, m
b = the axis length along Y axis of the ellipse, m
k = thermal conductivity, W/m.K
L = length, m
l = length, m
Q = heat flow, W
R = resistance, Ω
T = temperature, K
v = volume fraction
x = coordinate
y = coordinate

Subscripts

e = effective
f = fiber
m = matrix
p = parallel
s = series
t = total

Superscript

$+$ = dimensionless

Greeks

β = ratio of thermal conductivities of filler to matrix of composites, $=k_f/k_m$
ρ = ratio of axis lengths along x-axis to along y-axis, $=a/b$

References

[1] Levy, E. K., 1971, "Optimum Plate Spacing for Laminar Natural Convection Heat Transfer from Parallel Vertical Isothermal Flat Plates," ASME J. Heat Transfer, **93**, pp. 463–465.
[2] Bar-Cohen, A., and Rohsenow, W. M., 1984, "Thermal Optimum Spacing of Vertical, Natural Convection Cooled, Parallel Plates," ASME J. Heat Transfer, **106**, pp. 116–123.
[3] Anand, N. K., Kim, S. H., and Fletcher, L. S., 1992, "The Effect of Plate Spacing on Free Convection Between Heated Parallel Plates," ASME J. Heat Transfer, **114**, pp. 515–518.
[4] Hu, M. H., and Chang, Y. P., 1973, "Optimization of Finned Tubes for Heat Transfer in Laminar Flow," ASME J. Heat Transfer, **95**, pp. 332–338.
[5] Fabbri, G., 1998, "Heat Transfer Optimization in Internally Finned Tubes Under Laminar Flow Conditions," Int. J. Heat Mass Transfer, **41**, pp. 1243–1253.
[6] Kim, S. J., Yoo, J. W., and Jang, S. P., 2002, "Thermal Optimization of a Circular-Sectored Finned Tube Using a Porous Medium Approach," ASME J. Heat Transfer, **124**, pp. 1026–1033.
[7] Brown, A., 1965, "Optimum Dimensions of Uniform Annular Fins," Int. J. Heat Mass Transfer, **8**, pp. 662–665.
[8] Ulman, A., and Kalman, H., 1987, "Efficiency and Optimized Dimensions of Annular Fins of Different Cross-Section Shapes," Int. J. Heat Mass Transfer, **32**, pp. 1105–1110.
[9] Kundu, B., and Das, P. K., 2001, "Performance Analysis and Optimization of Annular Fin with a Step Change in Thickness," ASME J. Heat Transfer, **123**, pp. 601–604.
[10] Liu, C. Y., 1960, "On minimum Weight Rectangular Radiating Fins," J. Aerosp. Sci., **27**, pp. 871.
[11] Aziz, A., and Kraus, A. D., 1996, "Optimum Design of Radiating and Convective-Radiating Fins," Heat Transfer Eng., **17**, pp. 44–78.
[12] Krikkis, R. N., and Razelos, P., 2002, "Optimum Design of Spacecraft Radiators with Longitudinal Rectangular and Triangular Fins," ASME J. Heat Transfer, **124**, pp. 805–811.
[13] Ogiso, K., 2001, "Assessment of Overall Cooling Performance in Thermal Design of Electronics Based on Thermodynamics," ASME J. Heat Transfer, **123**, pp. 999–1005.
[14] Bejan, A., 1979, "A Study of Entropy Generation in Fundamental Convective Heat Transfer," ASME J. Heat Transfer, **101**, pp. 718–725.
[15] Mawardi, A., and Pitchumani, R., 2003, "Optimal Temperature and Current Cycles for Curing of Composites Using Embedded Resistance Heating Elements," ASME J. Heat Transfer, **125**, pp. 126–136.
[16] Vynnycky, M., Ferrari, J., and Lior, N., 2003, "Some Analytical and Numerical Solutions to Inverse Problems Applied to Optimizing Phase-Transformation Tracking in Gas Quenching," ASME J. Heat Transfer, **125**, pp. 1–10.
[17] Aung, W., 1988, Cooling Technology for Electronic Equipment, Hemisphere, New York.
[18] Bejan, A., 1997, "Constructal-Theory Network of Conducting Paths for Cooling a Heat Generating Volume," Int. J. Heat Mass Transfer, **40**, pp. 799–816.
[19] Neagu, M., and Bejan, A., 2001, "Constructal Placement of High-Conductivity Inserts in a Slab: Optimal Design of Roughness," ASME J. Heat Transfer **123**, pp. 1184–1189.
[20] Xia, Z. Z., and Guo, Z. Y., 2001, "Simulations on Optimization of Thermal Conduction by Life Evolvement Processes," Advances on Natural Science (in Chinese), **11**, pp. 845–852.
[21] James, B. W., and Keen, G. S., 1985, "A Nomogram for the Calculation of the Transverse Thermal Conductivity of Uniaxial Composite Lamina," High Temp. - High Press., **17**, pp. 477–480.
[22] Ramani, K., and Vaidyanathan, A., 1995, "Finite Element Analysis of Effective Thermal Conductivity of Filled Polymeric Composites," J. Compos. Mater., **29**, pp. 1725–1740.
[23] Islam, Md. R., and Pramila, A., 1999, "Thermal Conductivity of Fiber Reinforced Composites by the FEM," J. Compos. Mater., **33**, pp. 1699–1715.
[24] Springer, G. S., and Tsai, S. W., 1967, "Thermal Conductivities of Unidirectional Materials," J. Compos. Mater., **1**, pp. 166–173.
[25] Pitchumani, R., and Yao, S. C., 1991, "Correlation of Thermal Conductivities of Unidirectional Fibrous Composites Using Local Fractal Techniques," ASME J. Heat Transfer, **113**, pp. 788–796.
[26] Zou, M. Q., Yu, B. M., and Zhang, D. M., 2002, "An Analytical Solution for Transverse Thermal Conductivities of Unidirectional Fiber Composites With Thermal Barrier," J. Phys. D, **35**, pp. 1867–1874.
[27] Thornburg, J. D., and Pears, C. D., 1965, "Prediction of the Thermal Conductivity of Filled and Reinforced Plastics," ASME Paper 65-WA/HT-4.
[28] Zehnder, P., Schlunder, E. U., 1970, "Thermal Conductivity of Granular Materials at Moderate Temperatures (in German)," Chem.-Ing.-Tech., **42**, pp. 933–941.
[29] Hus, C. T., Cheng, P., and Wong, K. W., 1995, "A Lumped-Parameter Model for Stagnant Thermal Conductivity of Spatially Periodic Porous Media," ASME J. Heat Transfer, **117**, pp. 264–269.
[30] Yu, B. M., and Cheng, P., 2002, "Fractal Models for the Effective Thermal Conductivity of Bi-Dispersed Porous Media," J. Thermophys. Heat Transfer, **16**, pp. 22–29.
[31] Lu, S. Y., 1995, "The Effective Thermal Conductivities of Composites with 2-D Arrays of Circular and Square Cylinders," J. Compos. Mater., **29**, pp. 483–506.
[32] James, B. W., Wostenholm, G. H., Keen, G. S., and Mclvor, S. D., 1987, "Prediction and Measurement of the Thermal Conductivity of Composite Materials," J. Phys. D, **20**, pp. 261–268.

Turbulent Plane Couette Flow and Scalar Transport at Low Reynolds Number

Chun-Ho Liu

e-mail: liuchunho@graduate.hku.uk
Department of Mechanical Engineering,
The University of Hong Kong,
Hong Kong

The turbulence structure and passive scalar (heat) transport in plane Couette flow at Reynolds number equal to 3000 (based on the relative speed and distance between the walls) are studied using direct numerical simulation (DNS). The numerical model is a three-dimensional trilinear Galerkin finite element code. It is found that the structures of the mean velocity and temperature in plane Couette flow are similar to those in forced channel flow, but the empirical coefficients are different. The total (turbulent and viscous) shear stress and total (turbulent and conductive) heat flux are constant throughout the channel. The locations of maximum root-mean-square streamwise velocity and temperature fluctuations are close to the walls, while the location of maximum root-mean-square spanwise and vertical velocity fluctuations are at the channel center. The correlation coefficients between velocities and temperature are fairly constant in the center core of the channel. In particular, the streamwise velocity is highly correlated with temperature (correlation coefficient ≈ −0.9). At the channel center, the turbulence production is unable to counterbalance the dissipation, in which the diffusion terms (both turbulent and viscous) bring turbulent kinetic energy from the near-wall regions toward the channel center. The snapshots of the DNS database help explain the nature of the correlation coefficients. The elongated wall streaks for both streamwise velocity and temperature in the viscous sublayer are well simulated. Moreover, the current DNS shows organized large-scale eddies (secondary rotations) perpendicular to the direction of mean flow at the channel center. [DOI: 10.1115/1.1571084]

Keywords: Computational, Finite Element, Heat Transfer, Turbulence

1 Introduction

In addition to turbulent flow, turbulent transport of heat and mass is of great importance in most engineering applications. For example, indoor air quality, motorway/railway tunnel ventilation, atmospheric pollutant dispersal, and contaminant mixing in oceans and rivers. Recent developments in supercomputation, both hardware and software, have made the direct numerical simulation (DNS) of turbulence feasible. Even though the current DNS databases are restricted to low Reynolds number and simple flow geometry, they capture the detailed transient flow behaviors quantitatively. These flow parameters are usually unable to be measured experimentally to good accuracy (for example, near-wall fluctuating quantities and velocity-pressure correlation).

This study uses DNS to investigate the turbulent flow and scalar transport mechanism in plane Couette flow at Reynolds number, based on the relative speed and distance between the walls, equal to 3000. The velocity and scalar boundary conditions are kept constant at the walls, while they are periodic in the streamwise and spanwise directions. The similarities and differences between plane Couette flow and more well-studied forced channel flow are also compared.

Fully developed turbulent forced channel flow, because of its geometric simplicity, has been studied extensively from both experimental [1,2,3] and numerical approaches [4,5,6]. The flow between the upper and lower stationary walls is driven by a mean streamwise pressure gradient. The geometry of plane Couette flow is exactly the same as that of forced channel flow. However, instead of mean pressure gradient, the driving force in Couette flow

is a constant total shear stress through the fluid. The shear stress is maintained by either one moving wall and one stationary wall, or two walls moving in opposite directions.

Early studies focused on the transition from laminar to turbulence in Couette flow. Using DNS, Lundbladh and Johansson [7] found that the transitional Reynolds number is about 1500 (with our definition of Reynolds number). Measurements showed that the transitional Reynolds number is 1480±40, and fully developed turbulent flow can be obtained at Reynolds number equal to 1800 [8,9]. DNS of Couette flow at Re=12,000 [10] calculated coherent structure in the channel center core, that is in contrast to forced channel flow. Bech et al. [11] compared their DNS with measurements at Reynolds number equal to 5200, and they also reported the similarity (near-wall turbulence) and difference (non-zero turbulent kinetic energy production at the channel center) between Couette flow and forced channel flow. Regarding the coherent structure (roll cells) in Couette flow, Komminaho et al. [12] performed DNS sensitivity tests for the size of horizontal domain at Reynolds number equal to 3000, and found that the roll cells contain about 10% of the turbulent kinetic energy. By DNS at Re=10,640, Papavassiliou and Hanratty [13] further confirmed that the roll cells are spatially and temporally persistent, which can be considered as secondary flow rather than turbulence. Other factors affecting the turbulence structure in Couette flow, such as rotation [14,15] and wavy surface [16] have been reported elsewhere.

With the calculated flow field, the scalar distribution can be calculated by considering the scalar transport (advection-diffusion) equation. Kim and Moin [17] employed a DNS to study the heat transfer (mass transport) in forced channel flow for different Prandtl (Schmidt) numbers. The calculations agree well with experimental and empirical results, but the use of isothermal boundary conditions made the DNS less practical to realistic situations. Kasagi et al. [18] revisited the problems by employing a

more practical constant time-averaged heat flux boundary condition on the walls. However, the temperature field is no longer horizontally homogeneous and there is a mean temperature gradient in the streamwise direction. An extensive review on the methodology and contribution of DNS to turbulent transport was discussed in Kasagi and Shikazono [19]. Using DNS of forced channel flow at different Reynolds number (Re_τ=150, 180 or 395), several studies have focused on the effect of Prandtl number (Pr=0.025 to 10) to heat transfer [20,21,22]. Recently, Tiselj et al. [23] included simulating the unsteady heat condition on the walls for a forced channel flow at Re_τ=150 and Pr=0.71 or 7.

On the other hand, numerical studies of scalar transport in Couette flow are very limited. Instead of DNS, Torii and Yang [24] employed a $k-\epsilon$ model to study the heat transfer mechanism in Couette flow. They focused on the turbulence statistics, both flow and temperature, calculated by turbulence model.

The following sections describe the mathematical model, simulation parameters and computational details of the current DNS. Then the turbulence statistics, both calculated flow and scalar fields are discussed. Afterward, I discuss the turbulent kinetic energy budget balance and the large scale structures of flow and scalar transport. Finally, the conclusions are drawn in Section 5.

2 Mathematical Model

I consider incompressible flow of Newtonian fluid, in which the governing equations are the momentum equation

$$\frac{\partial u_i}{\partial t} + \frac{\partial}{\partial x_j} u_i u_j = -\frac{\partial p}{\partial x_i} + \frac{1}{Re} \frac{\partial^2 u_i}{\partial x_j \partial x_j} \quad (1)$$

and the continuity equation

$$\frac{\partial u_i}{\partial x_i} = 0, \quad (2)$$

where x_i (i=1,2,3) are the Cartesian coordinates, u_i are the velocity components, t is the time, p is the kinematic pressure, and Re ($=UH/\nu$, where ν is the kinematic viscosity) is the Reynolds number. The equations are expressed in tensor notation and the usual summation convention on repeated indices is employed. All variables in Eq. (1) and (2) are nondimensionalized by the reference length scale H and the reference velocity scale U.

With the calculated flow field, the temperature is obtained by integrating the equation of conservation of energy

$$\frac{\partial T}{\partial t} + \frac{\partial}{\partial x_i} T u_i = \frac{1}{Re\ Pr} \frac{\partial^2 T}{\partial x_i \partial x_i}. \quad (3)$$

T is the temperature which is nondimensionalized by the reference temperature scale T ($=\Delta T/2$, where ΔT is the temperature difference between the walls) and the Prandtl number is set to 0.71 (air). The buoyancy force is neglected and thus the temperature is considered as a passive scalar in this study. I use temperature as the scalar in this paper and present the DNS as a heat transfer problem. In fact, the temperature and Prandtl number can be replaced by scalar mixing ratio and Schmidt number, respectively, for mass transfer problems.

For turbulent shear flow, it is also convenient to use wall variables which are denoted by a superscript +. The reference velocity scale is the friction velocity $u_\tau = (\tau_w/\rho)^{1/2}$, where τ_w is the mean shear stress on the walls and ρ is the fluid density. The reference length scale is ν/u_τ. The reference temperature scale in wall variable is the friction temperature

$$T_\tau = \frac{\alpha \left.\frac{\partial\langle T\rangle}{\partial z}\right|_w}{u_r}, \quad (4)$$

where α is the thermal diffusivity and $\alpha\partial\langle T\rangle/\partial z|_w$ is the mean surface heat flux on the walls.

3 Computational Issues

3.1 Numerical Method. The current DNS is carried out by employing a finite element code solving Eq. (1), (2), and (3). The implicit dependence of velocity and pressure is decoupled by a fractional-step method, which is second-order accuracy in time. The Galerkin method is used to construct the weighted residual formulation of the mathematical model. The velocity, pressure and temperature are approximated by the same trilinear interpolating polynomials based on brick elements. The advection terms in skew-symmetric form $(\partial u_i u_j/\partial x_j + u_j \partial u_i/\partial x_j)/2$ are solved by the explicit third-order Adams-Bashforth method. The diffusion terms are solved by the implicit second-order Crank-Nicolson method. The detailed methodology is discussed elsewhere [25,26].

3.2 Computational Domain and Boundary Conditions The computational domain for plane Couette flow is a horizontally homogeneous rectangular channel of height H enclosed by two rigid walls at the top and bottom. The streamwise direction is x, the spanwise is y and the direction perpendicular to the channel walls is z. The dimensions of the computational domain are 6H $\times$5H$\times$H. The upper wall moves at constant velocity U while the lower wall is stationary. No-slip velocity and isothermal boundary conditions are applied on the walls. The dimensionless temperature boundary conditions are prescribed as -1 and 1 on the upper and lower walls, respectively. Periodic boundary conditions are assumed in the streamwise and spanwise directions for both flow and temperature calculations. Because of the boundary conditions, even we use an equal-order finite element method, pressure boundary conditions are not necessary and the velocity boundary conditions are sufficient to close the mathematical model.

3.3 Simulation Parameters. The computational domain is discretized into 144$\times$96$\times$128 brick elements in x, y, and z directions, respectively. The dimensionless element sizes in the streamwise and spanwise directions are evenly distributed (Δx =0.042,Δy=0.052). In the wall-normal direction, the elements are stretched away from the walls, in which the dimensionless element size Δz ranges from 0.0035 at the walls to 0.0172 at the channel center. In this study, the Reynolds number is prescribed as 3,000 that turbulence is fully developed. The dimensionless friction velocity is 0.0352 and the Reynolds number based on friction velocity Re_τ ($=u_\tau H/2\nu$) is 52.8. The dimensionless element sizes in wall units, ($\Delta x^+,\Delta y^+,\Delta z^+$), are (4.4352, 5.4912, 0.3696, to 1.8163). The spatial resolution employed in the current DNS is comparable to other numerical studies, and is adequate to capture the dissipation range at the Reynolds number considered. The dimensionless time incremental interval Δt is 0.005 (Δt^+ =$\Delta t u_\tau^2/\nu$=0.01859) that satisfies the Courant-Fredrichs-Lewy requirement of the third-order Adams-Bashforth method.

The current DNS was started from the analytical solution to laminar flow ($u=z$, $v=0$, $w=0$ and $T=1-2z$). With the buoyancy term switching on initially, the turbulence was triggered by small random perturbations imposed on the laminar temperature field. After 3 dimensionless time units (H/U), the buoyancy term was switched off and the calculation continued for another 100H/U for turbulence development and reaching statistically steady state. Afterward, the results were collected for another 500H/U (1858 viscous time unit) that were archived at every 0.5H/U.

4 Results and Discussions

4.1 Turbulence Statistics. The vertical profile of dimensionless mean streamwise velocity $\langle u\rangle$ in dimensionless global coordinates is shown in Fig. 1(a). Statistics are denoted by parentheses $\langle\ \rangle$, that are the spatial (in the streamwise and spanwise directions) and temporal averaging. The S-shape velocity profile is antisymmetric about the horizontal centerline, in which the flow velocity at the channel center is uniform while its gradient near
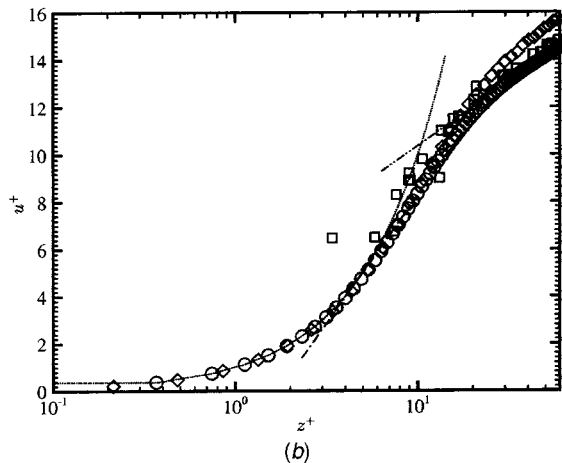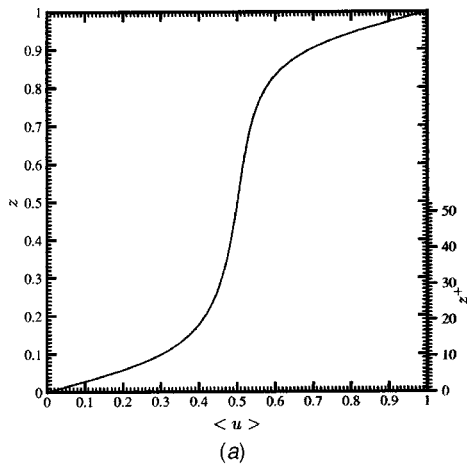
Fig. 1 Vertical profiles of dimensionless mean streamwise velocity $\langle u \rangle$ for turbulent Couette flow at Re=3000: (a) dimensionless global coordinates; and (b) wall coordinates. $\bigcirc$: present calculation, $\cdots\cdots$: $u^+ = z^+$, $-\cdot-\cdot-\cdot$: $u^+ = 4.7 \ln z^+ -2.56$, $-\cdot\cdot-\cdot\cdot-\cdot\cdot$: $u^+ = 2.33 \ln z^+ +4.96$, $\diamond$: DNS from Kim et al. [4], and $\square$: measurements from Žukauskas and Šlančiauskas [28].

Fig. 2 Vertical profiles of mean vertical turbulent flux $\langle u''w'' \rangle$ (——), mean viscous flux $-1/\text{Re}\,\partial\langle u\rangle/\partial z$ ($- - - - -$), and their sum ($\cdots\cdots$), normalized by u_τ^2 for turbulent Couette flow at Re=3000.

the walls is sharp. Unlike forced channel flow the velocity gradient at the channel center $\partial\langle u\rangle/\partial z|_{z=0.5}$ of Couette flow is non-zero ($=0.2$), whose magnitude is comparable to that calculated by Komminaho et al. [12]. The vertical profile of mean streamwise velocity in wall variables u^+ is illustrated in Fig. 1(b) in a semi-logarithmic form as a function of wall unit z^+. The mean streamwise velocity can be divided into a viscous sublayer ($u^+ = z^+$, $0 \leq z^+ < 5$), a buffer region ($u^+ = 5 \ln z^+ - 3.05$, $5 \leq z^+ \leq 30$ [27] p. 504), and a logarithmic region ($u^+ = 2.5 \ln z^+ + 5.5$ [4]) from $z^+ = 30$ extending to the channel center. With the fine spatial resolution, the viscous sublayer is well resolved that agrees with analytical solution, DNS for forced channel flow [4] as well as measurement [28]. Due to the domination of viscous motions in viscous sublayer, the mean streamwise velocity profile could be well represented by a linear function in wall units in either forced channel, Couette or open channel [29] flows. In the buffer region, the best-fit profile of the mean streamwise velocity based on the current DNS is $u^+ = 4.7 \ln z^+ - 2.56$, which is very close to that reported by Warsi [27]. Because of the small Reynolds number, the logarithmic region of the present DNS is small ($z^+ \leq 53$). The best-fit log-linear variation of mean streamwise velocity in the logarithmic region based on the current DNS is $u^+ = 2.33 \ln z^+ + 4.96$, which is different from that reported by other forced channel flows [4]. The reported log-law constants for

Couette flow from other numerical and experimental results in the form of $u^+ = A \ln z^+ + B$ are $2.3 \leq A \leq 2.55$ and $4.3 \leq B \leq 6.0$ [12,13,16]. Thus, the current DNS for Couette flow is consistent with other studies.

For plane Couette flow, the conservation of mean vertical momentum is

$$\frac{1}{\text{Re}}\,\frac{\partial\langle u\rangle}{\partial z} - \langle u''w'' \rangle = \frac{1}{\text{Re}}\,\frac{\partial\langle u\rangle}{\partial z}\bigg|_w, \qquad (5)$$

where the superscript $''$ denotes the deviation from statistical mean $u'' = u - \langle u\rangle$. Eq. (5) exhibits a constant total shear stress ($=$ wall shear stress) throughout the channel. The calculated total shear stress closely satisfies the exact solution Eq. (5) (Fig. 2) in which the error is no more than 2% comparing to the theoretical one. The central difference scheme is employed to calculate the velocity gradient whose truncation error is of first order of grid spacing $\mathcal{O}(\Delta z)$. The current error in the calculated total shear stress is thus consistent with the vertical grid spacing ($0.0035 \leq \Delta z \leq 0.0172$) employed. In forced channel flow, the total shear stress is a linear profile with zero shear stress at the channel center and maximum shear stress at the walls. On the contrary, in Couette flow the turbulent shear stress $-\langle u''w'' \rangle$ is symmetric about the channel horizontal centerline whose maximum is at the channel center. The non-zero turbulent shear stress and velocity gradient signify that the turbulence production $-\langle u''w'' \rangle\partial\langle u\rangle/\partial z$ is non-zero at the channel center and increases the local turbulent kinetic energy. The intersections of turbulent and viscous shear stresses as shown in Fig. 2 thus represent the locations of maximum turbulent kinetic energy production. The momentum transport is mainly accomplished by turbulent shear stress in the channel center core. Approaching the walls, the turbulent shear stress decreases, while the mean velocity gradient and thus the viscous shear stress $1/\text{Re}\,\partial\langle u\rangle/\partial z$ increase. The maximum turbulent shear stress is 96% of the total one locating at the channel center. Oppositely, in forced channel flow the maximum turbulent shear stress is about 75% of the total one locating in between the channel center and the walls.

The vertical profiles of root-mean-square velocity fluctuation normalized by friction velocity $\langle u_i'' u_i'' \rangle^{1/2}/u_\tau$ are shown in Fig. 3(a) in dimensionless global coordinates that, as expected, the profiles are symmetric about the horizontal centerline. In spite of the non-zero turbulence production in the channel center core, the dimensionless streamwise root-mean-square velocity fluctuation $\langle u''u'' \rangle^{1/2}/u_\tau$ has a local minimum at the channel center, while the local maxima are near the walls. On the other hand, the dimen-
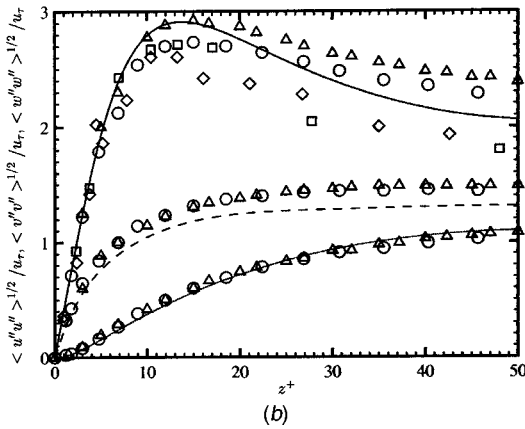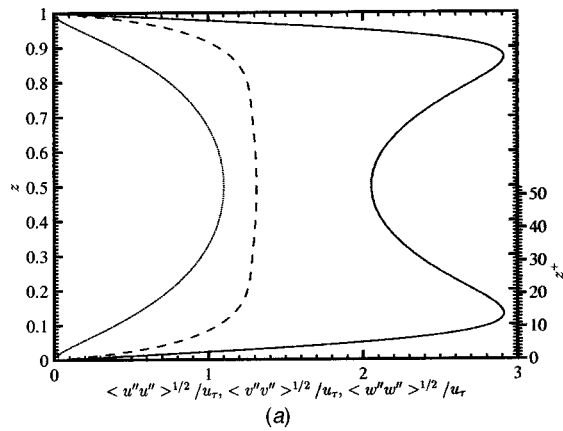
Fig. 3 Vertical profiles of root-mean-square velocity fluctuation normalized by wall friction velocity for turbulent Couette flow at Re=3000: (a) dimensionless global coordinates; and (b) wall coordinates. ——: $\langle u''u''\rangle^{1/2}/u_\tau$, — — — — —: $\langle v''v''\rangle^{1/2}/u_\tau$ and ·····: $\langle w''w''\rangle^{1/2}/u_\tau$. ◇: measurement from Aydin and Leutheusser [30], □: measurement from Bech et al. [11], △: DNS from Lee and Kim [10], and ○: DNS from Papavassiliou and Hanratty [13].

Fig. 4 Vertical profiles of dimensionless mean temperature $\langle T \rangle$ for turbulent Couette flow at Re=3000: (a) dimensionless global coordinates; and (b) wall coordinates. ○: present calculation, ·····: $T^+=\mathrm{Pr}z^+$, — · — · — ·: $T^+=2.63 \ln z^+ + 1.2$, □: measurement from Žukauskas and Šlančiauskas [28], △: DNS from Kim and Moin [17], and ◇: LES from Cabot and Moin [34].

sionless spanwise $\langle v''v''\rangle^{1/2}/u_\tau$ and vertical $\langle w''w''\rangle^{1/2}/u_\tau$ root-mean-square velocity fluctuations increase monotonically from zero at the walls to maximum at the channel center. However, the studies at higher Reynolds number (Re=8,000 [16] and Re =10,640 [13]) found slight local minima of spanwise and vertical root-mean-square velocity fluctuations at the channel center. The spanwise root-mean-square velocity fluctuation is fairly constant ($\langle v''v''\rangle^{1/2}/u_\tau=0.13$) in the channel center core while its vertical counterpart shows a gentle maximum ($\langle w''w''\rangle^{1/2}/u_\tau=0.11$). Oppositely, in forced channel flow all the minima of streamwise, spanwise and vertical root-mean-square velocity fluctuations locate at the channel center. Moreover, the magnitudes of dimensionless spanwise and vertical root-mean-square velocity fluctuations are almost the same (= 0.6 [4]). The spanwise root-mean-square velocity fluctuation calculated by the current DNS is 18% higher than its vertical counterpart at the channel center. In wall units (Fig. 3(b)), the current DNS agrees well with measurements [30,11] and DNS [10,13]. The local minimum dimensionless streamwise root-mean-square velocity fluctuation is 2 at the channel center, that is within the broad range from various existing experimental and numerical results. Indeed, the current calculated root-mean-square velocity fluctuations at the channel center are greater than those of forced channel flow by a factor of two. This would be due to the non-zero turbulence production at the channel center. The location of the present calculated maximum streamwise velocity fluctuation ($z^+=14$) agrees well with that calculated from other DNS of turbulent shear flow. The magnitude of

the maximum streamwise root-mean-square velocity fluctuation is more close to that calculated by Lee and Kim [10] than that from other experimental and numerical results. It is overpredicted by 5% compared with the well-accepted calculated values ($\langle u''u''\rangle^{1/2}/u_\tau=2.77$) in turbulent shear flow. This would be attributed to the different flow configurations.

Similar to the vertical profile of mean streamwise velocity, the vertical profile of mean temperature $\langle T \rangle$ is antisymmetric about the horizontal centerline as shown in Fig. 4(a). The mean temperature is more uniform in the channel center core while its gradient is steeper near the walls. In the current DNS the dimensionless friction temperature T_τ is 0.086 and the dimensionless mean temperature gradient at the channel center $\partial \langle T \rangle / \partial z|_{z=0.5}$ is -0.48. As shown in Fig. 4(b), near the walls ($z^+ \leq 5$) are conductive sublayers where molecular diffusion dominates the heat transfer. Moreover, the mean temperature profile (in wall variable) is a linear function of the distance (in wall units) from the wall ($T^+ = \mathrm{Pr}z^+$). For region farther away from the walls ($z^+ > 20$), the heat transfer is dominated by turbulent heat fluxes. The mean temperature profile could be approximated by a logarithmic distribution $T^+ = A \ln z^+ + B$ where A and B are constants. The value of A is barely affected by the flow in a wide range of Reynolds and Prandtl numbers ($1.83 \leq A \leq 2.1$), while B strongly depends on the Prandtl number of the working fluid. For Pr=0.71, B is 3.8 based on measurement [28]. The constants based on the best-fit profile of the current DNS are $A=2.63$ and $B=1.2$. The DNS of
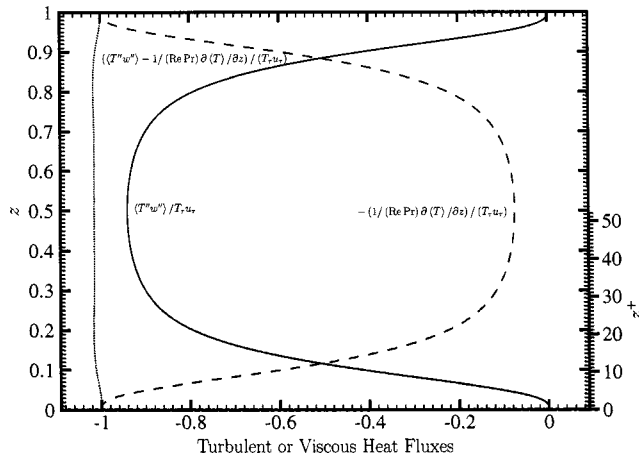
Fig. 5 Vertical profiles of mean vertical turbulent heat flux $\langle T''w''\rangle$ (——), mean vertical viscous heat flux $-1/(\mathrm{Re\,Pr})\,\partial\langle T\rangle/\partial z$ (− − − − − −), and their sum (······) normalized by $T_\tau u_\tau$ for turbulent Couette flow at Re=3000

Fig. 7 Vertical profiles of correlation coefficients between streamwise u'' and vertical w'' velocities (——), temperature T'' and streamwise velocity u'' (− − − − − −), and temperature T'' and vertical velocity w'' (······)

forced channel flow at $\mathrm{Re}_\tau=150$ and $\mathrm{Pr}=0.7$ [18] finds that the constants A and B are 2.78 and 2.09, respectively. At $\mathrm{Re}_\tau=180$ and $\mathrm{Pr}=2$, the DNS of open channel flow [31] finds $A=3.68$ and $B=10.1$. At $\mathrm{Re}_\tau=640$, the large-eddy simulation (LES) of forced channel flow [32] finds $A=2.12$ for $\mathrm{Pr}=1$, 100 and 200. Previous experimental, DNS and LES studies have shown a broad range of the values of the constant terms A and B. Thus, it is hard to draw a conclusion about the form of the logarithmic function in turbulent shear flow or even plane Couette flow. Further investigations are necessary to quantify the constant terms.

Ensemble averaging the energy conservation equation Eq. (3) we obtain the mean vertical heat fluxes equation

$$\frac{1}{\mathrm{Re\,Pr}}\frac{\partial\langle T\rangle}{\partial z}-\langle T''w''\rangle=\frac{1}{\mathrm{Re\,Pr}}\frac{\partial\langle T\rangle}{\partial z}\bigg|_w. \qquad (6)$$

Hence, the sum of conductive $1/\mathrm{Re\,Pr}\,\partial\langle T\rangle/\partial z$ and turbulent vertical heat fluxes $-\langle T''w''\rangle$ is constant ($=$wall surface heat flux) throughout the channel. The current DNS closely satisfies Eq. (6) (Fig. 5). The error of 2% of the calculated total heat flux is truncation error which is caused by calculating the temperature gradi-

ent by central difference method as discussed previously. Analogous to momentum transport, the vertical heat transfer is dominated by conductive diffusion in the near-wall regions, while it is generally governed by turbulent diffusion in the channel center core. Even though the Reynolds number in the current DNS is relatively small, the vertical turbulent heat flux is large which is 94% of the total one at the channel center. Because of the en-

(a)

(b)

Fig. 8 Vertical profile of root-mean-square temperature fluctuation $\langle T''T''\rangle^{1/2}$ normalized by friction temperature T_τ for turbulent Couette flow at Re=3000: (a) dimensionless global coordinates; and (b) wall coordinates.
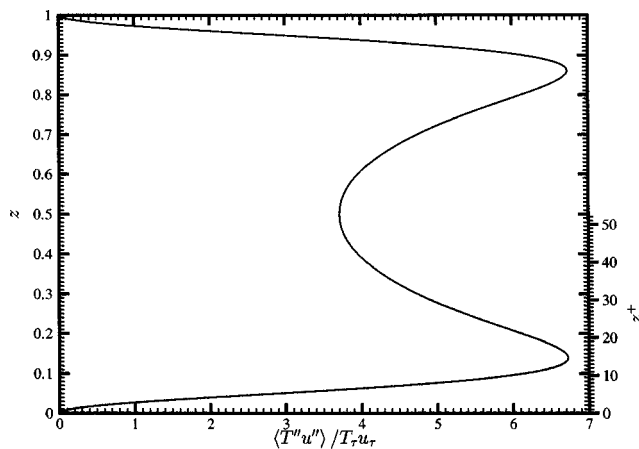

Fig. 6 Vertical profiles of mean streamwise turbulent heat flux $\langle T''u''\rangle$ normalized by $T_\tau u_\tau$ for turbulent plane Couette flow at Re=3000
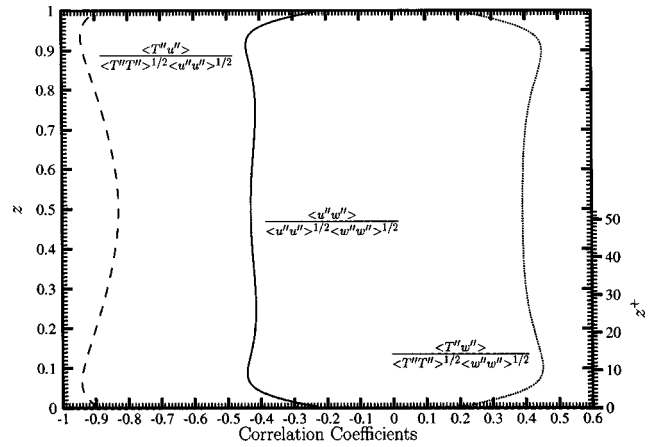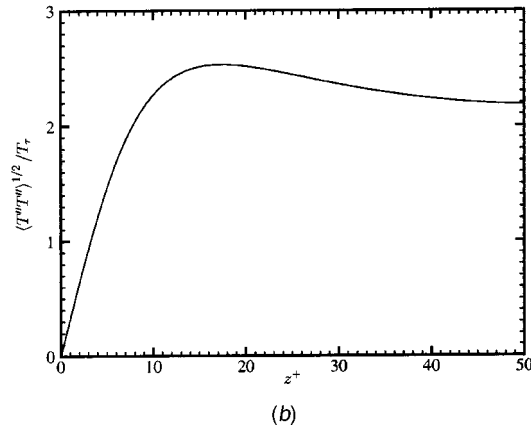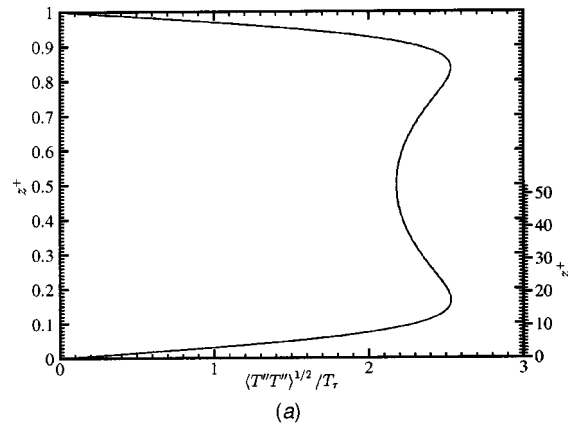
hanced turbulent mixing, the mean temperature is relatively gentler at the channel center as shown in Fig. 4(a). The maximum dimensionless vertical turbulent heat flux is slightly smaller than the maximum dimensionless vertical turbulent shear stress that would be caused by the magnitude of the Prandtl number. The Prandtl number used in this study is smaller than one, as a result, the proportion of conductive heat transfer (when compared with the total one) is greater than that of viscous momentum transfer. In forced channel flow, both conductive and turbulent vertical heat fluxes are zero at the channel center. Moreover, the maximum turbulent vertical heat flux is 70% of the total one [18,33] locating in between the channel center and the walls. The product of vertical turbulent heat flux and temperature gradient is the production term in the temperature fluctuation $\langle T''T'' \rangle$ budget. Thus, the production of turbulent temperature fluctuation is non-zero in the channel center core, and the locations of maximum production are the intersections of the curves in Fig. 5 ($z = 0.12$ and $z^+ = 12$).

The maximum dimensionless streamwise turbulent heat flux $\langle T''u'' \rangle / T_\tau u_\tau$ is 6.7 at $z^+ = 14$ (Fig. 6). Previous studies of heat transfer for forced channel flow have reported a wide range of the value of maximum streamwise turbulent heat flux. The DNS by Kim and Moin [17] and Kasagi et al. [18] find values of 5.5 and 6 (at $z^+ = 15$), respectively. The values obtained from LES [34,33] are 9. It is thus hard to assess the accuracy of the current DNS on calculating the streamwise turbulent heat flux. Nonetheless, the current DNS is reasonable in that regard. Unlike forced channel flow, the dimensionless mean streamwise turbulent heat flux in Couette flow is non-zero at the channel center that is equal to 3.7.

The vertical profiles of correlation coefficients between streamwise and vertical velocities, streamwise velocity and temperature, and vertical velocity and temperature are shown in Fig. 7. The correlation coefficient between streamwise and vertical velocities $\langle u''w'' \rangle / \langle u''u'' \rangle^{1/2} \langle w''w'' \rangle^{1/2}$ is fairly constant (-0.41 to -0.45) in

most part of the channel except in the viscous sublayers (-0.23 to -0.4). The maximum negative correlation coefficient is -0.45 in the near-wall region that is comparable to that obtained in forced channel flow [4]. The peaks locate at $z = 0.9$ ($z^+ = 10$), that are very close, but do not coincide exactly with the locations of maximum turbulence production in turbulent kinetic energy budget balance. The correlation coefficient between streamwise velocity and temperature is high ($-0.8 \leq \langle T''u'' \rangle / \langle T''T'' \rangle^{1/2} \langle u''u'' \rangle^{1/2} \leq -0.94$) throughout the channel whose negative maximum correlation coefficients are -0.94 at $z^+ = 6$. These calculated features in Couette flow are very similar to those obtained in forced channel flow [17,18]. In contrast, the negative correlation coefficient between streamwise velocity and temperature at the channel center in forced channel flow (-0.5) is much smaller than that in Couette flow (-0.83). The correlation coefficient between vertical velocity and temperature $\langle T''w'' \rangle / \langle T''T'' \rangle^{1/2} \langle w''w'' \rangle^{1/2}$ has minima (0.2) on the walls. It increases with increasing distance from the walls resulting in a peak (0.45) at $z^+ = 10$ and then decreases slightly thereafter. In fact, it is almost constant (0.4) in the channel center core.

The vertical profile of the calculated dimensionless root-mean-square temperature fluctuation $\langle T''T'' \rangle^{1/2} / T_\tau$ is shown in Fig. 8(a) in global dimensionless coordinates. Similar to the root-mean-square streamwise velocity fluctuation, the root-mean-square temperature fluctuation is symmetric about the horizontal centerline and its minimum (2.2) is at the channel center. The maximum dimensionless root-mean-square temperature fluctuation is 2.5 at $z^+ = 17$ as shown in Fig. 8(b).

4.2 Budgets for Turbulence Variables. In fully developed turbulent plane Couette flow, the dimensionless turbulent kinetic energy budget $\langle u_i'' u_i'' / 2 \rangle$ is governed by the following equation

$$\frac{D}{Dt}\left\langle \frac{1}{2} u_i'' u_i'' \right\rangle = \underbrace{-\langle u''w'' \rangle \frac{\partial \langle u \rangle}{\partial z}}_{\text{production}} \underbrace{- \frac{1}{\text{Re}} \left\langle \frac{\partial u_i''}{\partial x_j} \frac{\partial u_i''}{\partial x_j} \right\rangle}_{\text{dissipation}} \underbrace{+ \frac{1}{\text{Re}} \frac{\partial^2}{\partial z \partial z} \left\langle \frac{1}{2} u_i'' u_i'' \right\rangle}_{\text{viscous diffusion}} \underbrace{- \frac{\partial}{\partial z} \langle w''p'' \rangle}_{\substack{\text{velocity-pressure} \\ \text{gradient correlation}}} \underbrace{- \frac{\partial}{\partial z} \left\langle \frac{1}{2} u_i'' u_i'' w'' \right\rangle}_{\text{turbulent diffusion}},$$

$$\underbrace{\phantom{- \frac{\partial}{\partial z} \langle w''p'' \rangle - \frac{\partial}{\partial z} \left\langle \frac{1}{2} u_i'' u_i'' w'' \right\rangle}}_{\text{total diffusion}}$$

(7)

where $D/Dt = \partial/\partial t + \partial/\partial x_j$. The production term draws energy from the mean flow to the turbulence. The viscous diffusion, velocity-pressure gradient correlation and turbulent diffusion terms construct the total diffusion term, which redistributes the turbulent kinetic energy spatially (only vertically in horizontally homogeneous flow). Finally, the dissipation is an irreversible sink of turbulent kinetic energy. The above terms perform the energy cascade from large to small scale in turbulent flow. The vertical profiles of the terms in the turbulent kinetic energy budget for Couette flow are shown in Fig. 9. The most obvious difference compared with forced channel flow is the non-zero production and dissipation terms at the channel center. Moreover, the production and dissipation do not counterbalance each other. The production in the channel center core is not large enough for the energy loss by dissipation and velocity-pressure gradient correlation. The locations of maximum production are within the buffer regions ($z = 0.1$ and $z^+ = 10$). The energy then diffuses toward the channel center (mainly accomplished by turbulent diffusion) and the walls (accomplished by both turbulent diffusion and viscous diffusion). Turbulent kinetic energy is redistributed by viscous diffusion in the viscous sublayer where the production is much smaller than the dissipation. The locations of equal viscous diffusion and turbulent diffusion coincide with the locations of maximum produc-

tion. However, because of the velocity-pressure gradient correlation, the location of maximum negative total diffusion is slightly farther away from the walls than that of maximum production. At the walls, the energy loss by dissipation is totally counterbalanced by the energy gain by viscous diffusion.

The equation for vertical turbulent shear stress budget $\langle u''w'' \rangle$ for Couette flow is

$$\frac{D}{Dt} \langle u''w'' \rangle = \underbrace{-\langle w''w'' \rangle \frac{\partial \langle u \rangle}{\partial z}}_{\text{production}} \underbrace{- \frac{2}{\text{Re}} \left\langle \frac{\partial u''}{\partial x_i} \frac{\partial w''}{\partial x_i} \right\rangle}_{\text{dissipation}}$$

$$\underbrace{- \left(\left\langle u'' \frac{\partial p''}{\partial z} \right\rangle + \left\langle w'' \frac{\partial p''}{\partial x} \right\rangle \right)}_{\text{velocity-pressure gradient correlation}}$$

$$\underbrace{+ \frac{1}{\text{Re}} \frac{\partial^2}{\partial z \partial z} \langle u''w'' \rangle}_{\text{viscous diffusion}} \underbrace{- \frac{\partial}{\partial z} \langle u''w''w'' \rangle}_{\text{turbulent diffusion}}.$$

$$\underbrace{\phantom{+ \frac{1}{\text{Re}} \frac{\partial^2}{\partial z \partial z} \langle u''w'' \rangle - \frac{\partial}{\partial z} \langle u''w''w'' \rangle}}_{\text{total diffusion}}$$

(8)
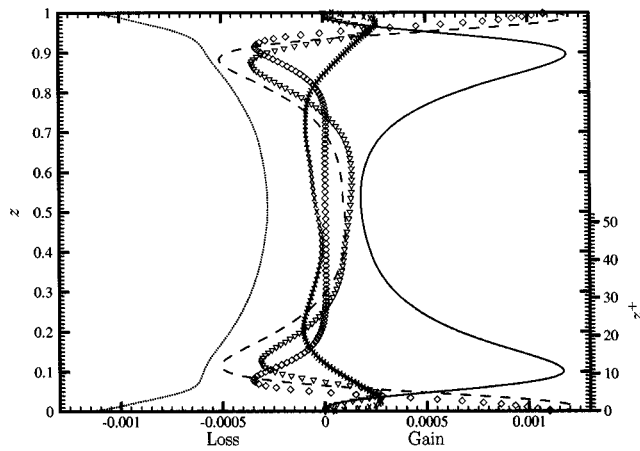
Fig. 9 Vertical profiles of the terms in turbulent kinetic energy $\langle u_i'' u_j''/2 \rangle$ **budget Eq. (7) for turbulent Couette flow at Re=3000.** —— **production,** ⋯⋯ **dissipation,** ◇ **viscous diffusion,** × **velocity-pressure gradient correlation,** ▽ **turbulent diffusion and** − − − − − − **total diffusion**

Fig. 10 Vertical profiles of the terms in Reynolds stress $\langle u'' w'' \rangle$ **budget Eq. (8) for turbulent Couette flow at Re=3000.** ——**turbulent production,** ⋯⋯ **dissipation,** ◇ **viscous diffusion,** ▽ **turbulent diffusion,** − − − − − − **total diffusion,** □ **velocity-pressure gradient correlation** $-\langle u'' \partial p''/\partial z \rangle$, △ **velocity-pressure gradient correlation** $-\langle w'' \partial p''/\partial x \rangle$ **and** — · — · — · **total velocity-pressure gradient correlation**

The vertical profiles of the terms in Eq. (8) are shown in Fig. 10. The vertical turbulent shear stress budget is generally dominated by the counterbalance between production and velocity-pressure gradient correlation, while the energy transport by total diffusion and dissipation is relatively small throughout the channel. Energy diffuses toward the walls and the channel center from locations of larger production (near-wall region, $z = 0.15$). Similar to the turbulent kinetic energy budget, the production is non-zero at the channel center, that is counterbalanced mainly by the velocity-pressure gradient correlation.

The equation for temperature variance budget $\langle T'' T'' \rangle$ for Couette flow is

$$\frac{D}{Dt} \langle T'' T'' \rangle = \underbrace{-2 \langle T'' w'' \rangle \frac{\partial \langle T \rangle}{\partial z}}_{\text{production}} - \underbrace{\frac{2}{\text{Pr}} \left\langle \frac{\partial T''}{\partial x_i} \frac{\partial T''}{\partial x_i} \right\rangle}_{\text{dissipation}}$$

$$+ \underbrace{\underbrace{\frac{1}{\text{Pr}} \frac{\partial^2}{\partial z \partial z} \langle T'' T'' \rangle}_{\text{molecular diffusion}} - \underbrace{\frac{\partial}{\partial z} \langle T'' T'' w'' \rangle}_{\text{turbulent diffusion}}}_{\text{total diffusion}}. \quad (9)$$

The vertical profile of the terms in the temperature variance budget is shown in Fig. 11. Unlike the temperature variance budget for forced channel flow [33], about 25% of the turbulent kinetic energy dissipated at the channel center is transported by diffusion from the buffer regions, in which turbulent diffusion dominates the energy transport. The maximum production locates at $z = 0.12$ ($z^+ = 12$), where both turbulent diffusion and viscous diffusion transport energy toward the channel center and the near-wall regions. The energy transport mechanism for temperature variance is similar to that of turbulent kinetic energy. The locations of maximum total diffusion coincide with those of maximum production, however, they do not coincide with the locations of maximum temperature variance. In the buffer regions, comparing to turbulent kinetic energy budget, the energy of temperature variance transported by molecular diffusion is greater than the turbulent kinetic energy transported by viscous diffusion. It is because the thermal diffusivity is greater than

the kinematic viscosity. Thus, we expect almost the same magnitude of molecular diffusion for turbulent kinetic energy and energy of temperature variance budget transfer if the Prandlt number is close to one. In the conductive sublayers, the dissipation is counterbalanced generally by the molecular diffusion. Kasagi et al. [18] finds a local minimum of dissipation at $y^+ = 8$ which is not observed in the current DNS. Instead, a region of relatively gentle change of dissipation is observed in the nearby location.

The equation for streamwise turbulent heat flux budget $\langle T'' u'' \rangle$ for Couette flow is

Fig. 11 Vertical profiles of the terms in temperature variance $\langle T'' T'' \rangle$ **budget Eq. (9) for turbulent Couette flow at Re=3000.** ——**turbulent production,** ⋯⋯ **dissipation,** ◇ **viscous diffusion,** ▽ **turbulent diffusion and** − − − − − − **total diffusion.**

$$\frac{D}{Dt}\langle T''u''\rangle = -\langle u''w''\rangle\frac{\partial\langle T\rangle}{\partial z} - \langle T''w''\rangle\frac{\partial\langle u\rangle}{\partial z} \underbrace{- \left(\frac{1}{\text{Re}} + \frac{1}{\text{Re Pr}}\right)\left\langle\frac{\partial u''}{\partial x_i}\frac{\partial T''}{\partial x_i}\right\rangle}_{\text{dissipation}} \underbrace{- \left\langle T''\frac{\partial p''}{\partial z}\right\rangle}_{\substack{\text{temperature-pressure}\\\text{gradient correlation}}}$$

$$\underbrace{+ \frac{1}{\text{Re}}\frac{\partial}{\partial z}\left\langle u''\frac{\partial T''}{\partial z}\right\rangle + \frac{1}{\text{Re Pr}}\frac{\partial}{\partial z}\left\langle T''\frac{\partial u''}{\partial z}\right\rangle}_{\text{molecular diffusion}} \underbrace{- \frac{\partial}{\partial z}\langle T''u''w''\rangle}_{\text{turbulent diffusion}}.$$

(The braces under "production" span the first two terms, and "total diffusion" spans molecular and turbulent diffusion.)

(10)

The vertical profiles of the terms in Eq. (10) are shown in Fig. 12. The temperature-pressure gradient correlation and the dissipation terms draw energy from the mean flow throughout the channel. In the near-wall region the energy sink is dominated by dissipation. However, at the channel center, the magnitudes of energy-sink from dissipation and temperature-pressure gradient correlation terms are almost the same. Similar to the turbulent kinetic energy budget balance, at the channel center the non-zero production is not large enough for energy loss. The energy gain at the channel center is generally accomplished by turbulent diffusion in addition to the production, so as to counterbalance the energy loss. The magnitudes of viscous diffusion and diffusive diffusion are similar in most part of the channel. While close to the viscous sublayer, the diffusive diffusion is about 30% higher than the viscous diffusion. The difference would be attributed to the thermal diffusivity, which is greater than the kinematic viscosity about 30% (Pr=0.71). A similar magnitude of viscous and diffusive diffusion is expected if the Prandlt number is about unity.

The equation for vertical turbulent heat flux budget $\langle T''w''\rangle$ for plane Couette flow is

$$\frac{D}{Dt}\langle T''w''\rangle = -\langle w''w''\rangle\frac{\partial\langle T\rangle}{\partial z} \underbrace{- \left(\frac{1}{\text{Re}} + \frac{1}{\text{Re Pr}}\right)\left\langle\frac{\partial w''}{\partial x_i}\frac{\partial T''}{\partial x_i}\right\rangle}_{\text{dissipation}} \underbrace{- \left\langle T''\frac{\partial p''}{\partial z}\right\rangle}_{\substack{\text{temperature-pressure}\\\text{gradient correlation}}} \underbrace{+ \frac{1}{\text{Re}}\frac{\partial}{\partial z}\left\langle w''\frac{\partial T''}{\partial z}\right\rangle + \frac{1}{\text{Re Pr}}\frac{\partial}{\partial z}\left\langle T''\frac{\partial w''}{\partial z}\right\rangle}_{\text{molecular diffusion}} \underbrace{- \frac{\partial}{\partial z}\langle T''w''w''\rangle}_{\text{turbulent diffusion}}.$$

(11)

The vertical profile of the terms in the vertical turbulent heat flux budget is shown in Fig. 13. Unlike the streamwise turbulent heat flux budget, the production and temperature-pressure gradient correlation almost counterbalance each other throughout the channel. The dissipation is negligible except in the viscous sublayer that is about 15% of the total energy loss. Even though the energy of the vertical turbulent heat flux transported by total diffusion is small, total diffusion transports energy toward the channel center to bal-

ance the energy loss by temperature-pressure gradient correlation, and transports energy toward the viscous sublayer to balance the energy loss by dissipation. The turbulent diffusion is generally greater than the viscous diffusion unless in the conductive sublayer.

4.3 Structure of the Flow and Temperature Fields. The previous sections describe the turbulence statistics and energy budget characteristics by looking into the statistical quantities.
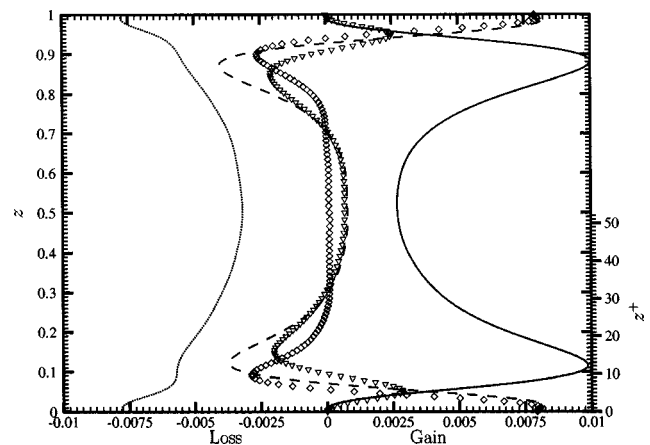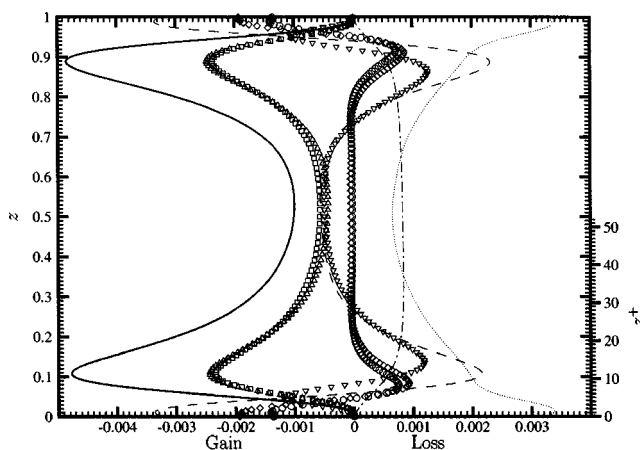

Fig. 12 Vertical profiles of the terms in streamwise turbulent heat flux $\langle T''u''\rangle$ budget Eq. (10) for turbulent Couette flow at Re=3000. □ turbulent production $-\langle u''w''\rangle\partial\langle T\rangle/\partial z$, △ turbulent production $-\langle T''w''\rangle\partial\langle u\rangle/\partial z$, —— total turbulent production, ⋯⋯ dissipation, ◇ viscous diffusion $1/\text{Re}\,\partial/\partial z\langle u'\partial T'/\partial z\rangle$, ○ conductive diffusion $1/(\text{Re Pr})\partial/\partial z\langle T'\partial u''/\partial z\rangle$, ▽ turbulent diffusion, − − − − − − total diffusion, and —·—·—·— temperature-pressure gradient correlation.
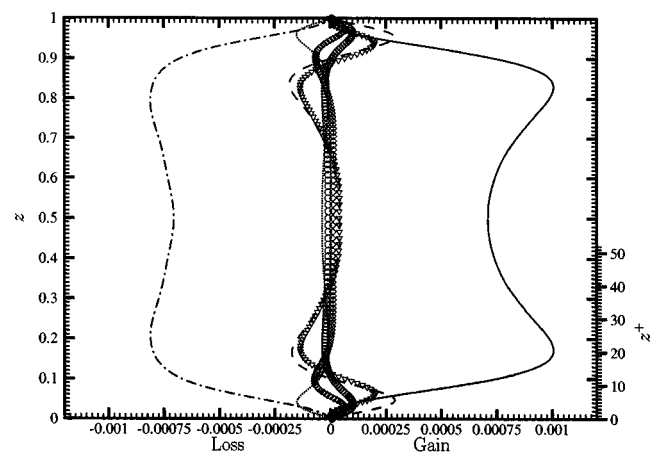
Fig. 13 Vertical profiles of the term in vertical turbulent heat flux $\langle T''w''\rangle$ budget Eq. (11) for turbulent Couette flow at Re=3000. ——total turbulent production, ⋯⋯ dissipation, ◇ viscous diffusion $1/\text{Re}\,\partial/\partial z\langle w'\partial T'/\partial z\rangle$, ○ conductive diffusion $1/(\text{Re Pr})\partial/\partial z\langle T'\partial w''/\partial z\rangle$, ▽ turbulent diffusion, − − −total diffusion, and —·—·—· temperature-pressure gradient correlation.
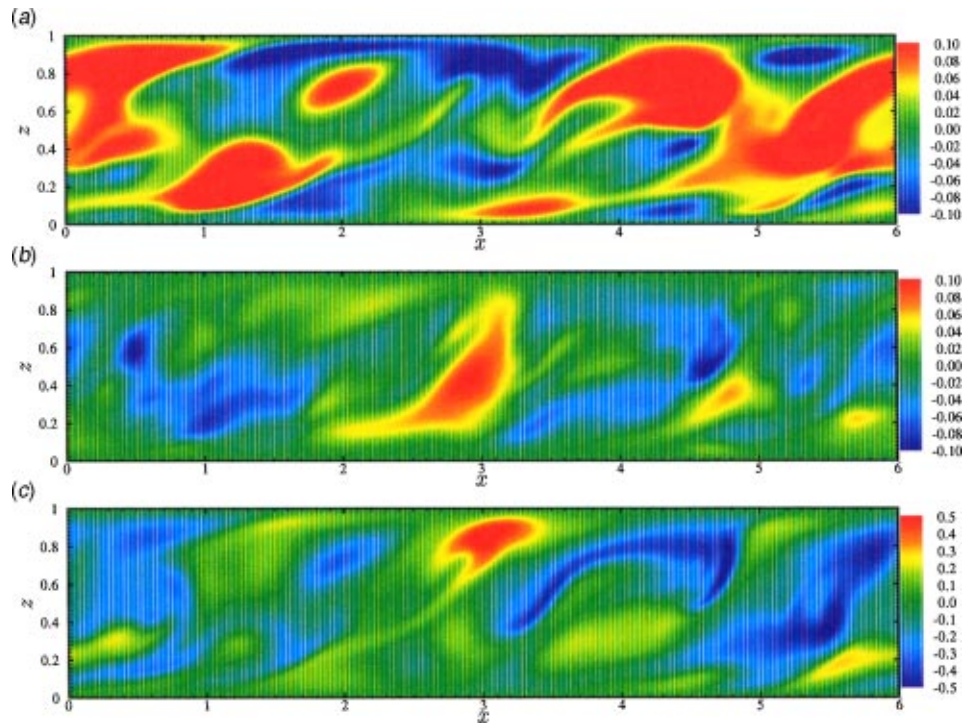
Fig. 14 Contours of fluctuating variables on the x-z plane in the middle of the y domain: (a) u'' contours; (b) w'' contours; and (c) T'' contours.
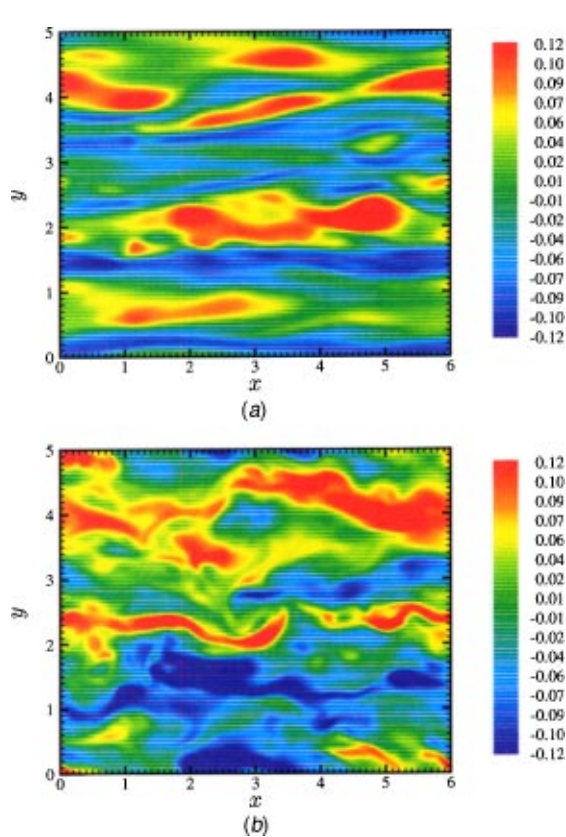
Fig. 15 Contours of streamwise velocity fluctuation u'' on the x-y plane at: (a) $z^+=5$ and (b) $z=0.5$.
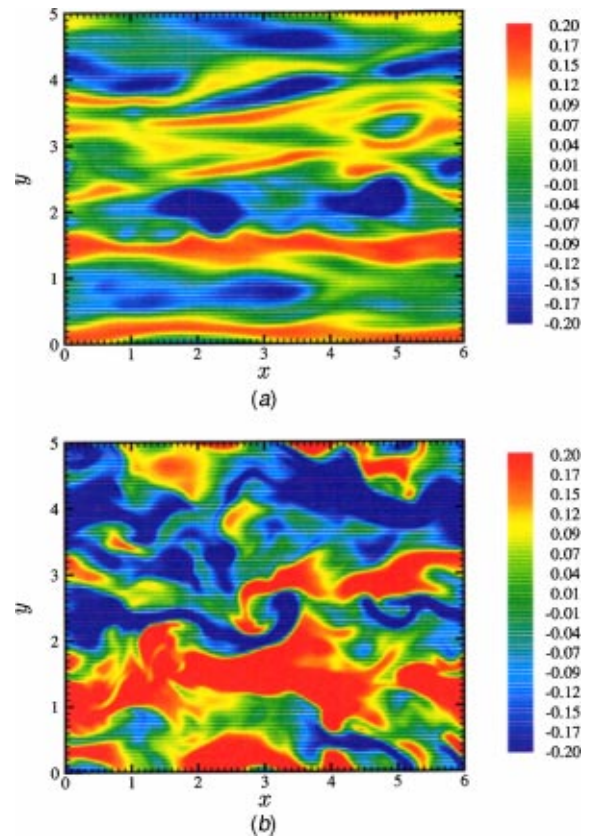
Fig. 16 Contours of temperature fluctuation T'' on the x-y plane at: (a) $z^+=5$ and (b) $z=0.5$.
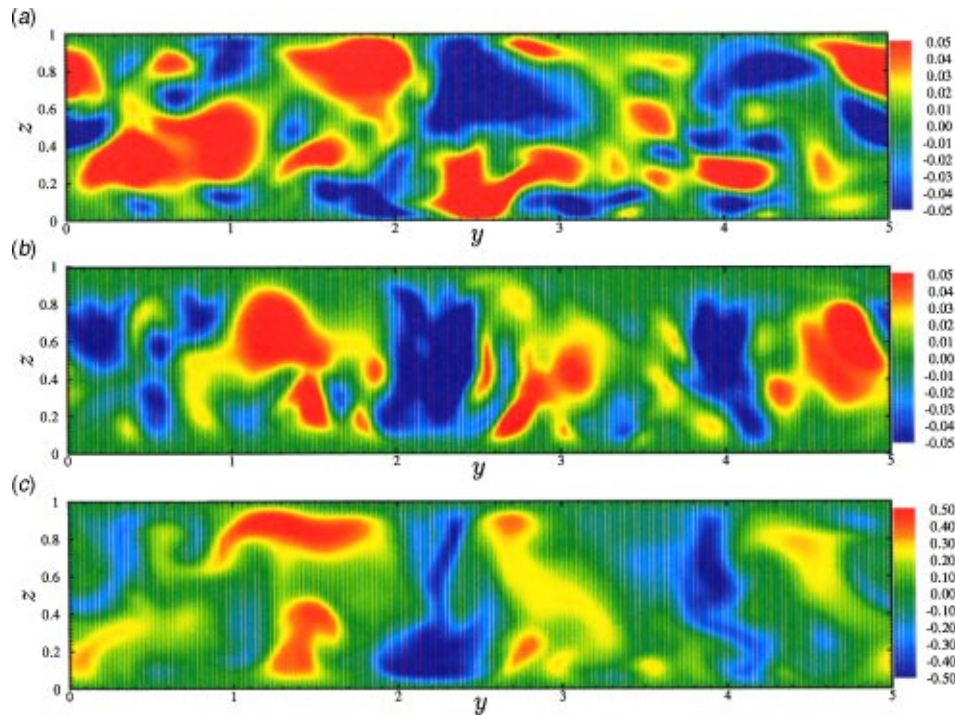
Fig. 17 Contours of fluctuating variables on the y-z plane in the middle of the x domain: (a) v'' contours, (b) w'' contours, and (c) T'' contours.

Additional perspective about transport mechanisms, both momentum and energy, could be obtained by looking into the instantaneous flow and temperature fields.

Figure 14 shows the contours of instantaneous fluctuating streamwise velocity u'', vertical velocity w'' and temperature T'' on the x-z plane in the middle of the y-domain ($y = 2.5$). These figures are snapshots of the DNS and are considered as typical flow and temperature structures. The negative correlation coefficient between streamwise and vertical velocities $\langle u''w'' \rangle / \langle u''u'' \rangle^{1/2} \langle w''w'' \rangle^{1/2}$ is also depicted in Fig. 14(a) and (b). Obviously, most regions of positive streamwise velocity fluctuation coincide with regions of negative vertical velocity fluctuation, and vice versa. As a result, the correlation coefficient between streamwise and vertical velocities is negative in most part of the computational domain. The nature of the correlation coefficients between streamwise velocity and temperature $\langle T''u'' \rangle / \langle T''T'' \rangle^{1/2} \langle u''u'' \rangle^{1/2}$, and vertical velocity and temperature $\langle T''w'' \rangle / \langle T''T'' \rangle^{1/2} \langle w''w'' \rangle^{1/2}$ can also be explained in a similar manner. Structure of hot and cold fluids in the form of S-shape are aligned across the channel as shown in Fig. 14(c). These large structures cross the centerline in Couette flow that enhance the heat transfer between the walls.

Figure 15(a) shows the contours of the instantaneous fluctuating streamwise velocity u'' on the x-y plane at $z^+ = 5$. The typical wall streaks for wall-layer turbulence in viscous sublayer is shown as elongated regions of high speed fluid located adjacent to the low speed fluid. The coherent structure of streaks is also observed in the center plane $z = 0.5$ as shown in Fig. 15(b) but it is not as elongated as that in the viscous sublayer. The temperature fluctuation T'' is also organized in streaks carrying elongated alternatively high and low contours in the conductive sublayer (Fig. 16(a)). The organized structure of temperature fluctuation is also observed at the channel center (Fig. 16(b)). Because of their high correlation coefficients, the contours of streamwise velocity and scalar fluctuations are highly correlated (positive streamwise velocity fluctuation and negative temperature fluctuation, and vice versa).

Papavassiliou and Hanratty [13] found organized large eddies in the center core of the channel perpendicular to the mean flow (roll cells). The effects of the secondary flow to the temperature distribution is depicted in Fig. 17. Unlike forced channel flow in which coherent structures are only observed in the near-wall region, large scale coherent structures of alternative positive and negative velocity fluctuations (both spanwise and vertical) are observed in the center core of Couette flow. The coherent structures are in the form of secondary rotations, resulting in the alternative high and low temperature fluctuation.

5 Conclusions

The turbulence structure and heat transfer mechanism in plane Couette flow at Reynolds number equal to 3000 is investigated by DNS. The numerical model is a three-dimensional finite element code with the use of Galerkin weighted residual method. I demonstrate the turbulence statistics, turbulent kinetic energy balance and large-scale coherent structures, and discuss the differences between turbulent Couette and forced channel flows. The mean velocity and temperature profiles for Couette flow are similar to those of forced channel flow that can be divided into viscous sublayer ($u^+ = z^+$), buffer region and logarithmic region. Based on the current DNS, the best-fit profile of the buffer and logarithmic regions are $u^+ = 4.7 \ln z^+ - 2.56$ and $u^+ = 2.33 \ln z^+ + 4.96$, respectively. The current DNS closely satisfies the analytical solution to the total shear stress for Couette flow which is constant throughout the channel. Unlike forced channel flow, the production terms of turbulent Couette flow are non-zero at the channel center. Moreover, the maximum turbulent shear stress (96%, locates at the channel center) is greater than its forced channel counterpart (75%, locates in-between the channel center and walls). Based on the current DNS data base, The root-mean-square velocity fluctuations are calculated that are comparable to other DNS and measurements. Similar to the mean velocity profile, the temperature profile for plane Couette flow can be divided into three characteristic regions as discussed above. The logarithmic tem-

perature profile based on the current DNS is $T^+ = 2.63 \ln z^+ + 1.2$. However, previous DNS, LES and measurements showed a block range of the values of the constant terms, further studies are required to quantify accurately the constant terms in the logarithmic region. Similar to the mean vertical momentum equation, the current DNS exhibits constant total heat flux across the Couette flow channel that agrees well with the analytical solution. The temperature is highly correlated with the streamwise velocity in which the correlation coefficient is as high as -0.8 to 0.94. The root-mean-square temperature fluctuation is computed whose dimensionless maximum is 2.5 locating at $z^+ = 17$. The energy budgets for the turbulence variables are also analyzed. In contrast to forced channel flow, production for the turbulence variables energy budgets is non-zero at the channel center. However, the production is unable to counterbalance the dissipation. The total diffusion transports energy to compensate the energy-sink. The nature of correlation coefficients of turbulent plane Couette flow is explained by looking into the instantaneous fluctuating variables. Similar to other turbulent shear flows, well organized and elongated streaks are observed in the viscous sublayer of turbulent Couette flow. In addition, large scale coherent structures and secondary rotations, and their effects to heat transfer in turbulent plane Couette flow are discussed.

Acknowledgments

References

[1] Eckelmann, H., 1974, "The Structure of the Viscous Sublayer and the Adjacent Wall Region in a Turbulent Channel Flow," J. Fluid Mech., **65**, pp. 439–459.

[2] Hussain, A. K. M. F., and Reynolds, W. C., 1975, "Measurements in Fully Developed Turbulent Channel Flow," J. Fluids Eng., **97**, pp. 568.

[3] Kreplin, H.-P., and Eckelmann, H., 1979, "Behavior of the Three Fluctuating Velocity Components in the Wall Region of a Turbulent Channel Flow," Phys. Fluids, **22**(7), pp. 1233–1239.

[4] Kim, J., Moin, P., and Moser, R., 1987, "Turbulence Statistics in Fully Developed Channel Flow at Low Reynolds Number," J. Fluid Mech., **177**, pp. 133–166.

[5] Moser, R. D., Kim, J., and Mansour, N. N., 1999, "Direct Numerical Simulation of Turbulent Channel Flow Up to $Re_\tau=590$," Phys. Fluids, **11**, pp. 943–945.

[6] Abe, H., Kawamura, H., and Matsuo, Y., 2001, "Direct Numerical Simulation of a Fully Developed Turbulent Channel Flow With Respect to the Reynolds Number Dependence," J. Fluids Eng., **123**, pp. 382–393.

[7] Lundbladh, A., and Johansson, A. V., 1991, "Direct Simulation of Turbulent Spots in Plane Couette Flow," J. Fluid Mech., **229**, pp. 499–516.

[8] Daviaud, F., Hegseth, J., and Bergé, P., 1992, "Subcritical Transition to Turbulence in Plane Couette Flow," Phys. Rev. Lett., **69**, pp. 2511–2514.

[9] Malerud, S., Maloy, K. J., and Goldburg, W. I., 1995, "Measurement of Turbulent Velocity Fluctuations in a Planar Couette Cell," Phys. Fluids, **7**, pp. 1949–1955.

[10] Lee, H. J., and Kim, J., 1991, "The Structure of Turbulence in a Simulated Plane Couette Flow," in Paper 5-3, *Proc. 8th Symposium on Turbulent Shear Flows*, Munich.

[11] Bech, K. H., Tillmark, N., Alfredsson, P. H., and Andersson, Helge I., 1995, "An Investigation of Turbulent Plane Couette Flow at Low Reynolds Numbers," J. Fluid Mech., **286**, pp. 291–325.

[12] Komminaho, J., Lundbladh, A., and Johansson, A. V., 1996, "Very Large Structures In Plane Turbulent Couette Flow," J. Fluid Mech., **320**, pp. 259–285.

[13] Papavassiliou, D. V., and Hanratty, T. J., 1997, "Interpretation of Large-Scale Structures Observed in a Turbulent Plane Couette Flow," Int. J. Heat Fluid Flow, **18**, pp. 55–69.

[14] Bech, K. H., and Andersson, H. I., 1996, "Secondary Flow in Weakly Rotating Turbulent Plane Couette Flow," J. Fluid Mech., **317**, pp. 195–214.

[15] Bech, K. H., and Andersson, H. I., 1997, "Turbulent Plane Couette Flow Subject to Strong System Rotation," J. Fluid Mech., **347**, pp. 289–314.

[16] Sullivan, P. P., McWilliams, J. C., and Moeng, C.-H., 2000, "Simulation of Turbulent Flow Over Idealized Water Waves," J. Fluid Mech., **404**, pp. 47–85.

[17] Kim, J., and Moin, P., 1989, "Transport of Passive Scalar in a Turbulent Channel Flow," *Turbulent Shear Flow* J.-C. Andre, J. Cousteix, F. Durst, B. E. Launder, F. W. Schmidt, and J. H. Whitelaw, eds., Springer-Verlag, Berlin, **6**, pp. 85–96.

[18] Kasagi, N., Tomita, Y., and Kuroda, A., 1992, "Direct Numerical Simulation of Passive Scalar Field in a Turbulent Channel Flow," Journal of Heat Transfer, **114**, pp. 598–606.

[19] Kasagi, N., and Shikazono, N., 1995, "Contribution of Direct Numerical Simulation to Understanding and Modelling Turbulent Transport," Proc. R. Soc. London, Ser. A, **451**, pp. 257–292.

[20] Kawamura, H., Ohsaka, K., Abe, H., and Yamamoto, K., 1998, "DNS of Turbulent Heat Transfer in Channel Flow With Low to Medium-High Prandtl Number Fluid," Int. J. Heat Mass Transf., **19**, pp. 482–491.

[21] Kawamura, H., Abe, H., and Matsuo, Y., 1999, "DNS of Turbulent Heat Transfer in Channel Flow With Respect to Reynolds and Prandtl Number Effects," Int. J. Heat Fluid Flow, **20**, pp. 196–207.

[22] Na, Y., and Hanratty, T. J., 2000, "Limiting Behavior of Turbulent Scalar Transport Close to a Wall," Int. J. Heat Mass Transf., **43**, pp. 1749–1758.

[23] Tiselj, I., Bergant, R., Mavko, B., Bajsic, I., and Hetsroni, G., 2001, "DNS of Turbulent Heat Transfer in Channel Flow With Heat Conduction in the Solid Wall," J. Heat Transfer, **123**, pp. 849–857.

[24] Torii, S., and Yang, W.-J., 1997, "Heat Transfer Analysis of Turbulent Parallel Couette Flows Using Anisotropic $k-\epsilon$ Model," Numer. Heat Transfer, Part A, **31**, pp. 223–234.

[25] Liu, C.-H., and Leung, D. Y. C., 2001, "Development of a Finite Element Solution for the Unsteady Navier-Stokes Equations Using Projection Method and Fractional-θ-Scheme," Computer Methods in Applied Mechanics and Engineering, **190**(32–33), pp. 4301–4317.

[26] Liu, C.-H., 2001, "A Cubic Finite Element Solution to the Unsteady Incompressible Navier-Stokes Equations," Computer Methods in Applied Mechanics and Engineering, submitted.

[27] Warsi, Z. U. A., 1992, *Fluid Dynamics: Theoretical and Computational Approaches*, CRC Press.

[28] Žukauskas, A., and Šlančiauskas, A., 1987, *Heat Transfer in Turbulent Fluid Flows*, Hémisphere Publishing Corporation.

[29] Yamamoto, Y., Kunugi, T., and Serizawa, A., 2001, "Turbulence Statistics and Scalar Transport in an Open-Channel Flow," Journal of Turbulence, **2**, pp. 1–16.

[30] Aydin, E. M., and Leutheusser, H. I., 1991, "Plane-Couette Flow Between Smooth and Rough Walls," Exp. Fluids, **11**, pp. 302–312.

[31] Handler, R. A., Saylor, J. R., Leighton, R. I., and Rovelstad, A. L., 1999, "Transport of a Passive Scalar at a Shear-Free Boundary in Fully Developed Turbulent Open Channel Flow," Phys. Fluids, **11**(9), pp. 2607–2625.

[32] Calmet, I., and Magnaudet, J., 1997, "Large-Eddy Simulation of High-Schmidt Number Mass Transfer in a Turbulent Channel Flow," Phys. Fluids, **9**(2), pp. 438–455.

[33] Wang, W.-P., and Pletcher, R. H., 1996, "On the Large Eddy Simulation of a Turbulent Channel Flow With Significant Heat Transfer," Phys. Fluids, **8**(12), pp. 3354–3366.

[34] Cabot, W., and Moin, P., 1993, "Large Eddy Simulation of Scalar Transport With the Dynamic Subgrid-Scale Model," *Large Eddy Simulation of Complex Engineering and Geophysical Flow*, Boris Galperin and Steven A. Orszag, eds., Cambridge University Press, New York, pp. 141–158.

Effect of Tip Clearance on the Thermal and Hydrodynamic Performance of a Shrouded Pin Fin Array

Kevin A. Moores
e-mail: kamoores@eng.umd.edu
CALCE Electronic Products and Systems Center,
Mechanical Engineering Dept.,
University of Maryland,
College Park, MD 20742

Yogendra K. Joshi
e-mail: Yogendra.Joshi@me.GaTech.edu
George W. Woodruff School of
Mechanical Engineering,
Georgia Institute of Technology,
Atlanta, GA 30332-0405

The effect of introducing tip clearance to a liquid cooled array of shrouded pins fins is examined. Three arrays of height to diameter ratio ranging from 0.5 to 1.1 were evaluated experimentally. The arrays were exposed to a uniform heat flux of 0.02 to 0.26 W/mm² and cooled with water through a nominal Reynolds number range of 200 to 10,000. Tip clearance of 0 to 25% of pin height was assessed. Mean heat transfer rates and adiabatic pressure drop across the array were determined and empirical correlations are proposed. The introduction of clearance was seen to increase overall heat transfer in some cases. [DOI: 10.1115/1.1621897]

Keywords: Channel Flow, Conjugate, Electronics, Heat Transfer, Heat Exchangers

Introduction

Shrouded pin fin arrays such as those shown at the top of Fig. 1 are a common geometry employed to enhance forced convection heat transfer in a variety of applications. A sizable body of work is available regarding the thermal and hydrodynamic performance of such arrays. By far, the most prominent application is in the cooling of the trailing edge of turbine blades, with the vast majority of shrouded pin fin literature having emerged from this field. In such cases, the pin fins are designed into the interior of the blade and act as both extended surfaces for heat transfer as well as cross-members between the upper and lower airfoil surfaces for structural integrity. Armstrong and Winstanley [1] provide a general review of pin fin heat transfer as applied to turbine cooling applications. More recent studies have been performed by Hwang [2–4], Chyu [5–10], Li [11,12] and Lau [13,14], among others.

Because the pin fins double as structural members in turbine blades, they normally span the full distance between the upper and lower endwalls as shown in Fig. 1(A). As a result, little attention has been paid to the effect of tip clearance (Fig. 1(B)) on the thermal and hydrodynamic performance of the cooling passages. However, the use of shrouded pin fin arrays is becoming increasingly more common in electronics cooling applications as well. In these applications, the pin fins generally extend from the base of a heat sink, with the tips of the pins flush against a flat shroud, which in essence is the same configuration employed in the turbine cooling passages. However in the case of electronics cooling systems, the pin fins normally are not required to perform a structural role. Therefore, in these cases, the inclusion of clearance above one end of the pins is feasible.

Only a handful of researchers have considered tip clearance in relation to pin fin arrays. Sparrow et al. [15] were the first to look at its effect on an array of cylindrical pin fins. They compared the overall heat transfer from arrays with tip clearances ranging from 14 to 244% of pin length. They found only a 20% decrease in Nu between these two extremes, but made no comparisons to the case of zero clearance. Peng [16] compared the performance of the standard turbine blade geometry (i.e., no clearance) to that where pin fins extend from each endwall, spanning less than half the channel height, thereby creating a clearance gap through the cen-ter of the channel. The tests included what amounts to 0, 50, and 200% tip clearance. It was found that while the overall heat transfer was lower with the partial pins, the ratio of $\overline{Nu}/f$ generally increased, thereby producing a higher rate of heat transfer per unit of pumping power.

Jubran et al. [17] considered the effect of transverse and streamwise pin spacing in addition to tip clearance. They considered both inline and staggered arrays of right circular cylinders with tip clearances of 0, 50, and 100% and proposed separate empirical heat transfer correlations for each case. More recently, Chyu et al. [10] looked at the relative performance for tip clearances of 0, 25, 50, 100, and 200%. They found the case of 25% clearance produced a $\overline{Nu}$ only 1.5% lower than that with no clearance, while 200% clearance resulted in a 45% reduction. Chyu's pin fins differed from those of the earlier studies and the current study in that they were of square cross-sectional area in an in-line arrangement, rather than cylindrical pins in a staggered arrangement

The authors are aware of no studies to date that have systematically considered the effect of low levels of tip clearance (between 0 and 25%) on the performance of a cylindrical pin fin array. With this in mind, there are a number of reasons to believe that the inclusion of such clearance can actually enhance the overall heat transfer capabilities of a given cooling system. The most obvious reason is that exposing the tips of the pin fins to the cooling fluid increases the total heat transfer area. In the case to be considered here, which is forced liquid cooling of power electronics, the pin fins tend to have relatively low height to diameter ratios (H/D) due to the high convection coefficients involved with liquid cooling. They are also closely packed, so the pin tip area can represent a considerable portion of the total area of the array.

There may be several less obvious reasons to introduce tip clearance as well. Sparrow [18] has shown that for a single pin fin attached to a wall at only one end, the relative rate of heat transfer is higher at, and adjacent to the tip of the fin, than along the lateral face of the pin away from the tip. In other words, the exposed tip of the pin not only increases the total heat transfer area, it may produce a higher rate of local heat transfer than the rest of the pin does on average. Another byproduct of tip clearance may be the introduction of three-dimensional behavior into the flow field around the pin fins. Chyu [10] reported increased heat transfer along the endwall, upstream of the array's leading edge, when tip
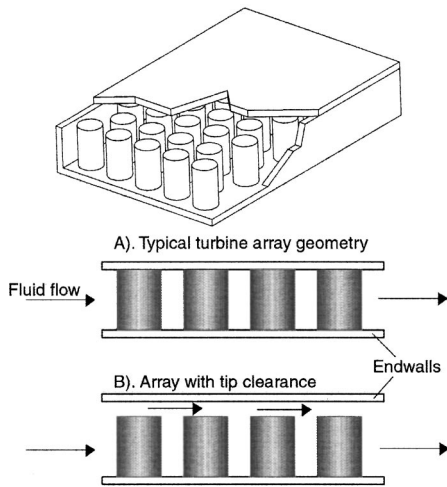
Fig. 1 Typical shrouded pin fin arrangement; (A) without and (B) with tip clearance

Table 1 Array dimensions and material properties

Plate:	#1	#2	#3
W_{bp}, W_A:		0.072, 0.054	
L_{bp}, L_A:		0.106, 0.065	
t_{bp}:		0.005	
H:	0.002	0.003	0.004
D_{ew}:	0.004	0.004	0.004
D_t:	0.00367	0.0035	0.00333
D_{ave}:	0.00384	0.00375	0.00367
S_T:	0.005	0.005	0.005
S_L:	0.00433	0.00433	0.00433
H/D_{ave}:	0.52	0.80	1.09
S_T/D_{ave}	1.3	1.33	1.36
S_L/D_{ave}	1.13	1.15	1.18
N:		15	
Pins/Row:		11/major row; 10/minor row	
k:		160	

clearance was present. He credited the production of vortices along the tips of the pin fins and their subsequent interaction with the endwall for this behavior.

Therefore, the aim of this study is to investigate in a parametric fashion, the effect of tip clearance on the mean heat transfer rate and pressure drop across a given array. Relative performance for nominal clearances of 0, 6, 12, 18, and 25% are investigated and discussed.

Experimental Apparatus

A series of three power electronics base plates were used as the test vehicles to evaluate pin fin performance as a function of tip clearance. The base plates were commercially manufactured,

composed of an AlSiC metal matrix composite, and formed into the shape shown in Fig. 2 through a molding process and high temperature infiltration stage. The base plate and pin fin array comprise a single, contiguous structure with uniform properties throughout. The pin fins have a 4.8 degree taper angle from base to tip to facilitate removal from the mold during manufacturing. As a result, the pin diameter varies slightly along the length of the fin.

The three base plates considered here are geometrically identical except for pin height, which varies from 2 mm to 4 mm. Correspondingly, non-dimensional length (H/D) ranges from 0.5 to 1.1. A summary of the base plate dimensions and material properties is provided in Table 1. The base plates were evaluated by mounting them on an open channel aluminum and Plexiglas housing as depicted in Fig. 3. The lower section of the housing was milled from a single piece of aluminum to provide good rigidity and strength to the assembly. Plexiglas was chosen as the upper section for its insulating properties and to allow visual access to the plate. Silicone rubber o-rings sealed the mating faces of the
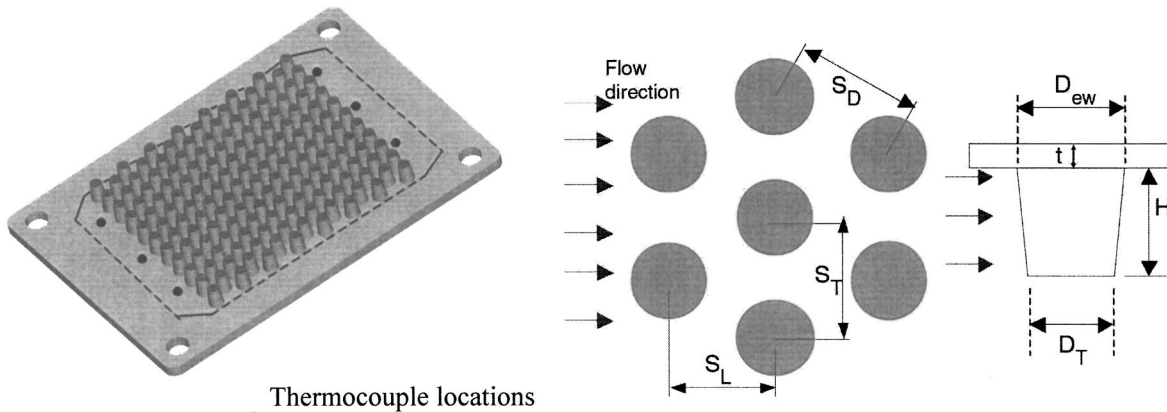
Fig. 2 AlSiC base plate pin fin array and geometry definitions
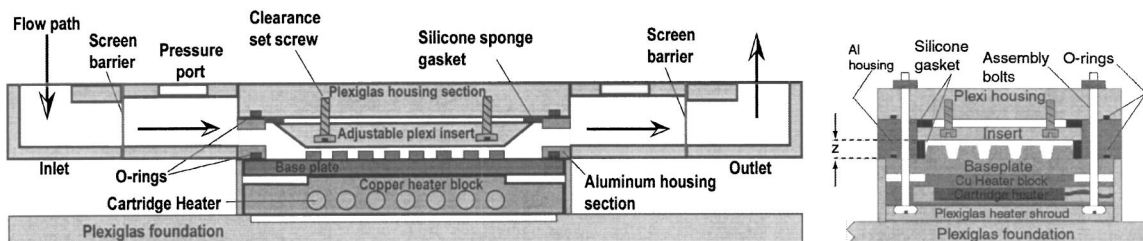
Fig. 3 Primary test assembly, side and end cross-sectional views
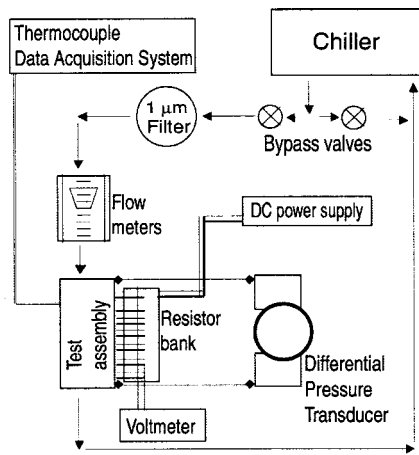
Fig. 4 Schematic of closed loop test facility

base plate and aluminum housing and those of the Plexiglas and Al housing. A Plexiglas insert sitting atop a silicone sponge gasket was situated between the tips of the pin fins and the Plexiglas housing. Four setscrews located at the corners of the insert and threaded into the body of the upper housing enabled the insert to be raised and lowered relative to the tips of the pin fins to control clearance. In the case of zero clearance, the set screws were removed and sufficient gasket material placed under the insert to insure that when the base plate was bolted onto the housing, the tips of the pins pressed down onto the insert, compressing the gasket material, and forcing good physical contact between the pins and insert across the entire array.

Pressure taps were located directly upstream and downstream of the main housing section and were ported to an Omega PX771-100WD1 piezo-resistive differential pressure transducer to measure pressure drop across the test section. Fiber glass window screening (7.1×6.3 mesh/cm; 0.028 cm wire diameter) was situated between each end section and the adjoining pressure tap section to promote a uniform flow field to the pin array, and for better mixing of the fluid downstream of the base plate to assist in bulk fluid temperature measurements. Beyond this, no attempt was made to characterize or condition the flow into the array due to limitations imposed by o-ring seal geometry.

A copper block with seven embedded cartridge heaters provided a uniform heat flux to the base plate. The face of the heater block was undercut so that it came in contact with the base plate only along the area corresponding to the pin array on the opposite side (see Fig. 3). The block was mechanically fastened to the base

plate and housing by machine screws, with thermal joint compound (Thermalloy Inc., Thermalcote II) applied at the heater-to-base plate interface to minimize contact resistance.

As depicted in Fig. 4, a Lauda WK500 chiller with integral pump located upstream of the test assembly, provided a continuous flow rate of distilled cooling water at constant temperature (± 1°C). Between the chiller and assembly were a pair of bypass valves to control flow rate to the test section, a 1 μm cartridge filter to remove any particulates in the flow stream, and a series of three variable area flow meters, (Blue-White Ind. models F-44[250/375/376]LH8), each for a different range and operating in parallel to measure flow rate through the system. Once the cooling fluid passed through the outlet section of the test assembly, it was returned directly to the chiller.

A Sorensen DHP200-10 DC power supply provided electrical power to the heaters. A 1 Ω precision resistor was connected in series between the power supply and each cartridge heater. The current through each heater was determined by monitoring the voltage across the resistor. This combined with the voltage measured across each heater was used to determine the total electrical power dissipation within the copper block.

Two thermocouples in the inlet section and three in the outlet section measured the bulk fluid temperature. Six thermocouples, as indicated in Fig. 2, were cemented to the base plate endwall using thermally conductive epoxy (Thermalloy Inc., #4952). An additional three thermocouples were embedded into the heater block itself, and two others were suspended in air to measure ambient temperature. A Labview based PC data acquisition system (Hewlett Packard 3852A) recorded temperature data.

Test Procedures

Tests were conducted through a nominal Reynolds number range of 2×10^2 to 1×10^4. Due to a limited pump head capacity of the chiller, some combinations of pin height and tip clearance were not tested through the full range. A summary of test ranges is provided in Table 2.

Each of the three base plates was tested at nominal tip clearances (C) of 0, 6, 12, 18, and 25% of pin fin height. Insert depth (z), shown in Fig. 3, was measured at nine points on the assembly using a Mitutoyo series 229 depth micrometer. This depth is the distance between the lower face of the aluminum housing section upon which the endwall of the base plate was mated, and the face of the Plexiglas insert. The difference between this distance and the height of the pins is the tip clearance. The average of the nine clearance measurements was taken to be the representative clearance for the plate. These average clearances and the standard deviation among the nine measurements are given in Table 3.

Each case was tested at ten flow rates within the given Re range at a constant nominal inlet temperature of 27°C (± 1°C). For each flow rate, a heat flux of 0.02 to 0.26 W/mm^2 was applied, resulting in a 3°C to 8°C average base plate temperature rise. During each test run, half the flow rates were repeated in random order at a heat flux approximately 10% higher or lower than used initially, to confirm repeatability of heat transfer results. In addition, 20% of the cases shown in Table 2 were repeated after completing the

Table 2 Re range covered in testing

C:	H/D: 0.5	H/D: 0.8	H/D: 1.1
0	427-10185	260-9980	379-6853
6	327-9370	208-8970	307-5564
12	279-6646	181-6927	260-5300
18	239-6851	319-5777	225-4074
25	205-5868	274-4968	188-3820

Table 3 Measured tip clearances

H/D	Nominal C	Heat transfer tests				Pressure drop tests			
		6	12	18	25	6	12	18	25
0.5	Avg. C	6.4	12.6	18.4	25.5	6.6	13.0	18.8	25.8
	σ	±0.6	±0.5	±0.6	±0.6	±1.1	±1.1	±0.9	±0.9
0.8	Avg.	5.5	11.1	18.2	25.2	6.4	12.6	17.9	24.9
	σ	±0.7	±1.2	±0.9	±0.7	±0.2	±0.4	±0.3	±0.4
1.1	Avg. C	6.2	12.2	18.2	27.2	6.2	12.1	18.3	25.1
	σ	±0.6	±0.7	±1.0	±1.5	±0.1	±0.5	±0.3	±0.4

initial test matrix. In each case, the experimental data showed good repeatability and were consistent with earlier trials.

Pressure drop measurements were conducted separately from the heat transfer tests. All trials were operated at zero heat flux at an inlet temperature of 27°C ($\pm$1°C). Due to limitations in setup accuracy, the tip clearances used during pressure measurements were similar, but not exactly the same as those in the heat transfer tests. The actual average clearances for the pressure tests are also shown in Table 3.

Calibration of Heat and Pressure Losses. The test section as designed, did not completely limit heat transfer to the array only. The area inside the dotted line of Fig. 2 indicates the wetted portion of the base plate, part of which lies outside the array itself. Exposed portions of the aluminum housing section also participated in heat transfer via forced convection. In addition, conduction from the heater block to the foundation was to be expected. To account for these losses and to determine the actual rate of heat transfer from the pin array itself, two sets of calibration tests were conducted.

The first set involved operating the assembly dry, with all internal test assembly surfaces exposed to quiescent air, thereby producing a relatively adiabatic condition at those surfaces. In such a configuration, the heat input into the base plate is dissipated by conduction through the foundation, or by natural convection from the outer walls of the assembly. Tests were conducted for $H/D=0.5$ through a range of input power levels (0.9–5.2 W). At each power level, the test was allowed to run for six hours or more to insure the system attained a steady state condition. This provided a quantitative relationship between average heater block temperature rise and heat lost through conduction and natural convection during subsequent testing.

A second set of tests was conducted to determine the relative amount of heat dissipated by forced convection from the wetted surface areas outside of the pin array itself. For this purpose, a flat aluminum base plate with a relatively non-conducting pin array was employed. Constructing an exact replica of the tapered cylindrical pin fins of the AlSiC base plates was not feasible. Therefore, an array of diamond shaped pin fins of approximately equivalent geometry was machined from a Plexiglas block and attached to the Al plate using silicone rubber adhesive. Since the thermal conductivity of Plexiglas is three orders of magnitude lower than AlSiC and Al, convection from the machined array can be considered negligible in this configuration. The preponderance of the heat transfer therefore occurs at the wetted surface areas outside the array while the rest of the assembly experiences a flow field similar to that experienced when the AlSiC base plate is in place. The aluminum plate was 6.25 mm thick, compared to the 5 mm thickness of the AlSiC base plate to account for the higher thermal conductivity of aluminum and maintain a consistent overall thermal resistance among the two plates. Calibration trials were conducted for $H/D=0.5$ at $C=0\%$, $H/D=0.8$ at $C=12\%$, and $H/D=1.1$ at $C=25\%$.

Like the heat transfer tests, pressure measurements required a separate set of calibration runs. A smooth flat aluminum plate was employed to determine the pressure drop inherent in the test assembly itself due to area constrictions and wall friction. Tests were run for flow areas equivalent to each combination of pin height and tip clearance.

Data Reduction and Uncertainties

The heat dissipated by the pin fin array itself was calculated as

$$Q_A = Q_H - Q_{L,\text{cond}} - Q_{L,\text{conv}} \tag{1}$$

A least square linear curve fit to the conduction loss calibration data gave

$$Q_{L,\text{cond}} = 0.242(T_H - T_{\text{amb}}) \tag{2}$$

Conduction losses were between 1 and 2% of total heater power.
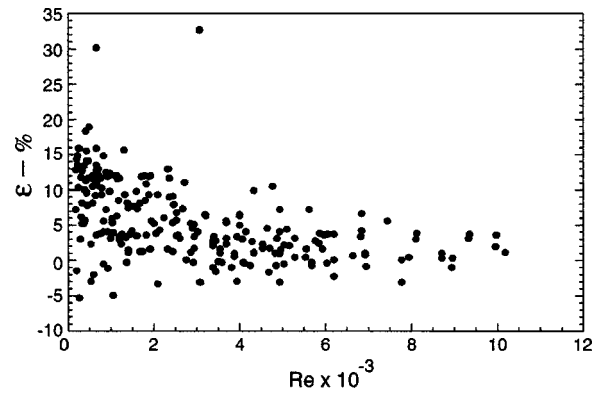
Fig. 5 Energy balance of heat transfer trial data

Similarly, the forced convection heat loss data were found to be extremely linear for a given flow rate. The results of these calibration trials were subsequently modeled by

$$Q_{L,\text{conv}} = (T_H - T_f)\tan\theta - Q_{L,\text{cond}} \tag{3}$$

where θ is measured in radians and is the angle the data makes with the horizontal at a given flow rate when heater block power dissipation (ordinate) is plotted against its temperature rise (abscissa). To preclude the need of a separate heat loss calibration equation for each combination of H/D, C, and U, a single fifth order least square polynomial curve fit to the test data was employed to estimate this angle for all test cases. This approximation greatly simplified data reduction efforts while introducing a maximum uncertainty in predicted convection heat loss of 8.3%. This corresponds to a maximum of 1.2% error in the total array heat load (Q_A). Convection losses ranged from 9.7 to 24.1%, with the vast majority being below 15% of total test power. Full details regarding the estimation of $Q_{L,\text{cond}}$ and $Q_{L,\text{conv}}$ are to be found in Moores [19].

Mean heat transfer from the pin fin array is calculated as:

$$\overline{\text{Nu}} = \frac{hD_{\text{ave}}}{k} \tag{5}$$

where the heat transfer coefficient (h) is defined as:

$$h = \frac{Q_A}{A(T_{ew} - T_f)} \tag{6}$$

and the area (A) is either the total wetted surface area of the pin array (A_w) or the projected area of the array (A_p). The representative fluid temperature (T_f) is estimated based on calorimetry according to

$$T_f = T_{\text{in}} + \frac{(Q_H - Q_{L,\text{cond}})}{2\dot{m}c_p} \tag{7}$$

To judge the propriety of this approach, an energy balance was performed on the fluid stream to compare the temperature rise of the water as measured to that which is expected based on the total energy imparted to the fluid by the heater. The relative ratio of the two temperature rises is then defined as

$$\varepsilon = \frac{(T_{\text{in}} - T_f) - (T_{\text{in}} - T_{\text{out}})}{T_{\text{in}} - T_f} \tag{8}$$

The results of the energy balance for all trials are shown in Fig. 5. In 78% of the cases, the energy balance is within $\pm$10% while 96% of the data lies within $\pm$15%. The highest deviations occurred almost exclusively at the low Re range where one would expect thermal stratification to be the most pronounced and therefore lead to nonrepresentative temperature measurements at the outlet. The results also show that with increasing Reynolds num-

ber and the added mixing that occurs, the measured and expected temperature rises were in very good agreement, thereby supporting the given approach to heat loss calibration and data reduction.

Heat transfer data were also processed to account for differences in fin efficiency to better compare the performance of the three fin heights. This also facilitates more meaningful comparisons between the results of the current study and the literature, particularly in cases where naphthalene sublimation is employed; a common technique in pin array studies, which by its nature produces results corresponding to 100% fin efficiency. Where indicated, the reported data have been prorated to 100% fin efficiency according to the relationship

$$h_{100} = \frac{h}{\eta} \qquad (9)$$

where the fin efficiency η is calculated as

$$\eta = \frac{\int_0^H \Theta_x dx}{\Theta_{ew} H} \qquad (10)$$

Θ_x is the temperature excess at any point along the length of a tapered pin fin relative to the bulk average fluid temperature as calculated by (Kraus and Bar-Cohen [20]):

$$\Theta_x = \frac{w_b^2}{w_x} \beta_2 \Theta_{ew} + \frac{32 n^2 b^2}{k \pi D_{ew}^2 w_b w_x} \beta_1 Q_{pf} \qquad (11)$$

where

$$\beta_1 = K_1(w_b) I_1(w_x) - I_1(w_b) K_1(w_x) \qquad (12a)$$

$$\beta_2 = K_2(w_b) I_1(w_x) + I_2(w_b) K_1(w_x) \qquad (12b)$$

To apply this relationship, Q_A and h are assumed to be uniform across the entire array, and the contributions of pin fin and end-wall heat transfer are determined iteratively based on the relationship:

$$Q_A = Q_{ew} + Q_{pf} = h A_{ew} \Theta_{ew} + h A_{pf} \Theta_{ew} \eta \qquad (13)$$

where A_{ew} is the wetted endwall surface area within the array, A_{pf} is the total wetted area of the pins only, and Q_{ew} and Q_{pf} are the heat rates dissipated across each of those areas, respectively.

Pressure drop results are reported in terms of friction factor

$$f = \frac{\Delta P_A}{2 \rho V_{max}^2 N} \qquad (14)$$

where N is the number of rows in the array.

The pressure drop across the array itself is determined from the difference between the pressure drop measured with a given base plate in place (ΔP_{bp}) and that produced when the flat plate (ΔP_{fp}) was installed

$$\Delta P_A = \Delta P_{bp} - \Delta P_{fp} \qquad (15)$$

Both heat transfer and pressure drop results are presented as a function of Reynolds number (Re). Many forms of Re have been used in past studies of shrouded pin fin arrays. Here, to account for the tip clearance we have adopted a modified form of Re originally proposed by Zukauskus [21] for the analysis of flow across tube banks

$$Re = \frac{V_{max} D_{ave}}{v} \qquad (16)$$

where V_{max} is the maximum estimated bulk velocity within the array based on the minimum cross-sectional flow area along the channel, including flow area beyond the tips, and is the greater of

$$V_{max} = U \frac{S_T(H+C)}{(S_T(H+C) - D_{ave}H)} \qquad (17a)$$

and

$$V_{max} = U \frac{S_T(H+C)}{2(S_D(H+C) - D_{ave}H)} \qquad (17b)$$

For the nonclearance case, this definition simplifies to the classic definition of V_{max} [21]. With two exceptions, all thermophysical values employed in data reduction were assessed at T_{in} and based on Incropera and Dewitt [22]. The density of the distilled water and the thermal conductivity of the AlSiC base plate were taken to be constant.

Estimated Uncertainties. The uncertainties in temperature and pressure measurements were estimated through direct calibration to be a maximum of 0.17°C and 2% of measured value respectively. Using the method of Kline and McClintock [23] and assuming uncertainties associated with array and channel dimensions to be negligible, the overall uncertainties in $\dot{V}$, Q_H, Re, $\overline{Nu}$, and f were found to be a maximum of 2.6, 1.4, 5.2, 14.3, and 4.5% respectively. The highest uncertainties in heat transfer occurred at the low end of the Reynolds number range (Re<1000). Through the majority of the flow range, uncertainties in $\overline{Nu}$ were in the range of 6–8%.

Results and Discussion

Figure 6 illustrates the effect of tip clearance on heat transfer for the given pin arrays. Shown is the resulting increase in $\overline{Nu}_p$ for each clearance set, relative to the zero clearance case. The data are presented for a range of flow rates and have not been modified to account for fin efficiency effects. The Nusselt number is based on
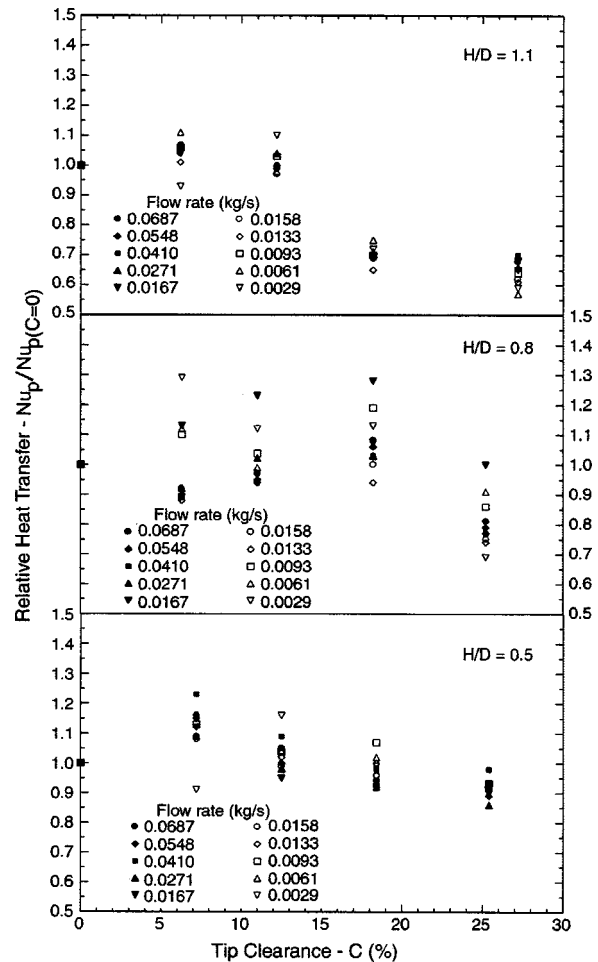
Fig. 6 Relative effect of clearance on Nu_p
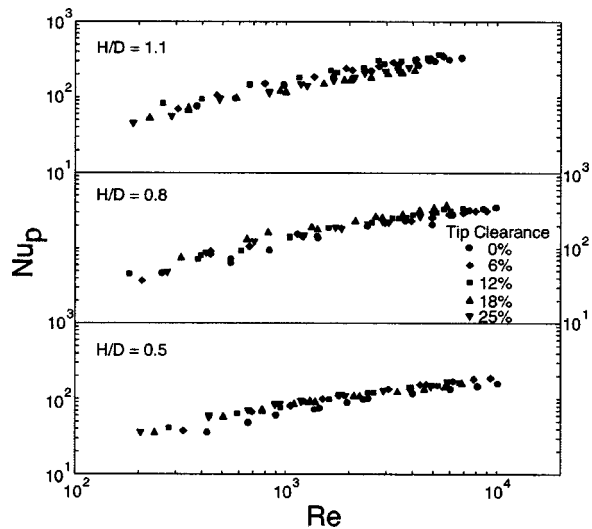
Fig. 7   Nu based array projected area

Fig. 8   Nu based on total wetted area of array

the projected area of the array, which is constant (3490 mm^2) regardless of clearance or pin height. This form of Nu reflects the behavior of the overall heat transfer from the array, as would be experienced by a heat source mounted on the flat side of the base plate, such as a semiconductor chip.

A large amount of scatter is present in the case of $H/D = 0.80$, however in general, the trends are consistent across the three cases. The results show an initial heat transfer enhancement at low levels of clearance as the pin tips become exposed to the cooling fluid and provide additional heat transfer area to the array. However, as the clearance is increased further, the effect of fluid bypassing the array becomes dominant, and the resulting reduction in flow rate within the array itself produces lower rates of relative heat transfer.

For $H/D = 0.5$, the heat transfer area increases by 49% when the tips are exposed. However, the maximum increase in Nu_p is only 13% on average, and occurs at 6% clearance, which is the minimum considered here. For $H/D = 1.1$, the heat transfer area increases by 26.7% when the tips are exposed, but produces an average of only 6% maximum increase in Nu_p. This is due in part to the fact that the added area is orientated parallel to the flow as opposed to the majority of the array which is perpendicular to the flow. It is therefore less effective in heat transfer. The second factor is of course the reduced flow rate within the array due to the overall larger flow area when tip clearance is present.

At the highest clearance, the relative heat transfer is lowered to an average of 94 and 65% for $H/D = 0.5$ and 1.1 respectively. The former is similar to that of Chyu et al. [10] who reported a 1.5% decrease in heat transfer for 25% clearance. Direct comparisons are difficult however, due to the differences in geometry between the array of Chyu and the current study. H/D in Chyu's array was nearly equivalent at 1.0, while the pin pitch (S/D) was approximately 50% larger, meaning Chyu's pins were spaced much further apart. More notably, the pins were square in cross-section and arranged in an online pattern.

In Fig. 7, $\overline{Nu}_p$ is presented as a function of Reynolds number. Since the chosen form of Re accounts for changes in flow area, enabling comparison between different clearances on an equivalent flow condition basis, this provides perhaps a truer picture of the impact of clearance on the array heat transfer behavior for a given flow condition. Maximum increases in heat transfer are found to be 23, 19, and 15% for $H/D = 0.5$, 0.8, and 1.1 respectively. This is in comparison to 49%, 36%, and 27% increases respectively in the overall heat transfer area of the arrays when tip
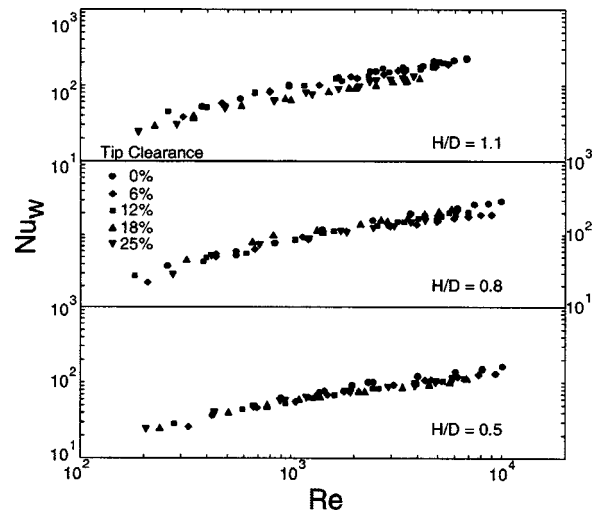
clearance is present. This suggests that the heat transfer rate from the tip area in these cases is roughly half that of the array as a whole, on a unit area basis.

Figure 8 depicts Nu_w, which is based on the total wetted area of the pin fin array, rather than the projected area, thereby accounting for the discrete jump in heat transfer area that occurs between the trials with no tip clearance and those with clearance. In this form, the non-clearance case produced the highest level of heat transfer for each base plate, again reflecting the poorer performance of the tip area. In addition, while not ruling out the occurrence of vortex shedding at the pin tips and other three-dimensional phenomena that might enhance heat transfer within the array, the current results suggest that such effects are at most a secondary influence on overall performance.

To correlate the data for all combinations of pin height and tip clearance, a nonlinear multiple regression analysis was performed using NLREG, a shareware curve-fitting program. The correlation was taken to be of the form

$$Nu_{w,100} = \alpha_0 \left(\frac{H}{D} \right)^{\alpha_1} \left(\frac{C+H}{H} \right)^{\alpha_2} Re^{\alpha_3} Pr^{0.36} \qquad (18)$$

Prandtl number was calculated at T_f and typically ranged between 5.4 to 5.7. The exponent of the Prandtl number is assumed to be
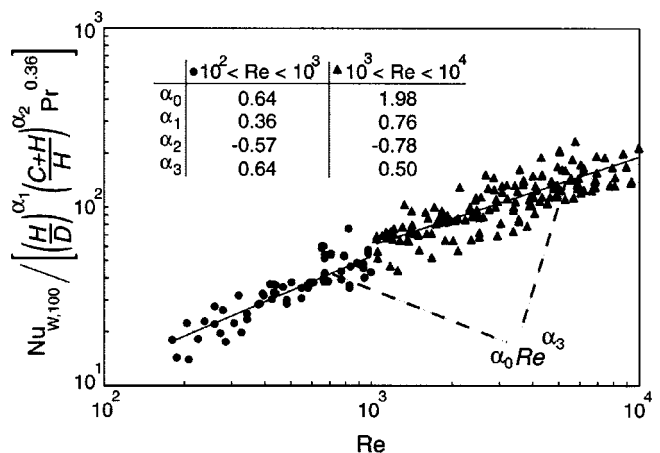
Fig. 9   Evaluation of $Nu_{w\text{-}100}$ correlation
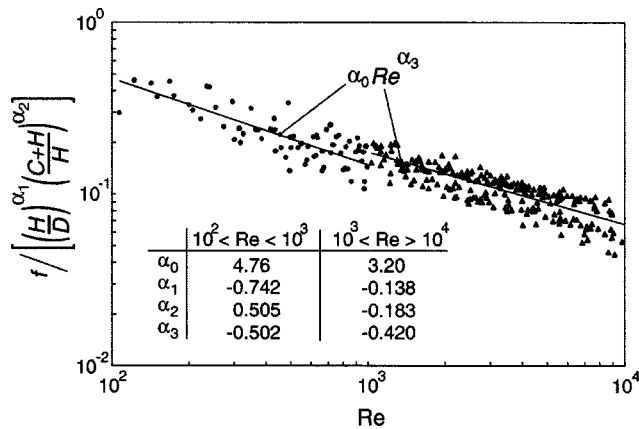
Fig. 10 Correlation of friction factor (f) data

	$10^2 < \text{Re} < 10^3$	$10^3 < \text{Re} > 10^4$
α_0	4.76	3.20
α_1	-0.742	-0.138
α_2	0.505	-0.183
α_3	-0.502	-0.420
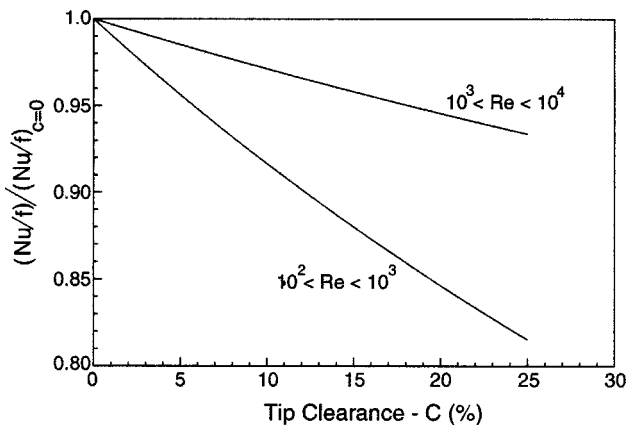
Fig. 11 Relative effect of clearance on heat transfer to pressure ratio

0.36 based on the work of Zukauskus [21], who found this power index to be valid for correlating heat transfer in a wide range of tube bank geometries.

Separate correlations have been developed for the range $10^2 < \text{Re} < 10^3$, which is predominantly laminar in nature, and $10^3 < \text{Re} < 10^4$, which represents the start of a transitional region from laminar to fully turbulent flow [21,24]. The correlations are based on efficiency corrected heat transfer data.

Figure 9 depicts an evaluation of the correlations and the calculated parameters for each region. A considerable amount of scatter is present, particularly at higher Reynolds numbers, with a standard deviation of 13.4 and 17.0% for the low and high range correlations, respectively. Several alternate forms of Re were considered, but none was found to improve the accuracy of the correlation.

The general trend is similar to that of Chyu et al. [8], who employed the naphthalene sublimation technique to investigate contributions of pin fin verses endwall heat transfer rates. For a staggered array of $H/D=1$, $S_T/D=2.5$, $S_L/D=2.5$, they correlated the mean heat transfer of the array to

$$\overline{\text{Nu}} = 0.320\,\text{Re}^{0.583} \tag{19}$$

within the Re range of 5×10^3 to 2.5×10^4. While Chyu's work considered only the nonclearance case, the power index of Re is in good agreement with that found in the current study.

Array pressure drop has also been correlated assuming a form similar to that for heat transfer:

$$f = \alpha_0 \left(\frac{H}{D}\right)^{\alpha_1}\left(\frac{C+H}{H}\right)^{\alpha_2}\text{Re}^{\alpha_3} \tag{20}$$

Separate curve fits were developed according to flow region and are depicted in Fig. 10. The laminar region data correlates poorly, but the transitional data is somewhat better correlated, with 85% of the data laying within a ±25% error band of the reduced correlation curve.

Lastly, employing Eq. (18) and (20), Fig. 11 illustrates the relative effect of clearance on the ratio of Nu_w/f, which is proportional to the rate of heat transfer per unit of pumping power. The results suggest that the introduction of clearance has a negative impact, with the influence being greater in the laminar region than the transitional region.

Conclusions

The effect of tip clearance on three selected pin fin arrays has been evaluated. The results show that for arrays of $0.5 \leqslant H/D \leqslant 1.1$, increased mean heat transfer and lower overall pressure drops can be realized by incorporating small amounts of clearance (<10% of pin height) between the pin tips and the surrounding shroud. Average improvements of up to 15% for a given flow rate, and 23% for a given Reynolds number were achieved. The increase in heat transfer rate appears to be primarily due to the additional surface area that is exposed to the cooling fluid when clearance is introduced. Any improvements from induced three-dimensional effects via vortex generation at the tips is apparently offset by the lower heat transfer efficiency of the tip area as compared to the array as a whole.

Acknowledgments

Nomenclature

A = area [m²]
b = endwall location relative to tip [m]
C = tip clearance [percent of H]
c_p = Specific heat [J/kg-K]
D = pin diameter [m]—average diameter when not subscripted
f = flow friction factor [nd]—Eq. (14).
H = pin fin height [m]
h = heat transfer coeff. [W/m² K]
I_z = modified Bessel function, first kind, order z [nd]
K_z = modified Bessel function, second kind, order z [nd]
k = thermal conductivity [W/m-K]
L = length [m]
$\dot{m}$ = mass flow rate [kg/s]
N = number of pin rows in array
n = $[(4h^2/D_{ew}^2 k^2)(4b^2 + D_{ew}^2)]^{1/4}$ [1/m⁰·⁵]
nd = non-dimensional
$\overline{\text{Nu}}$ = mean array Nusselt number [nd]—Eq. (5).
Pr = Prandtl Number [nd]
Q = heat dissipation [W]
Re = array Reynolds number [nd]—Eq. (16).
S = center-to-center pin spacing [m]
T = average temperature [°C]
t = thickness [m]
U = bulk mean inlet fluid velocity [m/s] $\dot{V}/A_c$
$\dot{V}$ = volumetric flow rate [m³/s]
$V_{\max}$ = max. estimated array velocity [m/s]—Eq. (17).
W = width [m]
w_x = $2nx^{1/2}$ [nd]

$w_b = 2nb^{1/2}$ [nd]

x = location along height of pin fin [m]

z = insert depth (see Fig. 3)

Greek Symbols

α = multiple regression coefficient

β = pin efficiency parameter [nd] Eq. (12)

ΔP = pressure drop [Pa]

ε = energy balance [percent/100]—Eq. (8)

η = pin efficiency [percent/100]—Eq. (10)

Θ_x = temperature excess along pin height relative to bulk fluid [°C] Eq. (11)

Θ_{ew} = temperature excess at endwall [°C]

θ = calibration angle [radians]

ρ = density [997 kg/m^3]

σ = standard deviation [percent of H]

ν = kinematic viscosity [m^2/s]

Subscripts

100 = corresponding to 100% fin efficiency

A = array

amb = ambient air

ave = average

bp = base plate

c = cross-section of channel

D = diagonal direction $S_D = [S_L^2 + (S_T/2)^2]^{1/2}$

ew = endwall

f = fluid

fp = flat calibration plate

H = heater block

in = inlet of test section

L = longitudinal direction

L,cond = losses via conduction and natural convection

L,conv = losses via forced convection outside array

out = outlet of test section

p = projected area (ie footprint) of array

pf = pin fin

t = pin tip

T = transverse direction

w = wetted area of array

References

[1] Armstrong, J., and Winstanley, D., 1988, "A Review of Staggered Array Pin Fin Heat Transfer for Turbine Cooling Applications," ASME J. Turbomach., **110**, pp. 94–103.

[2] Hwang, J. J., and Lu, C. C., 1999, "Detailed heat transfer characteristic comparisons in straight and 90-deg turned trapezoidal ducts with pin fin arrays," Int. J. Heat Mass Transfer, **42**, pp. 4005–4016.

[3] Hwang, J. J., Lai, D. Y., and Tsia, Y. P., 1999B, "Heat transfer and pressure drop in pin fin trapezoidal ducts," ASME J. Turbomach., **121**, pp. 264–271.

[4] Hwang, J. J., and Lu, C. C., 2001, "Lateral flow effects on endwall heat transfer and pressure drop in a pin-fin trapezoidal duct of various pin shapes," ASME J. Turbomach., **123**, pp. 133–139.

[5] Chyu, M. K., 1990, "Heat transfer and pressure drop for short pin-fin arrays with pin endwall fillet," J. Heat Transfer, **112**, pp. 926–932.

[6] Chyu, M. K., and Goldstein, R. J., 1991, "Influence of an array of wall-mounted cylinders on the mass transfer from a flat surface," Int. J. Heat Mass Transfer, **34**, pp. 2175–2186.

[7] Chyu, M. K., Hsing, Y. C., and Natarajan, V., 1998, "Convective heat transfer of cubic fin arrays in a narrow channel," ASME J. Turbomach., **120**, pp. 362–367.

[8] Chyu, M. K., Hsing, Y., and Shih, T. I. P., 1999, "Heat transfer contributions of pins and endwall in pin fin arrays: effects of thermal boundary condition modeling," ASME J. Turbomach., **121**, pp. 257–263.

[9] Chyu, M. K., Hsing, Y., Natarajan, V., and Chiou, J. S., 1999, "Effects of perpendicular flow entry on convective heat/mass transfer from pin-fin arrays," J. Heat Transfer, **121**, pp. 668–674.

[10] Chyu, M. K., Yen, C. H., Ma, W., and Shih, T. I. P., 1999, "Effects of flow gap atop pin elements on the heat transfer from pin fin arrays," ASME Paper 99-GT-47.

[11] Li, Q., Chen, Z., Flechtner, U., and Warnecke, H. J., 1996, "Konvective Warme/Stoff-Ubertragung und druckverlust in Rohrbundeln bestehend aus tropfenformigen rohren," Chem.-Ing.-Tech., **68**, pp. 1299–1302 (In German).

[12] Li, Q., Chen, Z., Flechtner, U., and Warnecke, H. J., 1998, "Heat Transfer and Pressure-Drop Characteristics in Rectangular Channels with Elliptic Pin Fins," Int. J. Heat Mass Transfer, **19**, pp. 245–250.

[13] Lau, S. C., Han, J. C., and Kim, Y. S., 1989, "Turbulent heat transfer and friction in pin fin channels with lateral flow ejection," J. Heat Transfer, **111**, pp. 51–58.

[14] Lau, S. C., Han, J. C., and Batten, T., 1989, "Heat transfer, pressure drop and mass flow rate in pin fin channels with long and short trailing edge ejection holes," ASME J. Turbomach., **111**, pp. 116–123.

[15] Sparrow, E. M., and Ramsey, J. W., 1978, "Heat transfer and pressure drop for a staggered cylinder wall attached array of cylinders with tip clearance," Int. J. Heat Mass Transfer, **21**, pp. 1369–1377.

[16] Peng, Y., 1984, "Heat transfer and friction loss characteristics of pin fin cooling configurations," ASME J. Eng. Gas Turbines Power, **106**, pp. 246–251.

[17] Jubran, B. A., Hamdan, M. A., and Abdualh, R. M., 1993, "Enhanced heat transfer, missing pin, and optimization for cylindrical pin fin arrays," J. Heat Transfer, **115**, pp. 576–583.

[18] Sparrow, E. M., Ramsey, J. W., and Altemani, C. A. C., 1980, "Experiments on In-line pin fin arrays and performance comparisons with staggered arrays," J. Heat Transfer, **102**, pp. 44–50.

[19] Moores, K. A., 2004, "Effect of Tip Clearance on the thermal and hydrodynamic performance of shrouded pin fin arrays," Ph.D. thesis, University of Maryland, College Park, MD.

[20] Kraus, A. D., and Bar-Cohen, A. B., 1995, *Design and Analysis of Heat Sinks*, John Wiley & Sons, New York, pp. 99–102.

[21] Zukauskas, A., 1972, *Heat transfer from tubes in crossflow, Advances in heat transfer*, J. Hartnett, and T. Irvine, eds., Academic Press, New York, **8**, pp. 93–160.

[22] Incropera, F. P., and Dewitt, D. P., 1985, *Fundamentals of heat and mass transfer*, second edition, John Wiley and Sons, New York, pp. 753–782.

[23] Kline, S. J., and McClintock, F. A., 1953, "Describing Uncertainties in Single Sample Experiments," Mech. Eng. (Am. Soc. Mech. Eng.), **75**, pp. 3–8.

[24] Short, B. E., 1994, "Pressure drop and heat transfer in cast pin fin coldwalls," Ph.D. dissertation, Southern Methodist University, Dallas, TX.

The Optimum Height of Winglet Vortex Generators Mounted on Three-Row Flat Tube Bank Fin

S. D. Gao

L. B. Wang
e-mail: lbwang@lzri.edu.cn

Y. H. Zhang

F. Ke

Department of Mechanical Engineering,
Lanzhou Jiaotong University,
Lanzhou, Gansu 730070, P.R. of China

Winglet vortex generators can be used to enhance the heat transfer performance of finned flat tube bank fin. The effects of the height of vortex generators (VG) on local heat transfer were studied using the naphthalene sublimation method and the optimum height of winglet VG are screened by using JF, a dimensionless factor of the larger the better characteristics. In order to get JF, the local heat transfer coefficient obtained in experiments and a numerical method were used to get the heat transferred from the fin. For the configurations studied in this paper: for local characteristic, as increasing height of VG, heat transfer is enhanced, but the mostly enhanced region moves away from the tube wall; with increasing height of VG to certain degree, the width of enhanced region does not increase significantly; the effects of VG's height on span-average Nusselt number (Nu) are more mixed on fin surface mounted with VGs and its back surface, with increasing height of VG, in some region heat transfer is worsened, and in other region heat transfer is enhanced; in real working condition, the heat transferred from fin surface mounted with VGs is larger than the heat transferred from the other surface of the fin; increasing the height of VG (H) increases average Nu and friction factor (f), but with considering the fin efficiency, there is an optimum H to get best heat transfer performance; the optimum height of VG is dependent on the thickness of fin and its heat conductivity, for mostly used fin thickness and material, the optimum height of VG is 0.8 times of net fin spacing.
[DOI: 10.1115/1.1621900]

Keywords: Enhancement, Experimental, Heat Transfer, Mass Transfer, Vortex

Introduction

The finned flat tube bank fin as shown in Fig. 1 is commonly used as heat exchanger on vehicles. To reduce the size and the weight of heat exchangers, various fin patterns have been developed to improve the fin heat transfer performance. The vortex generators (VGs) can generate developing boundary layers, swirl and flow destabilization. Various experimental and numerical studies were carried out, and reviewed by Fiebig [1,2] and Jacobi et al. [3].

The capacity of heat enhancement of VGs depends on their shape and other parameter such as angles of attack. The optimum geometric parameters of the VG also depend on the geometry of the flow passage and the flow structure. There are many types of VG such as delta wing, rectangular wing, delta winglet and rectangular winglet. The difference between wing and winglet is on what edge of wing is attached on the fin surface. When wing's trailing edge is attached to the fin we call wing, if wing's chord is attached to the fin we call winglet. According to the reports of Tiggelbeck et al. [4], the best performance is given by the delta winglets, closely followed by the rectangular winglets. The wings give considerably less enhancement than do the winglets. So in the reported studies delta winglet configurations were further investigated. Experimental investigation shows that heat transfer enhancement by mounted delta winglet VG in finned flat tube bank is more pronounced than in a finned circular tube bank in Fiebig et al. [5]. Numerical investigations show that aspect ratio (height to base length) of delta winglet, 2, provides the best ratio of heat transfer enhancement to flow loss penalty for a finned one-row oval tube bank in Chen et al. [6]. It was found that an aspect ratio variation between 1.5 and 2.0 influenced the global heat transfer results less than 5%. if other dimensionless parameters were not

changed, see Fiebig [1]. The mostly studied height of delta winglet VG is net fin spacing because one believes that VGs can also function as a pitch holder of the fin, but it may not be the case in real application. So far it seems that there is a shortage of investigation of the effects of VG height on the heat transfer enhancement for a finned flat tube bank.

Recently, analogy between heat and mass transfer has been used to investigate the local and average heat transfer over a finned three-row flat tube bank with four delta winglet vortex generators per tube fin in Wang et al. [7] and with six delta winglet vortex generators per tube fin in Wang et al. [8]. Several types of surfaces involved in heat transfer process were considered. The effects of VG parameters such as height and angle of attack on heat transfer and pressure drop were investigated. The local Nu distribution shows that VGs can efficiently enhance the heat transfer in the region near tube on the fin surface mounted with VGs. On its back surface the enhancement is also pronounced, but the mostly enhanced region is away from tube wall with some distance. The difference between the distributions of heat transfer coefficient on two surfaces of the fin is large. Average results show that increasing the height of VG increases the enhancement of heat transfer and pressure drop. The comparison of heat transfer enhancement with flat tube fin without VGs under identical mass flow rate, identical pumping power and identical pressure drop constraints was carried out. Without considering the efficiency of fin, the results show that the larger the height of VG, the better the heat transfer performance. This may not be the case in real working condition, because with increasing the height of VG, the mostly enhanced region may move away from the tube, the gain we get for heat transfer enhancement may be less than the companied penalty of flow loss.

In this paper the effects of height of VG on the local heat transfer coefficient of a three-row finned flat tube bank, as shown in Fig. 1, are studied using naphthalene sublimation method. The larger the better factor, *JF* in Yun et al. [9] is used as the criteria to
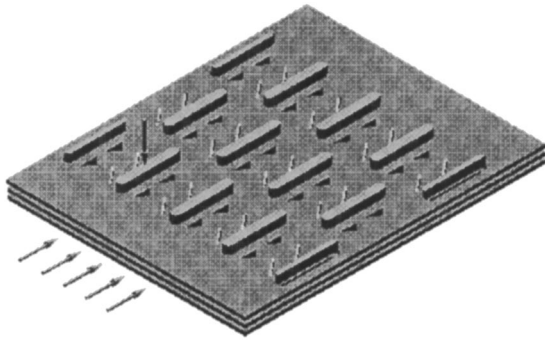
Fig. 1 Schematic view of a finned 3-row flat tube bank with mounted delta winglet vortex generators

Fig. 2 Experimental setup: (a) flow passages between fins; (b) plate forming flow passage; (c) fin surface I; (d) fin surface II; and (e) flat tube cast out of naphthalene.

screen the optimum height of VG. This factor is derived from the performance evaluation criteria based on area goodness factor, which has been proposed to compare the thermal and dynamic performance of heat exchangers. In order to get JF, the experimental results of local heat transfer coefficient are used and a numerical method is adopted to obtain the heat transferred from the fin.

Test Apparatus and Experimental Methods

In Fig. 2(a), the flow passages are presented. Two plates with 6 mm thickness, shown in Fig. 2(b), were used in the test channel. We put the measured plates, "fin surface I" and "fin surface II" in Figs. 2(c) and (d), into the void region on two plates such as shown in Fig. 2(b), respectively. One of the surfaces of measured plate was cast out of naphthalene. The naphthalene thickness is about 3 mm. In actual industrial applications, the VGs are punched into the fin surface rather than mounted. Due to the experimental difficulty of using punched VGs, in present study VGs are mounted on the surface. According to studies of Ref. [2], the punched VGs give slightly better performance than the mounted ones. Due to very small area ratio of VG surface and fin surface (in this study, it is 2.9%), this difference in configuration has only limited effect on the overall results. In order to model the two sides of the fin, the fin surfaces I and II were arranged face to face as Fig. 2(a) shows. We used the stakes of 8 mm in width and 5 mm in heights to support the plates and control the net fin spacing (T_p) near the lateral walls of test section in wind tunnel. VGs were manufactured from copper plate of 0.8 mm thickness by a line milling method. Two tubes cast from naphthalene shown in Fig. 2(e) were put in the regions labeled with B in Fig. 2(a) to measure the sublimation of tubes. Other tubes and plates did not participate directly in the mass transfer process. On one cross section just before the inlet of test elements (Fig. 2(a)) four pressure tips were mounted, as the same, four pressure tips were mounted on one cross section just after the outlet of test elements.

The flat tube fin geometries and positions of VGs are presented in Fig. 3. The geometric parameters are $S_1 = 40$ mm, $S_2 = 55$ mm, $b = 46.3$ mm, $b_{VG} = 27.7$ mm, and $a = 6.3$ mm. Figure 3(a) presents the arrangements of VG pair. In this study, the geometry of VG is shown in Fig. 3(b), and the aspect ratio is selected as 2. Three heights of VG, $H = 3$, 4, and 5 mm are studied at $\theta = 35$ deg and $T_p = 5$ mm. Some non-dimensional parameters often appeared in other references are: $a/b = 0.136$, $L_{pVG} = 4.62$, $B_{pT} = 8$, and $B_{pVG} = 5.48$.

The experimental method is the naphthalene sublimation technique via the heat-mass transfer analogy. The VGs were mounted at the given positions on fin surface I and the backside of fin surface II by quick-drying glue. Each cast plate was sealed in a special glass container and placed in a temperature-controlled experimental room with temperature fluctuation less than ± 0.1°C for a time period of about 24 hours prior to a test run. Measurements of the surface contour of the naphthalene plates before and
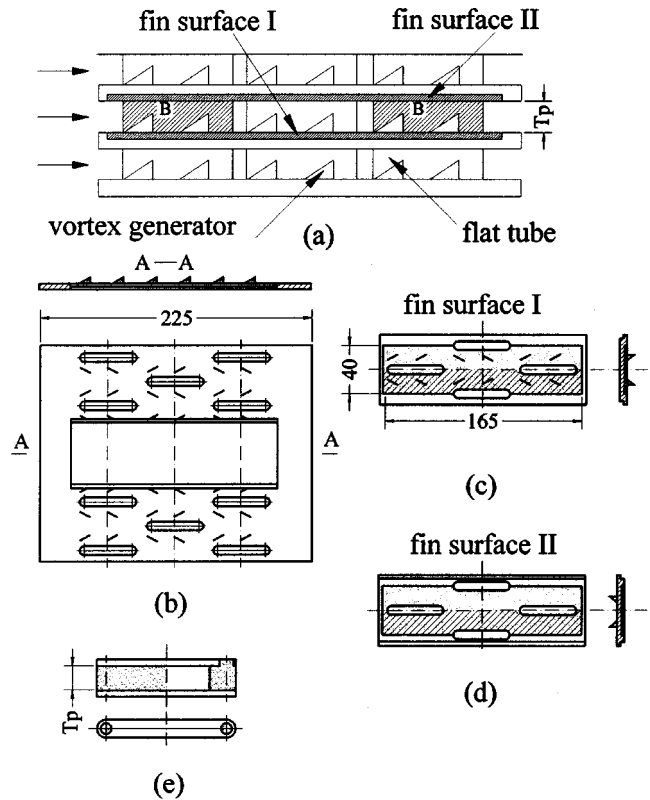
after a test run were made with a sensitive dial gauge with the resolution of 1 μm. The sublimation depth on the plate was measured on the total surface and a symmetrical mass transfer was obtained in some pre-test experiments. In the formal experiments, only half of the fin surfaces I and II were measured (hatched areas
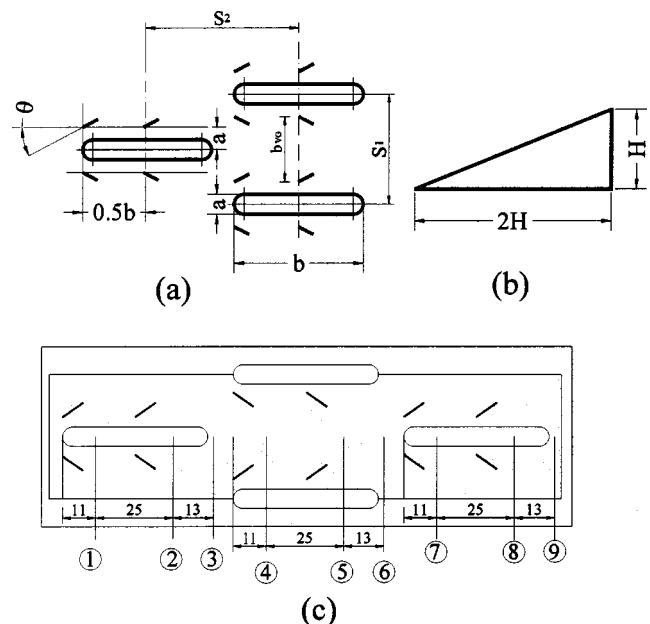
Fig. 3 Flat tube bank parameters and positions of VGs: (a) configuration; (b) shape of VG; and (c) positions of 9 labeled cross-sections.

in Fig. 2(c) and (d)) due to symmetry. The total measured points are 3300 on half of the fin surfaces I or II. The interval of any two neighboring points is 1 mm in both stream direction (x) and span direction (y). There is no naphthalene at the front and rear end of measured plates. It is very difficult for us to measure the sublimation depth of flat tube due to a more expensive special apparatus is required. The local measurement was not carried out for flat tubes. By weighting the tubes before and after running an average mass transfer coefficient was obtained and then an averaged Nu for flat tube. A volumetric flow meter was used to measure the airflow rate with precision of 0.1 m³/h. The temperature of air entering test section was measured by a precision grade laboratory thermometer, which can be read to 0.1°C. A digital timer was used to measure the duration of a test run as well as the time required for setting up the experiment and for executing the surface contour measurements.

Data Reduction

The local mass sublimation rate per unit area is evaluated from

$$m' = \rho_s \delta z / \delta \tau \tag{1}$$

Then the local mass transfer coefficient h_{local} can be determined as

$$h_{local} = m' / (\rho_{n,w} - \rho_{n,b}) \tag{2}$$

where $\rho_{n,w}$, is determined by using the perfect gas law and the vapor pressure-temperature relation for naphthalene and $\rho_{n,b}=0$, see Goldstein [10]:

$$\rho_{n,w} = P_{n,w} / (RT_w) \tag{3}$$

$$\log P_{n,w} = 11.55 - 3765/T_w \tag{4}$$

The local Sherwood number is defined as:

$$Sh_{local} = h_{local} \cdot d_h / D_{naph} \tag{5}$$

where D_{naph} is diffusion of naphthalene and d_h the hydraulic diameter of finned tube bank channel. The diffusion of naphthalene is calculated by [10]

$$D_{naph} = 0.0681(T/298.10)^{1.93}(1.013 \times 10^5/P_{atm}) \times 10^{-4} \tag{6}$$

The definition of d_h in the present study is

$$d_h = 4(S_1 - a)T_p / (2(S_1 - a) + 2T_p) \tag{7}$$

Nu_{local} is defined as

$$Nu_{local} = \alpha_{local} \cdot d_h / \lambda_{air} \tag{8}$$

After obtaining the local and average Sherwood number, the analogy between heat and mass transfer is employed to determine the local or average Nusselt number by

$$Nu = Sh(Pr/Sc)^n \tag{9}$$

Sc is calculated by [10]:

$$Sc = 2.28(T/298.10)^{-0.1526} \tag{10}$$

According to the suggestion of Goldstein [10] and the analysis of Saboya et al. [11] $n=0.4$ is adopted in this study.

The Reynolds number and the friction factor are defined as

$$Re = \rho \cdot u_{max} \cdot d_h / \mu \tag{11}$$

$$f = \Delta p d_h / (L\rho u_{max}^2/2) \tag{12}$$

where $u_{max} = V/A_{min}$.

The Parameter to Select the Optimum Height of VG

In general, an increase in heat transfer yields an increase in pressure drop, the trade-off between the increased heat transfer and the increased pressure drop should be considered. However, it is difficult to simultaneously evaluate both the heat transfer coefficient of the larger the better and the pressure drop of the smaller

the better. It is known that Colburn factor (j) and friction factor (f) are the relevant parameters used to characterize the heat transfer coefficient and the pressure drop, respectively, of a heat exchanger. But, a direct comparison on the basis of j and f factors is not useful in selecting the optimum heat exchanger, because if j is large, f also becomes large. The performance evaluation criterion based on area goodness factor has been proposed in Yun et al. [9] to compare the thermal and dynamic performance of heat exchangers. The proposed criterion is obtained by comparing a studied heat exchanger to a reference heat exchanger. From these two heat exchangers two ratios can be obtained. One is the ratio of the heat transfer rate per unit temperature difference, per unit surface area, and the other is the ratio of the friction power dissipated per unit surface area. A new ratio can be obtained through above-mentioned two ratios.

The friction power dissipated per unit surface area is

$$N/A = \Delta p u A_{front} = \left(\frac{\mu^3}{2\rho^2}\right) \frac{LA_{front}}{d_h A} f \left(\frac{Re}{d_h}\right)^3 \tag{13}$$

From definition $d_h = 4A_{front}/U$, $LU=A$, we have $LA_{front}/(d_h A) = 1$.

$$N/A = \left(\frac{\mu^3}{2\rho^2}\right) \cdot f \cdot \left(\frac{Re}{d_h}\right)^3 \tag{14}$$

From definition of the Colburn j factor, $j = \alpha Pr^{2/3}/(\rho c_p u)$, the heat transfer rate per unit temperature difference, per unit surface area is

$$\alpha = \left(\frac{\mu c_p}{Pr^{2/3}}\right) \cdot j \cdot \left(\frac{Re}{d_h}\right) \tag{15}$$

The ratio of the heat transfer rate per unit temperature, per unit area of studied surface or heat exchanger and reference surface or heat exchanger is

$$\frac{\alpha}{\alpha_R} = \left(\frac{j}{j_R}\right) \cdot \frac{(Re/d_h)}{(Re/d_h)_R} \tag{16}$$

The ratio of the friction power dissipated per unit area of studied surface or heat exchanger and reference surface or heat exchanger is

$$\frac{(N/A)}{(N/A)_R} = \left(\frac{f}{f_R}\right) \cdot \frac{(Re/d_h)^3}{(Re/d_h)_R^3} \tag{17}$$

Eliminating $(Re/d_h)/(Re/d_h)_R$ in Eqs. (16) and (17) we have

$$\frac{\alpha/\alpha_R}{\{(N/A)/(N/A)_R\}^{1/3}} = \frac{j/j_R}{(f/f_R)^{1/3}} \tag{18}$$

Therefore, we defined JF as

$$JF = \frac{\alpha/\alpha_R}{\{(N/A)/(N/A)_R\}^{1/3}} = \frac{j/j_R}{(f/f_R)^{1/3}} \tag{19}$$

In real working condition of heat exchanger, the heat transfer coefficient α is

$$\alpha = Q/F_f \Delta T_m \tag{20}$$

where, Q represents the amount of heat transferred from the fin surface, ΔT_m indicates the logarithmic mean temperature difference, F_f is the area of the fin surface. JF is a dimensionless factor of the larger the better characteristics.

From the experimental procedure mentioned above, we can get the local heat transfer coefficient at constant fin temperature (this is determined by the analogy between heat and mass transfer used in present experiments). In real condition, the temperature is not constant on the fin surface. In order to determine the heat transferred from the fin in real condition, the local temperature on the fin is required. Here we use a numerical method to get the local temperature on the fin surface. Figure 4(a) shows the model we
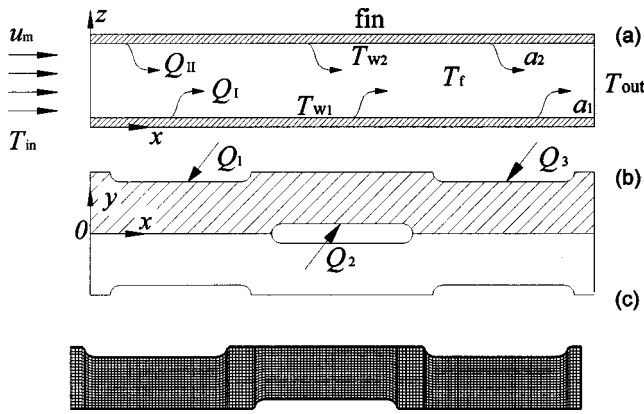
Fig. 4 Numerical model to get the heat transferred from fin: (a) channel of simulation model; (b) domain of simulation; and (c) grid system.

used to determine the heat transferred and temperature of fin surface. The inlet air temperature is T_{in}, the inlet airflow velocity is u_m, and the outlet temperature of air is T_{out}. The temperature of fin surfaces I and II is $T_{w1}(x,y)$ and $T_{w2}(x,y)$, respectively. The heat transferred from fin surface I and II is $Q_I(x,y)$ and $Q_{II}(x,y)$, respectively. $T_f(x)$ is the span-averaged bulk temperature of air. The experimental results of heat transfer coefficient on the fin surface are $\alpha_1(x,y)$ and $\alpha_2(x,y)$, respectively. The fin surface temperature is obtained by solving the heat conduction equation:

$$\lambda_{fin}\left(\frac{\partial^2 T}{\partial x^2}+\frac{\partial^2 T}{\partial y^2}+\frac{\partial^2 T}{\partial z^2}\right)=0 \tag{21}$$

The numerical simulation domain is the region hatched as shown in Fig. 4(b). The boundary conditions are: the temperature in the region where the fin contacts with tube is T_{tube}, and heat conduction insulating condition is applied to the other surfaces except fin surfaces I and II. On fin surfaces II and I, the following boundary condition is used, respectively.

$$\lambda_{fin}\frac{\partial T(x,y)}{\partial z}\bigg|_{z=0}=\alpha_2(x,y)(T_{w2}(x,y)-T_f(x)) \tag{22}$$

$$\lambda_{fin}\frac{\partial T(x,y)}{\partial z}\bigg|_{z=\delta}=\alpha_1(x,y)(T_{w1}(x,y)-T_f(x)) \tag{23}$$

The $T_f(x)$ and T_{out} are calculated using following equations:

$$Q(x)=\int_0^x\int_{l_y}[\alpha_1(x,y)\{T_{w1}(x,y)-T_f(x)\}$$
$$+\alpha_2(x,y)\{T_{w2}(x,y)-T_f(x)\}]dydx+Q_{tube}(x) \tag{24}$$

Because we only have the averaged experimental heat transfer coefficient for flat tube, the assumption that heat transfer coefficient and the temperature do not vary across the tube is needed. As for the configuration of this study, the area ratio of flat tube surface to total heat transfer surface is 11.5%, using of average instead of local Nu of flat tube will not cause significant difference to real case.

$$T_f(x)=T_{in}+Q(x)/(Ac_pu\rho) \tag{25}$$

$$T_{out}=T_{in}+Q(L)/(Ac_pu\rho) \tag{26}$$

The ΔT_m is calculated using

$$\Delta T_m=\{(T_{tube}-T_{in})-(T_{tube}-T_{out})\}/\ln\left(\frac{T_{tube}-T_{in}}{T_{tube}-T_{out}}\right) \tag{27}$$

For different height of VG, the heat transfer area of fin surface does not change. From Eq. (20), we have following JF expression.

$$JF=\frac{j/j_R}{(f/f_R)^{1/3}}=\frac{1}{(f/f_R)^{1/3}}\cdot\frac{Q/\Delta T_m}{(Q/\Delta T_m)_R} \tag{28}$$

The density and heat capacity is determined under the temperature of $(T_{in}+T_{out})/2$.

Due to the complex of computation domain, we use the curvilinear coordinate system to solve Eq. (6). The grid system in x-y plane is shown in Fig. 4(c). In calculating, the grid size of 165 $\times20\times10$ is used. Three different thickness, $\delta_{fin}=0.05$, 0.10, 0.15 mm in real geometry are considered, because the scale factor is 2.5 in the model of experiments, $\delta_{fin}=0.125$, 0.25 and 0.375 mm are used in calculation. Three different heat conductivities of fin, $\lambda_{fin}=50$, 100, 390 W/m·K are selected. The convergent solution is obtained when the relative error of the sum of the heat conducted from tubes and the sum of the heat transferred from fin surfaces I and II is less than 10^{-3}.

Validation of Experimental Method and Uncertainty

A group of test runs for finned flat tube bank without VG enhancement was carried out. We compared our results with published data obtained at real working conditions of a finned flat tube bank heat exchanger in Kylikof [12]. Although, the boundary condition of present experiments is not the same as real working condition, as shown in Fig. 3 of Wang et al. [7], the experimental results are found in good agreement with the published data. The minimal value can be read for naphthalene depth is 1 μm, for one test running, the smallest sublimation depth of all points measured is about 33 μm, considering nature convection sublimation in process of measurement, the uncertainty of sublimation depth is about 5.2%. The uncertainty of temperature is 0.034% in Kelvin scale. The uncertainty of time interval is 0.1%. The uncertainty of the density of naphthalene is 1.1%, $p_{n,m}$ is about 3.5%, considering the temperature effect, the uncertainty of $\rho_{n,m}$ is 4.03%, and D_{naph} is about 4.1%. The uncertainties of other data such as Sh or h_{local} were estimated by a single sample theory of Moffart [13]. From this theory the uncertainties of h_{local}, α_{local}, Sh, and Nu are 4.0, 4.0, 5.8, 5.9, and 5.9 percent, respectively. In average experiments at smallest Reynolds number case, the uncertainty of f is 7.1%. For the Reynolds number the local measurements were carried out, the uncertainty of f is about 2.3%.

In order to estimate the uncertainty of JF, the uncertainty of $Q/\Delta T_m$ is necessary, in this case we have to conduct some numerical simulations. In simulations, we considered one normal case and one worst case. For normal case, we used experimental results of local heat transfer coefficient, for the worst-case local experimental heat transfer coefficient (at all measured points) increased by +4.0%. The numerical simulation results found that the uncertainty of $Q/\Delta T_m$ is about 1.6%. According to the single sample theory of Moffart [13] The uncertainty of JF is

$$\frac{\delta JF}{JF}=\sqrt{\left\{\frac{\delta(Q/\Delta T_m)}{(Q/\Delta T_m)}\right\}^2+\left\{\frac{\delta(Q/\Delta T_m)_R}{(Q/\Delta T_m)_R}\right\}^2+\frac{1}{9}\left\{\frac{\delta f}{f}\right\}^2+\frac{1}{9}\left\{\frac{\delta f_R}{f_R}\right\}^2}$$

$$=\sqrt{(1.6\%)^2+(1.6\%)^2+(2.3\%)^2/9+(2.3\%)^2/9}=2.5\%$$

The heat transfer boundary condition analogy to the mass transfer boundary condition of this study is constant temperature. In heat transfer case, all surface are active heat transfer surface, in mass transfer experiments there were some surfaces such as front and rear end surfaces of the fin, and surfaces of VGs, which were not covered with naphthalene. The corresponding area ratios to total active surface are 0.2%, 2.9% for front or rear end surfaces and VG surfaces, respectively. Due to the small area ratio, it is reasonable to assume that without covering of naphthalene on these surfaces the effects on overall heat/mass transfer or thermal boundary layer are negligible. Furthermore, the start point of mass transfer boundary layer and the velocity layer is not the same point; this is not the case in real heat exchanger configuration. Large difference will come from the inlet effects on heat/transfer case if the test element length in stream direction is small. As for the configuration of this study, T_p/L (covered by naphthalene) $= 33$, so the inlet effect on overall results is very limited. For local heat transfer coefficient near inlet the experimental value will be lower than for real case, for which developing of velocity and thermal boundary layers starts at the same point. If all comparisons and evaluations were carried out for the same basic configuration as for the referenced one, the results of JF will be less affected by different start points of velocity and thermal boundary layers.

Results and Discussion

The Effect of Height of VG on Local Nu Distribution. Figure 5 shows the local Nu distribution on fin surface II for different H. Without VGs, Nu on fin surface has large values in a U-shaped band around tube, especially in the stagnation region as shown in Fig. 5(a). With VGs, for $H=3$ mm ($H/T_p=0.6$), VGs increase the Nu in a narrow region beside every tube row. Along the first tube row the enhancement of Nu is weaker than along the other two rows of tubes. With increasing H, the enhancement of heat transfer is intensified. In Fig. 5(d), there are some points at which Nu is large. These points correspond to the highest tips of VGs. Even though H is larger, the Nu along the first tube row is relative small, especially in the region between the first and the second
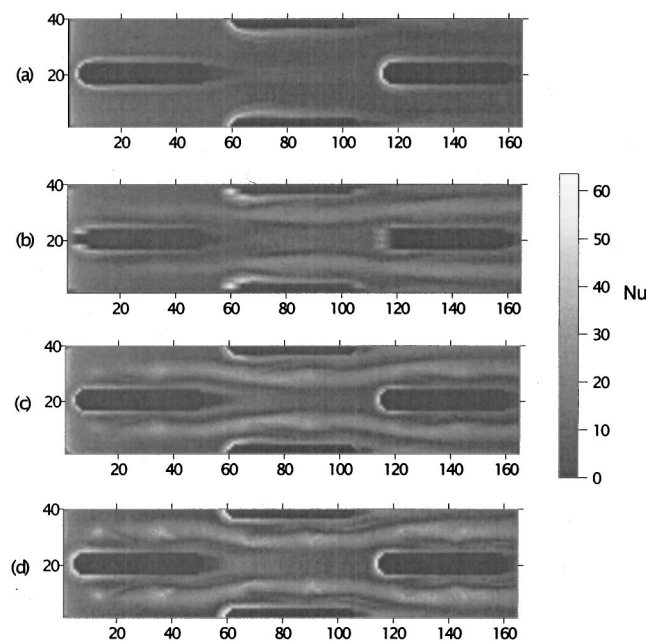
Fig. 5 Comparison of local Nu distribution on fin surface II: (a) without VGs, Re=1797; (b) with VGs, Re=1853, H=3 mm; (c) with VGs, Re=1836, H=4 mm; and (d) with VGs, Re=1796, H=5 mm.
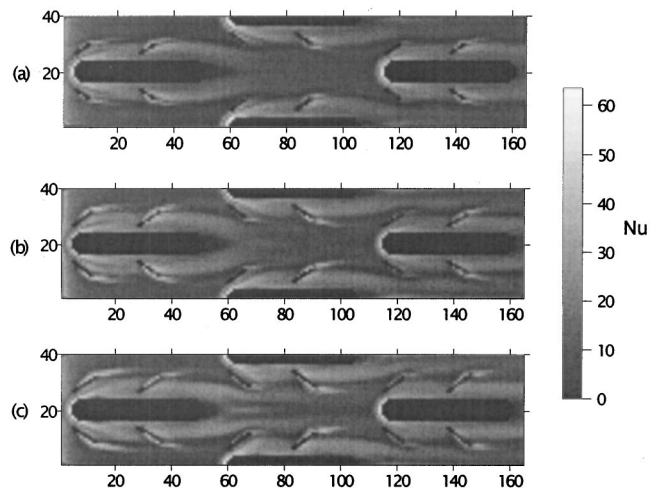
Fig. 6 Comparison of local Nu distribution on fin surface I: (a) with VGs, Re=1853, H=3 mm (b) with VGs, Re=1836, H=4 mm; and (c) with VGs, Re=1796, H=5 mm.

VG pairs. It seems that the oncoming vortices contribute to the enhancement of heat transfer downstream on this surface. The common characteristics of Figs. 5(b) to (d) are that the regions with large Nu are located beside tubes, between the enhanced region and tube there is a region with small Nu.

Figure 6 shows Nu distribution on fin surface I for different H. The measurements for the no VG case for fin surface I were also obtained, but are identical to those for fin surface II to within 4% for averaged Nu. When H is small, the width of the mostly enhanced region is small as shown in Fig. 6(a). From Figs. 6(b) and (c), it is showed that when H is greater than 4 mm the width of mostly enhanced region nearly has no change. This is contrary to one's expectation that the width of mostly enhanced region should increase, because in the experiments the aspect ratio is constant, 2, when H increases the base length of VG also increases. From this figure, it is clear that when H increases the heat transfer enhancement behind the trailing edge of VG is intensified. Unlike behind the trailing edge of other VG pairs, behind the trailing edge of the first VG pair of the second and the third rows of tubes there is no distinct enhanced region. The common characteristic of Figs. 6(a) to (c) is that the regions with large Nu are located near the tubes.

Figure 7 presents the local distribution of Nu_{VG}/Nu_0 on the fin surface II at 9 span-cross sections labeled in Fig. 3(c). Nu_{VG}/Nu_0 at the sections 1, 2, and 3 along the first tube row is smaller than at the periodically corresponding sections of the second and the third rows of tubes. Along the first tube row, with increasing H, Nu_{VG}/Nu_0 becomes larger and the width of enhanced region increases. The largest Nu_{VG}/Nu_0 occurred at section 3 with a value of 3 for $H=5$ mm at position $2.4S_1$. As shown at sections 4 through 6, the width of enhanced region increases as H increasing from 3 mm to 4 mm, but it is nearly the same when H is greater than 4 mm. At section 4, Nu_{VG}/Nu_0 is almost the same for H $=4$ mm and 5 mm with a largest value of 4.3 at position of $0.33S_1$, but the peak value for $H=3$ mm is only about 2.5 at position of $0.3S_1$. For sections 7 through 9, the width of enhanced region and Nu_{VG}/Nu_0 are nearly the same for $H=3$ mm and 4 mm, but are smaller than that for $H=5$ mm. The largest Nu_{VG}/Nu_0 is about 4.5 at section 7 for $H=5$ mm at position of $0.17S_1$. From this figure, we see that as increasing H, Nu_{VG}/Nu_0 increases, but the mostly enhanced region will move away from the tube wall. The increase of the average Nu_{VG}/Nu_0 does not necessary mean that we can get more heat transfer from the fin surfaces with reasonable flow loss penalty, if the temperature difference on fin surface is taken into consideration.

Figure 8 shows the local distribution of the Nu_{VG}/Nu_0 on fin

Fig. 7 Effects of *H* on spanwise local Nu/Nu₀ on fin surface II
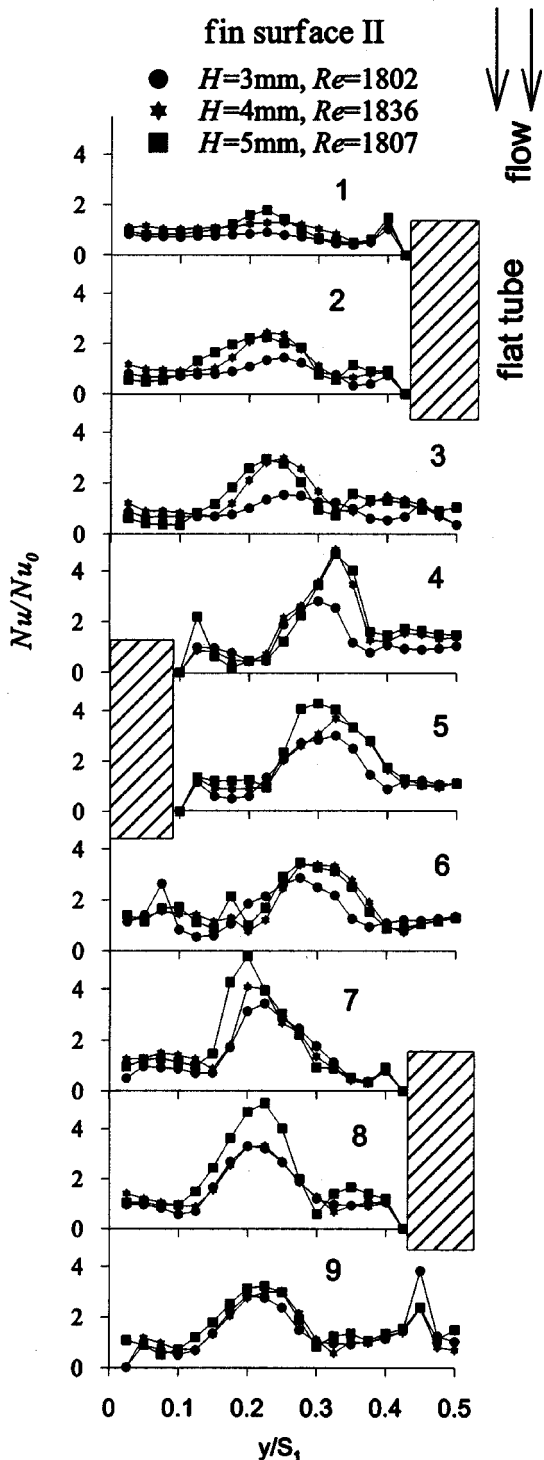
Fig. 8 Effects of *H* on spanwise local Nu/Nu₀ on fin surface I

surface I at 9 span-cross sections. At all sections presented, we can see that with increasing of H, $\mathrm{Nu_{VG}}/\mathrm{Nu_0}$ increases. The largest value of $\mathrm{Nu_{VG}}/\mathrm{Nu_0}$ is different for different tube row. For the first tube row the largest $\mathrm{Nu_{VG}}/\mathrm{Nu_0}$ is about 3.6 at section 3 for $H = 5$ mm at position of $0.35S_1$. The largest $\mathrm{Nu_{VG}}/\mathrm{Nu_0}$ is about 5.0 and 4.0 for the second and third rows of tubes at section 5 and section 8, respectively. Comparing the $\mathrm{Nu_{VG}}/\mathrm{Nu_0}$ along every tube row, its difference is smaller than that along every tube row on fin surface II. There are two peak values at sections 1 and 2, 4, and 5, and 7 and 8 for $H = 4$ mm and 5 mm. According to the
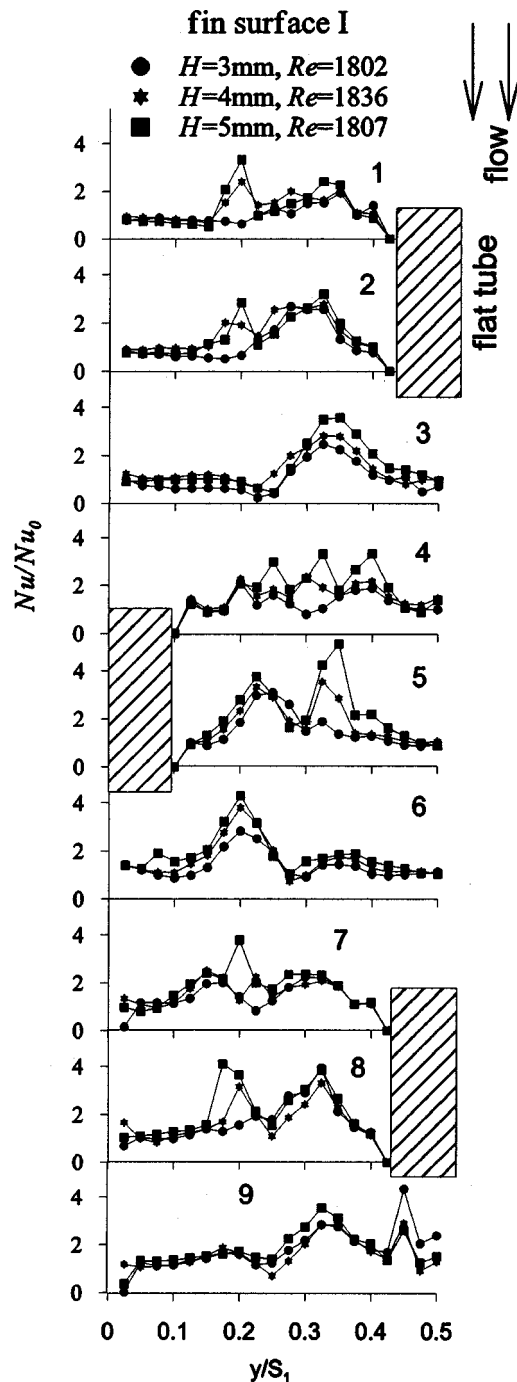
location of these sections, the peak value near to the wall of the tube comes from the main vortices generated by VG. The other comes from the vortices generated by the trailing edge of VG, although the increase of H contributes to great increase of these vortices and the increase of $\mathrm{Nu_{VG}}/\mathrm{Nu_0}$, from Fig. 6, such enhancement only occurred in a very small region. The dependence of $\mathrm{Nu_{VG}}/\mathrm{Nu_0}$ caused by vortices generated from trailing edge of VG on H may imply that due to the blockage of VGs, more fluid will move through the vacancy beside VGs. This will reduce the strength of main vortices generated by VGs. The enhancement of $\mathrm{Nu_{VG}}/\mathrm{Nu_0}$ caused by vortices generated from trailing edge will contribute to the average value of present experimental results, but may not contribute a lot to the real heat transfer, because the enhanced region is small and far from the tube wall.
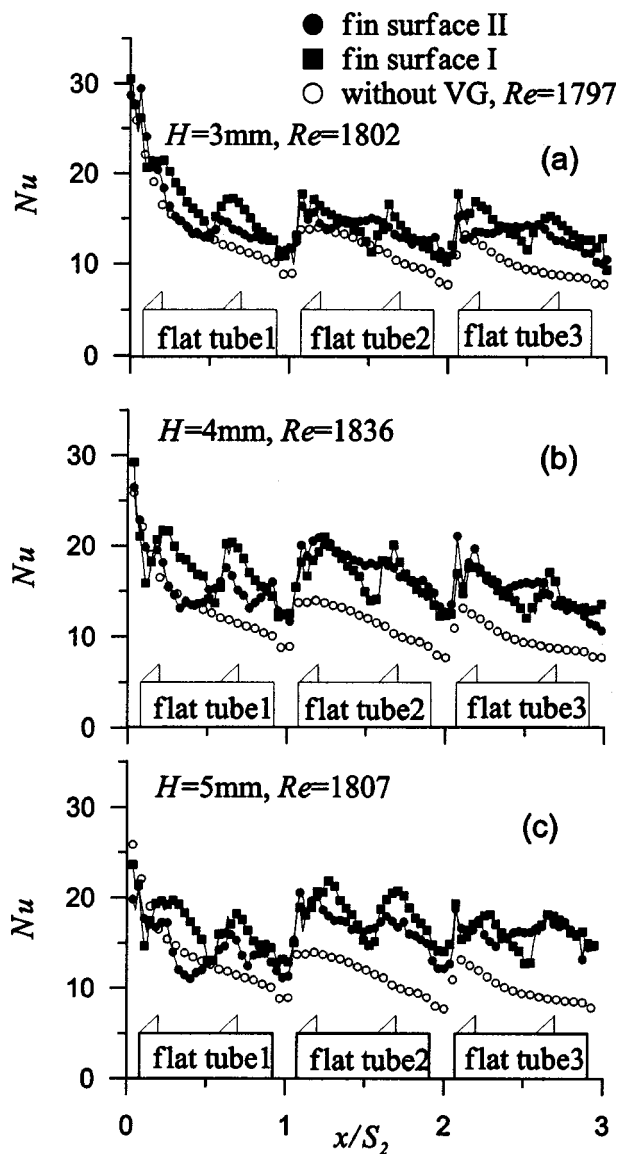
Fig. 9 Comparison of span-averaged Nu on the fin surfaces I and II at different *H*

Fig. 10 Effects of *H* on span-averaged Nu on the fin surfaces I and II

For the configurations studied, vortices generated by VGs of the first tube row have counter-rotating direction to the vortices generated by VGs of the next tube row. According to the studies made by Tiggelbeck et al. [14,15] and Chen et al. [6], the qualitative flow structure, the number of developing vortices per VG and their stream wise development are independent of whether the flow approaching the vortex generator is uniform or vortical. These phenomena can also be observed in Figs. 5(*b*) to (*c*) indirectly, because there is a similarity in the Nu distribution along three different tube rows on fin surface I. From Figs. 7 and 8, it is clear that the span position of peak values of Nu_{VG}/Nu_0 at three sections along three rows of tubes changes along stream direction. It seems that the centerlines of vortex cores beside the tube try to converge in the wake region of the tube. This displacement is caused by the lower pressure in the wake regions of tubes due to the change of cross section area of flow passage.

Effect of Height of VG on Span-Averaged Nu Distribution. Figure 9 shows the span-averaged Nu distribution in the stream direction and the comparison with the corresponding Nu of no enhanced one for the cases of $H=3$ mm, 4 mm, and 5 mm, respectively. On fin surface I, it can be seen that Nu is enhanced for all of H at most region except in the beginning region of the first tube row, where heat transfer is reversed at small region just ahead the first VG pair. The main reason is that due to flow blockage caused by the presence of the VG pair, the flow velocity near fin surface I decreases. From Figs. 9(*a*) to (*c*), it is clear that with increasing H, the reversed effect increases. On fin surface I, just behind every VG pair, there is a peak value of Nu. Along the second tube row Nu is larger than along other two rows of tubes at periodical corresponding position, and with increasing height of VG, Nu increases on this surface. On fin surface II, Nu increases greatly only further downstream. Along the first tube row, it is clear that when H is small, the enhancement of Nu is very limited. Between the first VG pair and the second VG pair of the tube row, Nu has almost no increase, see Figs. 9(*a*) and (*b*). It is surprising that when $H=5$ mm, Nu is reversed greatly in the region between the first and the second VG pairs of the first tube row as Fig. 9(*c*) shows. Although we cannot get the clear answer to this phenomena duo to the shortage of flow structure information, but the possible reason may be the great flow blockage caused by the increase of H, and most flow will not pass through the space over the VG, and will pass through the space beside VG. Furthermore, after flow passes over the VG, due to the abruptly change of the cross area of flow passage, a recycle flow may form near fin surface II. For three cases of H studied, along the first tube row the Nu on fin surface II is smaller than on fin surface I. With increasing H, along the second and the third rows of tubes, Nu on fin surface II becomes larger, and at some region it is larger than on fin surface I.

Figure 10 presents the comparisons of Nu on fin surfaces I and II at different H, respectively. It seems that the effects of H on Nu are more mixed on fin surfaces I and II, especially heat transfer enhancement is dependent on the location. On fin surface II, along the first tube row, increasing H will not enhance the heat transfer as $x/S_2<0.5$. When $0.5<x/S_2<2$, Nu for the case of $H=4$ mm is larger than Nu for cases of $H=3$ mm and 5 mm. Further downstream Nu for $H=5$ mm is larger than Nu for cases of $H=3$ and 4 mm. The more effective improvement of heat transfer occurs in the region around the second and third rows of tubes. On fin surface I, when $x/S_2<0.25$, Nu increases with decreasing H. In

Fig. 11 Effects of H on average Nu and f at different Re

will increase Nu and f. Without considering the fin efficient, so far, we still cannot determine the optimum height of VG in real working condition of heat exchanger.

Screening of Optimum Height of VG. As mentioned above, the numerical method is used to get the heat transferred from fin surfaces. In the calculation, the inlet temperature of air is set to 40°C and the tube wall temperature is set to 80°C. The airflow rate is determined through the three values used in local experiments, the average value of Re is 1815. The friction factor f for VG enhanced tube bank comes from Eqs. (15) and (16) in Wang et al. [7]. The experimental result of the friction factor of finned flat tube bank without VGs at $T_p = 5$ mm is $f = 2.98 \, \mathrm{Re}^{-0.483}$. At different heat conductivity and fin thickness, the results are present in the Tables 1–3. In Table 1, the results of referenced heat transfer exchanger (without VG enhancement) are presented. The effects of the H on the heat transfer performance are presented in Tables 2 and 3.

In Table 1, for the finned flat tube bank fin without VG enhancement, when heat conductivity $\lambda_{\mathrm{fin}} = 100$ W/m·K, the heat transferred from the fin increases with increasing fin thickness δ_{fin}. For example, the total heat transferred from the fin surface, Q, is 4.90, 5.54 and 5.82 W for $\delta_{\mathrm{fin}} = 0.05$, 0.1 and 0.15 mm (0.125, 0.250 and 0.375 mm in the Tables), respectively. For given λ_{fin} and δ_{fin} the heat transferred from the different row of tube is different. As shown in Table 1, for $\delta_{\mathrm{fin}} = 0.1$ mm and $\lambda_{\mathrm{fin}} = 100$ W/m·K the heat transferred from half tube of the three tubes rows is 2.28, 1.87 and 1.39 W, respectively. When δ_{fin} is constant, with increasing λ_{fin}, the heat transferred from the fin increases, for example, from 4.89 to 6.22 W as λ_{fin} changes from 50 to 380 W/m·K. The heat transfer per unit temperature difference also increases.

The effects of the H on the heat transfer performance of the finned flat tube bank with VGs are dependent on the fin thickness and heat conductivity of the fin. The dependence on the thickness of the fin is presented in Table 2. At constant λ_{fin} and small δ_{fin}, with increasing H, the JF decreases from 1.005 to 0.98. This means that the heat transfer performance will become worse when $H > 3$ mm. The heat transfer coefficient increase does not counterbalance the increase of penalty of flow loss. When δ_{fin} is 0.1 mm and 0.15 mm, with increasing H, the JF firstly increases and then decreases. For example, if $\delta_{\mathrm{fin}} = 0.1$ mm and λ_{fin}

the region $0.25 < x/S_2 < 1$, The Nu for the case of $H = 4$ mm is larger than for the cases of $H = 3$ and 5 mm. In the region $x/S_2 > 1$, with increasing H, Nu increases. More pronounced enhancement comes around the second row of tube.

Figure 11 presents the average Nu and f at various Reynolds numbers, Re, for different H. The Nu was averaged over two flat tube surfaces and surfaces I and II. It is clear that increasing H

Table 1 Summary of the numerical results of the finned flat tube bank without VG—reference data

δ_{fin} mm	λ_{fin} W/m·K	T_{out} °C	Q W	ΔT_m °C	$Q/\Delta T_m$ W/°C	f	Q_1 W	Q_2 W	Q_3 W	Q_I W
0.125	100	53.63	4.90	32.71	0.150	0.0794	1.82	1.74	1.35	2.45
0.250	100	55.41	5.54	31.67	0.175	0.0794	2.28	1.87	1.39	2.77
0.375	100	56.18	5.82	31.21	0.187	0.0794	2.45	1.94	1.43	2.91
0.250	50	53.59	4.89	32.74	0.149	0.0794	1.93	1.70	1.27	2.44
0.250	100	55.41	5.54	31.67	0.175	0.0794	2.28	1.87	1.39	2.77
0.250	380	57.30	6.22	30.53	0.204	0.0794	2.64	2.06	1.53	3.11

Table 2 The effects of the height of VG on the heat transfer performance of the finned flat tube bank VGs—dependence on the thickness of the fin

H/T_p	δ_{fin} mm	λ_{fin} W/m·K	T_{out} °C	Q W	ΔT_m °C	$Q/\Delta T_m$ W/°C	f	JF	Q_1 W	Q_2 W	Q_3 W	Q_{II} W	Q_I W
0.6	0.125	100	55.05	5.41	31.89	0.170	0.1137	1.005	2.05	1.90	1.46	2.68	2.73
0.8	0.125	100	55.64	5.62	31.54	0.178	0.1358	0.992	2.08	2.02	1.53	2.71	2.92
1.0	0.125	100	56.00	5.75	31.32	0.184	0.1559	0.980	2.09	2.08	1.59	2.80	2.96
0.6	0.250	100	57.27	6.21	30.56	0.203	0.1137	1.029	2.49	2.13	1.60	3.10	3.11
0.8	0.250	100	58.22	6.55	29.97	0.219	0.1358	1.046	2.64	2.30	1.62	3.18	3.37
1.0	0.250	100	58.62	6.70	29.72	0.225	0.1559	1.026	2.60	2.38	1.72	3.28	3.42
0.6	0.375	100	58.23	6.56	29.97	0.219	0.1137	1.039	2.68	2.22	1.66	3.28	3.27
0.8	0.375	100	59.37	6.97	29.25	0.238	0.1358	1.064	2.86	2.42	1.69	3.40	3.57
1.0	0.375	100	59.78	7.12	28.99	0.245	0.1559	1.046	2.81	2.52	1.80	3.49	3.62

Table 3 The effects of the height of VG on the heat transfer performance of the finned flat tube bank VGs—dependence on the heat conductivity of the fin

H/T_p	δ_{fin} mm	λ_{fin} W/m·K	T_{out} °C	Q W	ΔT_m °C	$Q/\Delta T_m$ W/°C	f	JF	Q_1 W	Q_2 W	Q_3 W	Q_{II} W	Q_I W
0.6	0.250	50	55.04	5.41	31.89	0.170	0.1137	1.012	2.09	1.89	1.44	2.68	2.73
0.8	0.250	50	55.62	5.62	31.55	0.178	0.1358	0.999	2.17	2.00	1.45	2.70	2.92
1.0	0.250	50	55.98	5.75	31.33	0.183	0.1559	0.981	2.17	2.06	1.52	2.79	2.96
0.6	0.250	100	57.27	6.21	30.56	0.203	0.1137	1.029	2.49	2.13	1.60	3.10	3.11
0.8	0.250	100	58.22	6.55	29.97	0.219	0.1358	1.046	2.64	2.30	1.62	3.18	3.37
1.0	0.250	100	58.62	6.70	29.72	0.225	0.1559	1.026	2.60	2.38	1.72	3.28	3.42
0.6	0.250	380	59.61	7.05	29.10	0.242	0.1137	1.052	2.92	2.38	1.76	3.55	3.50
0.8	0.250	380	60.05	7.57	28.18	0.269	0.1358	1.103	3.11	2.63	1.83	3.71	3.86
1.0	0.250	380	61.48	7.73	27.90	0.277	0.1559	1.084	3.05	2.38	1.95	3.80	3.92

$= 100$ W/m·K, the JF is 1.029, 1.046 and 1.026 for $H = 3$, 4 and 5 mm, respectively. It is clear that there is an optimum H as shown in Fig. 12. When $\delta_{fin} = 0.05$ mm, with increasing H, JF decreases monotonously, with increasing δ_{fin}, JF increases at same H and the optimum H becomes clear. From Table 2, the heat transferred from the fin surface II is smaller than the heat transferred from the fin surface I. For example, when $\delta_{fin} = 0.1$ mm, $\lambda_{fin} = 100$ W/m·K and $H = 4$ mm, $Q_{II} = 3.18$ W but $Q_I = 3.37$ W.

In Table 3, the effects of H on the heat transfer performance at different λ_{fin} are presented. At constant δ_{fin} and small λ_{fin}, with increasing H, the JF decreases from 1.012 to 0.981. This phenomenon is the same as that for the case with small fin thickness. When λ_{fin} is 100 and 380 W/m·K, with increasing H, the JF firstly increases and then decreases. If $\delta_{fin} = 0.1$ mm and $\lambda_{fin} = 380$ W/m·K, the JF is 1.052, 1.103, and 1.084 for $H = 3$, 4 and 5 mm, respectively. There is an optimum H as shown in Fig. 13.

With considering the fin efficiency, from Figs. 12 and 13, except the poor conduction in the fin ($\lambda_{fin} = 50$ W/m·K) and very small fin thickness ($\delta_{fin} = 0.05$ mm), the height of VG, H, has an optimum value. For the configurations studied in this paper, the optimum H is 4 mm, corresponding to $H/T_p = 0.8$. For very small fin thickness or very poor conductivity of the fin material, when H is greater than 4 mm, the heat transfer performance will become worse.

For the configurations studied, increase of VG height may not enhance the heat transfer on fin surface II as shown in Fig. 10, especially around the second tube row. From Fig. 10(a) it is clear that on fin surface II Nu around the second tube for $H = 5$ mm is a bit lower than Nu for $H = 4$ mm. As stated before this phenomenon may come from the interactions of vortices generated by VGs located around upstream tube row and VGs located around next tube row due to the vortices generated by these VGs located at different locations have counter-rotating direction. The interactions of these vortices will decrease the intensity of heat transfer enhancement. Increase of H will make the interactions of vortices more intensifying. On fin surface I, development of vortices in stream direction is independent of whether the flow approaching VG is uniform or vortical, so the heat transfer enhancement increases with increasing H. But on fin surfaces I and II, with increase of VG height the largely enhanced region will move away from flat tube wall, after considering of fin efficiency this enhancement will become less useful. Based on these reasons, it is clear that an optimal VG height exists.

Small JF does not mean that VGs cannot enhance heat transfer. As it is the general case that if one wants to enhance the heat transfer, one must spend more things such as power et al. It is very difficult to counterbalance the gain and the payment. Heat transfer can be enhanced if we pay more power. As shown in Figs. 12 and 13, for small fin thickness and heat conductivity, even JF is small than unit, but from Tables 1–3 the heat (**Q**) transferred from the fin surface considered in the manuscript is larger for VGs than for no VGs. For later two cases, more power is spent due to the increase of pressure drop. If JF greater than unit, that means we really enhance the heat transfer with reasonable payment.
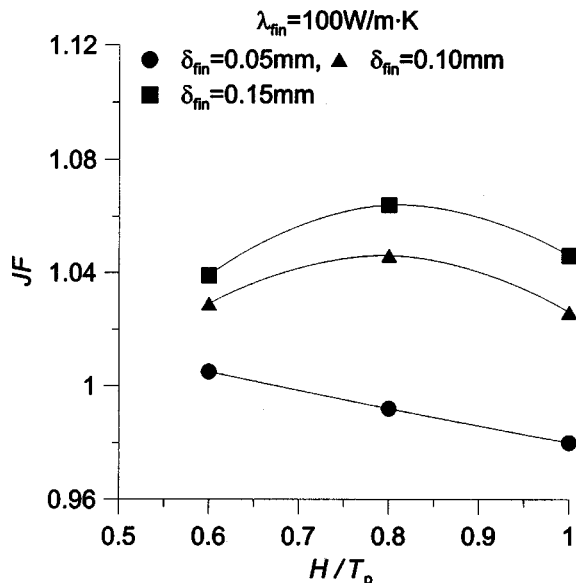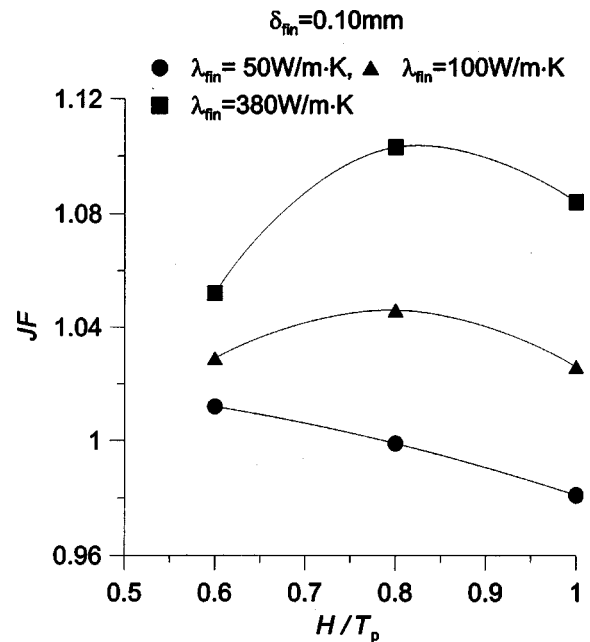

Fig. 12 Effects of fin thickness on optimum H

Fig. 13 Effects of fin materials (heat conductivity) on optimum H

Conclusions

Winglet vortex generators are used to enhance the heat transfer performance of finned flat tube bank fin. The effects of the height of VG on local heat transfer are studied using the naphthalene sublimation method and the optimum height of winglet VG are screened by using JF, a dimensionless factor of larger the better characteristics. In order to get JF, the local heat transfer coefficient obtained in experiments and a numerical method are used to get the heat transferred from the fin. As for the configuration studied in this paper, we get following conclusions:

1) For local characteristic, as increasing H, Nu_{VG}/Nu_0 increases, but the mostly enhanced region moves away from the tube wall.

2) With increasing H to certain degree, the width of enhanced region does not increase significantly.

3) The effects of H on span-averaged Nu are more mixed on fin surfaces I and II, and are dependent on the location. In real working condition, the heat transferred from fin surface I is larger than the heat transferred from fin surface II.

4) The average experimental results show that increasing H increases Nu and f, but with considering the fin efficiency, there is an optimum H to get best heat transfer performance.

5) The optimum H is dependent on the thickness of fin and its heat conductivity. For mostly used fin thickness and conduction, the optimum H is 4 mm, that is $H/T_p = 0.8$.

Acknowledgments

Nomenclature

A = heat transfer surface area [m^2]
A_{front} = cross section area of flow passage [m^2]
A_{mim} = minimum cross section area of flow passage [m^2]
a = width of flat tube [m]
b = length of flat tube [m]
b_{VG} = lateral pitch of vortex generator [m]
B_{pT} = lateral pitch of flat tube: $B_{pT} = S_1/T_p$
B_{pVG} = lateral pitch of vortex generators: $B_{pVG} = b_{VG}/T_p$
d_h = hydraulic diameter of flow channel [m]
D_{nath} = diffusion of naphthalene [m^2/s]
f = friction factor: $f = \Delta p d_h/(L\rho u_{max}^2/2)$
h = mass transfer coefficient [m/s]
H = height of winglet type vortex generators [m]
j = Colburn factor [-]
JF = a dimensionless ratio,
$JF = j/j_R/(f/f_R)^{1/3} = 1/(f/f_R)^{1/3} \cdot Q/\Delta T_m/(Q/\Delta T_m)_R$ [-]
L = streamwise length of fin [m]
L_{PVG} = longitudinal pitch of vortex generators divided by fin spacing: $L_{pVG} = l_{VG}/T_p$
l_{VG} = pitch of in-line vortex generators [m]
m = mass [kg]
m' = mass sublimation rate of naphthalene [kg/m$^2\cdot$s]
N = friction power dissipated (W)
Nu = Nusselt number: $Nu = \alpha d_h/\lambda$
P = pressure of naphthalene vapor [Pa]
p = non-dimensional pitch of in-line vortex generators: $p = l_{VG}/S_2$
Pr = Prandlt number [-]
Q = heat transfer rate [W]
R = universal gas constant [m^2/s$^2\cdot$K]
Re = Reynolds number: $Re = \rho \cdot u_{max} \cdot d_h/\mu$
S_1 = transversal pitch between flat tubes [m]
S_2 = longitudinal pitch between flat tubes [m]
Sc = Schmidt number [-]
Sh = Sherwood number: $Sh = hd_h/D_{naph}$
T_p = fin spacing [m]
T = temperature [K]
u_{max} = maximum velocity [m/s]
u = average velocity of air [m/s]
V = volume flow rate of air [m^3/s]
x, y, z = coordinates [m]
z = sublimation depth [m]

Greeks

α = heat transfer coefficient [W/m$^2\cdot$K]
λ = heat conductivity [W/m$\cdot$K]
μ = viscosity [kg/m$^2\cdot$s]
ρ = density [kg/m^3]
θ = attack angle of vortex generator [°]
τ = time interval for naphthalene sublimation [s]
δ = fin thickness, small value or interval
Δp = pressure drop [Pa]

Subscript

0 = without VG enhancement
1, 2, I, II = fin surface I, fin surface II, respectively
atm = atmosphere
f = fluid
local = local value
m = average
naph = naphthalene
n, b = naphthalene at bulk flow
n, w = naphthalene at wall
VG = with VG enhancement
w = wall or fin surface

References

[1] Fiebig, M., 1998, "Vortices, Generators and Heat Transfer," Chem. Eng. Res. Des., **76**(A2), pp. 108–123.
[2] Fiebig, M., 1995, "Vortex Generators for Compact Heat Exchangers," J. Enhanced Heat Transfer, **2**, pp. 43–61.
[3] Jacobi, A. M., and Shah, R. K., 1995, "Heat Transfer Surface Enhancement Through the Use of Longitudinal Vortices: A Review of Recent Progress," Exp. Therm. Fluid Sci., **11**, pp. 295–309.
[4] Tiggelbeck, S., Mitra, N. K., and Fiebig, M., 1994, "Comparison of Wing-Type Vortex Generators for Heat Transfer Enhancement in Channel Flows," J. Heat Transfer, **116**, pp. 880–885.
[5] Fiebig, M., Valencia, A., and Mitra, N. K., 1994, "Local Heat Transfer and Flow Losses in Fin-Tube Heat Exchanger With Vortex Generators: A Comparison of Round and Flat Tubes," Exp. Therm. Fluid Sci., **8**, pp. 35–45.
[6] Chen, Y., Fiebig, M., and Mitra, N. K., 1998, "Heat Transfer Enhancement of a Finned Oval Tube With Punched Longitudinal Vortex Generator In-line," Int. J. Heat Mass Transfer, **41**, pp. 3961–3978.
[7] Wang, L. B., Ke, F., Gao, S. D., and Mei, Y. G., 2002, "Local and Average Characteristics of Heat/Mass Transfer Over Flat Tube Bank Fin With Four Vortex Generators Per Tube," J. Heat Transfer, **124**, pp. 446–552.
[8] Wang, L. B., Zhang, Y. H., Su, Y. X., and Gao, S. D., 2002, "Local and Average Heat/Mass Transfer Over Flat Tube Bank Fin Mounted In-line Vortex Generators With Small Longitudinal Spacing," J. Enhanced Heat Transfer, **9**(2), pp. 77–87.
[9] Yun, Y. L., and Lee, K. S., 2000, "Influence of Design Parameters on the Heat Transfer and Flow Friction Characteristics of the Heat Exchanger With Slit Fins," Int. J. Heat Mass Transfer, **43**, pp. 2529–2539.
[10] Goldstein, R. J., 1995, "A Review of Mass Transfer Measurements Using Naphthalene Sublimation," Exp. Therm. Fluid Sci., **10**, pp. 416–434.
[11] Saboya, F., and Sparrow, E. M., 1974, "Local and Average Transfer Coefficients for One-Row Plate Fin and Tube Heat Exchanger Configurations," J. Heat Transfer, **96**, pp. 265–272.
[12] Kylikof, U. A., 1988, *The Cooling System of Diesel Locomotive*, Machine-Manufacturing, Moscow, (in Russian).
[13] Moffart, R. J., 1982, "Contribution to the Theory of Single-Sample Uncertainty Analysis," J. Heat Transfer, **104**, pp. 250–260.
[14] Tiggelbeck, S., Mitra, N. K., and Fiebig, M., 1992, "Flow Structure and Heat Transfer in a Channel With Multiple Longitudinal Vortex Generators," Exp. Therm. Fluid Sci., **5**, pp. 425–436.
[15] Tiggelbeck, S., Mitra, N. K., and Fiebig, M., 1993, "Experimental Investigations of Heat Transfer Enhancement and Flow Losses in a Channel With Double Rows of Longitudinal Vortex Generators," Int. J. Heat Mass Transfer, **36**, pp. 2327–2337.

A. Trombe

e-mail: trombe@insa-tlse.fr
Laboratoire d'Energétique,
Université Paul Sabatier,
Toulouse III,
118 Route de Narbonne,
31062 Toulouse Cedex 4,
France

A. Suleiman

Universite de Tichrin,
Faculté de Génie Mécanique et Electrique,
Lattaquié,
Syrie

Y. Le Maoult

Centre des Matériaux de l'Ecole des Mines
Albi-Carmaux,
Campus Jarlard,
Route du Teillet,
81103 Albi Cedex 09,
France

Use of an Inverse Method to Determine Natural Convection Heat Transfer Coefficients in Unsteady State

The purpose of this study is to evaluate the efficiency of an inverse method to determine the variation of convective heat transfer coefficients in the unsteady state inside building enclosures. The experimental system is mainly composed of a vertical, heated, flat plate where natural convection heat flow is generated and of a radiative source which can impose a known flux condition. The inverse method calculates the total heat flux by conduction along the vertical flat plate, together with surface temperatures. Subtracting the local contribution of the radiative heat flux from the total heat flux gives the average convective heat flux at different heights of the plate. For various boundary conditions, it is then possible to determine the values of the convective heat exchange coefficients. Uncertainty calculations relative to these results confirm the reliability of the inverse method developed. [DOI: 10.1115/1.1597611]

Keywords: Heat Transfer, Inverse, Natural Convection, Optimization, Unsteady

1 Introduction

The common approach for modeling internal surface convection is to employ the convective heat transfer relation Eq (1).

$$q_{cv} = h_{cv} \times (T_{\text{surf}} - T_{\text{air}}) \qquad (1)$$

This treats the room air as uniform and characterizes surface convection by a convection coefficient (h_{CV}) and by the temperature difference between room air (T_{air}) and the solid surface (T_{surf}). Note that, for thermal balance applications, the surface temperature is also assumed to be uniform. In this manner the surface convective term enters the energy balance of both the room air volume and the internal surface. Generally speaking, convection heat transfer can vary from surface to surface in the building, as well as with time, depending on local air flow patterns. That is to say that several convection regimes depending on various conditions (type of flow, operational states of equipment, external weather conditions, etc.) are commonly encountered in buildings.

This is the case for glazed spaces, such as verandas or atria, which have become a common feature in architecture. This type of space with great volumes is generally not heated. As the temperature varies freely, such volumes are more difficult to simulate than heated spaces. One of the difficulties encountered comes from the variations in the surface heat exchange coefficients due to the incoming radiative energy and particularly to direct beam radiation. To study this problem, several models have been developed in our laboratory [1,2]. These models can accurately determine the location and the flux density of the sun patch inside a dwelling even for complex enclosures. The intention of the present study is to evaluate the impact of the sun patch on the convective heat transfer value, Fig. 1. In our laboratory natural convection in building enclosures has been studied over many years using direct experimental approaches. The method for this type of study consists of measuring the temperature of the boundary layer with a very fine thermocouple [3–5], see Fig. 2. The temperature variation (slope) very near the surface studied leads

to a knowledge of the convective heat flux. Nevertheless, this type of heat transfer determination can also be subject to measurement errors and needs corrections [6].

Furthermore, this experimental method is not suitable for high fluxes such as those a direct beam can produce on thermocouple measurements. Consequently, the authors proposed to determine the convective heat transfer by a nondirect approach based on the use of an inverse method. Initial research work on this subject was carried out for the steady state by Cuniasse–Languans [7]. For various boundary conditions, the results obtained by the inverse method were validated by comparison both with an experimental method (direct method), Fig. 2, and with a relation from the literature (theoretical method), [8].

The results show that the inverse method is pertinent. However, as it is also subject to measurement errors, it must be constructed very carefully.

2 Experimental Setup

2.1 Description. The experimental setup mainly consisted of a uniformly heated vertical flat plate called ''the active plate'' throughout this study, and a light source.

The active plate was located in a small, open enclosure, Fig. 3, to avoid the influence of external turbulence (door openings, movements of persons) on the development of the boundary layer.

Two openings of small dimensions were made in this enclosure. The first opening, at the bottom of the active plate, created a leading hedge for the development of convection exchanges. The second, located at the top of the enclosure, was necessary to evacuate the heat coming from the active plate.

The dimensions of the active plate were: 1 meter height, 0.30 meter width and 0.008 meter thickness (resin only). It consisted, from the back face to the front face, of the following components, Fig. 4.

- A synthetic insulation material on all sides, except the front face of the plate, to provide adiabatic conditions.
- A heat exchanger with hot water circulating at a defined temperature.
- A copper plate to ensure uniform temperatures. On it were fixed several thermocouples allowing us to know the bound-
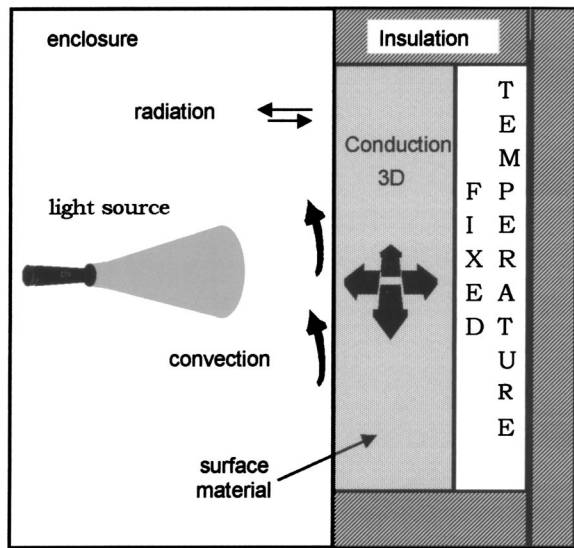
Fig. 1 Study of the impact of the solar patch on the convective heat transfer
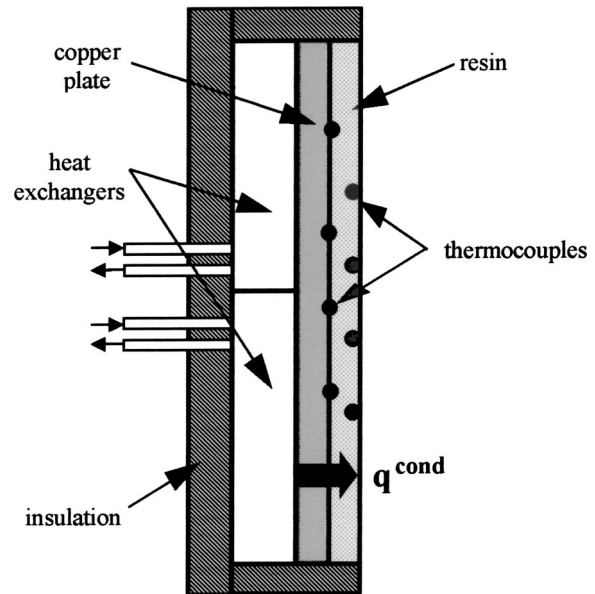
Fig. 4 Vertical section of the active plate

ary condition imposed at the back face of the resin. The range of variation of the temperatures measured by these sensors was lower than ±0.25 K around an average value for all the configurations studied.

• A synthetic material, a bi-component resin commercially available under the name of "Scotch weld −3524 B/A". In-
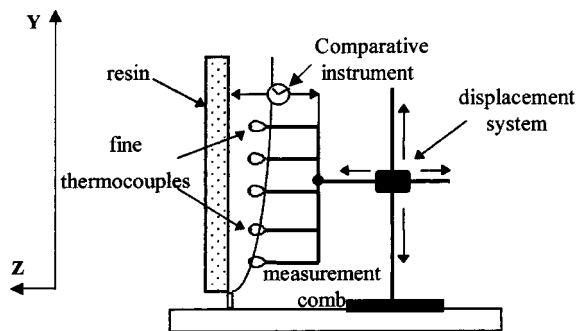
Fig. 2 Principle of the direct method
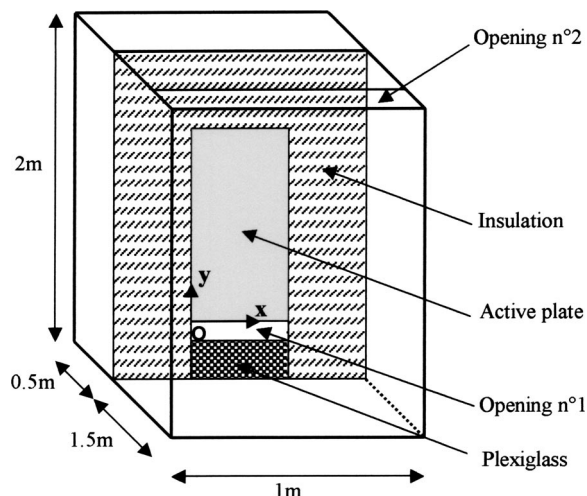
Fig. 3 Enclosure diagram in perspective

side that material, K type thermocouples with a 0.08 mm mean diameter and a thermal accuracy of ±0.15 K were buried 0.5 mm below the surface.

A light source was built during this experimentation. It consisted of an insulated box made of aluminum in which several short infrared lamps were located, Fig. 5.

The surface temperatures of the protection enclosure were also measured so that radiative exchanges could be calculated. It should be noted that surfaces having high emissivity ($\varepsilon > 0.9$) were chosen in order to correspond to those classically encountered in building enclosures.

2.2 Optimization. Preliminary studies were necessary to optimize both the choice of the front face material and also the location of the thermocouples inside it. This was done by successive numerical trials in the steady state (imposed temperature at the back face of the resin only) and unsteady state (imposed flux condition at the front face of the resin) and using the fictitious enclosure method [9], see Appendix A. This work allowed us to determine the sensitivity coefficients X_{ij} which are included in the sensitivity coefficient matrix X. With these values it is easy to calculate the criterion proposed by Blanc [10].
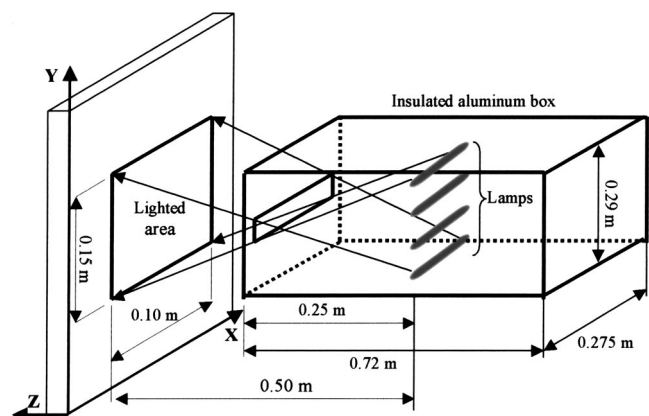
Fig. 5 Diagram of the radiative heat source

Table 1 Thermophysical properties of the resin

Material	Coefficient of conductivity $(W \cdot m^{-1} K^{-1})$	Heat capacity $(J \cdot kg^{-1} K^{-1})$	Density $(Kg \cdot m^{-3})$	Mean Emissivity
Resin	0.06	1454	480	0.95

This criterion is based on a quantity called the normalized ratio of representation, which is defined as follows Eq. (2).

$$\bar{\tau} = \frac{\tau_j}{\tau_{max}} \tag{2}$$

where

$$\tau_j = \sum_{i=1}^{m} X_{ij} \quad \text{for } j = 1 \text{ to } n$$

$$\tau_{max} = Max(\tau_j) \quad \text{with } 1 \leq j \leq n$$

This normalized representation ratio allows the sensitivity of the sensor to a flux density to be determined according to the location where it is used. It must satisfy the relationship (3).

$$\forall j, \quad 0.75 \leq \bar{\tau} \leq 1 \tag{3}$$

In fact, it is interesting to obtain high, uniform values of the normalized representation ratio. This generally leads to the sensors being placed as close as possible to the surface of the material. But for the proposed study we also had to use materials which are encountered in the real situations at wall surfaces. For that we studied several types of inside surface materials, such as plaster, wood or insulation materials. We finally chose a synthetic resin with thermophysical properties suitable for the planned studies, Table 1.

This material presents two advantages. First, it has a good insulation coefficient that keeps its sensitivity coefficient values high. This property is very interesting because it makes the estimation of fluxes less sensitive to measurement errors. Second, its volumic heat (product of the heat capacity by the density) is sufficient and very similar to that of plaster.

Therefore, the location and the number of thermocouples inside that material were determined in order to reach high values of the normalized representation ratio.

The location of the lamps inside the box was also optimized to obtain a uniformly lighted area and to impose a known flux boundary condition. Several preliminary numerical studies (not presented here) were carried out and led to the building of a radiative source able to deliver a variable power in the range 0 to 1600 $W \cdot m^{-2}$ Fig. 6.

Thickness of resin = 8 mm
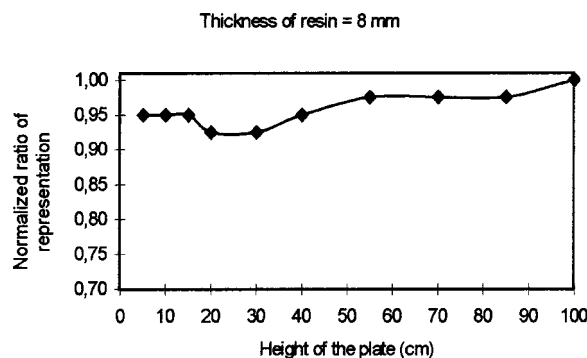
Fig. 6 Normalized representation ratio of thermocouples buried in the resin

All this optimization work is presented in Suleiman's Ph.D. thesis [11].

3 Inverse Identification Method

The inverse identification method developed used a numerical solution of the direct problem based on a finite volume technique [12]. It was a three-dimensional model because, for the sun patch study, we needed to know the temperature distribution inside the plate in all directions. Therefore, we stated the boundary conditions of our plate in a three-dimensional Cartesian system of coordinates. The mathematical representation is the following, Eq. (4).

$$\begin{cases} \alpha\left(\dfrac{\partial^2 T}{\partial x^2} + \dfrac{\partial^2 T}{\partial y^2} + \dfrac{\partial^2 T}{\partial z^2}\right) = \dfrac{\partial T}{\partial t} \\ \text{With:} \\ z = 0, \quad -\lambda\dfrac{\partial T}{\partial z}\bigg|_{z=0} = q_i^{cond} \\ z = (\text{Thickness})\, T = T_1, \quad \forall x, y = \text{known} \\ \text{At:} \\ x = 0 \quad \text{and} \quad x = \text{Width}, \quad \dfrac{\partial T}{\partial x} = 0, \forall y, z \\ y = 0 \quad \text{and} \quad y = \text{Height}, \quad \dfrac{\partial T}{\partial y} = 0, \forall x, z \end{cases} \tag{4}$$

The heat transfer flux is the sum of the radiative and the convective effects, so the inverse problem is linear. Furthermore, the heat transfer is also a function of the local surface temperature distribution.

To take these phenomena into account, a linear inverse method elaborated by Taler [13] was chosen. In this work we took the following hypotheses:

- The global heat flux arriving at the front face of the plate was divided into n components q_1, q_2, ..., q_n along the Y coordinate, Fig. 7. For the components which received the radia-
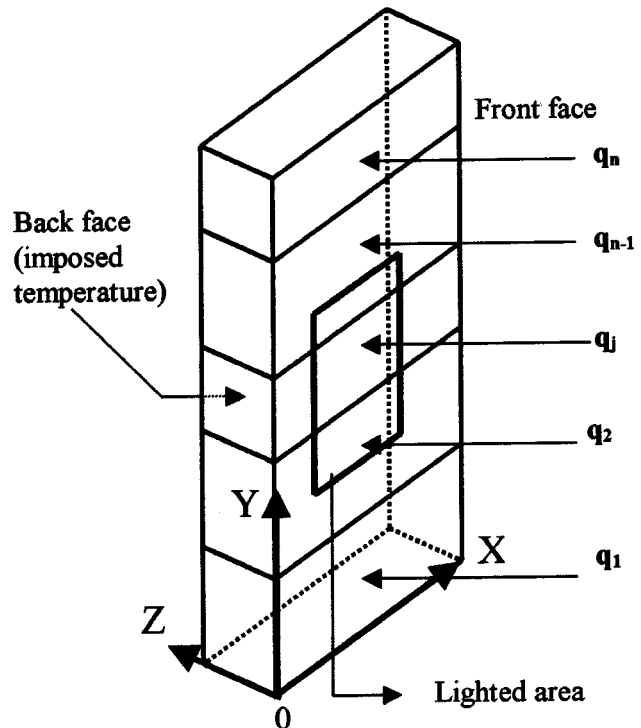
Fig. 7 Theoretical division of the active plate

tive source fluxes we took into account two distinct boundary conditions: one for the lighted areas the other for the non-lighted. This was done to determine the variations of temperatures and fluxes due to the irradiation.

- Consequently the convective heat flux was also divided into n components and, if necessary, in separated areas when receiving irradiation.

Here, with the following notation for the measured temperature (Y_i for $i = 1, m$) and the computed temperature (T_i for $i = 1, m$) and with $m > n$, the aim is to estimate $q = q_1, q_2, \ldots, q_n$ for the lowest deviation between Y_i and T_i, that is to say, Eq. (5):

$$T_i - Y_i \approx 0 \quad \text{for i varying from 1 to } m \tag{5}$$

Supposing that $\vec{q}^k = (q_1^k, \ldots, q_n^k)^T$ is a first estimation of the unknown flux, the temperatures are assumed to be continuous with the heat flux and a serial first order Taylor development, Beck [14], gives Eq. (6):

$$T_i^{k+1} = T_i^k + (q_1^{k+1} - q_1^k) \left. \frac{\partial T_i}{\partial q_1} \right|_{\vec{q} = \vec{q}^k} + \ldots + (q_n^{k+1} - q_n^k) \left. \frac{\partial T_i}{\partial q_n} \right|_{\vec{q} = \vec{q}^k} \tag{6}$$

By substituting Eq. (6) into Eq. (5) and simplifying, we obtain Eq. (7).

$$\sum_{j=1}^{n} \left. \frac{\partial T_i(q_1, \ldots, q_n)}{\partial q_j} \right|_{\vec{q} = \vec{q}^k} \times (q_j^{k+1} - q_j^k) + T_i^k(q_1^k, \ldots, q_n^k) - Y_i$$
$$\approx 0 \tag{7}$$

For i varying from 1 to m, this linear equation system can be written in matrix form, Eq. (8).

$$DT(\vec{q}^k) \cdot \vec{q}^{k+1} \approx DT(\vec{q}^k) \cdot \vec{q}^k - T(\vec{q}^k) + Y \tag{8}$$

Where:

$$DT(\vec{q}^k) = X : X = \begin{vmatrix} \frac{\partial T_1}{\partial q_1} & \frac{\partial T_1}{\partial q_2} & . & . & \frac{\partial T_1}{\partial q_n} \\ . & . & . & . & . \\ \frac{\partial T_m}{\partial q_1} & . & . & . & \frac{\partial T_m}{\partial q_n} \end{vmatrix}_{\vec{q} = \vec{q}^k}$$

is the $m*n$ Jacobi matrix of $T(\vec{q}^k)$.

Y and T are the m vectors of the discrete measurements and computed temperatures at the given sensor locations. The terms $\partial T_i / \partial q_j$ are the sensitivity coefficients X_{ij} that we calculate by progressive differentiation for the resin, Eq. (9).

$$\frac{\partial T_i}{\partial q_j} \approx \frac{T_i(\vec{q}^k + \delta_j \vec{e}_j) - T(\vec{q}^k)}{\delta_j} \tag{9}$$

The scalar δ_j is very small in comparison with the jth flux component q_j^k, and $\vec{e}_j$ is the jth column of the unit matrix. Two calculations of the temperature field were necessary to determine each column of matrix sensitivity coefficients:

- The first one with the flux value (q) for all the components together.
- The second one with the value ($q + \delta q$) for each component taken separately.

That is to say that, for the n components of the plate, the temperature field was calculated ($n + 1$) times.

Then we solved the three dimensional unsteady state heat conduction equation by a finite volume technique to reach values of the n components of the unknown flux $(q_j^{k+1})_{j=1,\ldots,n}$. As this resolution is an iterative process, it is solved again for these new flux values until the variation between two calculation steps reaches a low value, i.e., Eq. (10).

$$\left| \frac{q_j^{k+1} - q_j^k}{q_j^k} \right| < \varepsilon \quad \text{for } j = 1, \ldots, n \tag{10}$$

The set of Eq. (8) is over-determined. It takes the form $A q = b$ where A is a rectangular matrix of dimension $m*n$ with $m > n$. We cannot invert it to reach b. This problem was solved using the possibility of decomposition into a singular value and given by the Fortran program SVDCMP from Numerical Recipes [15].

The use of the inverse method gives the conductive heat flux q_i^{cond} arriving at the front face of the plate and the average surface temperature for each component of the plate. Therefore, before determining the convective heat flux q_i^{cv}, it was first necessary to calculate the radiative heat flux q_i^{rad} for each component of the plate. This was done using the classic radiosity method [16], which we briefly outline below. If we consider an enclosure composed of n gray surfaces where

- S_k is the kth surface of the enclosure.
- $q_{o,k}$ is the radiative heat flux per unit area leaving the surface k. It is called the radiosity and is given by Eq. (11).

$$q_{o,k} = \varepsilon_k \sigma T_k^4 + (1 - \varepsilon_k) q_{i,k} \tag{11}$$

$q_{i,k}$ is the radiative heat flux per unit area arriving on surface i.

In our case, as all the surface temperatures were known either by measurement or by simulation, we obtained a set of n equations for the n surfaces of the enclosure and hence all the values of $q_{o,j}$, Eq. (12).

$$\sum_{j=1}^{n} \left[\delta_{k,j} - (1 - \varepsilon_k) F_{k,j} \right] q_{o,j} = \varepsilon_k \sigma T_k^4 \tag{12}$$

where $\delta_{k,j} = 1$ if $k = j$ and 0 if $k \neq j$.

Then, to calculate the convective heat flux density q_i^{cv}, we applied the two following relations, corresponding to thermal balances of components located on the plate front face:

- the first one corresponds to locations outside the lighted area, Eq. (13).
- the second one corresponds to locations inside the lighted area, Eq. (14).

$$q_i^{cond} = q_i^{cv} + q_i^{rad} \tag{13}$$

$$q_i^{cond} + a \times q_{lighted} = q_i^{cv} + q_i^{rad} \tag{14}$$

4 Results

4.1 Presentation of the Results. The results concern particularly the thermocouple temperature variations, the flux variations and the convective exchange coefficient variations over the lighted area. For that study the active plate was divided into twelve components of which four received the radiation, Fig. 8. Various boundary conditions were tested. They corresponded to: a light flux density of 166 $W \cdot m^{-2}$ which was applied to the front face of the resin for 220 seconds; and different temperatures imposed at the back face of the resin allowing temperature differences $\Delta T = \bar{T}_{surf} - \bar{T}_{air}$ within the range 2.7 to 14.7°C.

Figure 9 shows the temperature variations of the thermocouples with the duration of illumination. During the illumination the range of temperature varied between 28.5 and 32.5°C for all the sensors. But two types of thermocouple thermal behaviors may be distinguished.

The first one corresponds to thermocouples 5 and 6, centrally located inside the lighted area. These thermocouples present the greatest amplitude of variation.

The second one is relative to the two thermocouples located at the limits of the lighted area (bottom or top). In that case, the variation amplitudes of the two thermocouples (4 and 7) were lower. The reason is that the energy emitted by the radiative source and absorbed by the resin is diffused towards the non-lighted area.
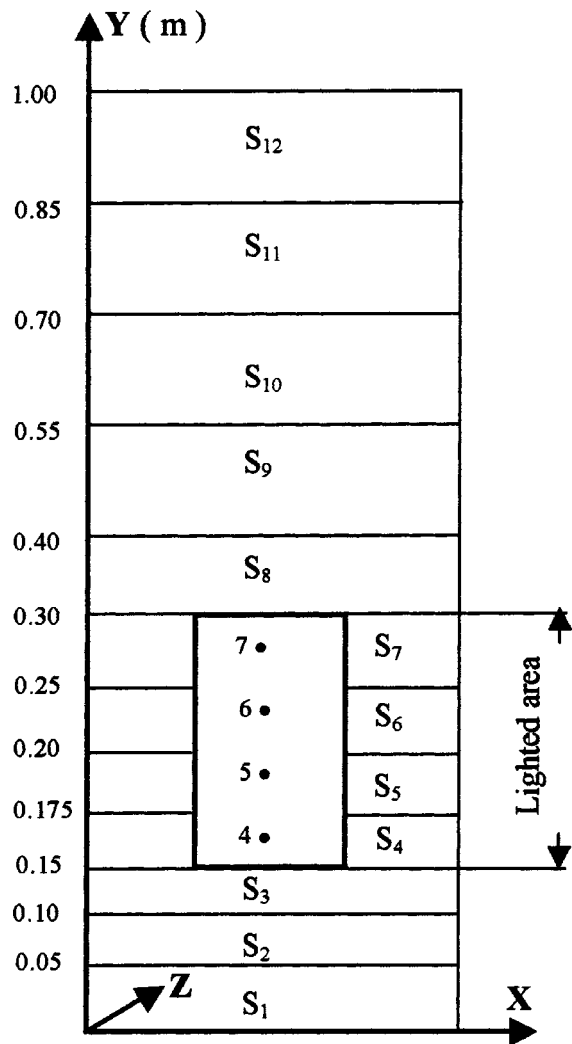
Fig. 8 Division of the active plate into components and location of the thermocouple sensors (•) inside the lighted area

Finally, we can see that the thermocouples 7 and 4, which are in the same situation (close to a non lighted area), present a small difference of temperature. This difference comes from the increase of air temperature due to the effects of natural convection.
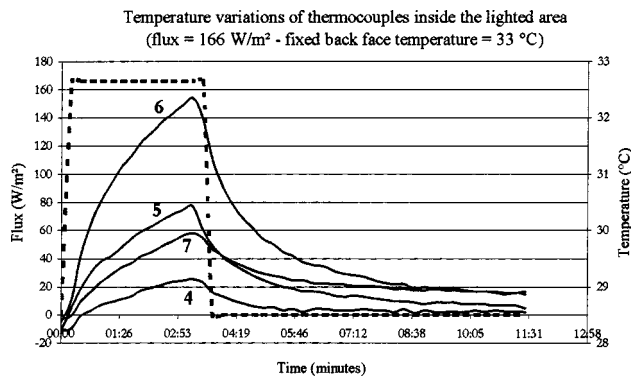
Fig. 9 Experimental temperature variations of thermocouples located inside the lighted area

Table 2 Characteristics of the configuration studied

$\bar{T}_{air}$ [°C]	$\bar{T}_{surf}$ [°C]	$\Delta T = \bar{T}_{surf} - \bar{T}_\infty$ [°C]	$\bar{G}r = \dfrac{\beta g \Delta T H^3}{\nu^2}$
23.7	[31.1–32.0]	[7.4–8.3]	$[8.99-10.05] \times 10^8$

4.2 Conductive, Convective, and Radiative Variations We chose experimental conditions that were representative of the general thermal behavior of the conductive, radiative and convective fluxes. They were a light flux density of 166 W·m^{-2} and other conditions indicated above, Table 2

The variations with time of six components are drawn on Figs. 10, 11, and 12. Four were located inside the lighted area (components 4, 5, 6, and 7), the two others (components 1 and 12) being outside that area, respectively at the bottom and at the top of the active plate.

Concerning the variation of conductive heat fluxes of the lighted components (4 to 7) we see, Fig. 10, that they decrease from the first moments of lighting. This phenomenon corresponds
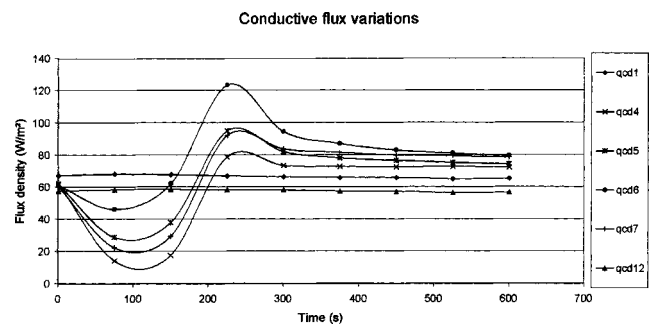
Fig. 10 Conductive heat flux variations for 7.4<ΔT<8.3°C
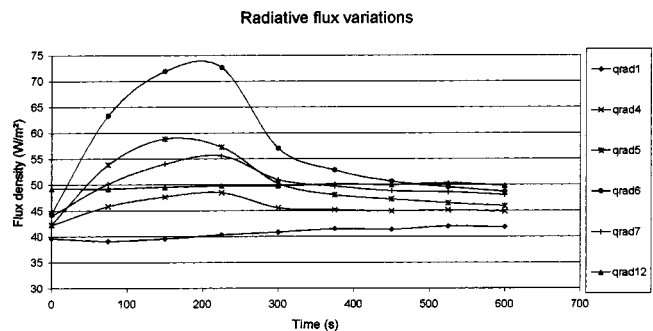
Fig. 11 Radiative heat flux variations for 7.4<ΔT<8.3°C
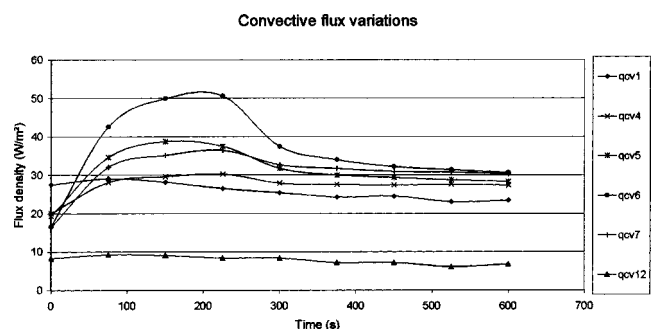
Fig. 12 Convective heat flux variations for 7.4<ΔT<8.3°C

Fig. 13 Convective heat exchange coefficient values for component 4
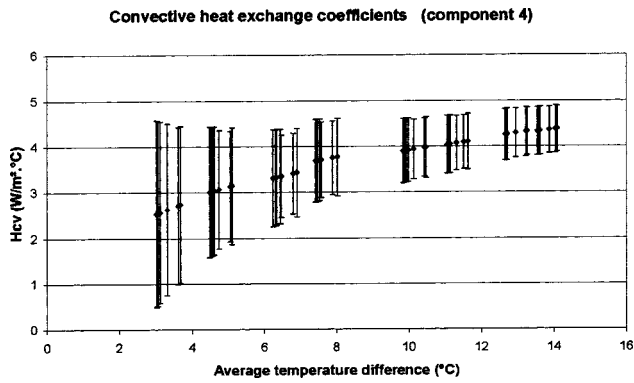
Fig. 14 Convective heat exchange coefficient values for component 5

to flux inversions which depend on the component locations. Then, just after the extinction of the radiative source, the conductive flux increases rapidly and reaches higher values during heat restitution because the material had stored heat in the previous periods.

Note that components 1 and 12, not located in the lighted area, do not present any significant variation during the lighting period.

Figures 11 and 12 for the radiative and the convective heat exchanges show, that the variations of components 4, 5, 6, and 7 located inside the lighted area are significant. Nevertheless, if we compare these two heat exchanges occurring at the solid surface the following observations can be made.

- The order of variations between the different components of the lighted area is respected. The central components (5 and 6) of the lighted area present the greatest temperature variations. For the other two, located in extreme positions (components 4 and 7), the variations are lower. We note again here, as mentioned in paragraph 4.1, that the energy emitted by the radiative source and absorbed by the resin is diffused towards the nonlighted area.
- The amplitudes of variations are different between the two types of exchanges. Due to the illumination, the convective heat exchange varies by more than twice its initial value before lighting. This is the case of the three upper components located in the lighted area, excepted for component "q_{cv4}". This may be explained, on the one hand, by heat restitution of the energy stored in the resin during lighting and, on the other hand, by the increase in air temperature due to convection effects from the bottom to the top of the plate.

Finally, if we consider now the two components 1 and 12 not located in the lighted area, we see that the illumination does not affect their variation in a significant manner. Nevertheless, a very slight variation may be observed, certainly due to the beam reflections of the radiative source inside the enclosure.

4.3 Convective Heat Exchange Coefficient Variations We present the variations of convective heat exchange coefficients with time, Figs. 13, 14, 15, and 16. They were calculated using the convective fluxes given by the inverse method and in terms of the average temperature difference $\Delta T = \bar{T}_{surf} - \bar{T}_{air}$ of each component. The uncertainty bars were calculated by a Monte-Carlo method [17]. We indicate the absolute errors on parameters such as emissivity or view factors and give informations about uncertainty calculations in the Appendix B.

These figures show that the variation of the convective heat exchange coefficient due to the light source may be high. It varied more than 50 percent between the two extremes of temperature mentioned above. This fact was observed for all the configurations studied.
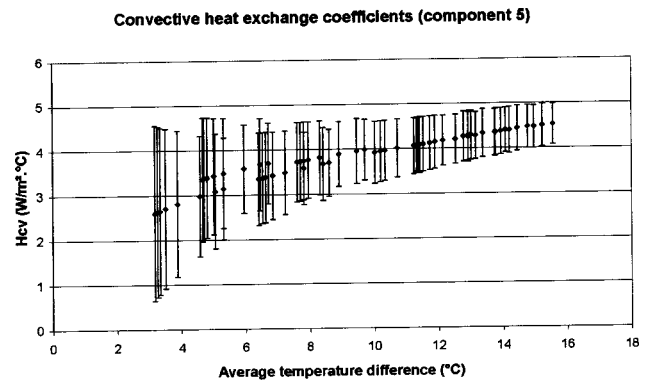
As was foreseeable, the figures indicate also, that uncertainties are high for low values of convective heat exchanges. This points out the weakness of the inverse method for such values.

The values of the coefficients allow us to obtain the different laws that govern the convective heat exchanges in terms of the average temperature difference of each component $\Delta T = \bar{T}_{surf} - \bar{T}_{air}$ of the lighted area. The laws fitting the calculated results obtained by the inverse method are as follows, Eq. (15).

- Component no. 4: $h_{cv} = 1.84 \times (\bar{T}_{surf} - \bar{T}_{\infty})^{0.33}$
- Component no. 5: $h_{cv} = 1.75 \times (\bar{T}_{surf} - \bar{T}_{\infty})^{0.35}$ (15)
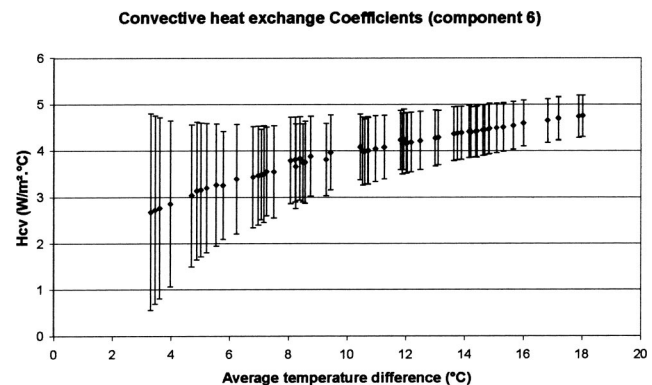
Fig. 15 Convective heat exchange coefficient values for component 6
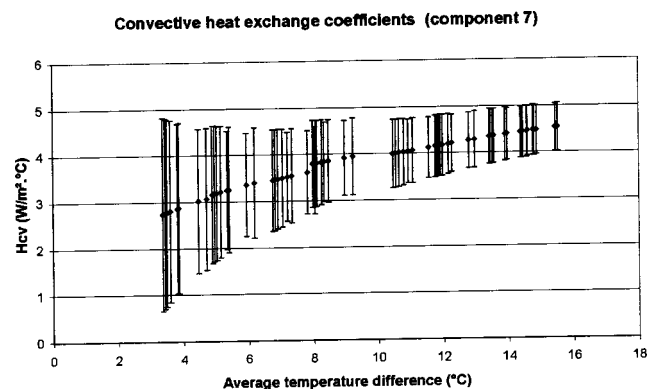
Fig. 16 Convective heat exchange coefficient values for component 7

Convective heat exchange coefficients

$$h_{cv} = 1.83 \left(\bar{T}_{surf} - \bar{T}_{\infty} \right)^{0.33}$$
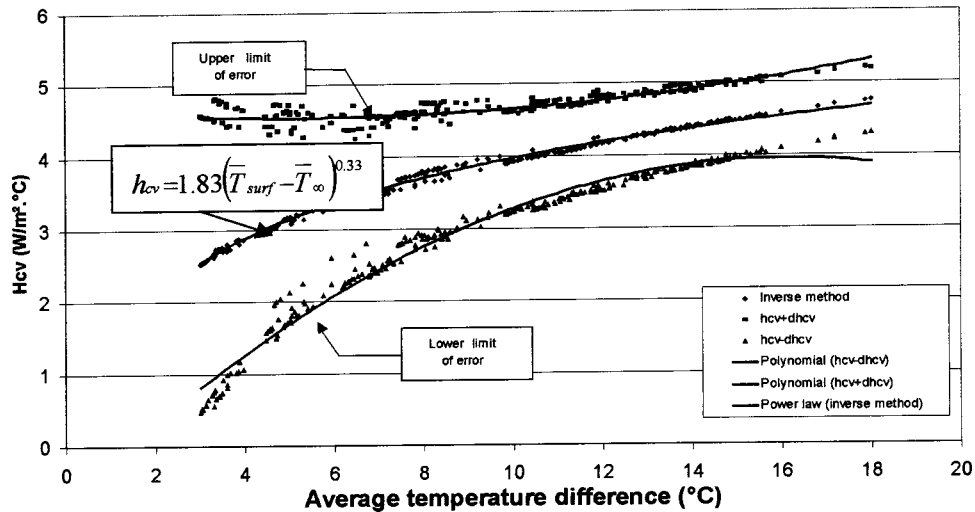
Fig. 17 Convective heat exchange law for the total lighted area

- Component no. 6: $h_{cv} = 1.91 \times (\bar{T}_{\text{surf}} - \bar{T}_{\infty})^{0.31}$

- Component no. 7: $h_{cv} = 1.86 \times (\bar{T}_{\text{surf}} - \bar{T}_{\infty})^{0.32}$

Note that these laws bear a power coefficient varying between 0.31 and 0.35. According to the literature on the subject, e.g. [18], this indicates a situation of turbulent flow. But we cannot conclude with certainty because, during the lighted period, the Grashof number varies with the increase of surface temperature and we may encounter several situations of flow regimes.

Nevertheless, as the temperature differences between all the components have small values, we determined a general convective exchange law for the lighted area, Eq. (16). This law has been drawn with the lower and the upper limits of errors, Fig. 17, mentioned before.

$$h_{CV} = 1.83 \times (\bar{T}_{\text{surf}} - \bar{T}_{\text{air}})^{0.33} \qquad (16)$$

This power law calculated with the results obtained by the inverse method may be compared with other laws provided in the literature by several authors. We have chosen laws corresponding to surfaces heated at constant temperature and for situations of vertical surfaces (free plates or included inside enclosures).

- The first type of law is reported by Roldan [19]. These laws give the convection heat exchange value in terms of the product of the average temperature difference $\Delta T = \bar{T}_{\text{surf}} - \bar{T}_{\text{air}}$ by a constant or their sum. For these relations, there are no indications given about the flow regime. Nevertheless, if we consider the power exponent affecting the temperature difference, these two laws correspond to situations of turbulent flow, Eq. (17) and Fig. 18.

- $h_{cv} = 1.88 \times (\bar{T}_{\text{surf}} - \bar{T}_{\infty})^{0.32}$ (Briss)

$$(17)$$

Convective exchange coefficients (first type of law)
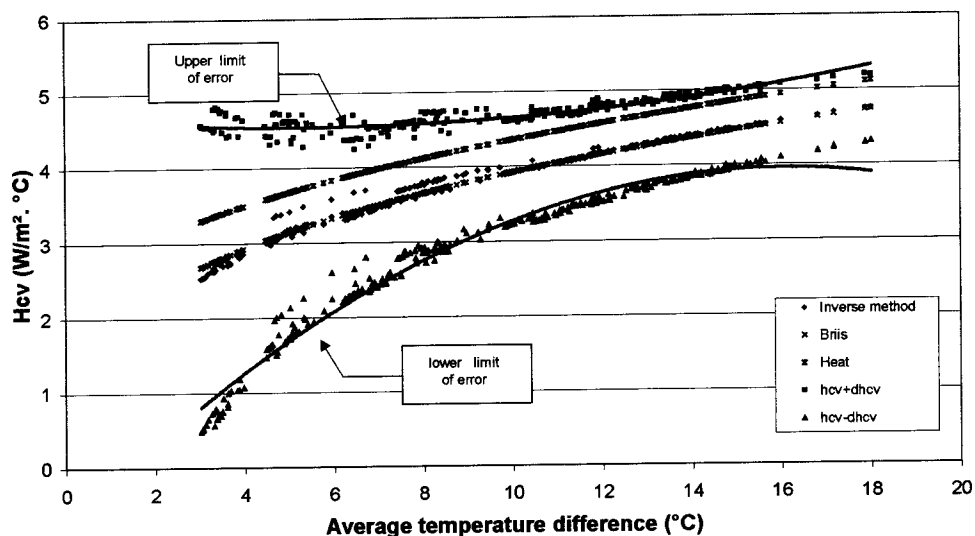
Fig. 18 Comparison of the inverse method law with laws of the first type

Convective exchange coefficients (second type of law)
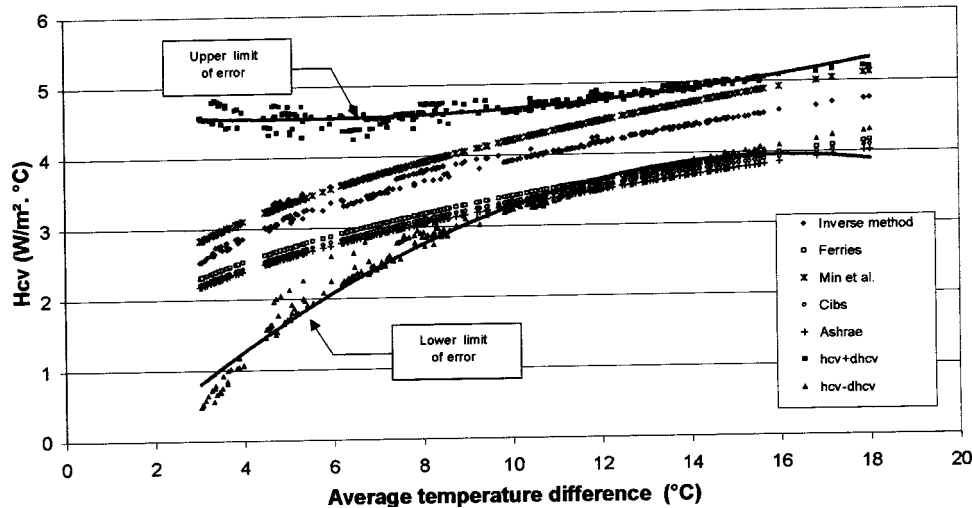
Fig. 19 Comparison of the inverse method law with laws of the second type

- $h_{cv} = 1.7 + (\bar{T}_{surf} - \bar{T}_\infty)^{0.425}$ (Heat)

- The second type of law is reported in the works of Dascali et al. [20]. These laws are given in terms of the Nusselt number, from which we can easily calculate the convective exchange coefficient, Eq. (18) and Fig. 19.

$$
\begin{aligned}
&\bullet \quad Nu = 0.117 Gr^{0.33} \quad \text{(ASHRAE)} \\
&\bullet \quad Nu = 0.119 Gr^{0.33} \quad \text{(Cibs)} \\
&\bullet \quad Nu = 0.124 Gr^{0.33} \quad \text{(Ferries)} \\
&\bullet \quad Nu = 0.197 Gr^{0.32} \quad \text{(Min \textit{et al.})}
\end{aligned}
\quad (18)
$$

If we consider the uncertainty domain, we can see, Figs. 18 and 19, that several laws are suitable to determine the convective heat exchanges with the active plate. Nevertheless, as we have seen before, the uncertainty decreases as the average temperature difference increases. For larger temperature differences, some laws of the second type go out of the uncertainty domain and are not suitable for such an application, Fig. 19. The inverse method appears more interesting in the case of large natural convection exchange coefficients, i.e., for large average temperature differences. But it can also be used for an approximate estimation of convective heat exchanges.

5 Conclusion

In this study, an inverse heat conduction method has been built to estimate convective heat fluxes at the surface of a vertical heated flat plate subject to natural convection and impacted by radiation. This method has been compared with various relations provided by the literature and according to thermophysical properties of building wall surfaces, particularly for high values of emissivity.

The results demonstrate the impact of a light source on convective heat exchanges. This proves that the inverse method is pertinent, even if it is subject to considerable uncertainties, particularly when the convective heat exchanges take weak values. However, for notable differences of temperature that we may encounter on surface walls of glazed spaces, this method could be useful.

The different algorithms and models developed in the study are robust and may be used for other types of applications. We par-

ticularly have in mind industrial processes as thermoforming of plastic bottles used for mineral water which need higher levels of temperature.

Nomenclature

$$
\begin{aligned}
a &= \text{absorptivity} \\
DT(\vec{q}^k) &= \text{sensitivity coefficient matrix for the } k\text{th} \\
&\quad \text{iteration of surface flux} \\
F_{k,j} &= \text{view factor between surfaces } k \text{ and } j \\
g &= \text{gravitational acceleration (m·s}^{-2}) \\
h_{CV} &= \text{convective heat transfer coefficient} \\
&\quad (\text{W·m}^{-2\circ}\text{C}^{-1}) \\
Gr_y &= \text{local Grashof number} \\
q &= \text{heat flux density (W·m}^{-2}) \\
q_i^{cond} &= \text{conductive heat flux density of the } i\text{th} \\
&\quad \text{component (W·m}^{-2}) \\
q_i^{cv} &= \text{convective heat flux density of the } i\text{th} \\
&\quad \text{component (W·m}^{-2}) \\
q_{lighted} &= \text{light flux density (W·m}^{-2}) \\
q_i^{rad} &= \text{radiative heat flux density of the } i\text{th} \\
&\quad \text{component (W·m}^{-2}) \\
q_{o,k} &= \text{radiosity of the } k\text{th surface of the enclo-} \\
&\quad \text{sure (W·m}^{-2}) \\
q_{i,k} &= \text{radiative heat flux arriving on surface } i \\
&\quad \text{of the enclosure (W·m}^{-2}) \\
\vec{q}^k = (q_1 \ldots q_n)^T &= \text{vector of surface flux density} \\
Nu_y &= \text{local Nusselt number} \\
Pr &= \text{Prandtl number} \\
m &= \text{number of thermocouple sensors in the} \\
&\quad \text{resin} \\
n &= \text{number of components of the heat flux} \\
t &= \text{time (s)} \\
S_i &= i\text{th surface area (m}^2) \\
T_i &= i\text{th numerical temperature (°C)} \\
T = (T_1, \ldots T_m)^T &= \text{vector of the } m \text{ numerical temperatures} \\
X &= \text{sensitivity matrix} \\
X_{ij} = \partial T_i / \partial q_j &= \text{sensitivity coefficient} \\
X, Y, Z &= \text{Cartesian coordinate system} \\
Y_i &= i\text{th measured temperature (°C)} \\
Y = (Y_1, \ldots Y_m)^T &= \text{vector of the } m \text{ measured temperatures} \\
&\quad (\text{°C})
\end{aligned}
$$

Greek Symbols

α = thermal diffusivity (m$^2\cdot$s^{-1})
β = coefficient of volume expansion (K^{-1})
δ = scalar or symbol of kronecker
ε = emissivity
ν = kinematic viscosity (m$^2\cdot$s^{-1})
σ = Stefan–Boltzmann constant (W$\cdot$m$^{-2}\cdot$K^{-4})
λ = thermal conductivity (W$\cdot$m^{-1}°C^{-1})
ρ = density (kg$\cdot$m^{-3})
$\bar{\tau}$ = normalized ratio of representation

Superscripts

$^{-}$ = average quantity
$( )^T$ = transposed quantity

Subscripts

air = ambient condition
surf = surface quantity

Appendix A

For the optimization of the surface material we used the fictitious enclosure method [9]. We consider that the fictitious enclosure is composed of two surfaces which are (i) the active plate and (ii) all the other surfaces of the enclosure taken together.

This assumption is valid if:

- The dimensions of the enclosure in the three directions are not very different; and
- The emissivity is uniform for a given surface

But, the temperature difference between the active plate and the other surfaces may be significant (e.g. active plate with radiative emission).

Then in the steady state we applied the relation $q_i^{cond}=q_i^{cv}+q_i^{rad}$ and we had have to determined both the convective and the radiative heat fluxes.

Concerning the Convective Heat Flux

- We used a relation from the literature which was integrated along the Y coordinate. This relation is the following and has been presented in [8]:

$$q_i^{cv}=\frac{K\cdot\left(\dfrac{\beta\cdot g}{v^2}\right)\cdot\lambda}{Y_2-Y_1}(T_{surf}-T_{\infty})^{1.25}\left[\frac{Y_2^{3/4}-Y_1^{3/4}}{0.75}\right]$$

where: "K" is a constant depending on the relation used.

Concerning the Radiative Heat Flux

- We estimated a linearized radiative heat exchange coefficient "h_r"

$$q_i^{rad}=h_r\times(T_{plate}-\bar{T}_{surf})$$

with:

T_{plate}=temperature of the active plate
$\bar{T}_{surf}$=average temperature of the other surfaces of the enclosure

A direct simulation allows us to determine the temperature field inside the active plate and to reach the best representation of the flux sought. This was done using the criterion of Blanc [10] by successive numerical trials taking into account the nature and thickness of the surface material, and the number and location of sensors inside it.

Appendix B

The uncertainty calculations of the convective heat exchange coefficients, in unsteady state, were determined from Eq. (14).

$$q_i^{cond}+a\times q_{lighted}=q_i^{cv}+q_i^{rad} \qquad (14)$$

Note that this expression depends on different parameters that enter into the thermal balance of the lighted area. Two literal expressions are necessary to reach this type of result.

The first gives the relative uncertainty on the convective heat flux.

$$\left(\frac{\Delta\varphi_{CV}}{\varphi_{CV}}\right)_{max}\leqslant\left|\frac{\Delta\varphi_{total}+\Delta\varphi_{radl}+\Delta\varphi_{abs}}{\varphi_{total}+\varphi_{abs}-\varphi_{rad}}\right|$$

The second gives the relative uncertainty on the heat exchange coefficient from the classical heat transfer law by convection.

$$\left(\frac{\Delta h_{cv}}{h_{cv}}\right)_{max}=\sqrt{\left(\frac{\Delta\varphi_{cv}}{\varphi_{cv}}\right)_{max}^2-2\left(\frac{\delta T}{\Delta T}\right)^2}$$

For these calculations, we took the following parameter uncertainties into account.

The absolute uncertainty on thermocouple accuracy was ±0.15 K. This type of error occurs in the calculation of the different flux components and we took this fact into account.

Concerning Conductive Exchanges

- The location error of thermocouples inside the resin was chosen to be 0.1 mm. We assumed that it was equivalent to a temperature error.

Concerning Radiative Exchanges

- relative error on view factors=1% (from numerical data)
- relative error on emissivity=2% (from experimental data)

Concerning the Radiative Source

The power of the radiative source has been determined by a specific experiment which is not presented. Consequently, it was subject to calibration errors which are included in the uncertainty bars relative to the results given for the convective heat exchange coefficients.

Generally speaking, these calculations were done using a Monte Carlo method [17]. For the case of temperature we followed the different stages:

1. With the help of a random noise generator and assuming a Gauss law probability distribution we can draw "m" values of the random variable $\delta(T)$ of temperature error.
2. These values were added to numerical temperatures given by the model to obtain noised temperatures.
3. Finally they were injected into the numerical model to obtain a first evaluation of the total flux component q_i^{cond} for example.

Stages 2 and 3 were repeated N times ($N\geqslant50$) to reach a statistical evaluation of the uncertainty.

References

[1] Mavroulakis, A., 1995, "Développement d'outils destinés à la modélisation des échanges radiatifs dans des enceintes de géométrie complexe. Calcul de facteurs de forme en présence d'obstacles," Ph.D. thesis, University P. Sabatier, Toulouse III, France.

[2] Serres, L., 1997, "Etude de l'impact d'une perturbation thermique locale de type tache solaire, Influence sur le confort thermique," Ph.D. thesis, INSA of Toulouse, France.

[3] El Alami, M., 1994, "Contribution à l'étude thermique et dynamique des écoulements le long d'une paroi non uniformément chauffée dans une cavité à grand nombre de Rayleigh," Ph.D. thesis, INSA of Toulouse, France.

[4] Lorente, S., 1996, "Contribution à l'étude des transferts thermiques dans les alvéoles verticales-Application aux produits de terre cuite, Modélisation et Expérimentation," Ph.D. thesis, INSA of Toulouse, France.

[5] El Khatib, H., and Javelas, R., 1998, "Etude de deux cas d'écoulement thermoconvectifs le long d'une plaque plane verticale uniformément chauffée dans une cavité," Rev. Gen. Therm., **37**(4), pp. 295–303.

[6] El. Khatib, H., and Javelas, R., 1996, "Modèle correctif de la mesure de température d'un gaz par couple thermoélectrique, Application à une zone à

fort gradient thermique,'' Rev. Gen. Therm., **35**, pp. 571–579.

[7] Cuniasse–Langhans, I., 1998, "Evaluation par méthode inverse de la distribution de flux de chaleur pariétaux le long d'une plaque plane verticale en convection naturelle,'' Ph.D. thesis, INSA of Toulouse, France.

[8] Cuniasse–Langhans, I., Trombe, A., Dumoulin, J., and Begue, M., 2001, "Efficiency of an Inverse Method to Determine Natural Convection Heat Transfer,'' Numerical Heat Transfer, Part B, **39**(6), pp. 603–615.

[9] Walton, G. N., 1980, "A New Algorithm for Radiant Interchange in Room Load Calculations,'' ASHRAE Trans., pp. 190–208.

[10] Blanc, G., 1996, "Problèmes inverses multidimensionels de conduction de la chaleur. Optimization du positionnement des capteurs et utilisation des mesures de thermodéformations,'' Ph.D. thesis, INSA of Lyon, France.

[11] Suleiman, A., "Evolution par méthode inverse de la distribution de flux de chaleur pariétaux d'une plaque plane verticale en présence d'une perturbation radiative,'' Ph.D. thesis, INSA of Toulouse, France.

[12] Patankar, S. V., 1980, *Numerical Heat Transfer and Fluid Flow*, Mac Graw Hill Book Company, New York.

[13] Taler, J., 1992, "Nonlinear Steady-State Inverse Heat Conduction Problem With Space-Variable Boundary Conditions,'' ASME J. Heat Transfer, **114**, pp. 1048–1051.

[14] Beck, J. V., Blackwell, B., and St-Clair, Jr., C. R., 1985, *Inverse Heat Conduction, Ill-Posed Problems*, Wiley-Interscience Publication.

[15] Press, W. H., Teukolsky, S. A., Vetterling, W. T., and Flannery, B. P., 1992, *Numerical Recipes in Fortran*, Cambridge University Press.

[16] Siegel, R., and Howell, J. R., 1992, *Thermal Radiation Heat Transfer*, Third edition, Hemisphere Publishing Corporation, Washington D.C.

[17] Beck, J. V., and Arnold, K. J., 1977, *Parameter Estimation in Engineering and Science*, John Wiley & Sons, New York.

[18] Bejan, A., 1993, *Heat Transfer*, John Wiley and Sons, Inc. New York.

[19] Roldan, A., 1985, "Etude thermique et aéraulique des enveloppes des bâtiments. Influence des couplages intérieurs et multizonages,'' Ph.D. thesis, INSA of Lyon, France.

[20] Dascali, E., Santamouris, M., Balaras, C. A., and Asimakopoulos, D. N., 1994, "Natural Convection Heat Transfer Coefficients From Vertical and Horizontal Surface for Building Applications,'' Energy Build., **20**, pp. 243–249.

A Natural Convection Model for the Rate of Salt Deposition From Near-Supercritical, Aqueous Solutions

Marc Hodes[1]
Department of Mechanical Engineering,
Massachusetts Institute of Technology,
Cambridge, MA 02139

Kenneth A. Smith
e-mail: kas@mit.edu
Department of Chemical Engineering,
Massachusetts Institute of Technology,
77 Massachusetts Avenue, Room 66-540,
Cambridge, MA 02139

Peter Griffith
e-mail: pgrif@mit.edu
Department of Mechanical Engineering,
77 Massachusetts Avenue, Room 7-044,
Cambridge, MA 02139

A model is developed for the rate of salt deposition by natural convection from aqueous salt solutions onto a horizontal cylinder heated beyond the solubility temperature for the dissolved salt. The model accounts for the deposition rate at the salt layer-solution interface (SLSI) formed on the cylinder, but it does not account for deposition which may occur inside the porous salt layer (PSL). Dissolved salt is transported to the SLSI by molecular diffusion (with advection) and subsequently nucleates heterogeneously there. The model is applied to the experimental deposition rate data acquired by Hodes et al. (1998, 2002) at conditions pertinent to Supercritical Water Oxidation (SWCO). The ratio of the predicted deposition rate to the measured one ranges from roughly 0.5 to 2 indicating that deposition inside the PSL can be considerable. [DOI: 10.1115/1.1603772]

1 Background

Supercritical Water Oxidation (SCWO) is a promising technology for the remediation of hazardous organic wastes as discussed by Shaw et al. [1]. However, scale buildup on reactor surfaces due to the production of ''sticky'' salts can be problematic. Research on phase behavior, heat transfer and salt deposition in supercritical water (SCW) has been reviewed by Hodes et al. [2]. The many reactor designs and operating techniques to control scale buildup during SCWO have been reviewed by Marrone et al. [3]. Very few investigators have examined deposition rates under carefully controlled conditions. For fully developed turbulent flow through a tubular reactor, Rogak and Teshima [4] measured sodium sulfate deposition rates and developed a predictive model. Rate data for deposition from near-supercritical, aqueous, sodium sulfate and potassium sulfate solutions to a heated cylinder have been obtained by Hodes et al. [5,6]. These data were accompanied by a simple model for the rate of deposition at the salt layer-solution interface (SLSI) formed on the heated cylinder and a more rigorous model is developed here.

The visually accessible test section used in the Hodes et al. experiments [5,6] is shown in Fig. 1 and described in detail by Hurst et al. [7]. At the system pressure of 250 bar, aqueous salt solutions preheated to within 3 to 8°C of the salt precipitation temperature flowed past a 5.08 mm (0.2 in) diameter heated cylinder. 10.61 W of (constant) power supplied to the cylinder increased its surface temperature beyond the solubility temperature of the salt in solution to drive deposition. Near the end of the 6–12 minute deposition period, the system was purged with nitrogen. Due to the difficulty of purging the high pressure (250 bar) system at elevated temperatures (about 375°C), it has been estimated that from 5 percent to 20 percent of the mass of salt deposited on the heated cylinder was removed in the process [6]. After purging, the heated cylinder was removed and the mass of salt deposited on it measured. It ranged from 0.27 grams to 1.96 grams and it was measured to within ±0.02 grams [6]. Natural convec-

tion dominated transport, but a weak cross flow of solution past the heated cylinder maintained the deposition driving force. Photographs of the heated cylinder before and after it was inserted into the cross flow of a 4 wt% aqueous sodium sulfate solution for about 15 minutes are shown in Fig. 2. The diameter of the SLSI is circular except in the region where a plume forms on the downstream side. A number of factors may contribute to the downstream roughness. Firstly, the (forced convective) Reynolds number based on the SLSI diameter was up to 200 during the deposition experiments; consequently, the turbulent and three-dimensional vortices shed in the wake of the (roughly cylindrical) SLSI could play a role in bump formation. Secondly, the maximum natural convection Rayleigh number based on the SLSI diameter was about 10^9, i.e., its transition value, hence there may have been some turbulence in the plume. Finally, the fluid in the pores of the PSL is buoyantly unstable on the downstream side of the plume and could induce secondary flows that could contribute to bump formation. In the potassium sulfate experiments, the downstream side of the SLSI is also rough; however, unlike the sodium sulfate deposits, the potassium sulfate deposits are dendritic [6].

The ratio of the measured mass of deposited salt to that predicted by the Hodes et al. [5,6] model was between about 1 and 4. Here, many of the assumptions invoked in the previous model are relaxed. First, the model is no longer restricted to linear solubility boundaries and allowance is made for the transient nature of the deposition rate. Moreover, depletion of salt in the bulk solution surrounding the SLSI is included in the model. Furthermore, the analogy between heat and mass transfer is not applied and buoyancy forces generated by both temperature and concentration gradients are taken into account. In both models, heat and mass transfer coefficients are calculated from results for a vertical flat plate geometry and deposition inside the porous salt layer (PSL) is not considered.

2 Development of the Model

2.1 Introduction. A generic temperature-composition phase diagram representative of the sodium sulfate-water and potassium sulfate-water systems at a pressure of 250 bar is shown in Fig. 3. The solubility line separates a single-phase fluid region from a
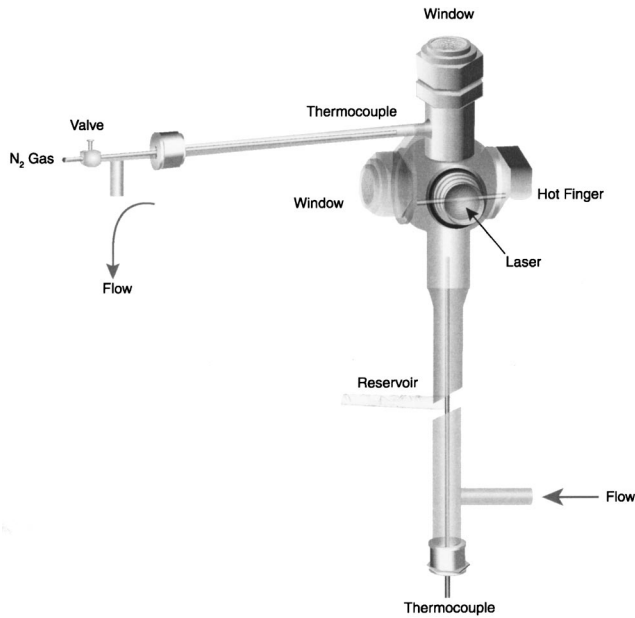

Fig. 1 Schematic of the test section used in the Hodes et al. deposition experiments [1,2] modeled here

two-phase (solid salt+fluid) region. Also shown on the generic solubility diagram are the the trajectories of (T, ω) states traversed by the bulk solution and by the SLSI as salt deposits on the heated cylinder, where ω represents salt mass fraction. The heat and mass transfer coefficients relate the heat and mass fluxes at the SLSI to their respective driving forces as shown. The bulk condition trajectory is qualitative, but it illustrates a number of relevant effects. Before deposition begins, the salt concentration in the bulk solution equals that in the inlet stream to the test cell (ω_{bo}) and the temperature of the bulk solution is designated by T_{bo}. At the onset of deposition, the material capacitance of the test cell is rapidly depleted (within 1 minute) and state "e" is reached. Between states "e" and "f," the concentration of salt in the bulk solution is further decreased because an increasing bulk solution temperature results in an increasing deposition rate. (The temperature of the bulk solution unavoidably drifted upward by about 3°C during the first 5 to 10 minutes of each run and was stable thereafter [6].) Once state "f" is attained, bulk temperature no longer increases. Then deposition rate decreases with time and, thus, bulk concentration increases. At steady-state conditions (designated by the subscript ∞), the salt concentration in the bulk solution equals that in the inlet stream and there is no deposition.

All of the (T, ω) states traversed by the SLSI are assumed to lie on the solubility boundary as shown in Fig. 3. The heat flux at the SLSI decreases with time because its area increases and the heater power is constant. Thus, the temperature and concentration differences across the boundary layer driving the natural convection flow which removes the heat supplied to the heated cylinder decrease with time and the SLSI condition moves towards the bulk solution condition until steady-state conditions are reached. At steady-state conditions there is heat transfer, but not mass transfer, between the SLSI and the bulk solution.

2.2 Mass and Energy Balances. Some further assumptions are given here before deriving the mass and energy balances at the SLSI. Firstly, diffusion of mass along temperature gradients and diffusion of energy along concentration gradients, i.e., the Sorét and Dufour effects, respectively, which can be important in supercritical fluids [2], are not considered. In addition, homogeneous nucleation is assumed not to occur in the bulk fluid, i.e., dissolved salt travels to the SLSI exclusively by molecular diffusion (with advection) and subsequently nucleates. The nucleation model of Smith et al. [8] predicts that homogeneous nucleation can not oc-

cur in the bulk solution during the experiments and this is supported by visual observations of deposition. It is further assumed that, once salt adheres to the SLSI, it can not be removed. The SLSI is modeled as a vertically oriented flat plate of height equal to half the circumference of the SLSI as justified in Section 2.3. Given that the SLSI is circular, except in the region of the plume as per Fig. 2, its perimeter is assumed to be circular. Finally, the detailed morphology of the SLSI is not considered.

The equations governing mass and heat transport at the SLSI are derived from the differential control volume shown in Fig. 4. Transport at the SLSI has been shown to be a weak function of azimuthal angle [6]; therefore, all variables are assumed to be independent of y. As the PSL thickness increases, aqueous salt solution is displaced and a salt mass balance at the SLSI yields:

$$\dot{m}_s'' = (\rho_s - \rho_A)(1-\phi)\frac{dx_i}{dt} = -[\rho_A v + J_{A,x}], \qquad (1)$$

where $\dot{m}_s''$ is the mass flux of salt deposited at the SLSI, ρ_s is the density of solid salt, ρ_A is the density of salt in solution, ϕ is the porosity of the salt layer, x_i is the position of the SLSI, $J_{A,x}$ is the diffusive flux of salt normal to the SLSI, and v is the normal velocity at the SLSI. The scale analysis discussed in Section 2.3 shows that advective transport of salt to the SLSI is negligible compared to that by diffusion.[1] Hence, it follows from the definition of the mass transfer coefficient that the salt mass balance becomes:

$$\dot{m}_s'' = (\rho_s - \rho_A)(1-\phi)\frac{dx_i}{dt} = h_m(\rho_{A,b} - \rho_{A,i}) \qquad (2)$$

An analogous mass balance on the the water component of the (binary) solution in the same control volume yields

$$\rho_B(1-\phi)\frac{dx_i}{dt} = \rho_B v - J_{B,x}, \qquad (3)$$

where ρ_B is the density of water in solution. Finally, an overall mass balance at the SLSI yields

$$(\rho_s - \rho)(1-\phi)\frac{\partial L}{\partial t}\bigg|_x = -\rho v \qquad (4)$$

An energy balance at the SLSI is also developed using the control volume in Fig. 4. The rate of accumulation of internal energy inside the control volume per unit area of the SLSI is denoted by dU''/dt. Specific internal energy is denoted by the variable u_i and has units of $J/(kg\ i)$; and u_s, u_A, and u_B represent the specific internal energy of solid salt, associated ion pairs of salt in solution and H_2O in solution, respectively. The result is

$$\frac{dU''}{dt} = [\rho_s u_s - \rho_A u_A - \rho_B u_B](1-\phi)\frac{dx_i}{dt} \qquad (5)$$

An overall energy balance at the PSL results in Eq. 6, where h_i is the specific enthalpy of species "i" in solution and has units of $J/(kg\ i)$. The first term on the right-hand-side of Eq. 6 accounts for the power supplied to the heated cylinder. (P'' is the total power supplied to the heated cylinder per unit area of the SLSI and η is the fraction of it that enters the PSL. The value of η was set equal to 0.90 based on the the heat conduction analysis done by Hodes [6].) The next two terms account for the energy fluxes associated with the mass fluxes of species A and B and flow work. The last term accounts for heat loss from the SLSI.

$$\frac{dU''}{dt} = \eta P'' - [\rho_A v + J_{A,x}]h_A - [\rho_B v + J_{B,x}]h_B - q_x'' \qquad (6)$$

---

[1]Advection is important, however, to the transport of water at the SLSI [2] because it is the nondilute component of the fluid.

Before Run **Upstream View**

Downstream View **Side View**
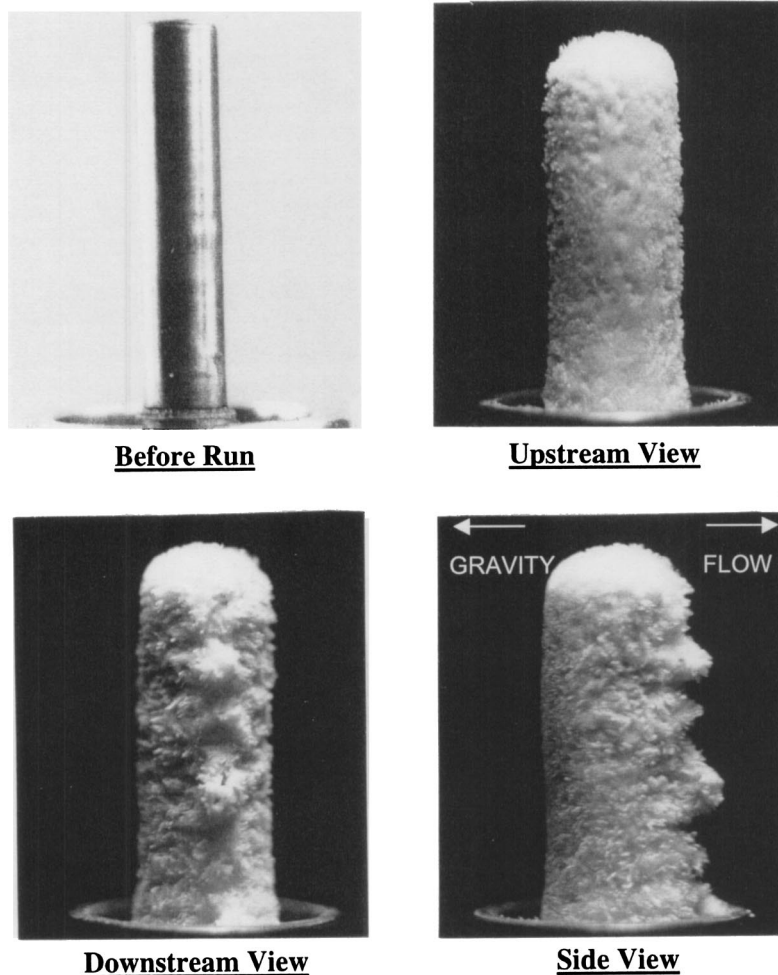
Fig. 2 Photograph of the 5.08 mm (outer) diameter heated cylinder before insertion into the cross flow of a 4 wt% aqueous sodium sulfate solution and upstream, downstream and side views of it after about 15 minutes of exposure. (Flow direction and gravity vector are shown in side view.) $[T_b=356°C, P=250 \text{ bar}, \dot{m}_{\text{soln}}=10.47 \text{ g/min.}]$

The net mass diffusive flux in the x-direction equals zero, i.e., $J_{A,x}=-J_{B,x}$; therefore, when taken together, Eqs. 5 and 6 become:

$$[\rho_s u_s - \rho_A u_A - \rho_B u_B](1-\phi)\frac{dx_i}{dt}$$
$$= \eta P'' - [\rho_A h_A + \rho_B h_B]v + J_{A,x}[h_B - h_A] - q_x'' \quad (7)$$

It is assumed that the specific internal energies of the condensed phases (solid salt, associated ion pairs of salt in solution and H_2O in solution) equal their respective specific enthalpies in solution [6]. Then combining the energy, salt mass, and water mass balances yields:

$$\rho_s[h_s - h_A](1-\phi)\frac{dx_i}{dt} = \eta P'' - q_x'' \quad (8)$$

The quantity $(h_A - h_s)$ is the (mass based) heat of dissolution and it is subsequently denoted by H_{diss}. (A negative value for H_{diss} implies endothermic precipitation.) From the definition of the heat transfer coefficient and the salt mass balance, the energy balance becomes

$$\eta P'' + \left(\frac{\rho_s}{\rho_s - \rho_A}\right)H_{\text{diss}}\dot{m}_s'' = h(T_i - T_b) \quad (9)$$

For the dilute salt concentrations of interest, solution density may be considered uniform and the term $\rho_s/(\rho_s - \rho_A)$ approximated as unity. The area available for deposition at the SLSI equals $\pi D_i L(1 + D_i/(4L))$, where (L) is the length of the heated cylinder, so that the mass and energy balances become

$$\frac{dm_s}{dt} = \rho_{soln} h_m \pi D_i L\left(1 + \frac{D_i}{4L}\right)(\omega_{A,b} - \omega_{A,i}) \quad (10)$$

$$\eta P + \frac{dm_s}{dt} H_{\text{diss}} = h \pi D_i L\left(1 + \frac{D_i}{4L}\right)(T_i - T_b) \quad (11)$$

where the term $(D_i/4L)$ accounts for the area at the tip of the heated cylinder.

2.3 Double-Diffusive Natural Convection. Double-diffusive natural convection may result when solution density is coupled to both temperature and solute concentration. It is the dominant mode of transport in the deposition experiments [6]. The mean Nusselt and Sherwood numbers for double-diffusive natural convective transport from/to an isothermal horizontal cylinder are functions of the Schmidt number ($Sc = \nu/D_{AB}$), the Prandtl number ($Pr = \nu/\alpha$), the Grashof number (Gr_D), and the dimensionless group $\tilde{N}$ where:
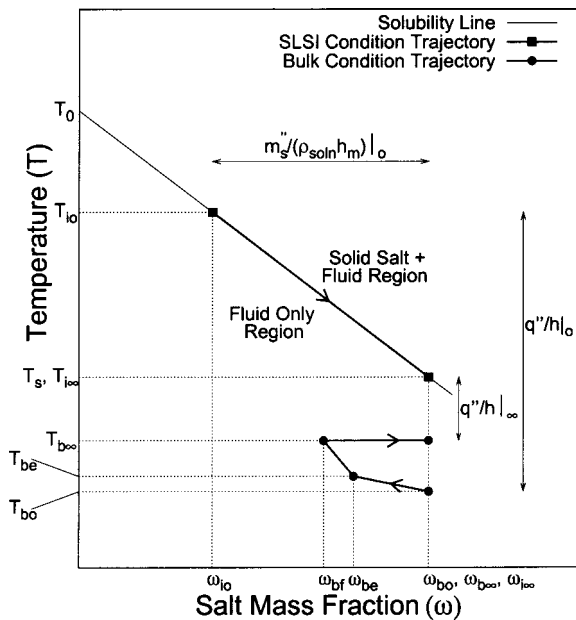
Fig. 3 Temperatures, concentrations and principles relevant to the deposition rate calculations plotted on a generic solubility diagram representative of the sodium sulfate-water and potassium sulfate-water systems at a pressure of 250 bar

$$\mathrm{Gr}_D = \frac{g(\beta(T_i - T_b) + \rho_{soln}\beta^*(\omega_i - \omega_b))D^3}{\nu^2} \quad (12)$$

$$\widetilde{N} = \frac{\beta^*(\rho_{A,i} - \rho_{A,b})}{\beta(T_i - T_b)} \quad (13)$$

The quantities β and β^* are the thermal expansion and species expansion coefficients, respectively, as defined by

$$\beta = -\frac{1}{\rho_{soln}} \left. \frac{\partial \rho_{soln}}{\partial T} \right|_{P, \rho_A} \quad (14)$$

$$\beta^* = -\frac{1}{\rho_{soln}} \left. \frac{\partial \rho_{soln}}{\partial \rho_A} \right|_{P, T} \quad (15)$$
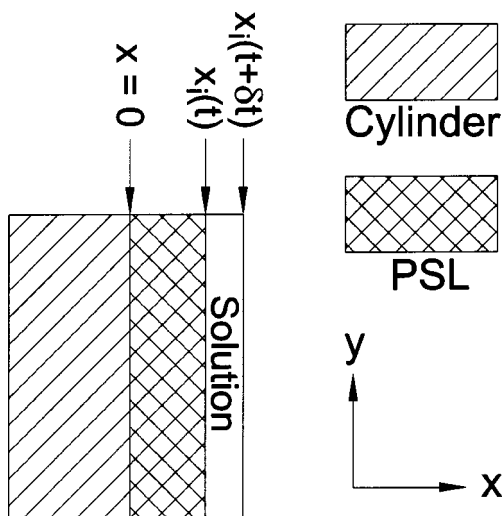
Fig. 4 Moving differential control volume used to derive the mass and energy balances at the SLSI

Buoyancy forces resulting from both temperature and concentration differences across the boundary layer are included in the definition of the Grashof number and the dimensionless group $\widetilde{N}$ represents their relative importance. The value of $\widetilde{N}$ is about 0.5–0.75 at the beginning of the sodium sulfate deposition experiments, but it can not be estimated for the potassium sulfate experiments because the required species expansion coefficient data do not exist [6]. As time increases, $\widetilde{N}$ decreases because a smaller fraction of the total natural convection driving force is provided by the concentration difference across the boundary layer. At steady state conditions, the temperature of the SLSI equals the solubility temperature corresponding to the salt concentration in the bulk solution and, thus, $\widetilde{N}$ equals zero.

Rayleigh Numbers (based on the diameter of the SLSI) for the present experiments range from 10^7 to 10^9. Since transition to turbulence is well known to occur at $\mathrm{Ra}_D > 10^9$, the flow may be assumed to be laminar. Furthermore, the problem may be treated as quasi-steady because the characteristic velocity in the boundary layer in the direction normal to the SLSI is much larger than the velocity at which the SLSI grows radially outward. The former velocity (V) scales as $\alpha \mathrm{Ra}_D^{**}(1/4)/D$. At the beginning of the deposition experiments, Ra_D is of order 10^7 and V is of order 10^{-4} m/s; whereas the velocity of the SLSI is of order $5*10^{-6}$ m/s, or about 20 times smaller. The characteristic value of the advective velocity in the boundary layer induced by mass transfer may be determined by scaling the overall mass balance at the SLSI (Eq. 4). It is two orders of magnitude smaller than the characteristic velocity in the boundary layer normal to the SLSI [6]; therefore, the effects of mass transfer on the quasi-steady velocity field in the boundary layer may be ignored. (Alternatively, if the boundary layer is modeled as a stagnant film and a blowing factor is calculated to correct for the effects of mass transfer on the quasi-steady velocity field, it is found that the mass transfer coefficient is changed by less than 1 percent.) Finally, examination of representative Nusselt number correlations for natural convection along a vertical flat plate and horizontal cylinder shows that both may be applied to either geometry with reasonable accuracy provided that the proper length scale is chosen. The well accepted correlation of McAdams [9], for example, states that $\overline{\mathrm{Nu}}_L = 0.59*\mathrm{Ra}_L^{**}1/4$ for $10^4 < \mathrm{Ra}_L < 10^9$ and, when $\pi D/2$ is substituted for L in both the $\overline{\mathrm{Nu}}_L$ and Ra_L numbers, the result is that $\overline{\mathrm{Nu}}_D = 0.53\mathrm{Ra}_D^{**}1/4$. This compares favorably with the correlation suggested by Morgan which states that $\overline{\mathrm{Nu}}_D = 0.48\mathrm{Ra}_D^{**}1/4$ for $10^4 < \mathrm{Ra}_L < 10^7$ based on a critical review of the literature [10]. Moreover, the analysis by Lienhard [11] provides an explanation of why the ratio of $\mathrm{Nu}/\mathrm{Ra}^{**}1/4$ is the same to within a few percent for laminar natural convection of wholly immersed bodies in general and suggests that this ratio may be set equal to 0.52 for all geometries provided the proper length scale is used. The procedure adopted here has been to use the results for an isothermal vertical flat plate and to set the plate height equal to half the perimeter of the cylinder.

Gebhart and Pera [12] provide the local Sherwood and Nusselt numbers for (laminar) double-diffusive natural convection on a vertically oriented, isothermal and constant concentration flat plate as

$$\mathrm{Sh}_y = \left[\frac{-\widetilde{C}'(0)}{\sqrt{2}} \right] \mathrm{Gr}_y^{1/4} \quad (16)$$

$$\mathrm{Nu}_y = \left[\frac{-\phi'(0)}{\sqrt{2}} \right] \mathrm{Gr}_y^{1/4} \quad (17)$$

where the quantities $-\widetilde{C}'(0)$ and $-\phi'(0)$ are tabulated as a function of Pr, Sc, and $\widetilde{N}$. Gebhart and Pera's results apply when the density difference across the boundary layer is small compared to bulk solution density, i.e., $\Delta\rho_{b-i}/\rho_b \lesssim 0.1$, which is true at conditions of interest [6]. Approximating the SLSI as a vertical

flat plate of height $\pi D_i/2$ in order to estimate the mean Sherwood and Nusselt numbers, the mass and energy balances become

$$\frac{dm}{dt} = K_A D_i^{3/4}\left(1 + \frac{D_i}{4L}\right)(\beta(T_i - T_b)$$
$$+ \rho_{soln}\beta^*(\omega_i - \omega_b))^{1/4}(\omega_b - \omega_i) \tag{18}$$

$$\eta P + \frac{dm}{dt}H_{diss} = K_B D_i^{3/4}\left(1 + \frac{D_i}{4L}\right)(\beta(T_i - T_b)$$
$$+ \rho_{soln}\beta^*(\omega_i - \omega_b))^{1/4}(T_i - T_b) \tag{19}$$

where

$$K_A = 0.84216(-\tilde{C}'(0))\rho_{soln}D_{AB}\pi L\left[\frac{g}{\nu^2}\right]^{1/4} \tag{20}$$

$$K_B = 0.84216(-\phi'(0))k\pi L\left[\frac{g}{\nu^2}\right]^{1/4} \tag{21}$$

Some care must be exercised when computing the parameters K_A and K_B. The thermophysical properties ρ_{soln}, D_{AB}, k and ν do not change significantly during the deposition period and may be treated as constants. The parameters $-C'(0)$ and $-\phi'(0)$, however, are functions of Pr, Sc, and $\tilde{N}$. At relevant conditions, representative values for Pr and Sc are about 1 and 4, respectively, for aqueous sodium sulfate solutions and 2 and 5, respectively, for aqueous potassium sulfate solutions [6]. (These moderate differences in Pr and Sc do not significantly affect the values of $-C'(0)$ and $-\phi'(0)$.) $\tilde{N}$ is about 0.5–0.75 at the beginning of the sodium sulfate deposition experiments, decreases by about 15 percent during the course of a run and equals zero at steady state. Conveniently, inspection of the Gebhart and Pera results shows that both $-C'(0)$ and $-\phi'(0)$ are relatively weak functions of $\tilde{N}$. For example, at Pr equal to 0.7 and Sc equal to 5.0, changing $\tilde{N}$ from -0.5 to 2 causes $-C'(0)$ and $-\phi'(0)$ to decrease by only 19.3 percent and 24.3 percent, respectively. Thus, for the purposes of calculating K_A and K_B, $-C'(0)$ and $-\phi'(0)$ are assumed constant. Characteristic values for Pr, Sc and $\tilde{N}$ are assumed to be 0.7, 5 and 0.5 respectively for all computations. With these assumptions, $-C'(0)$ and $-\phi'(0)$ are equal to 1.11689 and 0.46880, respectively [12].

2.4 Auxiliary Relationships. Deposition depletes the salt concentration in the bulk solution; therefore, it does not equal that in the inlet stream except at steady state conditions. If it is assumed that the bulk solution is perfectly well mixed, the salt concentration in the bulk solution equals that in the exit stream which may be determined from a material balance. Since the material capacitance of the test cell is negligible [6], it follows that:

$$\omega_b = \omega_{in} - \frac{1}{\dot{m}_{soln}}\frac{dm}{dt} \tag{22}$$

Calculation of the deposition rate requires an expression for the position of the SLSI as a function of the mass of salt deposited. This can be determined from the Hodes et al. [5] measurements of the salt layer porosity and the density of the precipitated (solid) salts. The result is that

$$D_i = \sqrt{D_{io}^2 + \frac{4m}{\rho_s\pi L(1-\phi)}} \tag{23}$$

where D_{io} is the diameter of the heated cylinder.

At the SLSI, concentration and temperature are related by the solubility correlations given by Hodes et al. [5] in the form $\omega_{sat} = f(T_{sat})$ since the system pressure is constant. Since these correlations are not valid at very low salt concentrations, they predict negative salt concentrations at sufficiently high temperatures. When this happens, the salt concentration at the SLSI is set equal to zero.

2.5 Overall Formulation

2.5.1 Numerical Solution Procedure. The material balance (Eq. 22), the relationship between the SLSI diameter and the mass of salt deposited on the heated cylinder (Eq. 23), and the solubility relationships were used to eliminate ω_b, D_i, and ω_i, respectively, from the mass and energy balances at the SLSI (Eqs. 18 and 19, respectively). Given the initial condition that the mass of salt on the heated cylinder equals zero at time equals zero, the resulting forms of the mass and energy balance equations contain two unknowns, namely dm/dt and T_i. To begin the solution process for the mass of salt deposited on the heated cylinder as a function of time, the mass and energy balances are recast into the form $f(dm/dt, T_i) = 0$ and $g(dm/dt, T_i) = 0$ and simultaneously solved for dm/dt and T_i at time equal to zero. Since these equations are nonlinear in both dm/dt and T_i, an analytical solution was not possible. The Newton-Raphson procedure was used to numerically solve for dm/dt and T_i at each time step. The required Jacobian matrices in the Newton-Raphson method were computed analytically and are provided by Hodes [2] and the FORTRAN 77 subroutine by Press et al. [13] was used for all computations. When either of two convergence criteria were met, the solution for dm/dt and T_i was considered to be converged. The first convergence criterion was that the sum of the absolute values for corrections in dm/dt and T_i for a given iteration was less than 0.0001. The second criterion was that the sum of the magnitudes of the functions $f(dm/dt, T_i)$ and $g(dm/dt, T_i)$ in a given iteration was less than 0.0001. After the values of dm/dt and T_i were determined at time equal to zero, the mass of salt on the heated cylinder during the next time step was calculated from dm/dt and the procedure repeated until steady-state conditions were reached. The foregoing solution process is subsequently referred to as the deposition rate formulation (DRF) and it is noted that it does not contain any adjustable parameters.

2.5.2 Numerical Uncertainty. All computations were performed in single precision with a (uniform) time step of 0.5 seconds. Decreasing the time step to 0.25 seconds in a selected run produced no discernible difference in the resulting plot of the mass of salt deposited versus time; therefore, the 0.5 seconds time step was considered sufficiently small. For a selected set of computations, both of the convergence criteria in the Newton-Raphson method were reduced from 0.0001 to $1*10^{-8}$ and the computations were performed in double precision. Since there were no discernible differences in the mass of salt deposited plotted as a function of time, the former criteria were considered to be sufficiently small.

2.6 Asymptotic Behavior. Since there is no deposition at steady-state conditions, natural convection is driven exclusively by the temperature difference between the SLSI and bulk solution. Thus the energy balance (Eq. 19) becomes:

$$\eta P = K_B D_{i\infty}^{3/4}\left(1 + \frac{D_{i\infty}}{4L}\right)\beta^{1/4}(T_s - T_b)^{5/4} \tag{24}$$

and it may be used to calculate the steady-state SLSI diameter ($D_{i\infty}$). The thermodynamic and transport properties (except β^* and D_{AB}) of the solution influence $D_{i\infty}$ because K_B is a function of $-\phi'(0)$ which, in turn, depends on these properties, albeit often weakly. The variables k, β, T_b, and ηP and the solubility boundary most strongly influence $D_{i\infty}$. The time required to establish steady-state conditions does not depend on the relevant variables in the same manner as the steady-state SLSI diameter and, additionally, it depends on β^* and D_{AB}. For example, the steady-state SLSI diameter is independent of the diffusion coefficient, but, as shown below, doubling the diffusion coefficient significantly decreases the time required to reach steady-state.

3 Estimation of Solution Properties

Since the temperature difference between the SLSI and the bulk solution is about 10°C at time equal to zero and monotonically decreases with time, it is a reasonable approximation to assume constant solution properties and evaluate them at the film temperature at time equal to zero. This holds even in the vicinity of the pseudocritical temperature of water (385°C at the system pressure of 250 bar) where the properties are the strongest functions of temperature [14]. (250 bar exceeds the critical pressure of H_2O by 13.2%, consequently, variations in properties near the critical temperature of pure water (374°C), despite being large, are far less dramatic than along the critical isobar.) Estimates of density, thermal expansion coefficient, species expansion coefficient, thermal diffusivity, binary molecular diffusion coefficient, and heat of dissolution of the aqueous salt solutions were possible as described below. The solutions were approximated as pure H_2O and the NBS Steam Tables [14] were used to determine the remaining properties. Densities of aqueous sodium sulfate solutions were computed from the model by Gallagher [15] which applies the equation of state developed by Anderko and Pitzer [16] for the NaCl-H_2O system above 573 K to the Na$_2$SO$_4$-H_2O system based on available, albeit somewhat sparse, experimental data. Thermal and species expansion coefficients were computed from these densities. The thermal diffusivity and the binary molecular diffusion coefficient have not been been measured in the aqueous salt solutions at relevant conditions. However, Butenhoff et al. [17] measured both in aqueous sodium nitrate solutions at near-supercritical conditions. The Butenhoff et al. [17] measurements show that the thermal diffusivities of pure water and aqueous sodium nitrate solutions are fairly close; therefore, the thermal diffusivity of pure water was used. The binary molecular diffusion coefficients of sodium sulfate and potassium sulfate in water at relevant conditions were assumed to equal $0.25*10^{-7}$ m^2/sec based on the Butenhoff et al. [17] data. Estimates for the heat of dissolution were based on the values reported by Zaytsev [18] for sodium sulfate and potassium sulfate in water at elevated temperatures.

4 Results

4.1 Sodium Sulfate. The predicted mass of salt on the heated cylinder as a function of time for the set of runs in which the sodium sulfate concentration in the inlet stream was 4 wt% is shown in Figs. 5 through 8. (Figures 5 and 7 are for the first 15 minutes of deposition and Figs. 6 and 8 extend to steady state.) A sensitivity analysis on (H_{diss}, D_{AB}, β^*, T_b, and ϕ) is performed relative to a baseline case which uses best estimates of all variables as these are the variables contributing the most uncertainty. The baseline heat of dissolution is set equal to zero because of the uncertainties associated with its estimation. The baseline binary molecular diffusion coefficient is set equal to $0.25*10^{-7}$ m^2/sec as discussed above. The baseline species expansion coefficient is set equal to -0.004 m^3/kg based on densities determined from the Gallagher model [15]. The baseline bulk solution temperature is set equal to that characterizing the end of the runs. Finally, the baseline porosity is assumed to be 2/3 based on porosity values measured in the deposition experiments [5,6]. Plots of the mass of salt on the heated cylinder versus time for the baseline case and for perturbations in the heat of dissolution and binary molecular diffusion coefficient are provided in Figs. 5 and 6. The experimental deposition rate data are shown in Fig. 5. The baseline predictions agreed with the experimental data to within 20 percent when the concentration of sodium sulfate in the inlet stream was 4 wt%.

Extrapolation of the Zaytsev [18] heat of dissolution values (at infinite dilution) to the film temperature characterizing the runs in which the concentration of sodium sulfate in the inlet stream was 4 wt% results in a value of $-2.24*10^6$ J/kg. (Precipitation is endothermic.) The predicted mass of salt on the heated cylinder when the heat of dissolution equals 0 and $\pm 2.24*10^6$ J/kg is

Fig. 5 Measured [1] and predicted mass of salt deposited versus time when the sodium sulfate concentration in the inlet stream is 4 wt%. Includes sensitivity analysis on H_{diss} and D_{AB}

shown as a function of time in Figs. 5 and 6. Relative to baseline conditions, for time scales on the order of the duration of the experiments, increasing the heat of dissolution from 0 to $2.24*10^6$ J/kg increases the predicted mass of salt deposited by close to 40 percent and decreasing it from 0 to $-2.24*10^6$ J/kg decreases the mass of salt deposited by about 25 percent. An exothermic precipitation process (positive heat of dissolution) increases the heat rate at the SLSI by $H_{diss}dm/dt$. Hence it increases temperature and decreases concentration at the SLSI. This results in an increase in the deposition driving force and, thus, the deposition rate. Analogously, for an endothermic precipitation process the mass of salt on the heated cylinder as a function of

Fig. 6 Predicted mass of salt deposited on the heated cylinder versus time when the concentration of sodium sulfate in the inlet stream was 4 wt% extended to steady-state conditions. Includes sensitivity analysis on H_{diss} and D_{AB}.
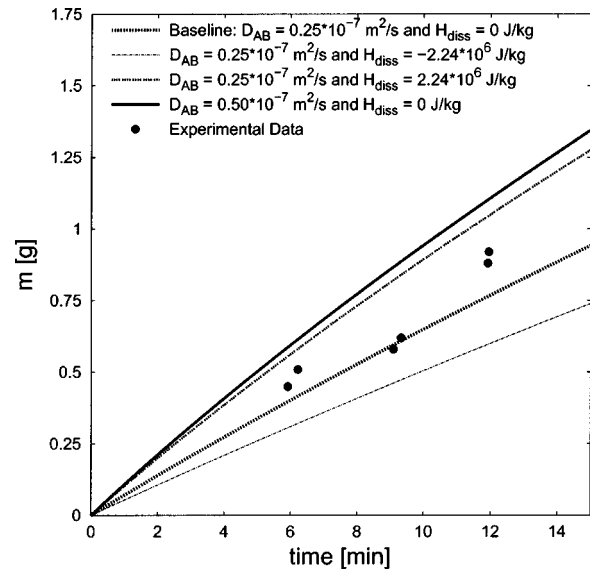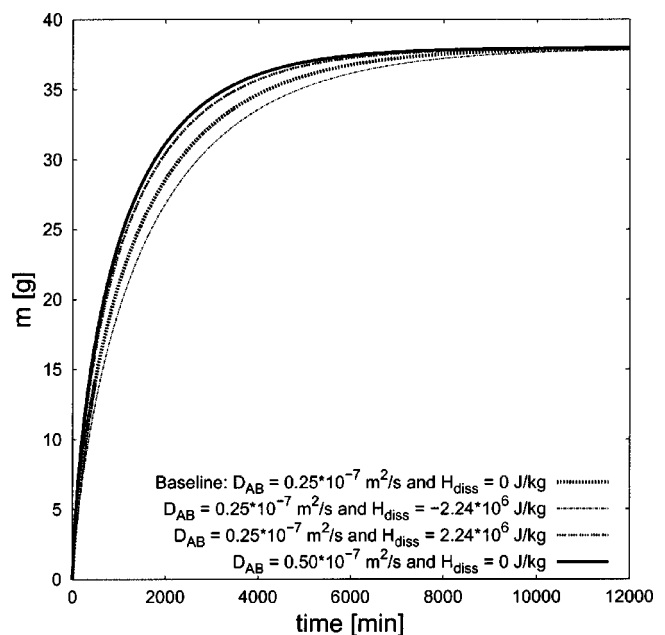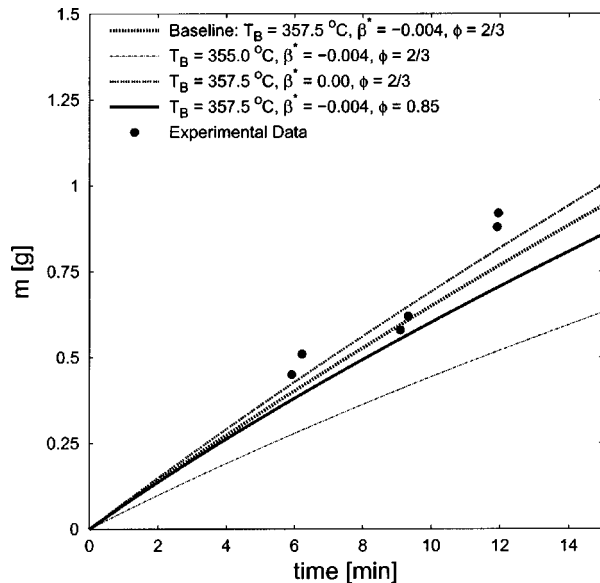
Fig. 7 Measured [1] and predicted mass of salt deposited versus time when the concentration of sodium sulfate in the inlet stream was 4 wt%. Includes sensitivity analysis on T_B, β^*, and ϕ.

time decreases relative to the baseline case. The importance of the heat of dissolution diminishes with time because the magnitude of $H_{diss} dm/dt$ decreases and the mass of salt on the heated cylinder at steady-state conditions is independent of the heat of dissolution. Finally, the time required to reach steady-state conditions is a weak function of the heat of dissolution.

The remaining curves in Figs. 5 and 6 show the effect of doubling the binary molecular diffusion coefficient on the deposition rate. Although the mass transfer coefficient is roughly proportional to the binary molecular diffusion coefficient, the deposition rate is not. This is largely because, as the mass transfer coefficient
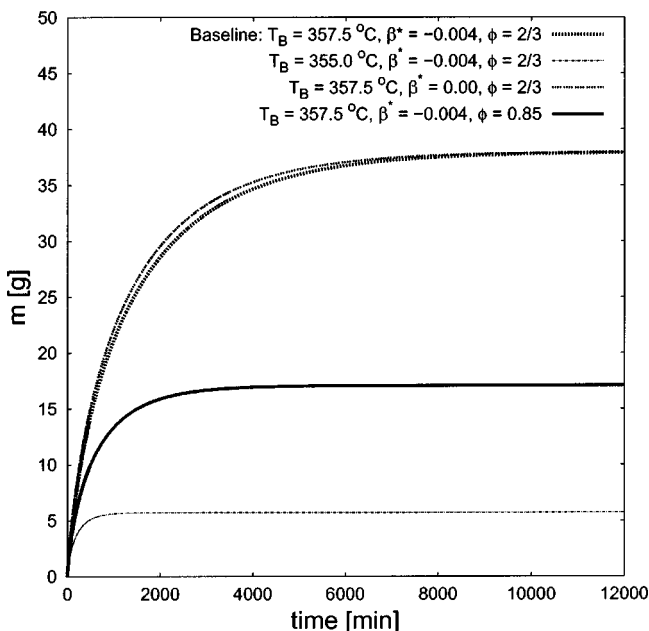

Fig. 8 Predicted mass of salt deposited on the heated cylinder versus time when the concentration of sodium sulfate in the inlet stream was 4 wt% extended to steady-state conditions. Includes sensitivity analysis on T_B, β^*, and ϕ.

and deposition rate increase, the depletion of salt in the bulk solution becomes more pronounced and this causes a reduction in the mass transfer driving force. Doubling the binary diffusion coefficient increases the mass of salt on the heated cylinder by about 40 percent for time scales on the order of the duration of the experiments and steady-state conditions are achieved about 10 percent faster.

Changing the species expansion coefficient from -0.004 m³/kg to zero increases the mass of salt on the heated cylinder as a function of time as shown in Figs. 7 and 8. This is an example of weakened transport increasing the deposition rate as elucidated by Hodes et al. [5]. Changing the species expansion coefficient from -0.004 m³/kg to zero reduces the transport coefficients corresponding to a given temperature difference between the SLSI and the bulk solution. Thus, a larger temperature difference across the boundary layer is required to remove the heat at the SLSI. This, in turn, increases the mass transfer driving force. The net effect of the reduced mass transfer coefficient and increased mass transfer driving force is an increased deposition rate. Thus the mass of salt on the heated cylinder as a function of time increases (albeit by only a few percent) relative to the baseline case until steady-state conditions are established as shown in Fig. 8.

The mass of salt on the heated cylinder as a function of time and at steady-state conditions is strongly influenced by bulk solution temperature and porosity as shown in Figs. 7 and 8. The bulk solution temperature at the beginning of the runs in which the sodium sulfate concentration in the inlet stream was 4 wt% was 355°C and increased to about 357.5°C by the end of each run. The temperature difference between the SLSI and the bulk solution is about 10°C during the experiments and it is a modest function of the bulk solution temperature. However, lowering the bulk solution temperature from 357.5°C to 355.0°C substantially decreases the amount by which the SLSI temperature exceeds the solubility temperature corresponding to the concentration of salt in the bulk solution. This substantially lowers the mass transfer driving force and the mass of salt deposited on the heated cylinder as a function of time. For time scales on the order of the duration experiments, the predicted mass of salt on the heated cylinder is reduced by a factor of about 1/3 when the bulk solution temperature is lowered from 357.5°C to 355.0°C. Decreasing the bulk solution temperature from 357.5°C to 355.0°C also reduces the mass of salt on the heated cylinder at steady state conditions from about 38 grams to about 6 grams, a more than sixfold effect, and drops the time required to reach steady-state conditions by an order of magnitude.

When the porosity of the salt layer is increased, less salt mass corresponds to a given SLSI diameter. The steady state SLSI diameter is independent of porosity; therefore, increasing porosity reduces the mass of salt on the heated cylinder at steady-state conditions. Increasing the porosity from 2/3 to 0.85 decreases the mass of salt on the heated cylinder at steady sate conditions by about 55 percent and the time required to reach steady state conditions by a factor of about 2/3. However, for time scales on the order of the duration of the experiments, increasing the porosity from 2/3 to 0.85 causes the mass of salt on the heated cylinder to decrease by only slightly more than 10 percent. As salt deposits, the driving force for deposition ($\omega_b - \omega_i$) and mass transfer coefficient are reduced, but the area available for deposition increases and, for time scales on the order of those in the experiments, the overall effect is modest. The measured porosity in the deposition experiments ranged from about 60 percent to 80 percent [5].

The predicted and measured mass of salt deposited on the heated cylinder for the runs in which the sodium sulfate concentration in the inlet stream was 2, 4, 6, and 8 wt% are plotted versus time in Fig. 9. (One curve represents the results for the 2 and 4 wt% inlet concentrations as the results are indistinguishable.) The amount by which the bulk solution temperature at time equal to zero was below the solubility temperature corresponding to the salt concentration in the inlet stream (ΔT_{s-bo}) monotoni-
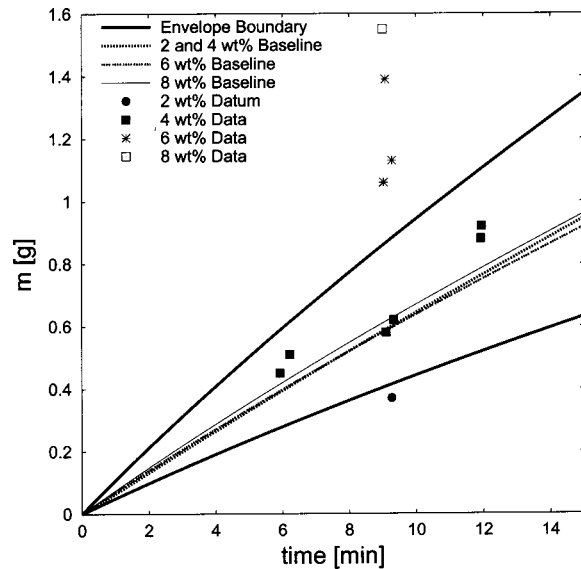
Fig. 9 Experimental data and predictions for all of the sodium sulfate deposition experiments. (One curve represents the results for the 2 and 4 wt% inlet concentrations as the results are indistinguishable and the same "envelope boundary" pragmatically bounds the predictions for all the experiments.)

Fig. 10 Experimental data and baseline predictions for the potassium sulfate deposition experiments

cally increased from 3.8 to 6.4°C as the salt concentration in the inlet stream increased from 2 to 8 wt%. Despite this fact, the DRF predicts that the mass of salt on the heated cylinder as a function of time is essentially independent of the inlet condition as shown in Fig. 9 for baseline conditions. If the solubility boundary were linear, increases in ΔT_{s-bo} with salt concentration would cause the deposition driving force to substantially decrease. However, the magnitude of the slope of the solubility curve for the Na_2SO_4/H_2O system at 250 bar decreases with increasing salt concentration and thus the concentration difference corresponding to a given temperature difference increases with increasing sodium sulfate concentration. At baseline conditions, the (initial) driving force for deposition at the SLSI (bulk salt concentration minus SLSI salt concentration) equals 1.4, 1.5, 1.5, and 1.6 wt% for the experiments in which the salt concentration in the inlet stream was 2, 4, 6, and 8 wt%, respectively.) Thermodynamic and transport properties also varied with the inlet conditions. The net effect is that the DRF predicts that the deposition rate is (pragmatically) independent of the inlet condition for time scales on the order of the duration of the experiments.

The preceding sensitivity analysis showed that the predicted deposition rate decreased the most relative to the baseline case if the bulk solution temperature were lowered to that at the beginning of the run and increased most if the binary molecular diffusion coefficient were doubled. Hence only the bulk solution temperature and binary molecular diffusion coefficient are examined in the sensitivity analysis for sodium sulfate deposition at different bulk concentrations. The results are shown in Fig. 9. For each inlet condition, the deposition rate changes by approximately the same magnitude when the bulk solution temperature is lowered from that corresponding to the end of the run to that corresponding to the beginning of the run (about 3°C) and when the binary molecular diffusion coefficient is doubled. Thus only one set of curves is included in Fig. 9 to represent the entire sensitivity analysis. For times on the order of the duration of the experiments, lowering the bulk solution temperature decreases the mass of salt on the heated cylinder by about 1/3 and doubling the diffusion coefficient increases it by about 40 percent. The data collected at salt concentrations of 2 and 4 wt% in the inlet stream almost fall within the bounds of the sensitivity envelope. When the concentration of salt in the inlet stream is 6 wt%, the data are
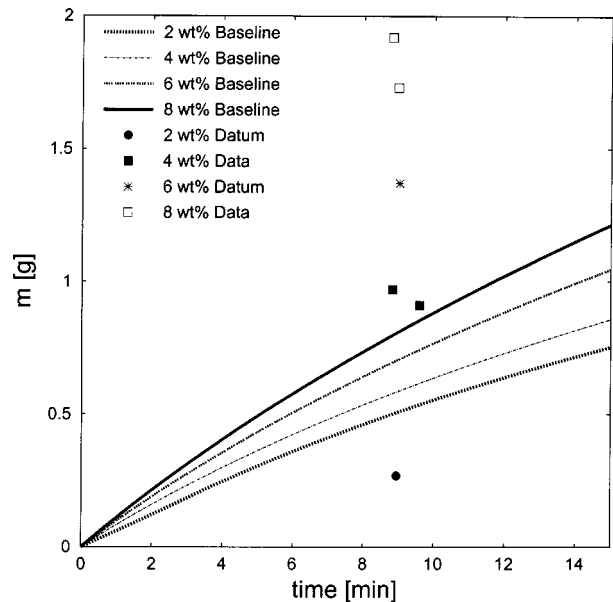
up to about 25% higher than the envelope boundary and those at 8 wt% are up to about twice the upper bound of the envelope. A logical explanation for the discrepancy between the predictions and data is that deposition inside the PSL becomes more important as the concentration of salt in the inlet stream increases as discussed below.

4.2 Potassium Sulfate. The potassium sulfate results are shown in Fig. 10. Whereas in the sodium sulfate deposition experiments the temperature difference between the solubility temperature corresponding to the salt concentration in the inlet stream and the bulk solution temperature (ΔT_{s-bo}) varied, it was held constant at 7°C in the potassium sulfate deposition experiments [6]. Moreover, because the solubility boundary is linear for the potassium sulfate-water system [6], it might be expected that the deposition rate at the SLSI should not vary with inlet concentration. The DRF, however, predicts that the mass of salt on the heated cylinder as a function of time is a substantial function of the inlet condition because of variations in thermophysical properties. For example, the heat capacity of pure water drops from 26.53 to 11.84 kJ/kg between the film temperatures characterizing the experiments for which the concentration of potassium sulfate in the inlet stream was 2 wt% and 8 wt%, respectively. Thermophysical property variations are more important in the potassium sulfate experiments than in the sodium sulfate experiments because potassium sulfate precipitates closer to the pseudocritical temperature of water at 250 bar.

The sensitivity analysis for the predictions of the potassium sulfate deposition experiments is provided by Hodes [6]. As with sodium sulfate deposition, when the concentration of salt in the inlet stream is 2 and 4 wt%, the data fall almost within the bounds of the sensitivity analysis. When the concentration of potassium sulfate is 6 and 8 wt% in the inlet stream, deposition inside the PSL is again a logical explanation for the discrepancy.

5 Transport Inside the Porous Salt Layer (PSL)

Once salt accumulates on the heated cylinder, the regions surrounding it contain various combinations of solid salt, pure water and aqueous salt solution as delineated in Fig. 11. Adjacent to the surface of the heated cylinder a region may exist which contains solid salt and (essentially) pure water. Solubility data reported by Rogak and Teshima [2] show that, at a pressure of 250 bar, so-
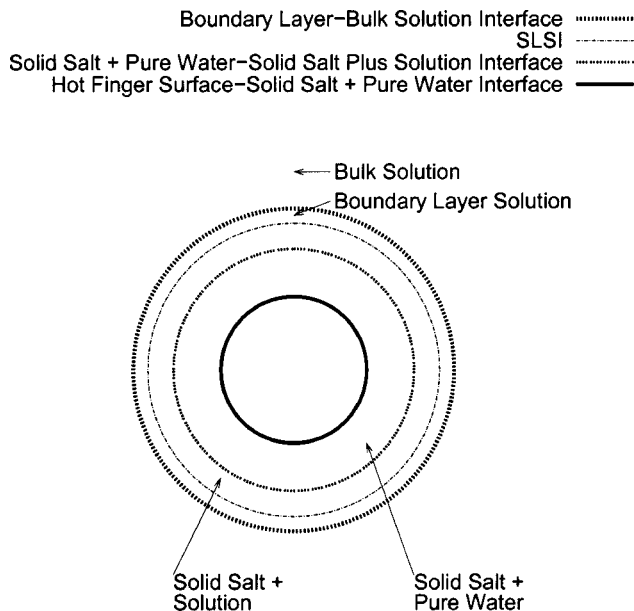
Fig. 11   Idealized boundaries between regions containing various combinations of solid salt, pure water and aqueous salt solution surrounding the heated cylinder

Fig. 12   Driving forces for deposition at the SLSI and in the PSL

dium sulfate becomes essentially insoluble in water for temperatures in excess of the pseudocritical value (385°C). During the experiments when the inlet stream concentration of sodium sulfate was 4 wt%, for example, the surface temperature of the heated cylinder reached about 390°C [2]; therefore, a mixture of solid sodium sulfate and (essentially) pure water was present adjacent to the heated cylinder. Similar arguments may be made for the potassium sulfate-water system. Beyond the radius at which temperature equals that corresponding to essentially zero salt solubility, lies a region containing a mixture of solid salt and aqueous salt solution. This region ends at the SLSI, beyond which solid salt is no longer present. Beyond the SLSI, the concentration of salt in solution increases to that in the bulk. The boundary layer around the SLSI is idealized as a thin annulus in Fig. 11 whereas the true boundary layer thickness is a (modestly) increasing function of y and a plume forms towards the top of the cylinder. Outside the boundary layer region, i.e., in the bulk solution, the concentration of salt in solution is assumed to be uniform.

An examination of the deposition driving forces present within the regions surrounding the heated cylinder delineated in Fig. 11 elucidates the importance of deposition within the PSL. The bulk solution temperature (T_b), the solubility temperature corresponding to the concentration of salt in the bulk solution (T_s), the SLSI temperature (T_i), the temperature corresponding to zero solubility (T_o) and the heated cylinder surface temperature (T_{HC}) are shown on a temperature-composition diagram in Fig. 12 for an arbitrary set of operating conditions. The driving force for salt deposition at the SLSI equals the salt concentration in the bulk solution (ω_b) minus that at the SLSI (ω_i) as shown. The driving force for deposition within the region containing solid salt and aqueous salt solution is more complex. At the outer boundary of this region the concentration of salt in solution corresponds to that at the SLSI, $\rho_{soln}\omega_i$. At the inner boundary of this region, the concentration of salt in solution equals (essentially) zero. Thus, a representative mass transfer driving force for this region is simply ω_i as shown in Fig. 12. However, the surface area available for deposition inside the PSL is important, but unknown. The driving forces for deposition at the SLSI and within the PSL pertain to two very different types of transport problems. The driving force for deposition at the SLSI is used to compute the rate of transport by natural convection. The driving force for deposition inside the PSL pertains to a volume in which diffusion is probably the dominant transport mechanism. Finally, for the innermost region of the PSL, the driving force for deposition is (essentially) zero.
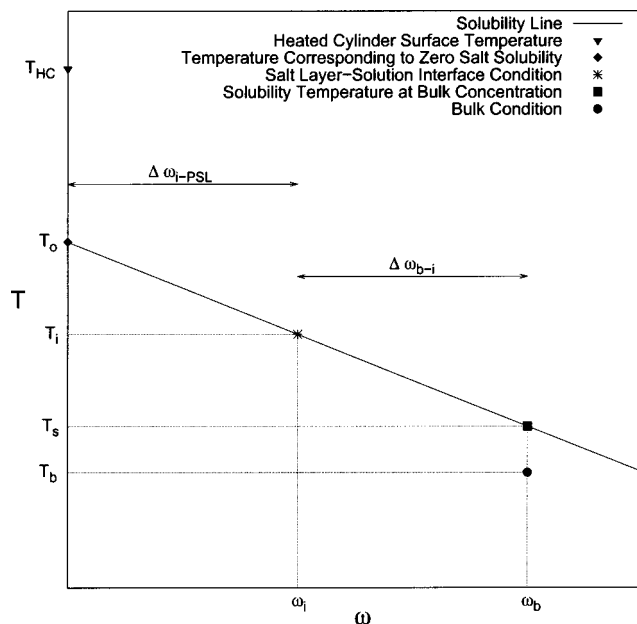
The analyses performed earlier suggest that, during all the experiments, the concentration of salt in the bulk solution approaches that in the inlet stream and the concentration of salt at the SLSI is about 2 wt% less than that in the bulk solution. Measurements of the heated cylinder surface temperature profile during selected deposition experiments show that it reaches or exceeds the temperature corresponding to zero salt solubility. It follows that, in general, the driving force for deposition at the SLSI equals roughly 2 wt% and the deposition driving force in the PSL equals roughly the inlet stream concentration minus 2 wt%. For example, in the experiments for which the concentration of salt in the inlet stream is 4 wt%, the driving forces for mass transfer to the SLSI (ΔC_{b-i}) and within the PSL (ΔC_{i-PSL}) are both approximately 2 wt%. In general, the driving force for deposition at the SLSI is, to a first approximation, independent of the concentration of salt in the inlet stream, but the driving force for deposition within the PSL is not. Deposition rates at the SLSI were computed earlier and compared to experimental data; however, deposition inside the PSL was neglected. The foregoing discussion suggests that deposition within the PSL increases with the concentration of salt in the inlet stream, but the deposition rate at the SLSI is essentially constant. Hence, it is not surprising that the deposition rate predictions agreed better with the experimental data when the concentration of salt in the inlet stream was 2 and 4 wt% than when the concentration of salt in the inlet stream was 6 and 8 wt%. The experimentally measured deposition rate increases monotonically with the concentration of salt in the inlet stream and this is also consistent with the results of this section.

Throughout this discussion, we have, for simplicity, depicted the SLSI as though it were a sharp interface. In truth, that cannot be the case and the porosity must be very high at the edge of the envelope which contains all of the solid salt. Indeed, there may be additional natural convection within this highly porous region just "below" the SLSI. It is likely that processes in this region are similar to those described by others in the context of the solidification of metals. (See, for example, Davis [19] or Beckermann and Viskanta [20].)

6 Implications on Scale Control in SCWO

Several techniques developed for scale control during SCWO rely on periodically removing salts deposited in the reactor. For example, Modell et al. [21] controlled scale in a tubular reactor by periodically sending a mechanical device, e.g., a bristle brush or metal ball, through it to remove deposited salt. Periodic flushing of SCWO reactors with pure water at a temperature low enough to redissolve deposited salts is another common technique used to control scale during SCWO [3]. When applicable, predictive models for deposition rates in SCW, e.g., that developed here and that by Rogak and Teshima [4] for turbulent forced convection in a tubular reactor, are useful in such scale control strategies to determine how often deposited salts must be removed. An important implication of the comparison between the current model and experimental data, however, is that, until predictive models account for salt deposition in the porous salt layers formed in SCWO reactors, the models will not be adequate for predicting when the reactors need to be flushed. This will be especially true with respect to the densification process that may take place within the PSL after a steady state scale thickness has been achieved. Denser material would presumably be more resistant to flushing.

7 Conclusions and Recommendations

A model for the rate of salt deposition by double-diffusive natural convection from aqueous salt solutions onto a cylinder heated beyond the solubility temperature of the salt in the surrounding solution has been developed. The model accounts for the deposition rate at the salt layer-solution interface (SLSI) formed on the cylinder, but does not account for deposition which may occur inside the porous salt layer (PSL). Dissolved salt is transported to the SLSI by molecular diffusion (with advection) and subsequently nucleates heterogeneously there. The model is applied to the experimental deposition rate data acquired by Hodes et al. [5,6]. The ratio of the predicted deposition rate to the measured values ranges from 0.5 to 2 allowing for realistic uncertainties in the variables input into the model. Omission of deposition inside the PSL in the model is thought to be largely responsible for the discrepancy (when present) between the model and the experimental data. Hence, it is recommended that future investigators focus on experiments and analyses which might elucidate this process.

Nomenclature

$-\tilde{C}'$ = dimensionless parameter defined by Eq. 16
D_{AB} = binary molecular diffusion coefficient [m^2/s]
D_i = salt layer-solution interface diameter [m]
g = acceleration due to gravity [m/s^2]
Gr = Grashof number
h = (mean) heat transfer coefficient coefficient [$W/m^2 \cdot K$]
h = enthalpy [J/kg]
h_m = (mean) mass transfer coefficient [m/s]
$J_{i,j}$ = mass diffusive flux of component i in j direction [$kg/m^2 \cdot s$]
K_A = constant defined by Eq. 20 [$kg/(sm^{3/4})$]
K_B = constant defined by Eq. 21 [$kgm^{5/4}/(s^3 K)$]
L = length of heated cylinder [m]
m = mass of salt on heated cylinder [kg]
m_s = mass of salt in differential control volume [kg]
$\dot{m}''_s$ = mass flux of salt deposited at SLSI [$kg/m^2 s$]
$\dot{m}_{soln}$ = mass flow rate of solution through test cell [kg/sec]
$\tilde{N}$ = dimensionless buoyancy parameter
Nu_x = local Nusselt number
P'' = heat flux on heated cylinder [W/m^2]
Pr = Prandtl number
q'' = heat flux [W/m^2]
Ra = Rayleigh number
Sc = Schmidt number
Sh_x = local Sherwood number

t = time [s or min]
T = temperature [°C]
u = internal energy [J/kg]
v = velocity [m/s]
x = direction perpendicular to salt layer-solution interface
x_i = position of SLSI [m]
U'' = internal energy flux at SLSI [W/m^2]
β = volumetric thermal expansion coefficient [1/K]
β^* = species expansion coefficient [m^3/kg]
η = fraction of power supplied to heated cylinder driving deposition
ρ_{soln} = density of aqueous salt solution [kg/m^3]
ρ_A = density of salt component in aqueous salt solution [kg/m^3]
ρ_B = density of water component in aqueous salt solution [kg/m^3]
ρ_s = density of solid salt [kg/m^3]
ϕ = porosity
$-\phi'(0)$ = dimensionless parameter defined by Eq. 17
ω = mass fraction of salt

SUBSCRIPTS DESCRIPTION

A = salt component of solution
b = bulk condition
B = water component of solution
bulk i = initial bulk condition
bulk f = bulk condition 2 minutes before end of run
e = time when material capacitance of cell becomes unimportant
HC = heated cylinder
i = salt layer-solution interface condition (SLSI)
in = inlet
o = time equal to zero
s = solubility
s = salt
sat = saturation
∞ = steady state condition

References

[1] Shaw, R. W., Brill, T. B., Clifford, A. A., Eckert, C. A., and Franck, E. U., 1991, "Supercritical Water: A Medium for Chemistry," Chemical and Engineering News, **26**, Dec. 23, pp. 26–39.
[2] Hodes, M., Marrone, P. A., Hong, G. T., Smith, K. A., and Tester, J. W., 2003, "Salt Precipitation and Scale Control in Supercritical Water Oxidation—Part A: Fundamentals and Research," accepted for publication in J. Supercrit. Fluids.
[3] Marrone, P. A., Hodes, M., Hong, G. T., Smith, K. A., and Tester, J. W., 2003, "Salt Precipitation and Scale Control in Supercritical Water Oxidation—Part B: Commercial/Full-Scale Applications," accepted for publication in J. Supercrit. Fluids.
[4] Rogak, S. N., and Teshima, P., 1999, "Deposition of Sodium Sulfate in a Heated Flow of Supercritical Water," AIChE J., **45**(2), pp. 240–247.
[5] Hodes, M., Smith, K. A., Hurst, W. S., Bowers, Jr., W., Griffith, P., and Sako, K., 2002, "Solubilities and Deposition Rates in Aqueous Sulfate Solutions at Elevated Temperatures and Pressure," submitted to AIChE J.
[6] Hodes, M., 1998, "Measurements and Modeling of Deposition Rates from Near-Supercritical, Aqueous, Sodium Sulfate and Potassium Sulfate Solutions to a Heated Cylinder," Ph.D. thesis, Massachusetts Institute of Technology, Cambridge, MA.
[7] Hurst, W. S., Hodes, M., Bowers, Jr., W. J., Bean, V. E., Maslar, J. E., Griffith, P., and Smith, K. A., 2002, "Optical Flow Cell and Apparatus for Solubility, Salt Deposition and Raman Spectroscopic Studies in Aqueous Solutions near the Water Critical Point," J. Supercrit. Fluids, **22**, pp. 157–166.
[8] Smith, K. A., Hodes, M., and Griffith, P., 2002, "On the Potential for Homogeneous Nucleation of Salt from Aqueous Solution in a Natural Convection Boundary Layer," ASME J. Heat Transfer, **124**(5), pp. 930–937.
[9] McAdams, W. H., 1954, *Heat Transmission*, 3rd ed., McGraw Hill, New York, Chap. 7.
[10] Morgan, V. T., 1975, "The Overall Convective Heat Transfer From Smooth Circular Cylinders," *Advances in Heat Transfer*, T. F. Irvine and J. P. Hartnett, eds., **11**, Academic Press, New York, pp. 199–264.
[11] Lienhard, IV, J. H., 1973, "On the Commonality of Equations for Natural Convection From Immersed Bodies," Int. J. Heat Mass Transfer, **16**, pp. 2121–2123.
[12] Gebhart, B., and Pera, L., 1971, "The Nature of Vertical Natural Convection Flows Resulting From the Combined Buoyancy Effects of Thermal and Mass

Diffusion,'' Int. J. Heat Mass Transfer, **14**, pp. 2025–2050.

[13] Press, W. H., Teukolsky, S. A., Vetterling, W. T., and Flannery, B. P., 1982, *Numerical Recipes in Fortran 77*, 2nd ed., Cambridge University Press.

[14] Gallagher, J. S., and Haar, L., 1985, NBS Standard Reference Data Base 10 Steam Tables, National Bureau of Standards in Gaithersberg, MD.

[15] Gallagher, J. S., 2000, ''A Model for the Liquid, Vapor and Supercritical Regions of Aqueous Solutions of Sodium Sulfate for Temperatures from 200 to 400°C and Pressures to 30 MPa,'' *Proc. 13th Int. Conf. on the Properties of Water and Steam*, NRC Press, Ottawa.

[16] Anderko, A., and Pitzer, K. S., 1993, ''Equation of State Representation of Phase-Equilibria and Volumetric Properties of the System NaCl-H_2O above 573 K,'' Geochim. Cosmochim. Acta, **57**, pp. 1657–1680.

[17] Butenhoff, T. J., Goemans, M., and Buelow, S. J., 1996, ''Mass Diffusion Coefficients and Thermal Diffusivity in Concentrated $NaNO_3$ Solutions,'' J. Phys. Chem., **100**, pp. 5982–5992.

[18] Zaytsev, I. D., and Aseyev, G. G., eds., 1992, *Properties of Aqueous Solutions of Electrolytes*, CRC Press.

[19] Davis, S., 2001, *Theory of Solidification*, Cambridge University Press.

[20] Beckermann, C., and Viskanta, R., 1993, ''Mathematical Modeling of Transport Phenomena during Alloy Solidification,'' Appl. Mech. Rev., **46**(1), pp. 1–27.

[21] Modell, M., Kuharich, E. F., and Rooney, M. R., 1993, ''Supercritical Water Oxidation Process of Organics with Inorganics,'' U.S. Patent #5,252,224.

Yuichi Mitsutake
e-mail: mitutake@me.saga-u.ac.jp
Research Associate,
Department of Mechanical Engineering,
Saga University,
1 Honjo-machi,
Saga city, 840-8502, Japan

Masanori Monde
e-mail: monde@me.saga-u.ac.jp
Professor,
Department of Mechanical Engineering,
Saga University,
1 Honjo-machi,
Saga city, 840-8502, Japan

Ultra High Critical Heat Flux During Forced Flow Boiling Heat Transfer With an Impinging Jet

An ultra high critical heat flux (CHF) was attempted using a highly subcooled liquid jet impinging on a small rectangular heated surface of length $5 \sim 10\,mm$ and width 4 mm. Experiments were carried out at jet velocities of $5 \sim 60\,m/s$, a jet temperature of $20°C$ and system pressures of $0.1 \sim 1.3\,MPa$. The degree of subcooling was varied from 80 to 170 K with increasing system pressure. The general correlation for CHF is shown to be applicable for such a small heated surface under a certain range of conditions. The maximum CHF achieved in these experiments was 211.9 MW/m^2, recorded at system pressure of 0.7 MPa, jet velocity of 35 m/s and jet subcooling of 151 K, and corresponds to 48% of the theoretical maximum heat flux proposed by Gambill and Lienhard. [DOI: 10.1115/1.1621899]

1 Introduction

As technology progresses, heat management, particularly cooling, is becoming increasingly important. For example, high-energy systems with high-density heat generation such as a diverter plate in a fusion reactor or a target plate in a proton accelerator require reliable cooling systems. The heat flux in such systems reaches the order of 10 MW/m^2, and can be expected to increase to more than 100 MW/m^2 in the future. The performance or operating conditions of such high-energy apparatus is strongly dependent on the upper limit of cooling, that is, the critical heat flux (CHF). Therefore, increasing the maximum heat flux level that can be handled by cooling systems, and determining the upper limit CHF are topics of intense interest.

Gambill and Lienhard [1] showed the theoretical upper limit of heat transmission with phase change assuming that vapor molecules behave as a Boltzman-Maxwellian gas, which is a reasonable approximation at low reduced pressure, and neglecting condensation on the liquid-vapor interface. The theoretical maximum heat flux $q_{max,max}$ determined in that study is given by

$$q_{max,max} = \rho_g h_{lg} \sqrt{RT/(2\pi M)} \qquad (1)$$

where ρ_g, h_{lg}, R, and M are density of vapor, latent heat of evaporation, universal gas constant and mass of molecular, respectively. T is the equilibrium gas temperature and taken as the saturation temperature. This equation can be easily proved based on the above assumptions and statistical thermodynamics [2]. As the saturation temperature T increases nonlinearly with system pressure P, $q_{max,max}$ increases sharply with P. For example, evaluating $q_{max,max}$ for water at 0.1 and 0.5 MPa gives very large heat fluxes of 223.4 and 994.2 MW/m^2, respectively. However, most CHF values obtained so far in boiling heat transfer experiments are about 10% of $q_{max,max}$.

It is known that the CHF is governed by the hydrodynamics of liquid-vapor flow in the vicinity of a heated surface [3]. For example, Haramura and Katto [4] proposed a hydrodynamic model to predict the CHF in which the critical film thickness of a macro liquid layer beneath a coalescent bubble is completely consumed by evaporation within an interval of liquid supply. Given this model, if the limitation of liquid supply due to the bubble or the

vapor flow can be eliminated by introducing an artificial device, the CHF may approach $q_{max,max}$. Several attempts have been made in this vein, including the use of a small heater with high mass flux and subcooled liquid flow [5–7], a swirl tape inside a tube [8], and a subcooled liquid jet flow [9,10], and all have effectively enhanced the CHF.

Nariai et al. [5] and Kureta et al. [6] studied the characteristics of the CHF for flow boiling of subcooled water in a small tube under atmospheric pressure. Nariai et al. achieved a maximum CHF of 65 MW/m^2 with an inner tube diameter d_i of 1 mm, tube length of 10 mm, mass flux G of 2×10^4 kg/m^2/s, and inlet subcooling $\Delta T_{sub,i}$ of 80 K. Kureta et al. reached 158 MW/m^2 under similar conditions ($d_i = 1$ mm, $\Delta T_{sub,i} = 90$ K, $G = 1.9 \times 10^4$ kg/m^2/s) with a shorter tube (5 mm). Kureta's result corresponds to 70% of $q_{max,max}$ and is the highest recorded CHF relative to $q_{max,max}$. Mudawar et al. [8] measured the CHF for vertical subcooled flow boiling in a small direct-heated tube and reached the highest absolute CHF of 274 MW/m^2 using a tube with inner diameter of 0.5 mm and length 5.5 mm, with inlet subcooling of 244 K, liquid mass flux of 10^5 kg/m^2/s (corresponding to a mean velocity of 98 m/s), and inlet pressure of 5.8 MPa. Monde et al. [9] and Inoue et al. [10] investigated the CHF of boiling subcooled impinging jet flow and showed that impinging jet cooling is a very effective method for enhancing the CHF. Monde et al. [9] also proposed a generalized correlation for the CHF, as given by

$$\frac{q_c}{q_{co}} = \frac{1 + \sqrt{1 + 4C\mathrm{Ja}}}{2} \qquad (2)$$

where q_c and Ja give the CHF of a subcooled impinging jet and Jacob number. q_{co} and C are the predicted CHF with a saturated impinging jet and the constant given by the following generalized correlations of Eqs. (3) and (4), respectively. This equation is applicable for subcooled impinging jet cooling within a density ratio ρ_l/ρ_g of $8.8 \sim 1605$, a jet velocity u of $5 \sim 34$ m/s, subcooling ΔT_{sub} of $0 \sim 115$ K, and a ratio of the characteristic diameter of the heater and jet diameter D/d of 20–30.

$$\frac{q_{co}}{\rho_g h_{lg} u} = 0.221(\rho_l/\rho_g)^{0.645}\left(\frac{2\sigma}{\rho_l u^2(D-d)}\right)^{0.343}(1+D/d)^{-0.364} \qquad (3)$$
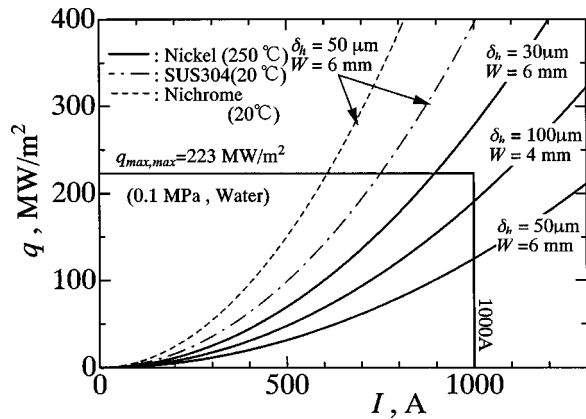
Copyright © 2003 by ASME

Fig. 1 Relationship between heat flux and current for various materials and sizes of direct heated rectangular surface

$$C = \frac{0.95(d/D)^2(1+D/d)^{0.364}}{(\rho_l/\rho_g)^{0.43}(2\sigma/\rho_l u^2(D-d))^{0.343}} \tag{4}$$

Equation (3) is applicable to a ρ_l/ρ_g of 5.3~1603, an inverse Weber number $2\sigma/\rho_l u^2(D-d)$ of 2×10^{-7} to 10^{-3}, and D/d of 5~30. The characteristic diameter D represents twice the distance between the stagnation point and the furthest point from it on the heated surface affected by the jet. Using only the characteristic diameter D, Eq. (2) is capable of predicting the CHF for any shape of heater or multiple impinging cooling jets. In the authors' previous study [11], Eq. (2) was verified for up to four jets.

If Eq. (2) were valid beyond its applicable range of D/d, a CHF equal to $q_{max,max}$ could be achieved at $D/d=2.5$, a jet velocity of 40 m/s, subcooling of 80 K, and atmospheric pressure. These conditions are not particularly severe, and can be realized experimentally. The objective of this study is to attempt to obtain a high CHF approaching the theoretical maximum heat flux $q_{max,max}$ and examine experimentally the extrapolation of the general correlation Eq. (2) to smaller D/d.

2 Experimental Apparatus and Procedure

2.1 Experimental Setup.

Heated Surface. Even if a good heat-conductive material like silver is used for a body that is heated indirectly by an external heater, a wall heat flux greater than 200 MW/m² generates a very high temperature gradient exceeding 500 K/mm inside the heated body, and the highest temperature may reach the melting temperature of silver. Only direct heating methods can avoid this problem at such a high heat flux.

The heater design focused on determination of the optimum material and electric conducting area of a rectangular heater (thickness $\delta_h \times$ width W) under the constraints of a maximum current of 1000 A at constant DC voltage and a moderate temperature gradient across the heater thickness. Figure 1 shows the relationship between heat flux and current for three materials, stainless steel, nichrome and nickel, for a range of thicknesses and widths. Nickel requires the smallest cross-sectional area among the tested materials to reach 200 MW/m² under the limitation of 1000 A because nickel has the smallest specific electric resistance.

The temperature difference across the heater was also calculated through one-dimensional steady heat conduction analysis with uniform volumetric heat generation. For example, the temperature differences at $\delta_h = 50~\mu$m and $q = 200$ MW/m² are 487, 383, and 140 K for stainless steel, nichrome, and nickel, respectively. The temperature differences for stainless steel and nichrome, are too high. However, a nickel heater can achieve 200 MW/m² given a heater width of only 4 mm and thickness of 0.1 mm.
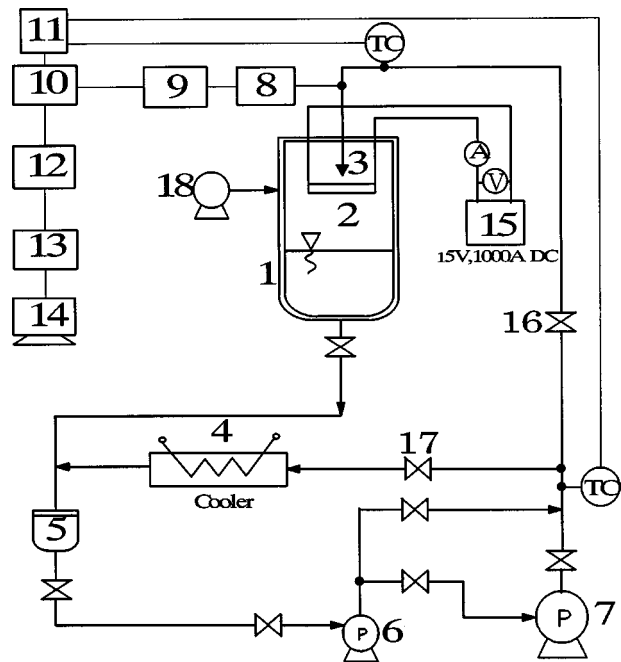
Fig. 2 Schematic of experimental apparatus (1. Pressure vessel, 2. Heated surface, 3. Circular nozzle, 4. Cooler, 5. Filter, 6. Low-pressure pump, 7. High-pressure pump, 8. Pressure transducer, 9. Strain meter, 10. Multiplexer, 11. Ice box, 12. Digital multimeter, 13. GPIB interface, 14. Personal computer, 15. DC power supply, 16. Flow control valve, 17. Bypass valve, 18. Nitrogen gas cylinder)

Experimental Apparatus. Figures 2 and 3 show the experimental apparatus and the details of the heater and nozzle setup. A circular jet nozzle was set at the top of the pressure vessel facing downward. The heated surface was mounted closely at 5 mm below the exit of the nozzle to prevent instability of the liquid jet affecting the liquid flow on the heated surface. The centers of the heated surface and the nozzle were carefully adjusted using a positioning jig. Liquid stored in the bottom of the pressure vessel was supplied to the nozzle by a low-pressure pump and high-pressure pump in series, capable of a maximum velocity of 60 m/s. The velocity was adjusted by a flow control valve and measured based on the pressure drop at the nozzle, and the flow coefficient of the nozzle was determined through nozzle calibration tests. As the circulating liquid is continuously heated by friction loss in the pumps, part of the flow was bypassed via a cooler to
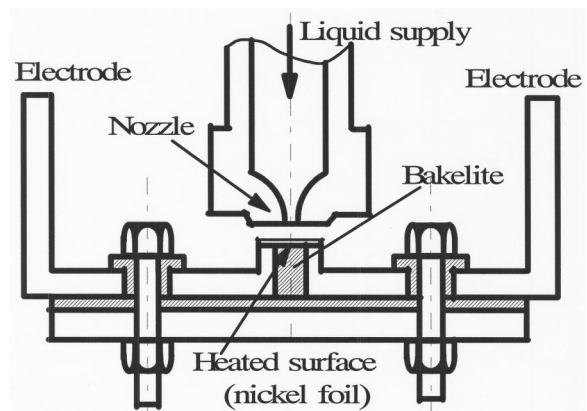
Fig. 3 Experimental setup of heated surface and nozzle

Fig. 4 Photograph of top view of a burnt-out surface

Table 1 Experimental range

Testing fluid	Water
Diameter of nozzle d, mm	2.0
Jet velocity u, m/s	5, 17, 35, 60
Jet temperature T_j, °C	20
System pressure P, MPa	0.1∼1.0
Subcooling of jet ΔT_{sub} corresponding to P, K	80∼170
Length of heated surface L, mm	5, 10
Width of heated surface W, mm	4
Ratio of characteristic diameter to jet diameter D/d	3.20, 5.39
Thickness of heated surface δ_h, mm	0.03, 0.05, 0.1, 0.3

maintain the liquid temperature at about 20°C, adjusted by controlling the bypass flow rate and the coolant flow rate of the cooler. In order to increase the degree of subcooling, the pressure vessel was pressurized at between 0.1 and 1.0 MPa by nitrogen gas, providing subcooling of 80 to 170 K depending on the system pressure.

As shown in Fig. 3, both ends of the rectangular nickel foil were soldered to the two electrodes. Special care was taken in soldering to ensure that the liquid flow on the surface remained smooth. The heated surface was made flush with the soldered areas, and obstacles such as spilled solder were removed completely. After soldering, the foil was pre-tensioned by extending the distance between electrodes slightly. A rectangular Bakelite block was inserted between the electrodes as an insulator. The foil was adhered to the Bakelite block with epoxy resin to prevent water from entering the clearance area. The wall temperature was not measured.

2.2 Experimental Procedure and Measurement of CHF. The jet velocity, jet temperature and nitrogen pressure were controlled to achieve the designated conditions. The heat flux q was calculated by the following equation:

$$q = \frac{V \times I}{L \times W} \tag{5}$$

where V is the voltage drop between the two electrodes, I is the electric current, and $L \times W$ is the rectangular heated area of the top side.
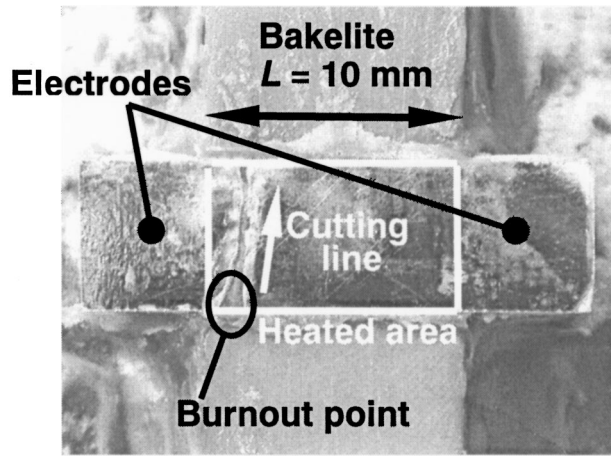
As shown in Fig. 4, the CHF was obtained as a physical burnout point where the melting of the heated surface proceeds from one of the four corners of the rectangular surface to the opposite side along the electrode. A preliminary experiment for each condition was conducted to determine a tentative CHF, followed by determination of accurate CHF through carefully repeated measurement until the reproducibility of the data was confirmed.

The experimental procedure was as follows:

1. The liquid temperature and jet velocity were controlled to designated values.
2. The voltage applied to the heated surface was gradually increased until the heat flux reached 50% of the tentative CHF.
3. The voltage was increased every 30 s until the CHF was detected. Each voltage increment was controlled so as to increase the heat flux by less than 5% of the previous heat flux. The 30-s interval was required to allow for CHF detection and to stabilize the wall temperature.

4. The CHF was detected by a sudden cut in the electric current due to breakdown of the heated surface. The heated surface was renewed in each experiment.

The voltage increment was controlled based on the electric resistance of the heater, as calculated from the measured current and voltage drop at each incremental step, such that the increment in heat flux was less than 5% until the CHF occurred. When the CHF occurred, the temperature excursion of the heater caused an increase in electric resistance and decrease electric current in a very short time (<0.2 s), and then the heater broke. Due to the difficulty in measuring the transient heat flux just before the CHF was reached, the CHF was defined as the heat flux calculated by adding the incremental heat flux to the stable heat flux measured in the previous step. Therefore, the CHF values can be considered to include an uncertainty of up to −5%.

The experiments were conducted over a wide range of jet velocity and jet subcooling, as listed in Table 1.

2.3 Assessment of Heat Losses. To assess heat losses from the heater to the electrodes and the bakelite block, steady-state heat conduction analyses were carried out for the simplified two-dimensional heater section model depicted in Fig. 5. The extent to which the heated wall area was affected by the adjacent cold electrodes was also evaluated because the CHF burnout always occurred near the electrode.

In Fig. 5, the calculation domain is taken as a half the heater area, using the symmetry of the heater. As no wall temperature information was obtained in the experiment, a uniform wall superheat ΔT_{sat} of roughly 50 K was adopted for each system pres-
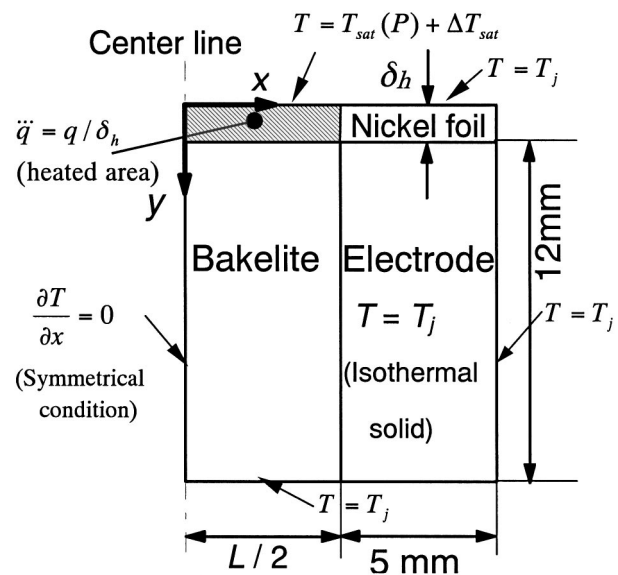

Fig. 5 Simplified two-dimensional heater assembly section model and prescribed boundary conditions to assess heat losses to the electrodes and bakelite block
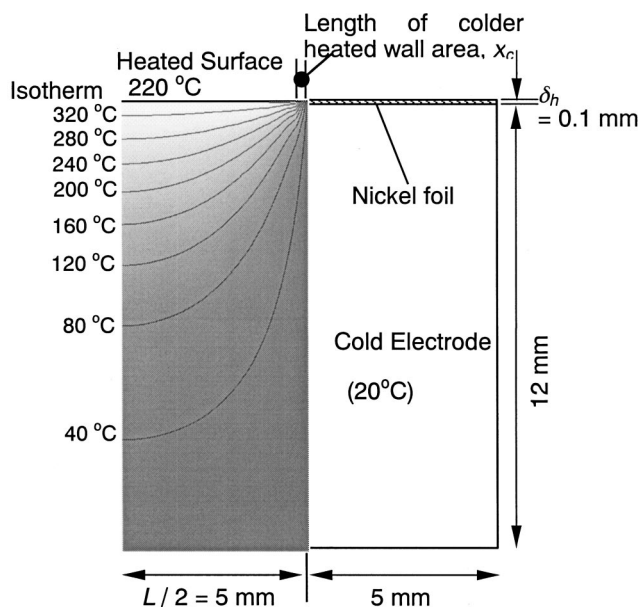
1040 / Vol. 125, DECEMBER 2003

Transactions of the ASME

Fig. 6 Steady-state temperature field in the nickel foil and the bakelite block for $q=200$ MW/m², $L=10$ mm, $\delta_h=0.1$ mm, $P=0.8$ MPa ($T_{sat}=170.4°C$), $\Delta T_{sat}=50$ K

Fig. 7 Estimated heat losses to the electrodes and the bakelite, and total heat loss with two-dimensional heat conduction analysis

sure P. This assumption is reasonable for a subcooling boiling region in which the CHF is reached, but may give an overestimated of the wall temperature in the stagnant region. For the other boundary conditions, the electrode was treated as an isothermal solid, and the bottom surface of the bakelite was considered to be isothermal, with temperatures the same as the jet temperature T_j. A uniform heat generation rate per unit volume q/δ_h was assumed for the nickel foil, and the heat flux was taken as 200 MW/m², which is comparable to the maximum CHF value. It should be noted that the assumptions of wall temperature and isothermal boundary condition may result in an overestimation of the heat loss, but errs on the side of safety.

Figure 6 shows a typical temperature distribution in the heater section at $q=200$ MW/m², $L=10$ mm, $\delta_h=0.1$ mm, $P=0.8$ MPa (corresponding saturation temperature $T_{sat}=170.4°C$), and $\Delta T_{sat}=50$ K. A distance from the electrode x_c as depicted in Fig. 6, was calculated to estimate a lower wall temperature area. For convenience the non-dimensional length x_c/L is defined as the distance at which the wall temperature recoveries

up to 95% of equilibrium wall temperature at the center portion. The value of x_c/L will be at most 0.025, 0.054, and 0.125 for the heater thickness of $\delta_h=0.03$, 0.1, and 0.3 mm. If we suppose that CHF occurs at the distance $(D/2-x_c)$ from the center of the jet, a predicted CHF with Eq. (2) may increase at most 4%, 9%, and 20% for $\delta_h=0.03$, 0.1, and 0.3 mm in the present experimental range.

Figure 7 shows the estimated heat loss for each heater length and thickness. The heat loss to the bakelite remains at approximately 5% for all heat flux levels under the present fixed heater dimensions. The heat loss to the electrodes increases from 1.0% to 7.4% as the heater becomes shorter and thicker, similar to the result for heat transfer in an extended fin. The total heat loss for $\delta_h=0.1$ mm, for which most of the CHF data was obtained, is 8.2% for a heater length $L=5$ mm, and 6.5% for $L=10$ mm.

2.4 Error Analysis. Uncertainty analysis was carried out according to the ASME Policy on Reporting Uncertainties in Experimental Measurements and Results. Table 2 shows the bias and precision limits and the uncertainties of measurements obtained from the specifications of the instruments, calibration tests, statistical data obtained from repeated measurements, and numerical analysis of the heat loss from the heated surface.

The bias limits associated with the measurements of voltage and current in the measurement of heat flux were ±0.045% and ±2.0% of reading, respectively. The dimensions of the heated surface were given accurately to within ±0.1 mm (length and width). The bias limit of the critical heat flux was calculated from

Table 2 Bias limits, precision limits and uncertainties associated with measurements

		Bias limit	
		$L=5$ mm	$L=10$ mm
Critical heat flux, B_q/q	$\delta_h=0.03$ mm	$-6.7\sim+2.8\%$	$-6.4\sim+2.2\%$
	0.1 mm	$-7.1\sim+2.8\%$	$-6.4\sim+2.2\%$
Jet subcooling, $B_{\Delta Tsub}$		±0.25 K at $P=0.1$ MPa	
Jet velocity, B_u		±1.33 m/s at $u=35$ m/s	
		Precision limit	
		$L=5$ mm	$L=10$ mm
Critical heat flux, P_q/q	$\delta_h=0.03$ mm	(min) $-7.3\sim+5.4\%$	(min) $-17.8\sim+17.1\%$
		(max) $-28.3\sim+27.9\%$	(max) $-34.5\sim+34.1\%$
	0.1 mm	(min) $-5.9\sim+3.2\%$	(min) $-7.8\sim+5.9\%$
		(max) $-22.2\sim+21.9\%$	(max) $-19.5\sim+18.8\%$
Jet subcooling, $P_{\Delta Tsub}$		±0.27 K at $P=0.1$ MPa	
Jet velocity, P_u		±0.06 m/s at $u=35$ m/s	
		Uncertainty	
		$L=5$ mm	$L=10$ mm
Critical heat flux, U_q/q	$\delta_h=0.03$ mm	(min) $-9.9\sim+6.1\%$	(min) $-18.9\sim+17.3\%$
		(max) $-29.1\sim+28.1\%$	(max) $-35.1\sim+34.2\%$
	0.1 mm	(min) $-9.3\sim+4.3\%$	(min) $-10.1\sim+6.3\%$
		(max) $-23.1\sim+21.6\%$	(max) $-20.5\sim+19.0\%$
Jet subcooling, $U_{\Delta Tsub}$		±0.37 K at $P=0.1$ MPa	
Jet velocity, U_u		±1.33 m/s at $u=35$ m/s	

Fig. 8 Effect of heater thickness on CHF

Fig. 9 Relationship between CHF and velocity

the root mean square of the bias limits and the total heat loss of the heater, as shown in Fig. 7. The jet velocity was calculated with accuracy of ±3.8% of reading, associated with the measurement of pressure drop in the circular nozzle, and the standard error estimation of the flow calibration curve. The subcooling of the jet was calculated from the system pressure and jet temperature. The system pressure was measured with a pressure gauge with accuracy of ±0.5% of the fu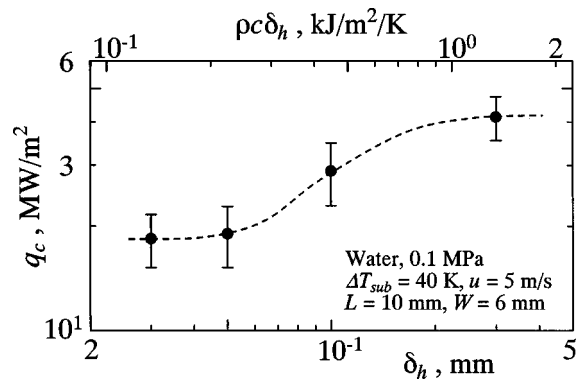ll scale, resulting in an error in saturation temperature of within ±0.2 K. The jet temperature was measured with an accuracy of ±0.15 K. To decide the precision limit, the standard deviations of jet velocity and jet subcooling were evaluated from more than 30 sampled data, and the precision limit of the CHF was calculated using repeatedly measured data at each experimental condition, incorporating the error of −5% associated with the determination of the CHF. The uncertainties were finally calculated from the root mean square of the bias and precision limits.

3 Results and Discussion

3.1 Effect of Heater Thickness on CHF.
The CHF taken in a steady state is independent of the thermal properties and thickness of the heater, as expressed in Eqs. (2)–(4). However, it is well known that a temporary dry patch appears repeatedly on a surface, reflected momentarily by a high heat flux near the CHF. The increase in the local wall temperature under the dry patch is greater at lower heater thickness or heat capacity. Therefore, the CHF may be triggered at lower heat flux than the steady-state CHF. Houchin et al. [12] and Tachibana et al. [13] reported the effect of heater thickness in pool boiling and showed that the effect of wall thickness disappears when the heat capacity per unit area $\rho c \delta_h$ becomes larger than 1 kJ/m²/K. In this study, a very thin direct heated surface was used to achieve the ultra high heat flux under investigation with limited power supply. As such, the effect of wall thickness on the CHF should be examined carefully.

Figure 8 shows the relationship between the CHF and the wall thickness for subcooling of 40 K, a jet velocity of 5 m/s, heater width of 6 mm, heater length of 10 mm, and system pressure 0.1 MPa. The upper abscissa scale of $\rho c \delta_h$ is given for nickel, and the dashed line denotes the tendency of the CHF for reference. The range bars denote the uncertainty ranges of the CHF. The CHF decreases by about 50% as the heater thickness is reduced from 0.3 to 0.03 mm, and seems to approach about 40 MW/m² asymptotically for $\delta_h > 0.2$ mm or the corresponding heat capacity $\rho c \delta_h > 0.8$ kJ/m²/K. It is noted that the CHF for $\delta_h = 0.1$ mm, at which most of the CHF data was measured, is at most 25% lower than that for 0.3 mm. As a result, a heater heat capacity of more than 0.8 kJ/m²/K appears to have no effect on the CHF, which is similar to the case for pool boiling. When the CHF data obtained with a very thin direct heated surface is applied to real applications, it is important to pay careful attention to the wall heat
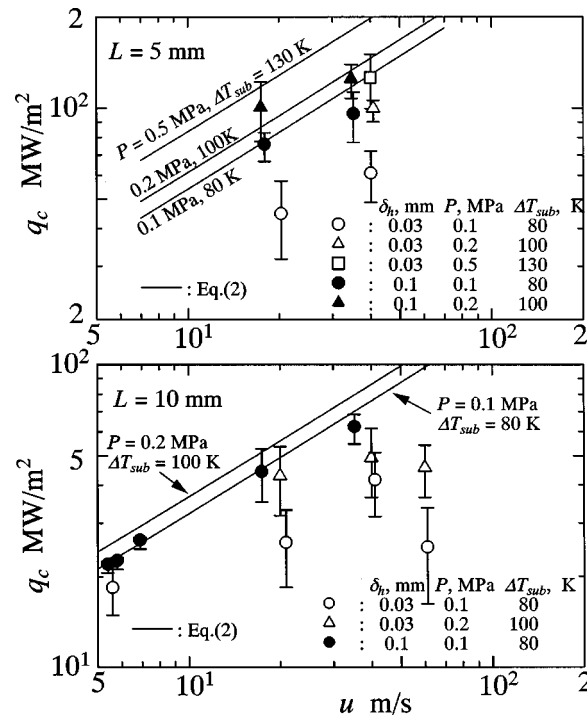
capacity because the wall thickness under heat load in a real apparatus is commonly quite thick so as to be robust under external forces or thermal stress.

Since the effect of thickness was only examined around $q = 40$ MW/m² due to the limit of the power supply, the result shown in Fig. 8 does not necessary hold for higher heat flux of up to 200 MW/m². However, as shown later, the CHF for $\delta_h = 0.1$ mm monotonously increases up to 200 MW/m² with jet velocity or jet subcooling in accordance with Eq. (2). From this, the effect of thickness on the CHF appears not to be strongly dependent on the level of the CHF for the fixed heater thickness of $\delta_h = 0.1$ mm.

3.2 Effect of Jet Velocity on CHF.
Figure 9 correlates the CHF data with velocity for heater lengths L of 5 and 10 mm, heater thicknesses δ_h of 0.03 and 0.1 mm, and degree of subcooling ΔT_{sub} of 80–130 K. The symbols and bars show the averaged CHF and the uncertainty range. The solid lines denote the CHF predicted by Eq. (2) for each system pressure and jet subcooling condition.

The CHF increases with jet velocity for each L, δ_h, and ΔT_{sub}. In particular, the CHF for $\delta_h = 0.1$ mm, denoted by solid symbols, agrees well with Eq. (2). Figure 9 indicates that the general correlation Eq. (2) holds for L up to 5 mm (corresponding to $D/d > 5.39$) at $\delta_h = 0.1$ mm. On the other hand, the CHF data for $\delta_h = 0.03$ mm (open symbols) is up to 40% lower than that for $\delta_h = 0.1$ mm. The uncertainty range for $\delta_h = 0.03$ mm is also much larger due to the larger precision limit of the CHF data. The relationship between CHF and jet velocity for $\delta_h = 0.1$ mm also tends to deviate from that described by Eq. (2), particularly at jet velocities over 40 m/s.

Error in the flatness of the heater surface or an inherent characteristic of the very thin heated surface is expected to be responsible for the larger uncertainty at $\delta_h = 0.03$ mm. Although the heated surface was made as flat as possible, a very small distortion of the surface was unavoidable, particularly for a very thin heater, which may generate a disturbance of the liquid film flow and hence affect the CHF. However, liquid flow on the surface could not be observed in detail due to splashing droplets.
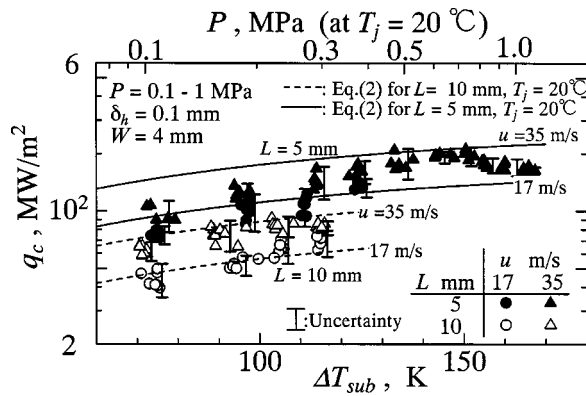
Fig. 10 Relationship between CHF and subcooling of jet

Fig. 11 Relative accuracy of the correlation Eq. (2)

3.3 Effect of Jet Subcooling on CHF. Figure 10 shows the effect of subcooling on the CHF at a jet velocity u of 17 and 35 m/s, heater length L of 5 and 10 mm, and fixed heater thickness δ_h of 0.1 mm. Bars denote the uncertainty range. Since the system pressure increased with subcooling, the corresponding system pressure for a jet temperature of 20°C is shown in the upper abscissa. The solid and dashed lines denote the CHF predicted by Eq. (2) for $L = 5$ and 10 mm, respectively.

The CHF increased with subcooling, and the trend for $L = 10$ mm is very close to that given by Eq. (2). In the case of $L = 5$ mm, Eq. (2) overestimates the CHF by up to 20%, and the deviation of the measured data from the prediction increases at lower and higher subcooling. Additionally, the change in CHF differs slightly from that described by Eq. (2), deviating most at $\Delta T_{sub} > 140$ K. However, there were no experimental observations such as change in boiling flow on the heated surface to explain this deviation. The maximum CHF of 211.9 MW/m^2 was recorded under the condition of $L = 5$ mm, $u = 35$ m/s, $\Delta T_{sub} = 151$ K, and $P = 0.7$ MPa. Comparing the flow condition of Mudawar's study [4] with that of the present study at a given level of CHF, this result shows that external flow boiling with an impinging jet can occur without extreme mass flux, liquid subcooling or system pressure.

The effects of subcooling and pressure on the CHF can both be seen in Fig. 10, because these two parameters vary jointly. As shown in the correlation of Eq. (2), the system pressure has no direct effect on the CHF, instead affecting it indirectly through the effects on saturation temperature and thermal properties such as latent heat and density ratio. For instance, Eq. (2) shows that the CHF increases by up to 3% when the system pressure increases from 0.1 to 1.0 MPa for fixed subcooling of $\Delta T_{sub} = 80$ K. Indeed, an increase in pressure experimentally enhances the CHF by a few
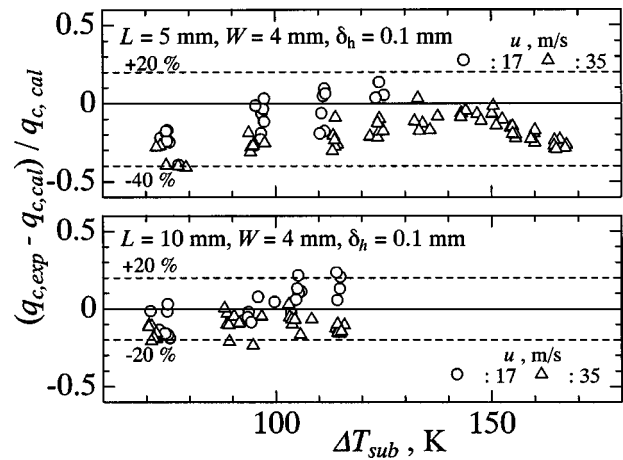
percent, but the increase appears to be largely due to the contribution of subcooling in the present narrow range of system pressure (corresponding reduced pressure is $4.5 \times 10^{-3} - 4.5 \times 10^{-2}$).

3.4 Effect of Nitrogen Gas on CHF. The effects of dissolution of the non-condensable nitrogen gas pressurizing the system into the liquid jet should also be discussed. Haramura [14] studied the effect of dissolved non-condensable gas such as air on the CHF and the behavior of bubbles and during pool boiling on a horizontal wire, and reported that the CHF for gas-saturated water is 25–30% lower than that for degassed water. The effect of dissolved gas on the CHF was explained as due to the accumulation of non-condensable gas into bubbles that stay on the water surface around the heated wire and re-dissolve into the surrounding liquid by mass diffusion.

As far as the authors know, there are no reports showing the definite effects of dissolved gas for external flow boiling. The existence of dissolved gas indeed activates nucleation at the inception of boiling, but this effect is not important in the high heat flux range near the CHF. Even though the concentration of dissolved nitrogen may become close to gas-saturation due to the long period of liquid-gas contact in the system loop, the effect of dissolved gas on CHF is considered to be unimportant in the present case, in contrast to subcooled pool boiling, because the high-speed liquid flow sweeps off the evacuated dissolved gas together with vapor, making it unlikely that non-condensible gas will accumulate in the vicinity of the heated surface. The good
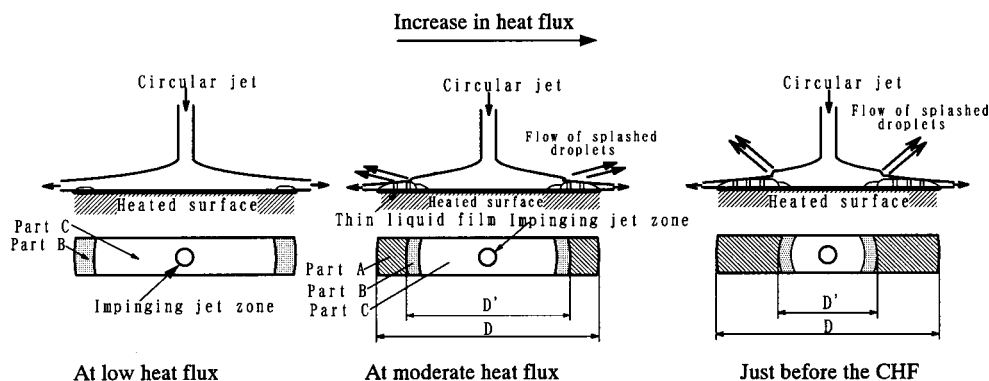
Fig. 12 Flow model in deriving the general correlation of CHF (Eq. (2)) (A: Saturated boiling region, B: subcooled boiling region, C: Single-phase flow region)
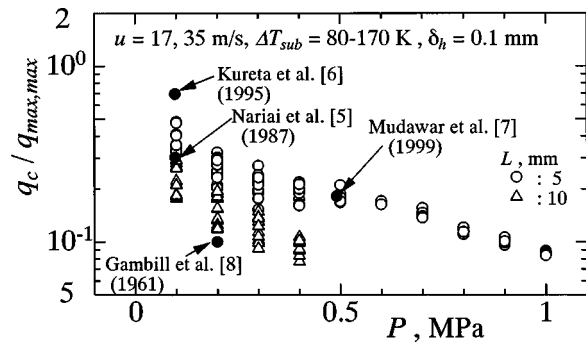
Fig. 13 Relationship between dimensionless CHF and system pressure

agreement between most of the CHF data and the extrapolation of Eq. (2) where a dissolved gas effect is not considered may support this fact.

3.5 Estimation Error for CHF Correlation. The relative estimation error for Eq. (2) at $\delta_h = 0.1$ mm is shown in Fig. 11. The relative error for $L = 5$ mm ranges from -40% to $+20\%$, while that for $L = 10$ mm is within $\pm 20\%$, equivalent to the estimation error of Eq. (2) in Ref. [9]. Thus, Eq. (2) is considered to be applicable for $D/d > 5.39$ ($L = 10$ mm), $u < 35$ m/s, $\Delta T_{sub} < 120$ K.

One of the possible reasons for the larger estimation error for $L = 5$ mm may be the assumptions in the flow model from which Eq. (2) derived, which may not be applicable for such a small heater. Figure 12 shows the flow model on the heated surface for different heat fluxes [9]. The heated surface is divided into three regions; A) saturated boiling region, B) subcooled boiling region, and C) single-phase flow region. Although Ref. [9] provides the details of derivation, Eq. (2) was essentially derived from the general correlation of saturation boiling given in Eq. (3). Here, the boiling length $D-d$ in Eq. (3) was evaluated with $D-D'$ for subcooled boiling, as shown in Fig. 12. To obtain the correlation of subcooled CHF explicitly by eliminating the unknown diameter of the subcooled boiling region D', a higher-order term of D'/D was neglected. This assumption may not be valid for $L = 5$ mm, resulting in the higher estimation error compared to $L = 10$ mm.

3.6 Comparison of CHF With the Maximum Heat Flux. The ratio of the measured CHF to $q_{max,max}$ represents one of the indices for evaluating the extent to which the CHF can be made approach to ultimate maximum heat flux. Figure 13 shows the ratio $q_c/q_{max,max}$ against system pressure. The solid symbols denote the data obtained by other researchers [4–7] for reference. As $q_{max,max}$ increases sharply with system pressure whereas the CHF does not, $q_c/q_{max,max}$ decreases monotonically with increasing system pressure. For the present results, $q_c/q_{max,max}$ reaches 48% at $u = 35$ m/s, $\Delta T_{sub} = 73$ K, $D/d = 3.2$, and $P = 0.1$ MPa.

4 Conclusions

High critical heat flux was measured with a highly subcooled impinging jet on a rectangular heated surface for a heated wall thickness of 0.03–0.3 mm, nozzle diameter of 2 mm, heated surface length of 5 and 10 mm, jet velocity of 5–60 m/s, jet subcooling of 80–170 K, and system pressure of 0.1–1.0 MPa.

The experimental results are summarized in the following conclusions.

1. The CHF around 40 MW/m^2 was found to decrease by about 50% as the thickness of the nickel foil heater was decreased from 0.3 to 0.03 mm. The effect of the wall thickness on the CHF disappeared when the heat capacity of unit area of the heated surface was larger than 0.8 kJ/m^2/K, which corresponds to a wall thickness of 0.2 mm for nickel.

2. The CHF for a heated wall thickness of 0.1 mm increased with increasing jet velocity and decreasing heater length in most cases, whereas no clear trend could be seen for a heated wall thickness of 0.03 mm due to the large data scattering.

3. The effect of jet velocity and subcooling on the CHF for a heated wall thickness of 0.1 mm correlates well with the general equation Eq. (2) for CHF under the condition: $D/d = 5.39$, $\Delta T_{sub} = 80-120$ K, $u < 40$ m/s. However, the characteristic of subcooling differs somewhat at $D/d = 3.20$, $\Delta T_{sub} > 140$ K.

4. The maximum CHF of 211.9 MW/m^2 was recorded at $L = 5$ mm, $W = 4$ mm, $d = 2$ mm, $P = 0.7$ MPa, $\Delta T_{sub} = 151$ K, and $u = 35$ m/s.

5. The CHF represents 48% of the theoretical maximum heat flux at the atmospheric pressure, $L = 5$ mm, $\Delta T_{sub} = 73$ K, and $u = 35$ m/s.

Acknowledgments

Nomenclature

c = specific heat of heated surface
c_p = specific heat of liquid at constant pressure
D = characteristic diameter of heated surface $(= (L^2 + W^2)^{1/2})$
d = diameter of liquid jet
I = electric current
J_a = Jacob number $(= (\rho_l/\rho_g)(c_p \Delta T_{sub}/h_{lg}))$
h_{lg} = latent heat of evaporation
L = length of rectangular heated surface
M = mass of molecular
q_c = subcooled critical heat flux
q_{co} = saturated critical heat flux
$q_{max,max}$ = maximum heat flux (Eq. (1))
P = system pressure
R = universal gas constant
T = temperature
T_{sat} = saturation temperature
T_j = temperature of liquid jet
u = velocity of liquid jet
V = voltage added to heated surface
x_c = length of colder surface area adjacent to a electrode
W = width of rectangular heated surface

Greek Letters

ΔT_{sub} = degree of subcooling of jet
δ_h = thickness of heated surface
ρ_g, ρ_l = densities of saturated vapor and liquid
ρ = density of heated surface
σ = surface tension

References

[1] Gambill, W. R., and Lienhard, J. H., 1989, "An Upper Bound for the Critical Boiling Heat Flux," ASME J. Heat Transfer, **111**(3), pp. 815–818.
[2] Bird, R. B., Stewart, W. E., and Lightfoot, E. N., 2002, *Transport Phenomena*, John Wiley & Sons, Inc., New York, pp. 39.
[3] Haramura, Y., 1989, "Characteristics of pool boiling heat transfer in the vicinity of the critical heat flux (relations between bubble motion and heat flux fluctuations)," Heat Transfer-Jpn. Res., **18**(3), pp. 18–31.
[4] Haramura, Y., and Katto, Y., 1983, "A new hydrodynamic model of critical heat flux, applicable widely to both pool and forced convection boiling on submerged bodies in saturated liquids," Int. J. Heat Mass Transfer, **26**(3), pp. 389–399.
[5] Nariai, H., Shimura, T., and Inasaka, F., 1987, "Critical heat flux of subcooled flow boiling in narrow tube," *ASME-JSME Thermal Engineering Joint Conference*, **5**, pp. 455–462.
[6] Kureta, M., Mishima, K., and Nishihara, H., 1995, "Critical heat flux for flow

boiling of water in small diameter tubes,'' ASME/JSME Thermal Engineering Joint Conference.

[7] Mudawar, I., and Bowers, M. B., 1999, ''Ultra-high critical heat flux (CHF) for subcooled water flow boiling, I: CHF data and parametric effects for small diameter tubes,'' Int. J. Heat Mass Transfer, **42**, pp. 1405–1428.

[8] Gambill, W. R., Bundy, R. D., and Wansbrough, R. W., 1961, ''Heat transfer, Burnout, and Pressure drop for Water in Swirl flow through tubes with internal twisted tapes,'' Chem. Eng. Prog., Symp. Ser., **57**(32), pp. 127–137.

[9] Monde, M., Kitajima, K., Inoue, T., and Mitsutake, Y., 1994, ''Critical Heat Flux in a Forced Convective Subcooled Boiling with an Impinging Jet,'' Heat Transfer, **7**, pp. 515–520.

[10] Inoue, A., Tanno, T., Takahashi, M., and Yamasaki, Y., 1995, ''Two-dimensional impinging jet cooling of high heat flux surfaces in magnetic con-finement fusion reactors,'' Fusion Eng. Des., **28**(1), pp. 81–89.

[11] Monde, M., and Mitsutake, Y., 1996, ''Critical heat flux in forced convective subcooled boiling with multiple impinging jets,'' ASME J. Heat Transfer, **118**(1), pp. 241–243.

[12] Houchin, W. R., and Lienhard, J. H., 1966, ''Boiling Burnout in Low Thermal Capacity Heater,'' *Proceedings of ASME Winter Annual Meeting 1966* (Heat Transfer Division), ASME, New York, pp. 1–8.

[13] Tachibana, F., Akiyama, M., and Kawamura, H., 1967, ''Non-Hydrodynamic Aspects of Pool Boiling Burnout,'' J. Nucl. Sci. Technol., **4**, pp. 121–130.

[14] Haramura, Y., 2003, ''Non-Condensible Gas Effect on Critical Heat Flux of Subcooled Pool Boiling of Water,'' *Proceedings of the 6th ASME-JSME Thermal Engineering Joint Conference*, pp. 278.

Round Turbulent Thermals, Puffs, Starting Plumes and Starting Jets in Uniform Crossflow

F. J. Diez

L. P. Bernal

G. M. Faeth
e-mail: gmfaeth@umich.edu

Department of Aerospace Engineering,
The University of Michigan,
Ann Arbor, MI 48109-2140

The self-preserving properties of round turbulent thermals, puffs, starting plumes and starting jets, in unstratified and uniform crossflow, were investigated experimentally. The experiments involved dye-containing fresh water (for nonbuoyant flows) and salt water (for buoyant flows) sources injected vertically downward into crossflowing fresh water within a water channel. Time-resolved video images of the flows were obtained using CCD cameras. Experimental conditions were as follows: source exit diameters of 3.2 and 6.4 mm, source Reynolds numbers of 2,500–16,000, source/ambient velocity ratios of 4–35, source/ambient density ratios (for buoyant flows) of 1.073 and 1.150, volumes of injected source fluid (for thermals and puffs) comprising 16–318 source diameters, streamwise (vertical) penetration distances of 0–200 source diameters and 0–13 Morton length scales (for buoyant flows) and crosstream (horizontal) penetration distances of 0–620 source diameters. Near-source behavior varied significantly with source properties and distance from the source but the flows generally became turbulent for streamwise distances within 5 source diameters from the source and became self-preserving for streamwise distances from the source greater than 40–50 source diameters. Crosstream motion satisfied the no-slip convection approximation. Streamwise motion for self-preserving conditions satisfied the behavior of corresponding self-preserving flows in still fluids: round thermals and puffs in still fluids for round thermals and puffs in crossflow and two-dimensional line thermals and puffs in still fluids for round starting plumes and jets in crossflow. The no-slip convection approximation for crossflow motion combined with self-preserving approximations for streamwise motion were also effective for predicting flow trajectories at self-preserving conditions for steady round turbulent plumes and jets in crossflow. [DOI: 10.1115/1.1622720]

Keywords: Heat Transfer, Jets, Plumes, Scaling, Thermal, Turbulence

Introduction

Recent theoretical and experimental studies of the temporal development of round turbulent thermals, puffs, starting plumes and starting jets in still fluids [1–3] were extended to consider the corresponding flows in unstratified uniform crossflow. Study of these flows is motivated by practical applications to the unconfined and unsteady turbulent flows resulting from the initiation of either interrupted or steady gas and liquid releases caused by process upsets, explosions and unwanted fires, among others. Due to their simplicity, these flows also are of interest as classical fundamental flows that illustrate the development of unsteady turbulent flows in a relatively simple way. As a result, observations of these flows are useful in order to provide data needed to evaluate methods of predicting their properties. Similar to past work [1–3], the present experiments emphasized conditions far from the source where effects of source disturbances are lost, and flow structure is largely controlled by its conserved properties. For such conditions, the flows approximate self-preserving turbulent behavior fixed by their conserved properties, and appropriately scaled flow properties are independent of streamwise distances. The particular advantages of self-preserving turbulent flows are that their flow properties considerably simplify both the presentation of measurements and execution of numerical simulations, because source disturbances do not affect flow properties which scale in a relatively compact manner as a result. Finally, extension of past work

in still fluids [1–3] to crossflow is desirable because most practical thermals, puffs, starting plumes and starting jets are exposed to crossflow.

Several reviews of past studies of round turbulent unconfined nonbuoyant and buoyant flows have appeared in the literature, see Turner [4,5], Tennekes and Lumley [6], Hinze [7], Chen and Rodi [8], List [9], Dai et al. [10], and references cited therein. As a result, the present discussion of the literature will be brief.

Past studies of the penetration properties of flows of interest during the present investigation—round turbulent thermals, puffs, starting plumes and starting jets—have emphasized the temporal properties of the flows in still environments. Some examples include: Diez et al. [3], Turner [4,5,13], Morton [11], Scorer [12], Fay and Lewis [14], Batt et al. [15] and Thompson et al. [16] for thermals; Sangras et al. [1,2], Richards [17] and Kovasznay et al. [18] for puffs; Diez et al. [3], Turner [4,5,19], Middleton [20], Delichatsios [21] and Pantzlaff and Lueptow [22] for starting plumes; and Witze [23], Johari and Paduano [24], Kato et al. [25], Kouros et al. [26], Adriani et al. [27] and Hill and Ouelette [28] for starting jets. These studies mainly sought the self-preserving scaling rules that describe the temporal penetration properties of the flows in still fluids, e.g., the maximum vertical and radial penetration distances of these flows into their surroundings as functions of time.

Measurements in this laboratory seeking to evaluate the self-preserving relationships for flows in still fluids were carried out considering round salt water jets in a still fresh water bath for thermals and starting plumes [3] and fresh water jets in a still fresh water bath for puffs and starting jets [1,2]. It was observed that the flows became turbulent within 5 source diameters in the

streamwise direction from the source and became self-preserving when streamwise penetration was greater than 20–30 source diameters from the source.

Most practical flows associated with buoyant and nonbuoyant sources are exposed to crossflow; therefore, there have been a number of studies seeking to extend the results just discussed for still fluids to the corresponding round turbulent buoyant sources in crossflow, e.g., Anwar [29], Lutti and Brzustowski [30], Andreopoulos [31], Alton et al. [32], Hasselbrink and Mungal [33], Baum et al. [34], and references cited therein, and to the corresponding round turbulent nonbuoyant sources in crossflow, e.g., Keffer and Baines [35], Kamotani and Greber [36], Chaissaing et al. [37], Kelso et al. [38], Smith and Mungal [39], and references cited therein. In spite of the importance of these flows in crossflow, however, measurements of their properties are limited and little is known about their self-preserving properties or about the conditions required for them to become self-preserving.

Motivated by the previous discussion, the objectives of the present investigation were to extend past work concerning the self-preserving properties of round turbulent thermals, puffs, starting jets and starting plumes in uniform and still fluids, in order to develop improved understanding of these flows in unstratified uniform crossflow, as follows:

1. Measure the streamwise (vertical), crosstream (horizontal) and radial penetration properties of the flows as a function of time for various source conditions typical of practical applications.
2. Formulate the self-preserving scaling relationships for the flows and exploit the new measurements of these flows to evaluate the effectiveness of their scaling relationships and to determine the empirical parameters within them.

Theoretical and experimental methods were similar to earlier studies of the present flows in still and uniform environments reported by Sangras et al. [1] and Diez et al. [2,3].

The present description of the research begins with a discussion of experimental methods. This is followed by scaling considerations for the present flows in both still and crossflowing environments. Experimental and scaling results are then considered, treating thermals, puffs, starting plumes and starting jets, all in uniform crossflow, in turn.

Experimental Methods

Test Apparatus. The experiments involved fresh and salt water sources injected into an unstratified and uniform fresh water crossflow produced by a water channel facility. The test section of the water channel had cross-section dimensions of 610×610 mm and a length of 2440 mm. The sides and bottom of the test section were constructed of 20 mm thick acrylic panels to provide optical access. Fresh water flow in the channel was driven by a propeller pump with variable test section velocities of 40–300 mm/s. The flow properties of the water channel were characterized using a hot film anemometer to calibrate the crossflow velocity as a function of propeller speed and to measure the uniformity and the turbulence levels of the crossflow. The contraction, flow straightener, screens, etc., of the water channel combined to yield a flow nonuniformity less than 1.5 percent, and turbulence intensity levels less than 1 percent in the test section.

The source flows were injected vertically downward into the fresh water channel flow through smooth round tubes having inside diameters of 3.2 and 6.4 mm. Injector passages had length/diameter ratios of 100 and 50, respectively, to help insure fully developed turbulent pipe flow at the source exit for sufficiently large injector Reynolds numbers [40]. The tubes were mounted vertically and discharged roughly 5 mm below the liquid surface. The tubes passed through a plane horizontal plexiglass plate (508 $\times$914 mm plan dimensions$\times$12 mm thick) having a tight fit. The tube (source) exits were mounted flush with the lower surface of the plexiglass plate to provide well-defined entrainment condi-

tions near the source exit. The source liquid was supplied to the tubes using either syringe pumps (Harvard Apparatus, PHD2000, Model 70-2000, with four 150 cc syringes having volumetric accuracies of ± 1 percent mounted in parallel), for small flow rates or a peristaltic pump (Masterflux L/S Digi-Staltic Disperser, Model 72310-0) for large flow rates. The pumps were computer controlled to start, stop and deliver liquid at preselected times and rates. The pumps were calibrated by collecting liquid for timed intervals. Pump delivery rates were essentially constant with the short transient flow development periods that were encountered during starting and stopping the pumps handled by extrapolating the constant delivery portion to the zero flow rate condition and finding an equivalent origin, t_d, for either start or stop times. A plot illustrating the pump flow rate transients when the syringe pumps were started and stopped appears in Sangras et al. [1]; the behavior of the peristaltic pump was similar.

The salt water source liquids were prepared by adding appropriate weights of salt (certified ACS crystal sodium chloride, 100.2 percent assay) to given volumes (weights) of water based on the tabulation of liquid densities as a function of salt concentration due to Lange [41]. These results were verified using precision hygrometers (Fisher Scientific, Cat. No. 11-583D having 0.2 percent accuracies). The absolute viscosities of the test liquids were measured directly using a Cannon/Fenske viscometer; this information was combined with the known densities to obtain kinematic viscosities for each source liquid considered during the present investigation. Red vegetable dye was added to the source liquids in order to facilitate flow visualization at a concentration of 0.15 percent dye by volume.

Instrumentation. Measurements of flow penetration properties as a function of time were obtained from video records. The water channel test section was illuminated for these observations using two 650W quartz lamps (Color-Tran quartz king dual 650, Model 116-011) and two 2000W quartz lamps (Mole-Richardson Type 2591 molequartz, 2k Baby "zip" softlite). The appearance of the dye-containing injected source liquid was recorded as a function of time using two 3CCD digital video camcorders (Canon Model XL1s) having 720×480 pixel arrays. Video records were obtained from side (frontal) views as well as bottom (plan) views of the flows.

The video records were analyzed to provide flow penetration properties, as follows: maximum mean streamwise (vertical), x_p, and crosstream (horizontal), y_p, penetration distances (taken as averages of the largest streamwise and crosstream distances of the injected source liquid from the jet exit) and the maximum mean radial (normal to the flow axis in a vertical plane), r_p, and maximum mean half-width (normal to the flow axis in a horizontal plane), w_p, all as a function of time from the start of injection. In addition, vertical, crosstream, radial and half-width penetration distances were measured as a function of crosstream distance from the source exit after steady conditions had been reached at given locations for the starting jets and plumes. All these mean parameters were obtained by averaging the results of three separate tests at a particular test condition; this yielded acceptable experimental uncertainties because each test condition provided numerous data points and rather dense plots of the data as will be seen in the following. Experimental uncertainties (95 percent confidence) of the measurements from the video records were as follows: less than 7 percent for times from the start of injection, less than 8 percent for mean maximum streamwise and crosstream penetration distances, and less than 15 percent for mean maximum radial and half-width penetration distances. Experimental uncertainties of all the penetration distances were largely governed by sampling errors due to the irregular turbulent boundaries of the present turbulent flows but also include fundamental accuracies of distance and time calibrations and measurements.

The virtual origins of each of the present flows were found by plotting $((t-t_o)/t^*)^n$ as a function of x_p/d for every test condition. A linear fit of the far-field data was then developed for each

Table 1 Summary of test conditions for round turbulent thermals, puffs, and starting plumes and jets, in unstratified uniform crossflow[a]

Flow	Nonbuoyant	Buoyant
Source fluid	Water	Salt water
Ambient fluid	Water	Water
Source fluid density, ρ_o (kg/m^3)	998	1070 & 1150
Ambient fluid density, ρ_∞ (kg/m^3)	998	998
Source fluid kinematic viscosity, ν_o (mm^2/s)	1.0	1.11 & 1.36
Source diameter, d (mm)	3.2 & 6.4	3.2 & 6.4
Source passage length, L/d	100 & 50	100 & 50
Source Reynolds number, $u_o d/\nu_o$	3,000–16,000	2,500–11,000
Source/ambient fluid density ratio, ρ_o/ρ_∞	1.00	1.073 & 1.150
Source/ambient fluid velocity ratio, u_o/v_∞	7–27	4–35
Source Morton length scale, ℓ_{Mp} or ℓ_{Mt}/d	∞	5–88
Source fluid discharged, $Q_o/(A_o d)$ or L_Q/d	16–318 (puffs)	18–318 (thermals)
Vertical penetration distance, $(x_p - x_o)/d$	0–160	0–200
Vertical penetration distance, $(x_p - x_o)/(\ell_{Mp}$ or $\ell_{Mt})$	0	0–13
Horizontal penetration distance, $(y_p - y_o)/d$	0–500	0–620

[a]Fresh (for nonbuoyant flows) and salt water (for buoyant flows) jets injected vertically downward from round tubes into uniform fresh water crossflows having a 610×610 mm crossection at an ambient pressure and temperature of 99.0±0.5 kPa and 297.0±0.5 K.

test condition so that solution of this fit at time $(t-t_d)=0$ determined the virtual origin, x_o/d. The values of x_o/d were relatively constant for each flow, see Diez et al. [2,3] for examples of this behavior for puffs and thermals in still fluids. As a result, a mean value of x_o/d could be found for each flow (along with its experimental uncertainty) as will be discussed later.

Test Conditions. Test conditions for the present measurements of round turbulent thermals, puffs and starting plumes and jets, in uniform crossflow are summarized in Table 1. The overall test conditions involved fresh water and salt water (for the buoyant flows) source flows in crossflowing fresh water, source diameters of 3.2 and 6.4 mm, source passage length/diameter ratios of 100 and 50, respectively, source/ambient density ratios of 1.073 and 1.150 (for the buoyant flows), source Reynolds numbers of 2,500–16,000, source/ambient velocity ratios of 4–35, volumes of source fluid discharged, $Q_o/(A_o d)$, of 16–318 (for the thermals and puffs), streamwise (vertical) penetration distances of 0–200 source diameters and 0–13 Morton length scales (the last for buoyant flows), and crosstream (horizontal) penetration distances of 0–620 source diameters. For the starting plume measurements in crossflow, it should be noted that source flows generally were over-accelerated flows, as defined by George et al. [42].

Scaling Considerations

Conditions for Self-Preservation. A parameter frequently used to estimate when round turbulent unconfined flows become self-preserving is the distance from the effective (virtual) origin of the flow normalized by the source diameter, $(x-x_o)/d$, (taken to be the streamwise (vertical) distance for purposes of this example) This parameter is a measure of conditions where distributions of flow properties appropriate for the often confined conditions of a source, have adjusted to reach distributions appropriate for an unconfined flow. The value of $(x-x_o)/d$ needed for self-preserving behavior depends on the nature of the flow, the properties of the source, and the property for which self-preserving behavior is sought. For example, results for steady round turbulent nonbuoyant jets suggest that values of $(x-x_o)/d$ greater than roughly 40 and 100 are required to obtain self-preserving behavior for distributions of mean and fluctuating (turbulent) properties, respectively [6]. In contrast, similar results for steady round turbulent buoyant plumes suggest that values of $(x-x_o)/d$ greater than roughly 90 are required to obtain self-preserving behavior for distributions of both mean and fluctuating (turbulent) properties [10]. Taken together, these results indicate effects of both the

property being observed and the nature of the flow on the conditions required to obtain self-preserving flow behavior.

Buoyant turbulent flows have more requirements for obtaining self-preserving flow than nonbuoyant turbulent flows. In this case, a second parameter that must be satisfied when steady buoyant turbulent plumes become self-preserving is that the streamwise (vertical) distance from the virtual origin normalized by the Morton length scale, $(x-x_o)/\ell_M$, must exceed a critical value as a measure of conditions where the momentum of the flow caused by effects of buoyancy is much larger than the original momentum of the flow at its source. For steady buoyant sources, e.g., starting or steady plumes, the Morton length scale is defined as follows [9,11]:

$$\ell_{Mp} = \dot{M}_o^{3/4}/\dot{B}_o^{1/2} \tag{1}$$

For steady round plumes having uniform properties defined at the source (similar to the flows of interest during the present investigation), the source specific momentum flux, $\dot{M}_o$, and the source specific buoyancy flux, $\dot{B}_o$, appearing in Eq. (1) can be computed as follows [9,10]:

$$\dot{M}_o = \dot{Q}_o u_o \tag{2}$$

$$\dot{B}_o = \dot{Q}_o g |\rho_o - \rho_\infty|/\rho_\infty \tag{3}$$

where an absolute value has been used for the density difference in Eq. (3) in order to account for both rising plumes having positive buoyancy and falling plumes having negative buoyancy. Substituting Eqs. (2) and (3) into Eq. (1) then yields the following expression for the Morton length scale of steady round turbulent buoyant plumes having uniform source properties:

$$\ell_{Mp}/d = ((\dot{Q}_o u_o^3/d^4)(g|\rho_o - \rho_\infty|/\rho_\infty)^2)^{1/4} \tag{4}$$

Then, since the volume flow rate of a uniform source flow can be represented as follows:

$$\dot{Q}_o = \pi d^2 u_o/4 \tag{5}$$

Eq. (4) can be written as follows:

$$\ell_{Mp}/d = (\pi/4)^{1/4}(\rho_\infty u_o^2/(g d|\rho_o - \rho_\infty|))^{1/2} \tag{6}$$

The corresponding formulation for the requirements of source momentum to become small compared to the momentum of flow due to effects of buoyancy for an interrupted source, e.g., a thermal, can be found in the same manner as the derivation of Eqs.

(1)–(6) for plumes. For a buoyant source involving a fixed quantity of fluid, Q_o, such as a thermal, the Morton length scale becomes:

$$\ell_{Mt} = M_o^{1/2}/B_o^{1/4} \qquad (7)$$

For round thermals having uniform properties defined at the source (similar to the flows of interest during the present investigation), the source specific momentum force, M_o, and the source specific buoyancy force, B_o, appearing in Eq. (7) can be computed as follows:

$$M_o = Q_o u_o \qquad (8)$$

$$B_o = Q_o g |\rho_o - \rho_\infty|/\rho_\infty \qquad (9)$$

where an absolute value has been used for the density difference in Eq. (9), as before, in order to account for both rising thermals having positive buoyancy and falling thermals having negative buoyancy. Substituting Eqs. (8) and (9) into Eq. (7) then yields an expression for the Morton length scale of a round turbulent buoyant thermal having uniform source properties, as follows:

$$\ell_{Mt}/d = ((Q_o/d^3)(\rho_\infty u_o^2/(gd|\rho_o - \rho_\infty|)))^{1/4} \qquad (10)$$

Then, since a uniform volume of source fluid can be represented as follows:

$$Q_o = \pi d^2 L_Q/4 \qquad (11)$$

Eq. (10) can also be written as follows:

$$\ell_{Mt}/d = ((\pi/4)(L_Q/d)(\rho_\infty u_o^2/(gd|\rho_o - \rho_\infty|)))^{1/4} \qquad (12)$$

Finally, a third criterion must be satisfied when self-preserving conditions are reached for buoyant turbulent flows; namely, that the flow should be ''weakly buoyant'' so that the density of the thermal or plume fluid is linearly related to the degree of mixing of the ambient and source fluid [10]. At self-preserving conditions in buoyant turbulent flows, all scalar properties are far removed from the complexities of practical sources of buoyancy, such as fires, and they are conveniently represented by functions of the mixture fraction, f (which corresponds to the mass fraction of source material in a sample), called state relationships [10]. At self-preserving conditions, typically $f \ll 1$ and the state relationship giving density as a function of mixture fraction can be linearized as follows [10]:

$$\rho = \rho_\infty + f\rho_\infty(1 - \rho_\infty/\rho_o), \quad f \ll 1 \qquad (13)$$

Buoyant turbulent flows mix very rapidly compared to other turbulent flows [10]. Therefore, the $f \ll 1$ criterion required for a linear relationship between mixture fraction and density is generally achieved relatively close to the source.

Scaling Relationships. Major assumptions used to find scaling relationships for self-preserving round turbulent thermals, puffs, starting plumes and starting jets, are as follows: physical property variations are small (i.e., buoyant flows are weakly buoyant so that density variations are linear functions of the degree of mixing represented by the mixture fraction), the flows are self-preserving so that effects of source disturbances have been lost, particular properties of each flow (to be specified later) are conserved, the times of source flow for thermals and puffs are assumed to be small compared to the flow times of interest, and source flows associated with starting plumes and jets begin abruptly and maintain steady source flow and property conditions thereafter. Under these assumptions, the temporal variation of the maximum streamwise (vertical) penetration distance can be expressed as follows, see Turner [4,5,19] and Morton [11]:

$$(x_p - x_o)/d = C_x((t - t_d)/t^*)^n \qquad (14)$$

where t_d is a virtual temporal origin used to handle source transients, t^* is a characteristic time that involves a conserved property of the flow, and the values of C_x and n vary depending upon

Table 2 Summary of equations for the self-preserving penetration properties of round turbulent thermals, puffs, starting plumes and starting jets in unstratified still fluids[a]

Conserved Property	n	t*	x*
Thermal: $B_o = Q_o g |\rho_o - \rho_\infty|/\rho_\infty$	1/2	$(d^4/B_o)^{1/2}$	$(B_o^{1/2}(t - t_d))^{1/2}$
Puff: $M_o = Q_o u_o$	1/4	d^4/M_o	$(M_o(t - t_d))^{1/4}$
Starting Plume: $\dot{B}_o = \dot{Q}_o g |\rho_o - \rho_\infty|/\rho_\infty$	3/4	$(d^4/\dot{B}_o)^{1/3}$	$(\dot{B}_o^{1/3}(t - t_d))^{3/4}$
Starting Jet: $\dot{M}_o = \dot{Q}_o u_o$	1/2	$(d^2/\dot{M}_o)^{1/2}$	$(\dot{M}_o^{1/2}(t - t_d))^{1/2}$

[a]Common equations: Streamwise penetration (d included): $(x_p - x_o)/d = C_x((t - t_d)/t^*)^n$. Streamwise penetration (d excluded): $(x_p - x_o)/x^* = C_x$. Radial penetration: $r_p/(x_p - x_o) = C_r$.

the particular flow being considered. Far from the source, in the self-preserving region of the flow, the source diameter is no longer relevant and can be eliminated from Eq. (14) to obtain the following expression for the streamwise (vertical) penetration distance:

$$(x_p - x_o)/x^* = C_x \qquad (15)$$

where x^* is a characteristic streamwise distance that involves a conserved property of the flow. Finally, within the self-preserving region, the radial penetration of the flows can be expressed as follows:

$$r_p/(x_p - x_o) = C_r \qquad (16)$$

where the value of C_r varies depending upon the particular flow being considered. Expressions for n, t^*, and x^* in Eqs. (14)–(16) can be found from the conserved property of each flow: the source specific buoyancy force, B_o, for thermals; the source specific momentum force M_o, for puffs; the source specific buoyancy flux, $\dot{B}_o$, for starting plumes; and the source specific momentum flux, $\dot{M}_o$ for starting jets. Given the conserved property of the flow, scaling considerations yield expressions for n, t^*, and x^* as described in detail by Turner [4,5,19] and Morton [11], among others. Specific expressions of this type for round turbulent thermals, puffs, starting plumes and starting jets, in still, unstratified and uniform fluids (all for uniform or given average source properties) from Sangras et al. [1] and Diez et al. [2,3] are summarized in Table 2 for reference purposes during the present investigation.

Results and Discussion

Overview. Note that the present flows involve either downwardly-injected nonbuoyant puffs and starting jets, or downwardly injected, negatively buoyant thermals and starting plumes. Rather than presenting the flows in this manner, however, they have been inverted in the following to show them as either upwardly injected nonbuoyant puffs and starting jets or upwardly injected, positively buoyant thermals and starting plumes. This was done due to the greater familiarity of most individuals with rising positively-buoyant flows. It should be noted that both rising and falling buoyant flows involve progressive approach of the flow density to the ambient density with increasing distance from the source, however, so that they have correspondingly similar buoyant flow properties.

Thermals. The test conditions for measurements of the properties of thermals in crossflow are summarized in Table 1, a visualization of a typical thermal in crossflow (inverted to appear to be a positively-buoyant flow as just noted) is illustrated in Fig. 1. These images include side and bottom views of a typical thermal, taken at the time when the thermal had reached the largest distance from the source where both the source and the thermal could be observed on one image. The length scale that appears on the images is appropriate for streamwise, radial and crossstream direc-
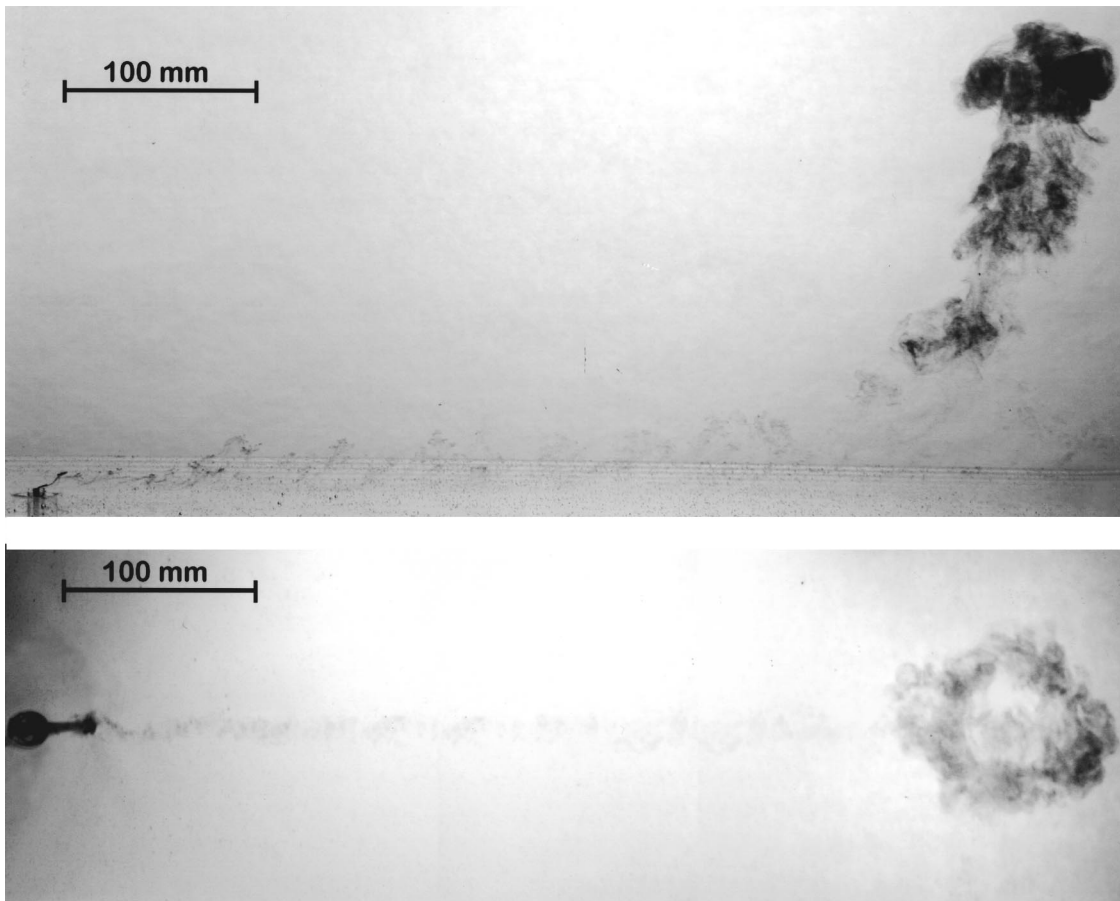
Fig. 1 Visualization of a thermal in crossflow (d=3.2 mm, Re_o=4,000, ρ_o/ρ_∞=1.150, $Q_o/(A_o d)$=223, ℓ_{Mt}/d =19, u_o/v_∞=11 and t=5.6 s)

tions. The thermal consists of a leading bulbous element mainly consisting of a starting circular vortex which is quite clearly seen in the bottom view. Given a sufficient amount of source fluid, the starting vortex is followed by a trailing plume-like region that extends from the bottom of the bulbous element. Progressive growth of the bulbous element suggests that the trailing plume-like region is being engulfed by the leading vortex. This engulfment process is relatively slow, however, and the thermals could not be observed far enough from the source for the trailing plume-like portion to be completely engulfed. In general, the thermals became turbulent within five source diameters from the source in the streamwise (vertical) direction and the dimensions of the thermals progressively increased with increasing distance from the source. The overall impression given by the visualizations of the thermals was that they rose in the streamwise (vertical) direction in the same manner as thermals in still fluids and that they were simply wafted along by the crossflow at the same time. The present self-preserving scaling considerations of the penetration properties of thermals were carried out based on this observation, as discussed next.

The assumptions for consideration of the scaling of self-preserving thermals in crossflow were the same as for thermals in still flow that were discussed earlier, and these assumptions will not be repeated here. In addition, the crossflow (horizontal) motion was assumed to be a uniform crossflow having negligible slip, whereas the streamwise (vertical) motion was assumed to be equivalent to the streamwise motion of a self-preserving thermal in a uniform and still environment. Thus, the maximum crosstream (horizontal) penetration distance was found from the

no-slip convection approximation, which implies that the flow moves in the crosstream (horizontal) direction at the crosstream (horizontal) velocity, as follows:

$$(y_p - y_o)/d = C_y(v_\infty(t - t_d)/d) \tag{17}$$

The diameter d factors out of Eq. (17) immediately to provide an equation in the self-preserving region that is properly independent of d. Penetration in the streamwise (vertical) and radial directions is still given by Eqs. (14)–(16), with the conserved property in the streamwise direction given by B_o, and with values of n, t^*, and x^* the same as for thermals in a still fluid from Table 2; these properties of self-preserving thermals in crossflow are summarized in Table 3 for comparison with the other flows in uniform crossflow considered during the present investigation.

Evaluation of the present self-preserving scaling relationships for thermals in uniform crossflow, as well as the best-fit values of C_y, C_x, and C_r and x_o/d based on the present measurements, will be considered next. The crosstream penetration distances of thermals in uniform crossflow are plotted in Fig. 2 according to the no-slip convection approximation. These results indicate that this approximation is satisfied for present measurements of thermals in crossflow, which extend from a crossflow displacement near zero, with $C_y = 1.0$ and $y_o/d = 0$. Normalized streamwise and radial penetration distances of thermals in crossflow are plotted according to the self-preserving relationships of Eqs. (15) and (16), with $n = 1/2$, and x^* for thermals in crossflow from Table 3, in Fig. 3. Near-source behavior differs depending on the source properties for each test condition and distance from the source but

Table 3 Summary of equations for the self-preserving penetration properties of round turbulent thermals, puffs, starting plumes and starting jets in unstratified uniform crossflow[a]

Conserved Property	n	t*	x*
Thermal: $B_o = Q_o g|\rho_o - \rho_\infty|/\rho_\infty$	1/2	$(d^4/B_o)^{1/2}$	$(B_o^{1/2}(t-t_d))^{1/2}$
Puff: $M_o = Q_o u_o$	1/4	d^4/M_o	$(M_o(t-t_d))^{1/4}$
Starting Plume: $B_o' = \dot{Q}_o g|\rho_o - \rho_\infty|/(\rho_\infty v_\infty)$	2/3	$(d^3/B_o')^{1/3}$	$(B_o'^{1/2}(t-t_d))^{2/3}$
Starting Jet: $M_o' = \dot{Q}_o u_o/v_\infty$	1/3	d^3/M_o'	$(M_o'^{1/2}(t-t_d))^{1/3}$

[a]Common equations: Streamwise penetration (d included): $(x_p - x_o)/d = C_x((t - t_d)/t^*)^n$. Streamwise penetration (d excluded): $(x_p - x_o)/x^* = C_x$. Radial penetration: $r_p/(x_p - x_o) = C_r$. Half-width penetration: $w_p/(x_p - x_o) = C_w$. Crossstream penetration (d included): $(y_p - y_o)/d = C_y(v_\infty(t - t_d)/d)$.

the thermals become self-preserving for these properties for $(x_p - x_o)/d > 40-50$, which is similar to the behavior of thermals in still fluids. Best-fit values of C_x, C_r, and x_o/d are readily obtained from the measurements and are summarized in Table 4 for comparison with corresponding results for thermals in still fluids. The magnitudes of these parameters are similar for the two flows although values of C_r suggest that thermals in still fluids have significantly larger penetration radii than those in crossflows. The reasons for this behavior, however, are not known at the present time.

Puffs. The test conditions for measurements of puffs in crossflow are summarized in Table 1. Visualizations of puffs in crossflow were qualitatively similar to those of thermals in crossflow, illustrated in Fig. 1 and will not be repeated here. Thus, puffs in crossflow involved a leading bulbous element which mainly consisted of a starting circular vortex. Given a sufficient amount of source fluid, the starting vortex was followed by a trailing jet-like region that extended from the bottom of the bulbous element. Similar to thermals, progressive growth of the bulbous element suggested that the trailing jet-like region was being engulfed by the leading vortex. Present results, however, were generally obtained before the trailing jet-like region was completely engulfed. Similar to thermals, the puffs became turbulent within five source
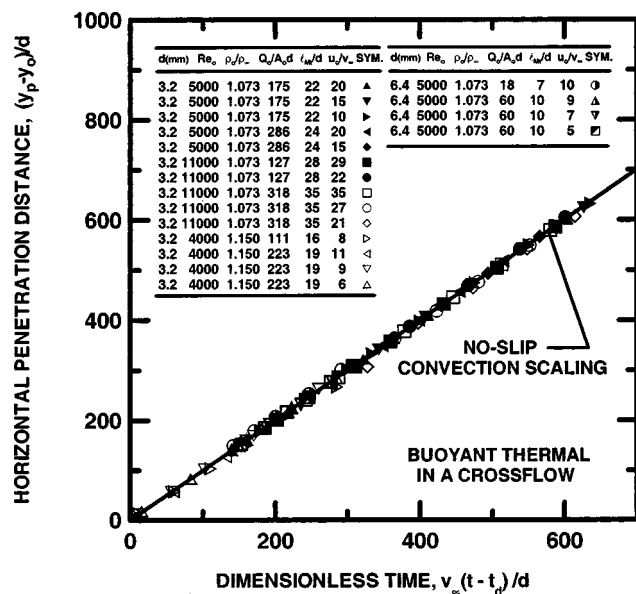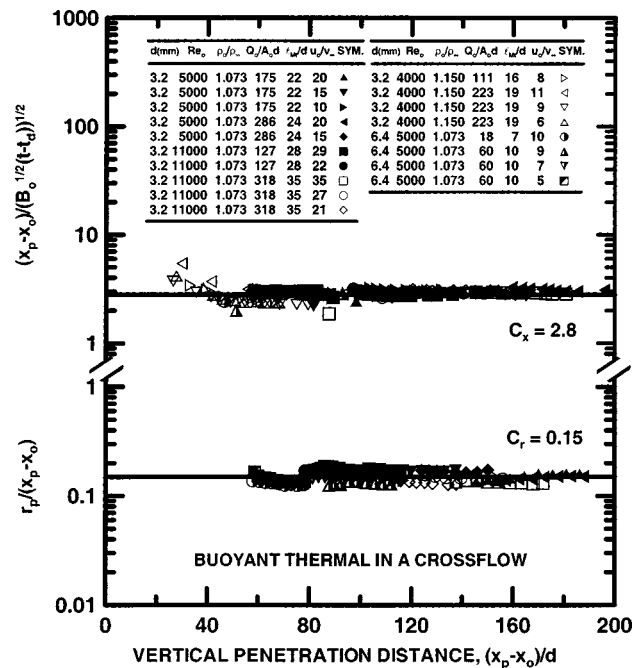

Fig. 3 Radial and streamwise (vertical) penetration distances of thermals in crossflow as functions of streamwise (vertical) penetration distance

diameters from the source in the streamwise (vertical) direction and the dimensions of the puffs progressively increased with increasing distance from the source. Finally, similar to thermals in crossflow, it generally appeared that the puffs in crossflow moved in the streamwise direction in the same manner as puffs in still fluids and that they were simply wafted along by the crossflow at the same time. The present self-preserving scaling considerations of the penetration properties of puffs were carried out based on this observation, as discussed next.

The assumptions for consideration of the scaling of self-preserving puffs in crossflow were the same as for puffs in still fluid as discussed earlier and these assumptions will not be repeated here. In addition, measurements of crossflow motion showed that the no-slip convection approximation was quite reasonable, with Eq. (17) satisfied for $C_y = 1.0$ and $y_o/d = 0$ as discussed for thermals in connection with Fig. 2. Penetration in the streamwise (vertical) and radial directions was still given by Eqs. (14)–(16), with the conserved property in this direction given by M_o, and with values of n, t^*, and x^* the same as for puffs in still fluid from Table 2; these properties of self-preserving puffs in crossflow are summarized in Table 3, as before.

The evaluation of the present self-preserving scaling relationships for puffs in crossflow, as well as the best-fit values of C_x, C_r, and x_o/d based on the measurements, will be considered next. Normalized radial and streamwise penetration distances of puffs in crossflow are plotted according to the self-preserving relationships of Eqs. (15) and (16), with $n = 1/4$ and x^* for puffs in crossflow from Table 3, in Fig. 4. Similar to the other flows that were studied, near-source behavior differs depending on source properties for each condition and distance from the source but the puffs become self-preserving for these properties for $(x_p - x_o)/d > 40-50$ which is similar to the behavior of puffs in still fluids. Best-fit values of C_x, C_r, and x_o/d from the self-preserving measurements illustrated in Fig. 4 for puffs are summarized in Table 4. The values for puffs in still fluids and crossflow are similar to each other in Table 4 but the values of C_r suggest enhanced radial growth of puffs in still fluids compared to crossflow, similar to the observations for thermals; the reasons for this behavior also are not known at the present time.

Fig. 2 Crosstream (horizontal) penetration distance of thermals in crossflow as a function of time

Table 4 Summary of the empirical parameters for the self-preserving penetration properties of round turbulent thermals, puffs, starting plumes and starting jets in unstratified still and uniformly crossflowing fluids[a]

Source	Ambient Flow	Re_o	ℓ_{Mt} or ℓ_{Mp}/d	u_o/v_∞	$(x_p-x_o)/d$	C_x	C_r	C_w	x_o/d
Thermal:									
Diez et al. [3]	Still	4,000–11,000	8–34	∞	0–110	2.7(0.05)	0.19(0.003)	$\cdots$	8.0(0.7)
Present	Crsfl.	2,500–15,000	7–35	4–35	0–200	2.8(0.05)	0.15(0.006)	$\cdots$	−12.5(1.5)
Puff:									
Diez et al. [2]	Still	3,000–12,000	∞	∞	0–100	2.6(0.06)	0.17(0.005)	$\cdots$	8.5(2.0)
Present	Crsfl.	3,000–16,000	∞	7–27	0–160	3.6(0.03)	0.12(0.003)	$\cdots$	−20.6(2.5)
Starting Plume:									
Diez et al. [3]	Still	4,000–11,000	9–74	∞	0–110	2.7(0.05)	0.16(0.006)	$\cdots$	7.0(1.7)
Present	Crsfl.	2,500–15,000	5–88	4–35	0–200	1.5(0.03)	0.24(0.005)	0.41(0.009)	17.9(3.1)
Starting Jet:									
Diez et al. [2]	Still	3,000–12,000	∞	∞	0–140	2.8(0.06)	0.15(0.003)	$\cdots$	0.0
Present	Crsfl.	3,000–16,000	∞	7–27	0–160	2.2(0.04)	0.20(0.004)	0.30(0.007)	2.0(3.7)

[a]Self-preserving behavior as summarized here was observed beyond 20–30 source diameters from the source for flows in still fluids and beyond 40–50 source diameters from the source for flows in uniformly crossflowing fluids. Experimental uncertainties (95 percent confidence) in parenthesis. Also $C_y=1.0$ and $y_o/d=0.0$.

Starting Plumes. The test conditions for measurements of the properties of starting plumes in crossflow are summarized in Table 1, a visualization of a typical starting plume in crossflow is illustrated in Fig. 5. Similar to the earlier visualization of a thermal in Fig. 1, these images include side and bottom views of a typical starting plume, taken at the time when the plume had reached the largest distance from the source where the source and the tip of the starting plume could be observed on one image. The length scales that appear on the images are appropriate for streamwise, radial and crosstream directions. An interesting feature of this visualization is that turbulent distortions of the lower surface of the flow (the side facing the source) are smoothed out because this region is stable to buoyant disturbances whereas turbulent distortions of the upper surface of the flow (the side facing away from the source) are enhanced because this region is unstable to buoyant disturbances. Next, the vertical self-preserving penetration velocity of starting plumes in crossflow progressively decreases with

increasing vertical distance (This velocity is proportional to $(t-t_d)^{-1/4}$ if the crossflow velocity is small compared to the streamwise velocity and the starting plume is nearly vertical from Table 2; whereas this velocity is proportional to $(t-t_d)^{-1/3}$ if the crossflow velocity is large compared to the streamwise velocity and the starting plume is nearly horizontal as will be demonstrated subsequently). As a result, the streamwise velocity eventually becomes small and the trajectory of the starting plume in crossflow becomes nearly horizontal far from the source where self-preserving flow is approached as illustrated in Fig. 5. When this condition is reached the aspect ratio (ratio of crosstream/streamwise penetration distances) of the flow is quite large and the streamwise penetration of the flow approximates a two-dimensional horizontal line thermal in a still fluid. Then, streamwise motion of the line thermal, retarded along its sides by the ambient fluid, naturally leads to the flow becoming two nearly horizontal counter-rotating vortices aligned along the axis of the starting plume as a whole. Evidence for this behavior is provided by the bottom view of the flow in Fig. 5, where the darker regions associated with the two vortices are separated by the lighter region between them. Clearly, this observation implies that the self-preserving motion in the streamwise direction should be based on a horizontal line thermal in a still fluid, rather than a starting plume in a still fluid for a starting plume in crossflow, even when the crosstream velocity is small. Finally, the two vortex basic flow configuration implies that maximum radial penetration normal to the flow axis in a vertical plane, r_p, and maximum radial penetration normal to the flow axis in a horizontal plane, taken as a maximum mean half-width, w_p, are not the same. Notably, the numerical simulations of plumes in crossflow due to Baum et al. [34] exhibit qualitatively similar behavior.

The assumptions for consideration of the scaling of self-preserving starting plumes in crossflow were the same as for buoyant thermals and starting plumes in still fluid discussed earlier and these assumptions will not be repeated here. In addition, measurements of crossflow motion showed that the no-slip convection approximation was quite reasonable, with Eq. (17) satisfied by $C_y=1.0$ and $y_o/d=0$, as discussed for thermals in connection with Fig. 2. Penetration in the streamwise, x_p, and radial, r_p, directions was still given by Eqs. (14)–(16). The conserved property in the streamwise direction is given by the source specific buoyancy flux per unit length of the line thermal, B'_o, associated with motion in this direction. The equation used to compute B'_o is summarized in Table 3. Values of n, t^*, and x^* were found in the same manner as for thermals and starting plumes in still fluid; these properties of starting plumes in crossflow are also summarized in Table 3 for convenience in comparing with other flows having uniform crossflow considered during the present investigation. Finally, radial penetration in the horizontal plane at

d(mm)	Re_o	Q_o/A_od	u_o/v_∞	SYM.
6.4	6000	16	12	▽
6.4	6000	16	8	△
6.4	6000	24	17	◁
6.4	6000	24	12	▷
6.4	6000	32	17	◇
6.4	6000	32	12	○
6.4	6000	32	8	⬦
6.4	6000	48	12	□
6.4	6000	48	8	⊕

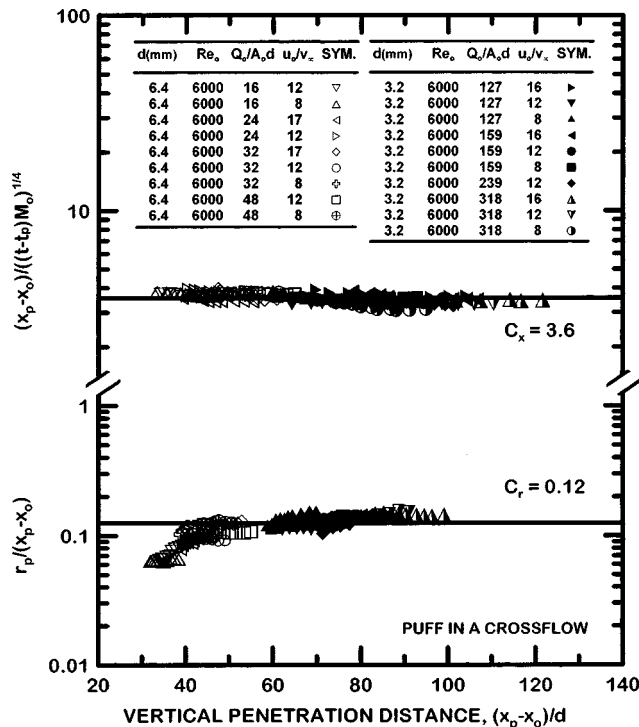| d(mm)	Re_o	Q_o/A_od	u_o/v_∞	SYM.
3.2	6000	127	16	▶
3.2	6000	127	12	▼
3.2	6000	127	8	▲
3.2	6000	159	16	◀
3.2	6000	159	12	●
3.2	6000	159	8	■
3.2	6000	239	12	◆
3.2	6000	318	16	▲
3.2	6000	318	12	▽
3.2	6000	318	8	◑

$C_x = 3.6$

$C_r = 0.12$

PUFF IN A CROSSFLOW

Fig. 4 Radial and streamwise (vertical) penetration distances of puffs in crossflow as functions of streamwise (vertical) penetration distance
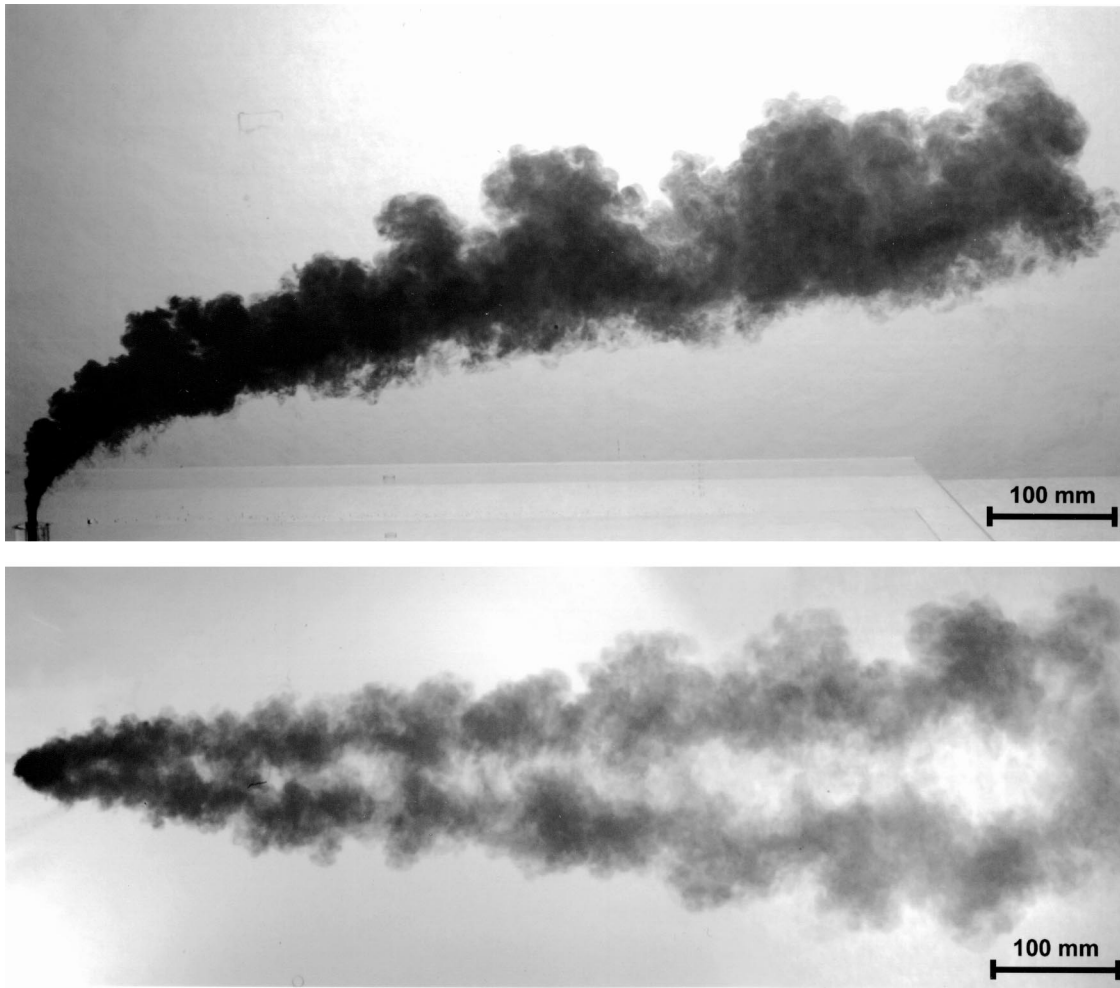
Fig. 5 Visualization of a starting plume in crossflow ($d=6.4$ mm, $Re_o=5,000$, $\rho_o/\rho_\infty=1.150$, $\ell_{Mp}/d=10$, $u_o/v_\infty=7$ and $t=3.4$ s)

self-preserving conditions, represented by the half-width parameter w_p, is given by an expression analogous to Eq. (16) for r_p, as follows:

$$w_p/(x_p-x_o)=C_w \qquad (18)$$

Evaluation of the present self-preserving scaling relationships for starting plumes in uniform crossflow, as well as best-fit values of C_x, C_r, C_w, and x_o/d based on present measurements, will be considered next. Normalized radial, half-width and streamwise penetration distances of starting plumes in crossflow are plotted according to the self-preserving relationships of Eqs. (15), (16), and (18), with $n=2/3$ and x^* for starting plumes in crossflow from Table 3, in Fig. 6. Near-source behavior varies depending on the source properties for each test condition and distance from the source but the starting plumes become self-preserving for all properties when $(x_p-x_o)/d>40-50$, similar to the other transient flows in crossflow that were considered. Best-fit values of C_x, C_r, C_w, and x_o/d are readily obtained from the measurements and are summarized in Table 4 for comparison with the corresponding results for other flows. The order of magnitude of these parameters is similar to the other flows studied during the present investigation. The details differ, however, because the counter-rotating vortex structure causes C_r to be larger for starting plumes in crossflow than in still fluids, whereas C_w is even larger yet as a result of the vortex structure.

Finally, the steady-state trajectory of a starting plume in crossflow can be observed by letting the flow run for a time after the tip

of the plume has passed a given location. Then the trajectory for steady plumes in crossflow can be obtained by noting that $(x_{ps}-x_{os})$, r_{ps} and w_{ps} are now functions of general displacement in the crosstream direction, $(y-y_o)$, rather than just a particular penetration distance. Then eliminating time from the expression for x^* for starting plumes in crossflow in Table 3, noting that the no-slip convection approximation in the crosstream direction implies that $(t-t_d)=(y-y_o)/v_\infty$ and recalling that $C_y=1$, a new scaling relationship for the streamwise penetration distance for a steady plume in crossflow is found as follows:

$$(x_{ps}-x_{os})/x_s^*=C_{xs} \qquad (19)$$

where the associated conserved property in the streamwise direction, B_o', and n and x_s^* are summarized in Table 5. Similarly, the other steady penetration properties of steady plumes in crossflow are found from equations analogous to Eqs. (16) and (18), as follows:

$$r_{ps}/(x_{ps}-x_{os})=C_{rs} \qquad (20)$$

and

$$w_{ps}/(x_{ps}-x_{os})=C_{ws} \qquad (21)$$

Present measurements of the trajectory properties of steady plumes in crossflow are plotted according to Eqs. (19)–(21) as functions of the normalized streamwise penetration distance in Fig. 7. Similar to earlier results for starting plumes in crossflow,

Fig. 6 legend — STARTING PLUME IN A CROSSFLOW

Vertical axes: $(x_p - x_o)/((B_o'^{1/2}(t-t_d))^{2/3})$ with $C_x = 1.5$; $r_p/(x_p - x_o)$ with $C_r = 0.24$; $w_p/(x_p - x_o)$ with $C_w = 0.41$. Horizontal axis: VERTICAL PENETRATION DISTANCE, $(x_p - x_o)/d$.

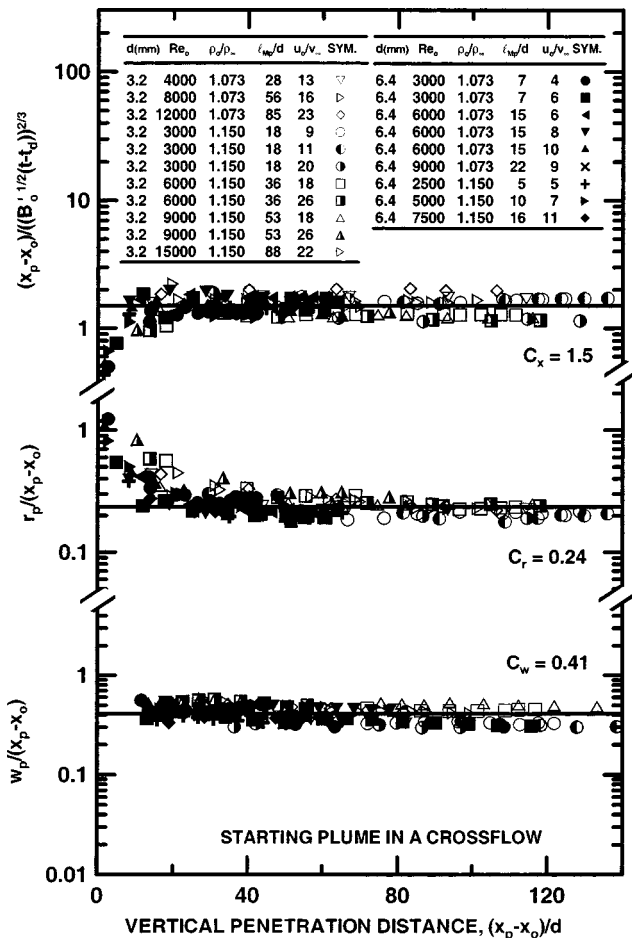| d(mm)	Re_o	ρ_o/ρ_∞	ℓ_Mo/d	u_o/v_∞	SYM.	d(mm)	Re_o	ρ_o/ρ_∞	ℓ_Mo/d	u_o/v_∞	SYM.
3.2	4000	1.073	28	13	▽	6.4	3000	1.073	7	4	●
3.2	8000	1.073	56	16	▷	6.4	3000	1.073	7	6	■
3.2	12000	1.073	85	23	◇	6.4	6000	1.073	15	6	◀
3.2	3000	1.150	18	9	○	6.4	6000	1.073	15	8	▼
3.2	3000	1.150	18	11	◑	6.4	6000	1.073	15	10	▲
3.2	3000	1.150	18	20	◐	6.4	9000	1.073	22	9	×
3.2	6000	1.150	36	18	□	6.4	2500	1.150	5	5	+
3.2	6000	1.150	36	26	▣	6.4	5000	1.150	10	7	▶
3.2	9000	1.150	53	18	△	6.4	7500	1.150	16	11	◆
3.2	9000	1.150	53	26	▲						
3.2	15000	1.150	88	22	▷						

Fig. 6 Radial, half-width and streamwise (vertical) penetration distances of starting plumes in crossflow as functions of streamwise (vertical) penetration distance

Fig. 7 legend — STEADY STATE PLUME IN A CROSSFLOW (TOP)

Vertical axes: $(x_{ps} - x_{os})/((B_o'^{1/2}(y-y_o)/v_\infty)^{2/3})$ with $C_{xs} = 1.9$; $r_{ps}/(x_{ps} - x_{os})$ with $C_{rs} = 0.36$; $w_{ps}/(x_{ps} - x_{os})$ with $C_{ws} = 0.49$. Horizontal axis: $(x_{ps} - x_{os})/d$.

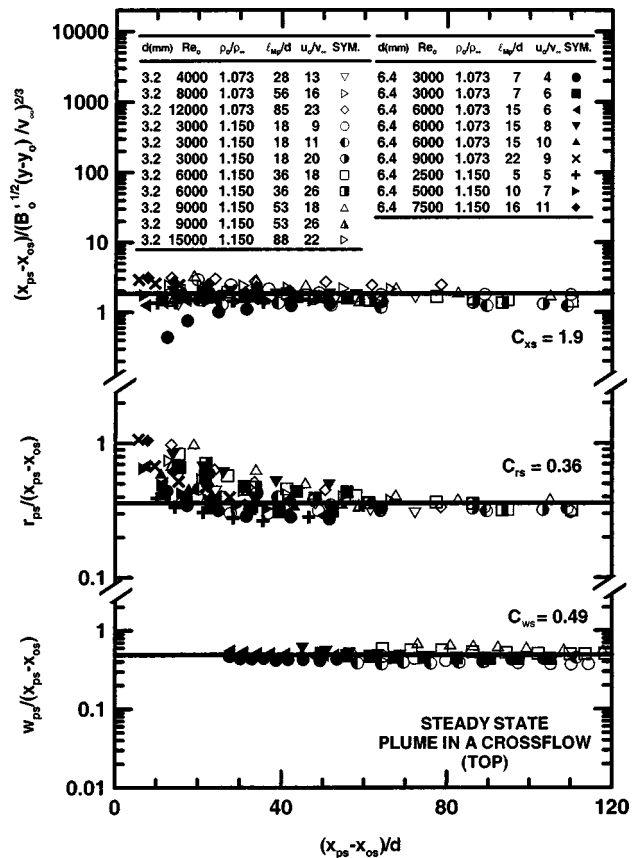| d(mm)	Re_o	ρ_o/ρ_∞	ℓ_Mo/d	u_o/v_∞	SYM.	d(mm)	Re_o	ρ_o/ρ_∞	ℓ_Mo/d	u_o/v_∞	SYM.
3.2	4000	1.073	28	13	▽	6.4	3000	1.073	7	4	●
3.2	8000	1.073	56	16	▷	6.4	3000	1.073	7	6	■
3.2	12000	1.073	85	23	◇	6.4	6000	1.073	15	6	◀
3.2	3000	1.150	18	9	○	6.4	6000	1.073	15	8	▼
3.2	3000	1.150	18	11	◑	6.4	6000	1.073	15	10	▲
3.2	3000	1.150	18	20	◐	6.4	9000	1.073	22	9	×
3.2	6000	1.150	36	18	□	6.4	2500	1.150	5	5	+
3.2	6000	1.150	36	26	▣	6.4	5000	1.150	10	7	▶
3.2	9000	1.150	53	18	△	6.4	7500	1.150	16	11	◆
3.2	9000	1.150	53	26	▲						
3.2	15000	1.150	88	22	▷						

Fig. 7 Radial, half-width and streamwise (vertical) penetration distances of steady plumes in crossflow as functions of streamwise (vertical) penetration distance

self-preserving penetration properties are reached for the steady plumes in crossflow when $(x_{ps} - x_{os})/d > 40$–50. The corresponding values of C_{xs}, C_{rs}, and C_{ws} are summarized in Table 5. In general, $C_{rs} > C_r$ and $C_{ws} > C_w$ for plumes in crossflow, suggesting gradual growth of the flow crossection of the plume until steady-state conditions are reached combined with greater horizontal width than vertical height due to the presence of the two parallel vortices along the axes of the plumes. Finally, $x_{os} > x_o$ for

Table 5 Summary of equations and empirical parameters for the self-preserving penetration properties of steady plumes and jets in unstratified and uniformly crossflowing fluids[a]

Flow	Conserved Property	n	x_s^*
Plume	$B_o' = \dot{Q}_o g|\rho_o - \rho_\infty|/(\rho_\infty v_\infty)$	2/3	$(B_o'^{1/2}(y-y_{os})/v_\infty)^{2/3}$
Jet	$M_o' = \dot{Q}_o u_o / v_\infty$	1/3	$(M_o'(y-y_{os})/v_\infty)^{1/3}$

Flow[b]	C_{xs}	C_{rs}	C_{ws}	x_{os}/d
Plume	1.9(0.08)	0.36(0.008)	0.49(0.015)	25.6(4.5)
Jet	2.3(0.08)	0.23(0.005)	0.31(0.011)	6.1(2.7)

[a]Common equations: Streamwise penetration: $(x_{ps} - x_{os})/x_s^* = C_{xs}$. Radial penetration: $r_{ps}/(x_{ps} - x_{os}) = C_{rs}$. Half-width penetration: $w_{ps}/(x_{ps} - x_{os}) = C_{ws}$.

[b]Self-preserving behavior summarized here was observed for the test conditions summarized in Table 4 for starting plumes and jets beyond $(x_{po} - x_{os})/d > 40$–50. Experimental uncertainties (95 percent confidence) in parentheses. Also $C_y = C_{ys} = 1$ and $y_o = y_{os} = 0.0$.

plumes in crossflow due to the increase of x_p at each crosstream position, y, as steady-state conditions are approached.

Starting Jets. The test conditions for measurements of the properties of starting jets in crossflow are summarized in Table 1. Visualizations of starting jets in crossflow were qualitatively similar to those of starting plumes in crossflow, illustrated in Fig. 5, and will not be repeated here. One change, however, is that buoyant stability is not an issue for starting jets; therefore, turbulent distortion of the boundary of the jets was similar in all directions around the axis of the jet. Similar to starting plumes, the streamwise self-preserving penetration velocity of starting jets in crossflow progressively decreases with increasing vertical distance (This velocity is proportional to $(t - t_d)^{-1/2}$ if the crossflow velocity is small compared to the streamwise velocity and the starting jet is nearly vertical from Table 2; whereas this velocity is proportional to $(t - t_d)^{-2/3}$ if the crossflow velocity is large compared to the streamwise velocity and the starting jet is nearly horizontal as will be demonstrated subsequently). As a result, the streamwise velocity eventually becomes small and the trajectory of the starting jets in crossflow becomes nearly horizontal far from the source where self-preserving flow is approached, giving a general appearance similar to the starting plume in crossflow illustrated in Fig. 5. When this condition is reached the aspect ratio (ratio of crosstream/streamwise penetration distances) of the flow is quite large and the streamwise penetration of the flow approximates a two-dimensional horizontal line puff in a still fluid. Then, streamwise motion of the line puff, retarded along its sides by the ambient fluid, naturally leads to the flow becoming two nearly horizontal counter-rotating vortices aligned along the axis of the starting jet as a whole. Evidence for this behavior was provided by the bottom views of the flow, which yielded images very similar

to the two-vortex images seen in the bottom view of the starting plume in crossflow illustrated in Fig. 5. Thus, the geometrical features of the flow structure of starting jets and plumes in crossflow are similar, with the properties of each crossection of the flow characterized by radial penetration, r_p, normal to the flow axis in a vertical plane, and radial penetration normal to the flow axis in a horizontal plane characterized by the half-width, w_p.

The assumptions for consideration of the scaling of self-preserving starting jets in crossflow were the same assumptions as nonbuoyant puffs and starting jets in still fluids discussed earlier and these assumptions will not be repeated here. In addition, measurements of crossflow motion showed that the no-slip convection approximation was quite reasonable, with Eq. (17) satisfied by $C_y = 1.0$ and $y_o/d = 0$. Penetration in streamwise, x_p, radial, r_p, and half-width, w_p, directions was still given by Eqs. (14), (16), and (18). The conserved property in the streamwise direction is given by the source specific momentum flux per unit length of the line puff, M_o', associated with motion in this direction. Values of n, t^*, and x^* were found in the same manner as for puffs and starting jets in still fluid. The resulting values of M_o', n, t^*, and x^* are summarized in Table 3 for convenience in comparing these properties with other flows in crossflow considered during the present investigation.

Evaluation of the self-preserving scaling relationships for starting jets in crossflow, as well as best-fit values of C_x, C_r, C_w, and x_o/d based on the present measurements, will be considered next. Normalized radial, half-width and streamwise penetration distances of starting jets in crossflow are plotted according to the self-preserving relationships of Eqs. (15), (16), and (18), with $n = 1/3$ and x^* for starting jets in crossflow from Table 3, in Fig. 8. Near-source behavior varies depending on the source properties for each test condition but the starting jets become self-preserving for all properties when $(x_p - x_o)/d > 40$–50, similar to the other transient flows in crossflow that were considered. Best-fit values of C_x, C_r, C_w, and x_o/d are readily obtained from the measurements and are summarized in Table 4 for comparison with the corresponding results for the other flows. The order of magnitude of these parameters is similar to the other flows studied during the present investigation. The values of C_r are larger for starting jets in crossflow than in still fluids, whereas the value of $C_w > C_r$ as a result of the two-vortex structure of the flow.

Finally, steady-state trajectories were observed for starting jets in crossflow similar to the starting plumes in crossflow. The trajectories were found for self-preserving conditions for starting jets similar to the earlier discussion of steady-state trajectories for starting plumes. Penetration properties of the steady jets in crossflow, e.g., x_{ps}, r_{ps}, and w_{ps}, are still given by Eqs. (19)–(21) but with the associated conserved properties in the streamwise direction, M_o', and n and x_s^* as summarized in Table 5.

Present measurements of the trajectory properties of steady jets in crossflow are plotted according to Eqs. (19)–(21) as functions of normalized streamwise penetration distance in Fig. 9. As before, self-preserving penetration properties are reached for steady plumes in crossflow when $(x_{ps} - x_{os})/d > 40$–50. The corresponding values of C_{xs}, C_{rs}, and C_{ws} are summarized in Table 5. In general, C_{rs} and C_{ws} are smaller for jets than plumes for the same reasons mentioned earlier for comparison of C_r and C_w for these flows. Finally, $x_{os} > x_o$ for jets in crossflow due to the increase of x_p at each crossstream position, y, as steady-state conditions are approached.

Conclusions

Scaling relationships for the temporal development of round turbulent thermals, puffs, and starting plumes and starting jets, were evaluated based on experiments emphasizing self-preserving behavior in unstratified crossflows having uniform velocities. The test conditions consisted of dye-containing fresh (for nonbuoyant flows) and salt water (for buoyant flows) sources injected verti-
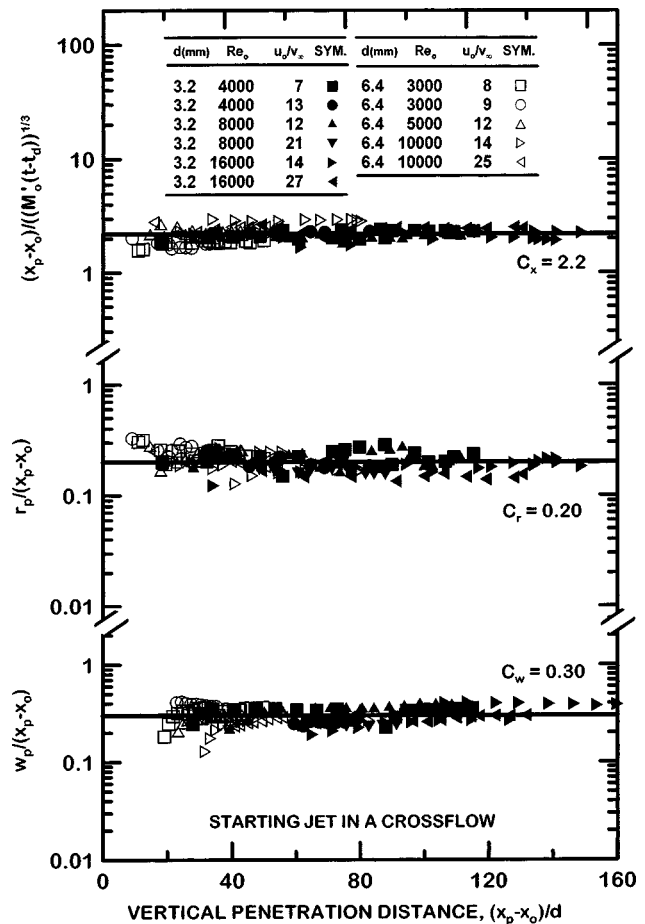

Fig. 8 Radial, half-width and streamwise (vertical) penetration distances of starting jets in crossflow as functions of streamwise penetration distance

cally downward into crossflowing fresh water within a water channel. The test conditions consisted of source exit diameters of 3.2 and 6.4 mm, source passage lengths in excess of 50 source exit diameters, source Reynolds numbers of 2,500–16,000, source/ambient velocity ratios of 4–35, source/ambient density ratios (for buoyant flows) of 1.073 and 1.150, volumes of injector source fluid (for thermals and puffs) consisting of 16–318 source diameters, vertical penetration distances of 0–200 source diameters and 0–13 Morton length scales (for buoyant flows) and horizontal penetration distances of 0–620 source diameters. Major conclusions of the study are as follows:

1) The flows became turbulent near the source exit, at streamwise distances of 0–5 source diameters from the source; although near-source behavior varied significantly with source properties and distance from the source, self-preserving behavior for all penetration properties generally was observed at streamwise (vertical) distances greater than 40–50 source diameters from the source.

2) For all the flows in crossflow considered during the present study, crossstream (horizontal) penetration of the flows was well represented by the no-slip convection approximation.

3) For all the flows in crossflow considered during the present study, streamwise (vertical) motion at self-preserving conditions scaled in a more complex way than crossstream (horizontal) motion. For puffs and thermals, self-preserving motion in the streamwise direction was identical to the self-preserving motion of the same flow in a still fluid. For starting jets and plumes, however, the self-preserving streamwise motion of these flows scaled according to associated flows, e.g., according to a horizontal line puff in a still fluid for a starting jet in crossflow and according to
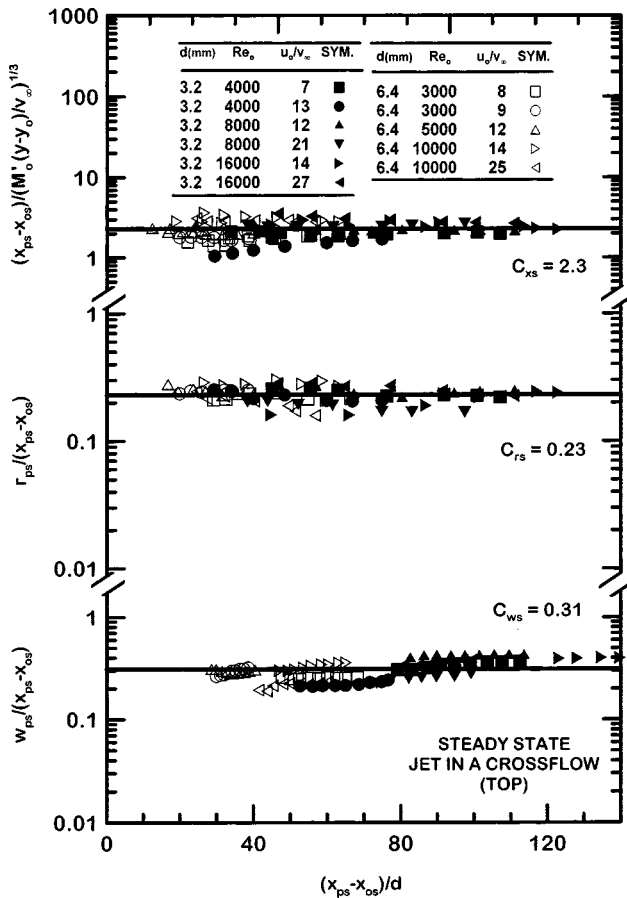
Fig. 9 Radial, half-width and streamwise (vertical) penetration distances of steady jets in crossflow as functions of stream-wise penetration distance

a horizontal line thermal in a still fluid for a starting plume in crossflow. This latter behavior for buoyant flows is qualitatively similar to the results of numerical simulations due to Baum et al. [34].

4) Turbulent distortion of starting jets in crossflow is similar for all azimuthal angles around the axis of the flow. This is not the case for starting plumes in crossflow, however, where distortion on the side toward the source is retarded due to the buoyant stability of this region whereas distortion on the side away from the source is enhanced due to the buoyant instability of this region.

5) Combining the no-slip convection approximation in the crossstream direction with self-preserving scaling in the streamwise direction yielded good predictions of the penetration trajectories within the self-preserving region of the flows. In addition, the same approach was successfully applied to correlating the steady trajectories of nonbuoyant jets and buoyant plumes in uniform crossflows.

It is somewhat surprising that the presence of crossflow did not modify the range of conditions where self-preserving behavior was observed compared to the present flows in still fluids. This behavior may very well change in the presence of stronger crossflow, however, and such conditions clearly merit further study in the future.

Acknowledgments

Nomenclature

A_o = source crosssectional area
B_o = source specific buoyancy force, Eq. (9)
$\dot{B}_o$ = source specific buoyancy flux, Eq. (3)
B_o' = source specific buoyancy flux per unit length for a line thermal, Tables 3 and 5
C_r = radial penetration coefficient, Eq. (16)
C_{rs} = radial penetration coefficient for steady plumes and jets, Eq. (20)
C_w = half-width penetration coefficient, Eq. (18)
C_{ws} = half-width penetration coefficient for steady plumes and jets, Eq. (21)
C_x = streamwise penetration coefficient, Eq. (14)
C_{xs} = streamwise penetration coefficient for steady plumes and jets, Eq. (19)
C_y = crossstream penetration coefficient, Eq. (17)
d = source diameter
f = mixture fraction, Eq. (13)
g = acceleration of gravity
L = source passage length
L_Q = length of source passage containing Q_o
ℓ_{Mp} = Morton length scalefor a plume, Eq. (1)
ℓ_{Mt} = Morton length scale for a thermal, Eq. (7)
M_o = source specific momentum force, Eq. (8)
$\dot{M}_o$ = source specific momentum flux, Eq. (2)
M_o' = source specific momentum flux per unit length for a line puff, Tables 3 and 5
n = time exponent, Eq. (14)
Q_o = volume of injected source fluid
$\dot{Q}_o$ = volumetric rate of injection of source fluid
Re_o = source Reynolds number, $u_o d/\nu_o$
r = radial penetration normal to flow axis in a vertical plane
t = time
t^* = self-preserving time scale, Eq. (14)
u = streamwise (vertical) velocity
v = crossstream (horizontal) velocity
w = radial penetration normal to flow axis in a horizontal plane
x = streamwise (vertical) distance
x^* = self-preserving length scale, Eq. (15)
y = crossstream (horizontal) distance
ν = kinematic viscosity
ρ = density

Subscripts

d = delay
p = maximum penetration location
s = steady-state flow property
o = source value or virtual origin location
∞ = ambient value

References

[1] Sangras, R., Kwon, O. C., and Faeth, G. M., 2002, "Self-Preserving Properties of Unsteady Round Nonbuoyant Turbulent Starting Jets and Puffs in Still Fluids," ASME J. Heat Transfer, **124**, pp. 460–469.
[2] Diez, F. J., Sangras, R., Kwon, O. C., and Faeth, G. M., 2003, "Self-Preserving Properties of Unsteady Round Nonbuoyant Turbulent Starting Jets and Puffs in Still Fluids," ASME J. Heat Transfer, **125**, pp. 204–205.
[3] Diez, F. J., Kwon, O. C., Sangras, R., and Faeth, G. M., 2003, "Self-Preserving Properties of Unsteady Round Buoyant Turbulent Plumes and Thermals in Still Fluids," ASME J. Heat Transfer, **125**, pp. 821–830.
[4] Turner, J. S., 1969, "Buoyant Plumes and Thermals," Annu. Rev. Fluid Mech., **1**, pp. 29–44.
[5] Turner, J. S., 1973, *Buoyancy Effects in Fluids*, Cambridge University Press, Cambridge.

[6] Tennekes, H., and Lumley, J. L., 1972, *A First Course in Turbulence*, MIT Press, Cambridge, pp. 113–124.

[7] Hinze, J. O., 1975, *Turbulence*, 2nd ed., McGraw-Hill, New York, pp. 534–584.

[8] Chen, C. J., and Rodi, W., 1980, *Vertical Turbulent Buoyant Jets: A Review of Experimental Data*, Pergamon Press, Oxford.

[9] List, E. J., 1982, "Turbulent Jets and Plumes," Annu. Rev. Fluid Mech., **14**, pp. 189–212.

[10] Dai, Z., Tseng, L.-K., and Faeth, G. M., 1994, "Structure of Round, Fully-Developed, Buoyant Turbulent Plumes," ASME J. Heat Transfer, **116**, pp. 409–417.

[11] Morton, B. R., 1959, "Forced Plumes," J. Fluid Mech., **5**, pp. 151–163.

[12] Scorer, R. S., 1957, "Experiments on Connection of Isolated Masses of Buoyant Fluid," J. Fluid Mech., **2**, pp. 588–594.

[13] Turner, J. S., 1964, "The Dynamics of Spheroidal Masses of Buoyant Fluid," J. Fluid Mech., **19**, pp. 481–490.

[14] Fay, J. A., and Lewis, D. H., 1976, "Unsteady Burning of Unconfined Fuel Vapor Clouds," Proceedings of the Combustion Institute, **16**, pp. 1397–1405.

[15] Batt, R. G., Brigoni, R. A., and Rowland, D. J., 1984, "Temperature-Field Structure Within Atmospheric Buoyant Thermals," J. Fluid Mech., **141**, pp. 1–25.

[16] Thompson, R. S., Snyder, W. H., and Weil, J. C., 2000, "Laboratory Simulation of the Rise of Buoyant Thermals Created by Open Detonation," J. Fluid Mech., **417**, pp. 127–156.

[17] Richards, J. M., 1965, "Puff Motions in Unstratified Surroundings," J. Fluid Mech., **21**, pp. 97–109.

[18] Kovasznay, L. S. G., Funjita, H., and Lee, R. L., 1974, "Unsteady Turbulent Puffs," Adv. Geophys., **18B**, pp. 253–263.

[19] Turner, J. S., 1962, "The Starting Plume in Neutral Surroundings," J. Fluid Mech., **13**, pp. 356–368.

[20] Middleton, J. H., 1975, "The Asymptotic Behavior of a Starting Plume," J. Fluid Mech., **72**, pp. 753–771.

[21] Delichatsios, M. A., 1979, "Time Similarity Analysis of Unsteady Buoyant Plumes," J. Fluid Mech., **93**, pp. 241–250.

[22] Pantzlaff, L., and Lueptow, R. M., 1999, "Transient Positively and Negatively Buoyant Turbulent Round Jets," Exp. Fluids, **27**, pp. 117–125.

[23] Witze, P. O., 1983, "Hot-Film Anemometer Measurements in a Starting Turbulent Jet," AIAA J., **21**, pp. 308–309.

[24] Johari, J., and Paduano, R., 1987, "Dilution and Mixing in an Unsteady Turbulent Jet," Exp. Fluids, **23**, pp. 272–280.

[25] Kato, S. M., Groenwagen, B. C., and Breidenthal, R. E., 1987, "On Turbulent Mixing in Nonsteady Jets," AIAA J., **25**, pp. 165–168.

[26] Kouros, H., Medina, R., and Johari, H., 1993, "Spreading Rate of an Unsteady Turbulent Jet," AIAA J., **31**, pp. 1524–1526.

[27] Adriani, R., Coghe, A., and Cossali, G. E., 1996, "Near-Field Entrainment in Unsteady Gas Jets and Diesel Sprays: A Comparative Study," Proceedings of the Combustion Institute, **26**, pp. 2549–2556.

[28] Hill, P. G., and Ouelette, P., 1999, "Transient Turbulent Gaseous Fuel Jets for Diesel Engines," ASME J. Fluids Eng., **121**, pp. 93–101.

[29] Anwar, H. O., 1969, "Experiment on an Effluent Discharging From a Slot Into Stationary or Slow Moving Fluid of Greater Density," J. Hydraul. Res., **7**, pp. 411–430.

[30] Lutti, F. M., and Brzustowski, T. A., 1977, "Flow Due to a Two-Dimensional Heat Source With Cross Flow in the Atmosphere," Combust. Sci. Technol., **16**, pp. 71–87.

[31] Andreopoulos, J., 1983, "Heat Transfer Measurements in a Heated Jet-Pipe Flow Issuing Into a Cold Cross Stream," Phys. Fluids, **26**, pp. 3200–3210.

[32] Alton, B. W., Davidson, G. A., and Slawson, P. R., 1993, "Comparison of Measurements and Integral Model Predictions of Hot Water Plume Behavior in a Crossflow," Atmos. Environ., Part A, **27A**, pp. 589–598.

[33] Hasselbrink, E. F., and Mungal, M. G., 1998, "Observations on the Stabilization Region of Lifted Non-Premixed Methane Transverse Jet Flames," Proceedings of the Combustion Institute, **27**, pp. 1167–1173.

[34] Baum, H. R., McGrattan, K. B., and Rehm, R. G., 1994, "Simulation of Smoke Plumes From Large Pool Fires," Proceedings of the Combustion Institute, **25**, pp. 1463–1469.

[35] Keffer, J. F., and Baines, W. D., 1963, "The Round Turbulent Jet in a Cross-Wind," J. Fluid Mech., **81**, pp. 45–62.

[36] Kamotani, Y., and Greber, I., 1972, "Experiments on a Turbulent Jet in Cross-flow," AIAA J., **10**, pp. 1425–1429.

[37] Chaissaing, P., George, J., Claria, A., and Sananes, F., 1974, "Physical Characteristics of Subsonic Jets in a Cross Stream," J. Fluid Mech., **62**, pp. 41–61.

[38] Kelso, R. M., Lim, T. T., and Perry, A. E., 1996, "An Experimental Study of Round Jets in Cross-Flow," J. Fluid Mech., **306**, pp. 111–144.

[39] Smith, S. H., and Mungal, M. G., 1998, "Mixing, Structure and Scaling of a Jet in Crossflow," J. Fluid Mech., **357**, pp. 83–122.

[40] Wu, P.-K., Miranda, R. F., and Faeth, G. M., 1995, "Effects of Initial Flow Conditions on Primary Breakup of Nonturbulent and Turbulent Round Liquid Jets," Atomization Sprays, **5**, pp. 175–196.

[41] Lange, N. A., 1952, *Handbook of Chemistry*, Handbook Publishers, Sandusky, OH, p. 1160.

[42] George, Jr., W. K., Alpert, R. L., and Tamanini, F., 1977, "Turbulence Measurements in an Axisymmetric Buoyant Plume," Int. J. Heat Mass Transfer, **20**, pp. 1145–1154.

Radiative Heat Transfer Properties of Electro-Controllable Fluids

Jeffrey B. Hargrove
Mem. ASME
e-mail: jhargrov@kettering.edu
Department of Mechanical Engineering,
Kettering University,
1700 W. Third Avenue,
Flint, MI 48504

John R. Lloyd

Clark J. Radcliffe

Department of Mechanical Engineering,
Michigan State University,
East Lansing, MI 48824

Active control of radiation heat transfer in liquids can be accomplished with the use of a class of fluids referred to here as electro-controllable (EC) fluids. EC fluids in general consist of a colloidal suspension of polarizable, micron-size particles dispersed in a carrier fluid with an appropriate dielectric constant. When an electric field is applied, the particles redistribute in the fluid, changing from a uniformly dispersed configuration to a tightly organized chain formation that follows the lines of the electric field, thus causing a change in the thermal radiation transport. In an example application, experiments are conducted and models are developed for thermal radiation transmittance through a composite window featuring a central layer of EC fluid. The specific EC fluids of this study are made of micron-sized Zeolite particles suspended in a light Silicone oil carrier fluid of appropriate dielectric strength. The incident thermal radiation ranged in wavelength between 500 nm and 800 nm, and the strength of the applied electric field ranged from 100 V/mm to 500 V/mm. The models are applicable for both the dispersed organizational state and the field induced chained state. Absorption was demonstrated to be the fundamental radiation transport property enabling the control process. The EC fluid transmittance predicted by these models are compared to the data obtained by experimental measurement demonstrate very good agreement. [DOI: 10.1115/1.1621894]

Keywords: Control, Heat Transfer, Modeling, Radiation, Rheological

Introduction

Electro-controllable (EC) fluids are suspensions of highly polarizable, micron-sized particles suspended in a carrier fluid of substantially different dielectric constant. When the fluid is subjected to an externally applied electric field of sufficient strength, the particles, which are initially uniformly dispersed, form particle chains that align with the electric field lines, as illustrated in Fig. 1. Upon removal of the electric field, the particles can resume their random distribution. The process of electrically induced chaining is reversible.

With the onset of field-induced particle chaining, the spatially averaged properties controlling conductive, convective and radiative thermal energy transport change [1]. Zhang and Lloyd [2,3] and more recently Yanju et al. [4] have demonstrated that radiative transmittance in EC fluids is significantly increased when the particles are in the field-induced chained state. Supporting work has shown that control of the electric field used to drive particle chain formation does indeed produce thermal fluid systems in which desired levels of energy transport can be actively controlled. The use of feedback control on internal particle organization has produced the ability to control effective thermal energy transport properties [5]. These studies motivate the development of a model that describes the controllable elements of the properties of the fluids. This suggests the possibility that the thermal transport properties could be controlled including the thermal radiant energy transport.

With a low concentration of particles in the fully dispersed state, under a zero-electric field condition, each particle acts to attenuate incident radiation by either scattering or by absorption. Upon the application of an external electric field, the process of chain formation begins (see Fig. 1), thus producing regions of attenuation by the chains and regions of energy transmission by

the void regions. Both regions are aligned with the direction of the electric field lines. This redistribution of the particles modifies the spatially averaged radiative transmittance [6].

Some particles scatter radiation [7,8] while others absorb radiation. Scattering and absorption together are typically termed extinction. Under the assumption that the multiple scattering does not exist, the classic Mie solution for light extinction [9–13] could be employed to model the radiative properties of an EC fluid.

The objective of the present investigation is to experimentally measure the radiative properties of absorption, transmission and reflection of an EC fluid, and to identify the dominant properties controlling radiative energy transport in EC fluids. Empirical models for absorption, reflection and transmittance as functions of particle size, volume fraction, radiation path length and applied electric field strength are developed. Strategies for control of the properties and the consequences of being able to control the properties are discussed.

Apparatus and Experimental Methods

In order to measure the radiative properties of the controllable fluids a glass-walled composite window was constructed as shown in Fig. 2. The composite window consisted of two pieces of 1 mm thick soda lime glass separated by a butadiene gasket. The center of the gasket was cut to form a chamber for the EC fluid sample. The composite window was mounted in a stainless steel support that was designed so that the incident radiation beam was always normal to the plane of the window.

The glass was coated with a 900 angstrom thick layer of indium-tin oxide (ITO) that served as the electrodes. This resulted in a uniformly distributed electric field across the window glass and through the EC fluid. The 900 angstrom coating resulted in a normal transmittance through the coated glass of 92 percent total transmission.

Other components in the apparatus (Fig. 3) used for taking radiative transport data consisted of a PC-based spectrometer, a tungsten-halogen lamp and associated optics. The light source provided energy in the wavelength range of 500 nm to 800 nm.

Copyright © 2003 by ASME
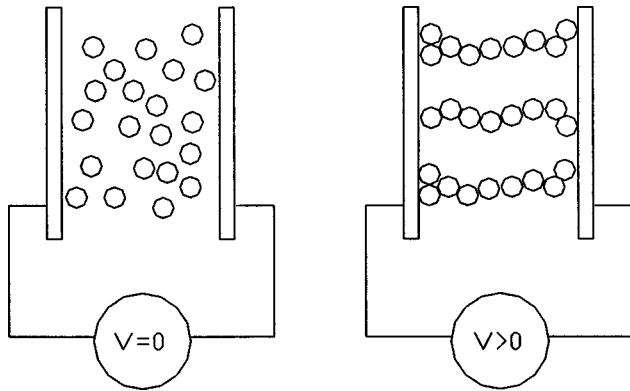
Fig. 1 Conceptual schematic of EC fluids

Fig. 4 Zeolite particles, average diameter 25 microns

Radiative energy was transmitted to the composite window using a 400 μm fiber optic cable with a 3-millimeter diameter collimating lens attached to its end. Radiation transmitted through the window was received by a similar collimating lens, which was positioned normal to the composite window connected to the input of the spectrometer by another fiber optic cable [14].

The electro-controllable fluids employed in this study were composed of particles of anhydrous crystalline Zeolite suspended in polysiloxane silicone oil. To insure control of water adsorption, and repeatability of experiments, the particles were baked at 150°C for 30 min. Measurements of particle weight were used during the baking process to determine when the particles were dry. Figure 4 shows an electron micrograph of 25 micron diameter Zeolite particles.

To insure uniform dispersion of the particles, the suspension was stirred prior to each experiment for 10 min, and then allowed to set for 10 min to eliminate all air bubbles created during the
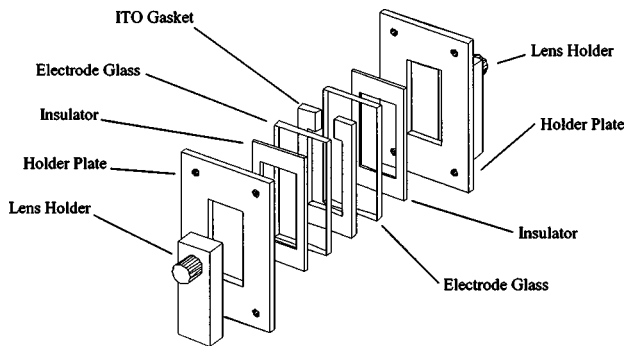
Fig. 2 Schematic of EC fluid window

Fig. 3 Schematic of experimental apparatus

stirring process. Prior to filling the cavity of the EC fluid window, baseline transmittance through the glass windows filled only with silicone oil was measured.

Parameters of the EC fluids studied and their ranges are given as follows:

- Particles of 11, 25, and 40-micron diameters were studied
- Particle volume fractions varied from 0.0025 (0.25 percent) to 0.0150 (1.5 percent)
- Electric field strengths ranged from $V_f = 100 \, V_{rms}$/mm to $V_f = 500 \, V_{rms}$/mm, at a frequency of 60 Hz
- Path lengths were varied between 0.7 mm and 2.2 mm

Model Development

Thermal radiation energy transport in an absorbing, emitting, and/or scattering medium is described by the radiation transfer equation [15]. Since operating temperatures involved with EC fluids are typically low, the contribution due to emission is neglected. Transport of a beam of energy of wavelength λ passing through a medium is a function of the transport properties of the medium and the path length through the medium, $0 \leq s \leq L$. The change in intensity of an incident beam, I, due to absorption in the distance ds is thus written as

$$dI_{abs} = -\kappa_\lambda I ds \qquad (1)$$

where the negative sign denotes a decrease in intensity, and κ_λ is the *absorption coefficient*. Similarly, the portion of the energy traveling through the medium that is redirected or scattered is given as

$$dI_{sca} = -\sigma_\lambda I ds \qquad (2)$$

where σ_λ is the *scattering* coefficient for all directions. When emission and in-scattering are neglected (i.e. $\beta_\lambda L \ll 1$), and if the medium is homogeneous, the simple Beer's Law relationship is appropriate

$$I(s) = I(0)e^{-\beta_\lambda s} \qquad (3)$$

where

$$\beta_\lambda = \kappa_\lambda + \sigma_\lambda \qquad (4)$$

is the extinction coefficient for the medium. For a particulate medium, the extinction coefficient may be written as

$$\beta_\lambda = N(C_{sca} + C_{abs}) \qquad (5)$$

where N is the number of particles per unit volume and C_{sca} and C_{abs} are the scattering and absorption cross-sections. Beer's Law gives an expression for the intensity of radiation at any point s along the path length as a fraction of the intensity entering the medium at $s = 0$. The ratio $I(s)/I(0)$ is the transmittance, and is denoted by the symbol τ.
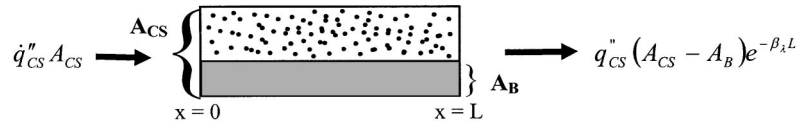
Fig. 5 Side view of volume of EC fluid with energy terms

A beam of light is attenuated by both absorption and scattering. Although absorption may be the dominant mode of attenuation, scattering is never entirely absent [13]. If the effect of scattering is minimal, the absorption can be modeled as the sole cause of attenuation.

Attenuation by particles is related to their size and optical properties. An electron micrograph of Zeolite, in Fig. 4, shows that the surface of the Zeolite particles is rough and dominated by pockets on the order of microns. Zeolite particles thus are expected exhibit significant absorption by multiple reflections within the pockets on its surface [15], which suggests that the particles may be modeled as black.

Since the surface characteristics indicate that absorption will be strong, we may presume that the absorptive index k is reasonably large. Considering the radiation wavelengths employed in this investigation, one can see that the value of the parameter

$$kx = 2k\pi a/\lambda \qquad (6)$$

will be much greater than one. Therefore, we may treat the particles as large opaque spheres and invoke the extinction paradox, which states that a large particle will remove twice the amount of light from an incident beam as it can intercept. Hence, the extinction efficiency, defined as

$$Q_{\text{ext}} = C_{\text{ext}}/\pi a^2 \qquad (7)$$

where

$$C_{\text{ext}} = C_{\text{abs}} + C_{\text{sca}} \qquad (8)$$

will always have a value of exactly two [9]. Since particles of this size are described well by geometric optics, where the projected area of a particle for absorption and reflection is πa^2, half of this extinction efficiency is due to diffraction. Exactly how much of the other half is due to absorption, and how much is due to reflection, will depend upon the reflectivity of the particle surface.

In an effort to determine the role of reflection in the energy transport through the EC fluid, the light sensor of the spectrometer was moved in small increments along a direction transverse to the incident beam and transmittance levels were measured. The results clearly showed that there was negligible transmittance in directions other than that of the beam [14]. Hence, it was assumed that the dominant mode of attenuation in these EC fluids is absorption and that reflection played at most a minor role.

Equation (3) may then be rewritten as (under the assumption of uniform distribution of the particles)

$$\tau = e^{-\beta_\lambda L} \qquad (9)$$

Combining Eqs. (5), (7), and (8) yields an expression for the extinction coefficient

$$\beta_\lambda = \pi a^2 N Q_{\text{ext}} \qquad (10)$$

The number of particles per unit volume may then be expressed as

$$N = \frac{f_v}{\text{Volume}_{\text{particle}}} \qquad (11)$$

and if the particles can be modeled as spheres of uniform size, this equation becomes

$$N = \frac{3f_v}{4\pi a^3} \qquad (12)$$

Substituting Eq. (12) into Eqs. (9) and (10) yields a simple model for transmittance in terms of the EC fluid particle volume fraction, path length and particle size

$$\tau = e^{-3f_v L/2a} \qquad (13)$$

The extinction coefficient is

$$\beta_\lambda = \frac{3f_v}{2a} \qquad (14)$$

Consider now the case where the particles form chains in the presence of an electric field V_f with field lines oriented parallel to a beam of incident radiant energy. We assume also that a uniform incident energy beam illuminates the EC fluid. The beam can be thought of as a cylinder of cross-sectional area A_{CS}, and its length is the path length L. Experimental observations [16] revealed that the optical path can be characterized as two parallel paths: one defined by the presence of the particle chains and by the presence of tubes of fluid and a small number of unchained particles at more or less random locations.

In some preliminary experiments, the authors observed that the base of the field-induced chains, which is immediately adjacent to the electrodes, contains multiple particles that form a typically conical geometry [16]. The incident radiant energy is completely absorbed by the particles of the base of these cones. There is then a portion of the cross-sectional area of the cylindrical volume (A_{CS}) that is completely blocked by the cumulative area defined by the base of the chains (A_B).

Consider then a beam of energy per unit area (q''_{CS}) with cross-section A_{CS}. As illustrated in Fig. 5, the total energy striking the EC fluid at x=0 is reduced as it passes through the fluid via two mechanisms: (1) a complete absorption of energy in the area blocked by the chains and their base, and (2) a partial absorption of energy via extinction by the remaining particles which exist in the fluid tubes. Thus, one can see that

$$\tau = \left(1 - \frac{A_B}{A_{CS}}\right) \cdot e^{-\beta_\lambda L} \qquad (15)$$

For the case where $A_B = A_{CS}$ transmittance will be zero, and the case where $A_B = 0$ transmittance will be given by the model for purely dispersed particles.

It remains now to determine A_B and β_λ as a function of the specific EC fluid properties and the applied field strength. The cross-sectional area of the beam (A_{CS}), the radiation path length (L) and the particle volume fraction (f_v) are not affected by field strength.

As stated previously, visual experimental observations revealed that a number of particles present in the EC fluid form conical geometries at the base of the chains [16]. The observed cone typically exhibited a tightly packed, hexagonal pattern similar to that shown in Fig. 6.

The base of the typical chain was approximately five particle diameters across. If we define the number of particles across the base as n (here $n=5$) then the total number of particles in the base layer is given by

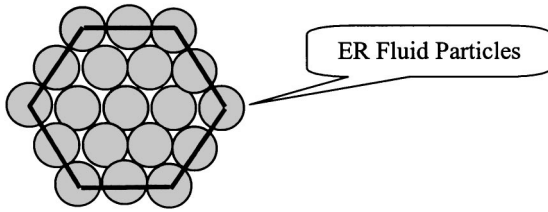$$P_{\text{BASE}} = n + \sum_{i=1}^{(n-1)/2} 2(n-i) \qquad (16)$$

Fig. 6 Modeled particle geometry at the base of the electrode

Fig. 7 Volumes excluded in the approximation of Eq. (28)

The area blocked by the base, A_{END}, is the area of the hexagon made by connecting the center points of the particles at the vertices of the hexagon of Fig. 6, the area of the outer portions of those six particles at the vertices, and the areas of the half-circles for the particles along the edges of the hexagon. Accordingly, the blocking area of the typical end of a chain is

$$A_{\text{END}} = \frac{3[(n-1)a^2]}{\sqrt{2}} + \left(\frac{3(n-1)-6}{2}\right)\pi a^2 + 6\left(\frac{2}{3}\pi a^2\right) \tag{17}$$

The number of potential chains present now remains to be determined. First, consider the number of particles that make up the conical structure at the ends of the chains. Particles will typically form in successive, distinct hexagonal layers of fewer particles away from the base layer. This continues until a chain of single particles is initiated which will in turn reach across the medium to the counterpart base formed at the opposite electrode. Thus, particles at the electrode will form a hexagonal shape with a number of particles across the base n. On top of that another hexagonal layer will form of $n-2$ particles across its base, followed by another of $n-4$ particles and so on until a single particle chain is initiated from the layer having a number of particles across its base given by $n=3$.

Thus the number of particles in a cone is given by

$$P_{\text{CONE}} = \sum_{j=1}^{(n-1)/2}\left[p + \sum_{i=1}^{(p-1)/2} 2(p-i) \right] \tag{18}$$

where

$$p = n - 2(j-1) \quad n = 3,5,7\ldots \tag{19}$$

The number of levels present in a cone is

$$N_{\text{LEVELS}} = \frac{n-1}{2} \tag{20}$$

Thus the total number of particles in a chain is determined by adding the particles present in the two base cones plus the particles forming a single chain between them

$$P_{\text{CHAIN}} = 2P_{\text{CONE}} + (L - 2N_{\text{LEVELS}}\cdot 2a)/2a \tag{21}$$

Equation (21) can be rewritten as

$$P_{\text{CHAIN}} = 2P_{\text{CONE}} + L/2a - 2N_{\text{LEVELS}} \tag{22}$$

or, in terms of the relationships so far developed

$$P_{\text{CHAIN}} = 2\sum_{j=1}^{(n-1)/2}\left[p + \sum_{i=1}^{(p-1)/2} 2(p-i) \right] + \frac{L}{2a} - 2\left(\frac{n-1}{2}\right) \tag{23}$$

It is also necessary to determine the number of particles available in a specified volume (N_V). Consider the ratio of volume fraction to the volume of particles as a measure of particles per unit volume. For the illuminated volume of Fig. 5, based on the assumption that the total number of particles is
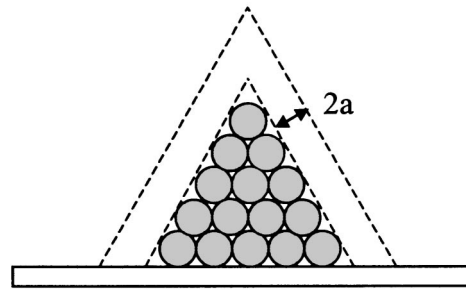
$$N_V = \frac{f_v}{V_{\text{particle}}}\cdot A_{CS}L = \frac{3f_v A_{CS}L}{4\pi a^3} \tag{24}$$

The maximum number of possible chains (C_{max}) is

$$C_{\text{max}} = \frac{N_V}{P_{\text{CHAIN}}} \tag{25}$$

This leads to an expression for the maximum total blocking area (A_B) as

$$A_B = IC_{\text{max}}\cdot A_{\text{END}} \tag{26}$$

where IC_{max} is defined as the integer value of C_{max}. The number of particles remaining that do not form chains, P_{DISP}, can now be determined

$$P_{\text{DISP}} = N_V - (IC_{\text{max}}\cdot P_{\text{CHAIN}}) \tag{27}$$

Naturally, when chains form there will remain a smaller volume for the unchained particles to reside. This is given by

$$V_{\text{DISP}} = A_{CS}L - (IC_{\text{max}}\cdot P_{\text{CHAIN}}\cdot 4/3\pi a^3) \tag{28}$$

Equation (28) is an approximation since it neglects the volume between two particles in a chain and the region defined by an outer shell a distance of $2a$ away from the cone where particles cannot reside. This is illustrated in Fig. 7.

Thus a new volume fraction (f_{vr}), which is the volume fraction of the unchained particles in the reduced volume, can be determined

$$f_{vr} = \frac{4/3\pi a^3 P_{\text{DISP}}}{V_{\text{DISP}}} \tag{29}$$

This reduced volume fraction is now used in the extinction coefficient term of the basic model Eq. (9)

$$\beta_{\lambda R} = \frac{3f_{vr}}{2a} \tag{30}$$

The primary effect of applied electric field is to form chains from otherwise dispersed particles. Very low field strengths often are observed to form small numbers of complete chains that reach from one electrode to the other. The actual number of chains thus can be less than C_{max}. Large field strengths create longer chains, approaching C_{max}. This gives rise to the concept of a chaining efficiency factor, $\eta(V_f)$, that is a function of field strength. Hence, the actual number of chains formed C is

$$\eta(V_f) \equiv \frac{C}{C_{\text{max}}} \tag{31}$$

An empirical relationship for chaining efficiency as a function of field strength was determined that best-fit the experimental data

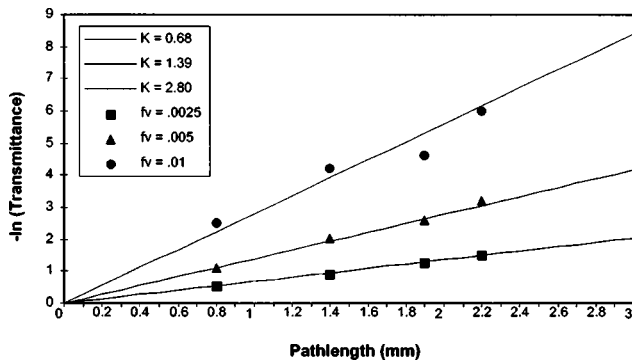$$\eta(V_f) = 0.96\left(\frac{V_f}{V_f+20}\right)^{0.7} \tag{32}$$

Fig. 8 Transmittance in dispersed state for varying volume fractions as a function of path length

It must be understood that this relationship is empirical and is representative of our experiments. The 0.96 factor is an empirical constant that ensures that $\eta(V_f) < 1$. The model for transmittance can now be written in the form:

$$\tau = \left[1 - \frac{\eta(V_f) IC_{\max} \cdot A_{\mathrm{END}}}{A_{CS}} \right] \cdot e^{-\beta_{\lambda R} L} \tag{33}$$

Values for $IC_{\max}$, A_{END}, and $\beta_{\lambda R}$ are determined from Eqs. (25), (17), and (30), respectively.

Experimental Uncertainty

Prior to the presentation of transmittance measurements, experimental uncertainty is addressed by considering Eq. (13) and rewriting transmittance in terms of transmitted energy through the EC fluid (I) divided by transmitted energy through an empty window (I_o). The measured energy transmitted through the EC fluid has been modeled as

$$I = I_o e^{-3f_v L/2a} \tag{34}$$

Measurement error levels acceptable in experimental analysis were determined, and the contribution due to measurement of volume fraction was found to be most critical. This was calculated by the formula:

$$\mathrm{ERROR} = \left[\left| \frac{\partial I}{\partial I_o} \delta I_o \right|^2 + \left| \frac{\partial I}{\partial f_v} \delta f_v \right|^2 + \left| \frac{\partial I}{\partial L} \delta L \right|^2 + \left| \frac{\partial I}{\partial a} \delta a \right|^2 \right]^{1/2} \tag{35}$$

Maximum errors in the experimental measurement of transmitted beam intensity were found to be 14.0 percent.

Results and Discussion

Experiments were conducted throughout the investigation in which data from multiple trials was collected. In all cases, measurements were made after sufficient time to observe a steady measurement on the instrumentation utilized in the experimental apparatus. In all cases, transmittance values were measured at a wavelength of 684 nm, which was representative of the location of average transmittance levels over the entire spectrum.

Consider first transmittance as a function of beam path length. Energy transmitted through EC fluids with particle volume fractions of 0.0025, 0.0050, and 0.0100 were first measured for path lengths ranging from 0.8 mm to 2.2 mm with no electric field applied. Each of these fluids used particles that had an average diameter of 11 microns. From measured transmittances for each volume fraction, Eq. (9) was used to determine corresponding extinction coefficients, and these coefficients were then averaged (K). Figure 8 shows the measured transmittance data points plotted on a natural logarithm scale with linear extinction lines drawn using the average extinction coefficients K.

Table 1 Experimentally averaged versus calculated extinction coefficients

Volume fraction	K (experimentally averaged)	β_λ (calculated)
0.0025	0.68	0.68
0.0050	1.39	1.36
0.0100	2.80	2.73

The experimentally averaged extinction coefficients of Fig. 8 were then compared to coefficients calculated directly from Eq. (14). The results are tabulated in Table 1. Note that the largest difference between experimental and calculated values is 2.6 percent.

In further experimental work, transmittance through EC fluids made with particles of varying size was measured. As stated earlier, the particle diameters ($2a$) were 11, 25, and 40 microns respectively. The volume fraction for each of these fluids was held at a constant value of 0.005. Again using Eq. (9), average extinction coefficients are determined based on these measurements. Figure 9 shows the measured transmittance data points with extinction lines drawn using the average extinction coefficients.

Once again, these average extinction coefficients are compared to theoretical values calculated directly from Eq. (14), with these results tabulated in Table 2.

Note here that the largest difference between experimental and calculated values is 3.7 percent.

Figure 10 presents experimental data of transmittance as a function of volume fraction taken at $V_f = 160$ V$_{\mathrm{rms}}$/mm. Superimposed against this is a line drawn to represent the model of Eq. (33). Table 3 summarizes comparisons of transmittance from experimental results to model prediction values. Note that the largest error difference between experimental and calculated values is 9.8 percent.

Experimental evidence of the effect of field strength is presented in Fig. 11. Here we see that the increase in transmittance as field strength increases is not dramatic, but is clearly significant. It is also evident that as field strength increases, the data scatter tends to decrease. This supports the concept that at higher field strengths, not only is the chaining efficiency greater, but also a higher order of uniform chain structure is realized. Thus, it is
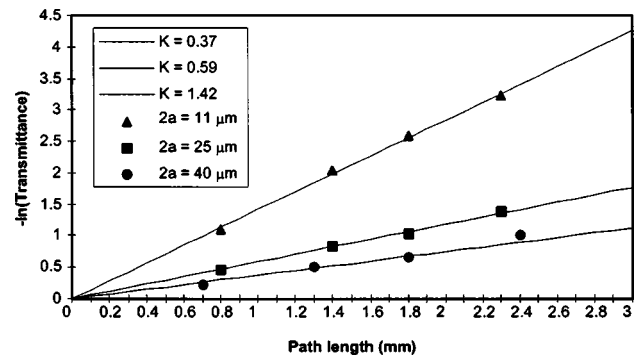

Fig. 9 Transmittance in dispersed state for varying particle sizes as a function of path length

Table 2 Experimental averaged versus calculated extinction coefficients

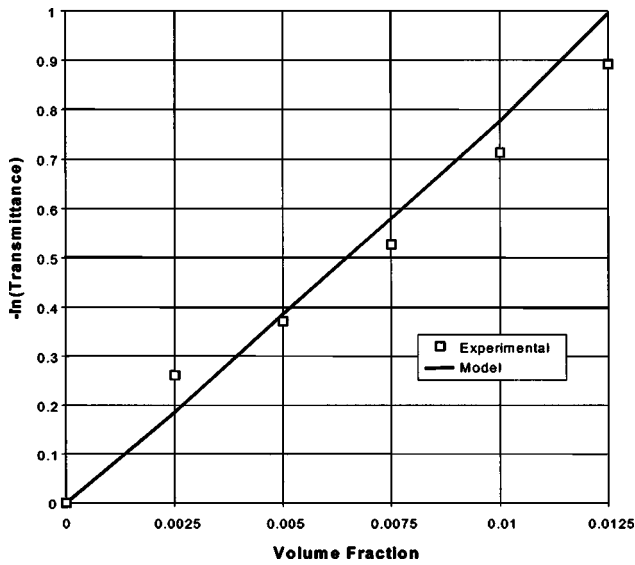| Particle Diameter	K (experimentally averaged)	β (calculated)
11 μm	1.42	1.36
25 μm	0.59	0.60
40 μm	0.37	0.38

Fig. 10 Transmittance in the chained particles state as a function of volume fraction (V_f=160 V_{rms}/mm, L=1.9 mm, $2a$=11 μm)

suggested that much more predictable transmittance levels can be obtained with higher field strengths. In the graphic, an EC fluid of volume fraction 0.0075 was subjected to increasing field strengths until arcing across the electrodes occurred.

Table 4 summarizes comparisons of transmittance from mathematically averaged experimental results to model prediction values. Note that the largest error difference between experimental and calculated values is 6.8 percent.

Table 3 Experimental versus calculated transmittance levels (V_f=160 V_{rms}/mm, L=1.9 mm, $2a$=11 μm)

Volume Fraction	Experimental Transmittance	Model Prediction (Eq. 33)
0.0025	0.77	0.83
0.0050	0.69	0.68
0.0075	0.59	0.56
0.0100	0.49	0.46
0.0125	0.41	0.37
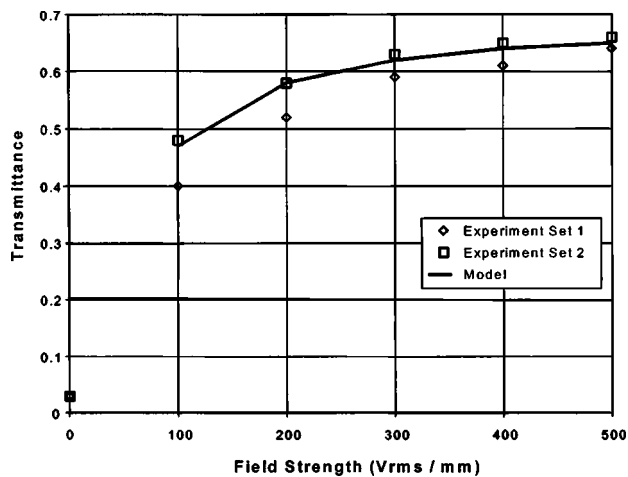
Fig. 11 Effect of field strength on transmittance (V_f=160 V_{rms}/mm, L=1.9 mm, $2a$=11 μm)

Table 4 Experimental versus calculated transmittance levels (V_f=160 V_{rms}/mm, L=1.9 mm, $2a$=11 μm)

Field Strength (V_{rms}/mm)	Average Experimental Transmittance	Model Prediction (Eq. 33)
100	0.44	0.47
200	0.55	0.58
300	0.61	0.62
400	0.63	0.64
500	0.64	0.65

Conclusions

An analytical/empirical model has been developed for EC fluids made of Zeolite particles that describes radiative heat transfer through a composite window. An empirical particle chaining efficiency coefficient for electric field strength is proposed. This model was developed based on the assumption that the dominant mode of attenuation is due to absorption, and that the role of scattering is negligible.

Experimental data was taken that shows excellent agreement between experimental levels of transmittance and those predicted from the model. This demonstrates that attenuation of radiation can be predicted by treating the dominant mode of extinction as absorption.

This basic model for describing radiative heat transfer in EC fluids provides a useful design tool for applications utilizing the uniquely controllable properties of EC fluids.

Acknowledgments

Nomenclature

a = mean particle radius
f_v = particle volume fraction
f_{vr} = reduced volume fraction
k = absorptive index
u = direction unit vector
A_B = area of blocking particle-chain face
A_{CS} = cross-sectional area
A_{END} = area blocked by end of particle chain
C = actual number of particle chains
C_{abs} = absorption cross section
C_{ext} = extinction cross section
C_{sca} = scattering cross section
C_{max} = maximum number of particle chains
q_s'' = beam energy per unit area
I = incident energy
I_{abs} = incident energy absorbed
I_o = incident energy through an empty window
I_{sca} = incident energy scattered
IC_{max} = integer value of maximum number of particle chains
K = calculated experimental average extinction coefficient
L = the extinction path length of EC fluid
n = number of particles across chain base
N = number of particles per unit volume
N_{LEVELS} = number of particle levels in a cone
N_V = total number of particles per volume of EC fluid
P_{BASE} = number of particles in the base layer
P_{CHAIN} = number of particles in a single chain
P_{CONE} = number of particles in the base cone
P_{DISP} = particles that do not form chains
Q_{ext} = extinction efficiency
s = directional variable
V_{DISP} = reduced volume for unchained particles

V_f = RMS voltage field strength (volts per millimeter)
$V_{particle}$ = volume of an individual particle
x = particle size parameter
β, β_λ = extinction coefficient
β_R = reduced extinction coefficient
η = efficiency factor
κ_λ = absorption coefficient
λ = incident radiation wavelength
σ_λ = scattering coefficient
τ = transmittance

References

[1] Shu'lman, Z. P., 1982, "Utilization of Electric and Magnetic Fields for Control of Heat and Mass Transfer in Dispersed Systems (Suspensions)," Heat Transfer-Sov. Res., **14**(5), p. 1.

[2] Zhang, C., and Lloyd, J. R., 1994, "Control of Radiation Heat Transfer Through a Composite Window Featuring ER Fluid: A Conceptual Investigation," Inzh.-Fiz. Zh., **6**(2), pp. 131–142.

[3] Zhang, C., and Lloyd, J. R., 1992, "Measurements of Radiation Heat Transfer in Electrorheological Fluid Based Composite Materials," *Developments in Radiative Heat Transfer*, 1992 National Heat Transfer Conference, HTD-Vol. 20, San Diego, CA, pp. 55–62.

[4] Yanju, L., Jinsong, L., and Dianfu, W., 2000, "Adaptive Optical Properties of ER Fluid Incorporating Composite Particles," Opt. Lasers Eng., **34**, pp. 47–53.

[5] Radcliffe, C. J., Lloyd, J. R., Andersland, R. M., and Hargrove, J. B., 1996, "State Feedback Control of Electrorheological Fluids," ASME International Mechanical Engineering Congress and Exhibition, Atlanta, Georgia, Nov. 1996.

[6] Tabatabai, S., 1993, "Aspects of Radiation Heat Transfer in ER Fluid Based Composite Windows," Studienarbeit (Student Thesis), Rheinisch-Westfalrsche Technische Hochschule Aachen/Michigan State University.

[7] Mimouni, Z., Bossis, G., Mathis, C., Meunier, A., and Paparoditis, C., 1990, "Field Induced Structure in a Colloidal Suspension," Prog. Colloid Polym. Sci., **81**, pp. 120–125.

[8] Ginder, J. M., 1993, "Diffuse Optical Probes of Particle Motion and Structure Formation in an Electrorheological Fluid," Phys. Rev. A, **47**(5), pp. 3418–3429.

[9] van de Hulst, H. C., 1957, *Light Scattering by Small Particles*, John Wiley and Sons, New York.

[10] Kerker, M., 1969, *The Scattering of Light and Other Electromagnetic Radiation*, Academic Press, New York.

[11] Brewster, M. Q., and Tien, C. L., 1982, "Radiative Transfer in Packed Fluidized Beds: Dependent Versus Independent Scattering," ASME J. Heat Transfer, **104**, p. 573.

[12] Buckius, R. O., 1986, "Radiative Heat Transfer in Scattering Media: Real Property Considerations," *Proc. of Eighth International Heat Transfer Conference*, **1**, p. 141.

[13] Bohren, C. F., and Huffman, D. R., 1983, *Absorption and Scattering of Light by Small Particles*, John Wiley and Sons, New York.

[14] Hargrove, J. B., Lloyd, J. R., and Radcliffe, C. J., 1996, "Radiation Heat Transfer Modeling in Electrorheological Fluids: Treatment as an Absorbing Medium," Conference Proceedings, ASME International Mechanical Congress and Exposition, Atlanta, GA.

[15] Modest, M. F., 1993, *Radiative Heat Transfer*, McGraw-Hill, New York.

[16] Cristescu, N., 2000, "Dynamic Simulation of the Electrorheological Effect in a Uniformly Distributed Electric Field," Master's thesis, Michigan State University, East Lansing, MI.

Yuan Zheng

Maurice J. Zucrow Laboratories,
School of Mechanical Engineering,
Purdue University,
West Lafayette, IN 47907-2014, USA

R. S. Barlow

Combustion Research Facility
Sandia National Laboratories
Livermore, CA 94550-0969, USA

Jay P. Gore

e-mail: gore@ecn.purdue.edu.
Maurice J. Zucrow Laboratories,
School of Mechanical Engineering,
Purdue University,
West Lafayette, IN 47907-2014, USA

Spectral Radiation Properties of Partially Premixed Turbulent Flames

Instantaneous spectral radiation intensities of three standard turbulent jet flames were measured and simulated in this study. In the simulation, a recently developed technique was adapted to reconstruct the local integral time and length scales in the flames. The simulated radiation properties, including mean, root mean square, probability density function, power spectral density and autocorrelation coefficient, were generally within 10% of the measurements. The macro time and length scales were found to increase with increasing distance from the axis and the radial averages of these scales were found to increase with down stream distance but decrease with Reynolds number.
[DOI: 10.1115/1.1621902]

Keywords: Combustion, Heat Transfer, Monte Carlo, Radiation, Turbulence

Introduction

This experimental and computational study is an extension of earlier work on the spectral radiation properties of standard turbulent jet flames [1,2]. Three non-sooting piloted CH_4/air flames from the workshop of Turbulent Nonpremixed Flames (TNF) [3] were considered in this study. Infrared (IR) flame radiation properties, including mean, root mean square (RMS), probability density function (PDF), power spectral density (PSD) and autocorrelation coefficient (ρ), were derived from the measured and the simulated instantaneous line-of-sight (LOS) spectral radiation intensities (I_λ) as described in the appendix. Time averaged radiation quantities of these flames, such as the total radiation heat loss, were reported in Ref. [4]. The present study of transient spectral radiation properties provides complementary and deeper information about the radiation heat transfer particularly with regards to the influence of turbulent fluctuations.

Accurate prediction on radiation heat transfer is important in modeling pollutant formation [4–6]. Experimental data are necessary for evaluating the radiation models. LOS spectral radiation intensities have been widely investigated experimentally in non-sooting [7,8] and sooting [6,9] turbulent flames. Most of these studies, however, were limited to radiation paths defined by the diameter of an imaginary circular cross section of the flames normal to the axis at fixed heights above the fuel injector. Extending the measurements to multiple chord-like paths parallel to the diameter in the same circular cross plane is very useful for better understanding of turbulent-radiation interactions (TRI) as indicated by recent studies [1,2]. Using a fast IR array spectrometer (FIAS) [10], our present measurements provide a more complete database of radiation properties for the three non-sooting flames. For these flames, detailed scalar property measurements have been made and examined by others with the best available instrumentation over the last 5 to 10 years [3]. The availability of scalar property measurements has contributed greatly to the studies of radiation properties. More reliable evaluation on the radiation models can be achieved without the uncertainties of the scalar predictions.

Inverse interpretation of radiation properties can provide insights into integral time (τ_I) and length scales (l_I) of the scalar fluctuations along a radiation path [1]. Although these macro scales are important characteristics of the turbulent flames, only a

few direct measurements of these quantities have been reported. Therefore, the behavior of macro scales in turbulent flames remains an active area of interest. Faeth et al. [7] measured l_I and τ_I for mixture fraction fluctuations in two turbulent carbon monoxide/hydrogen flames by using a two-point Mie-scattering technique. Renfro et al. [11] investigated τ_I for mixture fraction fluctuations in several turbulent non-premixed flames. They derived τ_I from inverse interpretation of the time series of minor-species from picosecond time-resolved laser-induced fluorescence (PITLIF) measurements. More recently, Karpetis and Barlow reported a study on mixture fraction length scales in a partially premixed methane/air flame by using line-imaging measurements [12]. In the present study, the tomography-like technique developed by Zheng et al. [1] is extended to reconstruct local integral time and length scales of scalar fluctuations along the radiation paths. The tomography-like technique includes inverse time and space series (TASS) calculations based on fitting the calculated RMS values and the autocorrelation coefficients of I_λ to the experimental data.

Experimental Method

The radiation measurements for the three piloted CH_4/air flames were conducted at the Turbulent Combustion Laboratory at Sandia National Laboratories. These are flames C, D, and E of the TNF workshop with nominal jet exit Reynolds number of 13,400, 22,400, and 33,600 respectively based on exit velocity, cold gas properties and fuel injector diameter. Flow facilities of the piloted flames have been discussed elsewhere [13] and will only be briefly described here. The piloted burner, on which flames are stabilized, has a main jet diameter (D) of 7.2 mm and a pilot diameter of 18.2 mm. The main CH_4/air jet is partially premixed with an equivalence ratio of 3.17 (25% CH_4 by volume). The lean premixed pilot flame burns a mixture of C_2H_2, H_2, CO_2, N_2 and air, having the same enthalpy and equilibrium composition as a CH_4/air flame with an equivalence ratio of 0.77. The burner can be moved in three dimensions for positioning. Air co-flows were fed through a wind tunnel with a co-flow velocity of 0.9 m/s for the piloted flames. The flow rates were carefully matched between the radiation and the scalar measurements even though these measurements were completed at different times.

For each flame, instantaneous I_λ for the diametric and many chord-like paths at three heights above the fuel injector were measured using the latest version of FIAS. The spectral range of this FIAS is from 1.4 to 4.8 μm with a mean resolution of 44 nm, covering the important molecular radiation bands of H_2O and

CO_2. The sampling rate for the individual wavelengths is 6250 Hz. The spatial resolution of the present measurements is 2 mm based on the FIAS optics. For each radiation path, 6000 samples were collected. The experimental uncertainties (95% confidence) of I_λ measurement were of the order of 10% [2] and repeatable within this range. The uncertainties were dominated by the effect of finite sampling time available in the continuous scanning process.

Computational Method

In present study, time and space series analysis (TASS) accounting for two-point/two-time statistics were used first to simulate instantaneous realizations of the scalar properties along a non-homogenous radiation path. Then, the instantaneous I_λ leaving that path were calculated by using RADCAL program with a narrow band radiation model [14]. The spectral radiation properties were extracted from the 6000 simulated realizations for each radiation path. The TASS based computational method, involving a tomography-like procedure to reconstruct the local integral time and length scales of scalar fluctuations along the radiation paths, has been discussed in detail elsewhere [1] and will only be briefly described here.

In the TASS simulation, specific stochastic processes are used to mimic the nature of turbulent fluctuations. Specifically, the temporal (τ) and spatial (k) evolutions of a normalized fluctuating scalar (z) were modeled by the following equation,

$$z_k(\tau) = \phi_1 z_{k-1}(\tau) + \phi_2 z_k(\tau - \Delta\tau) + a_k(\tau) \qquad (1)$$

The instantaneous scalar realizations were related to z through a mapping procedure [15]. Equation 1 can be extended to include influence from points outside the radiation path under consideration if computational resource is affordable. ϕ_1, ϕ_2 and the standard deviation of random shock (a) can be determined by the spatial and temporal correlation coefficients of scalar fluctuations $\rho(\Delta r)$, $\rho(\Delta\tau)$ [1], which were modeled with the integral time and length scales by the following equation,

$$\rho(\Delta r) = \exp(-\Delta r/l_I), \rho(\Delta\tau) = \exp(-\Delta\tau/\tau_I) \qquad (2)$$

In this study, τ_I and l_I were determined by an inverse calculation designed to match the RMS values and autocorrelation coefficients of the measured spectral radiation intensities. The single-point statistics (mean, PDF) of the TNF scalar data [3] were used as the inputs to the simulation.

In a previous study [1], the Taylor's hypothesis was adapted to relate l_I and τ_I. The Taylor's hypothesis, assuming that the turbulence pattern is translated at the local mean velocity, may not hold under some circumstances [16]. In addition, the velocity data may not be available for some of the cases. In present study, τ_I and l_I were determined independently from the spectral radiation data allowing a direct test of the Taylor's hypothesis. A least mean square (LMS) scheme was developed in the present work to determine the best-fit macro-scales. Spectral radiation intensities at two wavelengths (λ) were considered in order to minimize the computational time. Since the flame radiation under investigation was dominated by band radiation from water vapor and carbon oxide, wavelengths of (λ_1) 2.51 and (λ_2) 4.27 μm were selected to represent radiation from H_2O and CO_2 respectively. The procedure involved calculations of the RMS and ρ for the spectral radiation intensities and is briefly described as follows,

Step 1. Guess l_I and τ_I so that instantaneous I_λ can be simulated.

Estimates of l_I in a $CH_4/H_2/N_2$ jet flame from Ref. [1] were used as the initial guesses for flame D and the τ_I were guessed by using Taylor's hypothesis. The estimates of l_I and τ_I for flame D were also used as the initial guesses for flames C and E.

Step 2. Calculate RMS and ρ of the spectral radiation intensity from the simulated instantaneous values.

Step 3.1. Obtain the square of errors (e) between calculations (c) and data (d) in RMS for λ_1 and λ_2.

$$e_1 = ((I_{\lambda\text{rms}}/I_{\lambda\text{mean}})_c - (I_{\lambda\text{rms}}/I_{\lambda\text{mean}})_d)^2, \quad \lambda = \lambda_1 \qquad (3a)$$

$$e_2 = ((I_{\lambda\text{rms}}/I_{\lambda\text{mean}})_c - (I_{\lambda\text{rms}}/I_{\lambda\text{mean}})_d)^2, \quad \lambda = \lambda_2 \qquad (3b)$$

Step 3.2. Obtain the square of errors in ρ for λ_1 and λ_2. (ρ has n temporal components)

$$e_3 = \frac{1}{n}\sum_{i=1}^{n}(\rho_c - \rho_d)^2, \quad \lambda = \lambda_1 \qquad (4a)$$

$$e_4 = \frac{1}{n}\sum_{i=1}^{n}(\rho_c - \rho_d)^2, \quad \lambda = \lambda_2 \qquad (4b)$$

Step 3.3. Obtain the weighted mean square error.

$$e = \left(\frac{1}{4}\right)\sum_{i=1}^{4} e_i \qquad (5)$$

Step 4. Use the error minimization criteria to obtain new estimates of l_I and τ_I.

$$\frac{\partial e}{\partial l_I} = 0 \quad \text{and} \quad \frac{\partial e}{\partial \tau_I} = 0 \Rightarrow l_I, \tau_I \qquad (6)$$
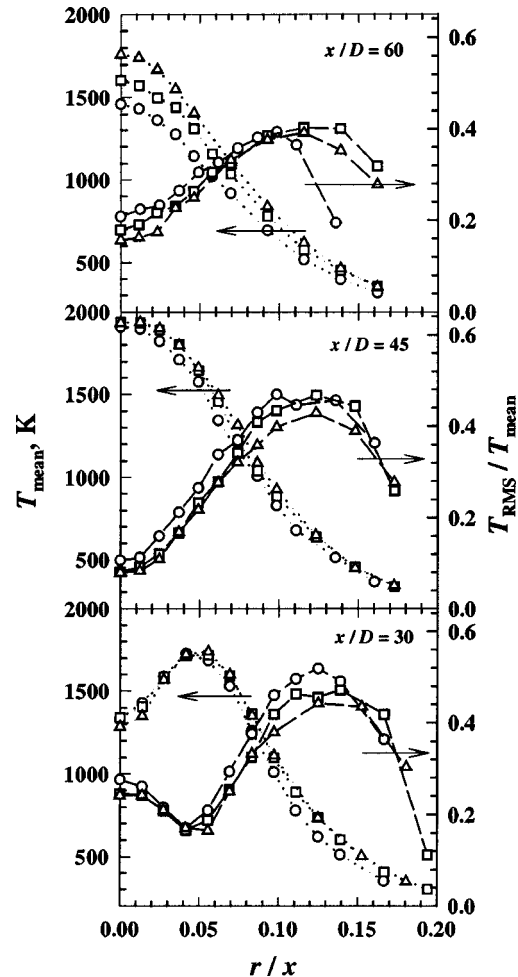

Fig. 1 Temperature distributions in flames C (circle), D (square) and E (triangular)
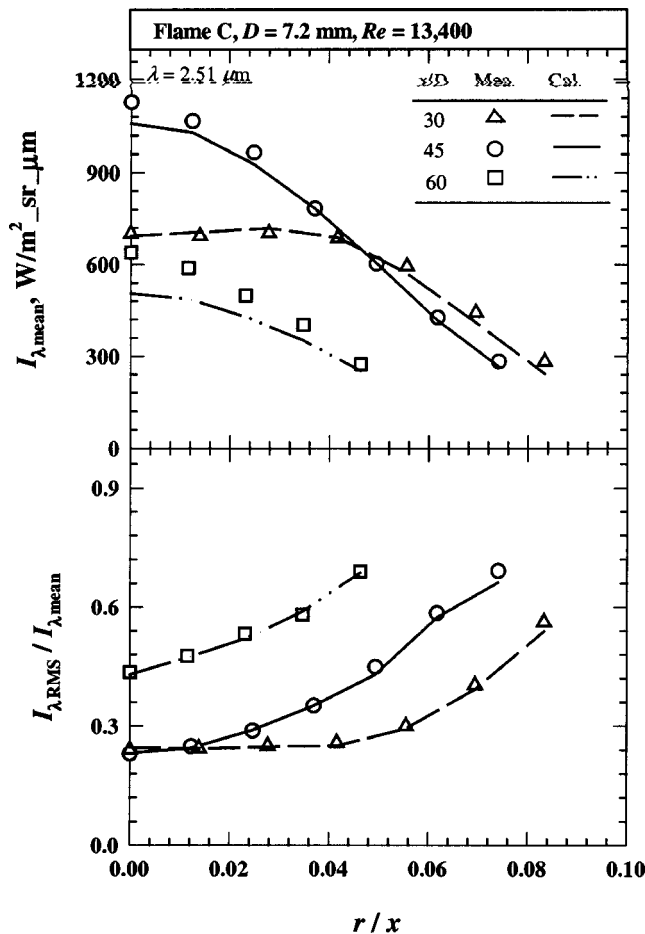
Fig. 2 Spectral radiation intensities of flame C at λ=2.51 μm

For the farthest downstream location of $x/D=60$ studied here, the maximum mean temperatures and the normalized temperature fluctuations both decrease compared to their values at the $x/D=45$ location. In contrast to those at the two upstream locations, the higher Reynolds number flames show significantly higher mean temperatures. The temperature fluctuations in the region near the axis at $x/D=60$ decrease with increase in the Reynolds number.

Results and Discussion

Measurements and calculations of mean and normalized RMS of I_λ emitted by flame C at $\lambda=2.51$ and 4.27 μm are illustrated in Figs. 2 and 3. The calculations captured the trends in the radial distributions of the mean and the normalized RMS of I_λ for different axial locations. The calculations were also generally in good agreement with the measurements with differences of between 10% and 20% at most locations. The mean intensities at $\lambda=4.27$ μm are about 5 times higher than those at $\lambda=2.51$ μm. The mean intensities for diametric path at $x/D=45$ are much higher than those for the diametric paths at downstream or upstream locations. At $x/D=30$, the mean I_λ increases slightly from the diametric path to the chord-like path at $r/x=0.05$ and then decreases to the flame edge. For the two upstream locations, the mean intensities for chord-like paths decrease with the radial distance as a combined result of shorter radiation path and less hot media being included. For all three axial locations, the fluctuations in radiation intensities increase with the radial distance. The radiation fluctuation levels at $x/D=60$, however, are much then those at two upstream locations. This is consistent with the scalar distributions depicted in Fig. 1, which shows that the normalized scalar fluctuations in flame C at $x/D=60$ are much higher than those at the upstream locations.
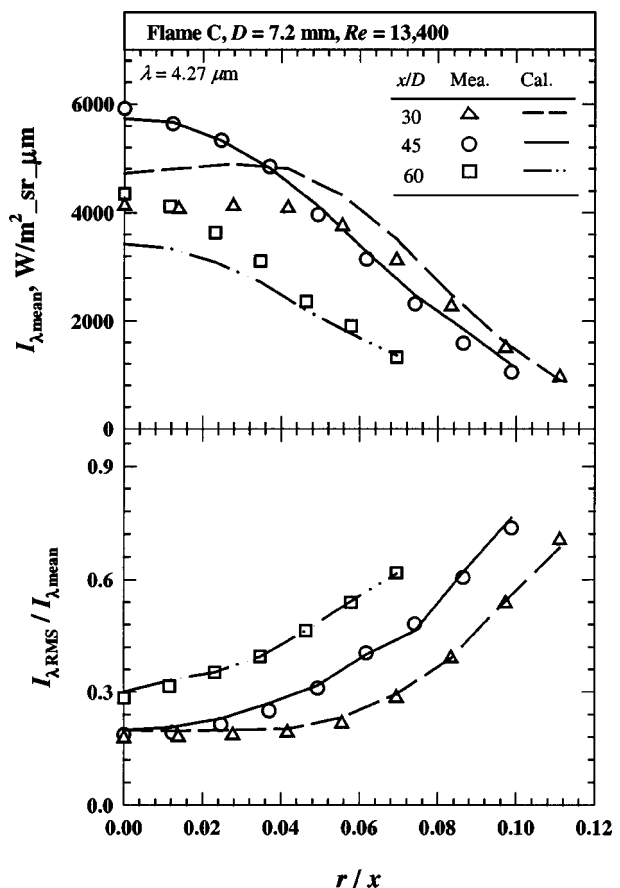
This iterative inverse process for estimation of l_I and τ_I involved between 5 to 10 iterations depending on the location before convergence to the least mean square error.

This methodology can also be applied to studies of premixed flames, where the length scales are important because of their relation to the chemical reaction rate as prescribed by the Bray-Moss-Libby (BML) combustion model [16].

Scalar Property Distributions

A preview of the scalar distributions that were used as inputs to the I_λ calculations is helpful in interpreting the measurements and calculations of the radiation intensities. Figure 1 shows the measured mean and normalized temperature fluctuations ($T_{\mathrm{RMS}}/T_{\mathrm{mean}}$) within flames C, D, and E [3]. At the axial location of $x/D=30$, the mean temperature distributions for the three flames are relatively close although the flow rate increases significantly from flame C to D and from flame D to E. The mean temperature increases in the radial direction from the jet axis to $r/x=0.05$, then it decreases towards the flame edge. The normalized temperature fluctuations in the flames, however, reach their peak values in the region farther away from the axis ($r/x=0.12$).

At the downstream location of $x/D=45$, where the flame tip is nearby ($x/D=47$ for all three flames [4]), the mean temperatures reach their peak values of around 1900 K at the jet axis. A slight increase of mean temperatures with the Reynolds number is observed. The normalized temperature fluctuations on the contrary have a minimum at the axis and increase to reach a maximum farther away from the axis before decreasing to their ambient values.

Fig. 3 Spectral radiation intensities of flame C at λ=4.27 μm
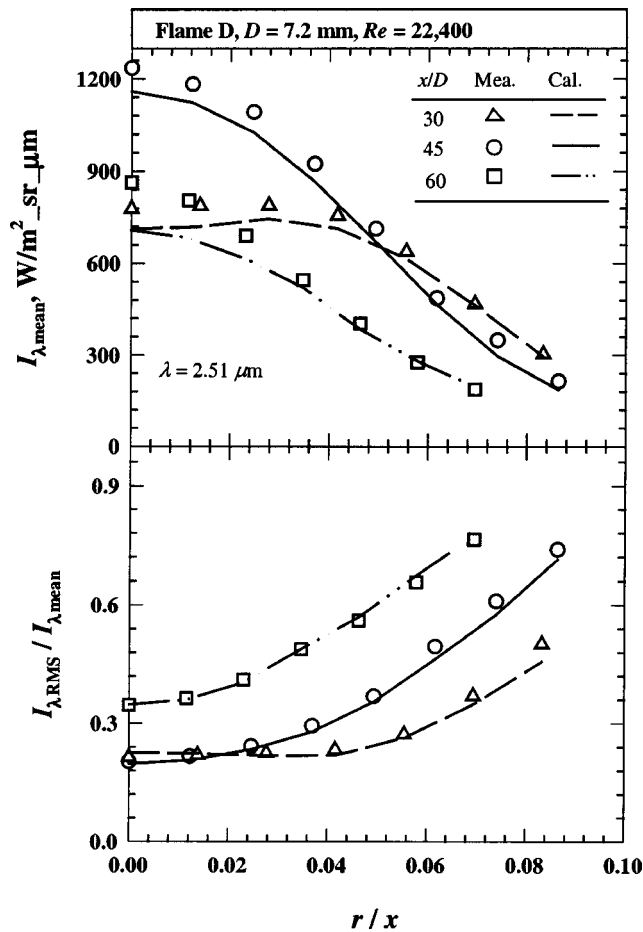
Fig. 4 Spectral radiation intensities of flame D at λ=2.51 μm

Fig. 5 Spectral radiation intensities of flame D at λ=4.27 μm

The measurements and calculations of mean and normalized RMS of I_λ emitted by flame D at the two selected wavelengths are illustrated in Figs. 4 and 5. The calculated intensities are within 10% and 20% of the data. The mean intensities at $x/D=45$ and 60 are 10~15% higher than those emitted by flame C due to the increase in the mean temperatures. This change in radiation intensities, however, is much smaller than the change in the flow rate, which is around 67%. The fluctuations of radiation intensities for the radiation paths near the axis at $x/D=60$ are smaller than those for flame C as a result of the lower normalized scalar fluctuations.

The measurements and calculations of mean and fluctuating radiation intensities for flame E are depicted in Figs. 6 and 7. The measurements and calculations are within 10 to 20% of each other for this flame as well. The mean intensities at $x/D=60$ for flame E are 15~25% higher than those of flame C. This change in radiation intensities, however, is small compared to the change in the flow rate of about 150%.

Representative measurements and calculations of the PDFs, the autocorrelation coefficients and the PSDs of I_λ fluctuations are reported next. The PDFs of I_λ fluctuations of all three flames at $x/D=45$ for the diametric path at λ=2.51 μm λ=4.27 μm are shown in Fig. 8. The measurements and the calculations both show a near Gaussian shape for the PDFs of the intensity fluctuations. The measurements and calculations are in excellent agreement with each other. The PDFs of I_λ fluctuations for the chord-like paths at $r/x=0.08$ are presented in Fig. 9. The shape of these PDFs is not Gaussian but shows a low end cutoff and a high end tail in the intensity distributions. The calculated PDFs match the measurements quite well.

Based on these data as well as examination of the PDFs for other axial locations and other flames, it can be concluded that the
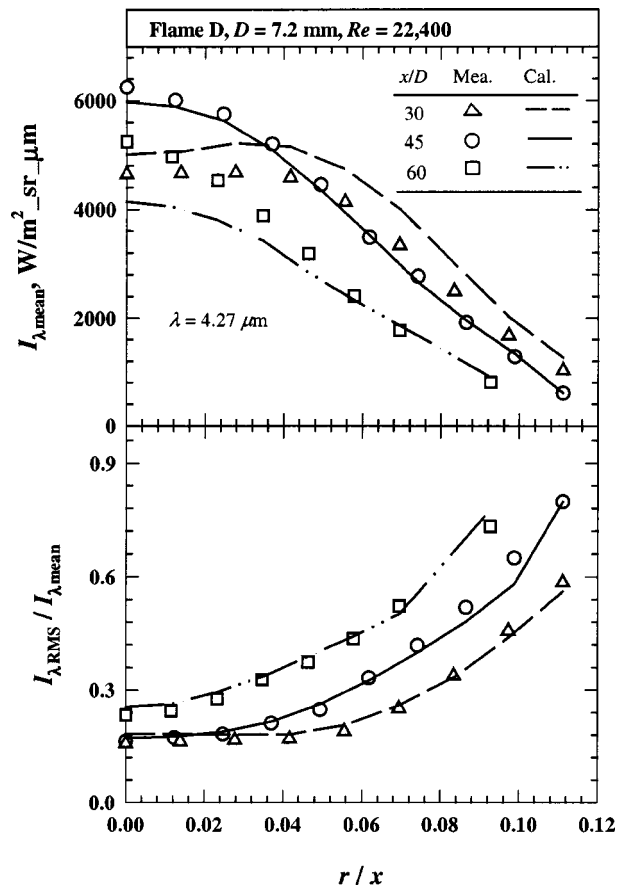
PDFs of I_λ fluctuations for the diametric paths are symmetric and generally Gaussian in shape. The data also show that the PDFs are skewed for chord-like paths and become increasingly skewed with increasing radial distance. The PDF peaks are skewed toward the lower I_λ side, since radiation intensities have a natural low end cutoff at zero. The intensities leaving a chord-like path can be zero because of scalar intermittency, which appears simultaneously with low mean radiation levels [7]. Consequently, the PDFs for the wavelength corresponding to the water vapor band have higher skewness as indicated in Fig. 9. The present calculations successfully capture these characteristic shifts in the shape of the PDF with wavelength and with radial location of the radiation path.

Figure 10 shows the autocorrelation coefficients of I_λ fluctuations at $x/D=45$ for the diametric paths in the three flames at the two wavelengths. The calculated autocorrelation coefficients match the measurements reasonably well at all locations for both wavelengths. The ρ decays very fast from 1 to 0 in less than 5 ms and the rate of this decay increases from flame C to E as the Reynolds number increases. This is expected because of the corresponding higher velocities. Figure 11 shows the autocorrelation coefficients of I_λ fluctuations for the chord like paths at $r/x=0.08$. The experimental data show significantly negative correlations of I_λ fluctuations for the chord-like paths far away from the jet axis. The present computational method is based on the assumption of an exponentially decaying autocorrelation model for the scalar fluctuations and did not capture the negative autocorrelations observed in the experiment. Improved models for the scalar autocorrelation coefficients and experimental validation are necessary for removing this deficiency. The calculations and measurements of the autocorrelation coefficients are in reasonable agreement for short time intervals depicted in Fig. 11.
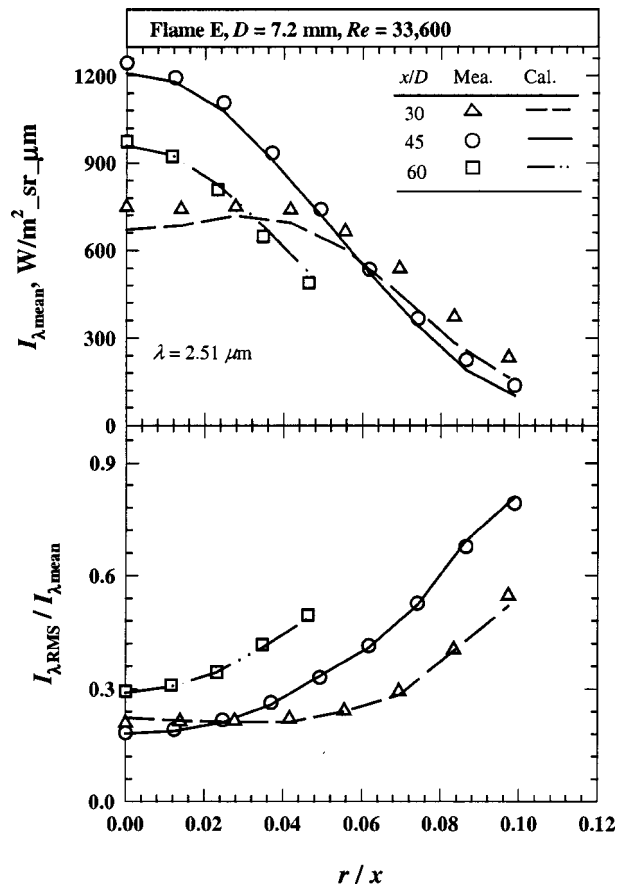
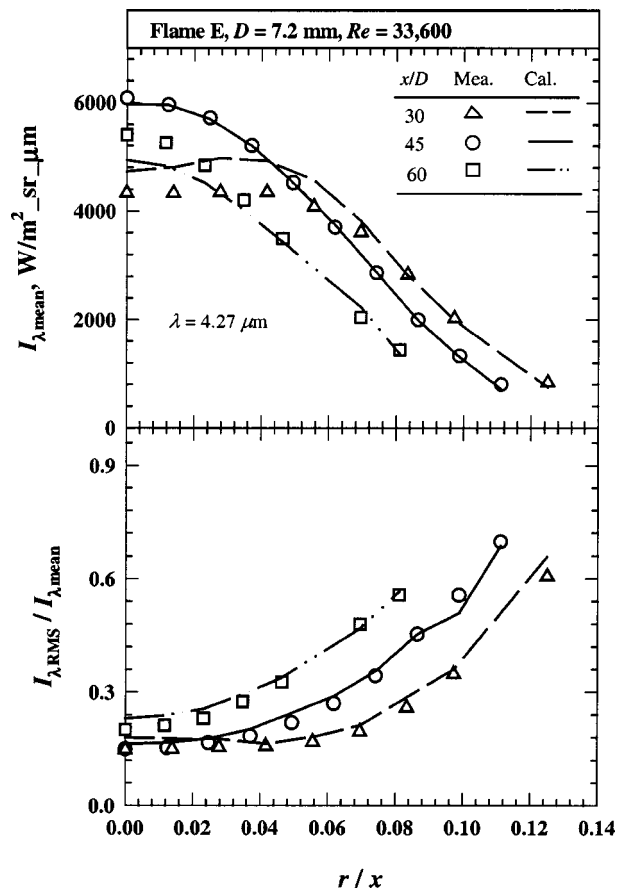**Fig. 6** Spectral radiation intensities of flame E at $\lambda = 2.51~\mu$m

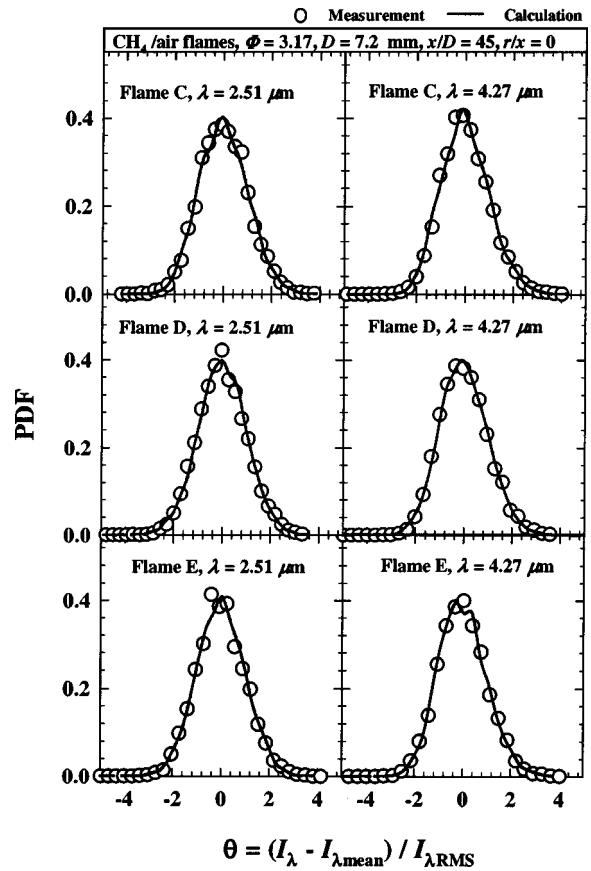**Fig. 7** Spectral radiation intensities of flame E at $\lambda = 4.27~\mu$m

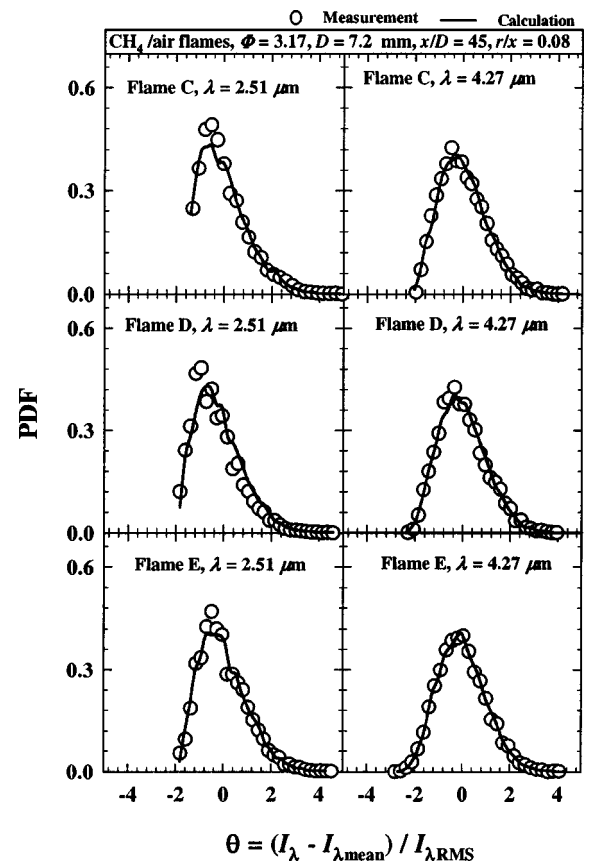**Fig. 8** PDF of spectral radiation intensities of flames C, D and E at $r/x = 0$

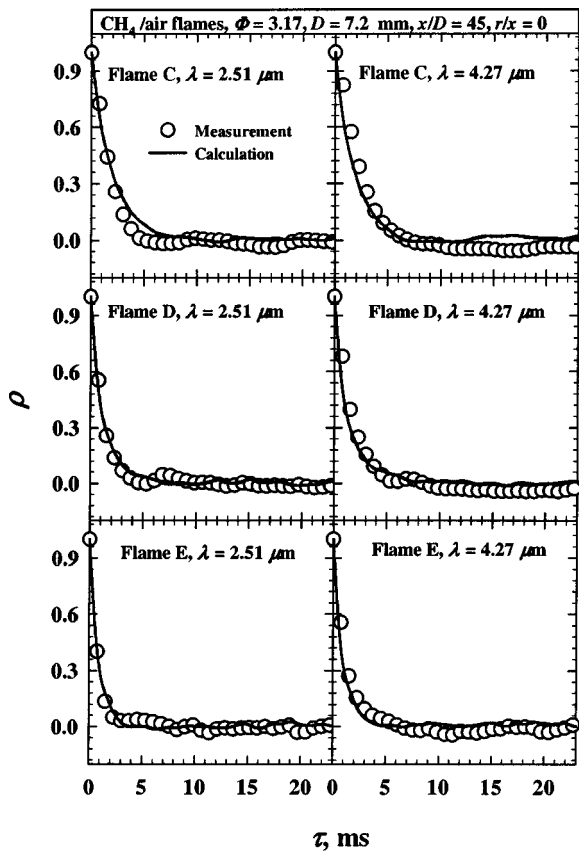**Fig. 9** PDF of spectral radiation intensities of flames C, D and E at $r/x = 0.08$

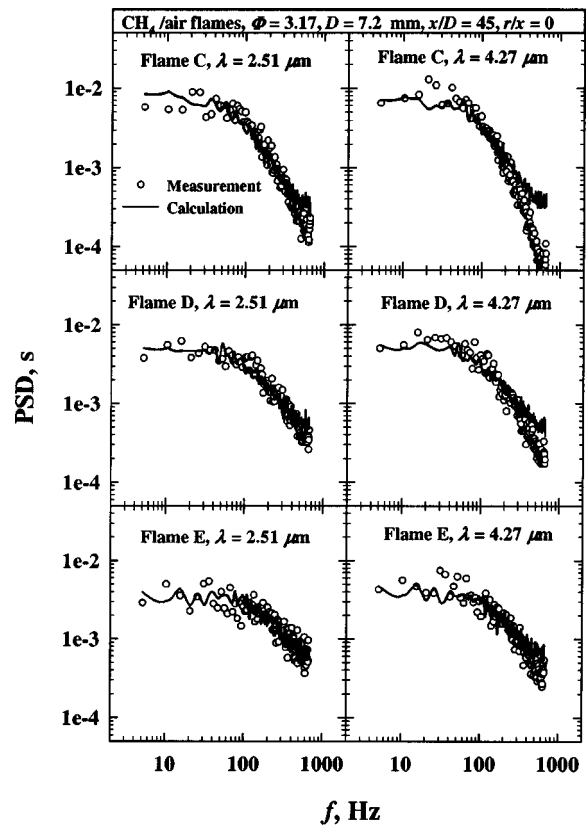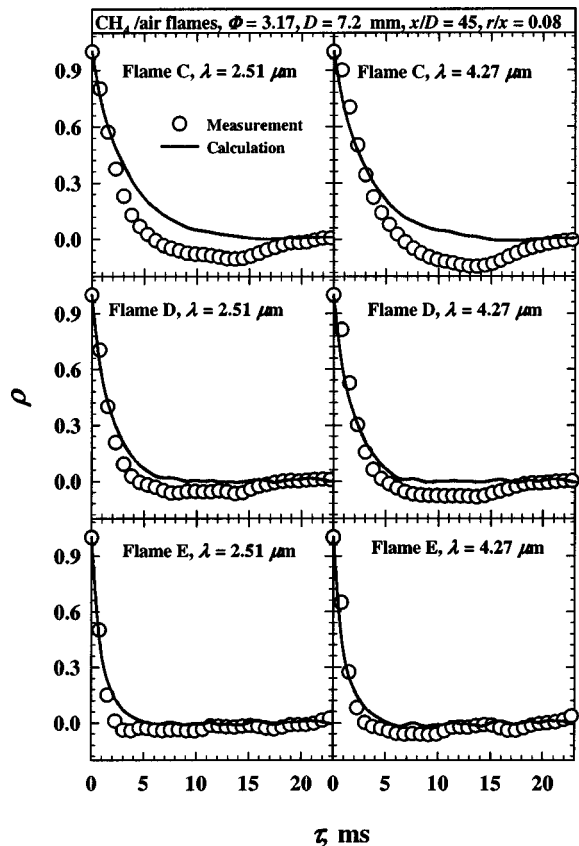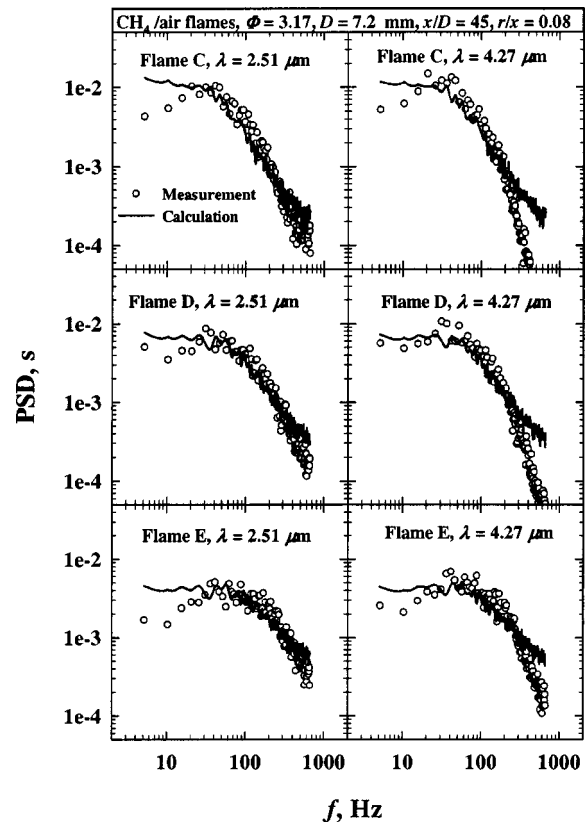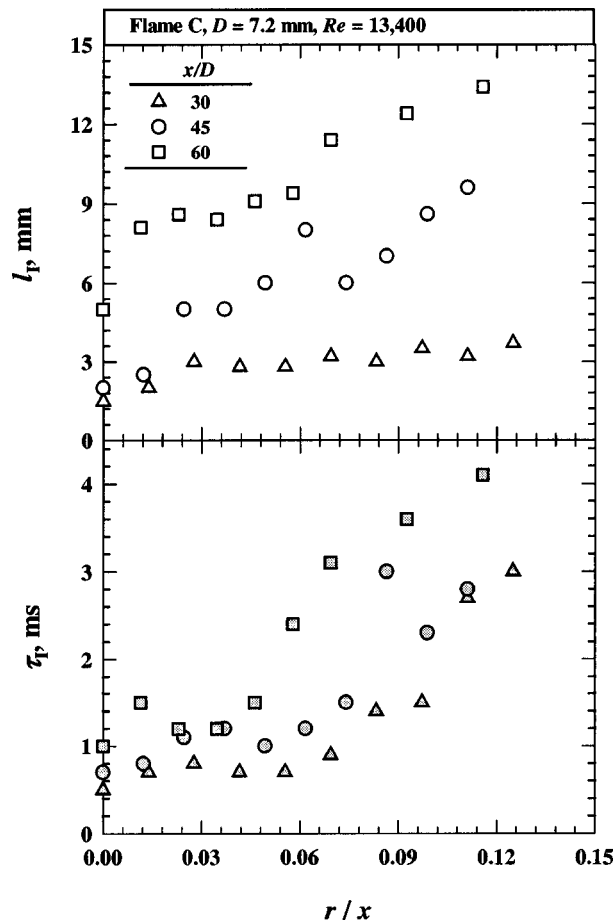**Fig. 10** Autocorrelation coefficient of spectral radiation intensities of flames C, D and E at $r/x = 0$

Fig. 12 PSD of spectral radiation intensities of flames C, D and E at $r/x = 0$

Fig. 11 Autocorrelation coefficient of spectral radiation intensities of flames C, D and E at $r/x = 0.08$

Fig. 13 PSD of spectral radiation intensities of flames C, D and E at $r/x = 0.08$

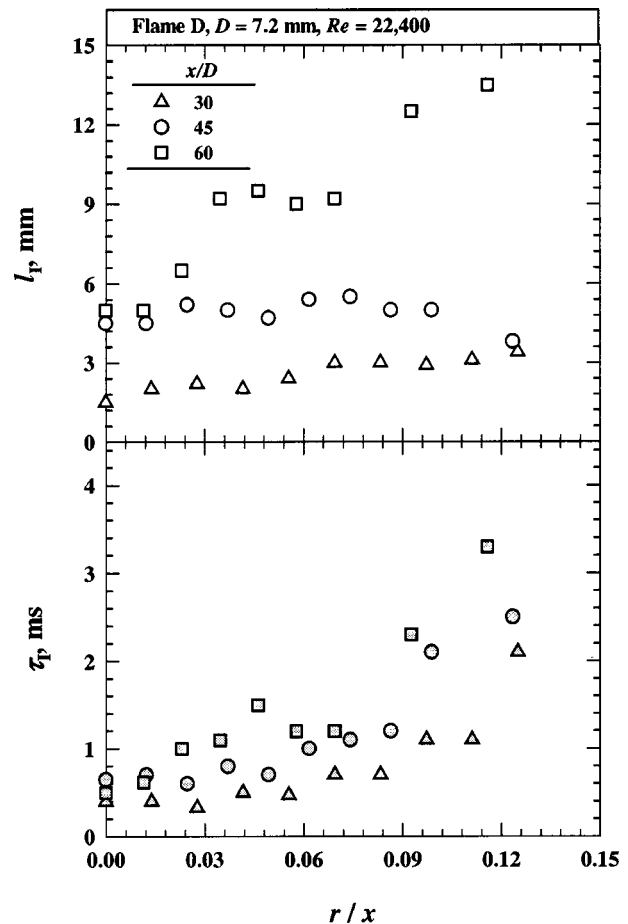**Fig. 14   Radial distributions of integral time and length scales in flame C**

Fig. 15   Radial distributions of integral time and length scales in flame D

The PSDs of I_λ fluctuations for diametric paths in flames C, D, and E at $x/D = 45$ are illustrated in Fig. 12. The present computations achieved fairly good agreement with the measurements. The PSD profile has a low-frequency energy-containing region up to a cut-off frequency. The measured and calculated cut-off frequencies are around 50, 75, and 100 Hz for flames C, D, and E respectively. Figure 13 presents the PSDs of I_λ fluctuations for chord-like paths (at $r/x = 0.08$) in flames C, D, and E at $x/D = 45$. The measured and calculated cut-off frequencies decrease to around 40, 60, and 80 Hz for flames C, D, and E respectively. The calculations captured these characteristic frequencies but underestimated the decay rate for the highest frequency regions. One explanation for this discrepancy is that the exponentially decaying correlation models used for the simulated scalar fluctuations may not properly truncate high-frequency fluctuations as turbulent micro-scales are approached [7].

As discussed above, the local integral time and length scales of scalar fluctuations were reconstructed during the TASS procedure. Radial distributions of l_I and τ_I in flame C at three axial locations are shown in Fig. 14. The l_I and τ_I at $x/D = 30$ increase from the jet axis to flame edge by factors of 2.5 and 6, respectively. The l_I and τ_I at $x/D = 45$ and 60 also generally increase with radial distance. However, there is some non-monotonic variation with radius similar to that observed by Renfro et al. [11] for time scales of mixture fractions based on OH radical concentrations measurements. Along the jet axis, both the length and the time scales increase with downstream distance. Radial distributions of l_I and τ_I are illustrated in Figs. 15 and 16 for flames D and E. Along the jet axis of these two flames, both length and time scale generally increase with downstream distance. Renfro et al. [11], however,

reported constant time scales for mixture fraction based on their measurements of OH radical concentrations along the axis in their flames.

For flame D, Karpetis and Barlow have reported measurements of macro length scales of mixture fraction fluctuations at $x/D = 7.5$, 15 and 30 [12]. The dependence of l_I on the radius has been tacitly suppressed in their work. In order to allow comparison with their data, the present l_I and τ_I were integrated and then averaged with respect to the radius. Figure 17 presents the radial averaged l_I and τ_I in flames C, D, and E from Ref. [12] and from the present estimates. The macro scales increase with downstream distance due to entrainment of surrounding air but decrease with Reynolds number owing to finer structures in higher speed flows. In flame D, the trend of increasing l_I with respect to the axial distance is observed in both the measurement of Ref. [12] and the present result. The present radial averaged length scale at $x/D = 30$ is 2.6 mm, which is some what lower but in general agreement with the experimental data of 3.2 mm from Ref. [12]. Data concerning macro time and length scales in flames are relatively sparse to allow more definitive comparisons.

Summary and Conclusions

Spectral radiation properties (mean, RMS, PDF, ρ, PSD) of three non-sooting partially premixed CH_4/air flames were studied by both experimental and computational methods. Also, local integral time and length scales in these flames were reconstructed using a tomography-like TASS procedure. The specific conclusions are as follows,
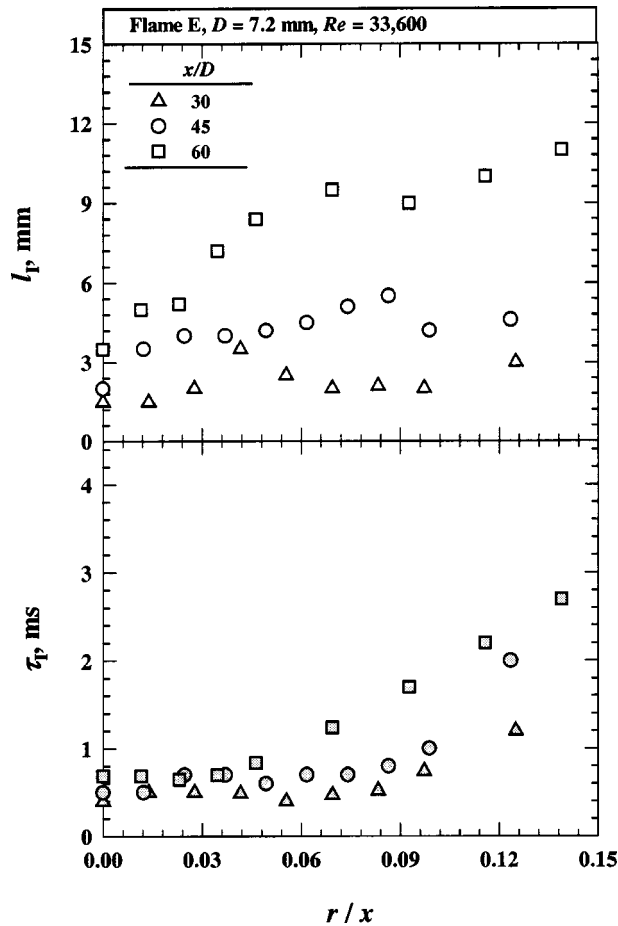
Fig. 16 Radial distributions of integral time and length scales in flame E
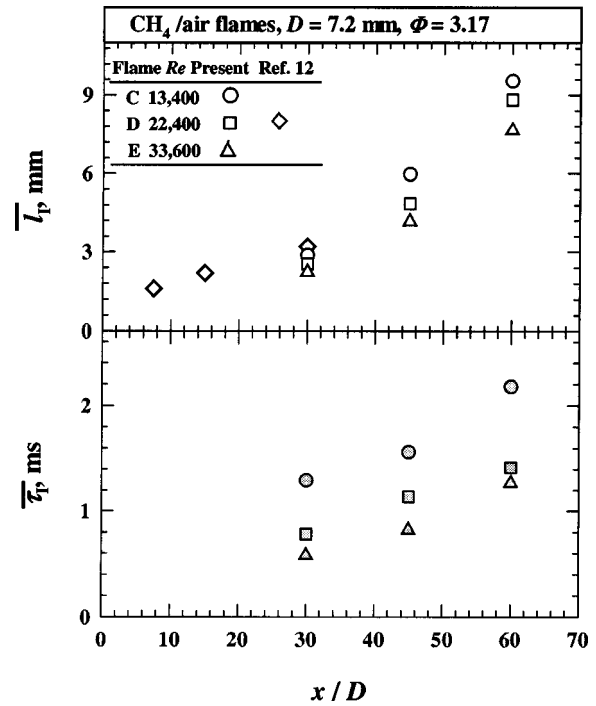

Fig. 17 Radial averaged integral time and length scales in flames C, D and E

Appendix

For a measured or simulated time series of random variable I with length N, the mean, root mean square (RMS), probability density function (PDF), autocorrelation coefficient (ρ) and power spectral density (PSD) of I are calculated following Bendat and Piersol [17]

$$I_{\text{mean}} = \bar{I} = \frac{1}{N} \sum_{k=1}^{N} I_k \tag{A.1}$$

$$I_{\text{rms}} = \left[\frac{1}{N-1} \sum_{k=1}^{N} (I_k - I_{\text{mean}})^2 \right]^{1/2} \tag{A.2}$$

$$\text{PDF}_i = \frac{N_i}{N}, \quad i = 1, 2, \ldots, m \tag{A.3}$$

where, N_i is the number of data fall in the ith bin with the width (W) determined by,

$$W = \frac{I_{\text{max}} - I_{\text{min}}}{m} \tag{A.4}$$

$$\rho(\Delta \tau) = \frac{\overline{(I(\tau) - I_{\text{mean}})(I(\tau + \Delta \tau) - I_{\text{mean}})}}{I_{\text{rms}}^2} \tag{A.5}$$

$$\text{PSD}(f) = \left| \Phi \left(\frac{I(\tau) - I_{\text{mean}}}{I_{\text{rms}}} \right) \right|^2 \tag{A.6}$$

where, $\Phi( )$ an f represent the complex Fourier transform and the frequency respectively.

1. The present TASS method achieved very encouraging agreement between computational and experimental values of spectral radiation properties generally within experimental uncertainties.
2. The PDF of spectral radiation intensities for diametric paths in the flames are symmetric and close to Gaussian in shape. The PDF for radiation paths away from the flame axis, however, are skewed because of intermittency. Experimental studies on the autocorrelation coefficients for radiation paths far away from the flame axis indicate negative correlations in scalar fluctuations near the flame edge.
3. Reconstructed integral time and length scales vary with radial distance with intermediate non-monotonic behavior.
4. Radial averaged integral time and length scales increase with downstream distance but decrease with Reynolds number. The present work indicates that investigating these macro scales only along the flame axis and in a radial averaged manner may both be inadequate.

Acknowledgment

References

[1] Zheng, Y., Sivathanu, Y. R., and Gore, J. P., 2002, "Measurements and Stochastic Time and Space Series Simulations of Spectral Radiation in a Turbulent Non-Premixed Flame," *Proc. of the Combustion Institute*, J. H. Chen and M. D. Colket, eds., The Combustion Institute, Pittsburgh, **29**, pp. 1957–1963.
[2] Zheng, Y., Barlow, R. S., and Gore, J. P., 2003, "Measurements and Calculations of Spectral Radiation Intensities for Turbulent Non-Premixed and Partially Premixed Flames," ASME J. Heat Transfer, **125**, pp. 678–686.

[3] International Workshop on Measurement and Computation of Turbulent Non-premixed Flames, 2003, www.ca.sandia.gov/TNF, Sandia National Laboratories.

[4] Frank, J. H., Barlow, R. S., and Lundquist, C., 2000, ''Radiation and Nitric Oxide Formation in Turbulent Non-Premixed Jet Flames,'' Proc. of the Combustion Institute, A. R. Burgess and J. P. Gore, eds., The Combustion Institute, Pittsburgh, **28**, pp. 447–454.

[5] Li, G., and Modest, M. F., 2002, ''Application of Composition PDF Methods in the Investigation of Turbulence-Radiation Interactions,'' J. Quant. Spectrosc. Radiat. Transf., **73**, pp. 461–472.

[6] Brookes, S. J., and Moss, J. B., 1999, ''Measurements of Soot Production and Thermal Radiation from Confined Turbulent Jet Diffusion Flames of Methane,'' Combust. Flame, **116**, pp. 49–61.

[7] Faeth, G. M., Kounalakis, M. E., and Sivathanu, Y. R., 1991, ''Stochastic Aspects of Turbulent Combustion Processes,'' Chemom. Intell. Lab. Syst., **10**, pp. 199–210.

[8] Ji, J., Sivathanu, Y. R., and Gore, J. P., 2000, ''Thermal Radiation Properties of Turbulent Lean Premixed Methane Air Flames,'' Proc. of the Combustion Institute, A. R. Burgess and J. P. Gore, eds., The Combustion Institute, Pittsburgh, **28**, pp. 391–398.

[9] Sivathanu, Y. R., Kounalakis, M. E., and Faeth, G. M., 1990, ''Soot and Continuum Radiation Statistics of Luminous Turbulent Diffusion Flames,'' Proc. of the Combustion Institute, The Combustion Institute, Pittsburgh, **23**, pp. 1543–1550.

[10] Ji, J., Gore, J., P., Sivathanu, Y. R., and Lim, J., 2000, ''Fast Infrared Array Spectrometer Used for Radiation Measurements of Lean Premixed Flames,'' Proc. of the 34th National Heat Transfer Conference, S. C. Yao and A. Jones, eds., ASME, New York, **2**, pp. 73–78.

[11] Renfro, M. W., Gore, J. P., and Laurendeau, N. M., 2002, ''Scalar Time-Series Simulation for Turbulent Nonpremixed Flames,'' Combust. Flame, **129**, pp. 120–135.

[12] Karpetis, A. N., and Barlow, R. S., 2002, ''Measurements of Scalar Dissipation in a Turbulent Piloted Methane/Air Jet Flame,'' Proc. of the Combustion Institute, J. H. Chen and M. D. Colket, eds., The Combustion Institute, Pittsburgh, **29**, 1929–1936.

[13] Barlow, R. S. and Frank, J. H., 1998, ''Effects of Turbulence on Species Mass Fractions in Methane/Air Jet Flames,'' Proc. of the Combustion Institute, A. R. Burgess and F. L. Dryer, eds., The Combustion Institute, Pittsburgh, **27**, pp. 1087–1095.

[14] Grosshandler, W. L., 1993, ''RADCAL: A Narrow-Band Model for Radiation Calculations in a Combustion Environment,'' NIST Technical Note 1402, U.S. Government Printing Office, Washington.

[15] Ji, J., 2000, ''Experimental and Theoretical Study of the Spectral Radiation Characteristics of Lean Premixed Flames,'' Ph.D. thesis, Purdue University, West Lafayette, IN.

[16] Shepherd, I. G., Cheng, R. K. and Goix, P. J., 1990, ''The Spatial Scalar Structure of Premixed Turbulent Stagnation Point Flames,'' Proc. of the Combustion Institute, The Combustion Institute, Pittsburgh, **23**, pp. 781–787.

[17] Bendat, J. S., and Piersol, A. G., 2000, Random Data: Analysis and Measurement Procedures, 3rd edition, John Wiley & Sons, Inc, New York.

An Experimental Study of Miniature-Scale Pool Boiling

Tailian Chen

Jacob N. Chung

Department of Mechanical and Aerospace
Engineering,
University of Florida,
P.O. Box 116300 Gainesville,
FL 32611, USA

By generating single bubbles on a micro-heater at different wall superheats, an experimental study of miniature-scale pool boiling heat transfer has been performed to provide a fundamental understanding of the heater size effect. In this study, the constant-temperature microheater is set at different temperatures by an electronic feedback control system. The heat transfer history during the lifetime of a single bubble which includes nucleation, growth, detachment and departure has been measured. The boiling curve obtained from the microheater is composed of two regimes which are separated by a peak heat flux. It is suggested that in the lower superheat regime, the boiling is dominated by liquid rewetting and micro-layer evaporation, while in the higher superheat regime, conduction through the vapor film and micro-convection plays the key heat transfer role as the heater is covered by vapor all the time. In general, boiling on microheaters is characterized by larger bubble departure sizes, smaller bubble growth rates due to the dryout of microlayer as the bubble grows, and higher bubble incipience superheat. As the heater size decreases, the boiling curve shifts towards higher heat fluxes with corresponding higher superheats. [DOI: 10.1115/1.1603773]

Keywords: Boiling, Bubble Growth, Heat Transfer, Microscale, Phase Change

Introduction

Applications of microtechnology often utilize components or systems with microscale fluid flow and heat transfer. As the size of individual components shrinks and the length scale decreases drastically, the transport mechanisms involved go beyond those covered by the traditional theories and understanding. The development of new theories and the fostering of up-to-date physical understanding have fallen behind the progress of micro machining and manufacturing. Recently Gad-el-Hak [1] gave a complete review on the fluid mechanics of micro-devices. He concluded that the technology is progressing at a rate that far exceeds our understanding of the transport physics in micro-devices. Therefore the study of micro-scale transport has become an integral part of not only understanding the performance and operation of miniaturized systems, but also designing and optimizing new devices. The current paper presents an experimental study of single bubbles generated on a constant-temperature microheater to examine the boiling characteristics and the size effect on boiling heat transfer. Microheaters have been found in many applications, for example, inkjet printerheads, and actuators and pumps in microfluidic systems.

Rainey and You [2] reported an experimental study of pool boiling behavior using flat, microporous-enhanced square heater surfaces immersed in saturated FC-72. Flush-mounted 2 cm $\times$ 2 cm and 5 cm $\times$ 5 cm copper surfaces were tested and compared to a 1 cm $\times$ 1 cm copper surface that was previously investigated. Heater surface orientation and size effects on pool boiling performance were investigated under increasing and decreasing heat-flux conditions for two different surface finish: plain and microporous material coated.

Results of the plain surface testing showed that the nucleate boiling performance is dependent on heater orientation. The nucleate boiling curves of the microporous coated surfaces were found to collapse to one curve showing insensitivity to heater orientation. The effects of heater size and orientation angle on CHF were found to be significant for both the plain and microporous coated surfaces.

Hijikata et al. [3] investigated boiling on micro-scale heaters to find the optimum thickness of the surface-deposited layer to enhance the heat removal from the heater in order to obtain the best cooling effect for a semiconductor. The square heaters they used were 50 μm and 100 μm. They claimed that the deposited layer conduction dominates the heat transfer due to the small sizes of the heater area. They also presented the nucleate boiling curves for the two heater sizes and different deposited layer thickness.

Rule and Kim [4] used a miniature heater (2.7 mm $\times$ 2.7 mm) which consisted of an array of 96 microheaters. Each of the microheaters was individually controlled to maintain at a constant temperature that enabled the mapping of the heat flux distributions during the saturated pool boiling of FC-72 fluid. They presented spatially and temporally resolved data for nucleate boiling, critical heat flux and transition boiling. Specifically, the outside edge heaters were found to have higher heat fluxes than those of the inner heaters.

Experimental System

Microheaters. The heater used in this experiment is one of the microheaters on a heater array similar to that employed in previous publications [4,5]. The heater array consists of 96 microheaters numbered from no. 1 to no. 96 as shown in Fig. 1. Each microheater is a platinum resistance element and manufactured on a quartz substrate using microfabrication technology. It has a serpentine pattern as shown in Fig. 2. On top of the platinum filaments a very thin layer of silicon dioxide was deposited. The heater filament has a dimension of 0.2 μm in thickness, 5 μm in width and 6000 μm in length. This design of microheaters allows a uniform heating of the surface and reduces the heat capacity effect to a maximum degree. Each microheater has a dimension of about 270 μm square, and a nominal electrical resistance of 750 Ω. The microheaters were wire-bounded through their pads to a pin grid array (PGA) and connected to an electronic circuit system.

Feedback Electronic Circuit for Temperature Control. Due to the linear relationship between the platinum resistance with its temperature, the temperature of each microheater can be set and maintained at a constant value by a feedback electronic circuit as shown in Fig. 3. A Wheatstone bridge and a feedback loop consist of the core of the circuit. $R1$, $R2$, $R3$, $R4$, $R7$, and $R8$ are metal film resistors whose resistances are not sensitive to their

Copyright © 2003 by ASME
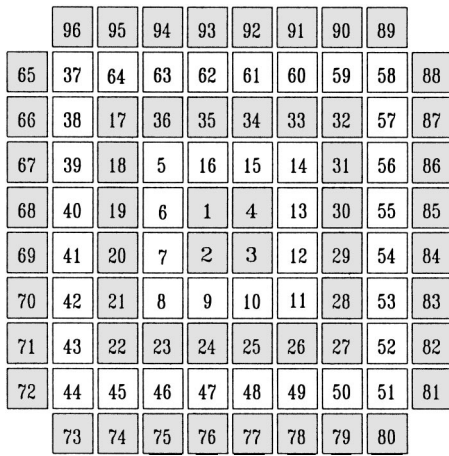
Fig. 1   Heater array containing 96 microheaters

Fig. 3   The electronics circuit for temperature control

temperatures. *Rh* is the platinum microheater. Its resistance is measured at 788 ohms at the room temperature. *Rd* is a digital potentiometer with a range from 0 to 10 k Ω set by digital signals from the computer. *R*1, *R*3, *Rh*, and *R*4 together with *Rd* form the Wheatstone bridge. The Op-Amp LTC1150 detects the imbalance in the bridge by measuring the voltage difference between *V*1 and *V*2. The transistor *Q*11 would then output the current that is needed to balance the bridge. When the bridge is balanced, *V*1 is equal to *V*2 and the following relationship is established:

$$\frac{R1}{R3} = \frac{Rh}{R4+Rd} \tag{1}$$

Therefore, the *Rh* value (thus, the heater temperature) is able to be set by adjusting the *Rd*. Calibration was required to find the linear relationship between the heater resistance and its temperature.

Boiling Conditions.   FC-72 is the boiling fluid in this experiment. It is widely used as the fluid in electronics cooling. Since it is dielectric, electrical conduction between the heaters can be avoided, thus each heater can be individually controlled. The bulk fluid was at the room condition (1 atm and 24.5°C), where its saturation temperature is 56°C. Therefore the experiment was performed in a subcooled condition. In the current experiment, only one single microheater (marked as no. 1 in Fig. 1) is heated to produce single bubbles. The experiment is started by setting the microheater at a temperature of 50°C where only natural convection occurs at this temperature. Then the temperature of the heater was incremented by 5°C at a time until the superheat reaches 114°C. For each increment, the heat dissipation by the heater was obtained by the data acquisition system through acquiring the voltages across the heater. In order to examine the effects of dis-
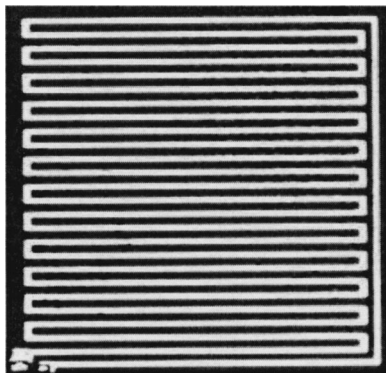
solved gas on the boiling heat transfer, boiling experiments were performed for two cases. One case is performed with the FC-72 fully gas-saturated, and the other one is with FC-72 fully degassed. The residual gas concentration was measured at less than 0.2×10^{-3} mole/mole for the fully degassed case. For both cases, the system was operated under the same pressure of 1 atm, and the same bulk liquid temperature of 24.5 ± 0.1°C.
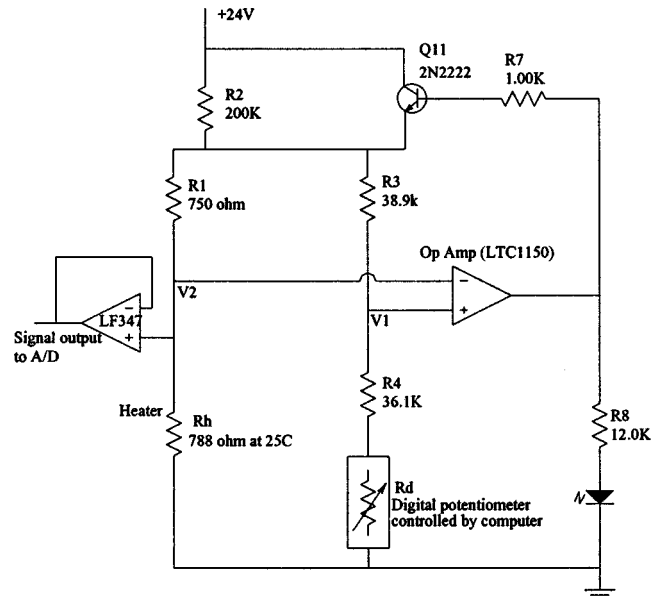
Data Acquisition and Visualization.   The data acquisition system consists of two *A/D* boards (ComputerBoards CIO-DAS48) and a *D/A* board (ComputerBoards CIO-DIO48) installed in a computer. The two *A/D* boards were used to acquire data and the *D/A* board was used to interface the computer signal with the electronic circuit system. The sampling rate in this experiment is about 4.5 kHz. Both the bottom and side views of boiling process were visualized. The semi-transparent nature of the heater substrate made it possible to take images from below the heater. The setup of the experiment is shown in Fig. 4. A high-speed digital camera (*Motion*Scope PCI 8000S) was used to take images at 1000 fps with a resolution of 240 pix.×210 pix. The bubble visualization was performed using the shadowgraph technique, in which the bubbles were illuminated from one side while the images were taken from the other side.

Data Reduction

Heat Transfer Path With Boiling.   The total heat dissipation rate from the heater when single bubbles are generated on it, q''_{raw1}, is obtained by directly measuring the voltage across the heater and its electrical resistance. The heat transfer path is shown in Fig. 5(*a*). q''_{raw1} includes the heat conduction to the substrate q''_{cond1}, the radiation to the surrounding, q''_{rad1}, and the boiling heat transfer to the liquid from the top surface of the heater, q''_{boi1}, which could be a complex combination of phase change heat transfer, micro-convection due to the bubble movement and natural convection due to the temperature gradient of the heater with the bulk fluid. Thus,

$$q''_{raw1} = q''_{cond1} + q''_{boi1} + q''_{rad1} \tag{2}$$

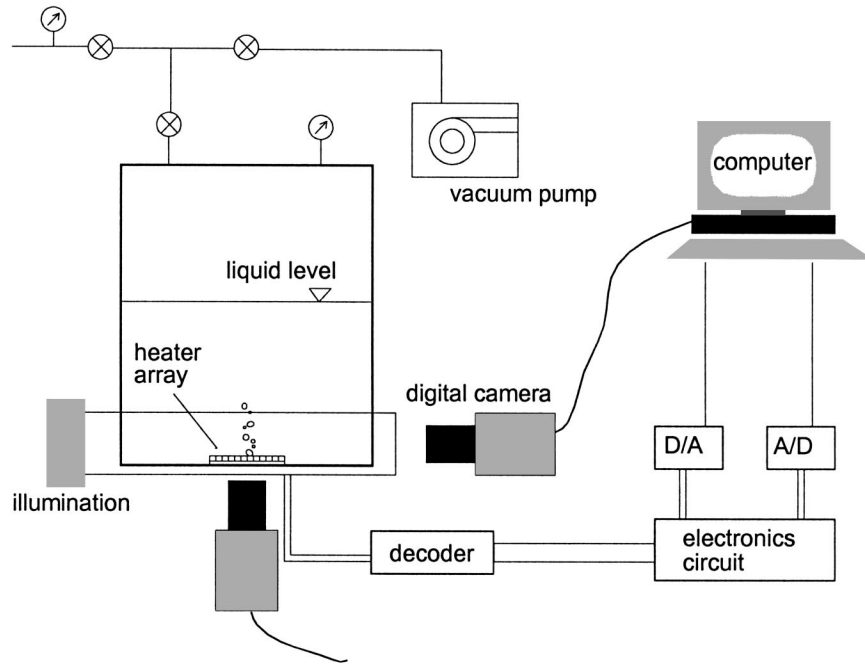**Fig. 2   One of the serpentine microheaters on the heater array**

Fig. 4 Schematic of experiment apparatus

Data Reduction Procedure. Our purpose here is to find q''_{boi1} and the data reduction procedure was designed to accomplish this goal. The method is explained as follows. Before the boiling experiment with the air-saturated case, the chamber was turned upside down, so that the heater is separated from the liquid FC-72 and facing downward to an almost air surroundings. Under this situation, the heater was powered to reach the various temperatures as those in the boiling experiment. For each heater temperature, the heater was allowed $20\sim30$ minutes to reach the steady state. Then the total heat dissipation rate, q''_{raw2}, was measured. The heat transfer path in this situation is shown in Fig. 5(b) and the total heat dissipation rate can be written as:

$$q''_{raw2} = q''_{cond2} + q''_{rad2} + q''_{cond3} \tag{3}$$

where q''_{cond2} is the conduction heat flux to the substrate, q''_{rad2} is the radiation heat flux from the heater, and q''_{cond3} is the conduction heat transfer downwards to the almost air environment.

Because that the conduction heat transfer media and the driving temperature difference are identical for the conduction heat transfer q''_{cond1} in Eq. (2) and the q''_{cond2} in Eq. (3), thus for the same heater temperature $q''_{cond1} = q''_{cond2}$.

From Eqs. (2) and (3), the boiling heat flux, q''_{boi1} can be derived as the following:

$$q''_{boi1} = q''_{raw1} - q''_{raw2} + q''_{rad2} - a''_{rad1} + q''_{cond3} \tag{4}$$

The only difference between the q''_{rad1} and q''_{rad2} is the media that the thermal radiation passes through. For q''_{rad1}, the medium is a liquid-vapor FC-72 two-phase volume, and for the q''_{rad2}, the medium is air. Since our heater was operated at lower than 170°C, intrinsically the radiation heat flux is much smaller than the boiling heat flux (even if we assume that the emissivity is one and the view factor is also one, with the maximum ΔT in a vacuum, the maximum radiation heat flux is about 0.174 W/cm^2 that is at most only 0.3 percent of the boiling heat flux $\sim$50 W/cm^2). Therefore, it is reasonable to neglect the radiation contribution. Furthermore, as indicated in Eq. (4), what we have neglected is actually the difference between q''_{rad2} and q''_{rad1} which is even smaller than either q''_{rad2} or q''_{rad1}. But we did take the neglect of the radiation heat flux difference into account in the uncertainty evaluation. As a result, to obtain the value of q''_{boi1} in Eq. (4), the conduction heat flux q''_{cond3} has to be evaluated. We used a commercial thermal-
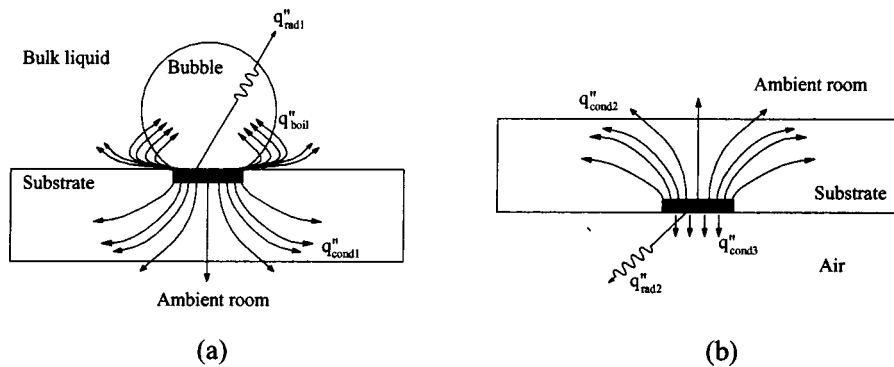

Fig. 5 Heat transfer path from the microheater: (a) boiling experiment; and (b) The heater was turned upside down.

fluid finite-element code FEMLAB to model our case exactly by its three-dimensional conduction module. The result shows that the conduction heat flux ranges from 1.27 W/cm^2 to 2.5 W/cm^2 for the heater temperature varying from 100°C to 170°C which covers the temperature range in the current study. We also double checked the FEMLAB results by the conduction shape factor method given in Incropera and DeWitt [6]. We approximated our square heater as a circular disk with identical surface area. The disk with a constant temperature T_1 is facing a semi-infinite medium of thermal conductivity k and temperature T_2. The q''_{cond3} obtained by two methods only differ by a maximum of 7 percent. Therefore, the boiling heat transfer can be simply obtained by:

$$q''_{boil} = q''_{raw1} - q''_{raw2} + q''_{cond3} \qquad (5)$$

Uncertainty Analysis. The uncertainties in this experiment include heater temperature uncertainty and heat flux uncertainty. The uncertainty sources from the heater temperature are estimated as follows: oil temperature fluctuation during calibration, $\varepsilon_{T1} = \pm 0.5°$C; discrete resistance increment of digital potentiometer, $\varepsilon_{T2} = \pm 0.05°$C; drift of offset voltage V_{off} of the Opamp, $\varepsilon_{T3} = \pm 0.1°$C; temperature fluctuation during boiling, especially during the vapor-liquid exchange process, $\varepsilon_{T4} = \pm 0.01°$C. Thus, the overall temperature uncertainty can be obtained by simply adding up all the uncertainties from each source, which gives an uncertainty of about $\pm 0.66°$C. The uncertainty sources associated with the boiling heat flux measurement can be summarized as follows: wire resistance from A/D boards to heater pads, $\varepsilon_{V1} = \pm 5$ percent, resolution of A/D boards, $\varepsilon_{V2} = \pm 0.03$ percent, voltage division device, $\varepsilon_{V3} = \pm 1.02$ percent. These three uncertainties ε_{V1}, ε_{V2}, and ε_{V3} all contribute to the uncertainty from acquiring the voltage of the heater. Thus, the total uncertainty for the voltage of the heater can be obtained: $\varepsilon_V = \varepsilon_{V1} + \varepsilon_{V2} + \varepsilon_{V3} = 5$ percent $+ 0.03$ percent $+ 1.02$ percent $= \pm 6.05$ percent which is only part of the overall heat flux uncertainty. Another part is due to the conduction heat transfer, q''_{cond3} in Eq. (3). The uncertainty for q''_{cond3} is estimated to be 10 percent. The last part of uncertainty comes from the neglect of the difference between the radiation heat fluxes q''_{rad1} and q''_{rad2} in the data reduction portion. Even the uncertainty is 100 percent, but due to the extremely small values of q''_{rad1} and q''_{rad2}, their contribution to the overall uncertainty is very minor. The uncertainty for the overall heat flux has been estimated by using the method of Kline and McClintock [7] to be around ± 1.5 percent. It is noted that this uncertainty is temperature dependent due to the different boiling transfer rates at different temperatures. This temperature dependence of the heat flux uncertainty is shown in Fig. 6.

Experiment Results and Analysis

Time-Averaged Boiling Curve. As the degree of superheat was increased to 54°C, single bubbles were seen to nucleate. The onset of nucleate boiling (ONB) for the single bubble experiment was observed at the superheat ΔT of 54°C to 59°C. After the ONB, the degree of superheat dropped to 34°C as the minimum superheat for stable boiling on the heater. Figure 7 shows the two measured boiling curves in linear scales where the superheat of the heater covers a range from 34°C to 114°C. The boiling curves were obtained based on the time-averaged heat flux (the averaging was carried out over several bubble cycles) for each superheat. One boiling curve was obtained when FC-72 was fully-gas saturated and the other one was obtained when FC-72 was fully degassed. Three runs were performed for each case to demonstrate the repeatability of the data. Our results show the following trends: (1) As shown in Fig. 7, except around the peak heat flux (at a superheat of 93°C), the gas-saturated case offers approximately 10 percent higher heat fluxes than the fully-degassed fluid. After the peak heat flux, there is not much difference between the two cases. (2) The dissolved gas heat transfer enhancement decreases with increasing heat flux. (3) Around the peak heat flux
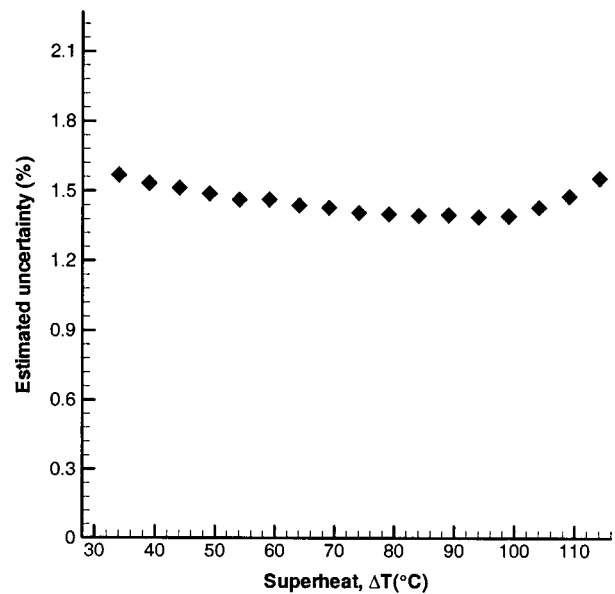

Fig. 6 The heat flux uncertainty at different heater superheats

area, on the average, the gas-saturated case exhibits a slightly higher heat flux level. The trends from our data are basically consistent with the data of You et al. [8] and Hong et al. [9] who also used the same fluid of FC-72 to conduct boiling experiment on small cylindrical wires. Since our results show that the dissolved gas effects are at most about 10 percent on the nucleate boiling heat fluxes, we agree with the assessment made by You et al. [8] that near the heater surface it is generally free of dissolved gas because once the gas is removed from the heater surface by earlier boiling bubbles, the diffusion of gas back to the heater surface is very slow. The slow rate for the gas to replenish near the heater surface is even more so for the current case of a micro flat heater due to the limited access than the cylindrical heater used by You et al. [8].

The classical boiling curve [10] which has three regimes separated by the CHF (critical heat flux) and the minimum heat flux (Leidenfrost point), respectively, is based on large heaters, where
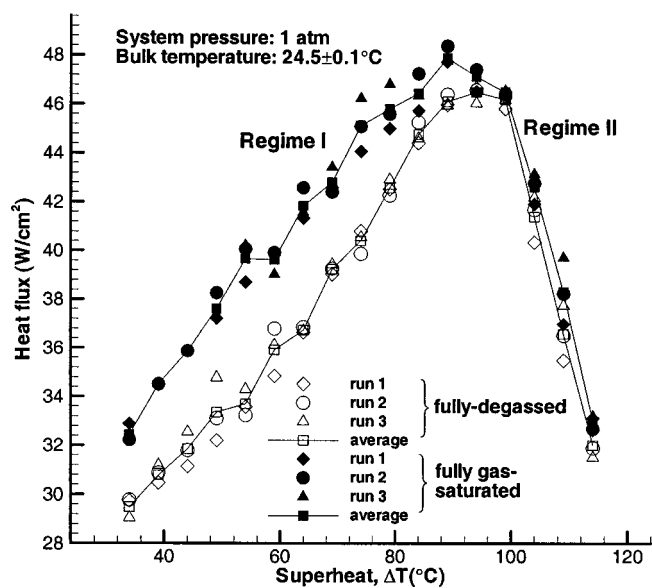

Fig. 7 The boiling curve for fully gas-saturated and fully degassed cases

the heater size is not a factor. For the current study, we have only identified two regimes (Regimes I and II) for the boiling curves in Fig. 7. For the classical case, it is widely accepted that the increase in the heat flux after the ONB (onset of nucleate boiling) as the heater superheat is increased is due to more activated nucleation sites, and bubble-bubble coalescence and interactions. In the current study, due to the very small heater size and a single bubble nature, nucleation sites and bubble-bubble interaction were not available and therefore are not responsible for the increase of the heat flux before the peak heat flux was reached. Instead, the high liquid evaporation rate of the microlayer and the higher bubble departure frequency were considered responsible for the heat flux increase in Regime I before the peak heat flux. The regime after the peak heat flux, where the heat flux decreases with increasing superheat is called the transition boiling in the classical pool boiling case while in the current study it is believed that the regime after the peak heat flux (Regime II) is similar to the film boiling regime in the classical case. In the classical case, the film boiling follows the transition boiling and is separated from it by the minimum heat flux. Therefore, we suggest that there is no transition boiling regime in the current study of a microheater with single bubbles that is basically due to the micro size of the heater and the lack of bubble-bubble interactions.

Temporally-Resolved Heat Flux at Different Superheats. Figure 8 provides the temporally-resolved heat flux history at different heater superheats (44°C to 114°C with increments of 10°C). For each superheat value, 3~4 bubble cycles are shown to demonstrate the repeatability of the single bubble boiling process. To further examine the characteristics of different boiling cycles, two cases are plotted in Fig. 9. We chose two different superheats of $\Delta T = 44°C$ and $\Delta T = 104°C$, in which the $\Delta T = 44°C$ case represents a typical lower superheat case and the $\Delta T = 104°C$ case represents a typical higher superheat case. For $\Delta T = 44°C$, a typical bubble cycle includes stages from [A] through [F] marked on the figure. [A] corresponds to a large spike which takes place during the combined process of bubble departure and new bubble formation. When the preceding bubble breaks from the heater surface, it leaves a vapor embryo for the new bubble as a result of the necking process caused by the surface tension during bubble detachment. The heater is then rewetted by the cooler bulk fluid. The establishment of the microlayer for the succeeding new bubble on the heater surface and the turbulent micro-convection induced by this vapor-liquid exchange lead to the large heat flux spike. [B] represents the short period when the succeeding bubble starts to grow after the vapor-liquid exchange. As the new bubble grows, the contact line, which is the three-phase division, expands outward. The bubble growth results in a larger dry area on the heater surface and thus the heat flux is decreasing. The low heat flux period indicated by [C], [D], and [E] corresponds to the slow growth period of the bubble. As the bubble size reaches to a certain value, the buoyancy force starts to overcome the forces which hold the bubble to the surface. However it is still not large enough to lift the bubble from the heater surface, causing the bubble to neck. During the necking process, the contact line starts to shrink, and the dryout area starts to decrease. Thus it was observed that the heat flux started to increase slightly with some oscillation of small-amplitudes. Finally, with the bubble growing further the buoyancy force is large enough to detach the bubble from the heater surface (point [F] in Fig. 9), and then another bubble ebullition cycle begins. For $\Delta T = 104°C$, a typical bubble cycle includes stages [A′] through [E′]. Again, [A′] represents the bubble departure and new bubble formation. It is noted that the bubble departure at higher superheats actually results in a heat flux dip rather than a spike. [B′] is the period of initial bubble growth and [C′]-[D′]-[E′] is the slow bubble growth period. Similarly, [F′] represents the necking and detachment process which is associated with bubble oscillations and heat flux fluctuations.

For all the heat flux history plots in Figs. 8 and 9, two general trends are observed. The first one, called Regime I, corresponds to lower superheats (44°C~74°C) where the bubble departure causes a heat flux spike and the slow bubble growth period is associated with relatively lower heat fluxes. However, the second one, called Regime II, corresponds to higher superheats (94°C–114°C) where the bubble departure causes a heat flux dip and the slow bubble growth period is associated with relatively higher heat fluxes. To further examine the temporally-resolved heat flux variations in more details, a close-up view on the heat flux histories are plotted at smaller time increments in Fig. 10. Some small-scale heat flux dips were recorded with the heat flux spikes. For superheats $\Delta T = 44°C$ and $54°C$, the heat flux dip was not seen. It is clear that at $\Delta T = 64°C$, the heat flux dip starts to be observable and becoming stronger in magnitude as superheat increases. A hypothetical model has been given in Fig. 11. Fig. 11(a) is for superheats ($\Delta T = 64°C$, $74°C$) where heat flux dips are observable but heater surface is still re-wetted significantly to produce a spike. Fig. 11(b) is for higher superheats ($\Delta T = 84°C$, $94°C$, $104°C$, $114°C$) where the heater surface is covered by the vapor all the time. As the leftover vapor embryo spreads over the surface, more surface area is covered by vapor, thus the dip in heat flux is formed. Figure 8 also reveals that the bubble departure frequency increases slightly with the heater temperature. At a heater superheat of 44°C, the departure frequency is 0.43 Hz, while at 84°C, it is 0.53 Hz.

Figure 12 shows the trends of the two characteristic heat fluxes during a bubble life cycle (Point [A] through Point [E] or Point [A′] through [E′]) in Fig. 8. The curve with diamonds, q_d'', represents either the peak heat flux of a spike or the minimum heat flux of a dip during the bubble departure (point [F] or [F′]) for various heater superheats. Based on Fig. 8, the bubble departure was observed to produce a spike for the heater superheat up to 84°C, after which a heat flux dip was observed. In Fig. 10, the curve with open circles, q_s'', shows the heat flux levels during slow bubble growth for superheats ranging from 44°C to 114°C. It is clear that the two curves exhibit opposite trends before they cross each other and similar trends after that.

Two-Regime Pool Boiling Model. As we examine Figs. 7–12 closely, all these figures consistently indicate that Regimes I and II in the boiling curves produced in the current study are dominated by two different transport mechanisms, respectively. In Fig. 7, the heat flux increases with increasing heater superheat in Regime I while the trend reverses in Regime II. In Figs. 8 and 9, we notice that a heat flux spike is associated with a bubble departure in Regime I (heater superheat up to 84°C) and a heat flux dip is seen to accompany a bubble departure in Regime II (starting at the superheat of 94°C). In Fig. 12, we found that the two curves cross each other at the heater superheat of 90°C which is the separating point between Regimes I and II. It is conjectured that in Regime I the bubble growth is mainly sustained by the mechanism of microlayer evaporation which follows the rewetting of the heater surface after the bubble departure. This scenario is supported by the presence of a heat flux spike recorded during the bubble departure. We suggested that the spike is produced when the heater surface is rewetted by the liquid with micro turbulent motion which in turn causes the microlayer to form and the ensuring evaporation of this layer facilitates the bubble growth. While for Regime II, because of the higher heater superheat, the heater is covered by vapor film all the time, even during the bubble departure. The heater surface is no longer re-wetted by the liquid flow, which results in the bubble growth controlled by conduction through a vapor film layer. The conduction-controlled scenario is supported by the presence of a heat flux dip recorded during the bubble departure in Regime II. It is suggested that the heat flux dip is mainly due to the necking process during the bubble departure. During the necking process, the top part of the bubble exerts an upward pulling force to stretch the neck (Fig.
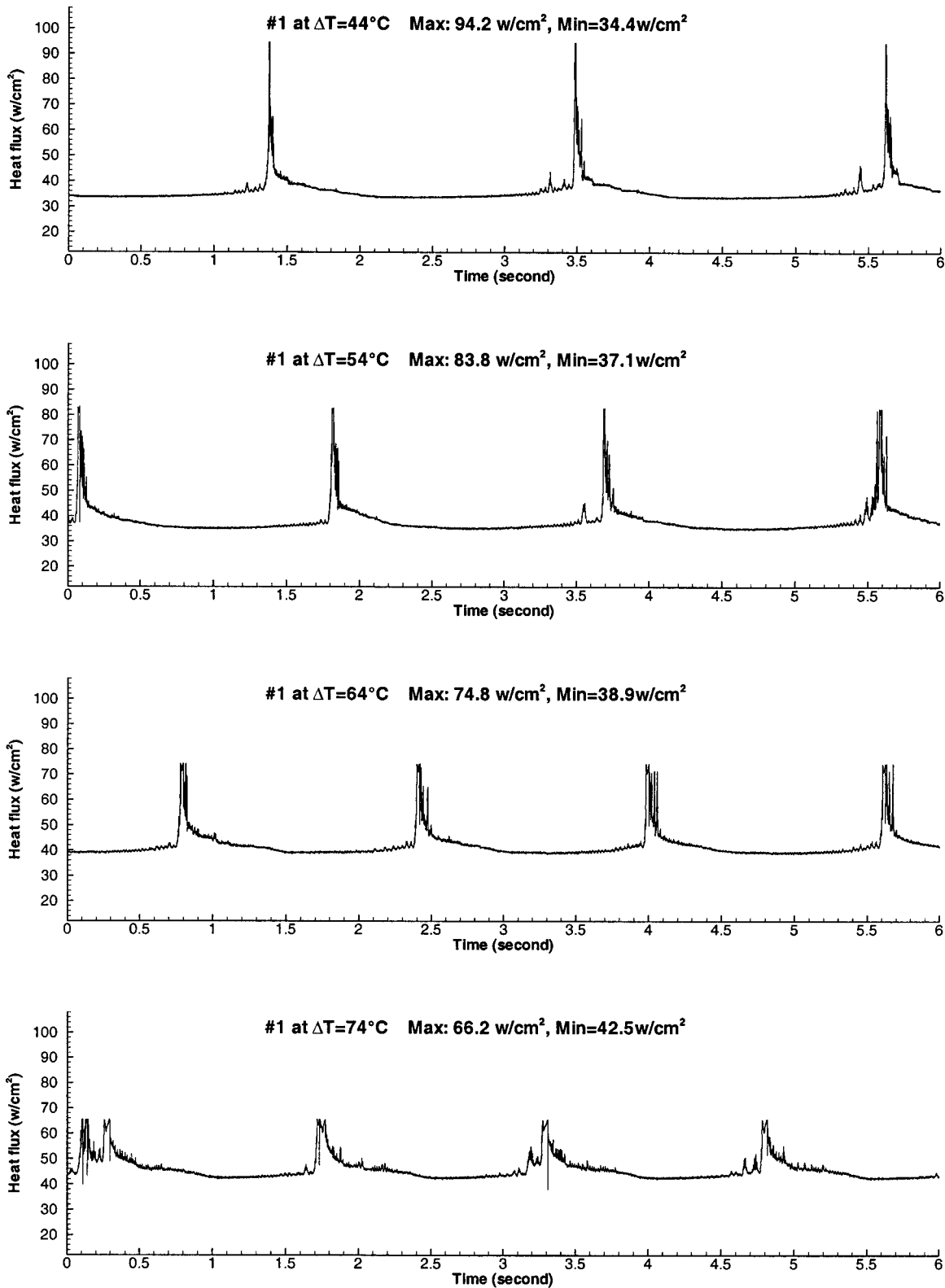
Fig. 8 Time-resolved heat flux traces at different superheats

11(b), Picture (a)). After the bubble severs from the base, the upward force disappears suddenly which allows the lower part of the neck to relax and spread so that the heater surface area is covered a layer of vapor film as illustrated in Fig. 11(b) (Picture (c)). Based on the necking process explained above, we have developed a simple vapor film conduction model to verify the heat

flux dip phenomenon. During the bubble growth period, the majority of heat transfer is going through the thin vapor film that is near the outer boundary of the bubble base area (as shown by the arrows in Fig. 11(b), Picture (a)). The base area that is directly under the neck does not conduct much heat because the temperature gradient is across the entire bubble height. Right after the
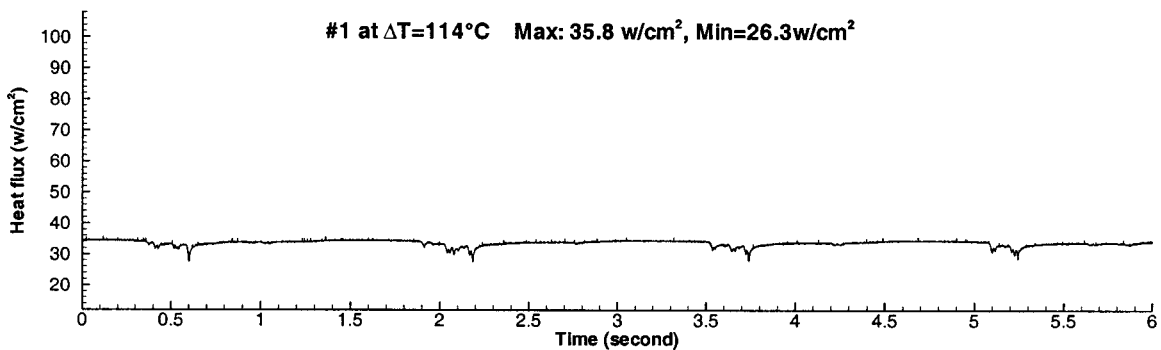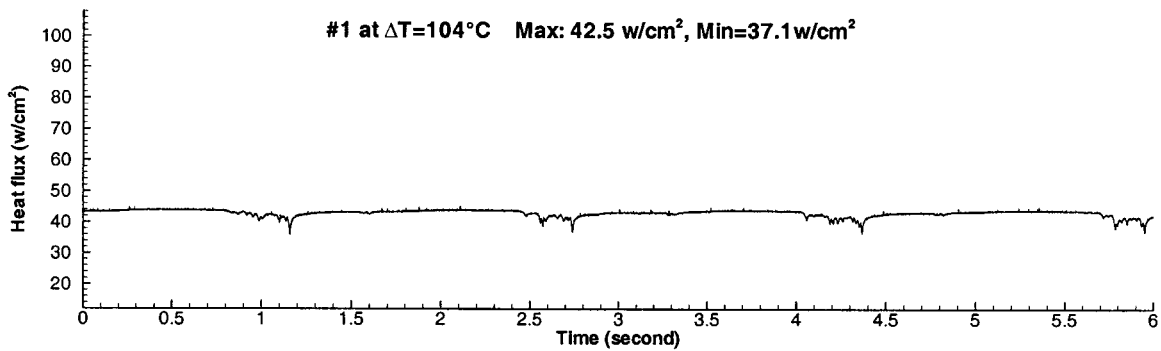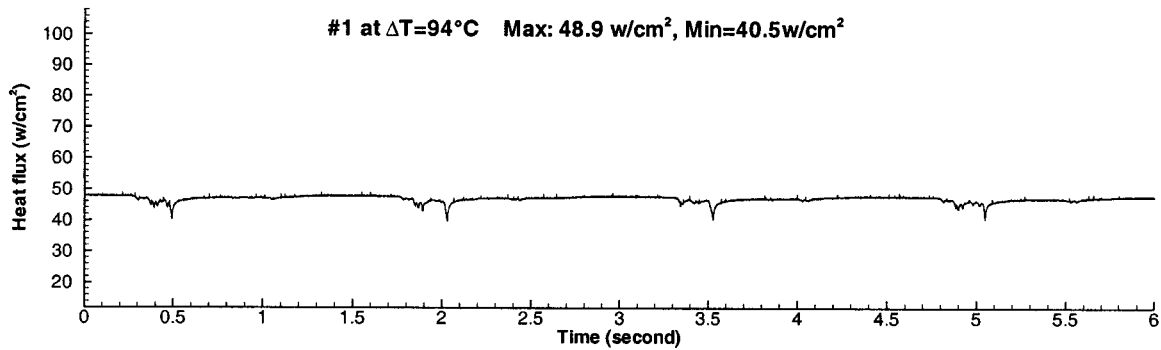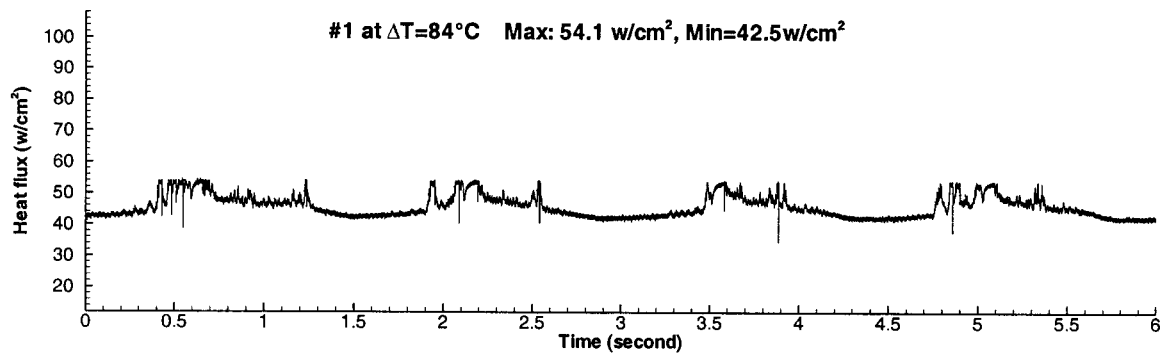
#1 at ΔT=84°C   Max: 54.1 w/cm², Min=42.5w/cm²

#1 at ΔT=94°C   Max: 48.9 w/cm², Min=40.5w/cm²

#1 at ΔT=104°C   Max: 42.5 w/cm², Min=37.1w/cm²

#1 at ΔT=114°C   Max: 35.8 w/cm², Min=26.3w/cm²

Fig. 8   (*continued*)

detachment, the relaxed and flattened vapor film covers the entire heater (as shown in Fig. 11(*b*), Picture (c)), therefore the entire heater surface is conducting heat through a relatively thicker vapor film. For the case of a superheat at 104°C, the model predicts the vapor film thicknesses of 1.9 μm and 2.55 μm for the bubble growth period ($q'' = 42.5$ W/cm²) and for the departure period

(minimum dip heat flux $q'' = 37.1$ W/cm²), respectively. The result of the model therefore supports the physical explanation given above for the Regime II.

Bubble Departure Size.   We observed that the bubble departure size increases slightly with heater superheat. Based on a cor-
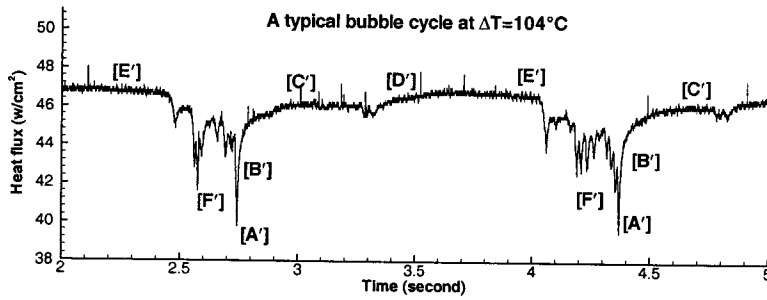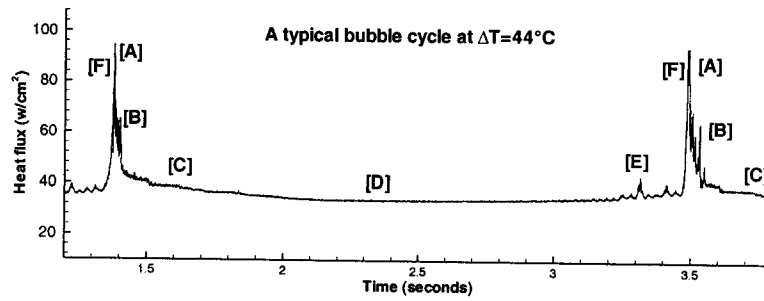
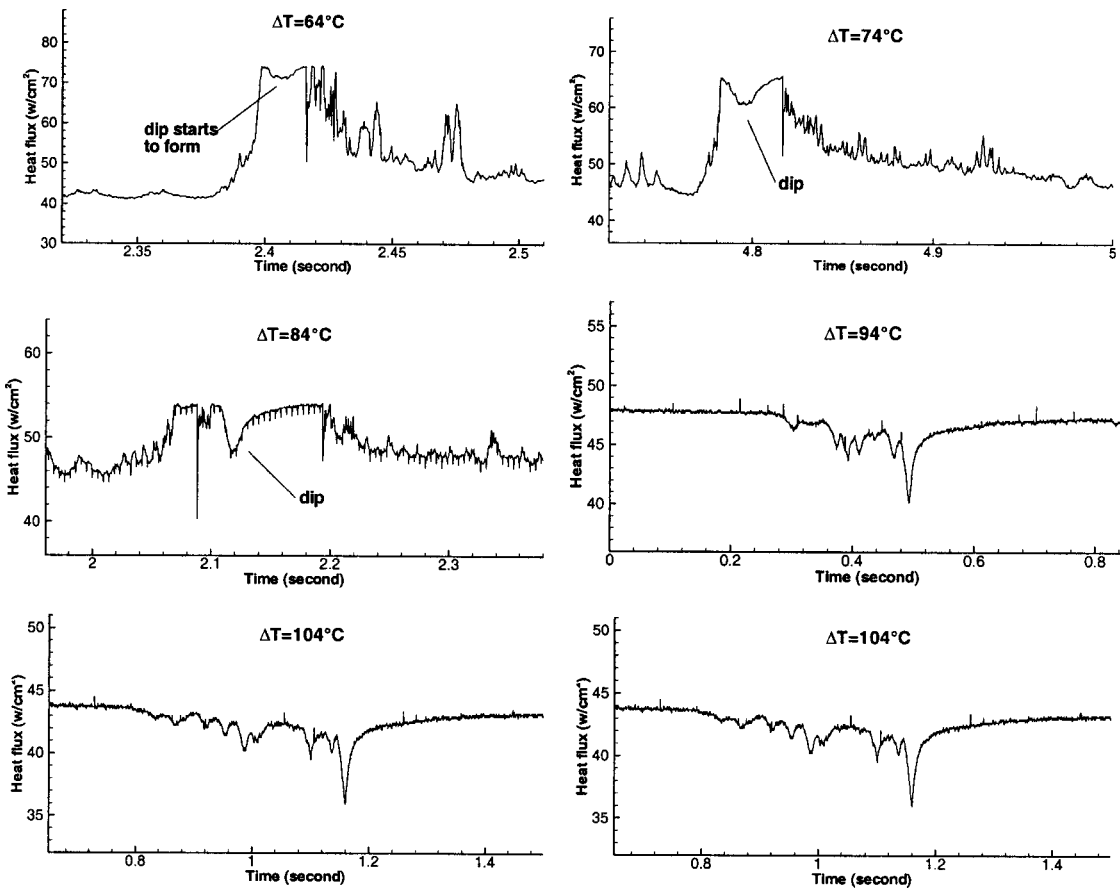**Fig. 9 Heat flux variations during one typical bubble cycle at two super-heats**

Fig. 10 A close-up view showing the heat flux dips at different superheats
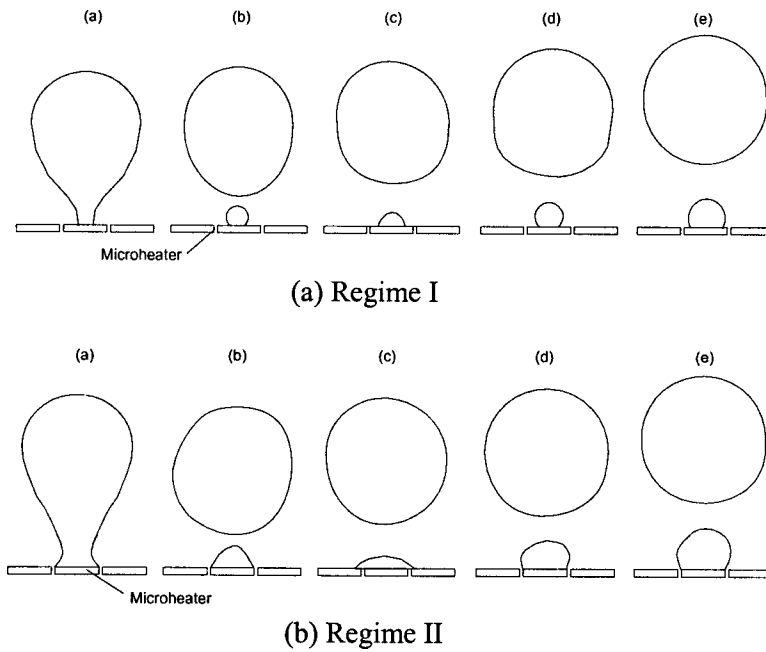
(a) Regime I

(b) Regime II

Fig. 11 Hypothetical models for bubble departure at the two regimes: (*a*) Regime I; and (*b*) Regime II.
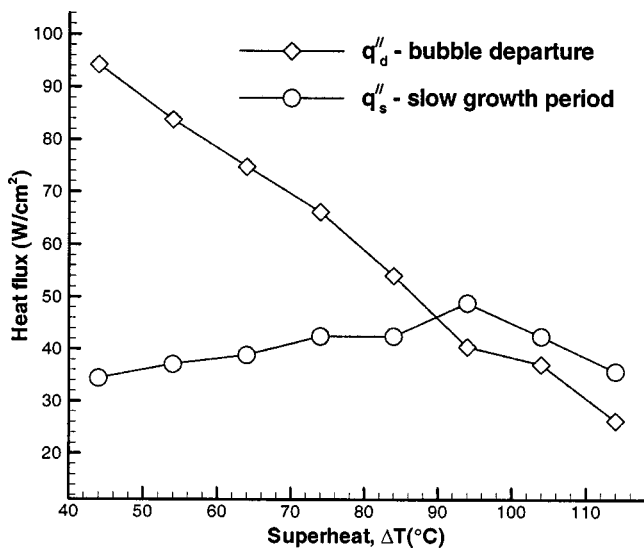

Fig. 12 The trend of max. and min. heat fluxes during one ebullition cycle with various heater superheats

relation proposed by Cole [11], the bubble departure diameter is given below

$$D_b = (0.004 \Delta T_{sup} C_{p\ell} \rho_\ell / \rho_v h_{fg})^{1/2} \sqrt{\sigma/g(\rho_l - \rho_v)} \qquad (6)$$

where ρ_l (liquid density), σ (surface tension), and h_{fg} (latent heat of vaporization) decrease with increasing temperatures, and $C_{p\ell}$ (liquid specific heat) and ρ_v (vapor density) increase with increasing temperatures. We have made a sample calculation showing that the departure diameter for superheat $\Delta T_{sup} = 74°C$ is 17 percent larger than that of superheat $\Delta T_{sup} = 34°C$. This result is supported by our bubble visualization photographs given in Fig. 13. The main contribution to the increase in diameter is due to the superheat increase.

Comparison and Discussion

Bubble Growth Rate. Figure 14 provides a sequence of bubble images during a typical bubble departure process on the microheater at a superheat of 54°C, where Fig. 14(*a*) gives the side view and Fig. 14(*b*) supplies the bottom view. It is worth noting that the embryo for the next bubble is formed when the departing bubble breaks away during the necking process. This phenomenon also demonstrates the combined process of bubble departure and embryo formation. Further more, the corresponding bubble size history was estimated from the image using the length of the microheater as a reference and plotted in Fig. 15. Also plotted in this figure is the theoretical prediction of bubble growth rates by Scriven [12]. As shown in Fig. 15, the initial growth rate
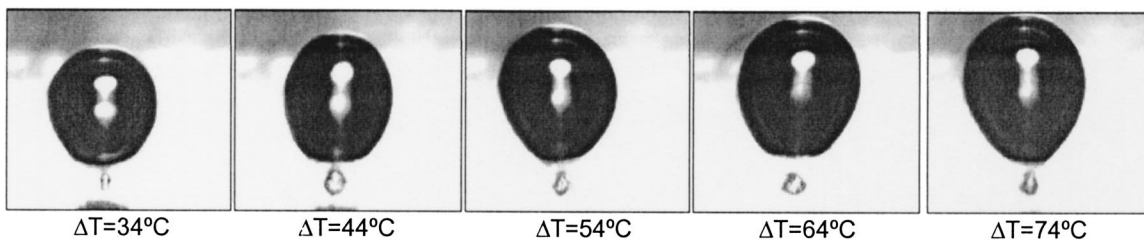

Fig. 13 Bubble departure sizes at different superheats
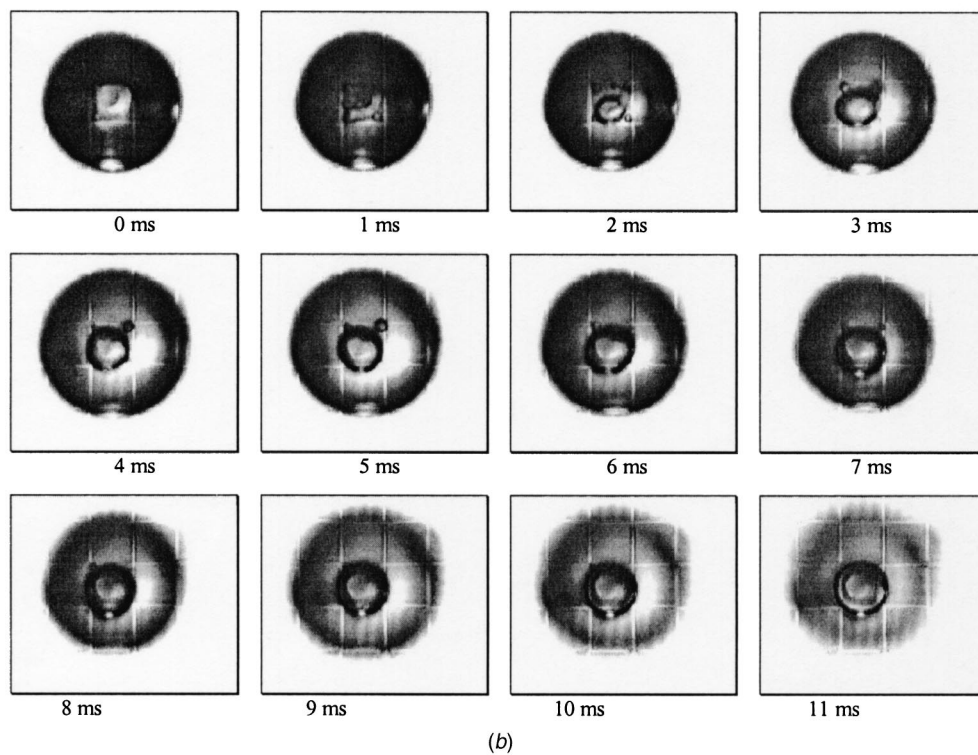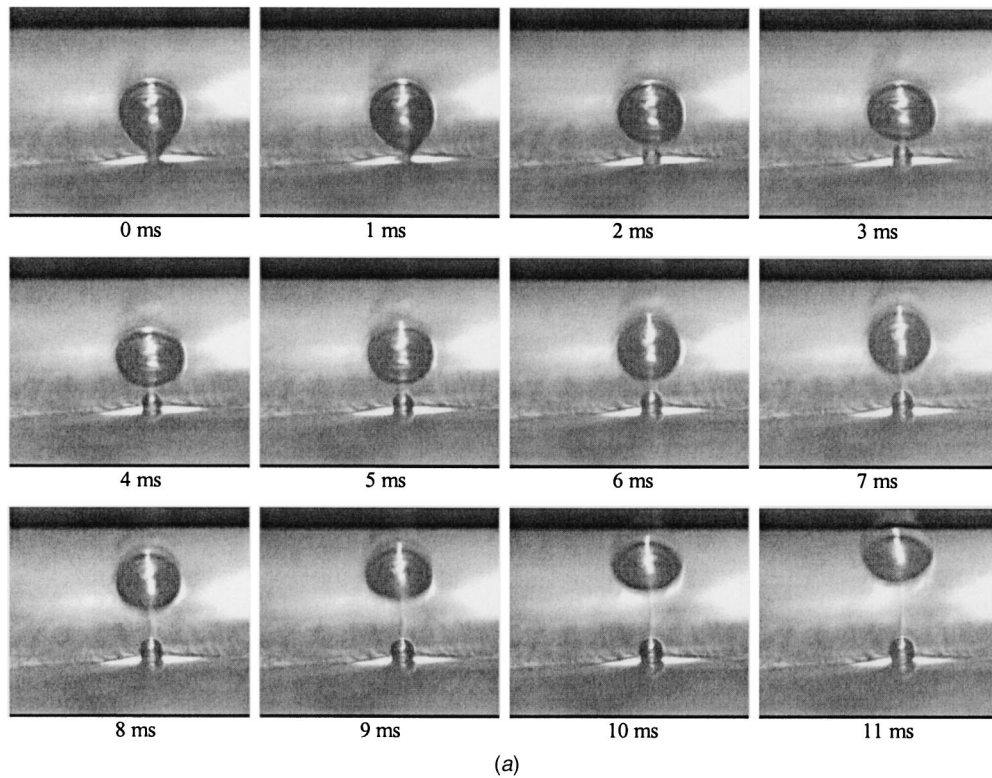
Fig. 14 The visualization results of bubble departure-nucleation process for #1 heater at ΔT $=54°C$: (*a*) the side views; and (*b*) the bottom views.

of our data conforms to the theory by Scriven [12]. After 0.02 second, the two curves start to deviate from each other. The reason for the deviation is suggested as follows: Scriven's model is based on a bubble suspended in a pool of superheated liquid of infinite extent. Therefore, the driving potential for heat transfer, which decreases with time for the current study of a bubble growing on a heater surface, stays constant for a suspended bubble all the time. The decrease in heat transfer is basically due to the drying outof more heater surface, a typical phenomenon of boiling on microheaters.

Fig. 15 Comparison of measured bubble growth rate with prediction by Scriven [12].

$$A = \sqrt{\frac{2\rho_v \Delta T_s H_{fg}}{3\rho_l T_s}} \quad B = Ja\sqrt{\frac{12}{\pi}\alpha_l} \qquad (8)$$

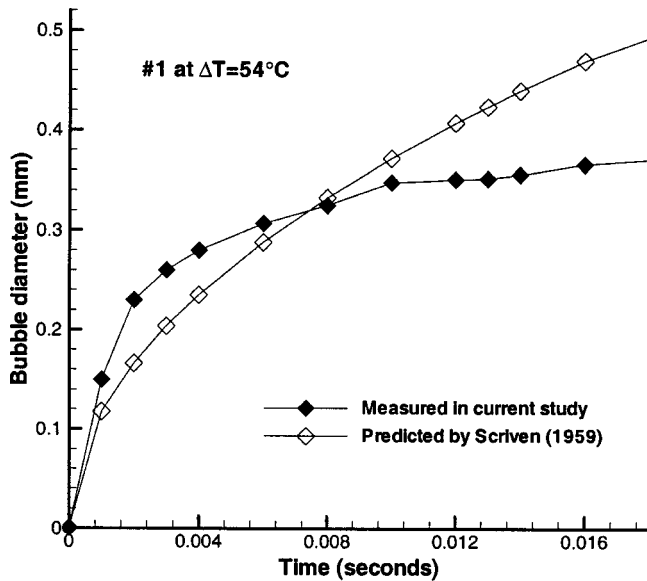$$\text{and} \quad \phi = \left[1 + \frac{1}{2}\left(\frac{\pi}{6Ja}\right)^{2/3} + \frac{\pi}{6Ja}\right]$$

For the current study, the measured bubble departure diameters and growth times at various heater surface superheats are given in Table 1. It is shown that the bubble growth time is inversely proportional to the superheat while the departure size only increases slightly with the increasing superheat as discussed above.

In order to compare our data with the correlation of Yang et al. [13], the data were converted to dimensionless forms according to Eqs. (7) and (8) using thermal properties given in Table 2. Figure 16 shows the comparison. In Fig. 16, previous results used by Yang et al. [13] to develop the correlation have been reproduced. Also included in this figure are the results from the current study based on the two dimensionless scales. Our data basically follow the trend of Yang et al. [13]. It is clear that the bubble dimensionless departure diameters are larger than those given by previous investigators, and the dimensionless bubble growth time is also longer.

Size Effects on Boiling Curve and Peak Heat Flux. It is also of importance to examine the heater size effect on the boiling curve. Boiling curves for heater sizes ranging from 50 μm, 100 μm, 270 μm, 2700 μm, 1 cm to 5 cm were plotted in Fig. 17. In order to ensure a meaningful comparison, all the curves in Fig. 17 are based on fluids with similar thermal properties. The trend is very clear that as the heater size decreases, the boiling curve shifts toward higher superheats and higher heat fluxes. The peak heat fluxes for different size heaters have been plotted in Fig. 18 for comparison, where the CHF values for heater sizes of 1 cm and 5 cm were given in Chang and You [14] and in Rainey and You [2], respectively. It is consistent that the peak heat flux increases sharply as the heater size approaches the micro-scale. It is noted that Hijikata et al. [3] reported that their linear boiling curves actually consist of two regimes where the nucleate boiling takes place at lower heat fluxes while the film boiling takes over at higher heat fluxes. There is no transition boiling and the two regimes continue from one to the other. The two-regime phenomenon is also shared by our boiling results. The film boiling heat fluxes measured by Hijikata et al. [3] are one to two orders of magnitude higher than those from our measurement.

Bubble Incipient Superheat. Bubble incipient superheat is relatively higher for the small size heater used in this experiment. This is consistent with the results given by Rainey and You [2], where they observed that the incipient superheat is about 16–17°C for 5 cm heater, 20~35°C for 2 cm heater, and 25~40°C for 1 cm heater. The incipient superheat observed in our experiment is about 45~55°C. The explanation for this phenomenon by

Bubble Departure Diameter. Recently Yang et al. [13] proposed a new model of characteristic length scale and time scale to describe the dynamic growth and departure process of bubbles. A correlation between bubble departure diameter and bubble growth time is established and a prediction formula for bubble departure diameter is suggested by considering the analogue between nucleate boiling and forced convection. The predictions by the model agree well with experimental results that were obtained with basically macro-scale pool boiling conditions.

Yang et al. [13] developed a new model of characteristic length scale and time scale to describe the dynamic growth and departure process of bubbles. They proposed a dimensionless bubble departure diameter D_b^+ and a corresponding dimensionless bubble growth time τ_g^+ to correlate the bubble departure diameter and the growth time from various experimental results. These scales are reproduced in Eq. (7) and Eq. (8).

$$D_b^+ = \frac{D_b}{L_o} = \frac{AD_b}{\phi B^2} \quad \tau_g^+ = \frac{1}{\phi}\left(\frac{A}{B}\right)^2 \tau_g \qquad (7)$$

where

Table 1 Bubble growth time and departure diameter

ΔT (K)	49	54	59	64	69	74	79	84	89	94	99	104
Growth time (seconds)	2.352	2.054	1.922	1.873	1.747	1.611	1.483	1.403	1.335	1.237	1.128	1.024
Departure diameter (mm)	0.823	0.824	0.829	0.833	0.832	0.836	0.839	0.843	0.850	0.859	0.866	0.875

Table 2 Properties of FC-72 at 56°C

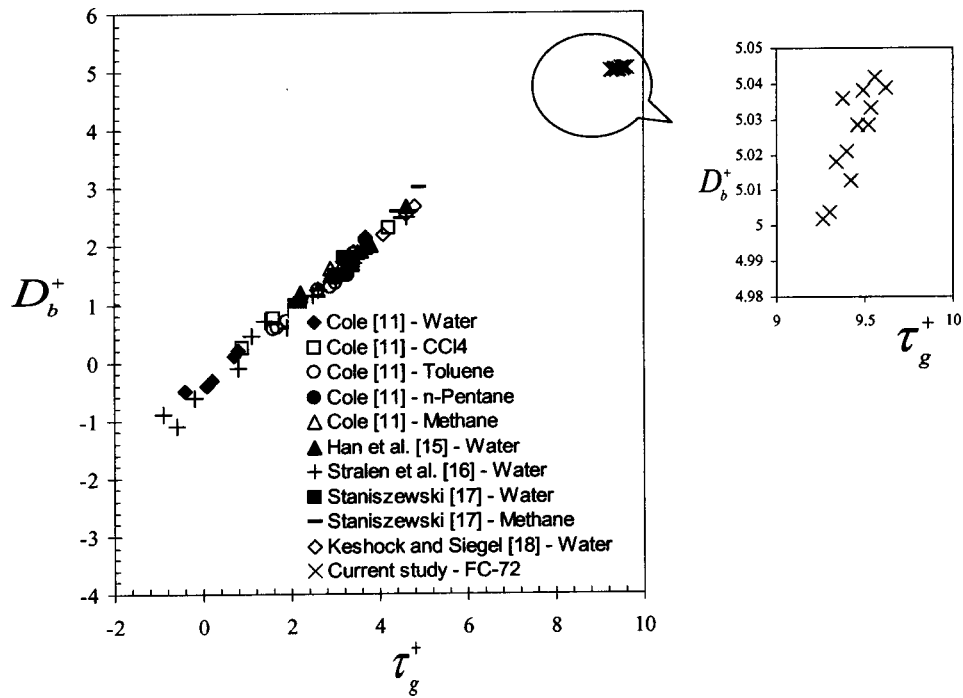| Properties	ρ_l (kg/m^3)	ρ_v (kg/m^3)	H_{fg} (kJ/kg)	C_{pl} (kJ/kg)	$\alpha_1 (10^8$ m^2/s)
Value	1680	11.5	87.92	1.0467	3.244

Fig. 16 Comparison of dimensionless growth time and bubble departure size

Rainey and You [3] is that larger heaters are more likely to have more surface irregularities and therefore a wider size range of cavities from which bubbles can nucleate [15–18].

Conclusion

An experimental study was performed to examine the effects of heater size on pool boiling. For a miniature-scale heater used in the current work, it was found that the boiling is controlled by the microlayer evaporation in the lower superheat regime while conduction through vapor film is the dominant heat transfer mechanism in the higher superheat regime. The two regimes are separated by the peak heat flux. The heat transfer is closely associated with the dynamics of the bubbles on the heater. During the bubble departure, a heat flux spike was observed in the lower superheat regime whereas a heat flux dip was found in the higher superheat regime. In general, as the heater size is reduced in pool boiling, the following characteristics may be summarized:

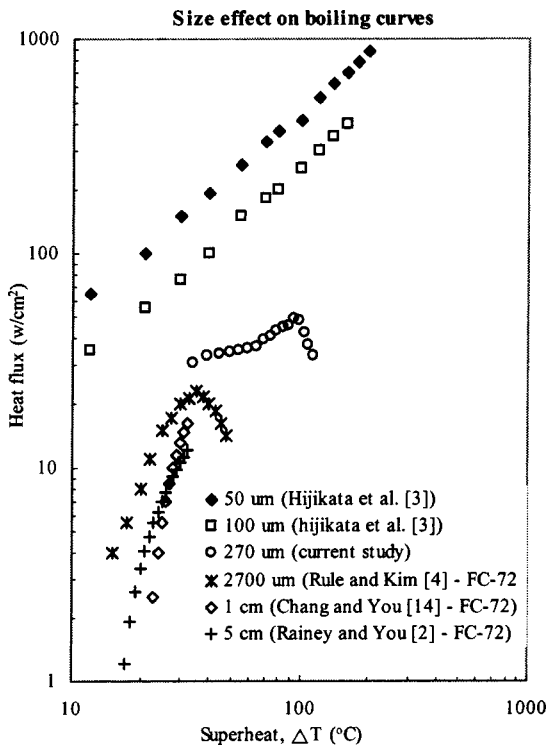1) The boiling curve shifts towards higher fluxes with corresponding increases in superheats.

Fig. 17 Comparison of boiling curves for different heater sizes
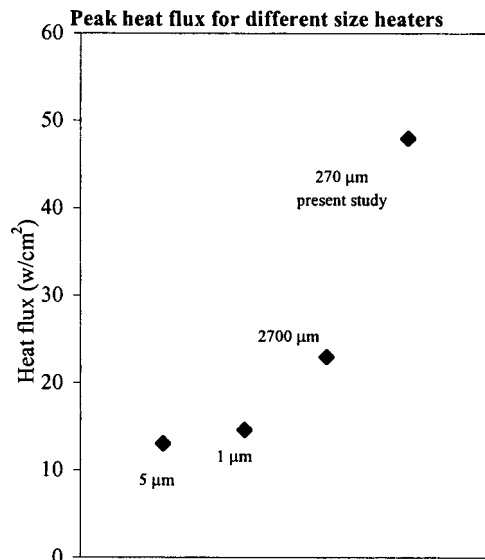

Fig. 18 Comparison of peak heat fluxes for different heater sizes

2) There is a very slow growth period before the bubble departure. This results in bubble growth times that are longer than those for boiling on larger heaters.
3) Bubble departure sizes are relatively larger.
4) Bubble incipience superheat increases as heater size decreases.

Acknowledgments

Nomenclature

C_{pl} = specific heat (kJ/kg·K)
D_b^+ = dimensionless bubble departure diameter
D_b = bubble departure diameter
g = gravitational acceleration constant
H_{fg} = latent heat of vaporization (kJ/kg)
Ja = Jakob number
L_o = heater characteristic length
q''_{cond1} = conduction heat transfer rate per unit area from a heater to substrate with boiling (W/cm^2)
q''_{cond2} = conduction heat transfer rate per unit area from a heater to substrate without boiling (W/cm^2)
q''_{cond3} = conduction heat transfer rate per unit area from a heater to air and vapor mixture (W/cm^2)
$q''_{natural}$ = natural convective heat transfer rate per unit area from a heater (W/cm^2)
q''_{rad1} = radiation heat transfer rate per unit area from a heater with boiling (W/cm^2)
q''_{rad2} = radiation heat transfer rate per unit area from a heater without boiling (W/cm^2)
q''_{raw1} = total heat transfer rate per unit area supplied to a heater with boiling (W/cm^2)
q''_{raw2} = total heat transfer rate per unit area supplied to a heater without boiling (W/cm^2)
T_s = heater temperature
V_{off} = offset voltage of the Opamp
ΔT_{sup} = heater surface superheat
ε = uncertainty
ρ_l = liquid density (kg/m^3)
ρ_v = vapor density (kg/m^3)
α_l = thermal diffusivity (kJ/kg·K)
τ_g^+ = dimensionless bubble growth time
τ_g = bubble growth time
σ = surface tension

References

[1] Gad-el-Hak, M., 1999, "The Fluid Mechanics of Microdevices—The Freeman Scholar Lecture," J. Fluids Eng., **121**, pp. 5–31.
[2] Rainey, K. N., and You, S. M., 2001, "Effects of Heater Size and Orientation on Pool Boiling Heat Transfer From Microporous Coated Surfaces," Int. J. Heat Mass Transfer, **44**, pp. 2589–2599.
[3] Hijikata, K., Yamamoto, N., and Takagi, S., 1997, "Boiling Heat Transfer From a Micro Heater," *Microelectronicsmechanical Systems (MEMS)*, ASME, New York.
[4] Rule, T., and Kim, J., 1999, "Heat Transfer Behavior on Small Horizontal Heaters During Pool Boiling of FC-72," Journal of Heat Transfer , **121**, pp. 386–393.
[5] Chen, T., and Chung, J. N., 2002, "Coalescence of Bubbles in Nucleate Boiling on Microheaters," Int. J. Heat Mass Transfer, **45**, pp. 2329–2341.
[6] Incropera, F. P., and DeWitt, D. P., 2002, *Fundamentals of Heat and Mass Transfer*, Fifth Edition, Wiley, New York.
[7] Kline, S. J., and McClintock, F. A., 1953, "Describing Uncertainties in Single-Sample Experiments," Mechanical Engineering, **75**, pp. 3–8.
[8] You, S. M., Simon, T. W., Bar-Cohen, A., and Hong, Y. S., 1995, "Effects of Dissolved Gas Content on Pool Boiling of a Highly Wetting Fluid," J. Heat Transfer, **117**, pp. 687–692.
[9] Hong, Y. S., Ammerman, C. N., and You, S. M., 1997, "Boiling Characteristics of Cylindrical Heaters in Saturated, Gas-saturated, and Pure-Subcooled FC-72," J. Heat Transfer, **119**, pp. 313–318.
[10] Nukiyama, S., 1934, "The Maximum and Minimum Values of Heat Transmittal from Metal to Boiling Water Under Atmospheric Pressure," J. Japan Soc. Mech. Eng., **37**, pp. 367–374.
[11] Cole, R., 1967, "Bubble Frequencies and Departure Volumes at Subatmospheric Pressures," AIChE J., **13**, pp. 779–783.
[12] Scriven, L. E., 1958, "On the Dynamics of Phase Growth," Chem. Eng. Sci., **90**, pp. 1–13.
[13] Yang, C., Wu, Y., Yuan, X., and Ma, C., 2000, "Study on Bubble Dynamics for Pool Nucleate Boiling," Int. J. Heat Mass Transfer, **43**, pp. 203–208.
[14] Chang, J. Y., and You, S. M., 1996, "Heater Orientation Effects on Pool Boiling of Micro-Porous-Enhanced Surfaces in Saturated FC-72," ASME J. Heat Transfer, **118**, pp. 937–943.
[15] Han, C. Y., and Griffith, P., 1965, "The Mechanism of Heat Transfer in Nuclear Pool Boiling—Part I," Int. J. Heat Mass Transfer, **8**, pp. 887–904.
[16] Stralen, S. J. D., Soha, M. S., Cole, R., and Sluyter, W. M., 1975, "Bubble Growth Rates in Pure and Binary Systems, Combined Effect of Relaxation and Evaporation Microlayers," Int. J. Heat Mass Transfer, **18**, pp. 453–467.
[17] Staniszewski, B. E., 1959, "Nucleate Boiling Bubble Growth and Departure," Tech. Rep. No. 16, Div. Sponsored Res. MIT, Cambridge, MA.
[18] Keshock, E. G., and Siegel, R., 1964, "Forces Acting on Bubbles in Nucleate Boiling Under Normal and Reduced Gravity Condictions," *NASA Tech. Note. TN D-2299*.

Inverse Determination of the Local Heat Transfer Coefficients for Nucleate Boiling on a Horizontal Cylinder

H. Louahlia-Gualous
Professor Assistant
e-mail: hasna.gualous@utbm.fr

P. K. Panday
Professor

E. A. Artioukhine
Professor

Centre de recherche sur les écoulements, les surfaces et les transferts, Laboratoire CREST UTBM_UFC UMR CNRS 6000, Site IGE, 2 avenue Jean Moulin, 90000 Belfort, France

This article treats the local heat transfer for nucleate pool boiling around the cylinder using the inverse heat conduction analysis. The physical model considers a half section of a cylinder with unknown surface temperature and heat flux density. The iterative regularization and the conjugate gradient methods are used for solving the inverse analysis. The local Nusselt number profiles for nucleate pool boiling are presented and analyzed for different electric heat. The mean Nusselt number estimated by IHCP is closed with the measured values. The results of IHCP are compared to those of Cornewell and Houston (1994), Stephan and Abdelsalam (1980) and Memory et al. (1995). The influence of the error of the measured temperatures and the error in placement of the thermocouples are studied. [DOI: 10.1115/1.1603776]

Keywords: Boiling, Heat Transfer

1 Introduction

Numerous investigations have been performed to explain the physical mechanism of boiling because it is an efficient heat transfer mode and finds applications in chemical, refrigeration, power and nuclear industries as well as in the cooling of electronic devices. The safe and efficient performance of heat transfer equipment requires knowledge of heat transfer coefficient, structure of flow, pressure loss, etc. Extensive experimental and theoretical studies on pool boiling have been reported in the literature [1,2]. A large amount of experimental research in pool boiling is oriented towards the study of mean heat transfer and the effects of different parameters on boiling such as: nucleation site density, bubble growth, bubble frequency, etc. Barthau [3] found that heat transfer of an individual active site is decreased by increasing pressure. Pioro [4] has measured the constants for the Rohsenow correlation for nucleate pool boiling on horizontal thick plates of four fluids. The influence of the coating thickness and porosity on enhancing mean heat transfer of nucleate boiling have been reported by Hsieh and Weng [5]. Hsieh and Hsu [6] have compared experimental results of boiling average heat transfer on plain and rib-roughened tube geometries for three different fluids (R114, R134a, and water). Erden and Balkan [7] and Gorenflo et al. [8] have measured average heat transfer coefficients in nucleate pool boiling of binary mixtures in order to determine the influence of mixture composition. Memory et al. [9] have analyzed the effect of R114-oil mixtures on average heat transfer of nucleate pool boiling on smooth and enhanced surfaces. Recently, nucleate pool boiling results for porous metallic coatings have been reported by Cieslinski [10] and the influence of PTFE coatings have been studied by Vittala et al. [11] for boiling of alcohols. Chang and You [12] have evaluated the effects of surface micro-geometry and macro-geometry on boiling mean heat transfer of FC-87 and R-123 on cylindrical heater surface. Kang [13] has conducted an experimental study of a tubular heat exchanger and found that the tube inclination influences average heat transfer for pool boiling. Cornwell and Houston [14] have noted that the local heat transfer

in pool boiling is due to liquid convection and evaporation under sliding bubbles and used bubble Reynolds number to correlate mean Nusselt number (Nu_m)

$$\frac{\mathrm{Nu}_m}{\mathrm{Re}_b^{0.67}\mathrm{Pr}^{0.4}} = 9.7 P_c^{0.5}\left[1.8\left(\frac{P}{P_c}\right)^{0.17} + 4\left(\frac{P}{P_c}\right)^{1.2} + 10\left(\frac{P}{P_c}\right)^{10}\right] \quad (1)$$

where Re_b is the boiling Reynolds number defined by $\mathrm{Re}_b = q_w D/\mu_L h_{fg}$.

Stephan and Abdelsalam [15] have applied the method of regression analysis to the many existing experimental results in order to establish one general form of equation to predict average heat transfer in pool boiling.

$$\mathrm{Nu}_m = 207\left(\frac{q_w D_b}{\lambda_L T_{\mathrm{sat}}}\right)^{0.745}\left(\frac{\rho_v}{\rho_L}\right)^{0.587}\mathrm{Pr}_L^{0.533} \quad (2)$$

where D_b is the equilibrium break-off-diameter defined by

$$D_b = 0.146\alpha\left(\frac{2\Omega}{g(\rho_L - \rho_v)^{0.5}}\right) \quad (3)$$

This brief bibliography shows that numerous studies on pool boiling are concerned only the evaluation of the average heat transfer but the local heat transfer in pool boiling has not retained much attention. This paper treats the local heat transfer for nucleate pool boiling on horizontal cylinder by solving inverse heat conduction problem (IHCP). Various numerical methods have been developed to solve IHCP for steady state (Martin and Dulikravich [16], Maillet et al. [17]) and transient problems (Lin et al. [18], Hantasiriwan [19], Abou khachfe and Jarny [20], Chen et al. [21]). In this study the iterative regularization method is applied because it can be easily extended to nonlinear as well as to transient problems. The physical model considers a cylinder with an unknown surface temperature and heat flux density. The temperature sensors are located inside the solid to measure the temperature profile. IHCP requires only these temperature measurements to determine the local thermal boundary conditions.

2 Physical and Mathematical Model

A long cylindrical tube of internal radius R_1 and external radius R_2 with nucleate boiling on the external surface is considered. The problem is assumed to be two-dimensional and symmetrical about
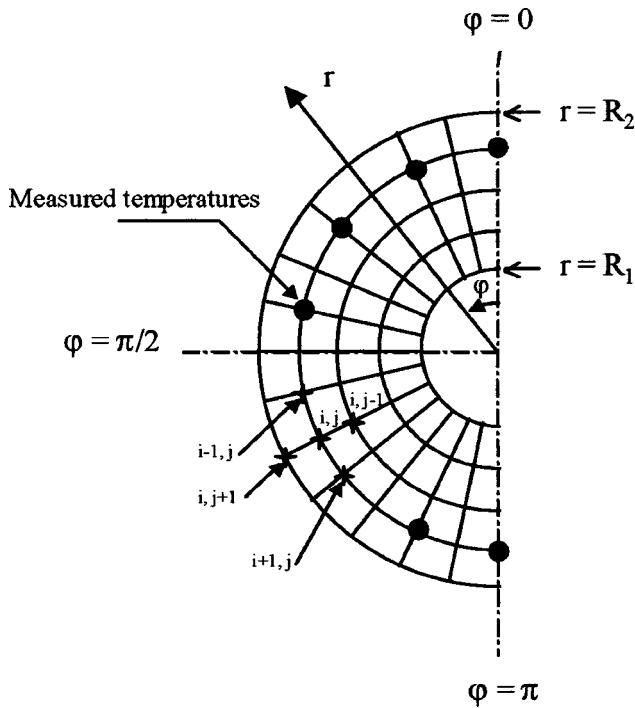
Fig. 1 Geometry of two-dimensional cylinder

the vertical plane through the axis (Fig. 1). The thermal conductivity of the cylinder is assumed constant and independent of temperature. The governing equation for the steady state heat conduction and the boundary conditions are expressed as

$$\frac{\partial^2 T(r,\varphi)}{\partial r^2} + \frac{1}{r}\frac{\partial T(r,\varphi)}{\partial r} + \frac{1}{r^2}\frac{\partial^2 T(r,\varphi)}{\partial \varphi^2} = 0,$$

$$(R_1 < r < R_2 \text{ and } 0 < \varphi < \pi) \qquad (4)$$

$$\frac{\partial T}{\partial \varphi}(r,0) = 0, \qquad (5)$$

$$\frac{\partial T}{\partial \varphi}(r,\pi) = 0, \qquad (6)$$

$$a\lambda\frac{\partial T}{\partial r}(R_1,\varphi) + bT(R_1,\varphi) = f(\varphi) \qquad (7)$$

The function $f(\varphi)$ represents either the heat flux density ($a=1, b=0$) or the temperature ($a=0, b=1$) imposed at the internal surface ($r=R_1$) of the cylindrical tube.

$$\lambda\frac{\partial T}{\partial r}(R_2,\varphi) = q_w(\varphi) \qquad (8)$$

The IHCP is used to estimate the unknown boundary condition $q_w(\varphi)$ from the additional data T_{meas} obtained during experiment. It consists in finding the optimal solution that minimizes the residual functional defined by the following equation:

$$J(q_w) = \frac{1}{2}\sum_{n=1}^{N_{\text{meas}}}[T(r_n,\varphi_n;q_w) - T_{\text{meas}}(r_n,\varphi_n)]^2 \qquad (9)$$

where the temperatures $T(r_n,\varphi_n;q_w)$ are the solution of the direct problem given by Eqs. (4–8) for an imposed heat flux density. The minimization is carried out by using the unconstrained conjugate gradient algorithm (Alifanov et al. [22]). The heat flux density $q_w(\varphi)$ is approximated in the form of a cubic B-spline and the IHCP is reduced to the estimation of a vector of parameters. The conjugate gradient procedure is iterative; at each iteration it the

successive improvements of desired parameters are built. The descent parameter is computed using a linear approximation as follows:

$$\gamma^{it} = \frac{\sum_{n=1}^{N_{\text{meas}}}[T^{it}(r_n,\varphi_n;q_w) - T_{\text{meas}}(r_n,\varphi_n)]\theta^{it}(r_n,\varphi_n;\delta q_w)}{\sum_{n=1}^{N}[\theta^{it}(r_n,\varphi_n;\delta q_w)]^2} \qquad (10)$$

The variation of temperature θ^{it} resulting from the variation of heat flux density is determined by solving the problem in variation. It is defined at the sensor locations (r_n,φ_n). The variation of functional $J(q_w)$ resulting from temperature variation is given by

$$\delta J(q_w,\delta q_w) = \sum_{n=1}^{N_{\text{meas}}}[T(r_n,\varphi_n;q_w) - T_{\text{meas}}(r_n,\varphi_n)]\theta(r_n,\varphi_n) \qquad (11)$$

where $\theta(r_n,\varphi_n;\delta q_w)$ is defined at the sensor locations (r_n,φ_n) and δq_w is approximated by a cubic **B**-spline.

2.1 Problem in Variation. The problem in variation is defined by the following equations:

$$\frac{\partial^2\theta}{\partial r^2} + \frac{1}{r}\frac{\partial\theta}{\partial r} + \frac{1}{r^2}\frac{\partial^2\theta}{\partial\varphi^2} = 0, \quad R_1 < r < R_2, \quad 0 < \varphi < \pi \quad (12)$$

$$\frac{\partial\theta}{\partial\varphi}(r,0) = 0, \qquad (13)$$

$$\frac{\partial\theta}{\partial\varphi}(r,\pi) = 0, \qquad (14)$$

$$a\lambda\frac{\partial\theta}{\partial r}(R_1,\varphi) + b\theta(R_1,\varphi) = 0, \qquad (15)$$

$$-\lambda\frac{\partial\theta}{\partial r}(R_2,\varphi) = \delta q_w(R_2,\varphi). \qquad (16)$$

2.2 Lagrangian Functional in Variation and Adjoint Problem. Using the Lagrange multiplier method, the Lagrangian functional is defined through Eqs. (10) and (11) with the constraints defined by Eqs. (12–15).

$$L(q_w) = \frac{1}{2}\sum_{n=1}^{N_{\text{meas}}}[T(r_n,\varphi_n;q_w) - T_{\text{meas}}(r_n,\varphi_n)]^2$$

$$+ \int_0^\pi\int_{R_1}^{R_2}\psi(r,\varphi)\left[\frac{\lambda}{r}\frac{\partial}{\partial r}\left(r\frac{\partial T}{\partial r}\right) + \frac{\lambda}{r^2}\frac{\partial^2 T}{\partial\varphi^2}\right]dr\,d\varphi$$

$$+ \int_{R_1}^{R_2}\xi(r)\lambda\frac{\partial T}{\partial\varphi}(r,0)dr + \int_{R_1}^{R_2}\omega(r)\lambda\frac{\partial T}{\partial\varphi}(r,\pi)dr$$

$$+ \int_0^\pi\gamma(\varphi)\left[\lambda\frac{\partial T}{\partial r}(R_2,\varphi) + q_w(\varphi)\right]d\varphi$$

$$\times \int_0^\pi\mu(\varphi)\left[a\lambda\frac{\partial T}{\partial r}(R_1,\varphi) + bT(R_1,\varphi) - f(\varphi)\right]d\varphi \qquad (17)$$

Let $\psi(r,\varphi)$, $\xi(r)$, $\omega(r)$, $\mu(\varphi)$, and $\gamma(\varphi)$ be the Lagrange multiplier. The necessary condition of the optimization problem is obtained from the following equation:

$$\delta L(q_w,\delta q_w) = 0 \qquad (18)$$

Let $\delta L(q_w,\delta q_w)$ be the variation of the Lagrangian functional. $\delta L(q_w,\delta q_w)$ is defined using the Eqs. (10–15).

$$\delta L(q_w, dq_w) = \frac{1}{2} \sum_{n=1}^{N_{\text{meas}}} [T(r_n, \varphi_n; q_w) - T_{\text{meas}}(r_n, \varphi_n)] \theta(r_n, \varphi_n)$$

$$+ \int_0^\pi \int_{R_1}^{R_2} \psi(r, \varphi) \left[\lambda \frac{\partial^2 \theta}{\partial r^2} + \frac{\lambda}{r} \frac{\partial \theta}{\partial r} + \frac{\lambda}{r^2} \frac{\partial^2 \theta}{\partial \varphi^2} \right] dr d\varphi$$

$$+ \int_{R_1}^{R_2} \xi(r) \lambda \frac{\partial \theta}{\partial \varphi}(r, 0) dr$$

$$+ \int_{R_1}^{R_2} \omega(r) \lambda \frac{\partial \theta}{\partial \varphi}(r, \pi) dr$$

$$+ \int_0^\pi \gamma(\varphi) \lambda \frac{\partial \theta}{\partial r}(R_2, \varphi) d\varphi$$

$$+ \int_0^\pi \mu(\varphi) \left[a\lambda \frac{\partial \theta}{\partial r}(R_1, \varphi) + b\theta(R_1, \varphi, t) \right] d\varphi$$

$$+ \int_0^\pi \gamma(\varphi) \delta q_w(\varphi) d\varphi \qquad (19)$$

The condition $\delta L(q_w, \delta q_w) = 0$ requires that all coefficients of the temperature variation $\theta(r, \varphi)$ are equal to 0. To satisfy this condition the necessary conditions of optimization are defined in the form of adjoint problem.

$$\lambda \frac{\partial^2 \psi}{\partial r^2} - \frac{\lambda}{r} \frac{\partial \psi}{\partial r} + \frac{\lambda}{r^2} \psi + \frac{\lambda}{r^2} \frac{\partial^2 \psi}{\partial \varphi^2} = S(r, \varphi),$$

$$R_1 < r < R_2, \quad 0 < \varphi < \pi, \qquad (20)$$

$$\frac{\partial \psi}{\partial \varphi}(r, 0) = 0, \qquad (21)$$

$$\frac{\partial \psi}{\partial \varphi}(r, \pi) = 0, \qquad (22)$$

$$a\lambda \frac{\partial \psi}{\partial r}(R_1, \varphi) + \left(b - a \frac{\lambda}{R_1} \right) \psi(R_1, \varphi) = 0 \qquad (23)$$

$$\lambda \frac{\psi(R_2, \varphi)}{R_2} = \lambda \left. \frac{\partial \psi(r, \varphi)}{\partial r} \right|_{r = R_2} \qquad (24)$$

$S(r, \varphi)$ represents the deviation between temperature measurements and computed temperatures. It is equal to 0 every where in the physical domain except at sensor locations (r_n, φ_n).

$$S(r, \varphi) = - \sum_{n=1}^{N_{\text{meas}}} \delta(r, r_n; \varphi, \varphi_n) [T(r_n, \varphi_n; q_w) - T_{\text{meas}}(r_n, \varphi_n)] \qquad (25)$$

where the Dirac function is defined by

$$\delta(r, r_n; \varphi, \varphi_n) = \delta(r - r_n) \delta(\varphi - \varphi_n) \qquad (26)$$

where $\delta(0) = 1$, $\delta(r) = 0$ for $r \neq 0$ and $\delta(\varphi) = 0$ for $\varphi \neq 0$. If the direct problem and the adjoint problem are verified, the variation of Lagrangian functional becomes:

$$\delta L(q_w, \delta q_w) = - \int_0^\pi \psi(R_2, \varphi) \delta q_w(R_2, \varphi) d\varphi \qquad (27)$$

2.3 Computation of the Vector Gradient. The variation of functional $J(q_w)$ can be approximated in the form

$$\delta J(q_w, \delta q_w) = - \int_0^\pi \int_{R_1}^{R_2} \left[\lambda \frac{\partial^2 \psi}{\partial r^2} - \frac{\lambda}{r} \frac{\partial \psi}{\partial r} + \frac{\lambda}{r^2} \psi \right.$$

$$\left. + \frac{\lambda}{r^2} \frac{\partial^2 \psi}{\partial \varphi^2} \right] \theta(r, \varphi) dr d\varphi \qquad (28)$$

Integration by parts gives

$$\bullet - \int_{R_1}^{R_2} \frac{\partial^2 \psi}{\partial r^2} \theta(r, \varphi) dr = - \left| \frac{\partial \psi}{\partial r} \theta - \psi \frac{\partial \theta}{\partial r} \right|_{r=R_1}^{r=R_2}$$

$$- \int_{R_1}^{R_2} \psi \frac{\partial^2 \theta}{\partial r^2}(r, \varphi) dr. \qquad (29)$$

$$\bullet \int_{R_1}^{R_2} \frac{\lambda}{r} \frac{\partial \psi}{\partial r} \theta(r, \varphi) dr = \left| \frac{\lambda}{r} \psi \theta(r, \varphi) \right|_{r=R_1}^{r=R_2}$$

$$- \int_{R_1}^{R_2} \left[\frac{\lambda}{r} \frac{\partial \vartheta}{\partial r} - \frac{\lambda}{r^2} \theta \right] \psi(r, \varphi) dr \qquad (30)$$

$$\bullet - \frac{\lambda}{r^2} \int_0^\pi \frac{\partial^2 \psi}{\partial \varphi^2} \theta(r, \varphi) d\varphi = - \frac{\lambda}{r^2} \left| \frac{\partial \psi}{\partial \varphi} \theta - \psi \frac{\partial \theta}{\partial \varphi} \right|_{\varphi=0}^{\varphi=\pi}$$

$$- \frac{\lambda}{r^2} \int_0^\pi \psi \frac{\partial^2 \theta}{\partial \varphi^2}(r, \varphi) d\varphi \qquad (31)$$

Substituting Eqs. (28–30) into Eq. (27), the variation of functional becomes using Eqs. (12–15)

$$\delta J(q_w, \delta q_w) = \int_0^\pi \left[-\lambda \frac{\partial \psi}{\partial r} \theta(R_2, \varphi) + \lambda \psi \frac{\partial \theta}{\partial r}(R_2, \varphi) \right.$$

$$\left. + \frac{\lambda}{R_2} \psi \theta(R_2, \varphi) \right] d\varphi \qquad (32)$$

Substituting Eqs. (15) and (25) into Eq. (31), $\delta J(q_w, \delta q_w)$ becomes

$$\delta J(q_w, \delta q_w) = - \int_0^\pi \psi(R_2, \varphi) \delta q_w(\varphi) d\varphi = \delta L(q_w, \delta q_w) \qquad (33)$$

By definition, the variation of functional is defined in the form of scalar product of gradient $J'_{q_w}(\varphi)$ and the variation of estimate function $\delta q_w(\varphi)$

$$\delta J(q_w, \delta q_w) = \int_0^\pi J'_{q_w}(\varphi) \delta q_w(\varphi) d\varphi \qquad (34)$$

Equations (32) and (33) implies that

$$J'_{q_w}(\varphi) = - \psi(R_2, \varphi) \qquad (35)$$

Using Eqs. (17) and (34) the variation of the functional $\delta J(q_w, \delta q_w)$ becomes

$$\delta J(q_w, \delta q_w) = \sum_{i=1}^m \left[\int_0^\pi - \psi(R_2, \varphi) \Phi_i d\varphi \right] \delta p_i \qquad (36)$$

This last equation implies that the components of the gradient J'_i in R^m space is defined as

$$J'_i = \int_0^\pi - \psi(R_2, \varphi) \Phi_i d\varphi, \quad i = 1, 2, ..., m \qquad (37)$$

where m is the number of approximation parameters and Φ_i are given basis cubic B-Spline.

2.4 Algorithm. The following iterative procedure is adopted to solve the IHCP: To start the calculations ($it = 1$) the heat flux density $q_w(\varphi)$ is taken equal to zero.
The following steps are then executed:

 i. solution of the direct problem,
 ii. calculation of the residual functional,
 iii. solution of the adjoint problem,
 iv. calculation of the components of the functional gradient,

v. calculation of the component of descent direction,
vi. solution of the problem in variation to determine the descent parameter,
vii. the new value of the heat flux density is corrected.

If the convergence criterion is not satisfied the iterative procedure is repeated.

The governing equations and the boundary conditions of the direct problem are discretized using the finite difference method. The energy balance is involved for node (i,j) in terms of the rate of heat flow by conduction to (i,j) from its neighboring nodes, the rate of internal heat generation in the control volume represented by (i,j) and the rate at which the control volume is rising in temperature. Let i and j be respectively the index of angular and radial coordinates. The same numerical discretization is adopted for adjoint problem and the problem in variation. The Gauss Seidel iterative procedure is used to solve the problem in variation and the direct and the adjoint problems (Holman [25]).

3 Regularization

The inverse problems are ill-posed and numerical solution depends on the fluctuation occurring at the measurements. Two approaches have been used to obtain a stable solution of the IHCP. The first one is the iterative regularization method. According to this method, the iterative improvements of the approximation parameters is terminated by choosing the residual criterion depending on the temperature errors

$$J(q_w) \approx \frac{1}{2} \xi^2 \tag{38}$$

where ξ^2 is the total measurement error defined as follows:

$$\xi^2 = \sum_{n=1}^{N_{\text{meas}}} \sigma^2(r_n, \varphi_n) \tag{39}$$

where $\sigma^2(r_n, \varphi_n)$ is the standard deviation for the temperature measured at the nth point.

If the number of measurement points N_{meas} is relatively small, the sensitivity of the residual functional to variations of the approximation parameters decreases rapidly (Blanc et al. [23]). To increase the sensitivity, a second approach based on smoothing the experimental data is applied (Loulou et al. [24]). This approach allows to interpolate the experimental temperatures values and to compute discrete temperatures at nodes (r_n, φ_n).

4 Experimental Setup

The experimental setup shown in Fig. 2 consists of a closed rectangular vessel filled with saturated fluid. A pressure gauge is used to measure the pressure in the vessel. A Pyrex glass plate is placed in front of the vessel to visualize the phenomena. Before each experiment the vacuum is drawn in the vessel and it is then filled with the working fluid (R-113). The heated test section is made of a smooth copper cylinder immersed in the liquid and thermally insulated at both extremities. The boiling occurs on a cylinder with 28 mm of outer diameter, 4 mm of thickness and 120 mm of length. The test section is heated by an electric heater of 2000 W and the heat flux is controlled by the electrical power input using an auto-transformer. The vapor generated from boiling is condensed in a water-cooled condenser. The mass flow of the coolant is controlled to maintain the saturation temperature at a constant value. The electrical power input is measured using an ammeter and a voltmeter. The temperatures of the liquid and vapor phases are measured by thermocouples. The temperatures inside the solid are measured with 200 μm diameter chromel-alumel calibrated thermocouples placed at 0.4 mm and at 1.5 mm from the wetted surface (Fig. 3). The wall temperatures were measured at two different sections as shown in Fig. 4. A Hewlett Packard data acquisition system is used to record all temperature measurements for an imposed wall electric heat. The full details of the
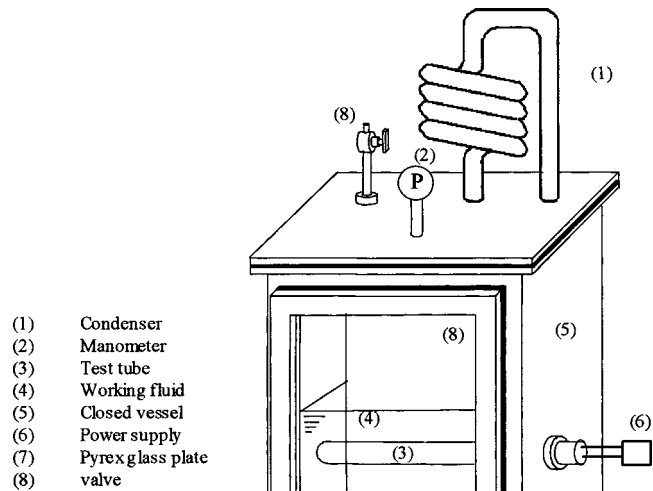

(1) Condenser
(2) Manometer
(3) Test tube
(4) Working fluid
(5) Closed vessel
(6) Power supply
(7) Pyrex glass plate
(8) valve

Fig. 2 Experimental apparatus

experimental set-up are given by Khan [26]. All the tests reported here have been made with refrigerant R-113 at a constant saturation temperature of 52.6°C.

5 Results and Discussions

The numerical procedure is verified by using the temperature data calculated from the direct problem for a known circumferential heat flux density to simulate the measured temperatures inside the cylinder for the inverse problem. The local heat flux required to solve the direct problem is assumed to be variable around the surface of cylinder. The local heat flux density determined from IHCP is closed to the exact heat flux density [27].

In this work, numerical calculations were carried out for a cylinder with internal radius $R_1 = 10$ mm and external radius $R_2 = 14$ mm. For all computations 31 nodes along the circumference and 16 nodes in the radial direction are used. The computations are conducted by using a uniform heat flux density as an imposed boundary condition at R_1. The measured wall temperatures (T_{meas}) at $R_{\text{meas}} = 13.6$ mm are used to calculate the residual functional.
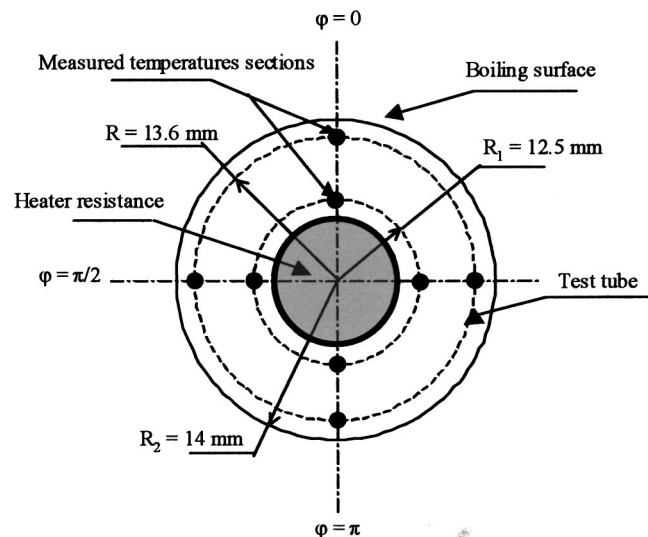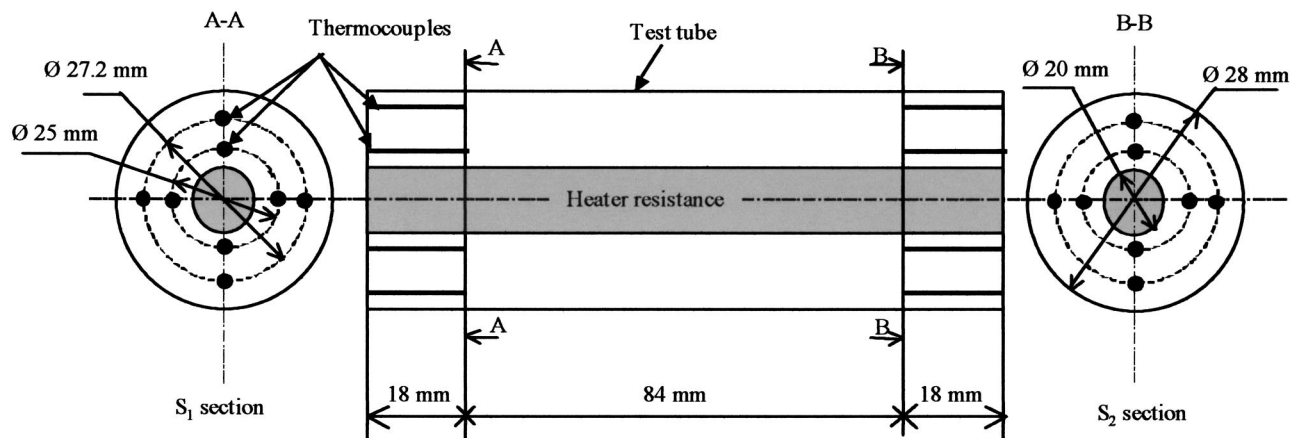

Fig. 3 Test section

Fig. 4 Measurement sections locations

5.1 Local Heat Transfer Results for Nucleate Pool Boiling.
The experimental study of boiling over a horizontal smooth tube
is conducted for electric heat varied from 400 W to 1500 W. The
test fluid is taken at a saturation temperature of 52.6°C. For each
electric heat, the temperatures (T_{meas}) are measured inside the
solid at R_{meas} = 13.6 mm and were represented by the polynomial
functions by using the least square method (95% confidence).

For each imposed electric heat, the local circumferential tem-
perature $T_c(\varphi)$ and heat flux density $q_w(\varphi)$ are determined by
solving IHCP. The local heat transfer coefficients h_φ were calcu-
lated from $q_w(\varphi)$ and the local difference between $T_c(\varphi)$ and the
saturation temperature T_{sat}. Thus:

$$h_\varphi = \frac{q_w(\varphi)}{(T_c(\varphi) - T_{sat})} \tag{40}$$

The estimated local Nusselt number Nu_φ is deduced from the
local heat transfer coefficient as

$$Nu_\varphi = \frac{h_\varphi D}{\lambda_L} \tag{41}$$

Figure 5(a–b) show that for each electric heat, the heat transfer
is highest at the top of the cylinder ($\varphi = 0$) and decreases steadily
around the tube to attain a minimum value at about $\pi/2$. Beyond
this point, heat transfer increases with increase of the angle φ to
attain another maximum value at the bottom of the cylinder ($\varphi
= \pi$). The non-uniform profile of heat transfer around the cylin-
der is due to the motion of bubbles after their detachment from the
nucleation site and the induced liquid convection. The heat trans-
fer is important in the zone where the bubbles are free to move
vertically under buoyancy after detachment from the nucleation
site. It has been observed that when the nucleation occurs at the
under-side of a horizontal cylinder, the bubbles slide along the
surface to a zone near the top before they leave the surface. This
sliding of the bubbles seems to introduce convection currents re-
sponsible for decrease of nucleation. At the bottom of the cylinder,
the nucleation is important because the small nucleating bubbles
cannot leave the boiling surface with ease because of the presence
of the cylinder. Figures 5(a–b) also show that the increase of
electric heat tends to increase the peripheral variation of boiling
heat transfer around the tube because of increased convection ef-
fect. At low electric heat the convection currents are week and the
suppression of the nucleation due to the convection is less impor-
tant. The variation of local pool boiling heat transfer are compa-
rable to those obtained by Parken et al. [28] for the boiling of
falling film on a cylinder. Generally, nucleate pool boiling on a
horizontal smooth cylinder induces a formation of a bubbly layer
around the tube. The local boiling heat transfer distribution de-
pends on two physical phenomena produced in this bubbly layer.

The first one is the convection of the liquid and the second is the
evaporation of the liquid thin layer under bubbles before
detachment.

The local temperature residuals resulting from these computa-
tions are defined as the difference between the measured and es-
timated temperatures. Figure 5(c) shows that the mean value of
the temperature residuals is about zero. The standard deviation of
temperature residuals for this computation is estimated to 0.8 C.
Figure 5(d) shows that the residual functional decreases when the
iteration index increases. For each imposed electric heat, the mea-
surement errors are not taken into account and the iterations were
continued till the minimization of residual functional is attained.

5.2 Mean Heat Transfer for Nucleate Pool Boiling. The
average heat transfer coefficient (h_m) is determined by using two
different procedures. The first one determines h_m from the total
electric power ($q_{w,e}$) imposed at the internal radius of the experi-
mental cylinder and the average circumferential temperature
($T_{c,m}$) determined by solving IHCP.

$$h_m = \frac{q_{w,e}}{(T_{c,m} - T_{sat})} \tag{42}$$

$$\text{where} : T_{c,m} = \frac{1}{\pi} \int_0^\pi T_c(\varphi) d\varphi$$

The second method consists to deduce h_m from the average heat
flux density ($q_{w,m}$) estimated by IHCP and the difference between
the temperatures $T_{c,m}$ and T_{sat}.

$$h_m = \frac{q_{w,m}}{(T_{c,m} - T_{sat})} \tag{43}$$

$$\text{where} : q_{w,m} = \frac{1}{\pi} \int_0^\pi q_w(\varphi) d\varphi$$

where $q_w(\varphi)$ is the local heat flux density estimated by solving
IHCP.

In the present study, the temperature inside the experimental
cylinder is measured at two different sections S_1 and S_2 84 mm
apart (see Fig. 4). Figure 6 shows for example, Nu_φ estimated for
S_1 and S_2 sections for electric heat of 1500 W. It is noted that
local heat transfer is not uniform along the axial direction of the
cylinder because of the non-uniformity of active nucleation sites
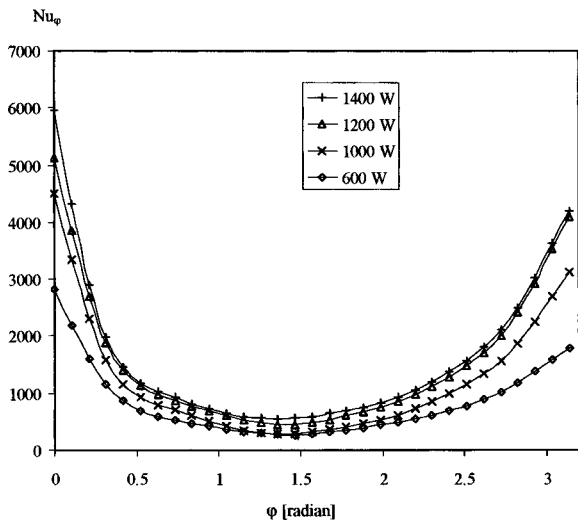distribution.

The mean heat flux density $q_{w,m}$ used in Eq. (43) represents the
average value of estimated heat flux density for S_1 and S_2 sec-
tions. Figure 7 compares the mean Nusselt number (Nu_m) de-
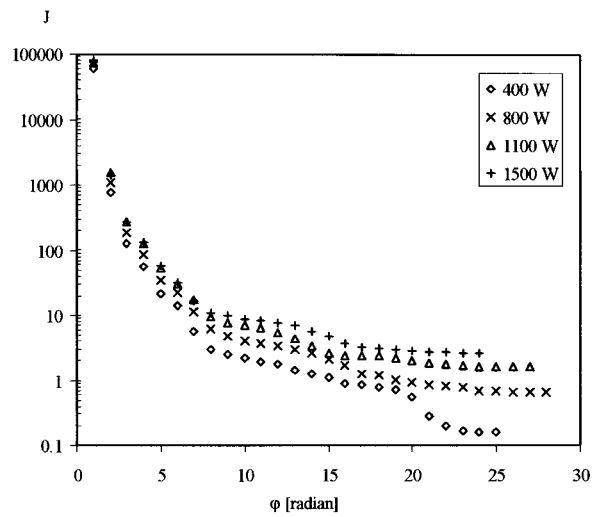duced from h_m determined from measured electrical heat flux Eq.
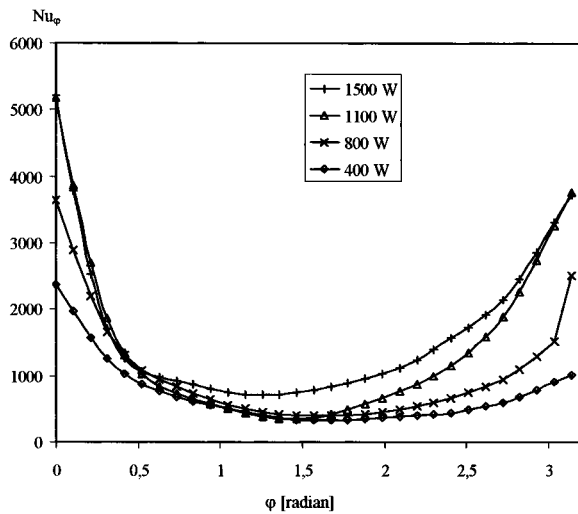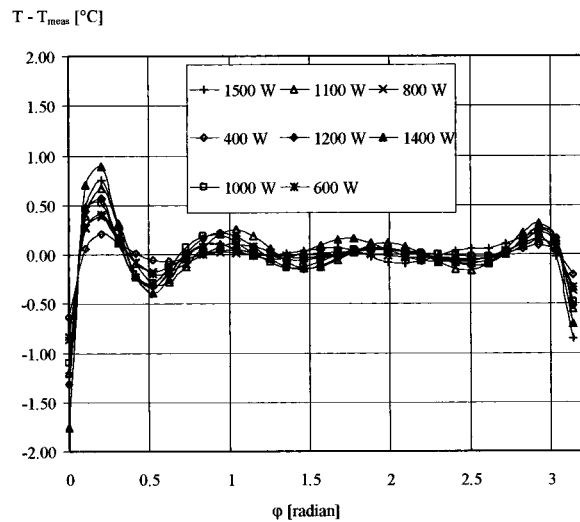
Fig. 5 Estimated results of IHCP: (*a*–*b*) circumferential Nusselt number versus φ, (*c*) local temperature residuals, and (*d*) criterion *J* versus iteration number.

(42) and estimated heat flux Eq. (43). It shows that the estimated mean heat transfer from IHCP and the measured heat transfer are in good agreement. At high heat flux, the measured Nu_m is relatively high than the estimated Nu_m because the energy loss is supposed negligible in the experimental procedure (Eq. 42). Figure 8 compares Nu_m determined by the inverse analysis and those obtained from the correlations of Cornwell and Houston [14], Stephan and Abdelsalam [15], and Memory et al. [9]. The estimated Nu_m are 15% lower than those obtained by Memory et al. correlation's and 11% lower than Nu_m predicted by Stephan and Abdelsalam correlations. The difference between Nu_m determined from IHCP and Nu_m calculated from the correlation of Cornwell and Houston is about $\pm 11\%$.

5.3 Errors Analysis. The temperature measurements are always associated with the errors whose magnitude is variable according to the measurement method.

Error in the Measured Temperatures. The influence of the measurement errors on the local heat transfer distribution is studied by adding the small random errors to the discrete temperature measurements. Thus the modified measured temperatures
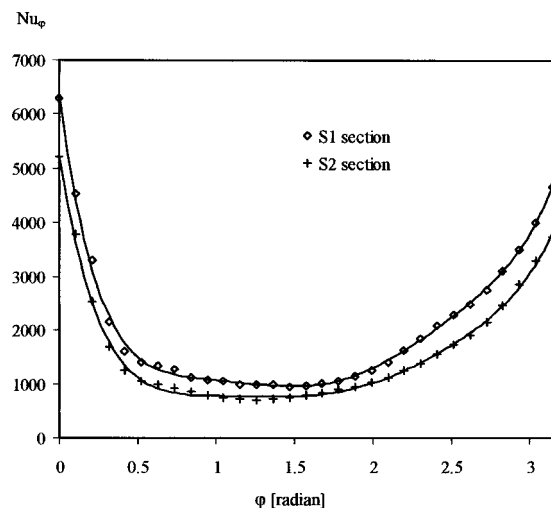

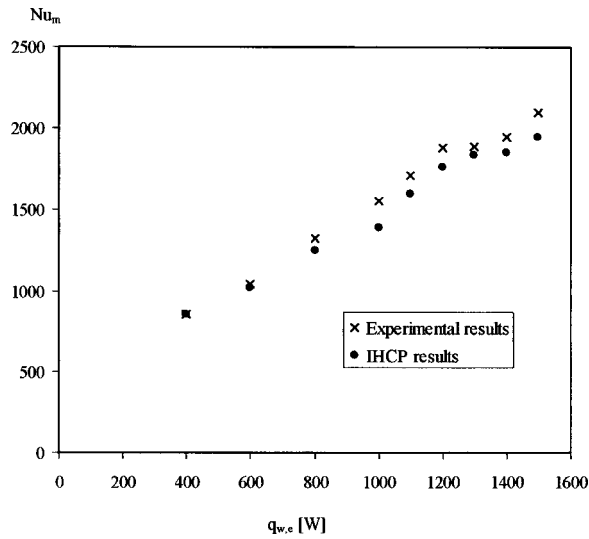Fig. 6 Comparison of local Nusselt number profiles in two locations

Fig. 7 Comparison of estimated and experimental results

($T_{\text{meas,new}}$) used in the inverse analysis in order to evaluate the influence of measurement errors were obtained from the following relation:

$$T_{\text{meas,new}}(\varphi) = T_{\text{meas}}(\varphi) + \omega \text{Max}[T_{\text{meas}}(\varphi)]\Delta \qquad (44)$$

where ω is a random number varied from -1 to 1, $\text{Max}[T_{\text{meas}}(\varphi)]$ is the maximum value of the measured temperature, Δ is the maximum magnitude of the disturbance.

Figure 9(a) shows an example of two profiles ($T_{\text{meas,new1}}$ and $T_{\text{meas,new2}}$) of the modified temperatures for $\Delta = 1\%$ obtained from the measured temperature profile (T_{meas}) for electric heat of 1200 W. For this computation, the maximum temperature error is about $\pm 0.8°$C. Figure 9(b) shows the local Nusselt number distribution $Nu_{\varphi 1}$ and $Nu_{\varphi 2}$ resulting respectively from the new temperature measurements $T_{\text{meas,new1}}$ and $T_{\text{meas,new2}}$ respectively. In the present computing procedure, when the iteration number increases the residual functional decreases and the iterative process is stopped at the optimal value of residual functional which satisfies the condition defined by Eq. (38). The error bars present the maximum difference between Nu_{φ} for $\Delta = 1\%$ and Nu_{φ} when measurement errors are not taken into account ($\Delta = 0\%$). For electric heat of 1200 W, the maximum variation of local heat transfer is about $\pm 15\%$ but the maximum variation of mean heat transfer is about
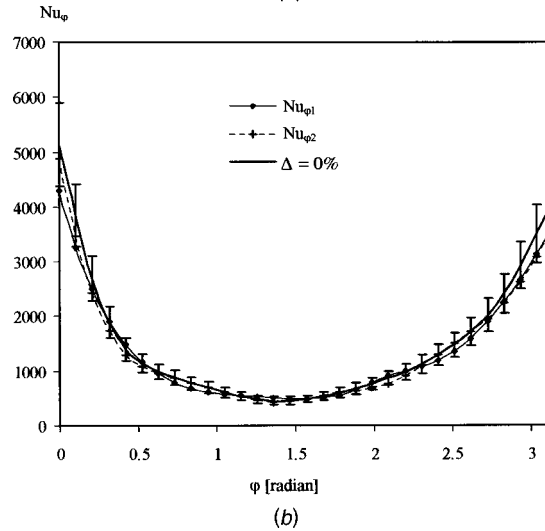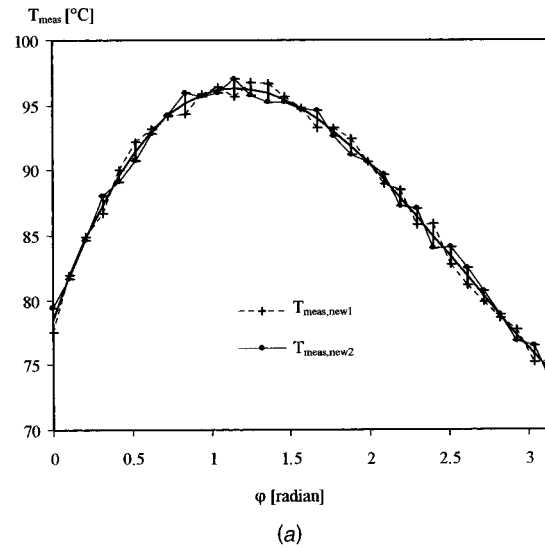

Fig. 8 Comparison of estimated and predicted mean heat transfer

(a)

(b)

Fig. 9 Influence of measurement errors for $q_{w,e} = 1200$ W: (a) measured temperatures profiles, and (b) local Nusselt number.

$\pm 4\%$. For electric heat varied from 400 W to 1500 W, Fig. 10 shows the influence of temperature errors on mean heat transfer when the maximum error in temperature is $\pm 0.8°$C ($\Delta = 1\%$). The error bars present the range of variation of Nu_m caused by the disturbance of temperature. It is noted that the maximum variation of Nu_m is about $\pm 6\%$.

Error in the Placement of Thermocouples. The influence of the systematic error resulting from the placement of the thermocouples inside the experimental cylinder is analyzed by computing local heat transfer for $R_{\text{meas}} = 13.8$ mm and $R_{\text{meas}} = 13.4$ mm. For electric heat of 1200 W, Fig. 11 shows the local Nusselt number profiles resulting from an error of ± 0.2 mm in placement of the thermocouples. The error bars are placed on the graph in order to define the range of local heat transfer. It is concluded that an error of 0.2 mm induced a maximum variation of local heat transfer of $\pm 10\%$. Figure 12 shows the influence of the error in the position of the thermocouples on the average heat transfer. The computation were carried out for electric heat varied from 400 to 1500 W by using $R_{\text{meas}} = 13.8$ mm or $R_{\text{meas}} = 13.4$ mm. The influence of the error in the placement of thermocouple increases with heat flux. The maximum variation of mean Nusselt number is about $\pm 12\%$.

Fig. 10 Influence of measurement errors on mean heat transfer

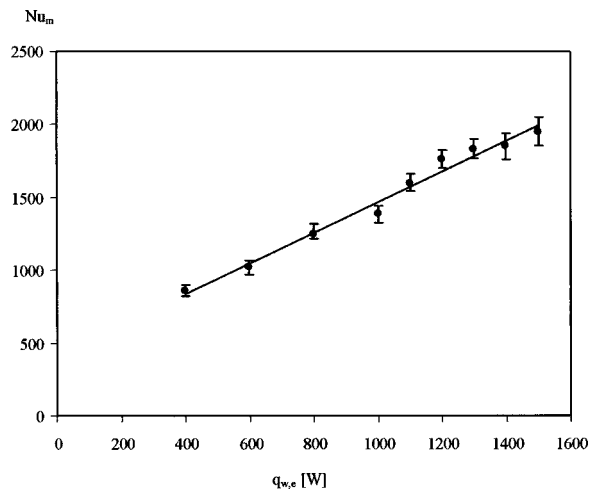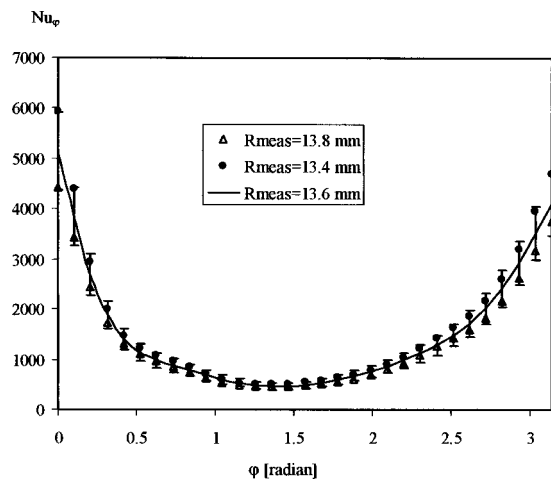**Fig. 11 Influence of systematic error on local heat transfer**
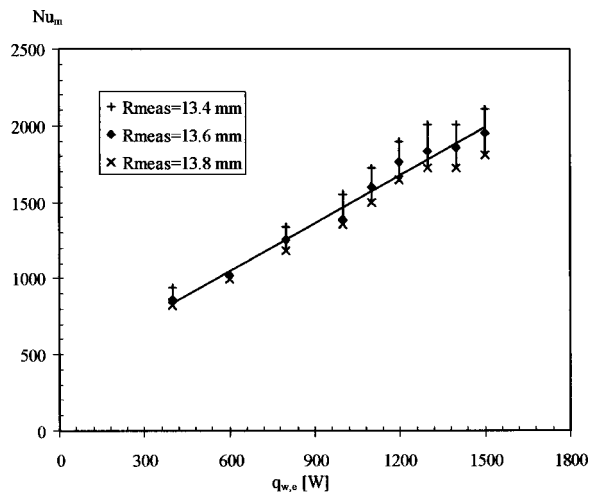

Fig. 12 Influence of systematic error on mean heat transfer

6 Conclusions

The local heat transfer for pool boiling around a smooth cylinder is successfully determined by the inverse heat conduction analysis using the iterative regularization method. The circumfer-

ential heat flux density and temperature are estimated by IHCP from the temperature measured inside the cylinder during experiments. The present paper shows the local Nusselt number profiles around the boiling surface for different electric heat. The non-uniform profile of heat transfer around the cylinder is due to the motion of bubbles after their detachment from the nucleation site and the induced liquid convection. The average heat transfer determined from IHCP is closed with the measured mean heat transfer by neglecting the energy loss. It is compared with the predicted mean Nusselt number from the experimental studies of Cornewell and Houston [14], Stephan and Abdelsalam [15] and Memory et al. [9]. The influence of measurements errors and the error in the placement of thermocouples on local and mean heat transfer are analyzed.

The described calculation procedure can be applied to solve inverse heat conduction problems for non-linear and transitory cases and also to evaluate the thermal boundary characteristics in two phase flows such as condensation and evaporation. The local results contribute to a better understanding of some of the physical factors influencing heat transfer in the studied phenomena.

Nomenclature

D = diameter of cylinder
g = acceleration of gravity
J = residual functional
J' = residual functional gradient
h = heat transfer coefficient
h_{fg} = enthalpy of evaporation
L = Lagrangian functional
Nu_m = mean Nusselt number
P = absolute pressure
P_c = critical pressure
Pr = Prandtl number
q = heat flux density
r = radius
T = temperature
Ω = surface tension
α = contact angle
φ = angle measured from the top
λ = thermal conductivity
μ = dynamic viscosity
ρ = mass density

Subscripts

L = liquid
v = vapor
w = wall

References

[1] Thome, J. R., 1990, *Enhanced Boiling Heat Transfer*, Hemisphere, Washington, DC.
[2] Webb, R. L., 1994, *Principles of Enhanced Heat Transfer*, Wiley, New York.
[3] Barthau, G., 1991, ''Active Nucleation Site Density and Pool Boiling Heat Transfer-An Experimental Study,'' Int. J. Heat Mass Transfer, **35**(2), pp. 271–278.
[4] Pioro, I. L., 1999, ''Experimental Evaluation of Constants for the Rohsenow Pool Boiling Correlation,'' Int. J. Heat Mass Transfer, **42**, pp. 2003–2013.
[5] Hsieh, S. S., and Weng, C. J., 1997, ''Nucleate Pool Boiling From Coated Surfaces in Saturated R-134a and R-407c,'' Int. J. Heat Mass Transfer, **42**, pp. 519–532.
[6] Hsieh, S. S., and Hsu, P. T., 1994, ''Nucleate Boiling Characteristics of R114, Distilled Water and R134a on Plain and Rib-Roughened Tube Geometries,'' Int. J. Heat Mass Transfer, **37**(10), pp. 1423–1432.
[7] Erden, A. H., and Balkan, F., 1998, ''Nucleate Pool Boiling Performance of Acetone-Ethanol and Methylene Chloride-Ethanol Binary Mixtures,'' *IJHMA*, **32**(12), pp. 2403–2408.
[8] Gorenflo, D., Gremer, F., Danger, E., and Luke, A., 2001, ''Pool Boiling Heat Transfer to Binary Mixtures With Miscibility Gap: Experimental Results for a Horizontal Copper Tube With 4.35 mm O.D,'' Exp. Therm. Fluid Sci., **25**, pp. 243–254.
[9] Memory, S. B., Sugiyama, D. C., and Marto, P. J., 1995, ''Nucleate Pool Boiling of R-114 and R114-oil Mixtures From Smooth and Enhanced Surfaces-I. Single Tubes,'' Int. J. Heat Mass Transfer, **38**, pp. 1347–1361.

[10] Cieslinski, J. T., 2002, "Nucleate Pool Boiling on Porous Metallic Coatings," Exp. Therm. Fluid Sci., **25**, pp. 557–564.

[11] Vittala, C. B. V., Gupta, S. C., and Agarwal, V. K., 2001, "Boiling Heat Transfer From a PTFE Coated Heating Tube to Alcohols," Exp. Therm. Fluid Sci., **25**, pp. 125–130.

[12] Chang, J. Y., and You, S. M., 1997, "Enhanced Boiling Heat Transfer From Micro-Porous Cylindrical Surfaces in Saturated FC 87 and R123," ASME J. Heat Transfer , **119**, pp. 319–325.

[13] Kang, M. G., 2000, "Effect of Tube Inclination on Pool Boiling Heat Transfer," ASME J. Heat Transfer, **122**, pp. 188–192.

[14] Cornwell, K., and Houston, S. D., 1994, "Nucleate Pool Boiling on Horizontal Tubes: A Convection-Based Correlation," Int. J. Heat Mass Transfer, **37**, Suppl. 1, pp. 303–309.

[15] Stephan, K., and Abdelsalam, M., 1980, "Heat Transfer Correlations for Natural Convection Boiling," Int. J. Heat Mass Transfer, **23**, pp. 73–87.

[16] Martin, T. J., and Dulkravich, G. S., 1998, "Inverse Determination of Steady Heat Convection Coefficient Distributions," ASME J. Heat Transfer, **120**, pp. 328–334.

[17] Maillet, D., Degiovanni, A., and Pasquetti, R., 1991, "Inverse Heat Conduction Applied to the Measurement of Heat Transfer Coefficient on a Cylinder: Comparison Between an Analytical and a Boundary Element Technique," ASME J. Heat Transfer, **113**, pp. 549–557.

[18] Lin, J. H., Chen, C. K., and Yang, Y. T., 2000, "The Inverse Estimation of the Thermal Boundary Behavior of a Heated Cylinder Normal to a Laminar Air Stream," Int. J. Heat Mass Transfer, **43**, pp. 3991–4001.

[19] Hantasiriwan, S., 2000, "Inverse Determination of Steady-State Heat Transfer Coefficient," Int. Commun. Heat Mass Transfer, **27**(8), pp. 1155–1164.

[20] Aboukhachfe, R., and Jarny, Y., 2001, "Determination of Heat Sources and Heat Transfer Coefficient for Two-Dimensional Heat Flow—Numerical and Experimental Study," Int. J. Heat Mass Transfer, **44**, pp. 1309–1322.

[21] Chen, H. T., Lin, S. Y., and Fang, L. Ch., 2001, "Estimation of Surface Temperature in Two-Dimensional Inverse Heat Conduction Problems," Int. J. Heat Mass Transfer, **44**, pp. 1455–1463.

[22] Alifanov, O. M., Artyukhin, E. A., and Rumyantsev, S. V., 1995, *Extreme Methods for Solving Ill-Posed Problems With Applications to Inverse Heat Transfer Problems*, Begell House, NY.

[23] Blanc, G., Raynaud, M., and Bardon, T. H., 1998, "A Guide for the Use of the Function Specification Method for 2D Inverse Heat Conduction Problem," *Revue Générale de la thermique*, **37**, pp. 17–25.

[24] Loulou, T., Artyukhin, E. A., and Bardon, J. P., 1996, "Estimation of the Time Dependent Thermal Contact Resistance at the Mold-Casting Interface," *The 2th Int. Conf. On Inverse Problems in Eng.*, Le Croisic, France.

[25] Holman, J. P., 1986, *Heat Transfer*, Mc Graw Hill Book Company.

[26] Khan, M., 1995, "Amélioration des échanges thermiques en ébullition nucléée de fluides frigorigènes sur des cylindres horizontaux et méthode optique de mesure des caractéristiques géométriques d'un film liquide," Thèse de Doctorat, Université de Franche Comté.

[27] Louahlia-Gualous, H., Artyukhin, E. A., and Panday, P. K., 2002, "The Inverse Estimation of the Local Thermal Boundary Conditions in Two-Dimensional Heated Cylinder," *4th Int. Conference on Inverse Problems in Engineering*, Brazil.

[28] Parken, W. H., Fletcher, L. S., Sernas, V., and Han, J. C., 1990, "Heat Transfer Through Falling Film Evaporation and Boiling on Horizontal Tubes," ASME J. Heat Transfer, **112**, pp. 744–750.

Experimental Study of Electrohydrodynamic Induction Pumping of a Dielectric Micro Liquid Film in External Horizontal Condensation Process

K. Brand
e-mail: karine.brand@wieland.de
Wieland-Werke AG,
Heat Transfer Engineering Department,
89070 Ulm, Germany

J. Seyed-Yagoobi
e-mail: yagoobi@iit.edu
Enhancement of Heat Transfer and Two Phase
Flow Laboratory,
Department of Mechanical, Materials, Aerospace
Engineering,
Illinois Institute of Technology,
10 West 32nd Street, E1,
Chicago, IL 60616

Electrohydrodynamic (EHD) induction pumping is based on charges induced in a dielectric liquid and delayed at a gradient or discontinuity of the electric conductivity. A traveling electric wave (AC) attracts or repels these induced charges, leading to liquid motion. EHD induction pumping of a dielectric micro condensation film, in an external horizontal configuration, is investigated experimentally. The pumping and its effect on heat transfer are explored by varying the voltage and frequency of the electric traveling wave, as well as the condensation heat flux. This study provides a fundamental understanding of induction pumping of micro liquid film and illustrates its potential for managing the flow and enhancing the heat transfer in the presence of phase change.
[DOI: 10.1115/1.1621890]

Keywords: Condensation, Enhancement, Film, Heat Transfer, Microscale, Phase Change

Introduction

Electrohydrodynamic (EHD) pumping is achieved when an electric field accelerates charges in a dielectric liquid. Due to viscous effects, these charges lose some of their momentum to the surrounding liquid, setting it to motion. The Coulomb force is the main mechanism of this interaction. EHD pumping of a two-phase medium is attractive for terrestrial and outer space applications since it is non-mechanical. In addition to pure pumping purposes, EHD pumps are also used for the enhancement of heat transfer, as an increase in mass transport or controlled flow management often translates to an augmentation of heat transfer. Applications, for example, include two-phase heat exchangers (evaporators and condensers) and two-phase systems such as heat pipes and capillary pumped loops. In a smaller scale, the EHD pumps can be used in electronic cooling applications. EHD pumps are lightweight, produce no vibrations, require little maintenance, are easily controlled by adjusting the applied voltage, and have very low electric power consumption.

Induction pumping is based on charges induced in a liquid and delayed at a gradient or discontinuity of the electric conductivity. An AC traveling electric wave attracts or repels these induced charges, leading to fluid motion. The concept of EHD induction pumping was introduced by Melcher in 1966 [1]. He illustrated the first experiment applying induction pumping on a two-phase media (liquid/air). Melcher later improved his theoretical model by considering the pumping of a liquid/liquid medium [2]. In these studies, he considered the charges being induced at the interface only. The further theoretical and experimental studies carried out by Melcher and Firebaugh [3], Wong and Melcher [4], Kervin et al. [5], Kuo et al. [6], Seyed-Yagoobi et al. [7,8], Margo and Seyed-Yagoobi [9] considered single-phase flows, with charges induced in the liquid bulk. More recently, Wawzyniak et al. [10,11,12] carried out an extensive theoretical and experimental study on EHD induction pumping of a stratified liquid/vapor medium in a rectangular channel configuration. They ex-

tended Melcher's work by taking into account the induction of charges in the bulk of the liquid (due to Joule heating) along with those induced at the interface. No work has ever been conducted in the area of enhancement of phase-change heat transfer by controlled flow management with EHD induction pumping phenomenon.

Enhancement of heat transfer in phase-change processes with refrigerants is essential for performance improvement and thus size reduction of HVAC&R equipment. More compact designs are necessary for material, refrigerant, and energy savings, which are of major importance for environmental protection. Significant enhancements have been achieved primarily with passive methods (i.e., structured surfaces) in the last decades. Further improvements, most likely, will have to be accomplished by combining passive and active techniques.

Effectively enhancing heat transfer in phase-change processes for industrial systems should be seen as a joined effort of an improvement at the small scale where the actual phase-change mechanism occurs, and an improvement at a large scale, which consists generally of a fluid flow management issue. As an example in evaporation applications, the overall process is improved drastically with an appropriate enhanced surface, only if the refrigerant liquid comes rapidly into contact with this surface, without the occurrence of dry-out locations. This limitation is an issue for falling-film evaporators. Whereas for condensation applications, the condensate should be removed as fast as possible from the chilled surface, to allow for the saturated vapor to get in contact with the surface. Therefore, a significant condensation heat transfer enhancement with a passive or active method on a small scale can result in a negligible or negative improvement on the heat exchanger scale, if the high condensate volume is not handled properly. In a horizontal shell and tube heat exchanger, this translates in flooding of the tubes by the condensate produced by the tubes above. As indicated by Nusselt [13], the impact of the flooding phenomenon can be predicted theoretically for smooth tubes by extending his analysis of condensation on the single horizontal smooth tube to an in-line bank of tubes. Each individual
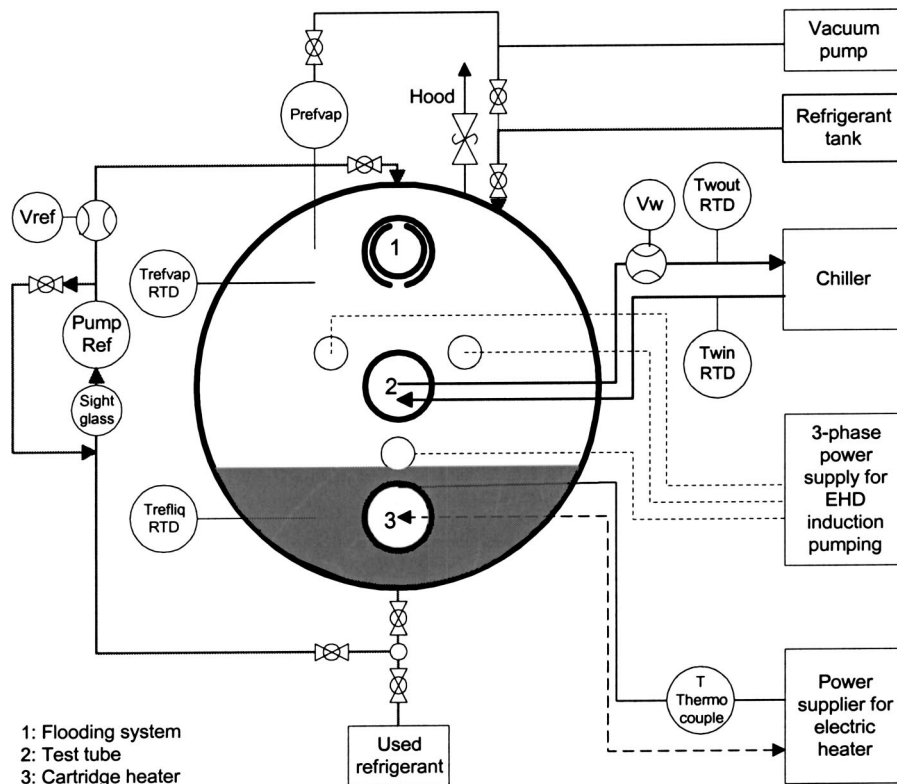
Copyright © 2003 by ASME

Fig. 1   Schematic of the condensation apparatus

tube in the bank is identical to that for a single tube, except that condensate from the tube immediately above is assumed to attach to the tube below. The result of this derivation shows that the mean heat transfer coefficient of a tube located at the nth row (the first row being at the top of the bundle) yields

$$h_n = (n)^{-1/4} h_1 \qquad (1)$$

From Eq. (1), it can be concluded that a loss of 50 percent in the performance can be expected at row 20. This analysis is highly idealized and gives only a crude idea of the effect of flooding. Considering further that the amount of condensate will increase by enhancing the heat transfer, adequate flow management becomes even more important when the heat transfer efficiency at the smaller scale is increased drastically.

EHD induction pumping shows a great potential for enhancing the heat transfer locally in phase-change processes, as well as for managing the fluid flow. Its mechanism can be used to pump a thin liquid film along the passively enhanced heat transfer surface. For the case of falling-film evaporation, the pumping action can be used to wet the surface properly. On the other hand, for the case of condensation, it can be applied to remove the condensate layer as it is formed, generating oscillations at the interface of the condensation film, and therefore improving the heat transfer.

Other EHD mechanisms have been explored in more details for enhancement of two-phase heat transfer processes. A recent and detailed literature review on this subject is presented in Seyed-Yagoobi and Bryan [14]. In particular, EHD extraction phenomenon has shown limited augmentation for evaporation and considerable enhancement for condensation applications, but has not yet been implemented in industrial applications. For condensation processes, it reduces the film thickness, resulting in increased heat transfer coefficients. The recent experimental investigations presented by Da Silva et al. [15] showed up to a three fold enhancement of the condensation heat transfer coefficient on a single structured tube in horizontal configuration. However, a limitation

of this mechanism is to transport the extracted condensate away from the heat transfer surfaces in the heat exchanger, especially in horizontal configuration.

EHD induction pumping of thin film for flow management, and hence heat transfer enhancement, in the presence of phase change has never been investigated. This work, concerned specifically with condensation on a horizontal tube, experimentally investigates this pumping technique. Its objective is to understand the behavior of longitudinal EHD induction pumping of the condensate (thickness of the liquid film under 100 μm) along a horizontal tube, under various heat flux, voltage, and frequency conditions. The working fluid is the refrigerant R123, commonly used in large chiller systems. The selected heat fluxes and saturation conditions correspond to HVAC&R systems. The experimental results presented here prove the promising potential of EHD induction pumping in phase-change systems to enhance the heat transfer through effective liquid film flow management.

Experimental Setup

The condensation apparatus is described in detail in Brand [16]. As shown in Fig. 1, it consists of a closed cylindrical chamber, 1050 mm in length and 150 mm in diameter, in which refrigerant is filled to about one third in height. The condensation test tube is located in the center of this cylinder, immersed in saturated vapor. It is cooled by running chilled water inside, resulting in condensation on its outer surface. A 4.9 kW capacity cartridge heater for evaporation is immersed in the refrigerant pool of liquid, below the test tube. It is controlled by a variac to allow the onset and control of the desired saturation conditions. An external loop allows pumping of refrigerant liquid from the bottom of the chamber to a distribution system placed above the test tube, generating flooding. However, the experiments reported here do not include flooding.

The inlet water temperature and velocity are maintained with a recirculating chiller. The water inlet and outlet temperatures of the

Table 1 Thermophysical and electric properties of R123 at 36.7°C

ρ^1 (kg/m^3)	μ^1 (Pa.s)	σ^2 (S/m)	k^1 (W/mK)	c_p^1 (J/kgK)	ε^2 (pF/m)
1315.1	4.804e-4	2.903e-8	0.0771	1005.5	40.74

[1]NIST Refprop, Version 6.01.
[2]Bryan [25].

test section are measured with RTDs. The water flow rate is measured at the outlet of the test tube with a turbine flow meter. The heat removed through the condensation process is calculated with these three terms. All tests are carried out with refrigerant R123 under the same saturation conditions, $T_{sat} = 36.7°C$ and $P_{sat} = 1.384$ bars. See Table 1 for the corresponding R123 thermophysical and electric properties.

As shown in Fig. 2, the electrodes are placed directly on the copper test tube, by winding simultaneously three insulated wires around it. The rated minimum breakdown voltage is 4.6 kV for the wire used (31 AWG). The three wires are tidily wrapped around the tube in small grooves, resulting in an almost smooth final condensing surface. This avoids any radial obstacles for the condensate, which has to be pumped longitudinally. A wavelength of 6 mm has been used for this study. Figure 2 also illustrates the principle of EHD induction pumping in repulsion mode, as is

expected form the present electrode configuration. By applying an electric field, charges are induced in the liquid bulk and at the liquid/vapor interface. These are repelled to liquid/vapor interface by the phase of opposite polarity. As the electric traveling wave moves in one direction, the charges are repelled in the other direction, leading the fluid into motion. More details can be found in Brand [16].

The custom built power supply utilized in this study to generate the three electric traveling waves is capable of generating sine, square and triangle waves at voltages of 0–15 kV (zero to peak) and frequencies of 0–30 Hz. The frequency can be increased to 60 Hz for voltages below 2 kV (zero to peak). The voltage, frequency, and phase shift are adjustable. For more details see Bohinsky [17].

A device has been constructed to collect axially pumped liquid at one extremity of the pumping section to quantify the pump performance. A 25 mm wide cup, with a volume of 33 ml, collects the condensate and can be emptied by sliding around the test tube through a gear system activated from the outside of the test section. The liquid rates are measured by placing the cup under the end of the pumping section and timing the collection time. This operation was repeated at least five times and the results were averaged.

Experimental Procedure and Data Uncertainties

The mean outside heat transfer coefficient is computed directly through Fourier's law in cylindrical coordinates

$$h_o = \frac{(\pi \cdot OD \cdot L)^{-1}}{(U \cdot A)^{-1} - (h_i \cdot \pi \cdot ID \cdot L)^{-1} - \ln(OD/ID)(2 \cdot \pi \cdot k_{copper} \cdot L)^{-1}} \tag{2}$$

where the overall heat transfer coefficient is calculated from

$$U \cdot A = q/\Delta T_{lm} \tag{3}$$

and the corresponding heat flux is determined based on the test tube internal surface area

$$q'' = \rho_w V_w c_{p,w}(T_{w,out} - T_{w,in})/(\pi \cdot ID \cdot L). \tag{4}$$

Note that the tube outside diameter (OD), inside diameter (ID), and surface area involved in the calculation above are based on the smooth tube and do not include any surface alteration due to the electrodes construction. The tested tube is smooth inside. A 30 mm long wire-insert was used at the entrance of the tube to ensure that the flow regime was fully developed at the test section entrance. Therefore, the inside heat transfer coefficient is calculated with the well-validated empirical Gnielinsky [18] correlation, where the friction coefficient is computed with the Pethukov [19] correlation. All water properties are calculated at the average temperature between the inlet and the outlet of the test tube. The Gnielinsky and Pethukov correlations are valid for $0.5 \leqslant Pr \leqslant 2.10^3$ and $3.10^3 \leqslant Re_D \leqslant 5.10^6$. For best accuracy, these correlations should be used for fully turbulent flow ($Re_D \geqslant 10^4$). All of the tests were carried out under fully turbulent flow conditions. Also, great care was taken to run tests with a water temperature difference between the inlet and the outlet of the test section lying between 1°C and 2°C. A too small difference would increase drastically the uncertainty in the temperature difference calculation, whereas a too large difference would compromise the accuracy of the above calculation procedure. In addition, keeping the temperature difference between 1 and 2°C allowed for the temperature difference between the vapor and the tube surface to remain as uniform as possible long the tube length. Furthermore, to minimize the errors, it was ensured that the heat transfer pro-

cess taking place on the outside of the tube was dominant (i.e., it represented the highest resistance to heat transfer).

Note also that the electric power dissipation (i.e., Joule heating) from the wire wound on the test tube, calculated from σE^2, had a negligible contribution, and hence was neglected in this investigation. In fact, it remained below 10^4 W/m^3, and the resultant heat flux from this volumetric heating was then below 10 W/m^2, which is over three orders of magnitude less than the imposed heat fluxes in this study.

A thorough uncertainty analysis has been performed for all measured data and calculated quantities, based on the methods described by Kline and McClintock [20], and Moffat [21]. The total uncertainty on the calculation of the inside heat transfer coefficient has been estimated to lie consistently below 5 percent. The test conditions resulting from the considerations described in the previous paragraph allow reaching the desired heat flux spectrum, by keeping an uncertainty on the outside heat transfer coefficient below 12 percent for the smooth tube, without any electrodes. The maximum calculated uncertainties on the external heat transfer coefficient for the tube with electrodes reach 14 percent at heat fluxes of 25 and 45 kW/m^2, and 20 percent at the lowest heat flux, 15 kW/m^2. The uncertainties on the heat flux calculations reach 8 percent, 7 percent, and 5 percent for the heat fluxes around 15, 25, and 45 kW/m^2, respectively. For more details, see Brand [16].

Experimental Results and Discussions

The experimental objective of this particular study is to investigate the behavior and effect of longitudinal EHD induction pumping of a thin film of condensate along a horizontal tube, under various heat flux, voltage and frequency conditions. Three heat fluxes representative of HVAC&R applications are chosen: 15, 25, and 45 kW/m^2, corresponding to average film thickness of
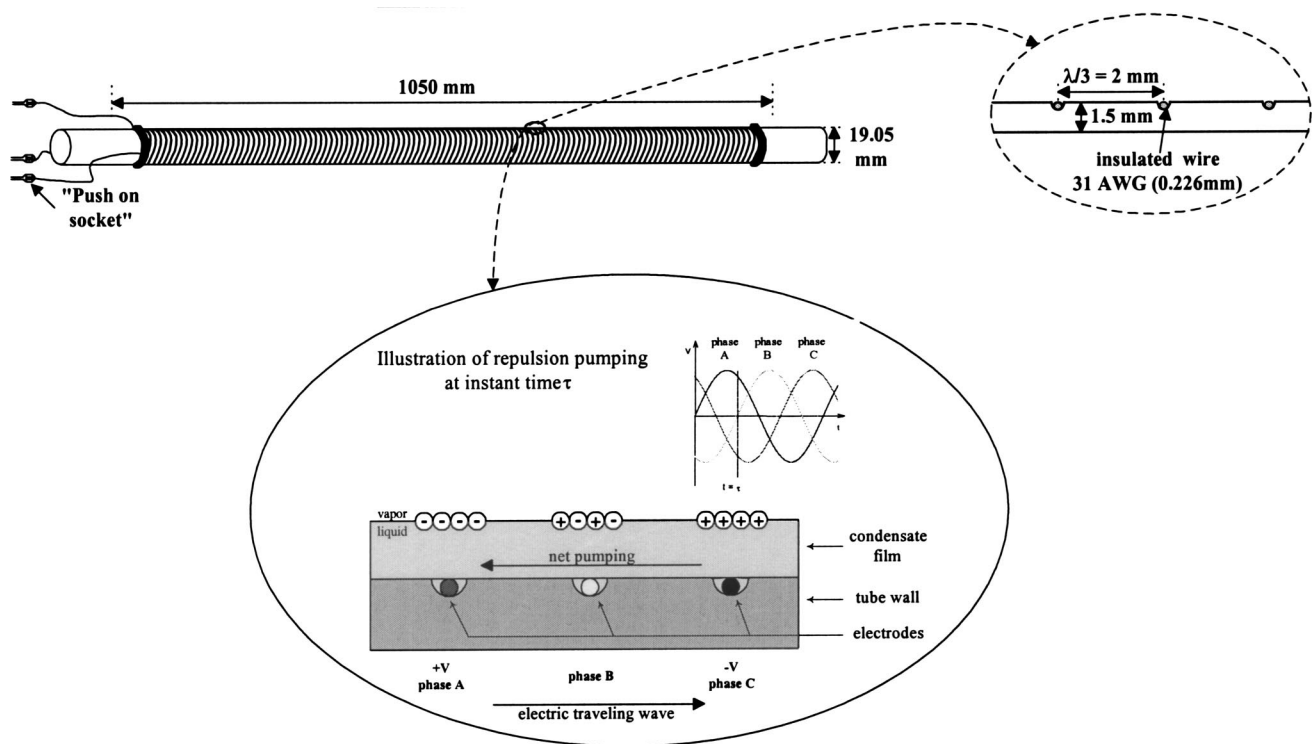
Fig. 2 Electrodes design

50–100 μm. Only a sinusoidal electric traveling wave is considered. Voltages of 1, 2, and 3 kV (zero to peak) are applied, for different frequencies ranging from 0 to 60 Hz for 1 and 2 kV, and from 0 to 30 Hz for 3 kV (due to the power supply constraint).

For the present electrode configuration, the liquid adjacent to the electrode has higher electric conductivity than the vapor positioned on the top of the liquid. Therefore, the pump is expected to operate in the repulsion mode (see Brand [16]), where the traveling electric wave will repulse the induced charges, leading to a fluid motion in a direction opposite to the traveling wave. Note that the pumping mode termed as attraction mode corresponds to fluid motion in the same direction as the electric traveling wave. However, depending on the pump geometry, operating conditions, and working fluid properties, the pump could operate in an unstable mode, meaning that multiple operating velocities satisfy simultaneously the required viscous and electric shear stress equilibrium. Instability can manifest itself in the establishment of a pumping motion in a direction opposite to the expected direction, or in a sudden drop or increase in the pump output. This aspect will be discussed in more details in the last section of this paper.

Figure 3 shows the average outside heat transfer coefficient as a function of the heat flux for a smooth tube. The results are compared to Nusselt's relation for the smooth tube, as well as to experimental results obtained at the Heat Transfer Laboratory of Wieland-Werke AG. Both experimental data sets provide almost identical results, and lie consistently for the whole heat flux range about 25 percent above the Nusselt's theoretical values. This trend has already been observed in the past by researchers with other refrigerants. The under predicting feature can be explained partially through two assumptions in the Nusselt's theory [13], which do not apply to actual condensation on a horizontal tube. Firstly, a condensation sheet is assumed all along the bottom of the tube, but in reality, droplet or column modes occur. Secondly, the velocity of the condensate is taken uniform around the tube, but due

to gravity effect, this can clearly not apply. However, the excellent match with the experimental results of Wieland-Werke AG give great confidence to the present data.

Figure 3 also illustrates the experimental results with EHD induction pumping under various applied potentials. At 0 kV, the outside heat transfer coefficient of the tube with electrodes is about 30 to 40 percent higher than the smooth tube. This is due to the surface area increase, the surface tension effects, and film perturbation, created by the groove/wire construction. The highest heat transfer enhancement at 0 kV occurs where the condensate
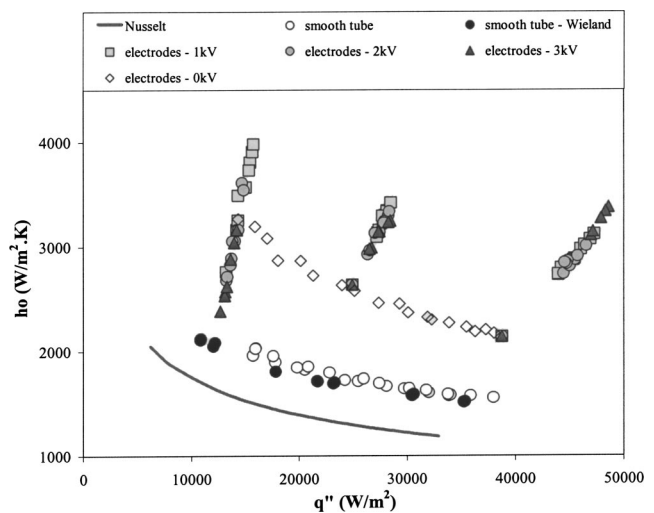

Fig. 3 Outside heat transfer coefficient as a function of heat flux for all voltages and all frequencies
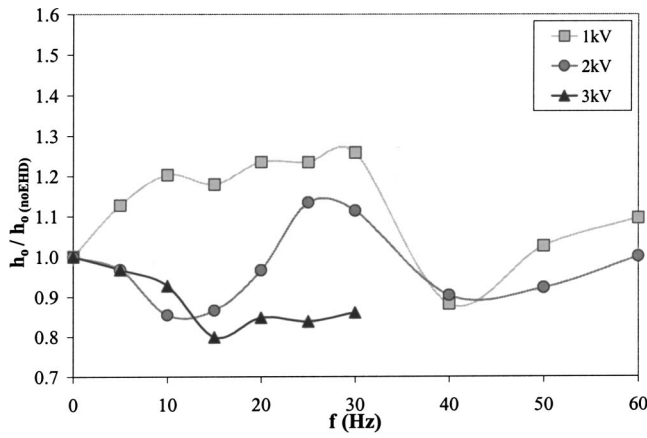
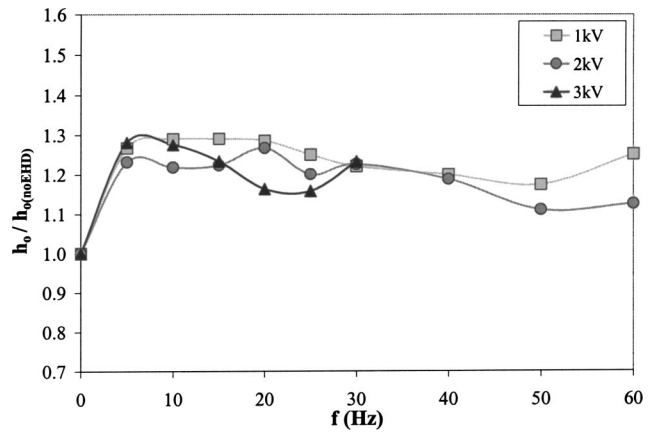**Fig. 4 Outside heat transfer coefficient ratio as a function of frequency at $q'' \approx 15$ kW/m^2**

Fig. 6 Outside heat transfer coefficient ratio as a function of frequency at $q'' \approx 25$ kW/m^2

film thickness is the smallest, i.e., where the heat flux is the smallest. The circumferencially averaged film thickness for the condensation process on the smooth tube for the three selected heat fluxes are 65 μm, 78 μm, and 95 μm for heat fluxes of 15, 25, and 45 kW/m^2, respectively. These values have been calculated with Nusselt's analysis for condensation on a horizontal smooth tube [13], which usually overpredicts actual condensate film thickness (see previous paragraph). For each of the three selected heat flux and voltage levels, multiple data points corresponding to various frequencies are displayed. The frequency impact cannot be visualized in the present plot. Its effect will be shown and discussed in subsequent figures.

The experimental data obtained by applying EHD induction pumping for the three selected heat fluxes show that its impact on heat transfer is clearly heat flux dependent, i.e., condensate film thickness dependent. At the lowest heat flux (around 15 kW/m^2), enhancement is observed for 1 kV and degradation for 3 kV, for all frequencies. Depending on the frequency level, enhancement or degradation occurs for the applied voltage of 2 kV. On the other hand, for heat fluxes of approximately 25 and 45 kW/m^2, the application of EHD results in heat transfer enhancement for all voltages and frequencies. This augmentation is largest for the highest heat flux and applied voltage.

For better evaluation, the data points are displayed for each heat flux separately in Figs. 4, 6, and 8, showing the ratio of the outside heat transfer coefficient with EHD to that of without EHD as a function of frequency, at various applied voltage levels. The corresponding flow rate measurements are presented in Figs. 5, 7, and 9, where the ratio between the collected condensate volume rate with EHD to that of without EHD is shown as a function of frequency, for the three voltages considered. The condensate is collected at the extremity of the tube corresponding to attraction pumping when liquid is pumped towards it in Figs. 5(a), 7(a), and 9(a), and to repulsion pumping in Figs. 5(b), 7(b), and 9(b). In these figures, a data point with a value greater than one means that attraction pumping is occurring for Figs. 5(a), 7(a), and 9(a), and that repulsion pumping is occurring for Figs. 5(b), 7(b), and 9(b). On the other hand, a data point with a value below one in both graphs indicates the occurrence of liquid retention on the heat transfer surface. This can be observed at all heat fluxes for operating conditions corresponding to small frequencies (below 10 Hz) and a peak voltage of 1 kV. In these instances, a shaking motion of the condensate appears on the tube while no net pumping occurs. The electric forces are too weak to induce a net pumping. In this particular case, the heat transfer is augmented through mixing of the liquid layer.
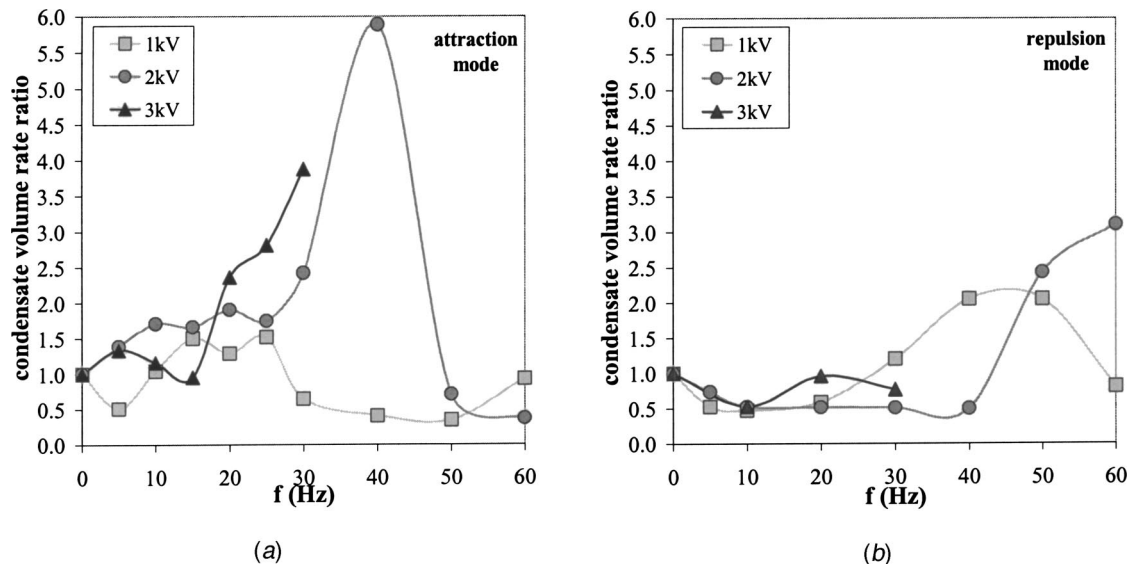

(a)

(b)

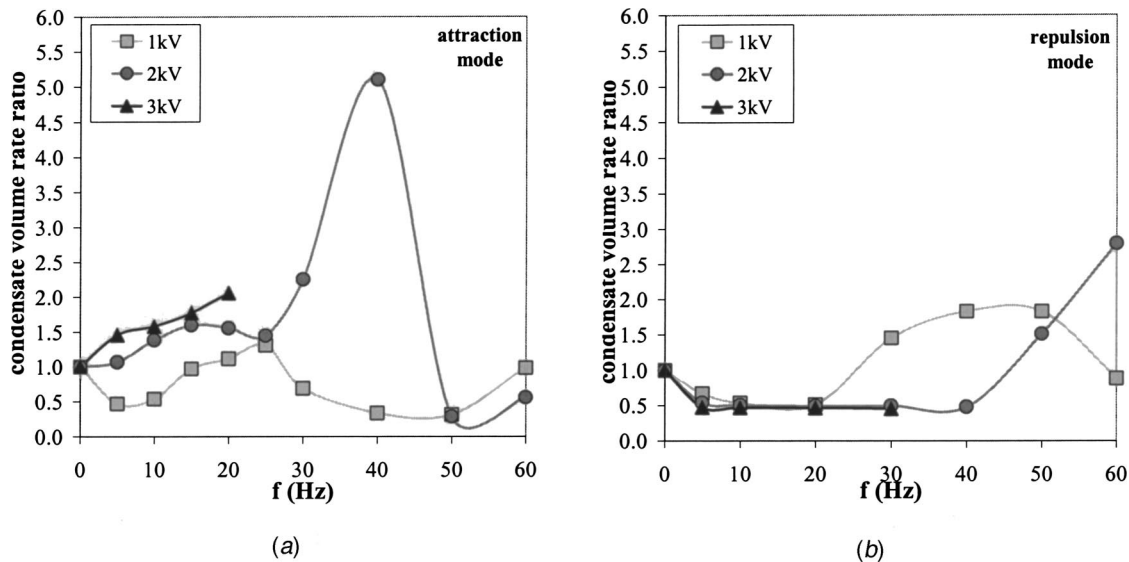**Fig. 5 Condensate volume rate ratio as a function of frequency at $q'' \approx 15$ kW/m^2**

Fig. 7 Condensate volume rate ratio as a function of frequency at $q'' \approx 25$ kW/m^2

Figures 5, 7, and 9 indicate that the net pumping direction switches from attraction to repulsion mode at high frequencies at all condensation heat fluxes. The pumping direction reversal from attraction to repulsion mode by increasing the frequency will be discussed in the last section of this paper. Figure 10 illustrates the pumping features corresponding to attraction and repulsion modes. Pictures of both ends and of the middle part of the pumping section are shown for each mode. In both modes, the fluid is pumped along the tube, leaving a dripping-free area at the start and creating a condensate stream at the end. At the starting region, no liquid dripping occurs. The condensate is pumped along the tube surface and accumulates till the film is so thick that it falls by gravity. From this location to the end of the pumping section, condensate drips regularly from the tube. The length of the dripping-free start and the intensity of the stream at the end of the tube depend on the pumping strength, varying strongly with liquid film thickness (i.e., heat flux level), voltage, and frequency. The maximum length observed for the dripping-free region was about 30 cm for $q'' = 15$ kW/m^2, a voltage of 2 kV, and a frequency of 40 Hz.

It is noteworthy that the appearance of attraction and repulsion pumping is very different. In the attraction pumping mode, the fluid motion appears extremely oscillatory (see middle picture of Fig. 10(a)), resulting in more fluid mixing. On the contrary, the

Fig. 8 Outside heat transfer coefficient ratio as a function of frequency at $q'' \approx 40$ kW/m^2

flow appears smooth in the repulsion mode (see middle picture in Fig. 10(b)). Note also that, as indicated by Figs. 5, 7, and 9, the pumping performance for both modes increases with increasing voltage for all heat fluxes, and with decreasing film thickness (i.e., decreasing heat flux). This trend is expected and predicted theoretically (see Brand [16], and Brand and Seyed-Yagoobi [22]). High voltage results in high electric field strength, producing effective pumping. Small film thickness also enhances the pumping performances due to higher electric field strength within the liquid film. However, when the film thickness approaches zero, the pumping strength drastically drops because of sudden increase in viscous shear stresses.

Enhancement or degradation of heat transfer is a direct consequence of the pumping performance and behavior. If the condensate film thickness is increased through pumping, the heat transfer will be degraded. If high mixing accompanies the pumping as for the attraction mode, it can result in heat transfer augmentation, especially for thicker liquid films. If the pumping action is strong and fast enough to remove the condensate more rapidly than it is produced, the heat transfer process will be enhanced. Modifying the heat flux, voltage, and frequency affects the condensate film thickness, the pumping strength, and the mixing intensity. Generally, as can be seen from Figs. 5, 7, and 9, the heat transfer enhancement increases with increasing heat flux for all voltages and frequencies. Note that the presented results correspond to pumping of the micro liquid film along the whole length of the test tube, resulting generally in an increase of the condensate film thickness due to axial pumping, and hence in poor heat transfer enhancement or even heat transfer degradation. If the liquid would be drained at some selected locations along the pumping length, the heat transfer would be expected to be much higher.

For a heat flux of 15 kW/m^2 (Figs. 4 and 5), the heat transfer enhancement for 1 kV is around 20 to 30 percent for low frequencies and it suddenly drops around the flow reversal frequency (30 Hz), resulting in heat transfer degradation. The additional mixing observed in attraction mode explains mainly the increased heat transfer. In repulsion mode, the sole pumping action results in larger film thickness, and therefore in small heat transfer enhancement or heat transfer degradation. By increasing the voltage to 2 and 3 kV, the stronger pumping generates degradation of heat transfer due to thicker condensate films. The best pumping performance (solely with regard to the fluid flow and not to heat transfer enhancement) was measured in attraction mode, at a voltage of 2 kV and a frequency of 40 Hz, where six times more condensate
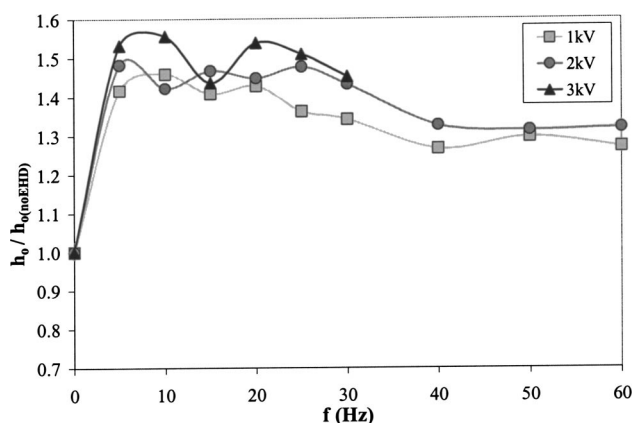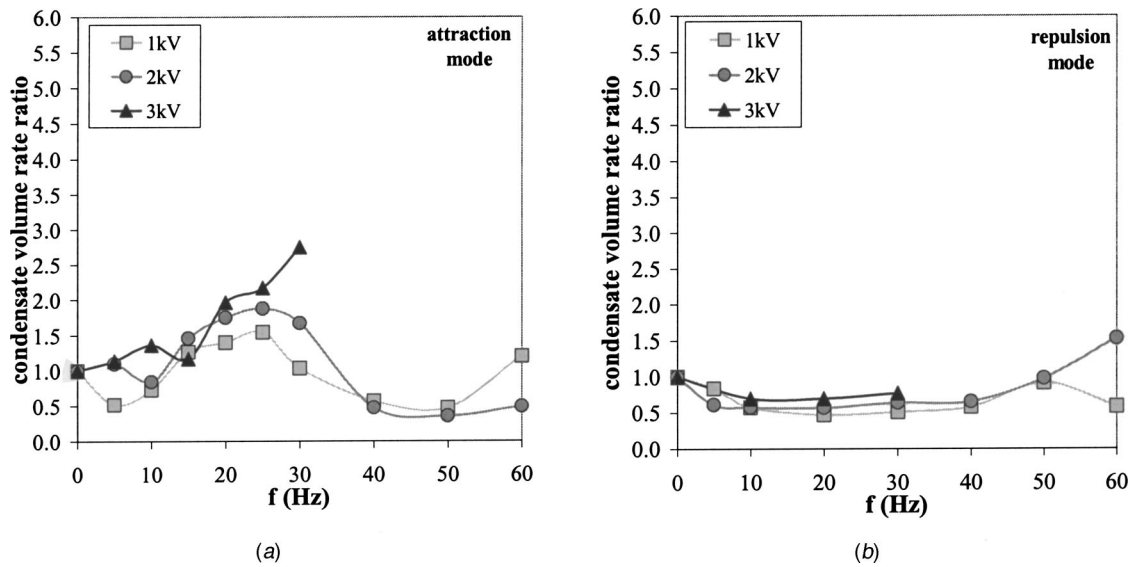
Fig. 9 Condensate volume rate ratio as a function of frequency at $q'' \approx 40$ kW/m^2

drained from the tube at its extremity. The best performance for repulsion mode lies at a frequency larger than 60 Hz and could not be measured.

For a heat flux of 25 kW/m^2 (Figs. 6 and 7), the heat transfer enhancement for attraction mode is around 30 percent and 20 perecent for 1 kV and 2 kV, respectively, with a decrease around 40 Hz for 1 kV, and 50 Hz for 2 kV. The results for 3 kV are similar to these obtained for 1 kV for the low frequency range, and decrease regularly. Again, Fig. 7 indicates that the change in pumping direction occurs at the frequency levels corresponding to the decrease of heat transfer enhancement, between 25 and 30 Hz for 1 kV, and between 40 and 50 Hz for 2 kV. The best attraction

pumping performance corresponds to 2 kV and 40 Hz. The best repulsion pumping performance is expected achieved at a frequency higher than 60 Hz. The oscillating fluid flow corresponding to attraction pumping versus the smooth flow in repulsion mode explains the highest heat transfer enhancement in attraction mode, where the condensate is highly mixed.

At a heat flux of 40 kW/m^2 (Figs. 8 and 9), the heat transfer is enhanced by 40 to 50 percent in attraction mode, and by 30 percent in repulsion mode, for all voltages considered. In this case, more liquid is present and any pumping mode increases the heat transfer process. The additional mixing in the attraction cases explains the better enhancement compared to the repulsion cases.

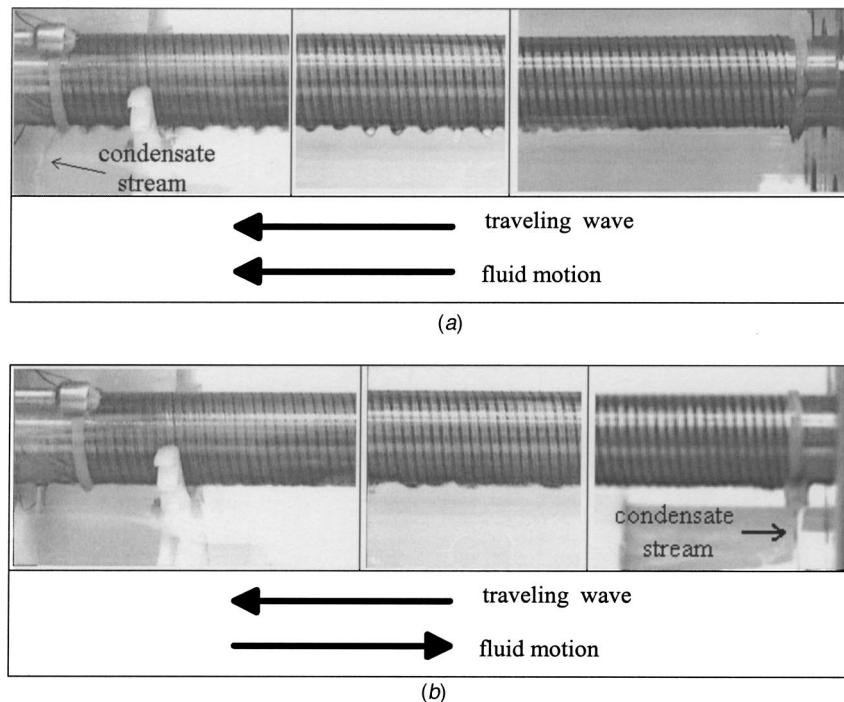**Fig. 10 Flow visualization of condensation process with EHD induction pumping in attraction and repulsion modes: (a) $q'' = 25$ kW/m^2, $\hat{\varphi} = 2$ kV, $f = 20$ Hz (attraction mode); and (b) $q'' \approx 25$ kW/m^2, $\hat{\varphi} = 2$ kV, $f = 50$ Hz (repulsion mode).**

Due to the larger condensate quantities, the pumping performance is reduced compared to the smaller heat flux levels. The repulsion pumping performance is not significant for the considered range of frequency, but may increase for frequencies beyond 60 Hz.

As predicted for single phase flow (Seyed-Yagoobi et al. [7,8]), as well as for two-phase flow (Wawzyniak and Seyed-Yagoobi [10,12], Brand and Seyed-Yagoobi [22]), the pumping performance is expected to rise to an optimum and then decrease with increasing frequency. In fact, at constant wavelength, very high frequencies correspond to small electric shear stresses, thus small mass fluxes. Therefore, the pumping performance as a function of frequency is expected to reach a peak, after which it decreases gradually. The frequency where the performance peak occurs depends on the pump geometry, and fluid physical and electric properties (see Brand [16]). For the experimental data presented here, this expected decrease in pumping does not appear for the range of frequency investigated.

The electric power consumption associated with the induction pumping of the liquid film presented in this paper, under all operating conditions, was minimal. In fact, the maximum measured electric power consumption in this study represented 0.022 percent of the test section heat transfer rate (see Brand [16]), which is practically negligible.

Pumping Direction Reversal

The pumping direction reversal from attraction to repulsion mode by increasing the frequency is due to the instability of EHD induction pumping. As discussed in Melcher [2], Crowley [23], and recently Wawzyniak and Seyed-Yagoobi [24], the velocity of the liquid/vapor interface is obtained by equating the electric and viscous shear stresses at the interface. Depending on the pump geometry, operating conditions, and working fluid properties, the resulting pumping velocity can have one or multiple solutions. The pump is termed as stable if only one operating point exists, whereas it is referred as unstable if multiple operating points exist. Instability can manifest itself in a sudden drop in pump output or alternating flow direction. Wawzyniak and Seyed-Yagoobi [24] developed non-dimensional stability criteria derived from the stress balance for a stratified liquid/vapor flow in a rectangular channel for four different pumping geometries. These derivations assumed charge induction present at the liquid/vapor interface only, and neglected bulk charge induction.

As shown in Brand [16], the electric shear forces are an order of magnitude higher than the gravity force, for the experimental conditions investigated in this study, where the liquid film thickness is below 100 μm. In addition, the curvature effect of the tube can be neglected since the liquid film thickness is very small compared to the tube diameter. Therefore, neglecting gravity and curvature, the present experimental case can be modeled as a two-dimensional stratified liquid/vapor medium. Furthermore, since the total length of the tube is equipped with electrodes, the adverse external pressure gradient in the liquid film is negligible. Following a similar approach to that of Wawzyniak and Seyed-Yagoobi [24], the corresponding viscous stress and electric shear stress balance for this configuration yields (see Brand [16] for detailed derivation):

$$v^3 - \frac{2\omega}{K}v^2 + \left(\frac{\omega^2}{K^2} + \frac{\sigma^2}{\varepsilon_0^2 \alpha K^2} + \frac{\eta}{\alpha K}\right)v - \frac{\eta\omega}{\alpha K^2} = 0, \quad (5)$$

where the parameters α and η are expressed as

$$\alpha = \left(\frac{1 + \dfrac{\varepsilon_0}{\varepsilon_s}\dfrac{\sinh(2Kh_s)}{\cosh(2Kh_s)+2}\tanh(Kh_v)}{\dfrac{\varepsilon_0}{\varepsilon_s}\dfrac{\sinh(2Kh_s)}{\cosh(2Kh_s)+2}+\tanh(Kh_v)}\tanh(Kh_l) + \frac{\varepsilon}{\varepsilon_0}\right)^2$$

$$(6)$$

and
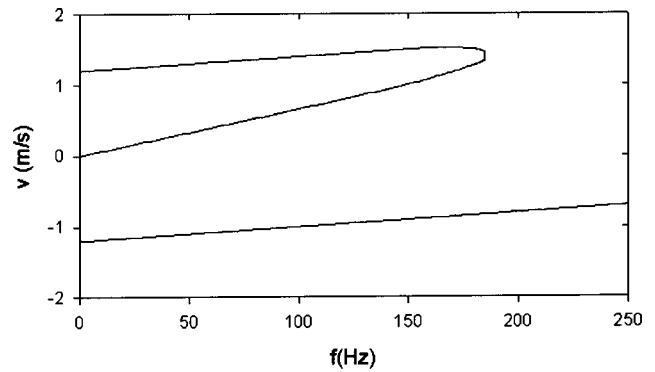

Fig. 11 Interfacial velocity as a function of frequency ($\varphi = 2$ kV, $h_l = 0.08$ mm, $h_v = 5$ mm, $\lambda = 6$ mm, R123 at $T_{ref} = 25°C$)

$$\eta = \frac{-\varepsilon \sigma h_l K^2 \hat{\varphi}^2}{2\varepsilon_0 \mu \cosh^2(Kh_l)} \frac{1 + \dfrac{\varepsilon_0}{\varepsilon_s}\dfrac{\sinh(2Kh_s)}{\cosh(2Kh_s)+2}\tanh(Kh_v)}{\dfrac{\varepsilon_0}{\varepsilon_s}\dfrac{\sinh(2Kh_s)}{\cosh(2Kh_s)+2}+\tanh(Kh_v)}.$$

$$(7)$$

Note that Eq. (5) yields multisolutions for the film velocity depending on the operating conditions.

By setting the peak voltage to 2 kV, the wavelength to 6 mm, the vapor thickness to 5 mm, and the liquid thickness to 80 μm (averaged thickness corresponding to a heat flux of 25 kW/m^2), and by solving Eq. (5) for the interfacial velocity as a function of the frequency, the results displayed in Fig. 11 are obtained. Three solutions for the equilibrium interfacial velocity (two positive and one negative) appear for lower frequencies, whereas only one negative solution appears for higher frequencies, meaning that the pump is unstable below a given frequency threshold and stable beyond it. As shown in Fig. 11, at zero frequency, a positive, a negative, and a zero velocity are mathematically obtained. However, only the zero velocity is practical and should be taken into consideration; the others are mathematical results of a nonlinear equation and cannot represent any physical behavior.

The curve corresponding to positive velocities shifts to lower frequency values by decreasing the applied voltage, increasing the wavelength, decreasing the liquid film thickness, and/or decreasing the refrigerant R123 temperature. For example, by increasing the wavelength from 6 mm to 7 mm, the calculated reversal frequency decreases from 185 Hz to 95 Hz. It is rather difficult to quantitatively compare the flow reversal frequency for different voltages and heat fluxes in the experimental results, because other parameters are varied simultaneously. In fact the film thickness is directly affected by the pumping itself and will, regardless, vary with frequency by keeping the voltage and heat flux constant. In addition, the temperature gradient across the condensate film is different from one heat flux to the other, since the cooling water entrance temperature (see Fig. 1) is varied from 25°C to 5°C to reach the desired heat flux level. The temperature change has mainly an impact on the viscosity and electric conductivity of the working refrigerant.

It has been observed (see Brand [16]) with a high-speed video camera that in the attraction mode, the liquid is pumped in two directions simultaneously, with the direction corresponding to the attraction mode being dominant. This was not observed in the repulsion mode, and explains the oscillating flow and the mixing effect accompanying the attraction mode (see Fig. 10).

The mathematical model presented above clearly explains the flow reversal phenomenon observed experimentally in induction pumping of the liquid film presented in the previous section. This model neglects charge induction in the bulk of the liquid, which is an important mechanism in the present configuration due to the

large temperature gradients across the condensate film. Furthermore, as mentioned previously, not knowing precisely the corresponding values of the key parameters such as the liquid film thickness, limits the prediction capability of the mathematical model. Therefore, Fig. 11 is not intended to predict the flow reversal frequency precisely, but to provide a fundamental understanding for the observed trend.

Conclusions

EHD induction pumping of thin liquid film for flow management, and hence heat transfer enhancement, in the presence of phase change was investigated for the first time. This experimental study provided a fundamental understanding for EHD induction pumping of condensation film along the outer surface of a horizontal smooth tube. The behavior of the EHD induction pumping of liquid condensate was explored by varying the electric traveling wave voltage and frequency, under three different heat flux conditions, representing HVAC&R applications.

Two different flow modes, attraction and repulsion modes, were observed experimentally and explained fundamentally with the aid of a mathematical model. The experimental observations along with the mathematical explanation of the bi-directional flow and flow reversal were neither observed nor reported in the literature. The attraction pumping mode seemed more desirable with respect to the pumping performance, and hence enhancement of heat transfer, under the operating conditions explored.

In summary, this study explored EHD induction pumping of micro liquid film, and showed its potential for improving the heat transfer in heat exchangers through flow management, especially in tube bundles. In fact, a controlled flow management on a single tube is expected to translate in an increased thermal performance in tube-bundle configuration, since the negative flooding effect would be minimized.

Acknowledgments

Nomenclature

A = surface area, m^2
c_p = specific heat, J/kgK
f = frequency, Hz
h = heat transfer coefficient, W/m^{2}K
h_l = liquid thickness, m
h_v = vapor thickness, m
h_s = solid thickness, m
h_{lv} = latent heat of vaporization per unit mass, J/kg
ID = tube inside diameter, m
k = thermal conductivity, W/mK
K = wave number = $2\pi/\lambda$, 1/m
L = length of the test tube, m
n = number of tubes
OD = tube outside diameter, m
Pr = Prandtl number = $c_p \mu/k$
q = heat rate, W
q'' = heat flux, W/m^2
Re_D = Reynolds number = $\rho v_w ID/\mu$
T = temperature, K
U = overall heat transfer coefficient, W/m^{2}K
V = volume flow rate, m^3/s
v = velocity, m/s
ΔT = temperature difference, K
α = parameter
ε = electric permittivity, F/m

ε_0 = electric permittivity of vacuum = $8.854.10^{-12}$ F/m
η = parameter
λ = wavelength, m
φ = zero to peak voltage, V
μ = dynamic viscosity, kg/ms
ρ = density, kg/m^3
σ = electric conductivity, S/m
ω = angular frequency = $2\pi f$, 1/s

Subscripts and Superscripts

i = inside
in = inlet
l = liquid
lm = log mean
o = outside
out = outlet
ref = refrigerant
s = solid
sat = saturation
w = water

References

[1] Melcher, J. R., 1966, "Traveling-Wave Induced Electro-convection," Phys. Fluids, **9**(8), pp. 1548–1555.
[2] Melcher, J. R., 1981, *Continuum Electromechanics*, The MIT Press, Cambridge, MA, pp. 5.49–5.54.
[3] Melcher, J. R., and Firebaugh, M. S., 1967, "Traveling-Wave Bulk Electro-convection Induced Across a Temperature Gradient," Phys. Fluids, **10**(6), pp. 1178–1185.
[4] Wong, J., and Melcher, J. R., 1969, "Thermally Induced Electroconvection," Phys. Fluids, **12**(11), pp. 2264–2269.
[5] Kervin, D. J., Crowley, J. M., Krein, P., and Chato, J. C., 1981, "Parametric Studies of a Large Thermal EHD Induction Pump," *Conference Record, IEEE-Industry Applications Society Annual Meeting*, IEEE, Piscatawy, NJ, pp. 1015–1020.
[6] Kuo, B. S., Chato, J. C., and Crowley, J. M., 1984, "Temperature Induced Electrohydrodynamic Pumping in Horizontal Pipes," ASME J. Heat Transfer, **106**, pp. 78–84.
[7] Seyed-Yagoobi, J., Chato, J. C., Crowley, J. M., and Krein, P. T., 1989, "Induction Electrohydrodynamic Pump in a Vertical Configuration, Part 1-Theory," ASME J. Heat Transfer, **111**, pp. 664–669.
[8] Seyed-Yagoobi, J., Chato, J. C., Crowley, J. M., and Krein, P. T., 1989, "Induction Electrohydrodynamic Pump in a Vertical Configuration, Part 2-Experimental Study," ASME J. Heat Transfer, **111**, pp. 670–674.
[9] Margo, B. D., and Seyed-Yagoobi, J., 1994, "Heat Transfer Enhancement Under Various Orientations Resulting From Attraction Mode Induction Electrohydrodynamic Pumping," ASME J. Heat Transfer, **116**, pp. 598–603.
[10] Wawzyniak, M., and Seyed-Yagoobi, J., 1997, "An Analytical Study of Electrohydrodynamic Induction Pumping of a Stratified Liquid/Vapor Medium," IEEE Trans. Ind. Appl., **35**(1), pp. 231–239.
[11] Wawzyniak, M., Seyed-Yagoobi, J., and Morrison, G. L., 2000, "An Experimental Study of Electrohydrodynamic Induction Pumping of a Stratified Liquid/Vapor Medium," ASME J. Heat Transfer, **122**, pp. 200–203.
[12] Wawzyniak, M., and Seyed-Yagoobi, J., 2001, "Electrohydrodynamic Induction Pumping of a Stratified Liquid/Vapor Medium in the Presence of Volumetric and Interface Electric Charges," IEEE Trans. Ind. Appl., **37**(4), pp. 950–958.
[13] Nusselt, W., 1916, "Die Oberflächenkondensation des Wasserdampfes," *Zeitschrift des Vereines Deutsche Ingenieure*, **60**, pp. 541–546, 569–575.
[14] Seyed-Yagoobi, J., and Bryan, J. E., 1999, "Enhancement of Heat Transfer and Mass Transport in Single-Phase and Two-Phase Flows with Electrohydrodynamics," Adv. Heat Transfer, **33**, pp. 95–186.
[15] Da Silva, L. W., Molki, M., and Ohadi, M. M., 2000, "Electrohydrodynamic Enhancement of R-134a Condensation on Enhanced Tubes," *Conference Record of the 2000 IEEE Industry Applications Conference*, **2**, pp. 757–764.
[16] Brand, K., 2002, "Enhancement of External Condensation Heat Transfer with Electrohydrodynamic Induction Pumping—Theoretical and Experimental Study," Ph.D. dissertation, Department of Mechanical Engineering, Texas A&M University, College Station, TX.
[17] Bohinsky, B. J., 1991, "An Experimental Study of Induction Electrohydrodynamic Pumping in a Horizontal Axisymmetric Configuration," Master of Science thesis, Department of Mechanical Engineering, Texas A&M University, College Station, TX.
[18] Gnielinski, V., 1976, "New Equations for Heat and Mass Transfer in Turbulent Pipe and Channel Flow," Int. Chem. Eng., **16**(2), pp. 359–368.
[19] Pethukov, B. S., 1970, "Heat Transfer and Friction in Turbulent Pipe Flow with Variable Physical Properties," Adv. Heat Transfer, **6**, pp. 503–564.
[20] Kline, S. J., and McClintock, F. A., 1953, "Describing Uncertainties in Single Sample Experiments," Mech. Eng. (Am. Soc. Mech. Eng.), **75**, pp. 3–8.
[21] Moffat, R. J., 1988, "Describing the Uncertainties in Experimental Results," Exp. Therm. Fluid Sci., pp., 3–17.

[22] Brand, K., and Seyed-Yagoobi, J., 2000, ''Electrohydrodynamic Induction Pumping of a Stratified Liquid/Vapor Medium in the Presence of Heat Transfer,'' *ASME International Mechanical Engineering Congress and Exposition*, HTD-Vol. 366-4, ASME, New York, pp. 153–160.

[23] Brand, K., and Seyed-Yagoobi, J., 2002, ''Effect of Electrode Configuration on Electrohydrodynamic Induction Pumping of a Stratified Liquid/Vapor Medium,'' IEEE Trans. Ind. Appl., **38**(2), pp. 389–400.

[24] Crowley, J. M., 1983, ''Stability of EHD Induction Pump,'' in *Conference Record of the IEEE-IAS Annual Meeting, Mexico City, Mexico*, pp. 1149–1153.

[25] Wawzyniak, M., and Seyed-Yagoobi, J., 1999, ''Stability of Electrohydrodynamic Induction Pumping of a Stratified Liquid/Vapor Medium in the Presence of an External Load,'' IEEE Trans. Ind. Appl., **35**, pp. 1211–1217.

[26] Bryan, J. E. 1998, ''Fundamental Study of Electro-hydrodynamically Enhanced Pool and Convective Boiling Heat Transfer,'' Ph.D. dissertation, Department of Mechanical Engineering, Texas A&M University, College Station, TX.

Theoretical Model for Nucleate Boiling Heat and Mass Transfer of Binary Mixtures

Jürgen Kern

Peter Stephan
e-mail: pstephan@ttd.tu-darmstadt.de

Chair of Technical Thermodynamics,
Darmstadt University of Technology,
Petersenstrasse 30, 64287 Darmstadt, Germany

A model is presented to calculate nucleate boiling heat transfer coefficients of binary mixtures. The model includes the governing physical phenomena, such as the variation of the phase interface curvature, the adhesion pressure between wall and liquid, the interfacial thermal resistance as well as the local variation of composition and liquid-vapor equilibrium. Marangoni convection is considered, too. The theoretical background of these phenomena is described and their implementation is explained. The model is verified by comparing calculated heat transfer coefficients of hydrocarbon mixtures with experimental data. Computational and experimental data are in good agreement. In the examples a considerable amount of the total heat flow passes through a tiny thin film area, called micro region, where the liquid-vapor phase interface is attached to the wall. Very high spatial gradients of heat flux and mixture concentration occur interacting with overall heat transfer performance. [DOI: 10.1115/1.1622717]

Keywords: Binary, Boiling, Heat Transfer, Modeling, Thin Films

1 Introduction

There are numerous applications where heat is transferred or substances are separated by nucleate boiling of binary mixtures, e.g., in chemical or process industries. Nevertheless, only a few correlations are available for special boiling conditions (pressure, heat flux or wall superheat, liquid mixture, wall material, surface structure, etc.). These equations serve their useful purpose only when they are applied in the range of parameters they were developed for. The main reason for this restriction is the huge number of physical phenomena governing the heat and mass transfer process. A review of experimental efforts to predict nucleate boiling heat transfer coefficients of binary mixtures can be found in [1–4].

In the last decade theoretical models have been developed for partial and fully developed nucleate boiling of pure substances [5–9]. Fundamentally, they are all based on a thin film evaporation concept of Wayner and co-workers [10]. They investigated the evaporation of a liquid meniscus in a tiny area where the liquid-vapor interface approaches the wall. In spite of the small geometrical dimensions (about one micrometer), a considerable amount of the supplied heat at the evaporator wall flows through the so-called "micro region." In this region, microscale effects such as adhesion forces and interfacial thermal resistance in combination with a strong curvature change of the phase interface significantly influence local heat and mass transfer.

Stephan and Busse [11] introduced a model to describe the heat and mass transfer in the micro region and combined it with a macroscopic model for heat pipes. Good agreement with measured heat transfer data was found. To calculate the nucleate boiling heat transfer coefficient of pure substances, the micro region model was implemented in a macroscopic vapor bubble growth model by several authors using different assumptions and simplifications [5–9]. As the micro region model proved to be successful in these studies, it might also be adapted and applied to liquid mixtures. In this work a single bubble model is presented to calculate nucleate boiling heat transfer of binary liquid mixtures. It is based on a previous model that was developed to predict nucleate boiling heat transfer of pure substances [6]. In contrast with the

mentioned correlations, the model is not restricted to a certain range of parameters. In chapter 2 basic assumptions of the developed model and the strategy of calculating heat transfer coefficients are presented. The theory includes a micro region model for binary mixtures that is described in chapter 3. The remaining area, called macro region, is treated in the proceeding chapter. Due to the significant influence of microscale heat and mass transfer phenomena on the overall heat transfer coefficient, some results of the micro region are shown. To verify the model, calculated heat transfer coefficients are compared with data from experiments.

2 Modeling Strategy

As long as neighboring bubbles do not interact, the boiling system can be divided into single bubble subsystems. This is fulfilled for low and intermediate heat fluxes. The subsystem consists of a single vapor bubble, surrounding liquid, and a part of the heated wall (Fig. 1). The shape of the bubble is assumed to be spherical, except for the tiny micro region. The bubble departure process where deviations from the spherical shape can be observed [7] is not taken into account. Using cylindrical coordinates (ξ, η), the diameter d_{sub} of the single bubble subsystems corresponds to the bubble site density (N_b). The vapor bubble is surrounded by liquid of the thermal boundary layer. Its thickness δ_{th} is calculated by means of a correlation for free convection assuming that heat is transferred within the thermal boundary layer only by conduction normal to the wall [12]. The subsystem includes a part of the heated wall because in experiments thermocouples are placed in a distance δ_w below the boiler surface.

Boundary conditions are the outside wall temperature T_{out} and the saturation temperature T_{sat} (Fig. 1). The model describes the heat and mass transfer in this subsystem for the time period when the bubble is growing from an infinitesimal size to the departure radius. As input parameters only values for the bubble site density and the departure diameter are required. This data can either be taken from measurements directly or can be obtained by using standard bubble departure diameter correlations, e.g., [13] and site density models [14]. The computation yields the time dependent local distribution of the heat flux $\dot{q}(\xi, r(t))$. The mean heat transfer coefficient α_m for one bubble growth period can be obtained using
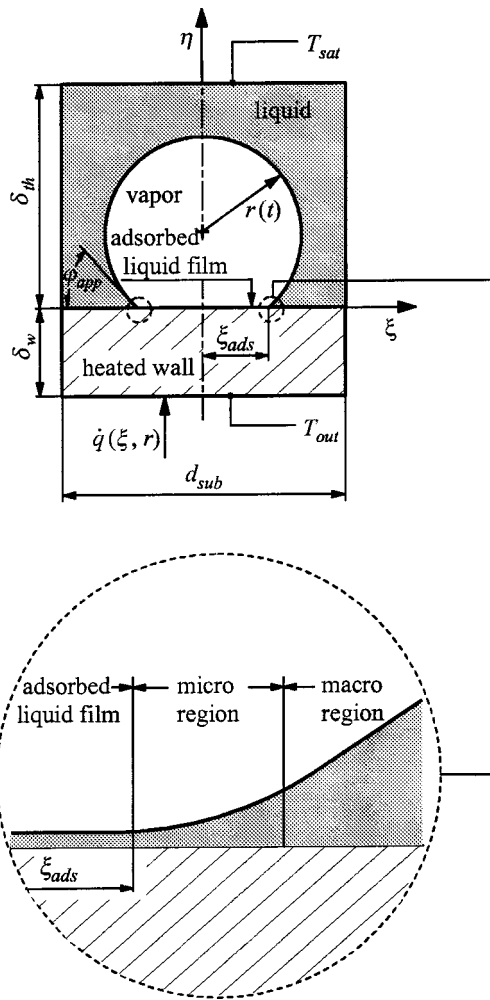
Fig. 1   Single bubble subsystem and computational domains

Fig. 2   Significant phenomena in the micro region

$$\alpha_m = \frac{\dot{q}_m}{T_{\text{out}} - T_{\text{sat}}} = \frac{1}{t_b} \int_0^{t_b} \alpha(t)\,dt \qquad (1)$$

where $\alpha(t)$ is an area-averaged heat transfer coefficient for a single bubble subsystem at a certain bubble radius $r(t)$:

$$\alpha(t) = \frac{1}{T_{\text{out}} - T_{\text{sat}}} \frac{2}{(d_{\text{sub}}/2)^2} \int_0^{d_{\text{sub}}/2} \dot{q}(\xi, r)\xi\,d\xi. \qquad (2)$$

To calculate the heat flux $\dot{q}(\xi, r)$ the computational domain is divided into two regions (Fig. 1):

- the tiny thin film area, called micro region, where the bubble is attached to the wall,
- and the liquid adjacent to the micro region as well as the wall, called macro region.

Transport phenomena within the vapor bubble are insignificant for overall heat transfer coefficients [15]. Therefore, the vapor is not included into one of these regions.

3   Microscale Heat and Mass Transfer

In Fig. 2 the micro region is plotted on a larger scale. The curved line represents the phase interface between liquid and vapor. In the macro region the interface has a constant curvature corresponding to the bubble radius $r(t)$. In the micro region the interface turns sharply and ends in a non-evaporating thin liquid film which is adsorbed at the wall. Attractive forces between the
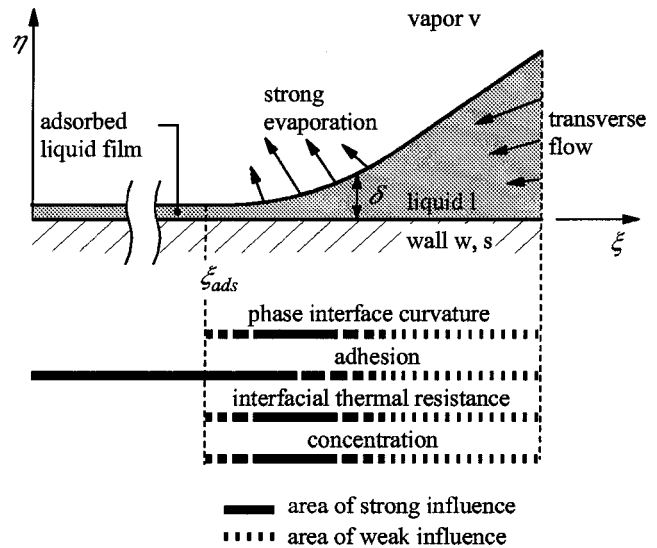
wall atoms and the liquid molecules inhibit evaporation. This film covers the whole wall underneath the vapor bubble (Fig. 1).

In most practical applications the thermal conductivity of the liquid is far smaller than that of the wall material. In this case the evaporation rate has a local maximum in the micro region. Most of the heat flows through the thin liquid film where the thermal resistance is small. The high local evaporation rate induces a transverse liquid flow into the micro region. The pressure drop is driven by the interface curvature effect and the adhesion force effect. Their spheres of influence are indicated schematically in Fig. 2. The interfacial thermal resistance is important in the central part of the micro region, because of the low thermal resistance of the thin liquid film and the high heat flux.

In a binary mixture one observes a preferential evaporation of one component. Thus, the concentration of this component decreases in the direction of the transverse liquid flow into the micro region. As a result of this liquid composition effect, the conservation equations have to be solved for variable thermophysical properties. Furthermore, the liquid-vapor equilibrium varies with the composition of the liquid. The surface tension changes with the composition, and hence a liquid flow is induced. This phenomenon is well-known as the Marangoni effect.

To gain the mathematical model for the micro region, in the following paragraphs, firstly, considerable interfacial phenomena with regard to binary mixtures are explained and their modeling equations are derived. Secondly, the conservation equations are simplified by means of a scale analysis. Solving heat, mass, and momentum balances as well as the thermodynamic equilibrium of the phase interface yields a mathematical model for the micro region. Finally, the numerical treatment of the differential equations is presented.

3.1   Interfacial Phenomena

3.1.1   Adhesion Pressure.   Long-range intermolecular forces cause adhesion of the liquid to the wall. These forces profoundly affect the performance of thin liquid film evaporation. The mechanic interpretation is a force per unit area acting perpendicular to the plane of the interface. If the liquid film thickness δ is so small that the adhesion pressure influences heat transfer in the micro region ($\delta \lesssim 20$ nm), disjoining pressure takes the form [16]

$$p_{\text{dis}} = \frac{A}{\eta^3} \qquad (3)$$

where η is the orthogonal distance between the wall and a parallel liquid layer. The dispersion constant A describes the London dis-
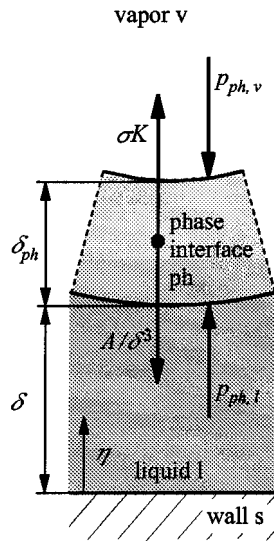
Fig. 3 Pressure balance at a curved liquid-vapor phase interface in the vicinity of a solid wall

persion interaction between two apolar molecules or atoms, the Debye induction interaction, and the Keesom orientation interaction. It can be calculated using the Lifshitz theory [17]. This theory utilizes the dispersion of light caused by the electronic structure of atoms and molecules. Based on dielectric and optical properties the dispersion constant for two identical media interacting across vacuum can be calculated, e.g., A_{ss} for the solid phase as well as A_{ll} for the liquid phase. Using combining laws [16] one derives (except for media with high dielectric constants)

$$A = A_{sl} = \sqrt{A_{ss} A_{ll}}. \tag{4}$$

In the case of liquid mixtures of similar components (such as two alkanes), the dispersion constant is a molar average of the values of the two pure components (A_{11} and A_{22}) [18]:

$$A_{ll} = x_{l,1} A_{11} + x_{l,2} A_{22}. \tag{5}$$

3.1.2 Pressure Difference at the Phase Interface. At a curved phase interface the surface tension causes a pressure difference between the liquid pressure $p_{ph,l}$ and the vapor pressure $p_{ph,v}$ at the phase interface. The corresponding Young-Laplace equation reads

$$p_{ph,v} - p_{ph,l} = \sigma K. \tag{6}$$

Equation (6) holds for the Gibbs assumption of a two-dimensional phase interface. This assumption is justified for phase interfaces that are not influenced by the vicinity of another interface (e.g., a wall). But for a liquid film thickness of the order of the phase interface thickness (about one nanometer) there is an additional contribution of the disjoining pressure (see Fig. 3). Assuming the vapor phase to be described by the ideal gas law, the enhanced Young-Laplace interfacial pressure difference model yields [19]

$$p_{ph,v} - p_{ph,l} = \sigma K + \frac{A}{\delta^3} = p_{\text{cap}}. \tag{7}$$

The pressure difference in Eq. (7) is called capillary pressure p_{cap}. In case of a spherical bubble the phase interface curvature K can be expressed as

$$K = \frac{d^2 \delta / d\xi^2}{[1 + (d\delta/d\xi)^2]^{3/2}} + \frac{1}{\xi} \frac{d\delta/d\xi}{[1 + (d\delta/d\xi)^2]^{1/2}}. \tag{8}$$

3.1.3 Interfacial Thermal Resistance. If the liquid film in the micro region becomes very thin the thermal resistance of the liquid is of the same order as the interfacial thermal resistance. In his

studies Schrage [20] used the kinetic theory of gases to develop the basics for the interfacial thermal resistance of pure substances. Extending his studies to binary mixtures the thermal resistance of the phase interface R_{ph} is gained [21]:

$$R_{ph} = \frac{2-f}{2f} \left[\Delta \bar{V} T_{\text{sat}} \sqrt{2 \pi \bar{R} T_{\text{sat}}} / \bar{H}_{lv} \Delta \bar{H} \left(\frac{x_{ph,v,1}}{\sqrt{M_1}} + \frac{x_{ph,v,2}}{\sqrt{M_2}} \right) \right]. \tag{9}$$

The coefficient f in Eq. (9) is usually called condensation coefficient. It is defined as the ratio of condensing molecules to vapor molecules striking the interface. Different values for the condensation coefficient are reported in the literature, often they are smaller than unity [22]. This might result from either a system contamination or deviations from the kinetic theory model used to define the condensation coefficient [23]. Both, no system contamination and the validity of the kinetic theory model are assumed in this investigation. Therefore, the condensation coefficient is unity.

3.1.4 Marangoni Convection. When a liquid-vapor interface is exposed to a concentration or temperature gradient parallel to it, a flow called surface tension-driven or Marangoni convection is induced. The origin of this kind of convection can be explained by a local imbalance of surface tension [24]. Applying Newton's law of viscosity, a balance between viscous shear stresses and surface tension forces at the phase interface yields the so-called Marangoni boundary condition

$$\tau_{ph,l} = \frac{d\sigma}{da} \tag{10}$$

where a is the coordinate parallel to the phase interface. Herein, it is assumed that the viscosity of the vapor is much smaller than that of the liquid, $\nu_v \ll \nu_l$.

3.2 Scale Analysis. The special geometrical conditions and the flow type allow to simplify the conservation equations for a Newtonian fluid by means of a scale analysis. In the micro region the reference film thickness δ_0 is far smaller than the reference length L_0 of the micro region:

$$\left(\frac{\delta_0}{L_0} \right)^2 \ll 1. \tag{11}$$

The transverse liquid flow (cf. Fig. 2) can be considered as a creeping thin film flow, i.e.,

$$\text{Re} = \frac{u_0 \delta_0}{\nu_0} \to 0 \tag{12}$$

where u_0 is the reference velocity in the film.

With characteristic quantities of the given problem the conservation equations are rearranged in dimensionless form. Using Eq. (11) and (12) the orders of magnitude of the terms are compared to each other and appropriate quantities are neglected [21].

The Navier-Stokes equations reduce to

$$\frac{\partial p_l}{\partial \xi} = \rho_l \nu_l \frac{\partial^2 u_\xi}{\partial \eta^2}, \tag{13}$$

$$\frac{\partial p_l}{\partial \eta} = \frac{\partial}{\partial \eta} \left(\frac{A}{\eta^3} \right). \tag{14}$$

Integration leads to a velocity component in ξ-direction (parallel to the wall)

$$u_\xi(\xi, \eta) = \frac{1}{\nu_l \rho_l} \left[\left(\frac{\partial p_l}{\partial \xi} \right) \left(\frac{\eta^2}{2} - \eta \delta \right) + \frac{1}{\sqrt{1 + (d\delta/d\xi)^2}} \frac{\partial \sigma}{\partial \xi} \eta \right] \tag{15}$$

where the last term takes into account the Marangoni boundary condition. The velocity component in η-direction $u_\eta(\xi, \eta)$ is obtained by evaluating the equation of continuity.
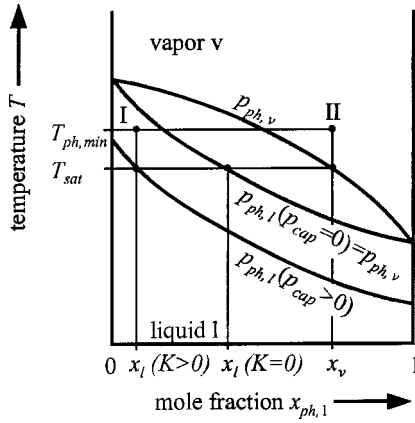
Fig. 4 Variation of the liquid-vapor equilibrium taking into account the influence of the capillary pressure effect

If the wall is impermeable, the concentration is only a function of the radial coordinate ξ according to the scale analysis of the equation of continuity for each component. Fick's law describes the diffusive mass flux j_1 of component 1 in component 2

$$j_1 = \rho_l D_{l,12}\left(\frac{dy_{l,1}}{d\xi}\right). \tag{16}$$

From the energy equation one obtains that in the liquid film heat is manly transferred by one-dimensional conduction normal to the wall (η-direction in Fig. 2) at a wall temperature $T_{w,\text{mic}}$. This yields

$$\dot{q} = \frac{T_{w,\text{mic}} - T_{ph,\min}}{\delta/\lambda_l + R_{ph}/\sqrt{1 + (d\delta/d\xi)^2}}. \tag{17}$$

In the above relation $T_{ph,\min}$ is the minimum phase interface temperature for evaporation of the fluid (see chapter 3.4), R_{ph} the interfacial thermal resistance at the phase interface according to Eq. (9), and $d\delta/d\xi$ the slope of the phase interface relative to the length coordinate ξ that is parallel to the wall (see Fig. 2).

3.3 Thermodynamic Equilibrium. The minimum phase interface temperature for evaporation $T_{ph,\min}$ is different from the saturation temperature T_{sat} if external forces such as surface tension or intermolecular adhesion act normal to the interface. The Thomson equation for binary mixtures [12] dictates that this shift is given by

$$T_{ph,\min} = T_{\text{sat}}\left(1 + \frac{x_{ph,v,1}V_{l,1} + x_{ph,v,2}V_{l,2}}{\Delta\bar{H}}p_{\text{cap}}\right) \tag{18}$$

The equation considers the influence of the capillary pressure (7) and liquid composition described by the partial molar volumes in the liquid $V_{l,1}$ and $V_{l,2}$. For the nucleate boiling process of a binary mixture one has to consider the following two effects on the liquid-vapor phase equilibrium (see Fig. 4). Firstly, the pressure difference at the phase interface, p_{cap}, leads to a lower liquid pressure $p_{ph,l}$ ($p_{\text{cap}} > 0$) than the vapor pressure $p_{ph,v}$ and hence a lower liquid mole fraction $x_{ph,l,1}$ ($p_{\text{cap}} > 0$) compared to a plane phase interface $x_{ph,l,1}$ ($p_{\text{cap}} > 0$) without adhesion forces. Secondly, the Thomson Eq. (18) describes the increase of the minimum phase interface temperature $T_{ph,\min}$ due to the capillary pressure effect. As a result one obtains the liquid-vapor phase equilibrium of a curved thin liquid film. In Fig. 4 the equilibrium state of the liquid at the phase interface is given by I and the equilibrium state of the vapor at the phase interface is given by II. It should be noted that the boiling curve for $p_{ph,l}$ ($p_{\text{cap}} > 0$) in Fig. 4 is the one that results from the thermodynamic equilibrium at a

curved phase interface with adhesion forces and is different from that at a plane phase interface without adhesion forces.

3.4 Mathematical Model and Numerical Treatment. The analysis of Eq. (15) to (18) together with a mass balance for each component leads to a set of six nonlinear ordinary differential equations:

$$\frac{d\delta}{d\xi} = \delta'$$

$$\frac{d\delta'}{d\xi} = \left(\frac{1}{\sigma}\left(p_{\text{cap}} - \frac{A}{\delta^3}\right) - \frac{1}{\xi}\frac{\delta'}{(1+\delta'^2)^{1/2}}\right)(1+\delta'^2)^{3/2}$$

$$\frac{dp_{\text{cap}}}{d\xi} = -3\frac{\nu_L}{\delta^3}\dot{M}_\xi - \frac{3}{2\delta\sqrt{1+(d\delta/d\xi)^2}}\frac{d\sigma}{d\xi} + 3A\frac{\delta'}{\delta^4}$$

$$\frac{d(\dot{M}_\xi\xi)}{d\xi} = \frac{\xi}{\Delta h_{1v}}\frac{T_{w,\text{mic}} - T_{\text{sat}}\left(\dfrac{x_{ph,v,1}V_{l,1} + x_{ph,v,2}V_{l,2}}{\Delta\bar{H}}p_{\text{cap}}\right)}{\delta/\lambda_1 + R_{ph}/\sqrt{1+\delta'^2}}$$

$$\frac{dy_{l,i}}{d\xi} = y'_{l,i}$$

$$\frac{dy'_{l,i}}{d\xi} = \frac{d(\dot{M}_\xi\xi)}{d\xi}\left(\frac{y_{ph,v,i} - y_{l,i}}{\xi\delta\rho_l D_{l,12}}\right) - y'_{l,i}\left(\frac{(\dot{M}_\xi\xi)}{\xi\delta\rho_l D_{l,12}} + \frac{1}{\xi} + \frac{\delta'}{\delta}\right)$$

$$+ -y'^2_{l,i}\left(\frac{1}{D_{l,12}}\frac{dD_{l,12}}{dy_{l,i}} + \frac{1}{\rho_l}\frac{d\rho_l}{dy_{l,i}}\right) \tag{19}$$

The differential equations of the micro region are integrated using a Runge-Kutta method. As a result, for a given radius $r(t)$ one gets the characteristic data of microscale heat and mass transfer, e.g., the liquid composition $y_{l,i}$, the shape of the liquid-vapor interface $\delta(\xi)$ including the apparent contact angle φ_{app} (see Fig. 1), and the local heat flux $\dot{q}(\xi)$.

4 Macroscale Heat and Mass Transfer

4.1 Modeling Equations and Boundary Conditions. The macro region consists of the liquid adjacent to the micro region and the wall. Heat transfer is modeled with simplifying assumptions. Energy storage can be neglected because the ratio of energy storage and heat of evaporation (see phase conversion number) is far smaller than one. Convective heat transfer within the thermal boundary layer is neglected, too [25,26]. Hence, to calculate heat transfer in the macro region the Laplace equations $\nabla^2 T = 0$ for the liquid and solid domain have to be solved. Nevertheless, one obtains a transient temperature field because of the moving boundary $r(t)$. Concentration changes only very slightly in the macro region (see Fig. 8). Therefore, the liquid concentration and the thermophysical properties are set constant outside the micro region.

The boundary conditions are shown in Fig. 5. Adiabatic boundaries are used due to the symmetry and the non-evaporating adsorbed liquid film.

4.2 Finite Element Method. To solve the Laplace equations the finite element code SEPRAN [27] is used. The mesh consists of triangular elements with quadratic functions (Fig. 6). The finite elements are distributed depending on the temperature gradient in the macro region. Hence, the grid width in the neighborhood of the micro region is extremely small and the number of elements therefore becomes very high.

5 Iteration Between Micro Region and Macro Region

The computation is started in the micro region with an assumed value of the wall temperature, $T_{w,\text{mic}}$. The initial data for equations (19) at $\xi = 0$ where the meniscus is connected to the non-
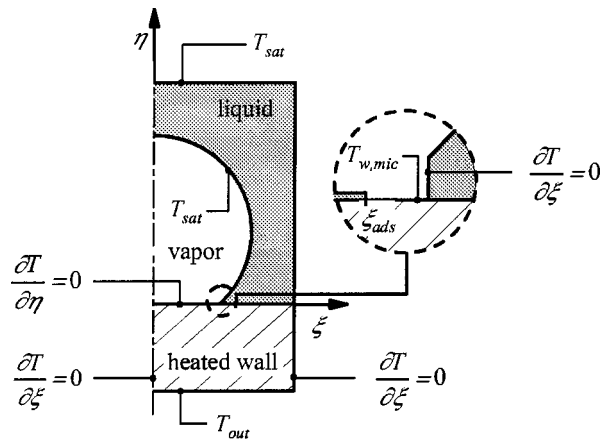
Fig. 5   Thermal boundary conditions in the macro region

Fig. 7   Liquid film thickness, heat flux, velocity vectors, and apparent contact angle in the micro region of the binary mixture propane/n-butane ($y_{l,1,\text{bulk}}=0.667$, $p^*=0.2$, $T_{\text{out}}-T_{\text{sat}}=10.74$ K, $\xi_{\text{ads}}=0.023$ mm, $r=0.057$ mm)

evaporating adsorbed liquid film is determined in an iterative procedure to match the macroscopic bubble radius, phase interface temperature, and liquid composition at the transition to the macro region. After computing the total heat that is transferred trough the micro region into the vapor, the chosen wall temperature in the micro region is used to calculate the heat that is conducted through the macro region into the micro region. If these two heat flows do not satisfy the energy balance at the interface between micro and macro region, the value of $T_{w,\text{mic}}$ is corrected and the calculation is started again. When the energy balance is fulfilled, the iteration ends and the heat transfer coefficient is calculated using Eqs. (1) and (2). A more detailed description of the iterative process, especially the used shooting method, is provided by [11,28].

6   Results

To verify the model, heat transfer in nucleate boiling of various binary mixtures of hydrocarbons on a copper plate is studied [21].
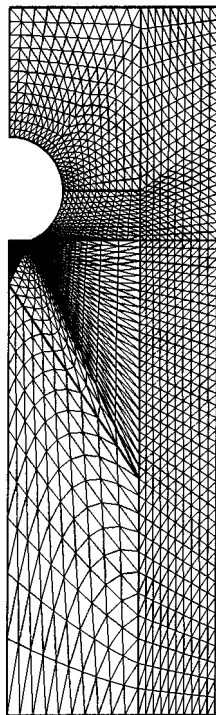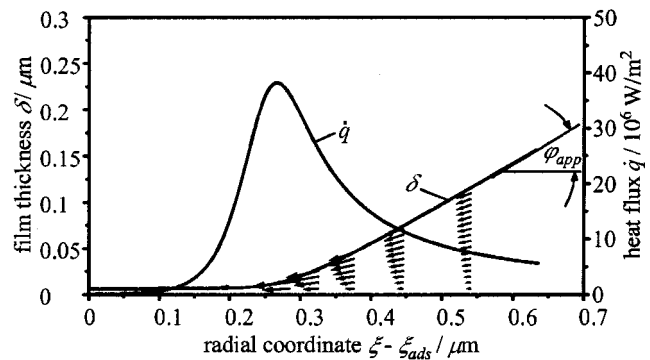

Fig. 6   Finite element distribution in the macro region

The examples correspond to experiments of Bednar and Bier [29] because in this work heat transfer coefficients, the related bubble site densities, and the departure diameters are measured simultaneously. Thermophysical properties are taken from [29,30].

6.1   Micro and Macro Region Results.   This paragraph deals with some numerical results of the micro region analysis for nucleate boiling of a propane/n-butane mixture on a copper plate. A mean heat flux of $\dot{q}_m=2\times10^4$ W/m² at the outer surface of the evaporator wall and a reduced pressure of $p^*=0.2$ are chosen. The liquid bulk mass fraction is $y_{l,1,\text{bulk}}=0.667$, the saturation temperature amounts to $T_{\text{sat}}=303.92$ K, and a bubble site density of $N_b=658/\text{cm}^2$ is determined. Thus, the diameter of the single bubble subsystem $d_{\text{sub}}=0.44$ mm is obtained. In the corresponding experiments [29], thermocouples were placed $\delta_w=0.5$ mm below the boiler surface. The boundary layer thickness $\delta_{th}=0.245$ mm results from the relations for natural convective heat transfer [12,31]. With the theory presented in paragraph 3.1.1 the dispersion constant $A=6.1\times10^{-21}$ J is calculated.

In Fig. 7 to 11 the micro region results for a single bubble with the radius $r=0.057$ mm are shown. An adsorbed film radius of $\xi_{\text{ads}}=0.023$ mm and a thickness of $\delta_{\text{ads}}=6.5$ nm are computed. In Fig. 7 the film thickness δ, the heat flux $\dot{q}$, and the velocity vectors of the transverse liquid flow are plotted versus the radial coordinate $\xi-\xi_{\text{ads}}$. The interface approaches the wall with nearly constant curvature, then turns sharply, and ends in the adsorbed film. The thermal resistance of the thin liquid film decreases with decreasing film thickness, and hence the heat flux increases. Close to the adsorbed film, where $\xi-\xi_{\text{ads}}\rightarrow0$, the heat flux is reduced by the adhesion pressure. These two opposite effects lead to a maximum of the heat flux which reaches a value of $\dot{q}=4\times10^7$ W/m² (Fig. 7), whereas the mean heat flux at the outer surface of the wall is only $\dot{q}_m=2\times10^4$ W/m². Due to the distribution of the heat flux the liquid flows wedge-shaped into the micro region and then turns increasingly towards the interface where evaporation takes place. Close to the adsorbed film the liquid velocity approaches zero. The apparent contact angle $\varphi_{\text{app}}=29,4°$ is a further result of the micro region analysis.

In Fig. 8 the distribution of the liquid and vapor mass fraction for the more volatile component propane in the micro region is shown. Due to the high evaporation rate and the preferential evaporation of propane, the mass fractions in the liquid and vapor phase decrease in the direction of the transverse liquid flow towards the adsorbed film. Strong concentration gradients occur. The variation of the liquid composition influences the local phase equilibrium and the thermophysical properties. With decreasing concentration of the more volatile component the saturation temperature T_{sat} increases (Fig. 9). At $\xi-\xi_{\text{ads}}=0$ the liquid-vapor phase interface is connected to the adsorbed film where the phase
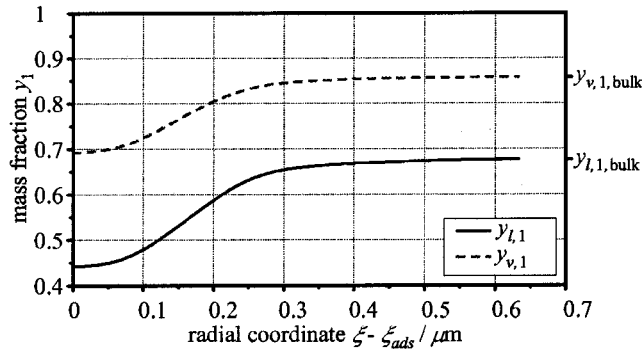
Fig. 8 Liquid and vapor mass fraction of the more volatile component propane in the micro region of the binary mixture propane/n-butane ($y_{l,1,bulk}$=0.667, p^*=0.2, T_{out}−T_{sat} =10,74 K, ξ_{ads}=0.023 mm, r=0.057 mm)

interface has a temperature T_{ph} equal to the wall temperature. Hence, no evaporation at the adsorbed film occurs. Within the micro region the difference between the wall temperature $T_{w,mic}$ and the minimum phase interface temperature $T_{ph,min}$, Eq. (17), drives the heat transfer at the interface. Liquid and vapor state can also be discussed in the phase equilibrium diagram (Fig. 10), where the states of liquid and vapor phase are marked at the transition from the micro to the macro region (I_{end} and II_{end}) and at the transition from the micro region to the adsorbed film (I_{ads} and II_{ads}). Within the micro region states change along the plotted lines in Fig. 10 according to Fig. 8 and Fig. 9.
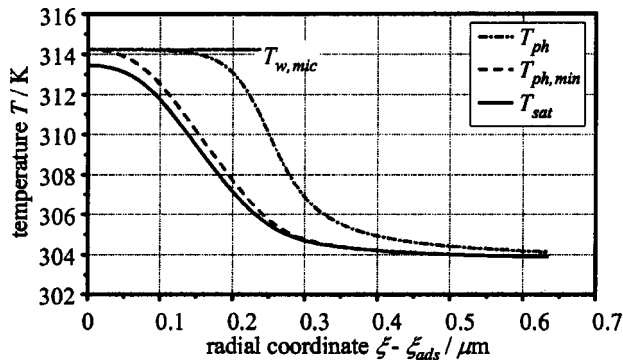

Fig. 9 Temperatures in the micro region of the binary mixture propane/n-butane ($y_{l,1,bulk}$=0.667, p^*=0.2, T_{out}−T_{sat} =10,74 K, ξ_{ads}=0.023 mm, r=0.057 mm)
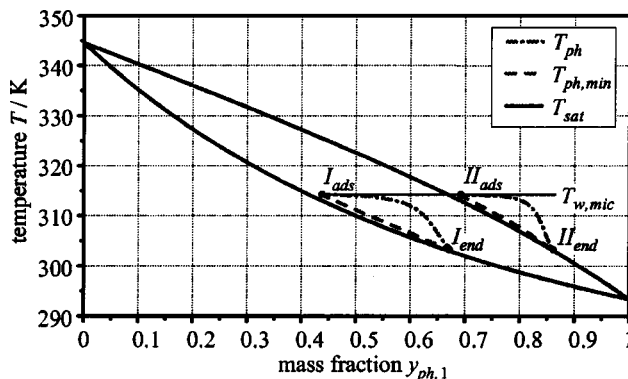

Fig. 10 Liquid-vapor phase equilibrium in the micro region of the binary mixture propane/n-butane ($y_{l,1,bulk}$=0.667, p^*=0.2, T_{out}−T_{sat}=10, 74 K, ξ_{ads}=0.023 mm, r=0.057 mm)
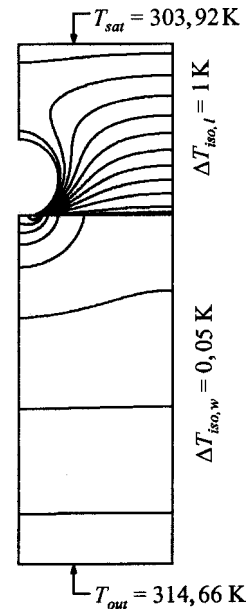
Fig. 11 Temperature distribution in the macro region of the binary mixture propane/n-butane ($y_{l,1,bulk}$=0.667, p^*=0.2, T_{out} − T_{sat}=10, 74 K, ξ_{ads}=0.023 mm, r=0.057 mm)

In the macro region two-dimensional heat conduction is calculated. Figure 11 depicts a plot of the macroscopic temperature distribution in the wall and in the liquid bulk. The isotherms indicate that the heat flow is concentrated towards the micro region. In this example about 30% of the total heat supplied at the outer surface of the evaporator wall passes through the micro region. The model computes a heat transfer coefficient α = 2594 W/(m²K) that belongs to a bubble radius of r = 0.057 mm (departure radius). For smaller bubble radii the calculated heat transfer coefficients are shown in Fig. 12. They depend linearly on the radius. Without bubbles (r=0) the calculated heat transfer coefficient corresponds to the thermal resistance of the liquid layer in natural convection.

For each value $r(t)$ a heat flow into the bubble $\dot{Q}_b$ is gained. The heat flow $\dot{Q}_b$ is related to the evaporating liquid mass flux and thus to the bubble growth rate. It follows

$$\dot{V}_b = \frac{\dot{Q}_b}{\Delta h_{lv}\rho_v} \qquad (20)$$

Fig. 12 Calculated heat transfer coefficients at different bubble radii of the binary mixture propane/n-butane ($y_{l,1,bulk}$ = 0.667, p^*=0.2, T_{out}−T_{sat}=10,74 K)
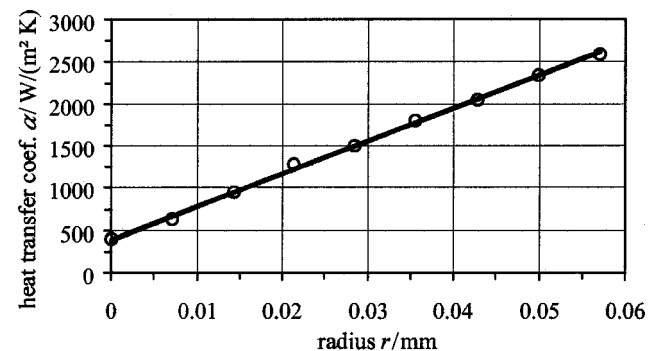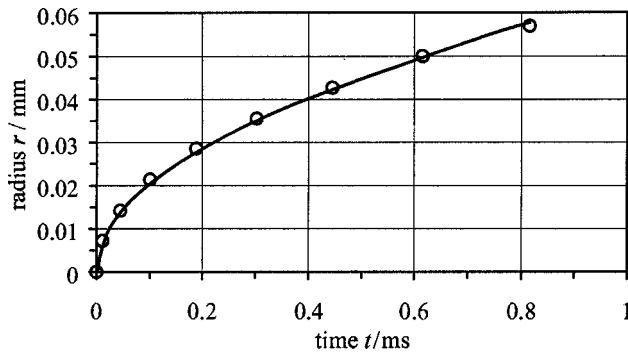
Fig. 13 Calculated bubble radii versus time of the binary mixture propane/n-butane ($y_{l,1,bulk}=0.667$, $p^*=0.2$, $T_{out}-T_{sat}=10,74$ K)

where $\dot{V}_b$ is the time derivative of the bubble volume. Integration of Eq. (20) over small time steps Δt yields the function $r(t)$. In Fig. 13 calculated radii are plotted versus the time. They can be correlated by a function of the form

$$r(t)=C\sqrt{t}. \tag{21}$$

In the present example one derives $C=2.0\times 10^{-3}$ ms$^{-0.5}$.

The numerical accuracy of the model is estimated by checking the energy balance and calculating its residual. First, at the interface between micro and macro region and second, at the outer boundaries of the macro region. We thereby estimate the numerical accuracy of calculated heat transfer coefficients to $\pm 5\%$.

6.2 Verification of Heat Transfer Coefficients. In order to compare computations with experiments the mean heat transfer coefficient is calculated according to Eq. (1) and Eq. (2). As input parameters the model needs bubble site densities which are reported in very few publications only. Therefore, experimental values are taken from Bednar and Bier [29]. They measured heat transfer coefficients on copper tubes and determined bubble site densities as well as departure diameters for various binary mixtures of hydrocarbons simultaneously. The error of measurement for the chosen data is in the range of $\pm 10\%$.

In Fig. 14–20 results for different compositions of the binary mixtures propylene/propane, propane/n-butane, and ethane/propane are shown. The model is capable to predict qualitatively the heat transfer coefficient as a function of composition for different mixtures and pressures. The model seems to describe well the typical mixture phenomena: the propylene/propene mixture shows almost no reduction of the heat transfer coefficient at intermediate bulk mole fractions (Fig. 14), because the components are rather similar once. The propane/n-butane and ethane/propane mixtures (Fig. 15–20), however, show the typical and well known reduction of the heat transfer coefficient at intermediate bulk mole fractions. The quantitative deviation between experimental and numerical values is less than 22% if the error of measurement ($\pm 10\%$) is not considered. As can be seen from the figures, in all cases numerical values are lower than experimental ones. The reason might be that the convective heat transfer around the rising bubble is not yet included in the model and that the single bubble model does not yet account for convection and flow effects around tubes. This explanation is strengthened by the fact that the deviation becomes smaller for increasing heat flux. With increasing heat flux the bubble site density also increases and this in turn leads to a decreasing influence of the heat transfer in the macro region where convective heat transfer is neglected so far. Furthermore, a study of the influence of convection on nucleate boiling heat transfer of pure substances around horizontal tubes [32] with the micro region model [6] seems to confirm this explanation.

Fig. 14 Comparison of computational results with data from experiments [26] of the binary mixture propylene/propane for different compositions ($p^*=0.03$, $\dot{q}_m=2\times 10^4$ W/m^2)

6.3 Simplified Approach for the Heat Transfer Coefficient. Due to the linear dependence of the heat transfer coefficient with the bubble radius (Fig. 12) and due to Eq. (21), integration of Eq. (1) and Eq. (2) yields

$$\alpha_m=\frac{1}{3}\alpha_{fc}+\frac{2}{3}\alpha(r_{dep}), \tag{22}$$

where α_{fc} is the heat transfer coefficient for free convection [31] and $\alpha(r_{dep})$ the heat transfer coefficient of the subsystem with a

Fig. 15 Comparison of computational results with data from experiments [26] of the binary mixture propane/n-butane for different compositions ($p^*=0.2$, $\dot{q}_m=2\times 10^4$ W/m^2)

Fig. 16 Comparison of computational results with data from experiments [26] of the binary mixture propane/n-butane for different compositions ($p^*=0.2$, $\dot{q}_m=2\times10^3$ W/m^2)

Fig. 18 Comparison of computational results with data from experiments [26] of the binary mixture propane/n-butane for different compositions ($p^*=0.1$, $\dot{q}_m=4\times10^3$ W/m^2)

bubble at departure radius. Equation (22) enables to predict the mean heat transfer coefficient by only one numerical calculation for the bubble departure radius r_{dep} and thus reduces the numerical expenditure enormously compared to the full time dependent computation.

7 Summary and Outlook

Confining ourselves to low and intermediate heat fluxes, nucleate boiling heat transfer of binary mixtures can be described theoretically using a single bubble model. The modeling equations are

derived by simplifying the conservation equations as well as considering special microscale and mixture effects. The resulting set of differential equations has to be solved numerically. As a result one gets the heat transfer coefficient of binary mixtures. Comparing this data with measurements from experiments implies good accuracy. As input parameters only the thermophysical properties as well as values for the bubble site density and the departure diameter are required.

Evaluating heat transfer in the subsystem indicates that the micro region has a strong influence on overall heat flow. A consid-
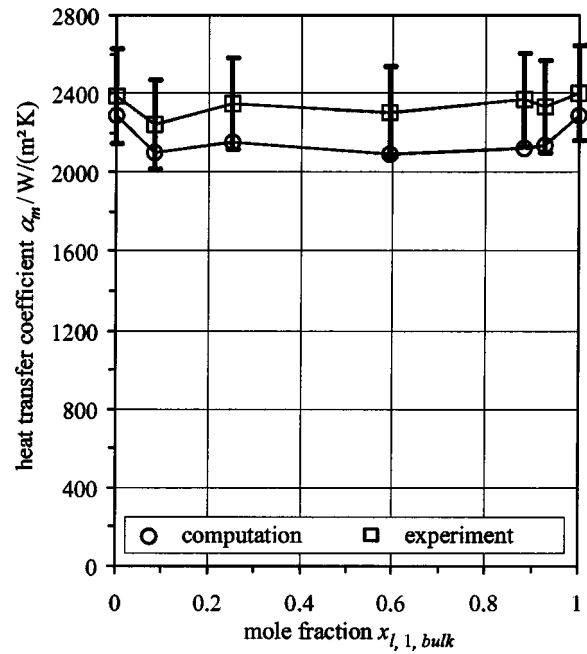

Fig. 17 Comparison of computational results with data from experiments [26] of the binary mixture propane/n-butane for different compositions ($p^*=0.1$, $\dot{q}_m=1\times10^4$ W/m^2)
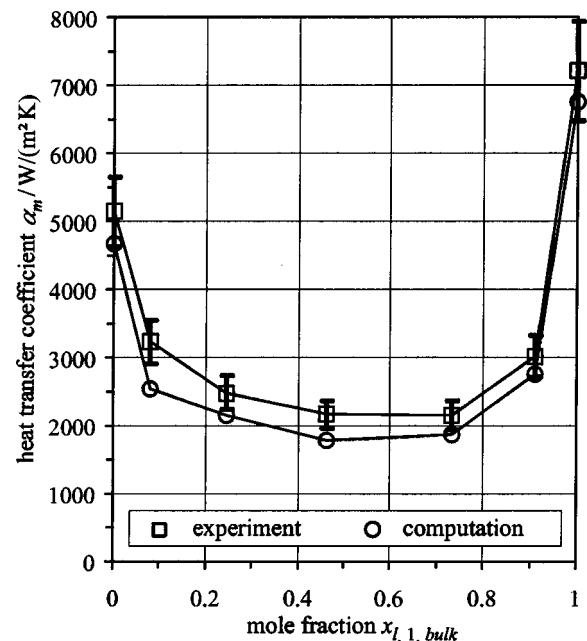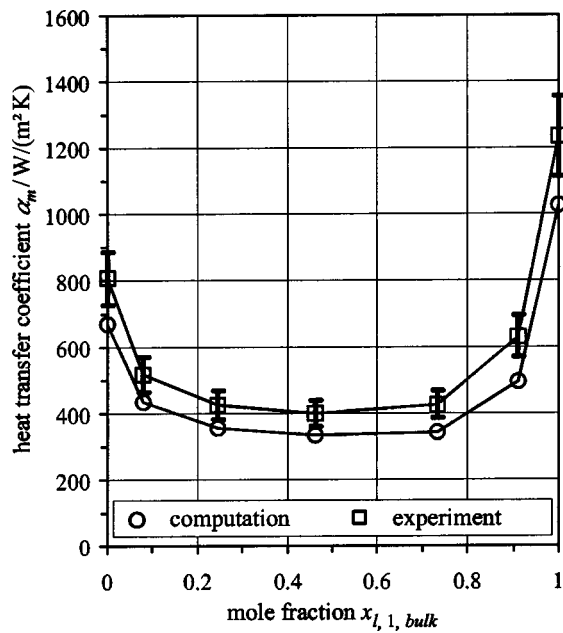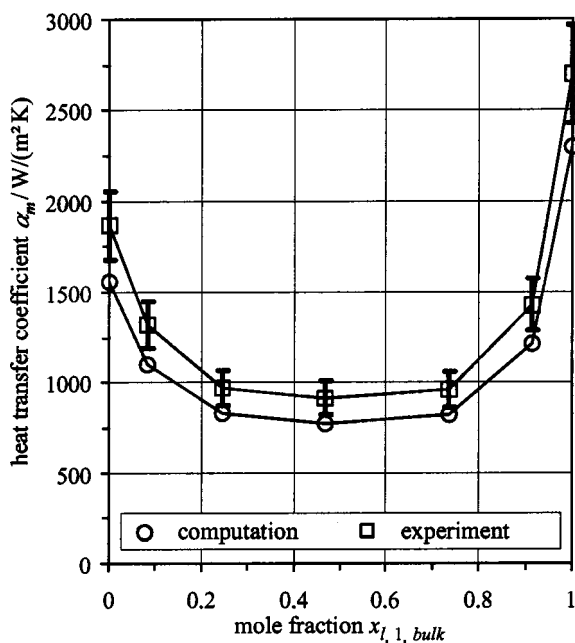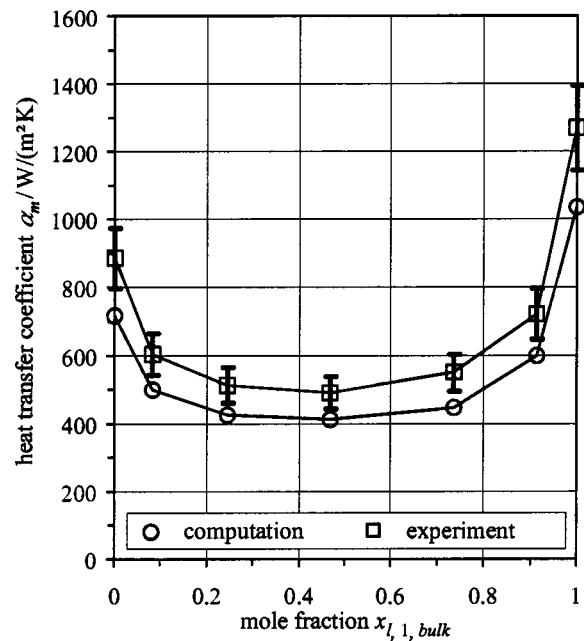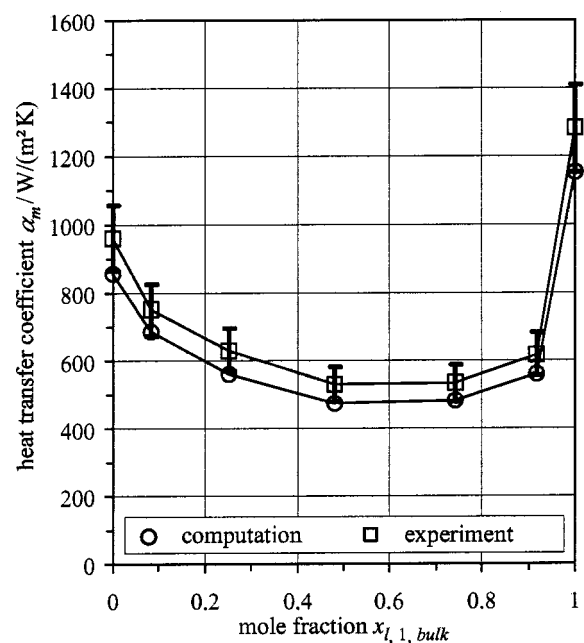

Fig. 19 Comparison of computational results with data from experiments [26] of the binary mixture propane/n-butane for different compositions ($p^*=0.03$, $\dot{q}_m=1\times10^4$ W/m^2)
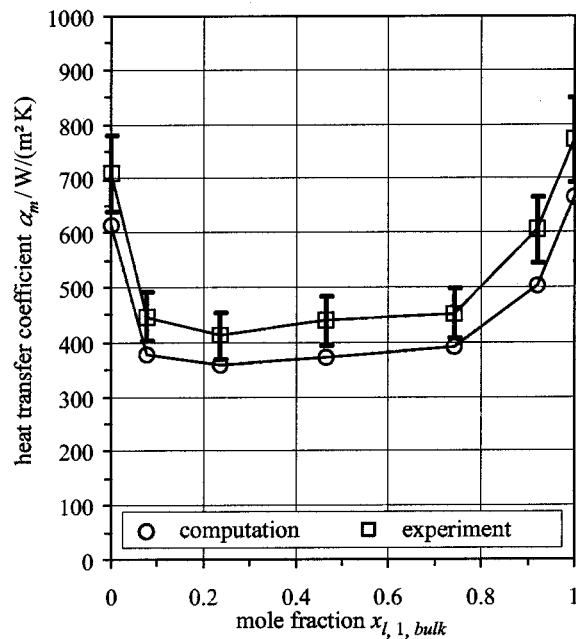
Fig. 20 Comparison of computational results with data from experiments [26] of the binary mixture ethane/propane for different compositions ($p^*=0.1$, $\dot{q}_m=2\times10^3$ W/m^2)

erable amount of the supplied heat at the evaporator wall flows through that region. In the micro region, the liquid-vapor equilibrium is influenced by the capillary pressure effect and the arising strong concentration gradients. Mixture effects, e.g., diffusive mass transfer and Marangoni convection, are also taken into account.

In literature there is no general agreement about the importance of different physical phenomena in nucleate boiling of binary mixtures. Using the developed model, one can identify dominant mixture effects as discussed in a proceeding paper.

Acknowledgments

Nomenclature

A = dispersion constant (J)
a = coordinate parallel to the phase interface (m)
C = constant (ms$^{-0.5}$)
D = diffusion coefficient (m^2/s)
d_{sub} = diameter of the subsystem (m)
f = condensation coefficient ($-$)
$\bar{H}_{lv}$ = molar heat of evaporation (J/kmol)
$\Delta\bar{H}$ = molar heat of total evaporation (J/kmol)
Δh_{lv} = latent heat of evaporation (J/kg)
j = diffusive mass flux (kg/(m^2 s))
K = curvature (1/m)
L = film length (m)
M = molar mass (kg/kmol)
$\dot{M}_\xi$ = integrated mass flux (kg/(ms))
N_b = bubble site density (1/m^2)
p = pressure (N/m^2)
p^* = reduced pressure (p/p_c) ($-$)
p_c = critical pressure (N/m^2)
p_{cap} = capillary pressure (N/m^2)
p_{dis} = disjoining pressure (N/m^2)
$\dot{Q}_b$ = heat flow into the bubble (W)
$\dot{q}$ = heat flux (W/m^2)

$\dot{q}_m$ = time- and area-averaged heat flux (W/m^2)
r = radius (m)
r_{dep} = departure radius (m)
$\bar{R}$ = universal gas constant (J/(kmol K))
R_{ph} = interfacial thermal resistance (m^2 K/W)
Re = Reynolds number ($-$)
T = temperature (K)
ΔT_{iso} = temperature difference of isotherms (K)
$T_{ph,min}$ = minimum phase interface temperature for evaporation (K)
t = time (s)
t_b = bubble growth time (s)
Δt = time step (s)
u = liquid velocity (m/s)
$\dot{V}_b$ = time derivative of the bubble volume (m^3/s)
$\Delta\bar{V}$ = molar volume difference of total evaporation (m^3/kmol)
$\bar{V}$ = partial molar volume (m^3/kmol)
x = mole fraction ($-$)
y = mass fraction ($-$)

Greek symbols

α = area-averaged heat transfer coefficient (W/(m^2 K))
α_m = time- and area-averaged heat transfer coefficient (W/(m^2 K))
δ = film thickness (m)
δ_{th} = thermal boundary layer thickness (m)
δ_w = wall thickness (m)
η = coordinate normal to the wall (m)
φ_{app} = apparent contact angle ($°$)
λ = thermal conductivity (W/(mK))
ν = kinematic viscosity (m^2/s)
ξ = coordinate parallel to the wall (m)
ρ = density (kg/m^3)
σ = surface tension (N/m)
τ = shear stress (N/m^2)

Subscripts

ads = adsorbed film
bulk = bulk
end = end of micro region (transition to the macro region)
fc = free convection
η = vertical direction
i = component
l = liquid
mic = micro region
out = outer surface of the wall
ph = phase interface
s = solid
sat = saturation
v = vapor
w = wall
ξ = radial direction
0 = reference quantity
1 = more volatile component
2 = less volatile component

References

[1] Kenning, D. B. R., 1997, "New Developments in Pool Boiling," Int. J. Refrig., **20**(8), pp. 534–544.
[2] Celata, G. P., Cumo, M., and Setaro, T., 1994, "A Review of Pool and Forced Convective Boiling of Binary Mixtures," Exp. Therm. Fluid Sci., **9**, pp. 367–381.
[3] Inoue, T., Kawae, N., and Monde, M., 1998, "Characteristics of Heat Transfer Coefficient During Nucleate Pool Boiling of Binary Mixtures," Heat Mass Transfer, **33**, pp. 337–344.
[4] Gorenflo, D., and Köster, R., 1999, "Pool Boiling Heat Transfer from Horizontal Tubes to Mixtures," *Convective Flow and Pool Boiling*, M. Lehner and F. Mayinger, eds., Taylor and Francis, Philadelphia, pp. 3–22.
[5] Dhir, V. K., 2001, "Numerical Simulations of Pool-Boiling Heat Transfer," AIChE J., **47**(4), pp. 813–834.

[6] Stephan, P., and Hammer, J., 1994, "A New Model for Nucleate Boiling Heat Transfer," Heat Mass Transfer, **30**, pp. 119–125.

[7] Mann, M., and Stephan, K., 2000, "Prediction of Bubble Departure Diameters in Nucleate Boiling," *Proceedings 3rd European Thermal Sciences Conference*, E. Hahne, W. Heidemann, and K. Spindler, eds., Edizioni ETS, pp. 749–754.

[8] Son, G., Dhir, V. K., and Ramaujapu, N., 1999, "Dynamics and Heat Transfer Associated with a Single Bubble During Nucleate Boiling on a Horizontal Surface," ASME J. Heat Transfer , **121**, pp. 623–631.

[9] Bai, Q., and Fujita, Y., 1999, "Numerical Simulation of the Growth for a Single Bubble in Nucleate Boiling," Therm. Sci. Eng., **7**, pp. 45–53.

[10] Wayner, P. C., Kao, Y. K., and LaCroix, L. V., 1976, "The Interline Heat Transfer Coefficient on an Evaporating Wetting Film," Int. J. Heat Mass Transfer, **19**, pp. 487–492.

[11] Stephan, P., and Busse, C. A., 1992, "Analysis of the Heat Transfer Coefficient of Grooved Heat Pipe Evaporator Walls," Int. J. Heat Mass Transfer, **35**(2), pp. 383–391.

[12] Stephan, K., 1992, *Heat Transfer in Condensation and Boiling*, Springer-Verlag, Berlin.

[13] Fritz, W., 1935, "Berechnung des Maximalvolumens von Dampfblasen," Phys. Z., **11**, pp. 379–384.

[14] Benjamin, R. J., and Balakrishnan, A. R., 1997, "Nucleation Site Density in Pool Boiling of Binary Mixtures: Effect of Surface Micro-roughness and Surface and Liquid Physical Properties," Can. J. Chem. Eng., **75**, pp. 1080–1089.

[15] Krupiczka, R., Rotkegel, A., and Ziobrowski, Z., 2000, "The Influence of Mass Transfer on the Heat Transfer Coefficients during the Boiling of Multicomponent Mixtures," Int. J. Therm. Sci., **39**, pp. 667–672.

[16] Israelachvili, J. N., 1992, *Intermolecular and Surface Forces*, Academic Press, Philadelphia.

[17] Dzyaloshinskii, I. E., Lifshitz, E. M., and Pitaevskii, L. P., 1961, "The General Theory of van der Waals Forces," Adv. Phys., **10**, pp. 165–209.

[18] Derjaguin, B. V., and Chureav, N. V., 1977, "Disjoining Pressure of Thin Layers of Binary Solutions," J. Colloid Interface Sci., **62**, pp. 369–380.

[19] Wayner, P. C., 1999, "Intermolecular Forces in Phase-Change Heat Transfer: 1998 Kern award review," AIChE J., **45**(10), pp. 2055–2068.

[20] Schrage, R. W., 1953, *A Theoretical Study of Interphase Mass Transfer*, Columbia University Press, New York.

[21] Kern, J., 2002, "Modellierung und numerische Berechnung des Wärmeübergangs beim Blasensieden binärer Gemische," Ph.D. thesis, Fortschritt-Berichte VDI, **3**(727), VDI-Verlag, Düsseldorf.

[22] Paul, B., 1962, "Compilation of Evaporation Coefficients," ARS Journal, **32**, pp. 1321–1328.

[23] Carey, V. P., 1992, *Liquid-Vapor Phase-Change Phenomena: An Introduction to the Thermophysics of Vaporization and Condensation Processes in Heat Transfer Equipment*, Hemisphere, Washington.

[24] McGillis, W. R., and Carey, V. P., 1996, "On the Role of Marangoni Effect on the Critical Heat Flux for Pool Boiling of Binary Mixtures," ASME J. Heat Transfer , **118**, pp. 103–109.

[25] Fuchs, T., 2001, "Modellierung und numerische Berechnung des konvektiven Wärme- und Stofftransports um eine wachsende Dampfblase," Diploma thesis, Chair of Technical Thermodynamics, University of Technology, Darmstadt.

[26] Genske, P., and Stephan, K., 2001, "Nucleate Boiling—Numerical Simulation of Heat Transfer at Moderate Heat Fluxes," paper B5.7, *Proc. of the International Institute of Refrigeration Conference, Commission B1, Thermophysical Properties and Transfer Processes of New Refrigerants*, Paderborn, Germany.

[27] Ingenieursbureau Sepra, 1993, SEPRAN, *A Finite Element Code. User manual*, Leidscham.

[28] Hammer, J., and Stephan, P., 1996, "The role of Micro-Region Phenomena on Nucleate Boiling Heat Transfer," *Proceedings 2nd European Thermal Sciences and 14th UIT National Heat Transfer Conference*, G. P. Celata, P. Di Marco, and A. Mariani, eds., Edizioni ETS, pp. 467–474.

[29] Bednar, W., and Bier, K., 1994, "Wärmeübergang beim Blasensieden von binären Kohlenwasserstoffgemischen," Ph.D. thesis, Fortschritt-Berichte VDI, **3**(357), VDI-Verlag, Düsseldorf.

[30] National Institute of Standards and Technology, 1998, *Standard Refence Database 23—Version 6.01*, Gaithersburg.

[31] *VDI-Wärmeatlas*, 1997, VDI-Verlag, Düsseldorf.

[32] Mann, M., and Stephan, K., 2000, "Influence of Convection on Nucleate Boiling Heat Transfer around Horizontal Tubes," Multiphase Sci. Technol., **12**(3), pp. 1–13.

Investigation of Decisive Mixture Effects in Nucleate Boiling of Binary Mixtures Using a Theoretical Model

Jürgen Kern

Peter Stephan
e-mail: pstephan@ttd.tu-darmstadt.de

Chair of Technical Thermodynamics,
Darmstadt University of Technology,
Petersenstrasse 30, 64287 Darmstadt, Germany

In the present paper an attempt is made to clarify the influence of mixture effects upon heat transfer in nucleate boiling of binary mixtures. The studies are based on a theoretical model that is briefly summarized. Evaluating heat and mass transfer around a single vapor bubble emphasizes a strong influence of the so-called micro region where the liquid-vapor phase interface approaches the wall. Due to the preferential evaporation of one component of the mixture, strong concentration gradients occur in the micro region. These microscale composition effects cause diffusive mass transfer, Marangoni convection, and a variation of the liquid-vapor phase equilibrium as well as a variation of the thermophysical properties. From a macroscopic point of view the bubble site density and the departure diameter vary with the composition of the liquid. By means of parameter studies decisive mixture effects are identified and their relevance in the nucleate boiling process is stated. The heat transfer coefficient crucially depends on the bubble site density and departure diameter. For increasing bubble site density, the influence of microscopic concentration gradients increases. But only the variation of liquid-vapor phase equilibrium becomes important, while diffusive mass transfer and Marangoni convection can be neglected. [DOI: 10.1115/1.1622716]

Keywords: Binary, Boiling, Heat Transfer, Modeling, Thin Films

1 Introduction

In the last decade many research projects were carried out on developing theoretical models to predict nucleate boiling heat transfer coefficients [1]. One of the aims was to supplement empirical correlations needed for the design of boilers. In a first step, investigations were confined on boiling of pure substances. Based on a modeling theory to compute the nucleate boiling heat transfer coefficient of pure liquids [2], the authors developed a model to calculate heat transfer coefficients of binary mixtures [3,4]. As input parameters only values for the bubble site density and the departure diameter are required. This data can either be taken from measurements directly or can be obtained by using standard bubble departure diameter correlations, e.g., [5] and site density models [6]. The model describes the heat and mass transfer in the liquid and wall around a single growing bubble (Fig. 1 left hand side). Computational results are in good agreement with data from experiments of Bednar and Bier [7]. The corresponding heat transfer coefficients are shown in Fig. 2. The error of measurement is in the range of ±10%. Furthermore, values of frequently used correlations are plotted in that figure. The correlations of Fujita and Tsutsui [8], Schlünder [9], and Stephan and Körner [10] also allow to calculate the heat transfer coefficient of binary mixtures, but only if the heat transfer coefficients of the two pure components are known. However, their correlations are partly based on different physical phenomena. Stephan and Körner take into account the local difference between liquid and vapor composition. Fujita and Tsutsui additionally consider the temperature difference between boiling and dew point curve at constant liquid concentration. Schlünder adds a diffusive mass transfer resistance in the near wall liquid layer.

Despite of a lot of publications and discussions on nucleate

boiling of binary mixtures, one hasn't come to an agreement concerning physical phenomena governing the heat and mass transfer process. Therefore, by utilizing the mentioned theoretical model [3,4], decisive mixture effects have been identified as presented in the proceeding chapters.

First of all, the used modeling theory is briefly summarized. The proceeding chapter is dedicated to the influence of mixture effects occurring in the tiny thin film area, called micro region, where the liquid-vapor phase interface approaches the wall. Finally, parameter studies are presented that inform on governing physical phenomena and especially on causal parameters responsible for the characteristic reduction of the heat transfer coefficient at intermediate compositions (see Fig. 2).

2 Single Bubble Model

The theoretical model that is summarized in this chapter is described in detail in [3,4]. The main ideas and assumptions are the following. As long as neighboring bubbles do not interact, the boiling system can be divided into small, symmetric subsystems, each of them containing a single vapor bubble. On the left hand side of Fig. 1 the single bubble subsystem is shown. The size of the system is chosen corresponding to the active bubble site density. Boundary conditions are the saturation temperature T_{sat} and the outside wall temperature T_{out}, where δ_{th} is the thickness of the thermal boundary layer and δ_w denotes for the position of the thermocouples underneath the boiler surface in experiments. The model calculates the heat flux $\dot{q}(\xi, r)$ for the time period when the bubble is growing from an infinitesimal size to the departure radius. After averaging the heat flux with respect to the heater area and the bubble growth time, the mean heat transfer coefficient is obtained using

$$\alpha_m = \frac{\dot{q}_m}{T_{out} - T_{sat}} \tag{1}$$

Copyright © 2003 by ASME
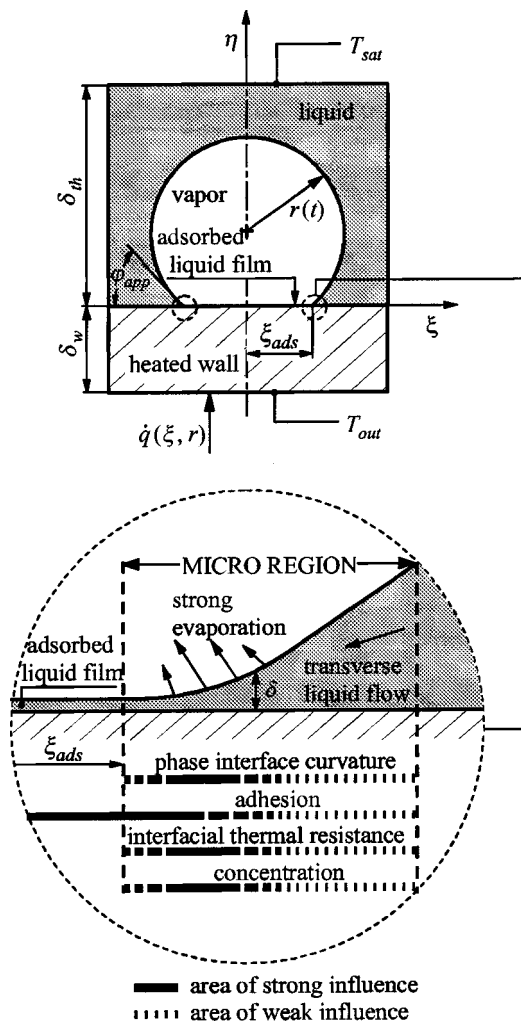
Fig. 1 Single bubble subsystem and significant phenomena in the micro region

Fig. 2 Comparison of computational results with data from experiments [5] and correlations [6–8] of the binary mixture ethane/propane for different compositions ($p^*=0.1$, $\dot{q}_m=4\times10^3$ W/m^2)

In order to calculate the heat flux, the computational domain is subdivided into two regions: the micro region, where the liquid-vapor phase interphase approaches the wall, and the liquid adjacent to the micro region as well as the wall, called macro region (see Fig. 1). In the macro region heat transfer is governed by two-dimensional heat conduction. The well known Laplace equations $\nabla^2 T=0$ are solved with a finite element method. In Fig. 1 the micro region is plotted on a larger scale. Whereas in the macro region the phase interphase has a constant curvature corresponding to the bubble radius, in the micro region the phase interphase turns sharply and ends in a non-evaporating thin liquid film which is adsorbed at the wall. Long range van der Waals forces between the wall atoms and the liquid molecules inhibit evaporation. This film covers the whole wall underneath the vapor bubble. In most practical applications the thermal conductivity of the liquid is far smaller than that of the wall material. In this case the evaporation rate has a local maximum in the micro region. Most of the supplied heat at the evaporator wall flows through the thin liquid film where the thermal resistance is small. The high local evaporation rate induces a transverse liquid flow into the micro region. The pressure drop is driven by the phase interface curvature effect and the adhesion effect. Their spheres of influence are schematically indicated in Fig. 1. The interfacial thermal resistance is important in the central part of the micro region, because of the low thermal resistance of the thin liquid film and the high heat flux. In a binary mixture one observes a preferential evaporation of one component

of the mixture. Thus, the concentration of this component decreases in the direction of the transverse liquid flow into the micro region. As a result of this concentration effect the conservation laws are solved for variable thermophysical properties, and Marangoni convection as well as diffusive mass transport are considered.

The aim of the present paper is to identify decisive mixture effects in nucleate boiling heat transfer using the above described theoretical model. Due to the separation of scales, the model distinguishes between microscale and macroscale mixture effects. The following microscale mixture effects caused by concentration gradients in the thin film area are considered in the model:

- diffusive mass transfer
- Marangoni convection due to surface tension gradients
- change of properties in general (e.g., density, viscosity, thermal conductivity, and latent heat of evaporation)
- change of equilibrium phase interface temperature (saturation temperature)

From the point of view of our model, macroscale mixture effects are:

- change of active site density with bulk concentration
- change of departure diameter with bulk concentration

3 Influence of Microscale Mixture Effects

To evaluate mixture effects in the micro region, our attention is drawn to a propane/n-butane mixture ($y_{l,1,\text{bulk}}=0.063$, $p^*=0.2$, $T_{\text{out}}-T_{\text{sat}}=7.87$ K). The saturation temperature amounts to $T_{\text{sat}}=335.45$ K.

In Figs. 3 and 4 the results for a single bubble with a radius $r=0.05$ mm are shown. An apparent contact angle of $\varphi_{\text{app}}=21.4°$ and an adsorbed film length of $\xi_{\text{ads}}=0.016$ mm are computed (see Fig. 1). In Fig. 3 the film thickness δ and the heat flux $\dot{q}$ are plotted versus the radial coordinate $\xi-\xi_{\text{ads}}$. Whereas the shape of the bubble is assumed to be spherical in the macro region, the curvature of the liquid-vapor phase interface changes strongly in the micro region. Towards the adsorbed liquid film the curvature approaches zero. The thermal resistance of the thin liquid film is

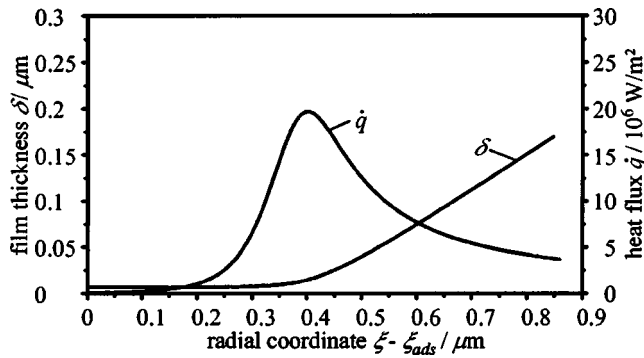**Fig. 3 Liquid film thickness and heat flux in the micro region of the binary mixture propane/n-butane** ($y_{l,1,\text{bulk}}=0.063$, $p^*=0.2$, $T_{\text{out}}-T_{\text{sat}}=7.87$ K, $\xi_{\text{ads}}=0.016$ mm, $r=0.05$ mm)

Fig. 5 Ratio of diffusive to convective mass flow of the more volatile component propane in the micro region of the binary mixture propane/n-butane ($y_{l,1,\text{bulk}}=0.063$, $p^*=0.2$, $T_{\text{out}}-T_{\text{sat}}=7.87$ K, $\xi_{\text{ads}}=0.016$ mm, $r=0.05$ mm)

becoming lower with decreasing film thickness, and hence the heat flux increases. Close to the adsorbed film, where $\xi-\xi_{\text{ads}}\rightarrow 0$, the heat flux is reduced by the adhesion pressure. These two opposite effects lead to a maximum of the heat flux, which reaches a value of $\dot{q}=2\times 10^7$ W/m^2 (Fig. 3), whereas the mean heat flux at the outer surface of the wall is only $\dot{q}_m=2\times 10^4$ W/m^2. Thus, in the present example 24% of the total heat supplied at the outer surface of the evaporator wall passes through the micro region.

In Fig. 4 the distribution of the liquid and vapor mass fraction of the more volatile component propane in the micro region are shown. Due to the high evaporation rate and the preferential evaporation of the more volatile component, the mass fractions decrease in the direction of the transverse liquid flow towards the adsorbed film. Strong concentration gradients occur. This in turn leads to an increase of the saturation temperature in the direction of the transverse liquid flow into the micro region (see Fig. 4).

3.1 Diffusive Mass Transfer. The differential equations of the micro region model are based on a scale analysis of the conservation equations. This analysis implies some simplifications [3,4]. One of them reads that diffusive mass transfer normal to the wall, i.e., in η-direction (Fig. 1) can be neglected. To evaluate diffusive mass transfer in radial direction (ξ) the calculated ratio of diffusive to convective mass flow of the more volatile component propane $\dot{J}_1/\dot{M}_1$ in the micro region of the binary mixture propane/n-butane is shown in Fig. 5. Diffusion contributes with 5 to 20% to mass transfer where $0\le\xi-\xi_{\text{ads}}\le 0.25\times 10^{-6}$ m, but only a very small amount of the heat flow passes through this area (see Fig. 3). For increasing values of $\xi-\xi_{\text{ads}}$ the diffusive contri-

bution tends to 0%. Therefore, diffusive mass transfer can be neglected in the micro region of this propane/n-butane mixture with a rather wide boiling range. It is unknown whether it is also negligible for mixtures with even wider boiling ranges, e.g., oil/water.
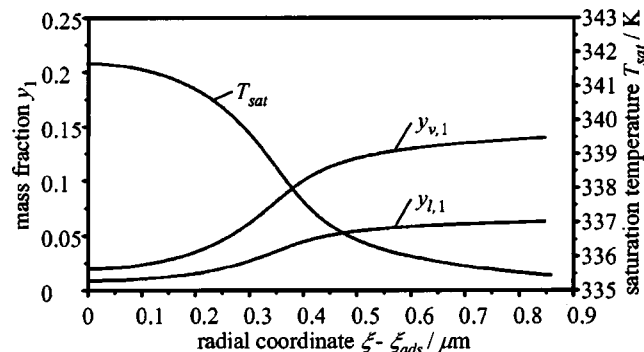
3.2 Marangoni Convection. The influence of Marangoni convection can be evaluated by considering the pressure gradient in the micro region [3,4]:

$$\frac{dp_l}{d\xi}=\frac{3\nu_l}{\xi\delta^3}(\dot{M}_\xi\xi)+\frac{3}{2\delta\sqrt{1+(d\delta/d\xi)^2}}\frac{d\sigma}{d\xi}. \tag{2}$$

The first term in Eq. 2 describes convection induced by evaporation and the second term describes the Marangoni convection. The ratio of the pressure gradient due to Marangoni convection and the total pressure gradient in the micro region of the binary mixture propane/n-butane is plotted in Fig. 6. It illustrates that Marangoni convection amounts to less than 3% of the total pressure gradient in the central part of the micro region and becomes important only towards the macro region. The plotted velocity profiles (Fig. 7) reveal a shear stress at the phase interphase that induces a weakening of the liquid flow into the micro region. This shear stress results from the fact that the surface tension decreases with decreasing mass fraction of the more volatile component propane $d\sigma(y_{l,1})/d\xi>0$. But Marangoni convection in the micro region does not influence heat transfer coefficients as shown below (chapter 3.4). In the macro region Marangoni convection is dominated by forced convection due to the growing vapor bubble [11]

Fig. 4 Liquid and vapor mass fraction of the more volatile component propane as well as saturation temperature in the micro region of the binary mixture propane/n-butane ($y_{l,1,\text{bulk}}=0.063$, $p^*=0.2$, $T_{\text{out}}-T_{\text{sat}}=7.87$ K, $\xi_{\text{ads}}=0.016$ mm, $r=0.05$ mm)

Fig. 6 Ratio of pressure gradient due to Marangoni convection and total pressure gradient in the micro region of the binary mixture propane/n-butane ($y_{l,1,\text{bulk}}=0.063$, $p^*=0.2$, $T_{\text{out}}-T_{\text{sat}}=7.87$ K, $\xi_{\text{ads}}=0.016$ mm, $r=0.05$ mm)

Fig. 7 Velocity profiles in the micro region of the binary mixture propane/n-butane ($y_{l,1,\text{bulk}}=0.063$, $p^*=0.2$, $T_{\text{out}}-T_{\text{sat}}=7{,}87$ K, $\xi_{\text{ads}}=0.016$ mm, $r=0.05$ mm)
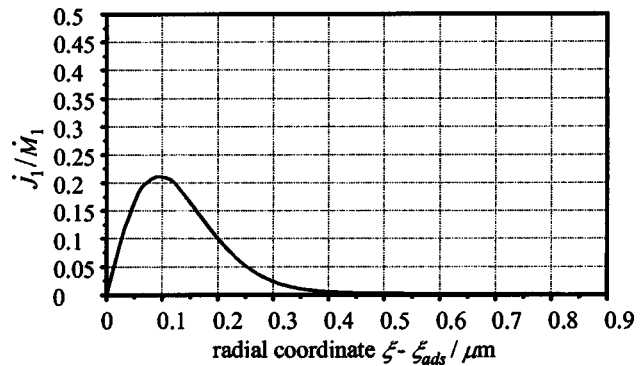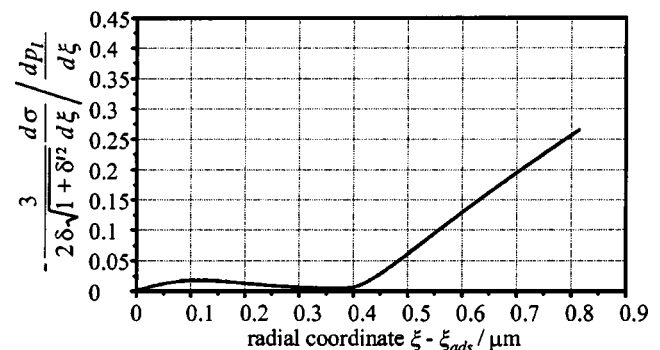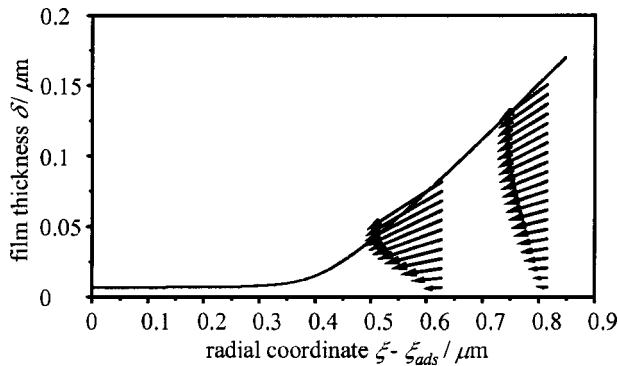
and therefore can be neglected in the macro region, too. Again, this conclusion may not be valid for mixtures with even wider boiling ranges, e.g., oil/water.

3.3 Change of Thermophysical Properties. Thermophysical properties vary with the composition of the liquid, and a variation of these properties influences the heat transfer coefficient. Table 1 contains tendencies obtained by several parameter studies. Thereby, mixtures have to be classified according to their concentration gradient in the micro region. Such a classification is shown in Fig. 8. In type A mixtures the concentration of the more volatile component increases in radial direction from the center of the single bubble subsystem, i.e., $dy_{L,1}/d\xi>0$. This is observed in zeotropic mixtures in general as well as in some azeotropic mixtures. In type B mixtures the concentration gradient has an opposite sign, i.e., $dy_{L,1}/d\xi<0$. This is only observed in some azeotropic mixtures as shown in Fig. 8. Table 1 indicates the influence of property changes with concentration on the heat transfer coefficient in type A and type B mixtures. For example, in a type A mixture the heat transfer coefficient decreases, if the surface tension increases with the mass fraction of the more volatile component, i.e., $\partial\alpha_m/\partial(d\sigma/dy_{l,1})<0$. Furthermore, influences of liquid density and viscosity changes, changes of liquid thermal conductivity, and heat of evaporation are presented in the table.

The main reasons for the observed tendencies might be the following: decreasing liquid density ρ_l and kinematic viscosity ν_l in the direction of the liquid flow into the micro region lead to a decrease of the viscosity effects in the Navier-Stokes equations and hence an increase of mass and heat transfer. An increase of thermal conductivity λ_l or latent heat of evaporation Δh_{lv} leads to

Table 1 Influence of variable thermophysical properties on the heat transfer coefficient

property	$dy_{L,1}/d\xi>0$ (type A mixture)	$dy_{L,1}/d\xi<0$ (type B mixture)
σ	$\dfrac{\partial\alpha_m}{\partial(d\sigma/dy_{l,1})}<0$	$\dfrac{\partial\alpha_m}{\partial(d\sigma/dy_{l,1})}>0$
ρ_l	$\dfrac{\partial\alpha_m}{\partial(d\rho_l/dy_{l,1})}>0$	$\dfrac{\partial\alpha_m}{\partial(d\rho_l/dy_{l,1})}<0$
ν_l	$\dfrac{\partial\alpha_m}{\partial(d\nu_l/dy_{l,1})}>0$	$\dfrac{\partial\alpha_m}{\partial(d\nu_l/dy_{l,1})}<0$
λ_l	$\dfrac{\partial\alpha_m}{\partial(d\lambda_l/dy_{l,1})}<0$	$\dfrac{\partial\alpha_m}{\partial(d\lambda_l/dy_{l,1})}>0$
Δh_{lv}	$\dfrac{\partial\alpha_m}{\partial(d\Delta h_{lv}/dy_{l,1})}<0$	$\dfrac{\partial\alpha_m}{\partial(d\Delta h_{lv}/dy_{l,1})}>0$
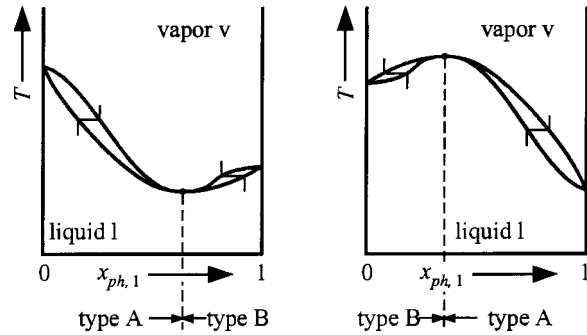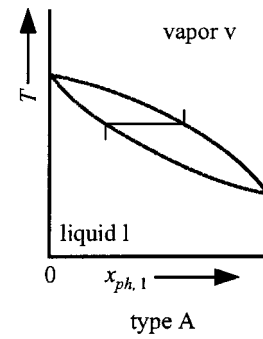
Fig. 8 Liquid vapor phase equilibrium diagrams of zeotropic and azeotropic mixtures. Classified with regard to the sign of the difference between liquid and vapor mole fraction at equilibrium.

an improvement of heat transfer towards the micro region. The gradient of surface tension results in a shear stress that influences liquid flow as stated in the preceding chapter.

3.4 Change of the Saturation Temperature. The influence of an increase of the saturation temperature (Fig. 4) on heat transfer in the micro region is determined by parameter studies. In these computations all mixture effects are switched off except for the variation of the saturation temperature with the concentration, i.e., no Marangoni convection is considered and the thermophysical properties are set constant corresponding to the values at bulk concentration $x_{l,\text{bulk}}$ in the macro region. The heat flow in the micro region $\dot{Q}_{\text{mic}}$ that is calculated with these assumptions then is compared to the heat flow in the micro region $\dot{Q}_{\text{mic}}$ ($x_l=$const.) without considering any mixture effects at all, i.e., concentration x_l is set constant. Figure 9 shows that the ratio of these heat flows is about 0.7 for the mixture at different bulk compositions (rectangles in Fig. 9), i.e., the increase of the saturation temperature towards the bubble center leads to a decrease of heat transfer in the micro region of about 30%. To compare this effect to the other two mixture effects, i.e., change of properties and Marangoni convection, the heat flow in the micro region is computed assuming that the change of concentration leads to Marangoni convection only (rhombi in Fig. 9) or a variation of thermophysical properties only (triangles in Fig. 9), respectively. But these two mixture effects alter heat transfer in the micro region very slightly as confirmed by a computation taking into account all mixture effects (circles in Fig. 9). We conclude that the variation of the saturation temperature with composition change in the micro region is quite important while the variation of properties and the Marangoni convection are almost negligible in the micro region.

Figure 10 shows the liquid film thickness and the heat flux in the micro region for the mentioned cases as well as for the "pure" case, i.e., the concentration x_l is set constant and no mixture effects at all are taken into account. Again, the figure indicates that the property change and the Marangoni convection are not decisive for the mixture behavior, but the change of saturation tem-

Fig. 9 Ratio of heat flow $\dot{Q}_{\text{mic}}$ considering selected effects and heat flow $\dot{Q}_{\text{mic}}(x_l = \text{const.})$ assuming constant liquid composition in the micro region of the binary mixture propane/n-butane ($p^* = 0.2$, $\dot{q}_m = 2 \times 10^4$ W/m², $r = d_A/4$)
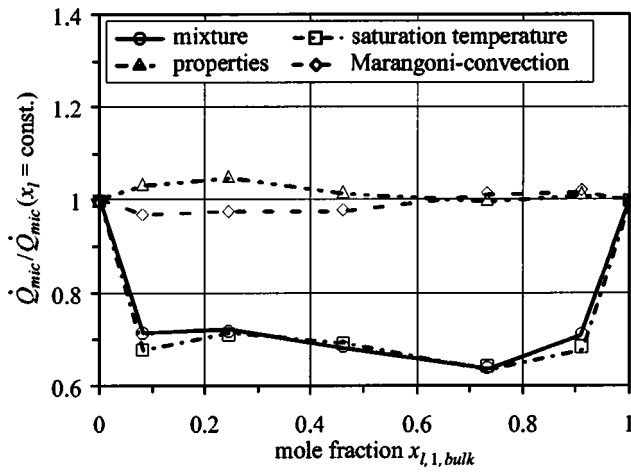
perature is important. The change of saturation temperature with composition leads to the following variations of liquid film thickness and heat flux in the micro region compared to the ''pure'' computations: the maximum heat flux is reduced and the apparent contact angle becomes lower.

Comparing calculated bubble growth cycles with and without mixture effects in the micro region shows a slower bubble growth when mixture effects are considered (Fig. 11). This can be explained by the lower heat transfer to vapor bubble due to mixture effects (see Fig. 9 and Fig. 10).

4 Identification of Decisive Mixture Effects for the Mean Heat Transfer Coefficient

The microscale mixture effects in the micro region are not the only reason for the characteristic reduction of the heat transfer coefficient for intermediate compositions (Fig. 2). Furthermore, bubble site density and departure diameter vary with the mixture composition influencing overall heat transfer performance. These two effects as well as the mentioned microscale mixture effects seem to explain the reduced heat transfer as the following parameter studies demonstrate. In these studies 4 different cases were investigated. The cases are (symbols in brackets are also used in the following figures):
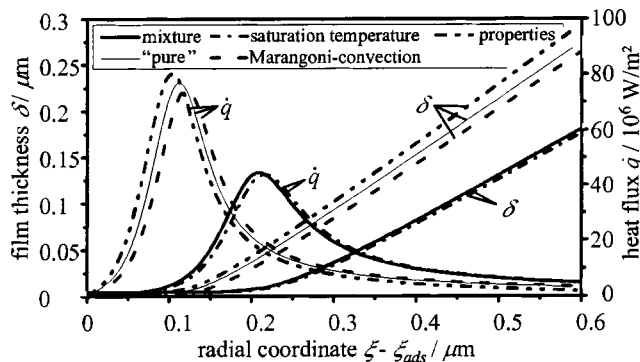
Fig. 10 Liquid film thickness and heat flux in the micro region of the binary mixture propane/n-butane considering selected effects ($y_{l,1,\text{bulk}} = 0.198$, $p^* = 0.2$, $T_{\text{out}} - T_{\text{sat}} = 7.87$ K, $r = 0.043$ mm)
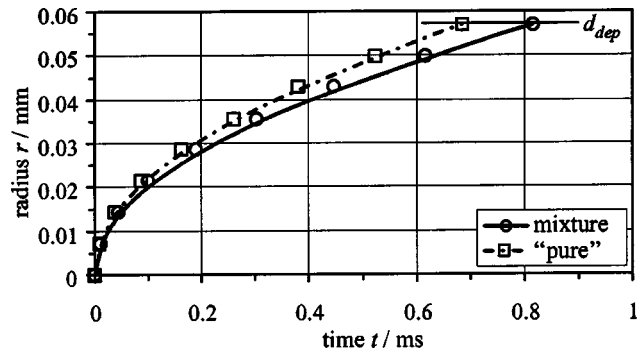
Fig. 11 Calculated bubble radii versus time of the binary mixture propane/n-butane ($y_{l,1,\text{bulk}} = 0.667$, $p^* = 0.2$, $T_{\text{out}} - T_{\text{sat}} = 7.87$ K)

1. *mixture* (○): comprehensive calculation considering all mixture effects.
2. *''pure''* (□): concentration in the micro region is kept constant corresponding to the bulk mole fraction, i.e., all mixture effects in the micro region are neglected.
3. *ideal bubble site density* (△): based on case 2 (''pure''), but using the ideal bubble site density (i.e., the molar average of the bubble site densities of the two pure components of the mixture) as input data for the model instead of the measured data at the bulk mole fraction.
4. *ideal departure diameter* (◇): based on case 3 (ideal bubble site density), but using the ideal departure diameter (i.e., the molar average of the departure diameters of the two pure components of the mixture) as input data for the model instead of the measured data at the bulk mole fraction.

4.1 Results for Ethane/Propane at Low Heat Flux. In Fig. 12 computed heat transfer coefficients for ethane/propane are plotted versus the liquid mole fraction of the bulk. The circles represent calculations with all mixture effects considered (case 1). If the microscopic concentration gradients and the related effects are neglected, heat transfer coefficients are only slightly higher (case 2, □ in Fig. 12). As is well known from experiments, bubble
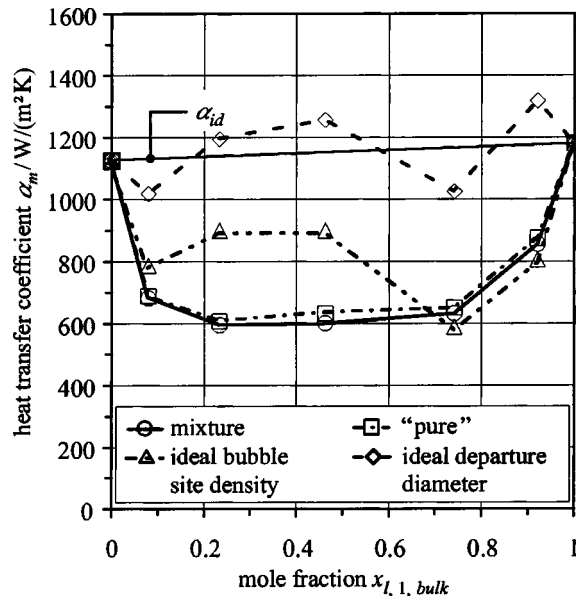
Fig. 12 Variation of decisive mixture effects. Calculated heat transfer coefficients of the binary mixture ethane/propane for different compositions ($p^* = 0.1$, $\dot{q}_m = 4 \times 10^3$ W/m²)

Fig. 13 Bubble site density and departure diameter of the binary mixture ethane/propane for different compositions ($p^* = 0.1$, $\dot{q}_m = 4 \times 10^3$ W/m^2)

Fig. 14 Variation of decisive mixture effects. Calculated heat transfer coefficients of the binary mixture propane/n-butane for different compositions ($p^* = 0.2$, $\dot{q}_m = 2 \times 10^4$ W/m^2).

site density and departure diameter of the mixture, that are still input values to the computation, clearly differ from the corresponding values of the two pure components of the mixture (Fig. 13). Introducing an ideal bubble site density and considering it as input parameter to the model, the calculated heat transfer coefficients are higher (case 3, $\triangle$ in Fig. 12) compared to case 2. Considering additionally the ideal departure diameter (Fig. 13) as input parameter, the resulting heat transfer coefficients are in the range of the ideal heat transfer coefficient (case 4, $\diamond$ in Fig. 12).

The study indicates that at least in this example the influence of microscale mixture effects is very small, while the influences of bubble site density and departure diameter are large. Microscale effects are obviously small because the mean heat flux at the outer surface of the heater wall is very low in this example. Only a few sites are active and most of the heat passes through the macro region. Therefore, the micro region has an inferior influence. In the next example a higher heat flux and hence a higher bubble site density are chosen.

4.2 Results for Propane/n-butane at High Heat Flux. Figures 14 and 15 contain calculated heat transfer coefficients, bubble site densities, and departure diameters of the binary mixture propane/n-butane at different bulk mole fractions. The same parameter studies are carried out as in the previous example. The heat transfer coefficients calculated using the ideal departure diameter (case 4, $\diamond$ in Fig. 14) are again in the range of the ideal heat transfer coefficient. Compared to the previous example, the influence of microscopic concentration gradients becomes higher (case 2, $\square$). This difference can be explained by the following
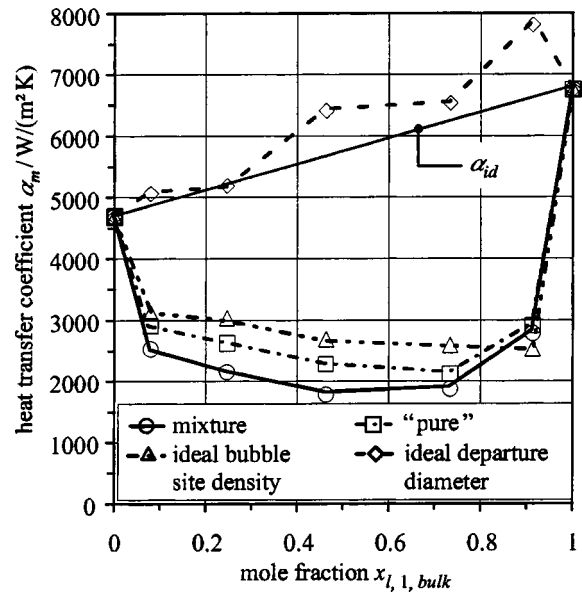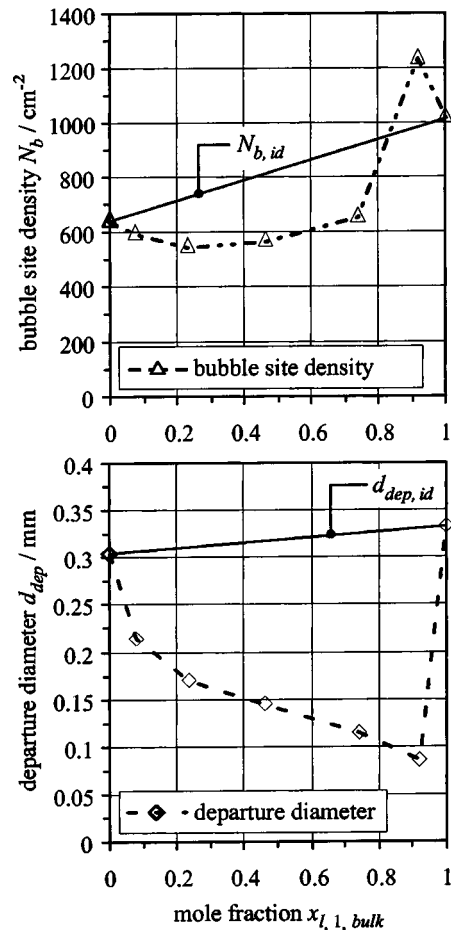
Fig. 15 Bubble site density and departure diameter of the binary mixture propane/n-butane for different compositions ($p^* = 0.2$, $\dot{q}_m = 2 \times 10^4$ W/m^2)

results: due to the higher heat flux and thus bubble site density in the second example, the proportion of the heat that passes through the micro region is far higher. In the micro region the heat transfer is reduced by mixture effects, mainly the increase of saturation temperature. Therefore, microscopic concentration gradients cause a stronger decrease of the overall heat transfer coefficient compared to the first example where heat flux and bubble site density are lower.

5 Summary and Conclusions

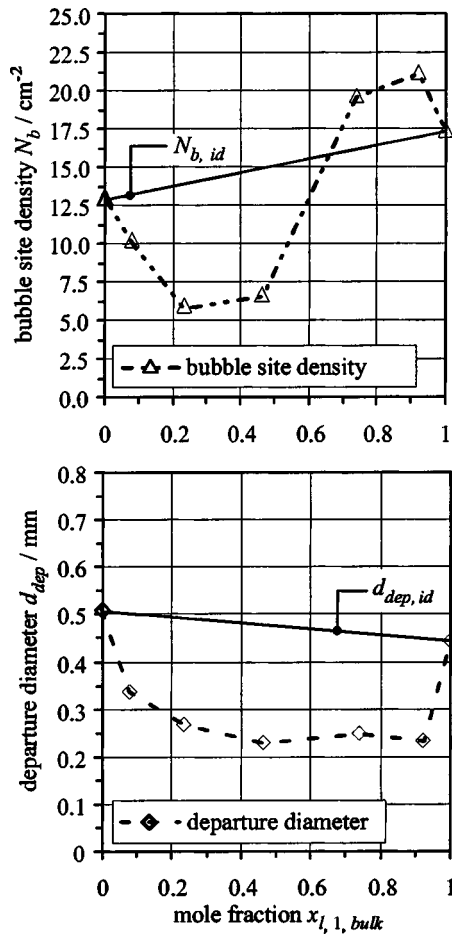The present study is based on a theoretical model to compute nucleate boiling heat transfer of binary mixtures. The model that was presented in an earlier publication [3] is briefly summarized. To identify decisive mixture effects in nucleate boiling of binary mixtures, several parameter studies are carried out. The results indicate that diffusive mass transfer and Marangoni convection have an almost insignificant influence on heat and mass transfer in the nucleate boiling process. In the micro region strong concentration gradients occur due to the preferential evaporation of one component of the mixture. The linked variation of thermophysical properties has only little impact on mass, momentum, and heat transfer, but the increase of the saturation temperature in the direction of the transverse liquid flow into the micro region can have a strong impact. In particular heat transfer in the micro region is reduced due to this rise in saturation temperature compared to a fictive pure substances at the same boiling conditions and thermophysical properties. This observation is very important because up to 30% of the total heat supplied at the evaporator wall passes through the micro region.

Apart from a microscopic increase of saturation temperature, the strong variations of bubble site density and departure diameter with the bulk concentration influence the overall heat transfer coefficient. In particular departure diameters at intermediate compositions are far smaller than the data of the pure components of the mixture, and hence this effect most reduces the heat transfer coefficient compared to the ideal heat transfer coefficient. The quantitative influence of the three decisive mixture effects, i.e., increase of saturation temperature induced by microscopic concentration gradients, variation of bubble site density with the bulk concentration, and variation of departure diameter with the bulk concentration strongly depends on the boiling conditions. The presented study indicates that future correlations and models should first of all describe these decisive mixture effects.

Acknowledgments

Nomenclature

$d_{\rm dep}$ = departure diameter (m)
Δh_{lv} = latent heat of evaporation (J/kg)
$\dot{J}$ = diffusive mass flow (kg/s)
$\dot{M}$ = mass flow (kg/s)
$\dot{M}_\xi$ = integrated mass flux (kg/(ms))
N_b = bubble site density (1/m^2)
p = pressure (N/m^2)
$p*$ = reduced pressure (p/p_c)
p_c = critical pressure (N/m^2)
$\dot{Q}$ = heat flow (W)

$\dot{q}$ = heat flux (W/m^2)
r = radius (m)
T = temperature (K)
t = time (s)
x = mole fraction (-)
y = mass fraction (-)

Greek Symbols

α = heat transfer coefficient (W/(m^{2}K))
α_{id} = ideal heat transfer coefficient (W/(m^{2}K))
δ = film thickness (m)
δ_{th} = thermal boundary layer thickness (m)
δ_w = wall thickness (m)
η = coordinate normal to the wall (m)
$\varphi_{\rm app}$ = apparent contact angle (°)
λ = thermal conductivity (W/(mK))
ν = kinematic viscosity (m^2/s)
ξ = coordinate parallel to the wall (m)
ρ = density (kg/m^3)
σ = surface tension (N/m)

Subscripts

ads = adsorbed film
bulk = bulk
id = ideal value (molar average of the values of the two pure components of the mixture)
l = liquid
m = mean value (time- and area-averaged)
mic = micro region
out = outer surface of the wall
ph = phase interface
sat = saturation
ν = vapor
1 = more volatile component

References

[1] Dhir, V. K., 2001, "Numerical Simulations of Pool-Boiling Heat Transfer," AIChE J., **47**(4), pp. 813–834.

[2] Stephan, P., and Hammer, J., 1994, "A New Model for Nucleate Boiling Heat Transfer," Heat Mass Transfer, **30**, pp. 119–125.

[3] Kern, J., and Stephan, P., 2003, "Theoretical Model for Nucleate Boiling Heat and Mass Transfer of Binary Mixtures," ASME J. Heat Transfer, **125**(6), pp. 1106–1115.

[4] Kern, J., 2002, "Modellierung und numerische Berechnung des Wärmeübergangs beim Blasensieden binärer Gemische," Ph.D. thesis, Fortschritt-Berichte VDI, **3**(727), VDI-Verlag, Düsseldorf.

[5] Fritz, W., 1935, "Berechnung des Maximalvolumens von Dampfblasen," Phys. Z., **11**, pp. 379–384.

[6] Benjamin, R. J., and Balakrishnan, A. R., 1997, "Nucleation Site Density in Pool Boiling of Binary Mixtures: Effect of Surface Micro-roughness and Surface and Liquid Physical Properties," Can. J. Chem. Eng., **75**, pp. 1080–1089.

[7] Bednar, W., and Bier, K., 1994, "Wärmeübergang beim Blasensieden von binären Kohlenwasserstoffgemischen," Ph.D. thesis, Fortschritt-Berichte VDI, **3**(357), VDI-Verlag, Düsseldorf.

[8] Fujita, Y., and Tsutsui, M., 1994, "Heat Transfer in Nucleate Pool Boiling of Binary Mixtures," Int. J. Heat Mass Transfer, **37**(1), pp. 291–304.

[9] Schlünder, E. U., 1986, "Heat Transfer in Nucleate Boiling of Mixtures," *Proceedings of 8th International Heat Transfer Conference*, C. L. Tien, V. P. Carey, and J. K. Ferrell, eds., Hemisphere, Washington, **4**(4), pp. 2073–2079.

[10] Stephan, K., and Körner, M., 1969, "Berechnung des Wärmeübergangs verdampfender binärer Flüssigkeitsgemische," Chem.-Ing.-Tech., **41**(7), pp. 409–416.

[11] Ammermann, C. N., You, S. M., and Hong, Y. S., 1996, "Identification of Pool Boiling Heat Transfer Mechanisms from a Wire Immersed in Saturated FC-72 Using a Single-Photo/LDA Method," ASME J. Heat Transfer , **118**, pp. 117–123.

An Improved Quasi-Steady Analysis for Solving Freezing Problems in a Plate, a Cylinder and a Sphere

Sui Lin

Department of Mechanical and Industrial
Engineering,
Concordia University,
1455 de Maisonneuve Blvd. W.,
Montreal, Quebec, Canada H3G 1M8

Zheng Jiang

Flomerics Inc.,
257 Turnpike Road,
Southborough, MA 01772, USA

Freezing processes taking place in a plate, a cylinder and a sphere are investigated by using the improved quasi-steady analysis model developed in the present study. In the improved quasi-steady analysis, an additional term is added to the temperature profile to simulate the transient effect on the temperature distribution in the solid phase. This additional term is based on the ratio of the heat flux at the phase boundary to that at the cooling surface, and physically, presents the thermal capacity effect in the frozen region. The maximum relative error of the moving phase front location obtained from the improved quasi-steady analysis is about 3% in comparison with that obtained from the exact solution of the freezing process in a plate. Since there is no exact solution available for the freezing process taking place in a cylinder or a sphere, the results obtained from the improved quasi-steady analysis are compared with results from references. The maximum relative errors of the improved quasi-steady analysis for the cylindrical and spherical cases are less than 4% while the maximum relative errors of the quasi-steady approximation are higher than 42%. It is evident that the improved quasi-steady analysis developed in the present study maintains the simplicity of the quasi-steady approximation while greatly increasing its accuracy. [DOI: 10.1115/1.1622719]

Keywords: Analytical, Cylinder, Heat Transfer, Plate, Solidification, Sphere

Introduction

The characteristics of freezing problems involve the coupling of the temperature distribution with the change rate of the moving boundary between the solid and liquid phases. As both the temperature and location of the phase boundary are unknown functions, the problem is nonlinear. Exact solutions of the non-linear problem are available only for a few specific cases (see, for example, Carslaw and Jaeger [1], and Lunardini [2]). For most cases, approximations are needed in obtaining analytical solutions.

The quasi-steady approximation does not consider the transient term in the differential equation; therefore the solution is extremely simple. However the validity of the solution is limited. The heat loss required to cool the solid phase to the temperature below the solidification temperature is neglected since it is considered to be small in comparison with the latent heat of solidification. London and Seban [3] solved the rate of freezing and thickness of ice formation by using the thermal resistance and capacity formulation in two idealized systems. The first of which neglected the ice capacity, while the second system had the capacity effect lumped at the center of the ice slab. It was concluded that the capacity effect was small, and this conclusion obtained whether or not it was lumped at the center of the ice resistance, or distributed throughout, as in the actual system. This argument suggested that the behavior of the first idealized system adequately approached the behavior of the actual system. Recent development of solving the freezing or melting problems is to use time-dependent boundary conditions at the cooling surface. For example, the coupled integral equation approach was used by Mennig and Ozisik [4], and the perturbation method was used by Caldwell and Kwan [5].

In this study an improved quasi-steady analysis is developed. In the improved quasi-steady analysis, an additional term is introduced to simulate the transient effect on the temperature profile in the solid phase. Physically, this term serves as a correction term for neglecting heat loss required to cool the solid phase to the temperature below the solidification point in the quasi-steady approximation. This additional term is determined based on an imposed condition that is the ratio of the heat flux at the phase boundary to that at the cooling surface. The heat flux at the cooling surface includes two parts, the heat flux at the moving phase boundary and the heat loss required to cool the solid phase to the temperature below the solidification temperature. As a result, the ratio of the heat flux at the phase boundary to that at the cooling surface has to be smaller than unity, which indicates the thermal capacity effect of the solid. Therefore, this ratio is appropriate for being the imposed condition in simulating the transient effect on the temperature profile in the frozen region. With this additional term, the improved quasi-steady analysis provides a significantly higher accuracy than the quasi-steady approximation and the method presented in [3].

Mathematical Formulation

Consider a one-dimensional freezing process taking place in a plate form of a thickness D, a cylindrical or a spherical form of radius r_0 as shown in Fig. 1. The freezing liquid in the plate, the cylinder or the sphere, is assumed initially at the solidification temperature T_s. From a definite time, $t=0$, the temperature of the surface at $x=0$ for the plate case, and at $r=r_0$ for the cylindrical and spherical cases, is suddenly dropped to a lower temperature, T_0, and this temperature is kept constant during the whole freezing process. The liquid starts to solidify with the solidification front moving in the x or r-direction. At the moving interface, the phase boundary between the solid and liquid phases, the temperature is equal to the solidification temperature, T_s. The latent heat of solidification released at the interface during the solidification
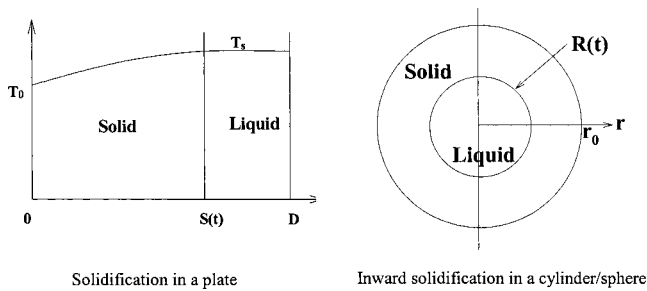
Fig. 1 Schematic diagram of freezing process in plate and cylinder/sphere coordinates

must be transferred by conduction through the solid phase. Assuming that all material properties are uniform and constant, the system of the equations formulating the problem of the freezing process in a plate, a cylinder or a sphere is described in the following sections.

Freezing Process for the Plate Case

The governing equation is

$$\frac{\partial T}{\partial t} = \alpha \frac{\partial^2 T}{\partial x^2} \quad 0 < x < s(t) \tag{1}$$

with boundary conditions

$$T = T_0 \quad \text{at} \quad x = 0 \tag{2}$$

$$T = T_s \quad \text{at} \quad x = s(t) \tag{3}$$

The energy balance equation at the solidification front can be expressed as

$$k \frac{\partial T}{\partial x} = \rho L \left(\frac{ds(t)}{dt} \right) \quad \text{at} \quad x = s(t) \tag{4}$$

where α is the thermal diffusivity, k the thermal conductivity, ρ the density, $s(t)$ the location of the phase boundary, and L the latent heat of the solidification. Since there is no solidification at the initial moment, the initial condition for the location of the phase boundary can be written as

$$s(t) = 0 \quad \text{at} \quad t = 0 \tag{5}$$

The exact solution of above system of equations is the known Neumann's solution [1,2] that can be expressed as

$$T = T_0 + (T_s - T_0) \frac{\text{erf}\left(\dfrac{x}{\sqrt{4at}} \right)}{\text{erf}(p)} \tag{6}$$

where erf( ) is the error function, and p is a constant defined by

$$s(t) = p \sqrt{4\alpha t} \tag{7}$$

The value of p is determined by Eq. (4) as follows:

$$\sqrt{\pi} p \exp(p^2) \text{erf}(p) = \frac{c}{L} (T_s - T_0) \tag{8}$$

where c is the specific heat of the material in the solid phase. This exact transient solution is to be used for comparison with the solutions obtained by the quasi-steady approximation and the improved quasi-steady analysis.

For the quasi-steady approximation and the improved quasi-steady analysis, Eq. (1), by neglecting the transient term on the left-hand side, becomes

$$\frac{\partial^2 T}{\partial x^2} = 0 \tag{1a}$$

while the boundary and initial conditions stated in Eqs. (2–5) remain the same. The solutions under the two conditions are analyzed below.

The Quasi-Steady Approximation. Solving Eq. (1a) with the boundary conditions, Eqs. (2) and (3) gives the temperature distribution of the quasi-steady approximation

$$T_{st} = T_0 + (T_s - T_0) \frac{x}{s(t)} \tag{9}$$

Substituting Eq. (9) into Eq. (4) and then integrating Eq. (4) yields the location of the phase front

$$s_{st}(t) = p_{st} \sqrt{4\alpha t} \tag{10}$$

with

$$2 p_{st}^2 = \frac{c}{L} (T_s - T_0) \tag{11}$$

The Improved Quasi-Steady Analysis. The temperature distribution of the improved quasi-steady analysis is obtained from the same system of Eqs. (1a), (2), and (3). However an additional term is added to the temperature profile to simulate the transient effect on the temperature distribution in solid. This additional term is determined based on an imposed condition which is the ratio of the heat flux at the phase boundary, $x = s(t)$, to that at the surface, $x = 0$. Physically, this term serves as a correction term for neglecting heat loss required to cool the solid phase to the temperature below the solidification point in the quasi-steady approximation. In the present study, the heat flux ratio is taken from the Neumann's solution as follows:

$$\frac{\left(\dfrac{\partial T}{\partial x} \right)_{x=s(t)}}{\left(\dfrac{\partial T}{\partial x} \right)_{x=0}} = e^{-p^2} \tag{12}$$

Assume that the temperature profile for the improved quasi-steady analysis can be expressed as

$$T = a_0(t) + a_1(t)x + a_2(t)x^2 \tag{13}$$

In order to satisfy the boundary conditions, Eqs. (2) and (3), and the imposed condition, Eq. (12), Eq. (13) becomes

$$T_m = T_0 + (T_s - T_0) \frac{\dfrac{x}{s(t)}}{[1 + \exp(-p^2)]} \left[2 - (1 - \exp(-p^2)) \frac{x}{s(t)} \right] \tag{14}$$

Substituting Eq. (14) into Eq. (4), and then integrating Eq. (4) with the initial condition, Eq. (5), one obtains the location of the solidification boundary as follows:

$$s_m(t) = p_m \sqrt{4\alpha t} \tag{15}$$

with

$$p_m^2 [1 + \exp(p_m^2)] = \frac{c}{L} (T_s - T_0) \tag{16}$$

Figure 2 compares the temperature distributions obtained from the exact solution, the quasi-steady approximation and the improved quasi-steady analysis with $T_s / T_0 = 1.5$ and $p = 1.0$. The maximum relative errors of the improved quasi-steady analysis and the quasisteady approximation are about 0.5 and 4.5 percent, respectively.

In comparison with the exact solution of the location of the phase boundary, Eqs. (7) and (8), the solutions obtained from the quasi-steady approximation, Eqs. (10) and (11), and these from the improved quasi-steady analysis, Eqs. (15) and (16), involve the relative errors, ε_{st} and ε_m, respectively, as follows:
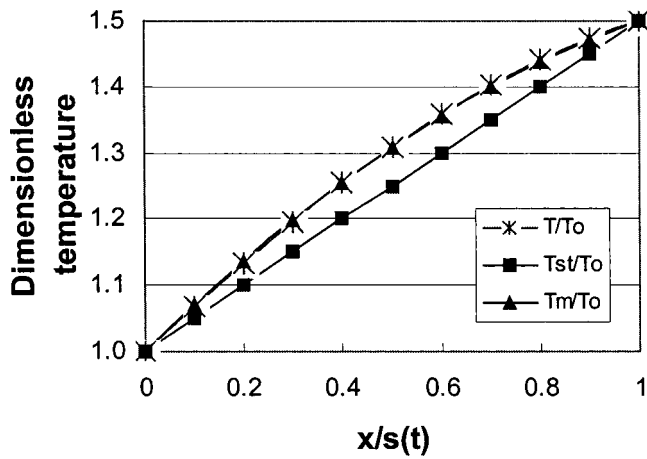
Fig. 2 Dimensionless temperature distributions, T/T_0 (exact solution), T_{st}/T_0 (quasi-steady approximation) and T_m/T_0 (improved quasi-steady analysis) with $T_s/T_0=1.5$ and $p=1.0$

$$\varepsilon_{st}=\frac{p-p_{st}}{p} \qquad (17)$$

and

$$\varepsilon_m=\frac{p-p_m}{p} \qquad (18)$$

Figure 3 shows the proportionality constants, p, p_{st}, and p_m as functions of $c/L(T_s-T_0)$. Figure 4 indicates the relative errors, ε_{st} and ε_m, as functions of $c/L(T_s-T_0)$. From Figs. 3 and 4, it can be concluded that the improved quasi-steady analysis gives a significant improvement to the results obtained from the quasi-steady approximation. The maximum relative error of the results obtained from the improved quasi-steady analysis is about 3 percent, while the maximum relative error of the result obtained from the quasi-steady approximation, at $c/L(T_s-T_0)=1.9$, is about 20 percent. It is noted that the relative errors of the temperature distributions are much smaller than those of the location of the phase boundaries, presented in Fig. 4.
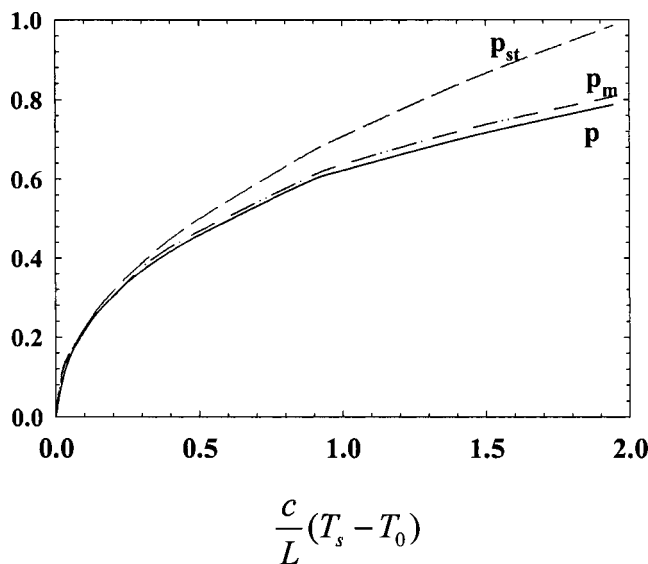
Fig. 3 Proportionality constants, p (exact solution), p_{st} (quasi-steady solution) and p_m (improved quasi-steady analysis) as functions of $c/L(T_s-T_0)$ for freezing process in a plate
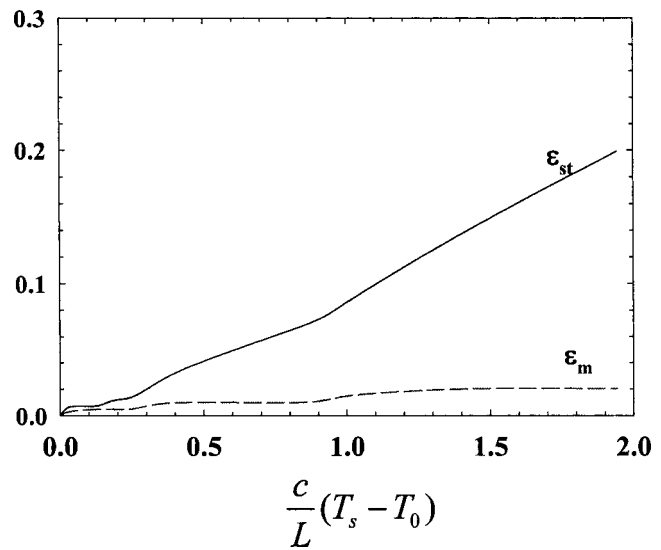
Fig. 4 Relative errors, ε_{st} (quasi-steady solution) and ε_m (improved quasi-steady analysis) as a functions of $c/L(T_s-T_0)$ for freezing process in a plate

It is worth noting that, with $\exp(-p^2)=1$ in Eq. (14), the results obtained from the improved quasi-steady analysis are identical to those obtained from the quasi-steady approximation. Therefore, in the following, we only consider the improved quasi-steady analysis in the cylindrical and spherical cases.

Freezing Processes for the Cylindrical and Spherical Cases

The system of equations formulating the freezing processes taking place in the cylindrical and spherical coordinates is as follows:

$$\frac{1}{\alpha}\frac{\partial T}{\partial t}=\frac{1}{r^n}\frac{\partial}{\partial r}\left(r^n\frac{\partial T}{\partial r}\right) \qquad R(t)<r<r_0 \qquad (19)$$

with $n=1$ for the cylindrical, and $n=2$ for the spherical problem. The boundary conditions are specified as

$$T=T_0 \quad \text{at} \quad r=r_0 \qquad (20)$$

$$T=T_s \quad \text{at} \quad r=R(t) \qquad (21)$$

The energy balance at the solidification front can be written as

$$k\frac{\partial T}{\partial r}=\rho L\left(\frac{dR(t)}{dt}\right) \qquad r=R(t) \qquad (22)$$

The initial condition of Eq. (22) is

$$R(t)=\mathrm{r}_0 \quad \text{at} \quad t=0 \qquad (23)$$

For the improved quasi-steady analysis, Eq. (19), by neglecting the transient term on left-hand side, becomes

$$\frac{\partial}{\partial r}\left(r^n\frac{\partial T}{\partial r}\right)=0 \qquad R(t)<r<r_0 \qquad (24)$$

The temperature distributions in the improved quasi-steady analysis for the cylindrical and spherical cases can be obtained, when the imposed condition, Eq. (12), for the plate case, is assumed also valid for the cylindrical and spherical cases.

For the cylindrical case, $n=1$,

$$\frac{T-T_0}{T_s-T_0}=\frac{1}{[1+\exp(-p^2)]}\frac{\ln\left(\frac{r}{r_0}\right)}{\ln\left(\frac{R}{r_0}\right)}$$

$$\times\left[2-(1-\exp(-p^2))\frac{\ln\left(\frac{r}{r_0}\right)}{\ln\left(\frac{R}{r_0}\right)}\right] \quad (25)$$

For the spherical case, $n=2$,

$$\frac{T-T_0}{T_s-T_0}=\frac{1}{[1+\exp(-p^2)]}\left[2\frac{R}{r}\left(\frac{r-r_0}{R-r_0}\right)\right.$$

$$\left.-(1-\exp(-p^2))\left(\frac{R}{r}\right)^2\left(\frac{r-r_0}{R-r_0}\right)^2\right] \quad (26)$$

Substituting Eqs. (25) and (26) into Eq. (22), and integrating Eq. (22) with the initial condition, Eq. (23), yields the locations of the solidification front for the cylindrical and spherical cases, for the cylindrical case, $n=1$,

$$\left(\frac{R}{r_0}\right)^2\ln\left(\frac{R}{r_0}\right)-\frac{1}{2}\left[\left(\frac{R}{r_0}\right)^2-1\right]=\frac{4}{1+e^{p^2}}S_T\tau \quad (27)$$

for the spherical case, $n=2$,

$$\frac{1}{3}\left(\frac{R}{r_0}\right)^3-\frac{1}{2}\left(\frac{R}{r_0}\right)^2+\frac{1}{6}=\frac{2}{1+e^{p^2}}S_T\tau \quad (28)$$

where S_T is the Stefan number and τ is the dimensionless time defined, respectively, by

$$S_T=\frac{c(T_s-T_0)}{L} \quad (29)$$

and

$$\tau=\frac{\alpha t}{r_0^2} \quad (30)$$

The time, τ_f, required for the complete solidification of the cylinder and the sphere, with $R=0$, is, for $n=1$

$$\tau_f=\frac{1+e^{p^2}}{8S_T} \quad (31)$$

for $n=2$,

$$\tau_f=\frac{1+e^{p^2}}{12S_T} \quad (32)$$

In order to compare the above results with the results obtained from the quasi-steady approximation, we set $\exp(p^2)=1$ in Eqs. (27), (28), (31), and (32) as follows:
  For $n=1$,

$$\left(\frac{R}{r_0}\right)^2\ln\left(\frac{R}{r_0}\right)-\frac{1}{2}\left[\left(\frac{R}{r_0}\right)^2-1\right]=2S_T\tau_{st} \quad (33)$$

$$(\tau_f)_{st}=\frac{1}{4S_T} \quad (34)$$

For $n=2$,

$$\frac{1}{3}\left(\frac{R}{r_0}\right)^3-\frac{1}{2}\left(\frac{R}{r_0}\right)^2+\frac{1}{6}=S_T\tau_{st} \quad (35)$$

$$(\tau_f)_{st}=\frac{1}{6S_T} \quad (36)$$

Evaluation of the Values of p for the Cylindrical and Spherical Cases

In deriving the temperature distributions of the improved quasi-steady analysis for the cylindrical and spherical cases presented in Eqs. (25) and (26), it is assumed that the imposed condition for the plate case, Eq. (12), is also valid for the cylindrical and spherical cases. However, the value of p for the plate is certainly different from that for the cylinder or sphere. In order to evaluate the values of p for the cylinder and sphere, the freezing processes taking place in the cylinder and sphere need to be transformed to the freezing processes in the plate.

We consider that the cylinder and sphere have the radius r_0, the surface area A_n, and the volume V_n, where the subscript $n=1$ refers the cylinder and $n=2$ refers to the sphere. The plate being transformed to has its thickness D that is equal to the radius r_0, surface A_p that is equal to the surface area A_n, and volume V_p that is equal to $A_p^*r_0$. The locations of entire solidification of the cylinder and sphere are taken as

$$r_0=p_n\sqrt{4\alpha t_f} \quad (37)$$

where p_n, corresponding to p in Eq. (7), is a constant for cylinder and sphere. The complete solidification time required, t_f, is assumed to be unchanged when transforming the volume of the cylinder of sphere, V_n, into the same volume of the plate. It is also assumed that the time required for the complete solidification of the plate volume, V_p, is equal to $(V_p/V_n)^*t_f$. The location r_0, in Eq. (37), is compared to the solidification location of the plate in the following two cases.

Case A. The solidification volume of the plate is equal to the volume of the cylinder or the sphere. Hence the solidification location of the plate is equal to $V_n/A_p=(V_n/V_p)^*r_0$, which can be expressed as $s(t)$ in Eq. (7). Replacing $s(t)$ in Eq. (7) by $(V_n/V_p)^*r_0$ yields

$$\frac{V_n}{V_p}r_0=p\sqrt{4\alpha t_f} \quad (38)$$

Case B. The solidification volume of the entire plate, V_p, corresponds to the solidification distance r_0. The time required for this solidification process is $(V_p/V_n)^*t_f$. Replacing t in Eq. (7) by $(V_p/V_n)^*t_f$, gives

$$r_0=p\sqrt{4\alpha\frac{V_p}{V_n}t_f} \quad (39)$$

Comparing Eq. (37) with Eqs. (38) and (39) gives p_n in Cases A and B, p_{nA} and p_{nB}, respectively, as

$$p_{nA}=\frac{V_p}{V_n}p \quad (40)$$

and

$$p_{nB}=\sqrt{\frac{V_p}{V_n}}p \quad (41)$$

The values of p_n required for the cylindrical and spherical cases are evaluated as the mean values of p_{nA} and p_{nB} in Eqs. (40) and (41), per unit dimension, as follows:

$$p_n=\frac{\left(\frac{V_p}{V_n}+\sqrt{\frac{V_p}{V_n}}\right)p}{n+1} \quad (42)$$

For the cylindrical case, $n=1$,

$$p_1=(2+\sqrt{2})\frac{p}{2}=1.707p \quad (43)$$

For the spherical case, $n=2$,

Table 1 Complete solidification of a circular cylinder

S_T			$\tau_f = a \cdot t_f / r_0^2$			
	Quasi-Steady	Riley (1974)	Poots (1962)	Beckett (1971)[b]	Allen & Severn (1962)[b]	Improved Quasi-steady
0.05	5.00	5.25	3.47	5.30	$\cdots$	5.1857
0.1	2.50	2.75	1.81	2.69	$\cdots$	2.6894
0.2	1.25	1.50	0.97	$\cdots$	$\cdots$	1.4466
0.25	1.00	1.25	0.81	1.19	$\cdots$	1.2004
0.641	0.39	0.64	0.40(0.52)[a]	$\cdots$	0.47	0.6200
1.0	0.25	0.50	0.31	$\cdots$	$\cdots$	0.5082

[a]Two-parameter method
[b]Numerical solution

$$p_2 = (3 + \sqrt{3})\frac{p}{3} = 1.577p \qquad (44)$$

The p value in Eqs. (43) and (44) can be found from Eq. (8) or in Fig. 3.

Verification of the Values of p_1 and p_2 in Eqs. (43) and (44)

Since there is no exact solution available for the freezing process in a cylinder and a sphere, the dimensionless times of the complete solidification in the cylinder and sphere, presented in Eqs. (31) and (32), with p_1 and p_2 replacing p in these equations, respectively, are compared with data in references. Lunardini [2] summarized the research results obtained by Riley et al. [6], Poots [7], Beckett [8], Allen and Severn [9], Tao [10] and Pedroso and Domoto [11]. Tables 1 and 2 show the comparison of the dimensionless time, τ_f, obtained from the improved quasi-steady analysis with the results from these references for the cylindrical and spherical cases, respectively. It should be noted that there exist two typographical errors in Table 8.4 of Ref. [2]: (1) the closure time for constant surface temperature spheres initially at freezing temperatures, τ_f, should be changed to $S_T^* \tau_f$; and (2) the result of 0.2168 obtained from Eq. (8.305) for $S_T = 0.3$ should be changed to 0.20578. These two errors are corrected in Table 2. Lunardini [2] indicated that the data given in Table 1 by Riley et al. [6] that used a perturbation method valid for small values of the Stefan number, and the relation obtained by the authors was probably the best one for determining the complete solidification time in a cylinder. In Table 1, the results obtained from the improved quasi-steady analysis agree very well with those obtained by Riley et al. [6] with the maximum relative error less than 4% and agree also very well with those obtained by Beckett [8] using numerical solutions, with the maximum relative error less than 3%. It was also indicated in Ref. [2] that, among the data for the closure time of spheres presented in Table 2, the superior result was given by Pedroso and Domoto [11] using a perturbation solution, and the relation obtained was accurate for $S_T \leq 1.0$. The results for $S_T \leq 1.0$ obtained from the improved quasi-steady analysis agree very well with those obtained by Pedroso and Domoto [11] with

the maximum relative error less than 4 percent as shown in Table 2. Based on this comparison, it can be concluded that the values of p_1 and p_2 determined from Eqs. (43) and (44) are reliable.

Figure 5 shows the relative errors ε_{st} of the quasi-steady solution and ε_m of the improved quasi-steady analysis, as functions of Stefan number, S_T. Figure 5(a) presents the results obtained from the quasi-steady approximation and the improved quasi-steady analysis in comparison with those obtained by Riley et al. [6] for the cylindrical case. Figure 5(b) shows the results obtained from the quasi-steady approximation and the improved quasi-steady analysis in comparison with those obtained by Pedroso and Domoto [11] for the spherical case. The relative errors ε_{st}, and ε_m are defined as follows:

For $n = 1$, the cylindrical case

$$\varepsilon_{st} = \frac{\tau_{fR} - \tau_{st}}{\tau_{fR}} \qquad (45)$$

and

$$\varepsilon_m = \frac{\tau_{fR} - \tau_m}{\tau_{fR}} \qquad (46)$$

For $n = 2$, the spherical case,

$$\varepsilon_{st} = \frac{\tau_{fP} - \tau_{st}}{\tau_{fP}} \qquad (47)$$

and

$$\varepsilon_m = \frac{\tau_{fP} - \tau_m}{\tau_{fP}} \qquad (48)$$

where τ_{fR} and τ_{fP} denote the dimensionless solidification time obtained by Riley et al. [6] and by Pedroso and Domoto [11], respectively. Figures 5(a) and 5(b) show that the maximum relative errors of the improved quasi-steady analysis for $n = 1$ and 2 are all less than 4%, while the maximum relative error of the quasi-steady approximation at $S_T = 1.0$ is 50% for $n = 1$ and

Table 2 Complete solidification of a sphere

S_T	Tao (1967)	Quasi-Steady	Pedroso (1973)	Riley (1974)	Poots (1962)	Improved Quasi-steady
			$\tau_f = a \cdot t_f / r_0^2$			
0.0					$\cdots$	
0.1	1.920	1.667	1.805	1.791	0.924	1.7733
0.3		0.556	0.686	0.649	0.368	0.6681
0.5	0.474	0.333	0.460	0.406	0.257	0.4519
0.8		0.208	0.333	0.256	0.195	0.3359
1.0	0.284	0.167	0.290	0.200	0.174	0.3001
2.0	0.180	0.083	0.204	0.062	0.132	0.2468

Fig. 5 Relative errors, ε_{st} (quasi-steady solution) and ε_m (improved quasi-steady analysis) as functions of Stefan number, S_T: (a) for cylindrical case: n=1; and (b) for spherical case: n=2.

42% for $n=2$. It is evident that the improved quasi-steady analysis significantly increases the accuracy over the quasi-steady approximation.

Discussion and Conclusions

Equations (7), (10), and (15) show that the locations of the solidification front, $s(t)$, $s_{st}(t)$, and $s_m(t)$, for the freezing processes in a plate are proportional to the dimensionless constants, p, p_{st}, and p_m, respectively. For the quasi-steady approximation, when the thermal capacity in the frozen solid is neglected, the temperature gradient at the solidification front is larger than that of the reality. As a result, the velocity of the moving solidification front is higher than the reality because this velocity is proportional to the temperature gradient at the solidification front as indicated in Eq. (4). Therefore, the value of the constant, p_{st}, determined by the quasi-steady approximation is larger than the p value from the exact solution as shown in Fig. 3. With the additional correction term presented, the improved quasi-steady analysis gives significantly higher accuracy than the quasi-steady approximation, as shown in Figs. 3 and 4, In comparison with the exact solution of the freezing process in a plate, the maximum relative error of the result obtained from the improved quasi-steady analysis is about 3 percent, while the maximum relative error of the result obtained from the quasi-steady approximation, at $S_T=1.9$, is about 20 percent.

In deriving the temperature profiles, Eqs. (25) and (26), for the cylinder and sphere, respectively, in the improved quasi-steady analysis, it is assumed that the imposed condition, Eq. (12), obtained for the plate case, is also valid for the cylindrical and spherical cases. However, the p value for the plate is different from that for the cylinder or the sphere. An evaluation method is developed to give the values of p_1 and p_2 in Eqs. (43) and (44), respectively. With the so-obtained p_1 and p_2, the dimensionless times of the complete solidification in the cylinder and sphere, presented in Eqs. (31) and (32), respectively, are compared with the results from other researchers using different analytical methods as shown in Tables 1 and 2. Figure 5 shows the relative errors, ε_{st} of the quasi-steady solution and ε_m of the improved quasi-steady analysis, as functions of Stefan number, S_T. The maximum relative errors of the improved quasi-steady analysis for $n=1$ and 2 are all less than 4%, while the maximum rel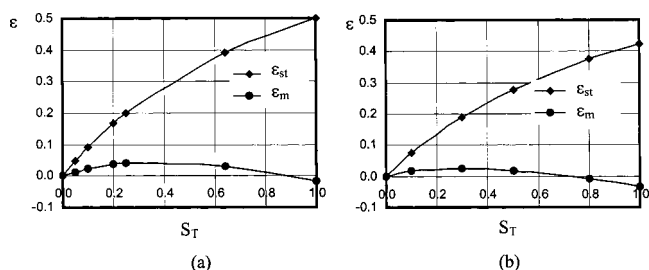ative errors of the quasi-steady approximation for $n=1$ and 2, at $S_T=1.0$ are 50% and 42%, respectively. It is evident that the improved quasi-steady analysis increases significantly the accuracy over the quasi-steady approximation.

From the above discussion, it can be concluded that the improved quasi-steady analysis developed in the present study maintains the simplicity of the quasi-steady approximation while greatly increasing its accuracy.

Acknowledgment

Nomenclature

a_i = i=0, 1, 2, coefficients used in Eq. (13)
A = surface area $[m^2]$
c = specific heat of solid phase material $[J/kg\,K]$
D = thickness of plate $[m]$
erf( ) = error function
exp( ) = exponential function
k = thermal conductivity $[W/Km]$
L = latent heat of solidification $[J/kg]$
n = $n=1$ and 2 referring to cylinder and sphere, respectively
p = dimensionless constant
r = radial direction of cylinder or sphere $[m]$
$R(t)$ = position of solidification front in cylindrical or spherical case $[m]$
$s(t)$ = position of solidification front in plate case $[m]$
S_T = Stefan number defined by Eq. (29)
t = time $[s]$
T = temperature $[K]$
V = volume $[m^3]$
x = space coordinate for plate $[m]$

Greek Symbols

α = thermal diffusivity $[m^2/s]$
ε = relative error
ρ = density of solid phase material $[kg/m^3]$
τ = dimensionless time defined by Eq. (30)

Subscripts

0 = at surface, $x=0$ or $r=r_0$
f = complete solidification of a cylinder or a sphere
m = improved quasi-steady analysis
n = n=1 and 2 referring to cylinder and sphere, respectively
p = plate
P = referring to Pedroso and Domoto [11]
R = referring to Riley et al. [6]
s = at solidification front, x=s(t) or r=R(t)
st = quasi-steady approximation

References

[1] Carslaw, H. S., and Jaeger, J. C., 1959, *Conduction of Heat in Solids*, Oxford University Press, London, Chap. XI.
[2] Lunardini, V. J., 1981, *Heat Transfer in Cold Climates*, Van Nostrand Reinhold Co., New York, Chap. 8.
[3] London, A. L., and Seban, R. A., 1943, "Rate of Ice Formation," Trans. ASME, **65**, pp. 771–778.
[4] Mennig, J., and Ozisik, M. N., 1985, "Coupled Integral Approach for Solving Melting or Solidification," Int. J. Heat Mass Transfer, **28**, pp. 1481–1485.
[5] Caldwell, J., and Kwan, Y. Y., 2003, "On the Perturbation Method for the Stefan Problem With Time-Dependent Boundary Conditions," Int. J. Heat Mass Transfer, **46**, pp. 1497–1501.
[6] Riley, D. S., Smith, F. I., and Poots, G., 1974, "The Inward Solidification of Spheres and Circular Cylinders," Int. J. Heat Mass Transfer, **17**, pp. 1507–1516.
[7] Poots, G., 1962, "On the Application of Integral Methods to the Solution of Problems Involving the Solidification of Liquid Initially at Fusion Temperature," Int. J. Heat Mass Transfer, **5**, pp. 525–531.
[8] Beckett, P. M., 1971, Ph.D. thesis, Hull University, England.
[9] Allen, D. N. de G., and Severn, R. T., 1962, "The Application of the Relaxation Method to the Solution of Non-Elliptic Partial Differential Equations," Q. J. Mech. Appl. Math., **15**, p. 53.
[10] Tao, L. C., 1967, "Generalized Numerical Solutions of Freezing a Saturated Liquid in Cylinders and Spheres," AIChE J., **13**(1), p. 165.
[11] Pedroso, R. I., and Domoto, G. A., 1973, "Perturbation Solutions for Spherical Solidification of Saturated Liquids," ASME J. Heat Transfer, **95**(1), pp. 42–46.

Direct Numerical Simulation of Turbulent Heat Transfer Across a Mobile, Sheared Gas-Liquid Interface

D. Lakehal[†]

M. Fulgosi

G. Yadigaroglu

Institute of Energy Technology,
Swiss Federal Institute of Technology,
ETH-Zentrum/CLT, CH-8092 Zurich,
Switzerland

S. Banerjee

Department of Chemical Engineering,
University of California,
Santa Barbara, CA 93106, USA

The impact of interfacial dynamics on turbulent heat transfer at a deformable, sheared gas-liquid interface is studied using Direct Numerical Simulation (DNS). The flow system comprises a gas and a liquid phase flowing in opposite directions. The governing equations for the two fluids are alternately solved in separate domains and then coupled at the interface by imposing continuity of velocity and stress. The deformations of the interface fall in the range of capillary waves of waveslope $ak=0.01$ (wave amplitude a times wavenumber k), and very small phase speed-to-friction velocity ratio, c/u_*. The influence of low-to-moderate molecular Prandtl numbers (Pr) on the transport in the immediate vicinity of the interface is examined for the gas phase, and results are compared to existing wall-bounded flow data. The shear-based Reynolds number Re_* is 171 and Prandtl numbers of 1, 5, and 10 were studied. The effects induced by changes in Pr in both wall-bounded flow and over a gas-liquid interface were analyzed by comparing the relevant statistical flow properties, including the budgets for the temperature variance and the turbulent heat fluxes. Overall, Pr was found to affect the results in very much the same way as in most of the available wall flow data. The intensity of the averaged normal heat flux at high Prandtl numbers is found to be slightly greater near the interface than at the wall. Similar to what is observed in wall flows, for $Pr=1$ the turbulent viscosity and diffusivity are found to asymptote with z^{+3}, where z^+ is the distance to the interface, and with z^{+n}, where $n>3$ for $Pr=5$ and 10. This implies that the gas phase perceives deformable interfaces as impermeable walls for small amplitude waves with wavelengths much larger than the diffusive sublayers. Moreover, high-frequency fluctuating fields are shown to play a minor role in transferring heat across the interface, with a marked filtering effect of Pr. A new scaling law for the normalized heat transfer coefficient, K^+ has been derived with the help of the DNS data. This law, which could be used in the range of $Pr=1$ to 10 for similar flow conditions, suggests an approximate $Pr^{-3/5}$ relationship, lying between the $Pr^{-1/2}$ dependence for free surfaces and the $Pr^{-2/3}$ law for immobile interfaces and much higher Prandtl numbers. A close inspection of the transfer rates reveals a strong and consistent relationship between K^+, the frequency of sweeps impacting the interface, the interfacial velocity streaks, and the interfacial shear stress. [DOI: 10.1115/1.1621891]

Keywords: Heat Transfer, Turbulence, Two-Phase, Interface

1 Introduction

Most investigations dealing with turbulent heat and mass transfer have traditionally focused on simple configurations involving rigid or flat surfaces. In practice, however, single-phase or two-phase flows may take place in the presence of boundaries which are neither flat nor rigid. In multi-phase flow systems involving immiscible fluids, the interface separating the fluids plays a role similar to that of an impermeable boundary. An example is the exchanges between the atmosphere and the oceans taking place across a continuously deforming interface. On a much smaller scale, gas-liquid exchange mechanisms across deformable interfaces may be encountered in annular flows, falling liquid films, etc.

Environmental studies on CO_2 absorption by the oceans [1,2] have focused on the proper scaling of the averaged mass transfer

coefficient with the Reynolds and Prandtl/Schmidt numbers. The principle consists in relating local mass transfer rates and scalar fluxes to the properties of the fluctuating velocity field. The classical approach uses the analogy between diffusion of momentum and of a scalar quantity (heat or mass), extending Fick's gradient laws up to the turbulent regime, i.e., the scalar turbulent diffusivity, α_t, is made proportional to the turbulent viscosity, ν_t. The surface renewal theory [3] has also been widely employed to parametrize gas-liquid mass transfer rates. Its principle consists in relating the mass transfer rate to the time between sweeps and bursts (τ_{ren}) impinging on the interface, assumed to be responsible for surface renewal, i.e., $K \equiv (\mathcal{D}/\tau_{ren})^{1/2}$, where $\mathcal{D} = \nu/Pr$ refers to molecular diffusivity of heat (or mass by simply replacing Pr with Sc, the Schmidt number).

Heat and mass transfer at interfaces depends on the resistance of diffusive layers with thickness $\delta_L \sim O$ (0.01 mm) on the liquid side and $\delta_G \sim O$ (1 mm) on the gas side. Accordingly the transport across both layers is controlled by fine-scale turbulence, so that the transport mechanisms can be faithfully simulated only by the use of DNS. The complexity of the problems increases if the interface is further sheared and free to deform, in which case an

extra transverse motion superimposed on the mean flow is expected to occur in the direction normal to the interface. The continuously deformable interface could then affect the heat/mass transport indirectly by modifying the turbulence in the vicinity of the interface, or more precisely by increasing the portion of frictional drag transferred into form drag. The importance of such phenomenon is not yet clear, but a higher impact is expected if the surface is populated by capillary waves with wavelengths up to an order of magnitude larger than δ_G. For longer waves, the time scale over which the surface renews its structure becomes too large compared to the turbulence time scale, and the movement of the interface does not affect the transport phenomena. In summary, momentum and heat/mass transfer across deformable, sheared interfaces depends on the nature of the waves, and hence on the interfacial shear inducing them. An important question that arises then is whether the interfacial heat transfer scales with the friction velocity based on frictional drag and kinematic viscosity.

Although confined to simple configurations involving flat and non-deformable interfaces, early DNS studies proved particularly efficient in providing insight into the scalar exchanges all the way down to the diffusive sublayer. The contributions have generally concentrated on two aspects: a first group essentially focused on modeling turbulent convection mechanisms [4–7], while a second dealt with mass transfer [8,9]. Wall flow simulations at similar Reynolds numbers, but for different thermal boundary conditions, produced DNS data for the development and calibration of turbulent scalar convection models. The studies involving heat and mass transfer are the most relevant ones for the present contribution. Campbell and Hanratty [8], who pioneered this class of DNS, were interested in identifying the frequency fluctuations controlling most of the transfer at the wall. McCready et al. [9] re-investigated the problem considering a flat, mobile gas-liquid interface. Lyons et al. [6] simulated the case of differential heating between channel walls. Calmet and Magnaudet [10] showed that similar results can be obtained for Sc=200 by use of LES, supporting the fact that the effect of high-frequency turbulence near the wall is filtered out by increasing Pr or Sc [9]. Na et al. [7] studied the effect of the Prandtl number on turbulent statistics characterizing transport and the spatial variation of the variance of the fluctuating temperature. The very recent contribution of Piller et al. [11] examines the influence of low Prandtl numbers (0.025– 1.0) on turbulent transport in channel flow. Their study has shown the molecular conductivity to act as a filter for high-frequency velocity fluctuations as Pr decreases, rendering them ineffective in the heat exchange processes.

Paralleling these studies, new results have been obtained in this area with the appearance of DNS of turbulent flows over wavy walls and sheared, gas-liquid interfaces [12–14]. Lombardi et al. [12] performed a DNS of coupled gas-liquid flows over a flat interface, which revealed that the interface appears to the gas phase almost like a rigid wall, whereas the liquid perceives the interface like a slip surface. De Angelis et al. [13] studied flows over rigid, sinusoidal wave trains. Their results show that fixed, high-amplitude waves exert significant effects on the mean flow and turbulence characteristics. De Angelis et al. [14] employed the same tools to study turbulent mass transfer at the sheared and deformable gas-liquid interface in the limit of capillary waves. A detailed comparison of the turbulence structure at the two different types of interface has been provided by Fulgosi et al. [15].

The objective of the present study is to complement the aforementioned contributions by exploring the heat transfer processes at a deformable interface, separating counter-flowing gas and liquid. The emphasis is on wave-induced mechanisms influencing the flow and the associated heat transfer in the context of low-to-moderate Pr numbers. The analysis is limited to the gas side, due to the presumed similarity between near-wall and near-interface turbulence. The effect of Prandtl number (Pr=1, 5 and 10) on the thermal field is investigated by means of a global analysis of the averaged heat fluxes, $\overline{u_i \theta}$, the temperature variance, $\overline{\theta^2}$, and the eddy diffusivity. Moreover, a scaling law for the heat transfer coefficient based on the effective viscous friction velocity is presented.

2 Mathematical Model and Numerical Strategy

The configuration of the problem is sketched in Fig. 1. The streamwise direction is denoted by x, the spanwise direction by y and the interface-normal (gravity) direction is referred to as z. The two phases are flowing counter-currently and are separated by an interface free to deform in three dimensions.

2.1 Transport Equations. The gas and liquid phases (designated by the subscripts G and L, respectively) are considered as Newtonian and incompressible fluids, flowing in separate domains, and driven by an imposed constant mean pressure gradient. The reference quantities employed for normalization in each domain are the effective shear velocity $u_* = \sqrt{\tau_{int}/\rho}$, where τ_{int} is the viscous interfacial shear stress, the half-depth of each computational domain h, and the kinematic viscosity ν. It is important to note that, at the beginning of the simulation when the interface is flat, the viscous interfacial shear stress balances exactly the mean pressure gradient driving the flow, and u_* corresponds to the shear velocity u_τ. As the waves start to form and develop, part of the energy is transferred into form drag, so that $u_* < u_\tau$.

The reference temperature T_* is defined as

$$T_* = \frac{q_{int}}{\rho c_p u_*}; \quad q_{int} = -\lambda \left(\frac{d\bar{T}}{dz} \right)_{int} \tag{1}$$

where q_{int} represents the interfacial heat flux. The time is made nondimensional using ν/u_*^2, and the length scales are normalized using u_*/ν. In each computational domain, the shear Reynolds number is defined as $Re_* = u_* 2h/\nu$.

With the reference quantities defined above, the Navier-Stokes and energy equations governing the flow in each domain can be written in nondimensional form as

$$\nabla \cdot \mathbf{u}^+ = 0 \tag{2}$$

$$\frac{\partial \mathbf{u}^+}{\partial t} + \nabla \cdot (\mathbf{u}^+ \mathbf{u}^+) = -\nabla p^+ + \frac{1}{Re_*} \nabla^2 \mathbf{u}^+ \tag{3}$$

$$\frac{\partial T^+}{\partial t} + \nabla \cdot (\mathbf{u}^+ T^+) = \frac{1}{Re_* Pr} \nabla^2 T^+ + \frac{u^+}{2 U_B^+} \tag{4}$$

where $\mathbf{u}^+ = (u^+, v^+, w^+)$ is the nondimensional (by u_*) velocity vector, p^+ is the dynamic pressure normalized by ρu_*^2, T^+ is the nondimensional temperature defined as $T^+ = (T - T_{int})/T_*$, and U_B^+ is the mean bulk velocity. The last term in Eq. (4) is the source term needed to accurately predict the scalar transfer rate at low Prandtl numbers [4]. The conventional notation

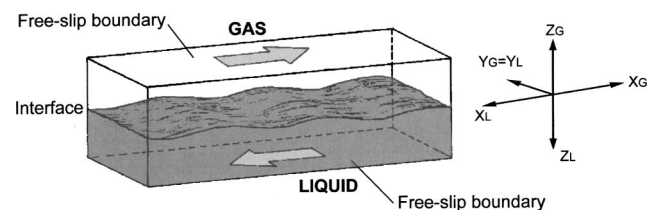$$\mathbf{u}^+(x,y,z,t) = \mathbf{U}^+(z) + u^+(x,y,z,t) \tag{5}$$

Fig. 1 Geometry of the simulated two-phase flow

$$T^+(x,y,z,t) = \Theta^+(z) + \theta^+(x,y,z,t) \tag{6}$$

is adopted to decompose the velocity and temperature fields into mean and fluctuating (turbulent) components.

2.2 Boundary Conditions. In the absence of phase change, the gas and liquid phases are coupled at the interface by the continuity conditions for normal and shear stresses, velocity and temperature (see, for example, Delhaye [16]), i.e.,

$$\begin{cases} \dfrac{1}{\mathrm{Re}_*}((\sigma_L^+ - \sigma_G^+)\cdot \mathbf{n})\cdot \mathbf{n} + p_G^+ - p_L^+ + \dfrac{1}{We}\nabla \cdot \mathbf{n} - \dfrac{1}{Fr}f^+ = 0 \\ ((\sigma_L^+ - \sigma_G^+)\cdot \mathbf{n})\cdot \mathbf{t}_i = 0, \quad i=1,2 \\ \mathbf{u}_L^+ = \mathcal{R}\mathbf{u}_G^+ \\ T_G^+ = T_L^+ \end{cases}$$

$$\tag{7}$$

where σ^+ is the viscous stress tensor, f^+ is a measure of the vertical displacement of the interface with respect to the mid plane, $\mathbf{n}$ and $\mathbf{t}_i$ are the normal and the two tangential unit vectors, respectively, and $\mathcal{R} = \sqrt{\rho_L/\rho_G}$ is the density ratio parameter. The Weber (We) and Froude (Fr) numbers are defined as

$$We = \frac{\rho_L h u_{*L}^2}{\gamma}, \quad Fr = \frac{u_{*L}^2 \rho_L}{gh(\rho_L - \rho_G)} \tag{8}$$

where γ is the surface tension.

The interface motion is simulated by solving a pure advection equation for the vertical elevation of the interface, $f(\mathbf{x},t)$, written in nondimensional form as

$$\frac{\partial f^+}{\partial t} + \mathbf{u}_L^+ \cdot \nabla f^+ = 0 \tag{9}$$

The approach based on advecting Eq. (9) and solving for the gas and the liquid fields separately is a boundary fitting method. In contrast to interface tracking methods, this approach cannot be extended to strong topological changes of the interface that might lead to the inclusion of one phase into the other, such as fragmentation and wave breaking [17].

Periodic boundary conditions are applied in the streamwise (x) and spanwise (y) directions. At the outer boundaries, symmetry boundary conditions are employed for the thermal field, whereas free-slip boundary conditions are imposed on the velocity field.

2.3 Numerical Procedure. The governing equations are solved using a collocation pseudo-spectral technique employing Fourier series in the homogeneous, streamwise and spanwise directions, and Chebychev polynomials in the non-uniform direction normal to the interface. The physical domain is mapped into a rectangular parallelepiped at each time step. Equations (2), (3), and (4) are first solved separately in each domain, then coupled at the interface (identified by solving Eq. (9)) through the continuity conditions (7): on the gas side, the interfacial conditions apply to velocities and the temperature, whereas on the liquid side they apply to stresses and the temperature. Procedures for de-aliasing the solutions based on the two-thirds rule apply in this context, too.

A modified version of the two-step fractional time splitting method introduced by Temam [18] is employed. In the first step, an intermediate value for the velocity $\hat{\mathbf{u}}$ is determined by solving the momentum equation, without the pressure gradient term

$$\frac{\hat{\mathbf{u}} - \mathbf{u}^n}{\Delta t} + \sum_{q=0}^{J-1} \beta_q \nabla \cdot (\mathbf{u}\mathbf{u})^{n-q} - \frac{1}{2\,\mathrm{Re}_*}\nabla^2(\hat{\mathbf{u}} + \mathbf{u}^n) = 0. \tag{10}$$
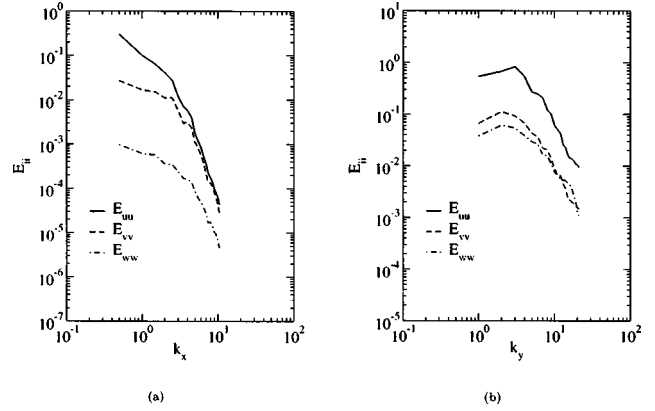

Fig. 2 Energy spectra at $z^+=5$ for the velocity components, in the gas phase: (*a*) streamwise direction; and (*b*) spanwise direction.

The convective term is explicit, with $J=2$, $\beta_0 = 3/2$ and $\beta_1 = -1/2$, as in the Adams-Bashforth (AB) scheme. The viscous term is implicit and discretized using the Crank-Nicholson (CN) semi-implicit scheme. The time marching is second-order accurate in the computation of the intermediate velocity $\hat{\mathbf{u}}$, the value of which is corrected in the next step using

$$\frac{\mathbf{u}^{n+1} - \hat{\mathbf{u}}}{\Delta t} + \nabla p^{n+1} = 0. \tag{11}$$

The unknown pressure field p^{n+1} can be obtained by taking the divergence of Eq. (11) which, using the condition that $\mathbf{u}^{n+1}$ is solenoidal, results in the Poisson equation

$$\nabla^2 p^{n+1} = \frac{1}{\Delta t}\nabla \cdot \hat{\mathbf{u}} \tag{12}$$

The energy Eq. (4) is also solved using a second-order accurate time differencing

$$\frac{T^{n+1} - T^n}{\Delta t} + \sum_{q=0}^{J-1} \delta_q \nabla \cdot (\mathbf{u}T)^{n-q} - \frac{1}{2\,\mathrm{Re}_*\,\mathrm{Pr}}\nabla^2(T^{n+1} + T^n) = 0 \tag{13}$$

where the explicit ($J=2$, $\delta_0 = 3/2$ and $\delta_1 = -1/2$) convective term is discretized using the AB scheme, and the implicit diffusive term is discretized by use of the CN scheme.

The size of each computational domain is $4\pi h \times 2\pi h \times 2h$ in streamwise, spanwise and interface-normal directions, corresponding to $1074 \times 537 \times 171$ wall units. As capillary waves do not produce significant domain distortion, a grid resolution (for each domain) of $64 \times 64 \times 65$ in the streamwise, spanwise and interface-normal directions was found to be appropriate for the solution of the isothermal flow field. This is proved in Fig. 2, displaying the energy spectra against wave numbers k_x and k_y for the three velocity components, evaluated at a distance of five wall units from the interface, in the gas side. The result shows no energy accumulation at high wave numbers, confirming that this resolution is sufficiently accurate for the solution of the velocity field. The extension of the spectrum to higher wave numbers, obtained by doubling the grid resolution in the interface-normal direction, did not show energy accumulation either (result not presented here). In their review of past DNS of heat transfer in channel flow, Piller et al. [11] note that the differences observed between some of the

Table 1 Computational parameters

	Pr=1	Pr=5	Pr=10
Re_*	171	171	171
We	4.8×10^{-3}	4.8×10^{-3}	4.8×10^{-3}
Fr	8.7×10^{-5}	8.7×10^{-5}	8.7×10^{-5}
$\Gamma=\sqrt{\rho L/\rho G}$	29.9	29.9	29.9
Grid points in each domain	$64\times64\times65$	$64\times64\times129$	$64\times64\times129$
Δx^+	16.77	16.77	16.77
Δy^+	8.38	8.38	8.38
Δz^+	0.102–4.191	0.026–2.096	0.026–2.096
Time Increment	$0.024\,\nu/u_*^2$	$0.012\,\nu/u_*^2$	$0.012\,\nu/u_*^2$

Fig. 3 Saturation spectra of the wave fields at the beginning (B_{in}) and at the end (B_{out}) of the sampling period

published results were chiefly due to insufficient statistical convergence, rather than to lower space resolution in the wall-normal direction.

2.4 Simulations. The shear Reynolds number Re_* is in each phase equal to 171. The inter-phase heat transfer does not include phase change. To limit the wave amplitude and steepness to the range of capillary waves, the Weber and Froude numbers were set equal to $We=4.8\times10^{-3}$ and $Fr=8.7\times10^{-5}$. The gas and liquid phases considered are such that $\mathcal{R}=29.9$. Three different thermal conditions have been investigated, namely Pr=1, 5 and 10. For Pr=1, the spatial resolution employed in each domain is $64\times64\times65$ (hereinafter referred to as G1), whereas for Pr=5 and 10, it was doubled in the direction normal to the interface, i.e. $64\times64\times129$ (referred to as G2). The grid resolutions in G1 ($\Delta x^+=16.77$, $\Delta y^+=8.38$, $\Delta z^+=0.102-4.191$) and G2 ($\Delta x^+=16.77$, $\Delta y^+=8.38$, $\Delta z^+=0.026-2.096$) are comparable to those employed by Tiselj et al. [19]. The time increments are $0.024\,\nu/u_*^2$ for the G1 grid, and $0.012\,\nu/u_*^2$ for G2.

After statistically stationary conditions were achieved in each run, the velocity and thermal fields were collected over $4000\nu/u_*^2$ nondimensional time units. The criterion used to establish steady state conditions was that the turbulent shear stress, $\overline{u^+w^+}$, and the turbulent heat flux, $\overline{w^+\theta^+}$, were no longer varying over a time interval of 1000 nondimensional time units. The simulation parameters are summarized in Table 1.

3 Interpretation of Results

Motivated by the uncertainties as to the existence of a similarity between near-wall and near-interfacial turbulence, Fulgosi et al. [15] studied the turbulent gas flow over the deformable interface, and compared the results to wall-bounded flow data at the same shear Reynolds number. In a time-averaged sense, the interfacial motion was seen to affect some features of the turbulence field in the near-interface region; the most pertinent effect is a general dampening of the turbulent fluctuating field which, in turn, leads to a reduction in the interfacial dissipation. Furthermore, the turbulence was found to be less anisotropic at the interface than at the wall. The analysis of the turbulent kinetic energy and Reynolds stress budgets revealed that the interface deformations mainly affect the so-called boundary term involving the redistribution of energy, and the dissipation terms, leaving the production terms almost unchanged. Away from the interface, the decomposition of the fluctuating velocity gradient tensor demonstrated that the fluctuating rate-of-strain and rate-of-rotation at the interface influence the flow throughout the boundary layer more vigorously.

Following this comparative strategy, in the present work, the interfacial turbulent heat transfer in the gas is investigated, and the results compared to wall-bounded flow data to reveal the effect of the interfacial deformation on heat transfer mechanisms for a range of low Prandtl numbers. As it is customary in DNS, the statistical analysis of the data is performed by averaging the collected velocity and thermal database over the two homogeneous directions (i.e., x-y plane average) and in time. For the flow under
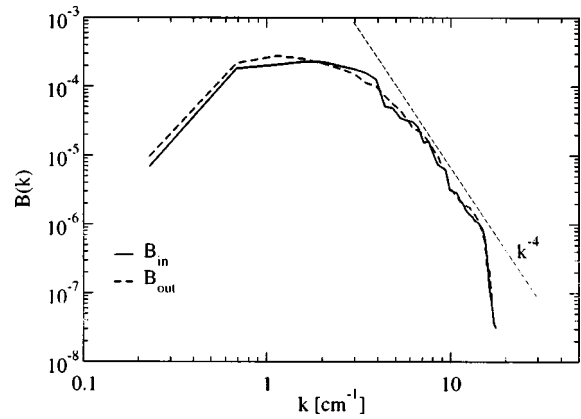
consideration here, this averaging procedure can be reliable only if the collected data cover a sufficiently large time interval over which the wave properties do not change. The statistical stationarity of the wave field is discussed below.

3.1 Characteristics of the Waves. The topology of the waves developing over a deformable free surface takes various forms, depending on the intensity of the interfacial shear stress caused by the nature of the underlying turbulence. The action of this shear is balanced by two stabilizing factors: one due to gravity and one caused by surface tension. The specialized literature [20] characterizes the wave field in terms of saturation spectrum

$$B(k)=k^2\Psi(k);\quad \Psi(k)=\frac{1}{2\pi}\int Z(\mathbf{r})e^{-i\mathbf{k}\cdot\mathbf{r}}dr, \qquad (14)$$

in which Ψ is the two-dimensional wave spectrum, and $Z(\mathbf{r})$ is the covariance of the instantaneous nondimensional surface displacement defined by

$$Z(\mathbf{r})=\overline{f(\mathbf{x},t_0)f(\mathbf{x}+\mathbf{r},t_0)} \qquad (15)$$

It is important to observe that, since the wavelength k is here defined in the dimensional space, Ψ has the dimension of $[L^2]$, so that a coefficient k^2 is needed in the definition of the saturation spectrum (14). The reader is referred to Phillips [20] for further theoretical details. The wave saturation spectra, obtained using grid G1, are plotted in Fig. 3 at two different times during the simulation: at the early stage (referred to as B_{in} in Fig. 3) and at the end (referred to as B_{out}) of the time interval over which the statistical analysis has been performed. The graph clearly indicates that the wave properties did not change significantly within this time interval, confirming the existence of the saturation or equilibrium range, which is synonymous to convergence in this context. The impact of the interfacial motion can then be inferred in an average sense.

3.2 Statistics of the Thermal Field. The mean temperature profiles plotted against the distance to the interface are shown in Fig. 4(a) for all Prandtl numbers. The results obtained by Kawamura et al. [5] at $Re_\tau=180$ for Pr=1 and Pr=5, and by Tiselj et al. [21] at $Re_\tau=171$ for Pr=1 and Pr=5.4 (for an isothermal wall boundary condition) have been included for comparison. For Pr=10 the present DNS has been compared to that of Na et al. [7] at $Re_\tau=150$. For Pr=1 the present results agree fairly well with both databases [5,21], whereas for Pr=5 the agreement is better with the data of Kawamura et al. [5] than with those of Tiselj et al. [21]. For Pr=10 the comparison with the data of Na et al.
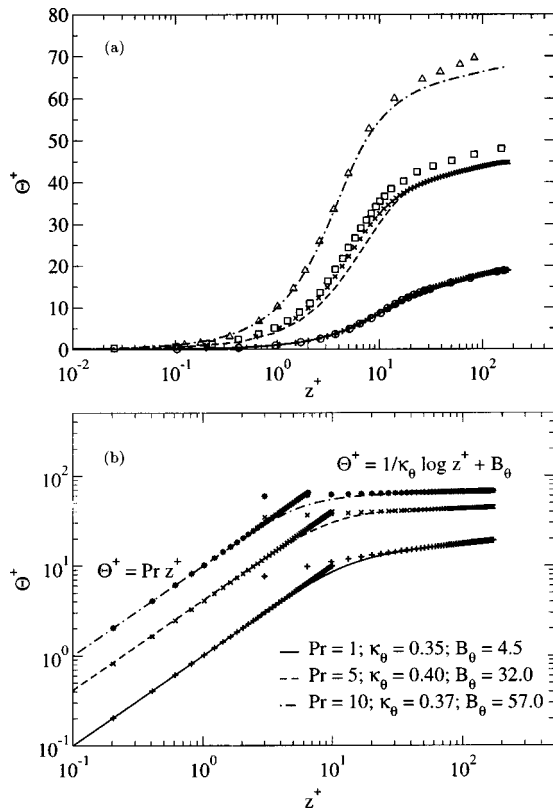
Fig. 4 Mean temperature profiles. (*a*) Comparison with other DNS databases. Lines are used to identify the present DNS result: ——, Pr=1; — — —, Pr=5; -----, Pr=10. Symbols identify respectively: +, Pr=1 and ×, Pr=5: DNS of Kawamura et al. [5]; ○, Pr=1 and □, Pr=5: DNS of Tiselj et al. [21]; △, Pr=10: DNS of Na et al. [7]. (*b*) Present DNS extrapolated data; lines are used to identify present DNS results and symbols to identify the fitting equations.

[7] is overall satisfactory. Figure 4(*b*) shows that inside the diffusive sublayer, the mean temperature profiles are in agreement with the linear relation $\Theta^+ = \text{Pr} \cdot Z^+$.

Further analysis of the data also permits to identify the extent of the logarithmic layer, where $\Theta^+ = 1/\kappa_\theta \ln z^+ + B_\theta$. Both the slope, κ_θ^{-1}, and the shift, B_θ, are found to vary with Prandtl number, though without leading to the establishment of a clear relationship. The diffusive sublayer exists in all three flows, with thicknesses Δ_θ^+ decreasing with increasing Prandtl number, i.e., $\Delta_\theta^+ \approx 6$, 4 and 2 wall units, respectively, for Pr=1, 5 and 10. While the results for Δ_θ^+ agree with those of Na et al. [7] and Kawamura et al. [5], those for the slope and the shift deviate appreciably from the data of Na et al. [7]. These deviations are perhaps due to the lower Reynolds number used by Na et al. [7] rather than the wall boundary conditions employed in their simulation. The difference in the slopes, in particular, suggests that the intensity of turbulence in [7] is simply weaker.

The behavior of the fluctuating temperature field near the wall/interface is generally accepted as a good indicator of the way scalar turbulent transport operates. An important feature requiring understanding is the effect of the Prandtl number on the interplay between molecular and turbulent transport near the wall. The r.m.s. values of the temperature fluctuations are presented in Fig. 5, where the results of Kawamura et al. [5] and Tiselj et al. [21] for Pr=1 and Pr=5, and those of Na et al. [7] for Pr=10, are again included for comparison. As can be observed, in both wall-bounded and interfacial flows, the increase in Prandtl number corresponds to a shift of the maximum of the temperature fluctuations
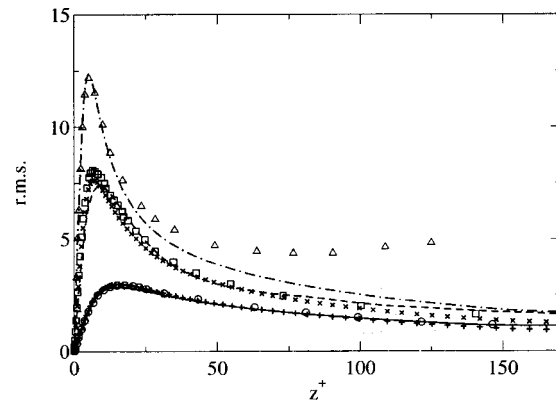

Fig. 5 Root mean square value of temperature fluctuations. Lines are used to identify the present DNS result: ——, Pr=1; — — —, Pr=5; -----, Pr=10. Symbols identify respectively: +, Pr=1 and ×, Pr=5: DNS of Kawamura et al. [5]; ○, Pr=1 and □, Pr=5: DNS of Tiselj et al. [21]; △, Pr=10: DNS of Na et al. [7].

towards the boundary. Both the present results and those of Kawamura et al. [5] for Pr=1, the maximum of the temperature fluctuations is located around $z^+ = 17$. Increasing the Prandtl number to 5 shifts the peak location to about $z^+ = 7$ in the wall-bounded flow, and to around $z^+ = 9$ in the flow over the deformable interface. The wall flow data of Na et al. [7] show the maximum of the temperature fluctuations located around $z^+ = 3$, whereas the present study shows that location to be around $z^+ = 5$. It is interesting to note that the exact location of the maximum r.m.s. value is not correlated with the position of the edge of the diffusive sublayer Δ_θ^+: the two locations tend to coincide with increasing Prandtl number.

The first important conclusion to be drawn from the above comparisons is that, as in wall flows, the most relevant statistical quantities scale with the friction velocity, based on frictional drag. The ratio of frictional drag to total drag (including form drag) was found to be around 0.98. The second important finding is the appreciable effect of Pr on $\overline{\theta^{+^2}}$, indicating that the range of wave numbers in the thermal fluctuating field increases with Pr, for which the spectral functions of the velocity field are negligible.

3.3 Turbulent Fluxes and Inter-Phase Heat Exchange. Figure 6 shows the nondimensional averaged turbulent heat flux (THF), $\overline{u^+ \theta^+}$, in the streamwise direction versus the dimensionless distance to the interface/wall. The data are compared to the wall-bounded flow DNS of Kawamura et al. [5]. For Pr=1 the streamwise THF over the deformable interface compares very
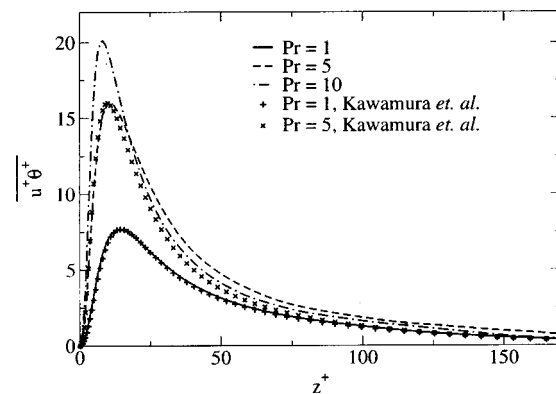

Fig. 6 Streamwise turbulent heat flux and comparison with Kawamura et al. [5]
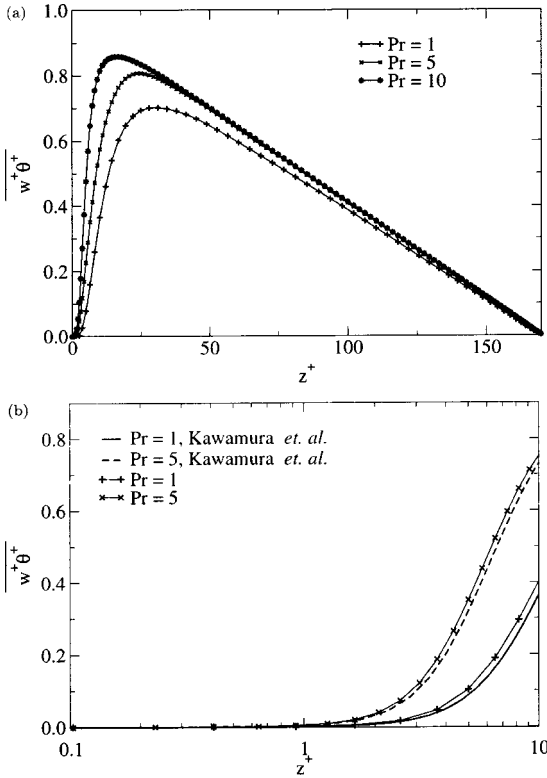
Fig. 7 Interface-normal turbulent heat flux: (*a*) boundary layer; and (*b*) near interface/wall region and comparison with Kawamura et al. [5].

Fig. 8 Heat transfer coefficient

well with the wall data; the behavior is similar and the peak value in both cases is located at the same distance from the interface/wall, $z^+ \approx 18$, which corresponds to the location of the maximum r.m.s. value of the temperature fluctuations. For Pr=5, the streamwise THF near the interface exhibits some differences compared to that near the wall, but peak values are almost identical and are furthermore reached almost at the same location from the interface/wall ($z^+ \approx 11$). Beyond the peak location, however, the THF for the flow over the deformable interface remains slightly higher than for the wall flow. For Pr=10 the streamwise THF peak location occurs at $z^+ \approx 8$. This analysis confirms that increasing the molecular Prandtl number substantially increases the intensity of the heat flux when approaching the wall/interface, depending on the thickness of the thermal boundary layer. Away from the diffusive thermal sublayer, the value of the THF drops faster for higher Prandtl numbers. Deeper in the bulk flow, heat transfer by turbulent transport does not depend much on the Prandtl number.

Figure 7(a) presents the distribution of the nondimensional averaged THF in the direction normal to the interface, $\overline{w^+\theta^+}$. We note that, as the molecular Prandtl number increases, the peak location moves closer to the interface, and so does the intensity of the flux. The differences between the near-interface and near-wall values (at $z^+ < 10$) of the normal THF are analyzed in detail in Fig. 7(b). For both Pr=1 and Pr=5 the flux intensity near the deformable interface is higher than at the wall. This implies that the interfacial dynamics leads to an increase in the vertical THF as compared to the situation near the rigid wall. The only plausible explanation for this difference is that the waves promote the velocity fluctuating field normal to the interface. Fulgosi et al. [15] indeed report that the turbulent kinetic energy decays faster at the
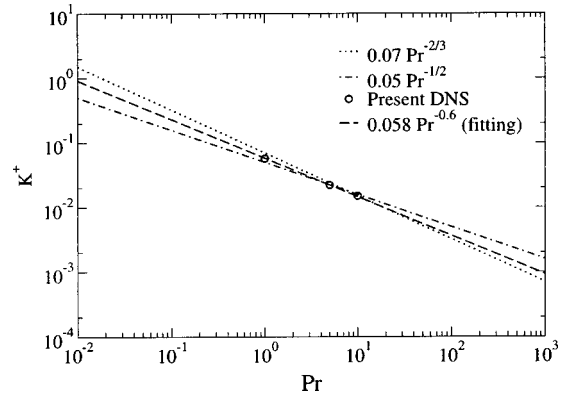
wall than at the mobile interface. The differences between the streamwise and vertical THFs will be explained more fully in Section 3.5, where the budget equations for the heat fluxes are compared term by term.

The nondimensional heat transfer coefficient (HTC) is defined as

$$K^+ = \frac{9_{\text{int}}}{\zeta C_p \Delta \bar{T} u} = \frac{1}{Pr} \frac{1}{(\bar{T}_{\text{top}} - \bar{T}_{\text{int}})} \left.\frac{d\bar{T}}{dz^+}\right|_{\text{int}}, \qquad (16)$$

where $\bar{T}_{\text{top}}$ represents the mean temperature at the upper boundary of the gas domain (in [22], $\bar{T}_{\text{top}}$ was taken at the center of the closed channel). Note, too, that K^+ is normalized by the effective friction velocity associated with a frictional drag $u_* = 0.98 u_\tau$. The scaling of the heat transfer coefficient with the effective frictional velocity u_* has so far shown that it scales with $Pr^{-1/2}$ at mobile interfaces, and with $Pr^{-2/3}$ at immobile interfaces [9]. De Angelis et al. [14] have shown the $Pr^{-2/3}$ scaling to also hold on the gas side of wavy gas-liquid interfaces, but for high-Sc numbers only.

Figure 8 presents the values of the nondimensional HTC obtained for the gas side in the present DNS as a function of Prandtl number. For the range of Pr investigated here, the present DNS provides the following variation of the HTC

$$K^+ = 0.058 \ Pr^{-3/5}, \qquad (17)$$

which can be seen to vary between $\propto Pr^{-1/2}$ for free surfaces and $\propto Pr^{-2/3}$ for immobile interfaces for much higher Prandtl numbers. For instance, the DNS of Na et al. [7] delivered smaller values for both the coefficient of proportionality and the exponent, i.e., 0.0509 and 0.546, respectively. A parameterization of the scalar transfer rate by reference to the surface renewal theory, using the above result, yields

$$K^+ = 0.41 \ \tau_{\text{ren}}^{+ -0.5} \ Pr^{-0.6}, \qquad (18)$$

where the normalized (by ν/u_*^2) mean time between sweeps, τ_{ren}^+, given by the DNS is approximately equal to $f_{\text{sweep}}^{-1} = 50$, where f_{sweep} denotes the frequency of sweeps ejections. Banerjee [23] obtained a similar relationship for high-Sc mass transfer at solid walls based on the Leveque boundary layer solution, reading
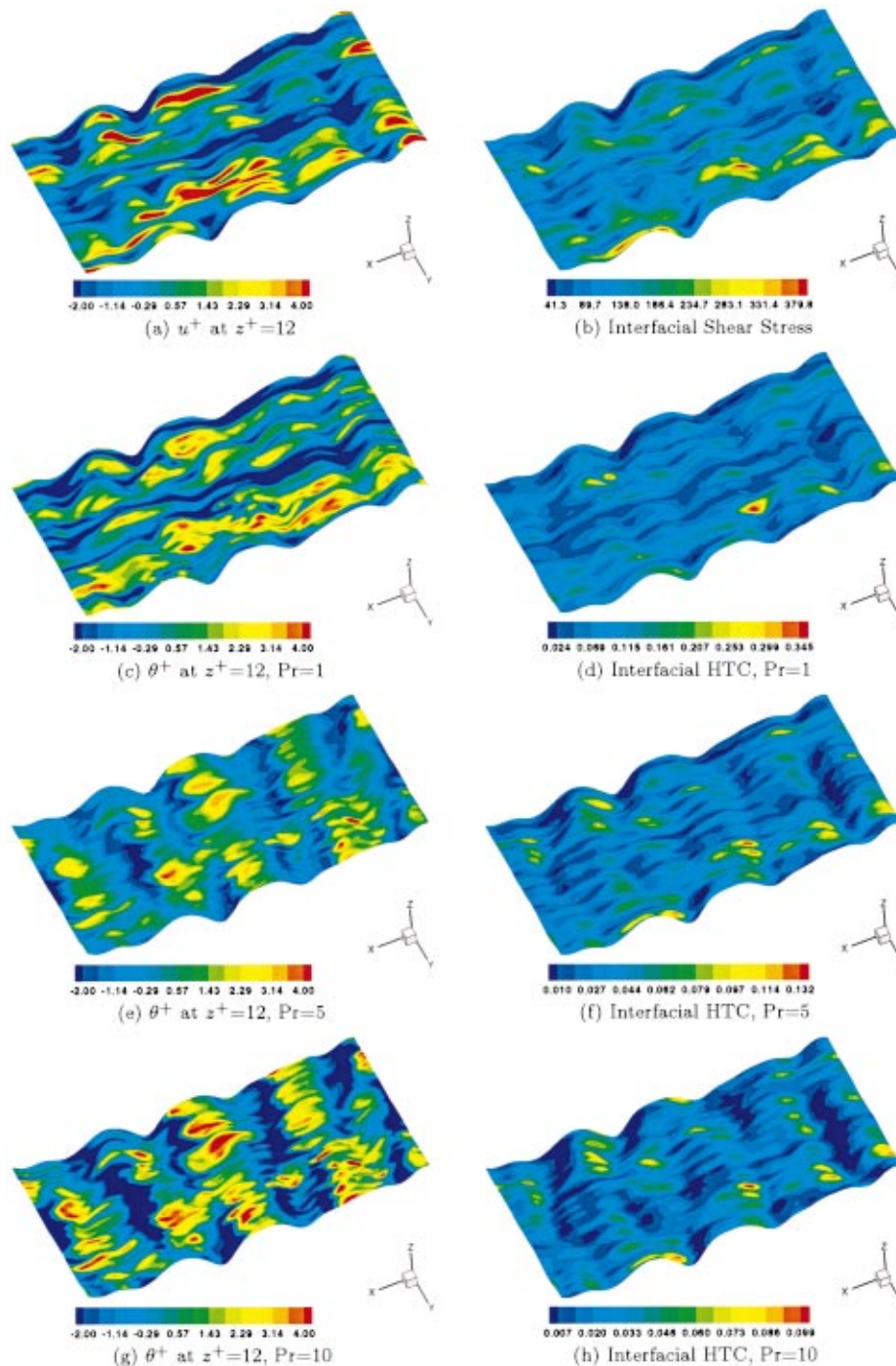
Fig. 9 The elevation of the waves is amplified by factor 10: (a) u^+ at $z^+=12$; (b) interfacial Shear Stress; (c) θ^+ at $z^+=12$, Pr=1; (d) interfacial HTC, Pr=1; (e) θ^+ at $z^+=12$, Pr=5; (f) interfacial HTC, Pr=5; (g) θ^+ at $z^+=12$, Pr=10; and (h) interfacial HTC, Pr=10.

$$K^+ = 0.68\, \tau_{\text{ren}}^{+\,-0.5}\ Sc^{-0.66}, \tag{19}$$

in which both the constant and the Sc power are actually functions of the Schmidt number. A close inspection of the Polhausens's boundary layer solution reveals on the other hand that the best fit for Sc in the range of Pr=5 to 15 is obtained with the constant fixed to 0.6 and the Sc exponent to -0.6.

Contours of the instantaneous HTC at the interface are shown in Figs. 9(d), 9(f), and 9(h), for Pr=1, 5 and 10, respectively, and are compared with the thermal streaks represented by contours of

θ^+ at $z^+=12$, shown in the neighboring left panels (Figs. 9(c), 9(e), 9(g)). The comparison also includes contours of instantaneous velocity streaks, marked by contours of u^+ at $z^+=12$ (Fig. 9(a)), and of the instantaneous shear stress at the interface (Fig. 9(b)). The three-dimensional interfacial waves can be seen to develop and propagate in the direction of the gas-flow (in the pictures the wave amplitude has been magnified by a factor ten). Regions of high shear-high heat transfer rates at the crests can be clearly distinguished from regions of low shear-low heat transfer rates at the troughs. The streaky structure of the velocity field is

well represented by contours of u^+, similar to what is observed in wall flow [24], and is shown to conform to the thermal streaks for Pr=1. This result indeed confirms the Reynolds analogy between diffusion of momentum and diffusion of heat; the deviations become evident with increasing Prandtl number.

Observing the HTC contours also reveals that heat transfer rates correlate with the interfacial shear; the largest values, occurring at the bulges imposed by turbulent motions, correspond to strongly positive shear values and positive u^+ levels, presented in Fig. 9(a). According to the quadrant analysis of near-wall/interface turbulence structure [12], this scenario is the signature of sweep events through which the surface renews its structure, leading to high scalar transfer rates. By controlling surface renewal throughout the migration of high momentum fluid towards the interface, sweep motions create regions of high interfacial shear stress, leading in turn to high heat transfer rates. The scalar transfer rate reaches its peak value when the sweep impinges on the surface; during the decay time the diffusive layer saturates by the actions of molecular diffusion. On the other hand, increasing Pr produces a much finer thermal streaky structure and a decrease in heat transfer rate (note that the scale of the plots changes with Pr).

3.4 Temperature Variance. As the turbulent kinetic energy represents an integral measure of the energy associated with the fluctuating velocity field, the variance of the fluctuating temperature $\overline{\theta^2}$ may be regarded as the energy carried by the fluctuating temperature field. The equation for the evolution of the temperature variance can be written in compact form (see, for example, Nagano [25]) as

$$\frac{D\overline{\theta^2}}{Dt} = \mathcal{D}_\theta + \mathcal{T}_\theta + \mathcal{P}_\theta - \varepsilon_\theta \qquad (20)$$

where D/Dt is the substantial derivative. The first and second terms on the right-hand side of this equation represent the diffusion by molecular actions and the diffusion due to turbulent transport, respectively. The third term is the production of $\overline{\theta^2}$ by the interactions between heat fluxes and mean temperature gradients. The last contribution represents the dissipation of the variance.

Figure 10 presents the budget terms obtained, for the gas side, from the present DNS. For the smaller Prandtl numbers, Pr=1 and 5, results are again compared to the data of Kawamura et al. [5]. For Pr=1, there are only small differences in the contributions to the balance (Fig. 10(a)), which conforms with previous results regarding the thickness of the thermal and momentum boundary layers and averaged heat fluxes. The effects of interfacial motion on the fluctuating thermal field are negligible at this Prandtl number. As the molecular Prandtl number increases (Fig. 10(b)), minor deviations from the wall-bounded flow data begin to appear, in particular concerning the production and turbulent diffusion terms. A comparison of the averaged normal heat fluxes in Fig. 7(b) explains why the production in wall flow is stronger than in the flow over the deformable interface.

The budget for Pr=10 presented in Fig. 10(c) indicates that the contribution of the production term becomes important with increasing Prandtl number, which is also true of the dissipation. In particular, these two contributions can be compared to the results of Na et al. [7] (their Figs. 7 and 13), which also show the values of $\mathcal{P}_\theta$ and ε_θ at the wall to increase drastically for Pr=10. The behavior of the dissipation in the diffusive thermal sublayer appears to be much more flat than for the case of the wall flow, and the starting value is also smaller.

3.5 Turbulent Heat Fluxes. In turbulence modeling, the most sophisticated approach accounting for the effects of turbulence-induced stresses in the heat transport consists in solving the transport equation for the turbulent heat fluxes, $\overline{u_i\theta}$, rather than resorting to the eddy diffusivity concept. In compact form, this transport equation can be written as

Fig. 10 Budget for the temperature variance in the near interface/wall region. Lines are used to identify the results of the present DNS and symbols to identify the wall-bounded DNS results of Kawamura et al. [5]. (a) Pr=1; (b) Pr=5; (c) Pr=10.

$$\frac{\overline{Du_i\theta}}{Dt} = \mathcal{P}_i^\theta + \Pi_i^\theta + \mathcal{D}_i^\theta - \varepsilon_i^\theta \qquad (21)$$

where the first term, $\mathcal{P}_i^\theta$, represents the mean flow production due to the combined actions of mean temperature gradients and mean velocity gradients. The second term is the pressure-temperature correlation, $\Pi_i^\theta \equiv -\overline{\theta\nabla p}$. The third contribution, $\mathcal{D}_i^\theta$, designates the diffusive transport comprising molecular, $\mathcal{D}_i^{m\theta}$, and turbulent counterparts, $\mathcal{D}_i^{t\theta}$. The last term, ε_i^θ, refers to the dissipation of turbulent heat flux (see, for example, Kasagi et al. [4] or Nagano [25] for the exact definition of each contribution).

Budgets of the streamwise heat flux, $\overline{u^+\theta^+}$, for the gas flow data obtained by the present DNS were compared (results not included here) to the channel-flow data of Kawamura et al. [5], for Pr=1 and 5. The comparison revealed the same behavior as observed before: the production becomes more important with increasing Pr, the molecular diffusion dominates as a positive con-
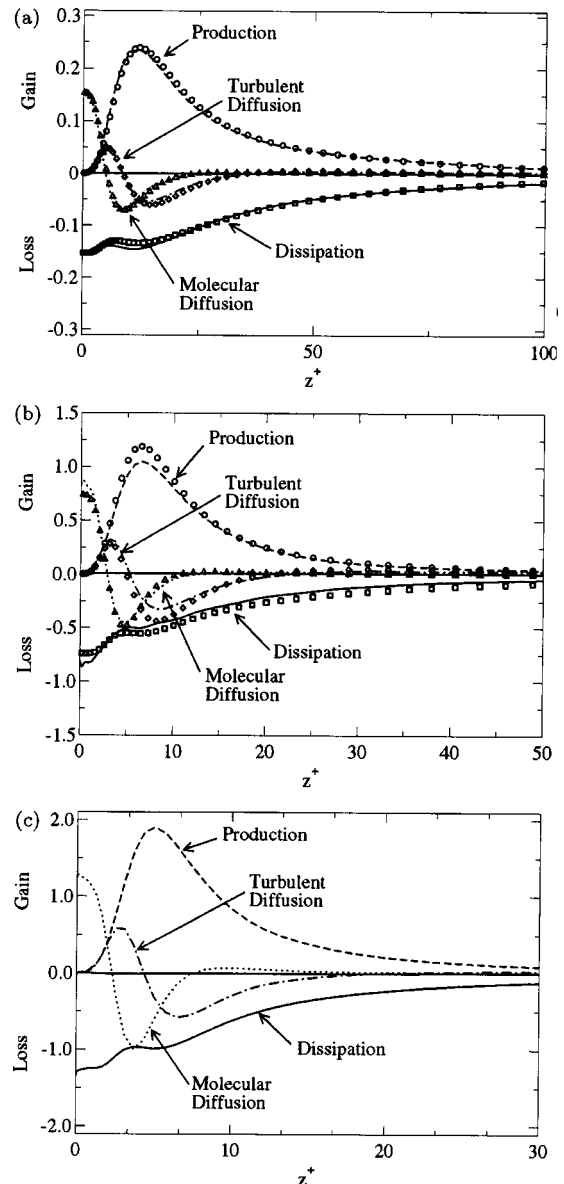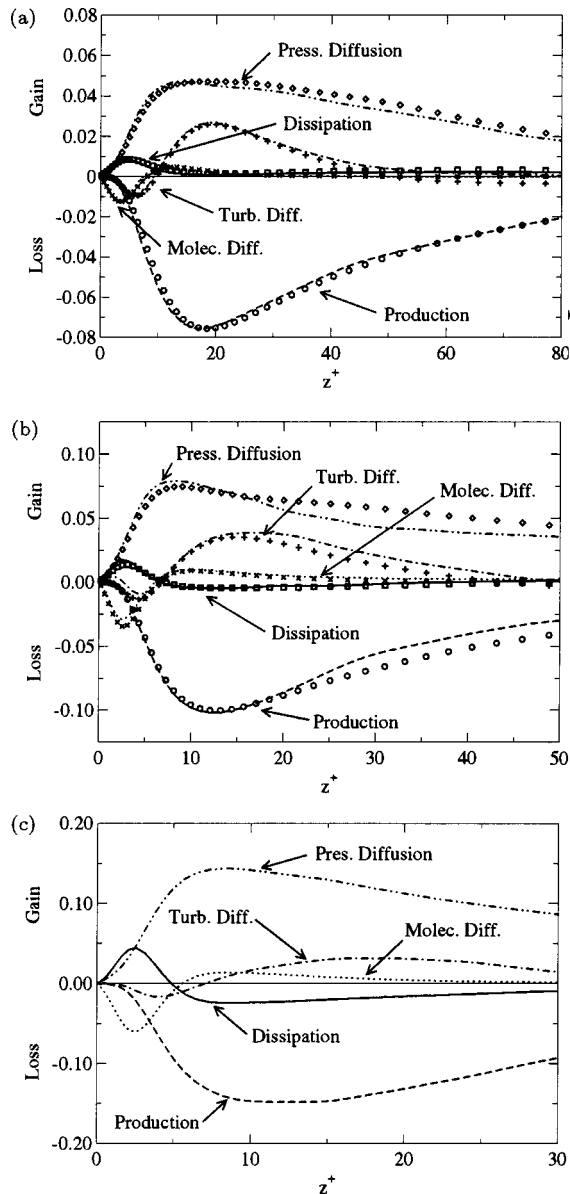
Fig. 11 Budget for the vertical turbulent heat flux in the near interface/wall region. Lines are used to identify the results of the present DNS and symbols to identify the wall-bounded DNS results of Kawamura et al. [5]. (a) Pr=1; (b) Pr=5; (c) Pr=10.

Fig. 12 (a) Turbulent diffusivity; and (b) Turbulent diffusivity in the vicinity of the deformable interface.

tribution in the diffusive sublayer and is balanced by the dissipation, while away from the wall/interface the production is balanced by the dissipation. The behavior of the dissipation, ε_i^θ, was particularly interesting: for Pr=1 its level gradually decreases away from the wall/interface, whereas for Pr=5 and 10 it marks a sharp drop at locations around the edge of the diffusive sublayer.

The effect of varying Prandtl number on the wall/interface-normal heat flux balance, $\overline{w^+\theta^+}$, is discussed in relation to Fig. 11, comparing the wall and the present deformable interface databases. Again, the production, which is negative in this case, gains in importance with increasing Pr, with the peak location always moving closer to the wall. In contrast to the streamwise component, the production in the normal direction is balanced by the pressure-gradient correlation $\Pi_3^\theta \equiv -\overline{\theta \partial_z p}$, and to a small extent by the turbulent diffusion $\mathcal{D}_3^{t\theta}$. The dissipation again shows an interesting behavior: the peak value of ε_3^θ in the diffusive sublayer increases with the Prandtl number. For Pr=1 the dissipa-
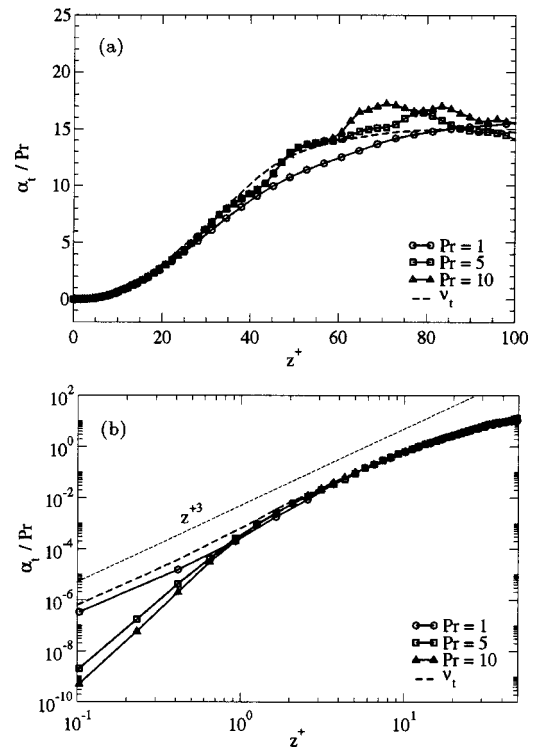
tion converges asymptotically almost to zero at $z^+ \approx 20$. For higher Prandtl numbers, the sign of ε_3^θ reverses exactly where the molecular and turbulent diffusion contributions change sign, too, indicating that in some flow regions the dissipation contributes positively as a gain. This was already revealed by Kasagi et al. [4] and Kawamura et al. [5], and was attributed to the fact that the dissipation takes place in the large-scale structures.

3.6 Turbulent Thermal Diffusivity. Turbulent thermal diffusivities were determined by averaging the thermal stress data and temperature gradients in the homogeneous directions and in time. The turbulent thermal diffusivity, α_t, was defined by applying the simplified Gradient Diffusion Hypothesis (GDH)

$$\overline{w^+\theta^+} = -\alpha_t \frac{d\Theta^+}{dz^+}. \tag{22}$$

The impact of varying Pr on the distribution of eddy diffusivity scaled by Pr is shown in Fig. 12(a), where the eddy viscosity—determined by use of GDH—is also included for comparison. For Pr=1 the data show the natural increase of α_t with distance to the interface, converging towards 15.5 at $z^+=100$. An increasing Prandtl number has no effect on α_t in the region close to the interface ($z^+<40$), but a larger one away from it. The eddy diffusivity is shown to gain almost 30% in this flow region. An attempt to infer values of the turbulent Prandtl number from this plot would not be conclusive, owing to the ragged profiles of α_t in the core flow region. Again, there is no clear picture on the exact dependence of α_t on Pr away from the interface.

The limiting behavior of the thermal diffusivity in the vicinity of the deformable interface is presented in Fig. 12(b), where the turbulent diffusivity for momentum is also included. For Pr=1 both α_t and ν_t vary with z^{+3}, as in wall flows. This again lends support to the hypothesis that the interface appears to the lighter phase like a wall. On the other hand, the result confirms the analogy between the diffusivities of momentum and heat for Pr=1.

However, at the same time it is noted that the slope of $\alpha_t / z^{+n}(n>3)$ increases with Pr as the interface is approached. This result suggests that $\alpha_t \sim z^{+3}$ cannot be justifiably generalized. The results of Na et al. [7] reveal the existence of a conductive layer at the wall, where α_t / z^{+3} appears to be constant, although it is decreasing with increasing Pr.

In summary, deformable, sheared interfaces populated by capillary waves with small wavelength play a similar role in heat transfer as solid walls. In particular, the near-interface limiting behavior is such that the normal velocity varies quadratically with the distance to the interface, and therefore the shear stress $\overline{u^+ w^+}$ and the heat flux $\overline{w^+ \theta^+}$ vary with z^{+3}. The scaling for α_t is, however, strongly tied to the Prandtl number, in that the variation with z^{+3} holds only for Pr=1. For Pr=5 and 10, on the other hand, the variation is proportional to z^{+n}, where $n>3$.

4 Concluding Remarks

Turbulent heat transfer across a mobile, sheared gas-liquid interface has been studied using direct numerical simulation. The purpose of the investigation was to examine the impact of the interfacial dynamics on turbulent heat transfer, and to investigate the influence of the Prandtl number on the transports by comparing the results to existing wall flow data. The motivation arose from the fact that investigations dealing with turbulent scalar transfer have focused on simple configurations involving rigid, flat surfaces, while in multicomponent systems the flow necessarily involves interfaces that are neither flat nor rigid.

The flow system studied comprises counter-flowing gas and liquid phases, each at a shear-based Reynolds number of 171. The interface deformations were limited to capillary-wave ripples with waveslope $ak=0.01$. Since, for high density ratios, interfaces play a role similar to that of a solid boundary, emphasis has been placed on the gas side. For both Pr=1 and Pr=5 the flux intensity near the deformable interface was found to be higher than at the wall. This implies that the interfacial dynamics leads to an increase in the vertical THF as compared to its value near the rigid wall. The explanation for this difference is that the waves enhance the velocity fluctuating field normal to the interface, as was revealed in [15]. The effect of Prandtl number (Pr=1, 5, and 10) on the averaged heat flux, the temperature variance, the eddy diffusivity, and the heat transfer scaling laws has been examined.

The changes in Pr were indeed found to affect the average results, but in very much the same way as in available wall flow data. This was particularly true for the way the thickness of the diffusive sublayer reduces with increasing Pr, and in reference to the induced influence on the production of heat flux and variance. It was also noticed that the pressure diffusion and dissipation contributions to the normal heat flux balance change with varying Prandtl number. The most relevant statistical quantities were found to scale with the friction velocity. This is an important result, since the capillary waves are expected to modify the local rate of heat transfer only through a reduction of the frictional drag in favor of form drag. This tendency accentuates with increasing waveslope caused by increasing u_*. In the present case, the imposed shear velocity at the beginning of the computations led to a ratio of frictional drag to total drag (including form drag) of 0.98.

Another important result is the appreciable effect of Pr on $\overline{\theta^{+2}}$, and also on the thermal time scale $\tau_\theta \equiv \overline{\theta^{+2}}/\epsilon_0$ (results not included), indicating that the range of spectral functions for the thermal fluctuating field increases with Pr.

The scaling law for the normalized heat transfer velocity K^+ on the gas side suggests an approximate $Pr^{-3/5}$ relationship, varying between $Pr^{-1/2}$ for free surfaces and $Pr^{-2/3}$ for immobile interfaces and much higher Prandtl numbers. The parameterization of the heat transfer rates based on the surface renewal theory delivers values for the constant of proportionality and the Pr-power that conform with both the Leveque and the Polhausens boundary layer solutions. A close inspection of the transfer rates reveals a strong and consistent relationship between the transfer rate, the frequency of sweeps impacting the interface, the interfacial velocity streaks, and the interfacial shear stress. Similarly to what is observed in wall flows, for Pr=1 the turbulent viscosity/diffusivity was found to asymptote with z^{+3}. For higher Pr, however, the scaling was seen to change to z^{+n}, with $n>3$. In the viscosity-affected layer the assumption that $\alpha_t \sim \nu_t$ was found to hold in this context, too, whereas in the outer core flow, α_t was greater than ν_t, and no clear picture emerged as to the distribution of the turbulent Prandtl number.

The present study has addressed only some of the many issues of this complex problem. It would be intriguing to see how statistical quantities scale with higher imposed shear velocities, i.e., in the presence of higher amplitude waves.

References

[1] Komori, S., Nagaosa, R., and Murakami, Y., 1993, "Turbulence Structure and Mass Transfer Across a Sheared Air-Water Interface in Wind-Driven Turbulence," J. Fluid Mech., **249**, p. 161.

[2] Rashidi, M., Hetsroni, G., and Banerjee, S., 1992, "Wave-Turbulence Interaction in Free-Surface Channel Flows," Phys. Fluids A, **4**, p. 2727.

[3] Danckwerts, P. V., 1951, "Significance of Liquid Film Coefficients in Gas Absorption," Ind. Eng. Chem., **43**, p. 1460.

[4] Kasagi, N., Tomita, Y., and Kuroda, A., 1992, "Direct Numerical Simulation of Passive Scalar Field in a Turbulent Channel Flow," ASME J. Heat Transfer, **114**, p. 598.

[5] Kawamura, H., Ohsake, K., Abe, H., and Yamamoto, K., 1998, "DNS of Turbulent Heat Transfer in Channel Flow With Low to Medium-High Prandtl Number," Int. J. Heat Fluid Flow, **19**, p. 482.

[6] Lyons, S. L., Hanratty, T. J., and McLaughlin, J. B., 1991, "Large-Scale Computer Simulation of Fully Developed Turbulent Channel Flow With Heat Transfer," Int. J. Numer. Methods Fluids, **13**, p. 999.

[7] Na, Y., Papavassiliou, D. V., and Hanratty, T. J., 1999, "Use of Direct Numerical Simulation to Study the Effect of Prandtl Number on Temperature Fields," Int. J. Heat Fluid Flow, **20**, p. 187.

[8] Campbell, J. A., and Hanratty, T. J., 1983, "Mechanisms of Turbulent Mass Transfer at Solid Boundaries," AIChE J., **29**, p. 221.

[9] McCready, M. J., Vassiliadou, E., and Hanratty, T. J., 1986, "Computer Simulation of Turbulent Mass Transfer at a Mobile Interface," AIChE J., **32**, p. 1108.

[10] Calmet, I., and Magnaudet, J., 1997, "Large-Eddy Simulation of High-Schmidt Number Mass Transfer in a Turbulent Channel Flow," Phys. Fluids, **9**, p. 438.

[11] Piller, M., Nobile, E., and Hanratty, T. J., 2002, "DNS Study of Turbulent Transport at Low Prandtl Numbers in a Channel Flow," J. Fluid Mech., **458**, p. 419.

[12] Lombardi, P., De Angelis, V., and Banerjee, S., 1996, "Direct Numerical Simulation of Near-Interface Turbulence in Coupled Gas-Liquid Flow," Phys. Fluids, **8**, p. 1643.

[13] De Angelis, V., Lombardi, P., and Banerjee, S., 1997, "Direct Numerical Simulation of Turbulent Flow Over a Wavy Wall," Phys. Fluids, **9**, p. 2429.

[14] De Angelis, V., Lombardi, P., Andreussi, P., and Banerjee, S., 1997, "Micro-Physiscs of Scalar Transfer at Air-Water Interfaces," in *Proceedings of Wind-Over-Wave Couplings: Perspectives and Prospects*, S. G. Sajjadi, N. H. Thomas, and J. C. R. Hunt, eds., Oxford University Press.

[15] Fulgosi, M., Lakehal, D., Banerjee, S., and De Angelis, V., 2003, "Direct Numerical Simulation of Turbulence in a Sheared Air-Water Flow With Deformable Interface," J. Fluid Mech., **482**, p. 319.

[16] Delhaye, J. M., 1974, "Jump Conditions and Entropy Sources in Two-Phase Systems. Local Instant Formulation," Int. J. Multiphase Flow, **1**, p. 305.

[17] Lakehal, D., Meier, M., and Fulgosi, M., 2002, "Interface Tracking Towards the Direct Simulation of Heat and Mass Transfer in Multiphase Flows," Int. J. Heat Fluid Flow, **23**, p. 242.

[18] Temam, R., 1979, *Navier-Stokes Equations*, North-Holland, Amsterdam.

[19] Tiselj, I., Bergant, R., Mavko, B., Bajsic, I., and Hetsroni, G., 2001, "DNS of Turbulent Heat Transfer in Channel Flow With Heat Conduction in the Solid Wall," ASME J. Heat Transfer, **123**, p. 849.

[20] Phillips, O. M., 1997, *The Dynamics of the Upper Ocean*, Cambridge University Press, Cambridge, UK.

[21] Tiselj, I., Pogrebnyak, E., Li, C., Mosyak, A., and Hetsroni, G., 2001, "Effect of Wall Boundary Condition on Scalar Transfer in a Fully Developed Turbulent Flume," Phys. Fluids, **13**(4), p. 1028.

[22] Papavassiliou, D. V., and Hanratty, T. J., 1997, "Transport of a Passive Scalar in a Turbulent Channel Flow," Int. J. Heat Mass Transfer, **40**, p. 1303.

[23] Banerjee, S., 1971, "A Note on Turbulent Mass Transfer at High Schmidt Numbers," Chem. Eng. Sci., **26**, p. 989.

[24] Lam, K., and Banerjee, S., 1992, "On the Condition of Streaks Formation in a Bounded Turbulent Flow," Phys. Fluids A, **4**, p. 306.

[25] Nagano, Y., 2002, "Modelling Heat Transfer in Near-Wall Flows," in *Closure Strategies for Turbulent and Transitional Flows*, B. Launder and N. Sandham, eds., Cambridge University Press.

Heat Transfer Characteristics of a Pair of Impinging Rectangular Flame Jets

L. L. Dong[1]

C. W. Leung

C. S. Cheung

Department of Mechanical Engineering,
The Hong Kong Polytechnic University,
Hung Hom, Kowloon, Hong Kong

Experiments were carried out to study the heat transfer characteristics of a pair of premixed, laminar, rectangular, butane/air flame jets impinging vertically upon a water-cooled flat plate. The effects of jet-to-jet spacing and the nozzle-to-plate distance on heat transfer were examined. The Reynolds number of the exit flow was 800. The non-dimensional jet-to-jet spacing ranged from 0.9 to 4.1, while the non-dimensional nozzle-to-plate distance varied from 1 to 6. The between-jet interference decreased with increasing jet-to-jet spacing and nozzle-to-plate distance. Both the maximum local and average heat flux occurred at a moderate jet-to-jet spacing of twice effective nozzle diameter, and when the nozzle-to-plate distance was equal to the effective diameter of the nozzle. The heat flux decreased faster along the shorter sides of the slot jets than the longer sides.
[DOI: 10.1115/1.1621901]

Keywords: Combustion, Flame, Heat Transfer, Impingement, Jets

Introduction

Multiple impinging jets have been used widely in industrial and domestic applications. The flow structures and heat transfer characteristics of multiple isothermal air jets have been studied extensively [1–4]. However, little information is available on multiple impinging flame jets, especially rectangular jets, despite their popularity in application. In order to provide fundamental understanding of the heat transfer characteristics, experimental studies of a pair of rectangular flame jets were carried out in the present study.

Mikhail et al. [5] investigated a pair of laminar impinging slot air jets numerically. They found that a recirculation zone was formed where the two adjacent spreading wall jets were facing with each other and were forced to turn downwards due to the positive pressure around the between-jet midpoint, which led to the separation and recirculation of the wall jets. Thus vortex was formed and characterized by high-level turbulence. This turbulence was found to enhance the heat transfer coefficient on the impingement surface around the midpoint between the jets. They also found that the average heat flux was considerably enhanced by reducing the between-jet spacing. Laschefski et al. [6] attributed the increase of the heat transfer coefficient at the between-jet midpoint to the thinning of the boundary layer with strong fluctuations caused by the collision of the adjacent wall jets. Tanaka et al. [7,8] also found the positive pressure region around the midpoint after the collision of the two air jets. In comparison to the numerous studies on the multiple impinging air jets, very little research has been carried out to study the multiple impinging flame jets. The previous investigations have been focused on the fluid flow and heat transfer characteristics of single circular or rectangular impinging flame jet [9–13]. However, using information for a single jet to design a multiple-jet system is usually not valid, due to the influence of the between-jet interaction, which could change the flow and heat transfer behavior of each jet in the system [14]. The available information on multiple impinging flame jets was related to the study of radial jet reattachment flames and the multi-jets used in the rapid heating furnace. Mohr

et al. [15] and Wu et al. [16] investigated the effects of the between-jet spacing and nozzle-to-plate distance on flame structure and heat transfer characteristics of a row of two and three radial flame jets. Malikov et al. [17] studied the heat transfer in a rapid heating furnace with a multi-jet combustion chamber. Dong et al. [18] studied the heat transfer characteristics of a row of three circular in-line flame jets. However, there is a lack of information on multiple impinging rectangular flame jets, although they are widely used in many domestic applications. Therefore, the present study was motivated to examine the heat transfer characteristics of a pair of impinging rectangular flame jets.
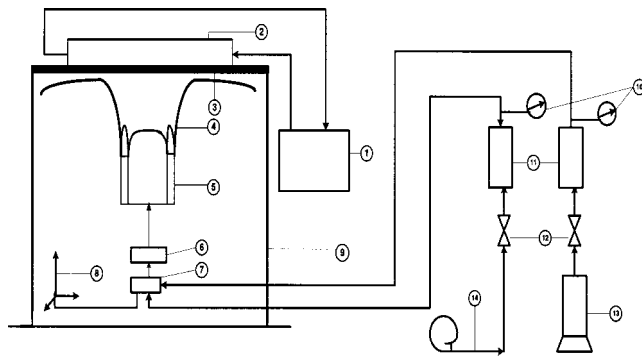
Experimental Method and Error Analysis

Experiments were performed to investigate the effects of non-dimensional nozzle-to-plate distance (i.e., H/d_e) and jet-to-jet spacing (i.e., S/d_e) on the heat transfer characteristics of a pair of impinging rectangular flame jets. The H/d_e ratio was selected from 1 to 6. The S/d_e ratio was varied from 0.9 to 4.1 to cover small, moderate and large spacings. The jet exit Reynolds number was fixed at 800 to ensure laminar flames. All the tests were preformed at stoichiometric condition.

The flame jet impingement system was composed of two parts: the heat generation system and the heat absorption system, as shown schematically in Fig. 1. The flame holders were two identical rectangular brass tubes and each of them had large and small side lengths of 9 mm and 3 mm, respectively. Metered butane and compressed air were premixed in a brass cylinder, before entering the cylindrical aluminum equalization chamber via a 200 mm long stainless steel tube. The equalization chamber was filled with stainless steel beads to produce uniform flow and prevent the flame from flashing back. The fuel/air mixture then entered the flame holder with a pre-determined equivalence ratio, and was ignited and stabilized at the tube rim. The internal surfaces of the brass tubes were polished to smoothen the exit velocity profile. The three-dimensional positioner enabled each of the attached burners to be fixed at a desired position relative to the impingement surface.

The flame impingement surface was a rectangular copper plate 200 mm long, 200 mm wide and 8 mm thick. It was uniformly cooled on its backside by a cooling water jacket. Copper was selected because of its high thermal conductivity. The top plate of the cooling water jacket was made of plexiglass to enable a view of the water flow. A stainless steel frame was used to support the

Copyright © 2003 by ASME

1. Thermostat
2. Cooling Water Jacket
3. Impingement Plate
4. Flame Jet
5. Nozzle
6. Equilizating Chamber
7. Premixed Chamber

8. 3-D Positioner
9. Angle Steel Holder
10. Pressure Gauge
11. Flow Meter
12. Valve
13. Fuel Tank
14. Compressed Air Line

Fig. 1 Coordinate system of the impingement plate

Fig. 2 Coordinate system of the impingement plate

copper plate and the cooling water jacket, so that the plate could be placed either horizontally or tilted at a selected angle relative to the burner. After a change in the operating condition, measurements were only made after the steady-state condition had been established again and exit temperature of the cooling water had been stabilized.

The local heat flux from the flame to the plate was measured with a small ceramic heat flux transducer having an effective sensing area of 3 mm$\times$3 mm. It was attached directly to the copper plate. The heat flux distributions in the x and y-directions were measured by moving the three-dimensional burner positioner as mentioned previously.

A PC-acquisition system was used to record the heat flux. Every data reported here was the average value of the data obtained consecutively in 30 seconds at a rate of 500 samples/second. Shapes of flame had also been recorded with a digital camera to facilitate a better understanding.

An error analysis was performed with the method proposed by Kline and McClintock [19]. Using a 95 percent confidence level, the maximum and minimum uncertainties of the presented local heat flux were 13.3 percent and 3.4 percent, respectively. Three tests with identical operating conditions were conducted. The data were then averaged to give the final result. The maximum and the minimum deviation in the heat flux value from the averaged value were 13.2 percent and 1.7 percent, respectively.

Results and Discussions

Effects of S/d_e and H/d_e ratios on flame shape and heat transfer rate of the twin rectangular jets were examined. The coordinate system of the test rig was shown in Fig. 2.

Flame Shape. Photographs of impinging flame jets with small, moderate and large jet-to-jet spacings, i.e., $S/d_e=0.9$, 2, 4.1, under small, moderate and large H/d_e ratios of 1, 2, and 6 were shown from Figs. 3–5. All the flames under investigation were laminar, with each of them having a thin blue inner cone and a light blue outer layer. However, the impinging flame shapes were varied due to the different between-jet interference, which resulted from the variation in S/d_e and H/d_e ratios.

It could be clearly observed from Figs. 3(a) to 3(c) that at a small S/d_e ratio of 0.9, only two flame outer layers, rather than four, were found. This is because the two flame jets have merged into one big jet before impingement due to the strong between-jet interference, as clearly shown in Fig. 3(c). It is known that the impinging jet can entrain the surrounding fluid after exiting from the nozzle. Therefore, a sub-atmospheric pressure region is pro-
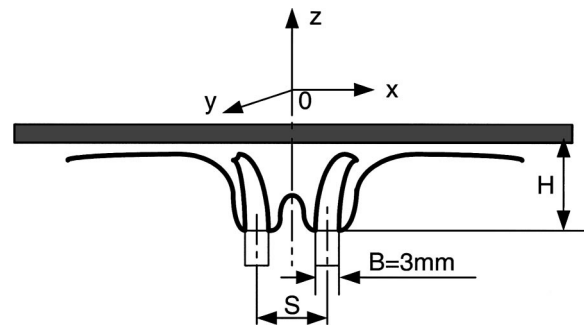
duced, which causes the neighboring jets to attract each other. When the S/d_e ratio is small, the between-jet entrainment is strong enough to cause the mergence of the two adjacent jets. It was found from Fig. 3(a) that under a small H/d_e ratio of 1, the inner cone reached the impingement plate and was deformed. Shape of the flame cross-section was no longer a quasi-isosceles triangle. The inner cone tip was not in-line with the nozzle axis, but shifted further outwards. This is due to the strong between-jet interference obtained under the small S/d_e ratio. It has been found that the third stagnation point (the first and the second stagnation points are around impingement midpoint of each jet, respectively) formed in the midway of the neighboring jets in a two-jet impingement system [20,21]. Because of the presence of this additional stagnation point, the flame jets in the interacting side encountered a negative pressure gradient when they spread radially. Therefore, the flames in the interacting side were pushed outwards to deform. As the H/d_e ratio was increased to 2, deformation of the inner cone was not as significant as that under $H/d_e=1$. When the H/d_e ratio was further increased to 6, this deformation was decreased further accordingly. The flame shapes along the y-axis were shown in Figs. 3(d) to 3(f). It was found that shape of the inner cone layer was quasi-trapezoid. No flame tip was found. This is formed under the effects of the uniform jet exit velocity profile and a longer side length in the y-direction.

When the between-jet spacing was a moderate value of $S/d_e=2$, the between-jet interference was reduced due to the increased spacing. No evident deformation of the inner cone was found, as shown in Figs. 4(a) to (c). Under the small H/d_e ratio of 1, the between-jet interference caused the outer flame layers in the interacting side to turn downwards after colliding with each other at the between-jet midpoint. When the H/d_e ratio was increased to two, such deformation of the outer flame layers was no longer found, and they merged with each other before impingement. When the H/d_e ratio was further increased to 6, the two jets looked like two separate single jets, and no deformation was found before and after impingement.

As the S/d_e ratio was further increased to 4.1, flame deformation due to the between-jet interference was very small for both under H/d_e ratios of 1 and 2, as shown in Figs. 5(a) and (b). The flame outer layers were just touching each other at the midpoint in the interacting side, which produced a slightly downward flow.

Heat Transfer Characteristics

The detailed heat transfer results were obtained under different S/d_e and H/d_e ratios. Their effects on the heat transfer characteristics of the twin rectangular flame jets were presented and discussed as below.

Effects of S/d_e Ratio. The effect of S/d_e ratio on the local heat flux distribution under small H/d_e ratio of 1 was shown in Fig. 6. It was found from Fig. 6(a) that a decrease of heat flux occurred around the mid-line of $x/d_e=0$. Apart from this, the value of heat flux decreased gradually from the maximum value as the x/d_e and y/d_e ratios were increased, which was also clearly
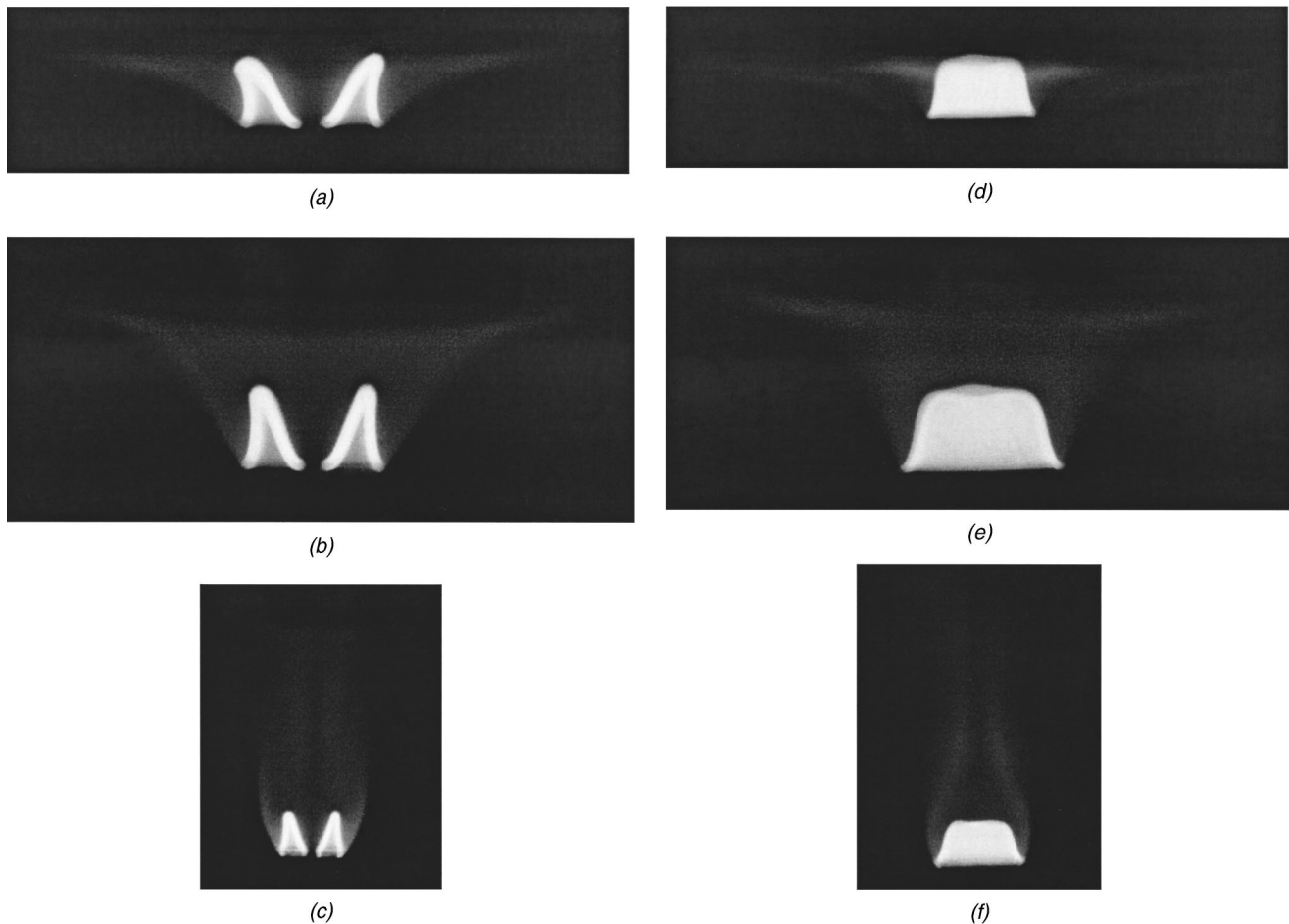
Fig. 3 (*a*) Photographs of impinging flame jets along the *x*-axis (Re=800; S/d_e=0.9; H/d_e=1; ϕ=1); (*b*) Photographs of imping-ing flame jets along the *x*-axis (Re=800; S/d_e=0.9; H/d_e=2; ϕ=1); (*c*) Photographs of impinging flame jets along the *x*-axis (Re=800; S/d_e=0.9; H/d_e=6; ϕ=1); (*d*) Photographs of impinging flame jets along the *y*-axis (Re=800; S/d_e=0.9; H/d_e=1; ϕ=1); (*e*) Photographs of impinging flame jets along the *y*-axis (Re=800; S/d_e=0.9; H/d_e=2; ϕ=1); and (*f*) Photographs of impinging flame jets along the y-axis (Re=800; S/d_e=0.9; H/d_e=6; ϕ=1).

shown in Fig. 6(*a*). Considering the quasi-symmetric distribution of the heat flux, further discussion was based on the right half of the heat flux contour in Fig. 6(*b*). It was found that the maximum heat flux occurred at the area between x/d_e=0.45 and 0.7, and the y/d_e ratio ranging from −0.8 to 0.8. Referring to the flame shape as shown in Fig. 3(*a*), it was found that this area is where the tip of the flame inner cone was just touching the impingement plate. This indicated that occurrence of the highest heat flux is related to the impingement of the flame inner cone with very high tempera-tures. It was also found from Fig. 6(*a*) that heat flux decreases faster at *y*-axis than at *x*-axis. This is due to more flow exiting from *x*-direction than *y*-direction [22].

As the S/d_e ratio was increased to 2, similar heat transfer char-acteristics were found as those obtained at S/d_e=0.9. The maxi-mum heat flux occurred at the area around x/d_e=1, as shown in Fig. 6(*b*), which is around the intersection of the jet axis and the impingement plate (i.e., the stagnation point of the flame jet). The heat flux contour generally exhibited a quasi-elliptic shape, with the heat flux decreasing more rapidly in *y*-axis than *x*-axis. When the S/d_e ratio was further increased to 4.1, the maximum heat flux occurred at the area around x/d_e=2.05, as shown in Fig. 6(*c*), which is also around the stagnation point. It was also found that the heat flux decreased slowly in the interacting side than the non-interacting side, which indicated that the between-jet interfer-ence induced turbulence enhanced the heat transfer rate.

Heat flux distributions along the streamwise axis (i.e., the *x*-axis) at different S/d_e ratios under the H/d_e ratios of 1, 2, and 4, were shown in Fig. 7. It was observed that the highest heat flux occurred at S/d_e=2 under H/d_e=1. This was the situation where moderate between-jet interference was induced, while the inner flame cone with high temperature just touched the impingement plate. It was found from Fig. 7(*a*) that in the interacting region, the heat fluxes were lower at S/d_e=0.9 than those at S/d_e=2. This indicated that the strong between-jet interference induced by the small between-jet spacing of $0.9d_e$ hindered the complete combustion, such that the heat transfer rate was decreased. It could also be found from Figs. 7(*a*) to 7(*c*) that after the maxi-mum heat flux was occurred, the decrease in heat flux gradient was smaller in the interacting side than in the non-interacting side. This is due to the enhanced convective heat transfer coefficient in the interacting side caused by the between-jet interference induced turbulence.

Effect of H/d_e Ratio. Comparison of the heat flux distribu-tions along *x*-axis under different H/d_e ratios with small, moder-ate and large S/d_e ratios of 0.9, 2, and 4.1, were shown in Fig. 8. It was found from Figs. 8(*a*) to 8(*c*) that for all the S/d_e ratios from 0.9 to 4.1, the heat flux increased generally with decreasing H/d_e ratio. There was a considerable increase in the heat fluxes in the interacting side when H/d_e ratio reduced from 2 to 1. This indicated that the optimal nozzle-to-plate distance was the flame inner cone length in terms of increasing heat transfer. As further increasing H/d_e ratio greater than 1, the temperatures of the flame
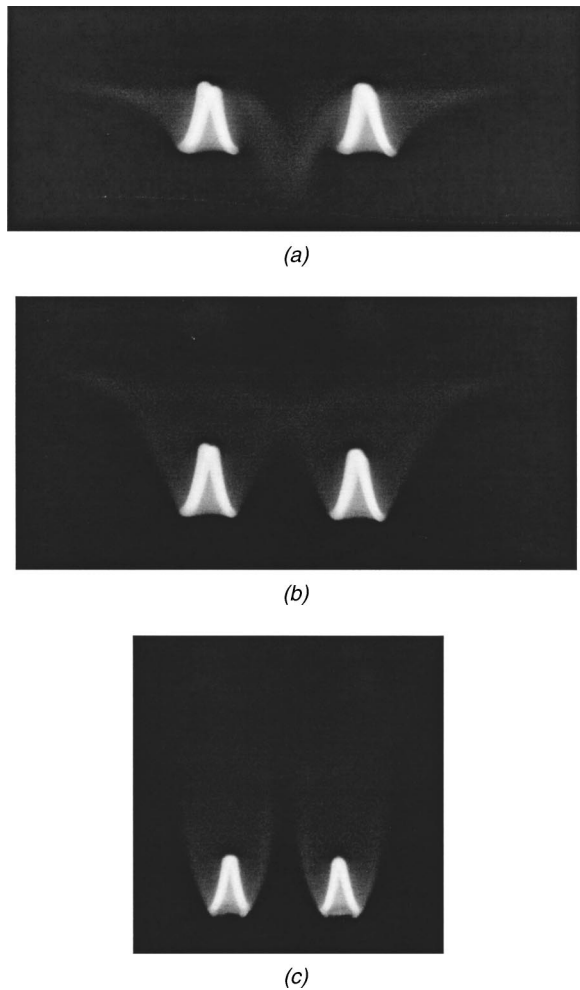
(a)

(b)

(c)

Fig. 4 (*a*) **Photographs of impinging flame jets along the *x*-axis (Re=800; *S*/*d*$_e$=2; *H*/*d*$_e$=1; ϕ=1); (*b*) Photographs of impinging flame jets along the *x*-axis (Re=800; *S*/*d*$_e$=2; *H*/*d*$_e$=2; ϕ=1); and (*c*) Photographs of impinging flame jets along the *x*-axis (Re=800; *S*/*d*$_e$=2; *H*/*d*$_e$=6; ϕ=1).**

(a)

(b)

Fig. 5 (*a*) **Photographs of impinging flame jets along the *x*-axis (Re=800; *S*/*d*$_e$=4.1; *H*/*d*$_e$=1; ϕ=1); and (*b*) Photographs of impinging flame jets along the *x*-axis (Re=800; *S*/*d*$_e$=4.1; *H*/*d*$_e$=2; ϕ=1).**

which contacted the plate decreased gradually when the nozzle was away from the impingement plate, and thus the heat fluxes decreased accordingly. This was because when $H/d_e > 1$, the part of flame which touched the plate was in the post-flame zone, where the temperatures decreased as increasing flame length, i.e., increasing nozzle-to-plate distance. It was also found that for $S/d_e = 0.9$, when $H/d_e \geqslant 4$, the maximum heat flux occurred at the midpoint. This was because at $S/d_e = 0.9$, the strong between-jet interference merged the two jets into one bigger jet before impingement, as shown in Fig. 3(*c*). Thus the relatively high temperature of the flame around the midpoint and the strong turbulence induced by the between-jet interference in this region resulted in the peak heat flux occurred at the midpoint. In other cases, such merging of the two jets before impingement was not occurred. The peak heat flux value was located around the stagnation point of each jet in these cases.

Average Heat Flux Distribution

The local heat fluxes along the streamwise (i.e., *x*-axis) and spanwise (i.e., *y*-axis) directions were integrated with trapezoid method to produce the average heat fluxes. The average heat flux distributions along the x and y-axes under different S/d_e and H/d_e ratios were shown in Fig. 9. It was found from Fig. 9(*a*) that the maximum average heat flux occurred at x-axis when $S/d_e = 2$ and $H/d_e = 1$, which was also the condition where the maximum local
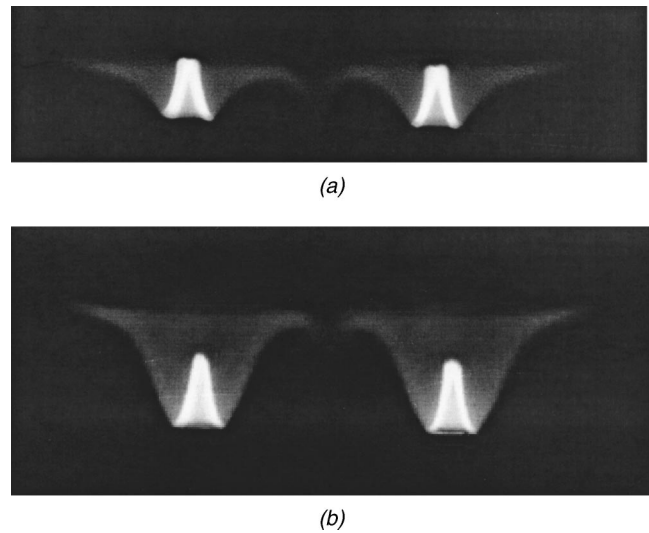
heat flux occurred, as discussed previously. When $S/d_e = 0.9$, the average heat fluxes along the x and *y*-axes were of similar values when $H/d_e = 1$. Then with further increasing H/d_e ratio, the average heat flux along *y*-axis was higher than that along *x*-axis. When $S/d_e = 4.1$, the average heat flux along the *x*-axis was always larger than that along the y-axis. While for a moderate S/d_e ratio of 2, the average heat fluxes along *x* and *y*-axes were close to each other in quantity. This indicated that moderate between-jet spacing characterized the uniform heating capacity. Figure 9(*b*) showed the heat fluxes averaged over the *x* and *y*-axes. It was found that the peak value still occurred when $S/d_e = 2$, and $H/d_e = 1$. When the value of H/d_e exceeded 2, the average heat flux increased with decreasing S/d_e ratio.

Comparison With Single Jet

To help understand better the influence of the between-jet interference on heat transfer enhancement in the two-jet impingement system, Comparison of the stagnation point heat flux of each jet in the two-jet impingement system was made with those of a single jet obtained with both experimental and semi-analytical methods. The comparison was shown in Fig. 10.

Considering an uniform flow of infinite extent impinging on a body of revolution, where the flow only changed in the boundary layer, the semi-analytical solution of heat transfer from the flow to the forward stagnation of the revolution body has been obtained by Sibulkin [23], which was shown as follows:

$$\dot{q}_s = 0.763(\beta_s \rho_e \mu_e)^{0.5} \mathrm{Pr}_e^{-0.6} C_{p_e}(T_e - T_w) \qquad (1)$$

β_s was obtained using the potential flow solution for flow normal to a disk according to van der Meer [24]:

$$\beta_s = 4u/\pi D_b \qquad (2)$$

It was observed from Fig. 10 that for all the H/d_e ratios varied from 1 to 6, the stagnation point heat fluxes in the two-jet array impingement system were significantly enhanced comparing with those obtained in a single-jet system. The stagnation point heat fluxes obtained with the semi-analytical method were lower than those from experiments. This is because in Sibulkin's solution, the Lewis number was kept unity. However, in the practical flame impingement system, the flame will dissociate when the temperature is high, e.g., in the area around the flame inner cone. When these dissociated species impinge on the cold plate, they will re-
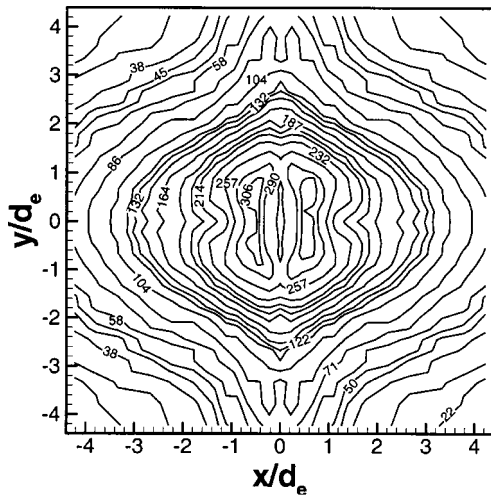
(a)
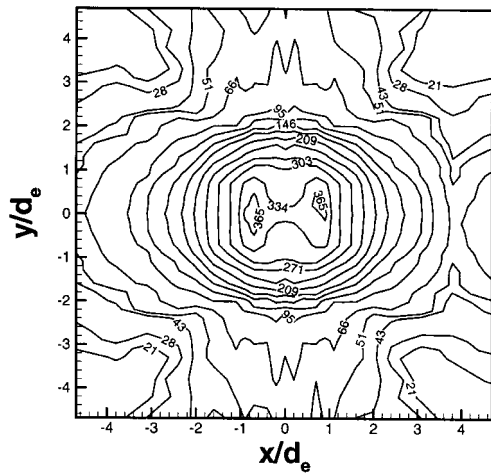
(b)
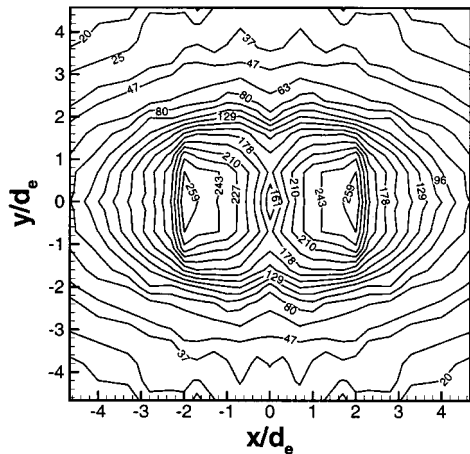
(c)

Fig. 6 (*a*) Heat flux contour at Re=800, S/d_e=0.9, H/d_e=1 and ϕ=1; (*b*) Heat flux contour at Re=800, S/d_e=2, H/d_e=1 and ϕ=1; and (*c*) Heat flux contour at Re=800, S/d_e=4.1, H/d_e=1 and ϕ=1.

(a)

(b)

(c)

Fig. 7 Effect of S/d_e on heat flux distribution along the *x*-axis

combine into stable molecules releasing heat energy, and thus enhances the convective heat transfer from the flame to the impingement plate. This deviation between the experimental and semi-analytical results became larger when the dissociation-recombination effect was more significant, as shown in Fig. 10, where the largest deviation occurred under $H/d=1$. Under this condition the flame reaction zone just touched the cold impingement plate, and the large temperature difference between them caused the dissociation-recombination effect to be more significant.

Conclusions

Effects of the S/d_e and H/d_e ratios on heat transfer characteristics of a pair of impinging rectangular flame jets had been examined in the present study. It was found that the between-jet

(a)

(b)

(c)

Fig. 8   Effect of H/d_e on heat flux distribution along the x-axis

(a)

(b)
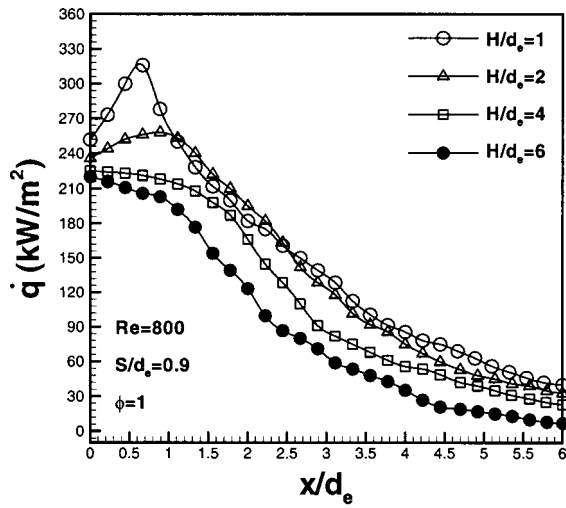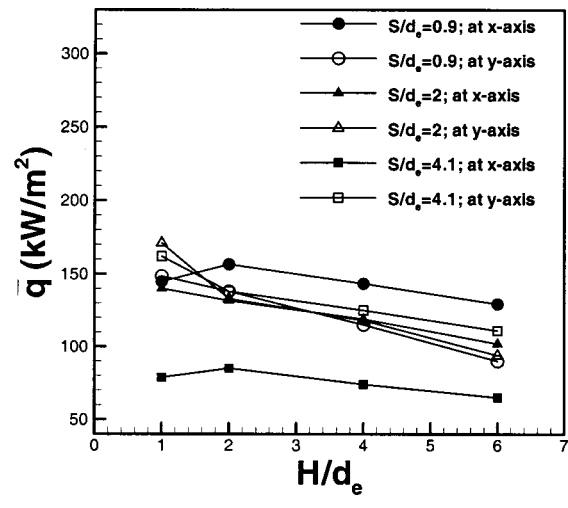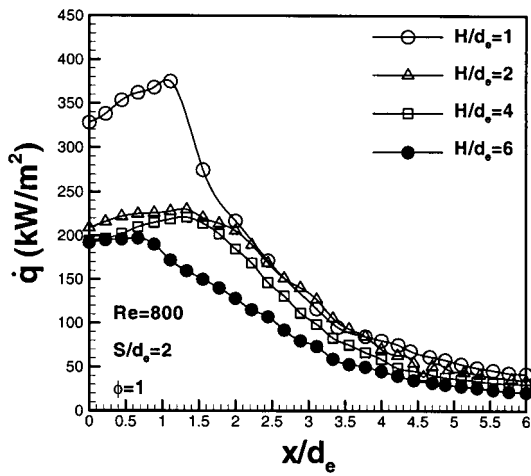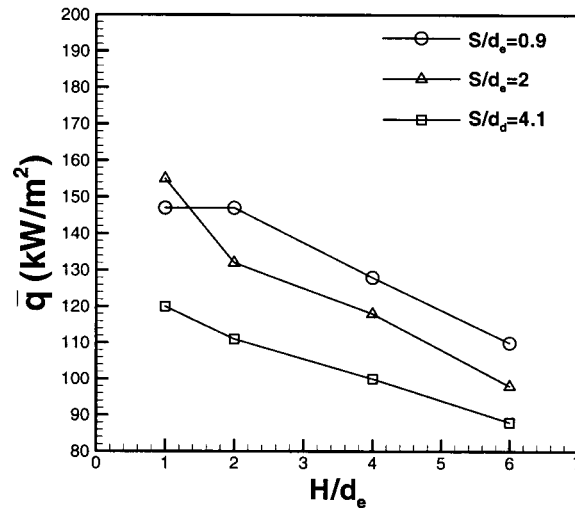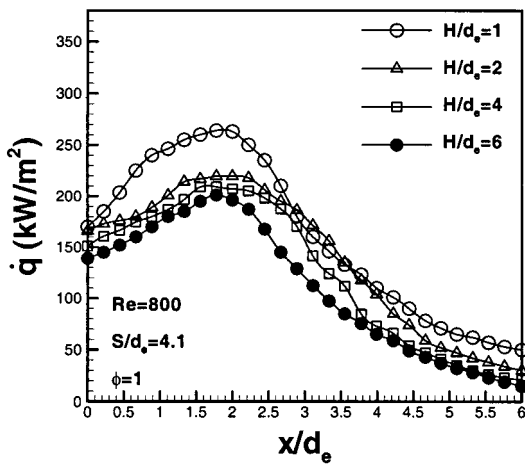
Fig. 9   Comparison of average heat fluxes at x and y axes

Fig. 10   Comparison of stagnation point heat flux with single jet at Re=800

interference decreased with increasing S/d_e and H/d_e ratios. Both the maximum local heat fluxes and maximum average heat fluxes were obtained at a moderate S/d_e ratio of 2 with a moderate between-jet interference, and when $H/d_e = 1$, where the high temperature inner cone of the flame was just reaching the impingement plate. The small S/d_e ratio could induce such strong

between-jet interference as to deform the inner reaction cone of the flame and thus hinder the complete combustion and reduce the heat transfer rate. For all the flames investigated, the heat flux was found to decrease with increasing H/d_e ratio from 1 to 6. Moderate S/d_e ratio of 2 could produce more uniform heating over the streamwise and spanwise directions.

Acknowledgment

Nomenclature

B = rectangular nozzle width (m)
C_P = specific heat of fluid (J/(Kg K))
D = diameter (m)
d_e = effective nozzle exit diameter (m) ($d_e = (4BL/\pi)^{1/2}$)
H = distance between the nozzle and the impingement plate (m)
L = rectangular nozzle length (m)
Pr = Prandtl number
$\dot{q}$ = local heat flux density (W/m^2)
$\bar{q}$ = average heat flux density (W/m^2)
r = radial distance from midpoint of the two nozzles (m)
Re = Reynolds number ($= u_{out}d_e/\nu$)
S = distance between the centers of the two nozzles (m)
T = temperature (K)
u = velocity of butane/air mixture (m/s)
v = flame velocity near the stagnation point (m/s)
x = central streamline (m)
y = central spanwise line (m)

Greek Symbols

ρ = gas density (kg/m^3)
μ = dynamic viscosity (kg/m.s)
ν = kinematic viscosity (m^2/s)
ϕ = equivalence ratio (=(stoichiometric air/fuel volume ratio)/(actual air/fuel volume ratio))
β = the velocity gradient near the stagnation point ($= (dv/dr)_{r\to 0}$)

Subscripts

b = stagnation body or target
f = for the flame jet
out = at the nozzle exit
p = at the impingement plate
s = at the stagnation point

References

[1] Koopman, R. N., and Sparrow, E. M., 1976, "Local and Average Transfer Coefficients Due to an Impinging Row of Jets," Int. J. Heat Mass Transfer, **19**, pp. 673–683.
[2] Saad, N. R., Polat, S., and Douglas, W. J. M., 1992, "Confined Multiple Impinging Slot Jets Without Crossflow Effects," Int. J. Heat Fluid Flow, **13**, pp. 2–14.
[3] Martin, H., 1977, "Heat and Mass Transfer Between Impinging Gas Jets and Solid Surfaces," Adv. Heat Transfer, **13**, pp. 1–60.
[4] Polat, S., Huang, B., Mujumdar, A. S., and Douglas, W. J. M., 1989, "Numerical Flow and Heat Transfer Under Impinging Jets: A Review," Annu. Rev. Numer. Fluid Mech. Heat Transfer, **2**, pp. 157–197.
[5] Mikhail, S., Morcos, S. M., Abou-Ellail, M. M. M., and Ghaly, W. S., 1982, "Numerical Prediction of Flow Field and Heat Transfer From a Row of Laminar Slot Jets Impinging on a Flat Plate," Heat Transfer, **3**, pp. 377–382.
[6] Laschefski, H., Cziesla, T., Biswas, G., and Mitra, N. K., 1996, "Numerical Investigation of Heat Transfer by Rows of Rectangular Impinging Jets," Numer. Heat Transfer, Part A, **30**, pp. 87–101.
[7] Tanaka, E., 1970, "The Interference of Two-Dimensional Parallel Jets (First Report, Experiments on Dual Jet)," Bull. JSME, **13**, pp. 272–280.
[8] Tanaka, E., 1974, "The Interference of Two-Dimensional Parallel Jets (Second Reports, Experiments on the Combined Flow of Dual Jet)," Bull. JSME, **17**, pp. 920–927.
[9] Baukal, C. E., and Gebhart, B., 1997, "Surface Condition Effects on Flame Impingement Heat Transfer," Exp. Therm. Fluid Sci., **15**, pp. 323–335.
[10] Hargrave, G. K., Fairweather, M., and Kilham, J. K., 1987, "Forced Convective Heat Transfer From Premixed Flames—Part 1: Flame Structure," Int. J. Heat Fluid Flow, **8**, pp. 55–63.
[11] Hargrave, G. K., Fairweather, M., and Kilham, J. K., 1987, "Forced Convective Heat Transfer From Premixed Flames—Part 2: Impingement Heat Transfer," Int. J. Heat Fluid Flow, **8**, pp. 132–138.
[12] Viskanta, R., 1993, "Heat Transfer to Impinging Isothermal Gas and Flame Jets," Exp. Therm. Fluid Sci., **6**, pp. 111–134.
[13] Viskanta, R., 1998, "Convective and Radiative Flame Jet Impingement Heat Transfer," Int. J. Transport Phenomena, **1**, pp. 1–15.
[14] Saad, N. R., Polat, S., and Douglas, W. J. M., 1992, "Confined Multiple Impinging Slot Jets Without Crossflow Effects," Int. J. Heat Fluid Flow, **13**, pp. 2–14.
[15] Mohr, J. W., Seyed-Yagoobi, J., and Page, R. H., 1997, "Heat Transfer From a Pair of Radial Jet Reattachment Flames," ASME J. Heat Transfer, **119**, pp. 633–635.
[16] Wu, J., Seyed-Yagoobi, J., and Page, R. H., 2001, "Heat Transfer and Combustion Characteristics of an Array of Radial Jet Reattachment Flames," Combust. Flame, **125**, pp. 955–964.
[17] Malikov, G. K., Lobanov, D. L., Malikov, Y. K., Lisienko, V. G., Viskanta, R., and Fedorov, A. G., 1999, "Experimental and Numerical Study of Heat Transfer in a Flame Jet Impingement System," J. Inst. Energy, **72**, pp. 2–9.
[18] Dong, L. L., Leung, C. W., and Cheung, C. S., 2003, "Heat Transfer of a Row of Three Butane/Air Flame Jets Impinging on a Flat Plate," Int. J. Heat Mass Transfer, **46**, pp. 113–125.
[19] Kline, S. J., and McClintock, F. A., 1953, "Describing Uncertainties in Single Sample Experiments," Mech. Eng. (Am. Soc. Mech. Eng.), **75**, pp. 3–8.
[20] Baydar, E., 1999, "Confined Impinging Air Jet at Low Reynolds Numbers," Exp. Therm. Fluid Sci., **19**, pp. 27–33.
[21] Huber, A. M., 1993, "Heat Transfer With Impinging Gaseous Jet Systems," Ph.D. thesis, Purdue University, West Lafayette, IN.
[22] Dong, L. L., Cheung, C. S., and Leung, C. W., 2002, "Heat Transfer From an Impinging Premixed Butane/Air Slot Flame Jet," Int. J. Heat Mass Transfer, **45**, pp. 979–992.
[23] Sibulkin, M., 1952, "Heat Transfer Near the Forward Stagnation Point at a Body of Revolution," J. Aeronaut. Sci., **19**, pp. 570–571.
[24] Van der Meer, Th. H., 1987, "Heat Transfer From Impinging Flame Jets," Ph.D. thesis, Delft University of Technology, Netherland.

Nanoparticles Formed in Picosecond Laser Argon Crystal Interaction

Xinwei Wang

e-mail: xwang3@unl.edu
Department of Mechanical Engineering,
N104 Walter Scott Engineering Center,
The University of Nebraska-Lincoln,
Lincoln, NE 68588-0656

Xianfan Xu

School of Mechanical Engineering,
Purdue University,
West Lafayette, IN 47907-1288

In this work, Molecular Dynamics simulations are conducted to attain thermal and mechanical characteristics of nanoparticles formed in laser materials interaction. It reveals that nanoparticles originate from intense vapor phase explosion. A gas-like structure is observed in nanoparticles in the initial stage of formation. After a short time of evolution, a typical liquid structure is revealed in particles. As a direct consequence of atoms escaping from the particle surface, the temperature of nanoparticles reduces to an undercooling point from the initial super-heating state. Furthermore, it indicates that movements of nanoparticles are dominated by those normal to the target surface.
[DOI: 10.1115/1.1621898]

Keywords: Heat Transfer, Laser, Molecular Dynamics, Nanoscale, Thermophysical

Introduction

In recent years, it has become more tempting to attach significant research interest to nanoparticles formed in short pulsed laser materials interaction due to their strong impact on micro/nanoscale manufacturing and thin film deposition. Ultrafast pulsed laser heating and the extremely small particle size impose considerable difficulty on experimental studies of the underlying physical origins as well as the in-situ thermal and mechanical characteristics associated with nanoparticles.

Interaction of the ultrafast laser pulse with the target material and the resulting material ablation are endowed with strong nonlinear, coupled optical, thermal, and mechanical processes that significantly complicate theoretical analysis. Molecular Dynamics (MD) simulation, which studies physical processes at the molecular/atomic level, is capable of providing systematic and integrated information of laser heating, material evaporation and nanoparticle formation.

A number of MD simulations have been reported on studying laser interaction with various targets. For semi-conductor materials, Kluge et al. [1] studied picosecond (ps) laser heating of a small silicon target comprising 216 atoms. Recently, ultrashort pulsed laser interaction with a larger silicon target constituted of 23,000 atoms was investigated by Herrmann et al. [2]. Laser-induced ultrafast phase transition in carbon was explored by Jeschke et al. [3] for a target of 216 atoms. As for laser metal interaction, laser heating of a metal surface was considered by Häkkinen and Landman [4] with taking into account the two-step heat transfer [5], and by Ohmura and Fukumoto [6]. Interaction of ultrafast laser with dielectrics and organic materials has been addressed by Kotake and Kuroki [7] and Zhigilei et al. [8], respectively. The quantum-mechanical effects in ultrashort laser materials interaction have been explored by Shibahara and Kotake [9] and Silverstrelli and Parrinello [10]. More recently, substantial details about the thermal and thermomechanical phenomena in ps laser interaction with large targets were reported by Etcheverry and Mesaros [11] and Wang and Xu [12,13]. Despite the large number of MD work pertinent to laser materials interaction, few MD simulations investigated nanoparticles formed in pulsed laser materials interaction [14–16]. Considerable details pertaining to the ablation process from which clusters originate have been reported by Zhigilei et al. [15] on the basis of the MD simulation of

ps laser organic solid interaction. It was pointed out by Ohmura et al. [16] that nanoparticles formed in ps laser metal interaction ejected from the target surface at a speed of several thousands of meters per second. To date, knowledge of formation and evolution of nanoparticles, as well as their in-situ thermal and mechanical properties are still lacking, thereby placing impediments on further understanding and optimizing pulsed laser materials processing.

In this work, MD simulations are carried out to investigate ps laser material interaction. Emphasis is placed on formation and evolution of nanoparticles during and after laser heating. Moreover, thermal and mechanical characteristics of nanoparticles, such as structure, temperature, and velocities are addressed in considerable detail. In this paper, methodologies employed in the MD simulation are outlined first, and then MD simulation results are presented to address various thermal and mechanical issues associated with nanoparticles.

Methodologies of the MD simulation

The problem to be studied in this work is associated with an argon crystal at an initial temperature of 50 K subjected to ps pulsed laser heating. The basic problem involves solving the Newtonian equations for each atom interacting with its neighbors,

$$m_i \frac{d^2 r_i}{dt^2} = \sum F_{ij} \tag{1}$$

where m_i and r_i are the mass and position of atom i, respectively, and m_i is taken as 6.63×10^{-26} kg for argon. F_{ij} stands for the interaction force between atoms i and j, and is computed from the Lennard-Jones (LJ) potential as $F_{ij} = -\partial \phi_{ij}/\partial r_{ij}$ with $r_{ij} = r_i - r_j$. The Lennard-Jones potential ϕ_{ij} is of the form

$$\phi_{ij} = 4\varepsilon \left[\left(\frac{\sigma_e}{r_{ij}} \right)^{12} - \left(\frac{\sigma_e}{r_{ij}} \right)^6 \right] \tag{2}$$

where ε is the LJ well depth parameter, and the corresponding value for argon is 1.653×10^{-21} J. σ_e is referred to as the equilibrium separation parameter, and is 0.3406 nm for argon [12].

A time step of 25 fs is applied in the simulation [11]. The interaction between particles is neglected when their distance exceeds a particular length r_c, namely, the cutoff distance. For ar-

gon, the widely accepted value of $2.5\sigma_e$ for r_c is applied in this work [12]. Details of the computation are published elsewhere [12,17].

Laser beam absorption in the target is achieved by exciting the kinetic energy of atoms, which is fulfilled by scaling the velocities of atoms with an appropriate factor. This factor is calculated as

$$\chi = \left[1 + \frac{\Delta E}{\frac{1}{2}\sum_{i=1}^{N} m_i \cdot [(v_{i,1}-\bar{v}_1)^2 + (v_{i,2}-\bar{v}_2)^2 + (v_{i,3}-\bar{v}_3)^2]} \right]^{1/2}$$

(3)

where $v_{i,j}$ and $\bar{v}_j$ ($j=1,2,3$) are velocities of atom i and the average velocity in the x, y, and z directions for atoms in a layer normal to the laser beam. ΔE is the laser beam energy deposited in the layer during one time step, and N is the number of atoms within the layer. The new velocity $v'_{i,j}$ of atom i is calculated as

$$v'_{i,j} = (v_{i,j}-\bar{v}_j)\cdot\chi + \bar{v}_j \qquad j = 1,2,3$$

(4)

This laser energy absorption model de-emphasizes the details of laser materials interaction, for which the quantum-mechanical effect needs to be accounted for, but is not predominant. The characteristic time of laser material interaction (<1 ps) is much smaller than the time associated with the laser pulse in this work. Hence nanoparticle formation and the thermal and mechanical information associated with them can still be investigated using the current absorption model in the absence of detailed knowledge of laser materials interaction. Exponential laser beam absorption is presumed in the computation with an absorption depth of τ. In this work, in lieu of recovering a specific experimental condition, the value of τ is chosen to reflect the fact of volumetric absorption of the laser beam. The presumed value (2.5 nm) of τ indicates that the laser beam will be absorbed within a distance of about 10 nm from the target surface. Therefore, the back side of the target will not see the direct effect of laser beam absorption. The laser pulse assumes a temporal Gaussian distribution with a FWHM (full width at half maximum) of 5 ps centered at 10 ps.

The MD computational domain is constructed in a fashion to embody extra spaces above and below the target, allowing macromotion of atoms in the z direction. Periodic boundary conditions are applied at the boundaries in the x and y directions, and free boundary conditions at the boundaries in the z direction. The target is initially constructed based upon the fcc (face-centered cubic) lattice structure of a lattice constant 0.5414 nm [12] with the (100) surface facing the laser beam. Initial velocities of atoms are specified randomly from a Gaussian distribution based on the expected temperature of 50 K. Before laser heating starts, the sample is thermalized for 100 ps to reach thermal equilibrium [11,12].

Results and Discussion

In the results that follow, a freestanding film of 90 fcc unit cells (48.73 nm) in the x and y directions, and 60 fcc unit cells (32.48 nm) in the z direction is irradiated with a single laser pulse of 1.2 J/m^2. This laser energy was proved high enough to induce phase explosion and formation of nanoparticles for argon crystal [12]. The thickness of the sample (32.48 nm) is much larger than the penetration depth of the laser beam ($\sim$10 nm), which ensures complete absorption of the laser beam. The computational domain measures 48.726 nm in the x and y directions, and 553.94 nm in the z direction with the back side of the film located at 8.55 nm. Schematic of the computational domain is shown in Fig. 1. A total of 1,944,000 atoms are tracked in the simulation. Parallel computation was conducted on a two-processor Xeon workstation using OpenMP (Open Multiple Processing).
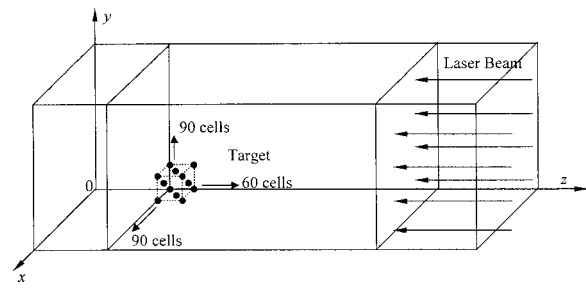

Fig. 1 Schematic of the computational domain

Formation of Nanoparticles. The manner in which nanoparticles are formed in ps laser argon interaction is delineated in Fig. 2, which presents snap shots of atomic positions at different moments. For the purpose of illustration, only the domain of $0 \le x \le 20$ nm, $0 \le y \le 20$ nm, and $30 \le z \le 90$ nm is illustrated. It is important to note that when the laser pulse stops ($t=15$ ps), thermal expansion is predominant and intense movements of atoms are observed at the target surface. Between 20 and 40 ps, phase explosion is taking place and becoming more intense with time. At 40 ps, it is evident that the thermal expansion of the material is replaced by an intense phase explosion indicated by the strong non-uniform atomic distribution in space. Plots at 60 ps through 150 ps are characterized by large clusters separating from each other to form individual particles. As a direct consequence of the surface tension force, the initial irregular nanoparticles gradually change to spheres. This process is demonstrated in plots of 200 ps through 500 ps.

The detailed formation process of a particular particle is delineated in Fig. 3. For the purpose of citation, this particle is termed particle β in the following sections. Since Fig. 2 only displays part of the computational domain, particle β can not be identified in Fig. 2. It is much pronounced in Fig. 3 that the particle starts with an irregular shape (70 ps) and concludes with a spherical one (500 ps). Before 70 ps, this particle does not separate from the target and can not be well defined. The initial irregular shape originates from the non-uniform phase explosion, and it takes quite a long time ($\sim$400 ps) for the particle to become a sphere. From 125 ps to 300 ps, the nanoparticle experiences an oscillation process, which diminishes gradually due to the presence of the inherent retarding force. The particle formation is also characterized by a shrinking process indicated by the presence of the initial loose atom distribution in space and the final much more dense distribution.

Figure 4(a) presents the variation of the particle number versus time, while Fig. 4(b) details the onset of particle formation. In Fig. 4, particle sizes are roughly sorted into several groups based on the number of atoms in a particle. This rough classification can readily reveal the trend of the formation of particles during laser-material interaction. Detailed particle size distribution was discussed elsewhere [18]. To define a particle, two atoms are treated as within the same particle if their distance does not exceed 0.40 nm, which is the nearest neighbor distance of argon atoms at the boiling point. It is found that particles defined by this criterion precisely represent the particles observed in the snap shot of atomic positions (Fig. 2). In Fig. 4 it is apparent that single atoms start coming out substantially at 10 ps through 30 ps, and stabilize at a number of about 50,000 after 200 ps. For dimers and particles comprising 3~100 atoms, their populations quickly reach a peak value at about 25 ps, and decay over a quite long time of about 300 ps. The reduction of the particle number is a consequence of losing atoms from the particle surface or smaller particles combining to form a bigger one. Particles consisting of 101 ~1000 atoms are characterized with an emergence time delay of 10 ps in comparison with smaller particles and single atoms. In
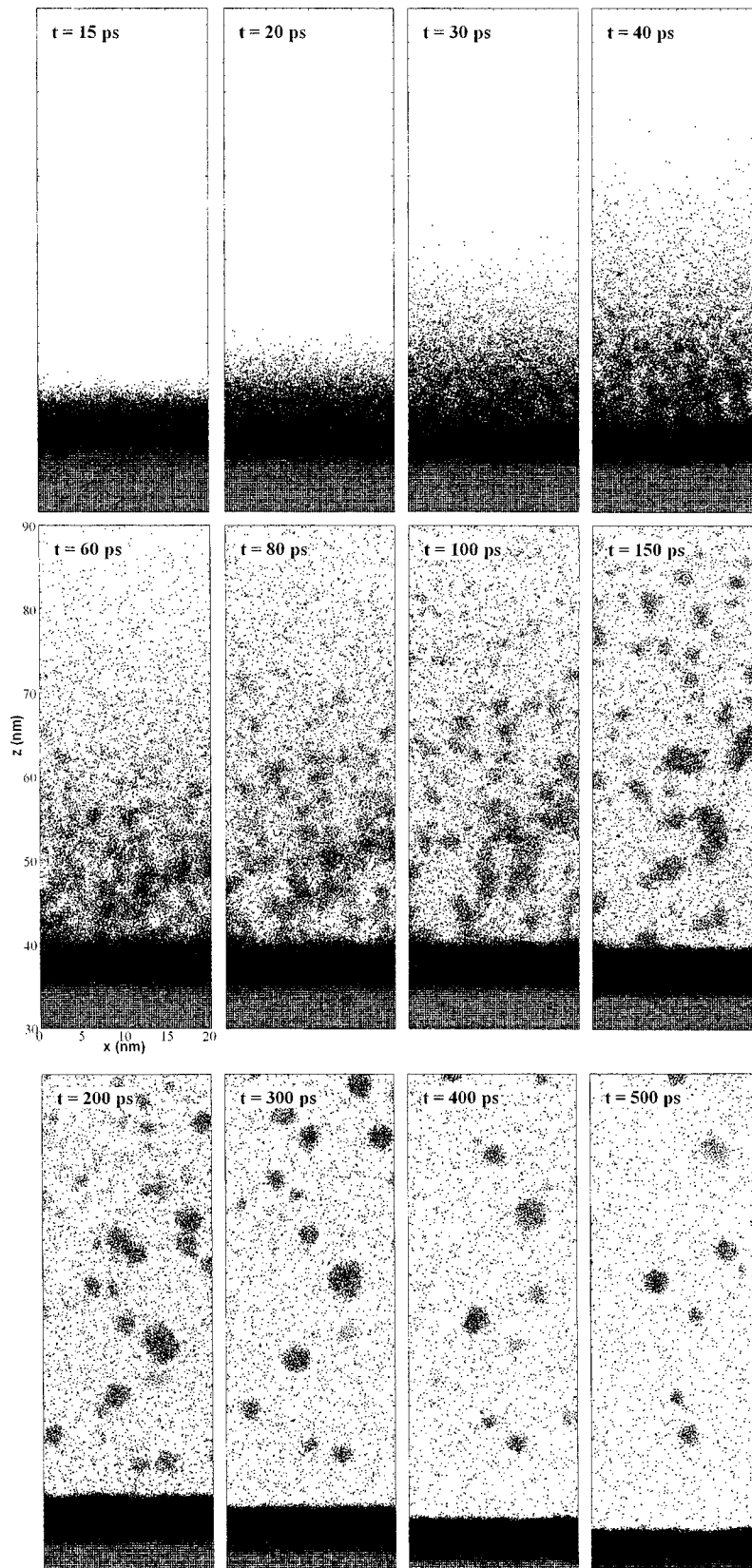
Fig. 2 Snap shots of atomic positions at different moments

other words, particles composed of 100 atoms or less start emerging during laser heating (10 ps), while particles comprising 101 atoms or more start appearing after laser heating (20 ps).

Escape of atoms from the particle surface could reduce the size of the particle substantially, and this effect is delineated in Fig. 5, which presents the temporal variation of the diameter of particle
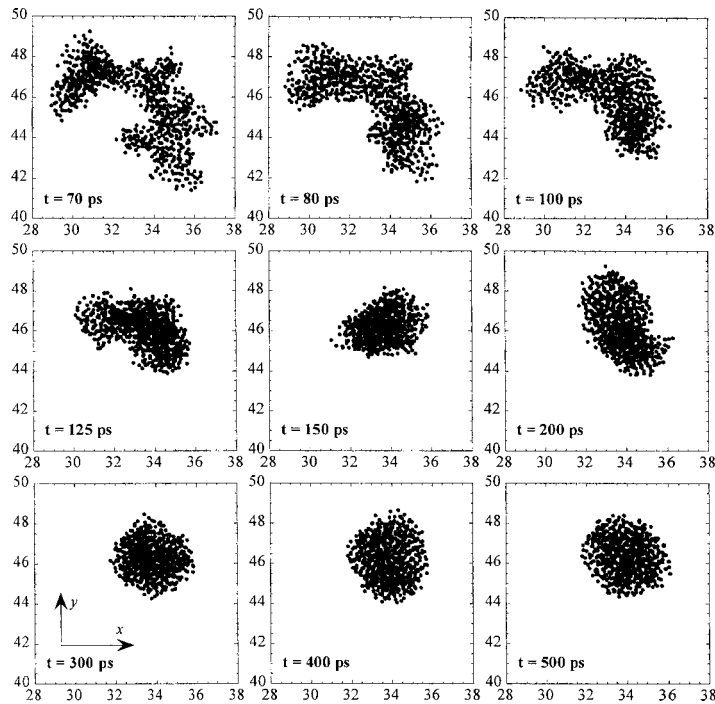
Fig. 3 Detailed formation process of particle β. The unit of the coordinates is nm.

β. The diameter of the nanoparticle is an effective value corresponding to a sphere comprising the same number of atoms at a fixed density that is evaluated at 500 ps. The sudden and temporary drop of the diameter at 110 ps is attributed to a temporary separation of a cluster from the particle. When this cluster separates from the particle, it is not accounted for when defining the particle volume, thereby inducing a temporary reduction in the particle diameter. It is seen in Fig. 5 that after 500 ps the diameter of the particle decreases by 7%, meaning a volume reduction of about 20%.

Structure of Nanoparticles.   It is a common practice to work with the radial distribution function when studying material structure. In general, the radial distribution function is defined as the ratio of the number of atoms at a distance r from a given atom compared with the number of atoms at the same distance in the ideal gas with the same density. In lieu of using the time-varying density of the particle as the reference, a constant reference density is used which is evaluated at 500 ps. The manner in which the

Fig. 4 Variation of the particle number versus time. Units of particle numbers are: 10^4 for monomers, 10^3 for dimers and particles consisting of 3 to 10 atoms, 10^2 for particles consisting of 11−100 atoms, and 10 for particles consisting of 101−1000 atoms.
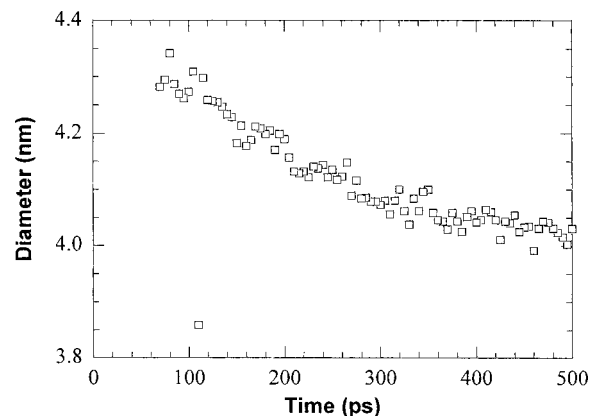
Fig. 5 Temporal variation of the diameter of particle β
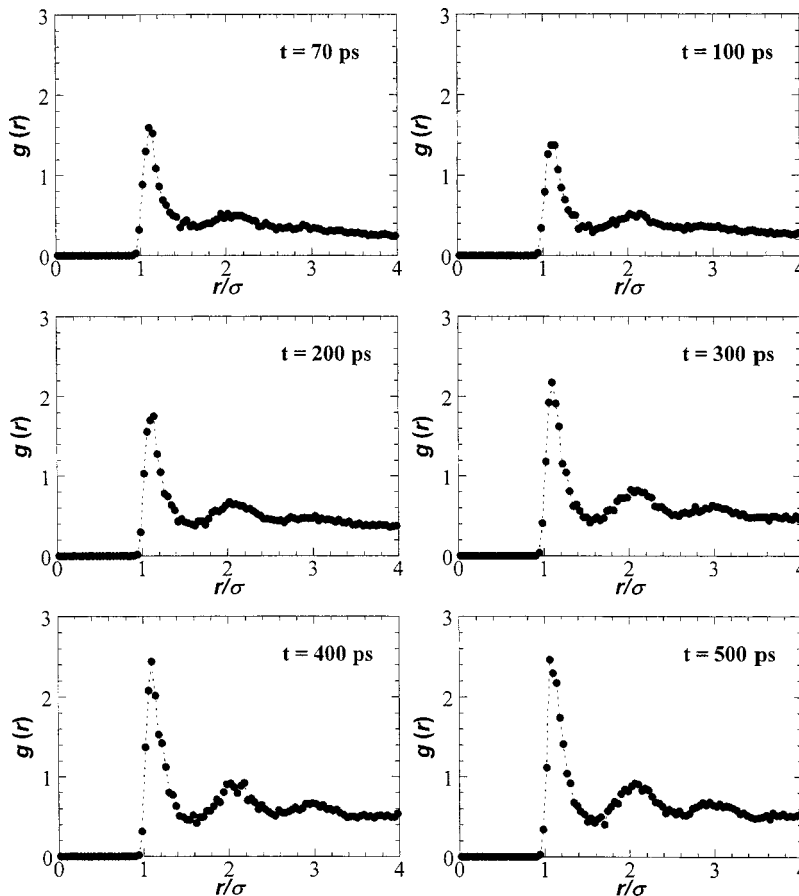
Fig. 6   Radial distribution function within particle β at different times

radial distribution function is modified makes it possible to acquire knowledge of the material density by looking into the absolute value of the radial distribution function while its shape reflects the material structure.

The radial distribution function $g(r)$ for particle β is plotted in Fig. 6. It is observed that the evolution of the radial distribution function is characterized with two features. One feature 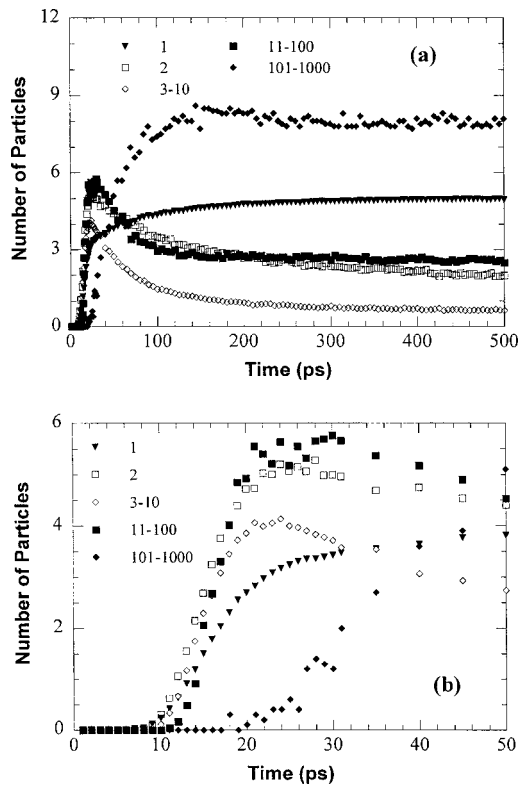is that the structure of the particle undergoes a transition from the initial gas-like structure to the final typical liquid structure. At 70 ps, it is pronounced that only the short-range order is preserved, and the long-range order is insignificant as indicated by the presence of the second weak peak. This gas-like structure remains until 300 ps while the second peak is becoming more prominent. At 300 ps, a weak third peak emerges, indicating that the liquid structure is becoming significant. After another 200 ps transition, the liquid structure is predominant, which is dictated by the three strong peaks in the radial distribution function at 500 ps.

The other feature characterizing the structural variation is the continuous condensation of atoms in space. The absolute value of the radial distribution function provides a measure of the amount by which the number density of atoms is evaluated. It is evident in Fig. 6 that besides the shape transition of the radial distribution function, its absolute value increases over the 500 ps period. In particular, the first peak has a maximum value of 1.6 at 70 ps, and this number increases to 2.6 at 500 ps. For $g(r)$ of $r/\sigma = 4.0$, its value increases substantially from 0.25 at 70 ps to 0.54 at 500 ps. The increase of the radial distribution function suggests that at a distance r from a given atom, more atoms can be found, meaning atoms are getting closer to each other. Based on the absolute value of the radial distribution function, the number density of atoms of particle β almost doubles to a first approximation.

Based on the definition of the radial distribution function used in this work, the average density (n) of the particle is related to $g(r)$ as

$$n \propto \int_0^{r_{\max}} g(r) r^2 dr \tag{5}$$

Figure 7 presents the density of particle β calculated using Eq. (5). In Fig. 7, it is evident that the density increases with time. The density at 500 ps is 12.78, which is 1.78 times the density at 70 ps (7.19), confirming the approximation conducted above. Both losing atoms from the particle surface and the decrease in intermo-

Fig. 7   Density of particle β at different times
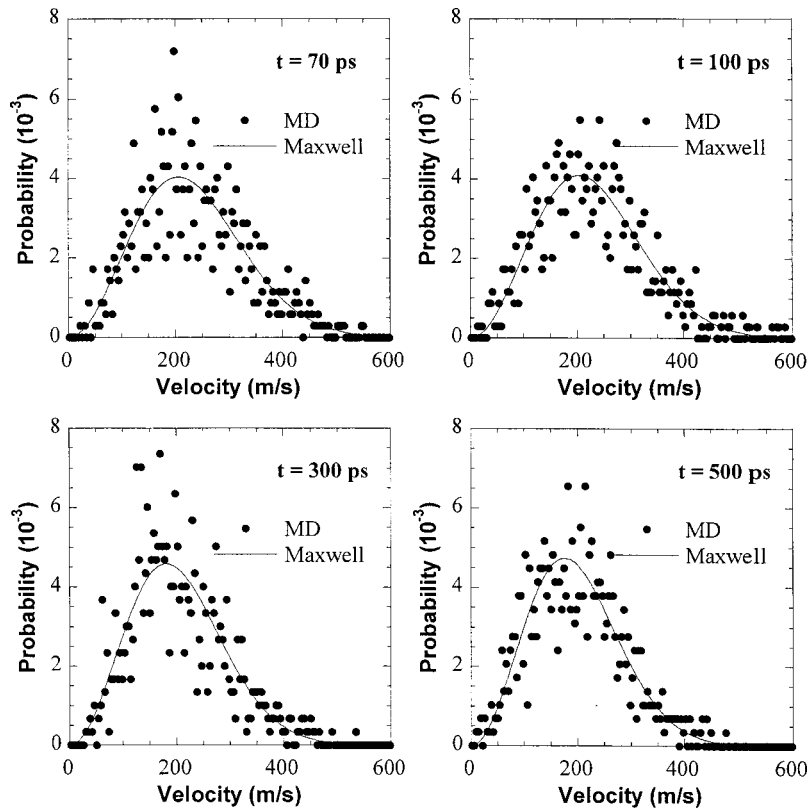
Fig. 8 Velocity distribution in comparison with the Maxwellian distribution within particle β

lecular spacing could reduce the size of the particle. As seen in Fig. 7, the decrease of intermolecular spacing can reduce the volume of the particle by about 44%. As discussed above (Fig. 5), escape of molecules from the particle surface reduces t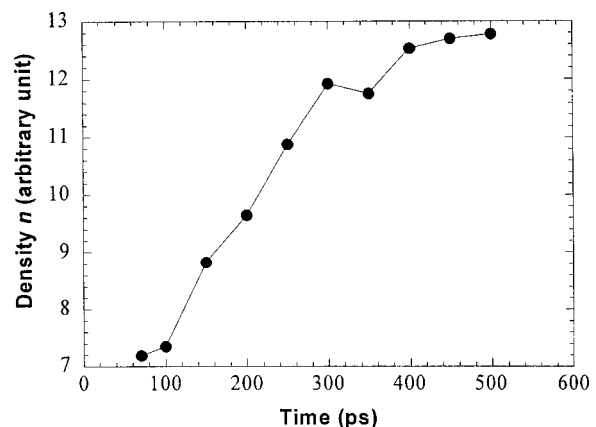he volume of particle β by about 20% (Fig. 5), which is smaller than, but comparable to, the effect of decrease of intermolecular spacing.

Temperature of Nanoparticles. It is important to be cognizant of the thermal equilibrium status of nanoparticles when exploring their temperature variation. The thermal equilibrium status is examined by comparing the atom velocity distribution with the Maxwellian distribution. Figure 8 shows the comparison of the velocity distribution of atoms within particle β. It is evident that at all times the velocity distribution follows the Maxwellian distribution well yet with noticeable deviations attributed to the small number of atoms within the particle.

The temperature of the particle is calculated using

$$\frac{3}{2}Nk_BT=\sum_{i=1}^{N} m_i\frac{1}{2}(v_{i,1}^2+v_{i,2}^2+v_{i,3}^2) \qquad (4)$$

where N is the number of atoms within the particle, k_B is the Boltzmann's constant $(1.38\times10^{-23}$ J/mol·K), and $v_{i,j}$ ($j=1,2,3$) is the velocity of atom i in the x, y, and z directions.

Temporal variation of the temperature of particle β is plotted in Fig. 9. It is prominent that the temperature decays with time. Atoms escaping from the particle surface take away a considerable amount of energy. As a result, the particle temperature experiences a decaying process as illustrated in Fig. 9. At 70 ps, the particle is at a temperature above 100 K, which exceeds the boiling point (87.3 K) of argon, indicating the existence of superheating. On the other hand, the particle temperature reduces to as low as 75 K at 500 ps, much lower than the melting point of argon

(83.8 K) while the particle is still at the liquid state as described before. Hence under-cooling occurs for particles formed in ps laser materials interaction. This phenomenon is attributed to the rapid cooling induced by escape of atoms from the particle surface while the particle itself does not have enough time to solidify.

The temperature variation described in the preceding paragraph exists for all particles comprising a large number of atoms for which the temperature concept is still valid. Figure 10 presents the temperature distribution versus the particle size at different times. For particles of less than 2 nm in diameter, their temperature cannot be defined in the strict physical sense since thermal equilibrium can not establish due to the small number of atoms within the particle. Hence Fig. 10 only plots the temperature of particles with a diameter of 2 nm or greater. It is evident that at 500 ps all

Fig. 9 Temperature of particle β at different times

Fig. 10 Temperature distribution versus the particle size at different times

particles are at temperatures below the melting point of argon even though their initial temperatures (50 ps) are above the boiling point.
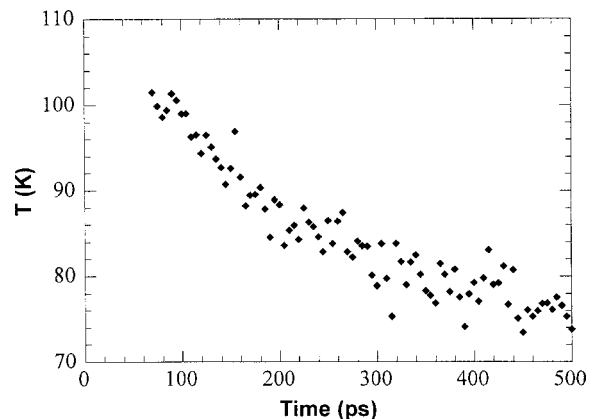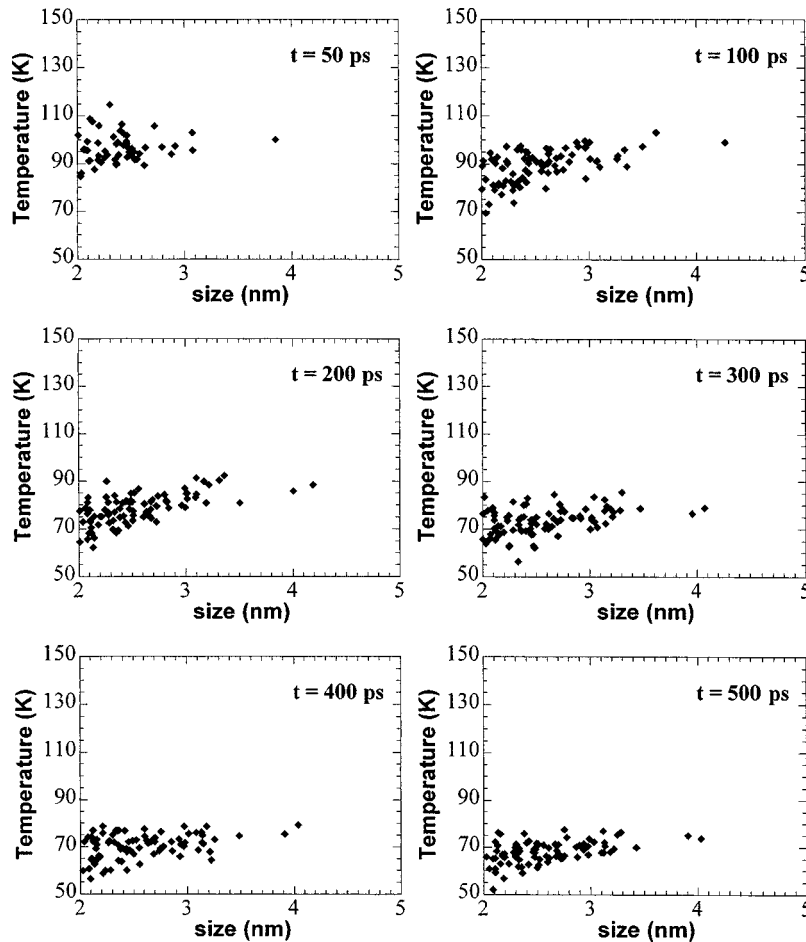
Velocities of Nanoparticles. The temporal variation of velocities of particle β is presented in Fig. 11. It is much noticeable in Fig. 11 that velocities in the x and y directions are one order of magnitude smaller than that in the z direction. Therefore, movements of the particle are dominated by those in the z direction. It is observed that initially the particle has a relatively high velocity in the x and y directions ($\sim$8 m/s) and conclude with a much smaller velocity of about 3 m/s. For the movement in the z direction, the particle starts with a velocity of about 130 m/s and picks up speed to a higher level of about 143 m/s at 500 ps. The velocities presented in Fig. 11 shows oscillation with time, which is attributed to escape of atoms from the particle surface. When an atom escapes from the particle, the momentum (velocity) of the particle changes accordingly due to momentum conservation. Since atoms escaping from the particle surface have different momentum, velocities of the particle show some up-and-down behavior with time.

Velocities of particles versus the diameter are shown in Fig. 12. It is apparent that the maximum velocity of smaller particles exceeds that of larger ones. For larger particles, their velocity is only about tens of meters per second or less in the x and y directions, while the maximum velocity in the z direction is about 100 m/s or less. This demonstrates that the z direction movement is predominant for nanoparticles formed in ps laser materials interaction. Another noticeable characteristic of the particle movement is that

particles move with the same probability in the opposite x and y directions. In contrast, for movement in the z direction, the velocity in the negative z direction is observed for smaller particles, but is insignificant in comparison with that in the positive z direction. For larger particles, only few move slowly in the negative z direction while most of them move in the positive z direction.

Conclusion

In this work, MD simulations were carried out to study nanoparticles formed in ps laser materials interaction. Substantial details of nanoparticle formation as well as their thermal and mechanical characteristics were uncovered. It was revealed that nanoparticles originated from an intense vapor phase explosion process. Small particles started coming out during laser heating while larger ones emerged after laser heating. Nanoparticles started with a gas-like structure of a super-heating state and concluded with a typical liquid structure at an under-cooling state. The temperature reduction of nanoparticles was attributed to atoms escaping from the particle surface. Moreover, nanoparticles underwent a substantial volume reduction due to the atomic escape from the particle surface and a decrease of intermolecular spacing. Movements of nanoparticles were dominated by those in the z direction. In the x and y directions, nanoparticles have the same probability of moving in opposite directions, while in the z direction, the movement in the positive direction is predominant.
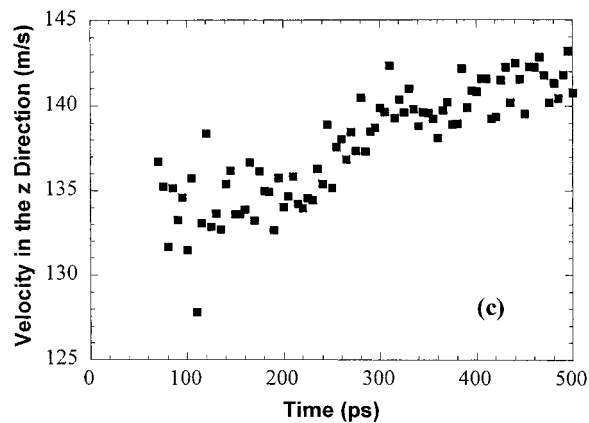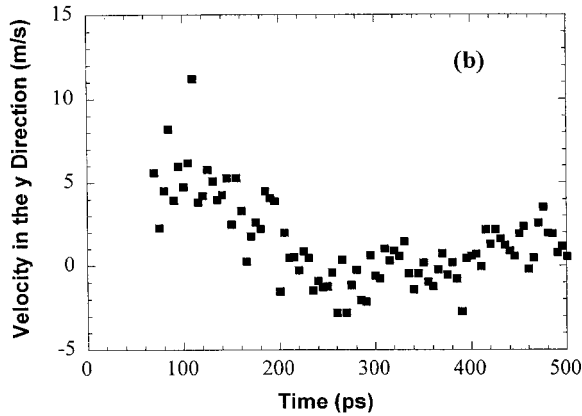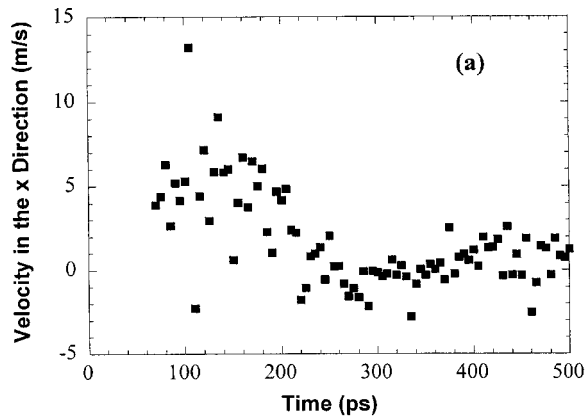
Fig. 11 Temporal variation of velocities of particle β
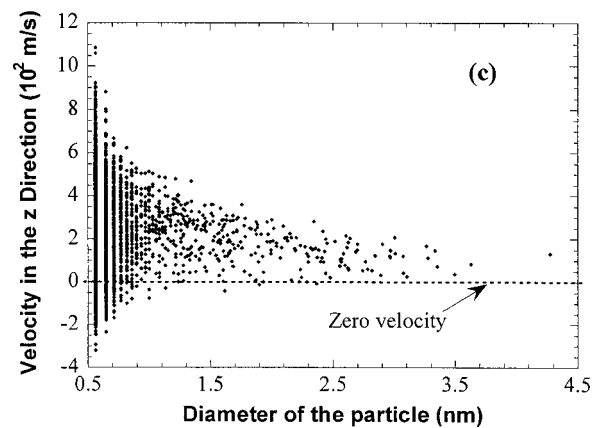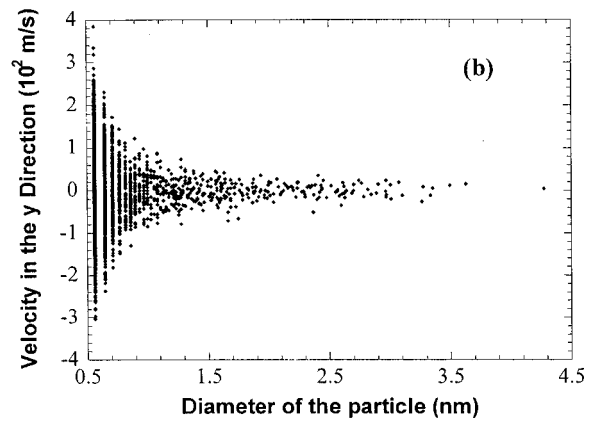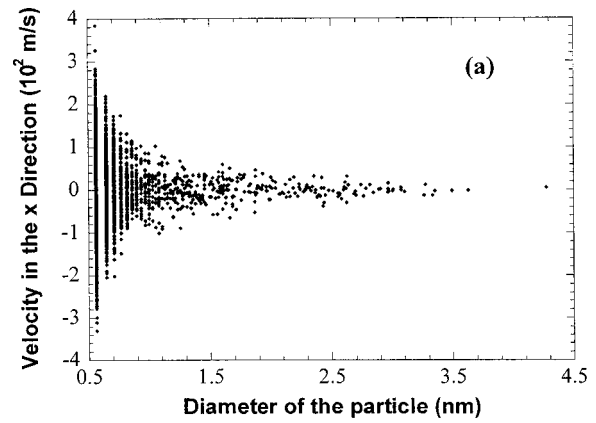
Fig. 12 Velocity distribution versus the diameter of particles at 100 ps

Acknowledgment

Nomenclature

ΔE = the laser energy absorbed by a layer during one time step
F_{ij} = interaction force between atoms i and j
$g(r)$ = radial distribution function
k_B = Boltzmann's constant
m = atomic mass
n = number density of atoms within a particle
N = number of atoms
r = position of the atom
r_c = cutoff distance
r_{ij} = the distance between atoms i and j
t = time
T = temperature
v = velocity of atoms
v' = velocity of atoms after scaling
$\bar{v}$ = average velocity of atoms

Greek Symbols

χ = scaling factor for the velocity of atoms
ε = LJ well depth parameter
ϕ = Lennard-Jones potential
σ_e = equilibrium separation parameter

τ = optical absorption depth

Subscripts

i = index of the atom
j = index of the atom/direction

References

[1] Kluge, M. D., Ray, J. R., and Rahman, A., 1987, "Pulsed Laser Melting of Silicon: A Molecular Dynamics Study," J. Chem. Phys., **87**, pp. 2336–2339.

[2] Herrmann, R. F. W., Gerlach, J., and Campbell, E. E. B., 1998, "Ultrashort Pulse Laser Ablation of Silicon: an MD Simulation Study," Appl. Phys. A: Mater. Sci. Process., **66**, pp. 35–42.

[3] Jeschke, H. O., Garcia, M. E., and Bennemann, K. H., 1999, "Theory for Laser-induced Ultrafast Phase Transitions in Carbon," Appl. Phys. A: Mater. Sci. Process., **69**, pp. S49–S53.

[4] Häkkinen, H., and Landman, U., 1993, "Superheating, Melting, and Annealing of Copper Surfaces," Phys. Rev. Lett., **71**, pp. 1023–1026.

[5] Anisimov, S. I., Kapeliovich, B. L., and Perelman, T. L., 1974, "Electron Emission from Metal Surfaces Exposed to Ultra-short Laser Pulses," Sov. Phys. JETP, **39**, pp. 375–377.

[6] Ohmura, E., and Fukumoto, I., 1996, "Molecular Dynamics Simulation on Laser Ablation of fcc Metal," Int. J. Jpn. Soc. Precis. Eng., **30**, pp. 128–133.

[7] Kotake, S., and Kuroki, M., 1993, "Molecular Dynamics Study of Solid Melting and Vaporization by Laser Irradiation," Int. J. Heat Mass Transfer, **36**, pp. 2061–2067.

[8] Zhigilei, L. V., Kodali, P. B. S., and Garrison, B. J., 1997, "Molecular Dynamics Model for Laser Ablation and Desorption of Organic Solids," J. Phys. Chem., **101**, pp. 2028–2037.

[9] Shibahara, M., and Kotake, S., 1998, "Quantum Molecular Dynamics Study of Light-to-heat Absorption Mechanism in Atomic Systems," Int. J. Heat Mass Transfer, **41**, pp. 839–849.

[10] Silvestrelli, P. L., and Parrinello, M., 1998, "Ab Initio Molecular Dynamics Simulation of Laser Melting of Graphite," J. Appl. Phys., **83**, pp. 2478–2483.

[11] Etcheverry, J. I., and Mesaros, M., 1999, "Molecular Dynamics Simulation of the Production of Acoustic Waves by Pulsed Laser Irradiation," Phys. Rev. B, **60**, pp. 9430–9434.

[12] Wang, X., and Xu, X., 2002, "Molecular Dynamics Simulation of Heat Transfer and Phase Change during Laser Material Interaction," ASME Journal of Heat Transfer, **124**, pp. 265–274.

[13] Wang, X., and Xu, X., 2003, "Molecular Dynamics Simulation of Thermal and Thermomechanical Phenomena in Picosecond Laser Material Interaction," Int. J. Heat Mass Transfer, **46**, pp. 45–53.

[14] Zhigilei, L. V., and Garrison, B. J., 1999, "Molecular Dynamics Simulation Study of the Fluence Dependence of Particle Yield and Plume Composition in Laser Desorption and Ablation of Organic Solids," Appl. Phys. Lett., **74**, pp. 1341–1343.

[15] Zhigilei, L. V., Kodali, P. B. S., and Garrison, B. J., 1998, "A Microscopic View of Laser Ablation," J. Phys. Chem. B, **102**, pp. 2845–2853.

[16] Ohmura, E., Fukumoto, I., and Miyamoto, I., 1999, "Modified Molecular Dynamics Simulation on Ultrafast Laser Ablation of Metal," *Proceedings of the International Congress on Applications of Lasers and Electro-Optics*, pp. 219–228.

[17] Allen, M. P., and Tildesley, D. J., 1987, *Computer Simulation of Liquids*, Clarendon Press, Oxford.

[18] Wang, X., and Xu, X., 2002, "The Formation Process of Nanoparticles in Laser Materials Interaction," *2002 ASME International Mechanical Engineering Congress & Exposition*, Paper No. 33857, ASME, New York.

Phonon Transport in Anisotropic Scattering Particulate Media

Ravi Prasher
e-mail: ravi.s.prasher@intel.com
Sr. Thermal Engineer,
Assembly Technology Development,
Ch5-157, Intel Corporation,
Chandler, AZ 85226-3699

Equation of phonon radiative transport (EPRT) is rewritten to include anisotropic scattering by a particulate media by including an acoustic phase function and an inscattering term which makes EPRT exactly same as equation of radiative transport (ERT). This formulation of EPRT is called generalized EPRT (GEPRT). It is shown that GEPRT reduces to EPRT for isotropic scattering and is totally consistent with phonon transport theory, showing that transport cross section is different from the scattering cross section. GEPRT leads to same formulation for transport cross section as given by phonon transport theory. However GEPRT shows that transport cross section formulations as described by phonon transport theory are only valid for acoustically thick medium. Transport cross section is different for the acoustically thin medium leading to the conclusion that mean free path (m.f.p) is size dependant. Finally calculations are performed for two types of scatterers for acoustic waves without mode conversion: (1) acoustically hard Rayleigh sphere; and (2) large sphere in the geometrical scattering regime. Results show that the scattering from these particles is highly anisotropic. It is also shown that for geometrical scattering case isotropic scattering leads to the conclusion of total internal reflection at the particle/medium interface. [DOI: 10.1115/1.1622718]

Keywords: Conduction, Heat Transfer, Microscale, Nanoscale, Scattering

Introduction

Equation of phonon radiative transport (EPRT) [1] is widely used for predicting the thermal conductivity of microstructures. EPRT is valid only for isotropic scattering of phonons by particles. Recently Prasher [2] extended EPRT by including an inscattering term. It is very well known that scattering of phonons even by symmetrical particles such as spheres can be highly anisotropic and asymmetrical depending upon the acoustic mismatch between the particles and the host medium [3]. It was also pointed out by Majumdar [1] that EPRT is similar to equation of radiative transport (ERT) except that (1) EPRT does not contain an in scattering term where as ERT does, and (2) in ERT the emission and absorption of photon energy imply transfer of photon energy to other particles such as electrons and or phonons, where as this does not exist for phonons. In reality EPRT does contain an inscattering term which will be proven in this paper. The Umklapp process can also be thought of as emission of phonons when 1 phonon gives out two phonons and absorption of phonons when 2 phonons combine together to give out 1 phonon. Note that Umklapp scattering is an inelastic scattering process. Other types of inelastic scattering process are also possible such as scattering between phonons and electrons. In this paper EPRT is written in a form where the inelastic and elastic scattering terms are separated and is called generalized EPRT (GEPRT) which means inclusion of an acoustic phase function. From this general formulation it is shown that EPRT can be derived from GEPRT if the scattering is isotropic.

It is typically assumed that transport cross section [1] is same as the scattering cross section which basically amounts to isotropic scattering. This lead to the conclusion, for example in the geometrical scattering regime that total internal reflection of acoustic wave takes place which will be shown later in this paper. It is well known that the transport cross section of carriers such as phonons or electrons is different from the scattering cross section [3]. It will be shown that solution of GEPRT is totally consistent with the transport theory of phonons in the acoustically thick regime. In the acoustically thin regime GEPRT shows that transport cross

section or alternately the mean free path (m.f.p) of the phonon is different from the m.f.p in the acoustically thick regime. This makes m.f.p due to particle scattering dependent on the acoustic thickness of the medium.

This paper is divided in six sections. In section one detailed development of GEPRT is shown. Section two provides details on the acoustic phase function. Section three deals with the solution of GEPRT for spherical particles. Section four provides a brief discussion on meaning of transport cross section and shows that GEPRT is totally consistent with transport theory in the diffusive regime. Mean free path of some mathematically simple scatterers is calculated in section five using GEPRT. Section six discusses the usefulness and application of GEPRT.

1 Generalized Equation of Phonon Radiative Transport [2]

All the equations developed in this paper are for steady-state one-dimensional slab, but can be easily extended for three-dimensional geometry. We start with steady state EPRT which can be written [1]

$$\mu \frac{\partial I_\omega}{\partial x} = K_u(I_\omega^0 - I_\omega) + K_p(I_\omega^0 - I_\omega) \tag{1}$$

where μ is the direction cosine, I the intensity, I^0 the equilibrium intensity, ω the frequency, K_u and K_p are the scattering coefficient for Umklapp (or an inelastic scattering process) and particle scattering (elastic process), respectively. ω in the subscript indicates that I is a function of ω. K_u and K_p is given by [1]

$$K_p = \frac{1}{l_p}, \quad K_u = \frac{1}{l_u} \tag{2}$$

where l_p and l_u are the m.f.p due particle and Umklapp scattering respectively and also

$$K_p = n\sigma \tag{3}$$

where n is the number of particles per unit volume and σ is the scattering cross section of a single particle.

ERT in one-dimension can be written as [4]

Copyright © 2003 by ASME

$$\mu \frac{\partial I_\omega}{\partial x} = K_a(I_\omega^0 - I_\omega) - K_p I_\omega + \frac{K_p}{4\pi} \int_{4\pi} \Phi(\Omega_i \to \Omega) I_\omega(\Omega_i) d\Omega_i$$

$$(4)$$

where K_a is the absorption coefficient, Φ the phase function for the scattered wave from solid angle Ω_i to Ω. Since the phase function term arises in radiative transport only if there are particles present in the medium which leads to scattering of the EM waves, it is reasonable to expect that even for phonons there should be a phase function if particles such as defects are present in the medium. Considering this EPRT is written as

$$\mu \frac{\partial I_\omega}{\partial x} = K_u(I_\omega^0 - I_\omega) - K_p I_\omega + \frac{K_p}{4\pi} \int_{4\pi} \Phi(\Omega_i \to \Omega) I_\omega(\Omega_i) d\Omega_i$$

$$(5)$$

This equation is referred to as GEPRT in the manuscript. Note that the last two terms in the right hand side of Eq. (5) are due to elastic scattering of phonons and the term in the bracket is due to inelastic scattering of phonons. The term involving the phase function in Eq. (5) is the in-scattering term. Φ also satisfies the following equation [5].

$$\frac{1}{4\pi} \int_{4\pi} \Phi(\Omega_i \to \Omega) d\Omega_i = 1 \qquad (6)$$

and $\Phi = 1$ for isotropic scattering.

This equation has an interpretation exactly similar to ERT. Umklapp process is like emission and absorption of phonons and other terms account for scattering with physical particles. Equation (6) can be further written as

$$\mu \frac{\partial I_\omega}{\partial \delta} = -I_\omega + (1 - w_\omega)I^0 + \frac{w_\omega}{4\pi} \int_{4\pi} \Phi(\Omega_i \to \Omega) I_\omega(\Omega_i) d\Omega_i$$

$$(7)$$

where

$$w_\omega = \frac{K_p}{K_u + K_p} = \frac{l_u}{l_u + l_p} \qquad (8)$$

$$\delta = K_e x \qquad (9)$$

$$K_e = K_u + K_p \qquad (10)$$

where w_ω is the scattering albedo for phonons, δ the acoustic dimension, and K_e the extinction coefficient.

Under radiative equilibrium dq/dx is zero, where q is the heat flux. It can be shown that for radiative equilibrium [5]

$$\frac{1}{4\pi} \int_{4\pi} I_\omega(\Omega_i) d\Omega_i = I^0 \qquad (11)$$

Substituting Eq. (11) in Eq. (5) and assuming $\Phi = 1$ (isotropic scattering) GEPRT reduces to EPRT. Therefore EPRT in its original form is valid only for isotropic scattering.

It is to be noted that both ERT and GEPRT are valid for a particulate media only if the energy transport inside the particles fall in the wave regime, i.e., the m.f.p of phonon or photon is much larger than the characteristic dimension of the particle. Phase function is derived solely based on matching the boundary conditions at the particle/medium interface assuming wave behavior. The implicit assumption inside the particle is that energy transport can still be treated like waves. However, absorption of energy inside the particle in ERT can still be handled by assigning an imaginary wave vector to the electromagnetic wave equation. If the particle diameter is much larger than the energy carrier m.f.p then neither ERT nor GEPRT is valid for the particulate media as a whole. In that situation ERT and GEPRT have to be applied separately in the particle and the medium and the boundary conditions have to be matched at the particle/medium interface.
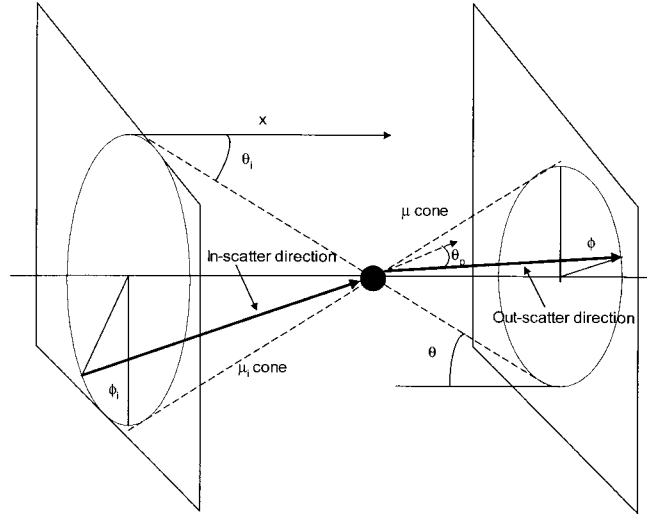
Fig. 1 Slab and single-particle scattering angles

2 Phase Function

The single-scattering phase function is typically known as a function of the particle single-scattering polar angle θp as shown in Fig. 1. Note that the subscript p denotes the particle in Fig. 1 and elsewhere in the manuscript. One needs to express Φ in terms of the slab angles to solve Eq. (7). A relation that gives the particle single-scattering polar angle θp as function of slab angles θ_i, ϕ_i, θ, and ϕ can be obtained from analytical geometry [6]

$$\cos \theta_p = \mu_i \mu + \sqrt{1 - \mu_i^2} \sqrt{1 - \mu^2} \cos(\phi - \phi_i) \qquad (12)$$

where $\mu_i = \cos(\theta_i)$ and $\mu = \cos(\theta)$. Definition of these angles is shown in Fig. 1. For scattering in a planar slab with azimuthal symmetry, slab $\Phi(\mu_i, \mu)$ can be obtained from $\Phi(\mu_p)$ from the following expression [4]

$$\Phi(\mu_i, \mu) = \frac{1}{\pi} \int_{\mu_{p\pi}}^{\mu_{p0}} \frac{\Phi(\mu_p) d\mu_p}{[(1 - \mu_i^2)(1 - \mu^2) - (\mu_p - \mu_i \mu)^2]^{1/2}}$$

$$(13)$$

where

$$\mu_{p0} = \mu_i \mu + \sqrt{1 - \mu_i^2} \sqrt{1 - \mu^2}, \quad \mu_{p\pi} = \mu_i \mu - \sqrt{1 - \mu_i^2} \sqrt{1 - \mu^2}$$

$$(14)$$

For the azimuthal symmetry case if the phase function $\Phi(\mu_p)$ can be expressed as a series of Legendre function (P) such that

$$\Phi(\mu_p) = \sum_{i=0}^{N_L} a_i P_i(\mu_p) \qquad (15)$$

where a is the coefficient of various terms in the series, then $\Phi(\mu_i, \mu)$ can be expressed as [4]

$$\Phi(\mu_i, \mu) = \sum_{i=0}^{N_L} a_i P_i(\mu_i) P_i(\mu) \qquad (16)$$

3 Solution of GEPRT for Spherical Particles

An asymmetry factor, $\langle \Phi \rangle$ is defined to solve problems in an anisotropic scattering media [5].

$$\langle \Phi \rangle = \frac{1}{4\pi} \int_{4\pi} \Phi(\Omega_p) \cos(\theta_p) d\Omega_p \qquad (17)$$

For spherical particles Eq. (17) reduces to

$$\langle\Phi\rangle = \frac{1}{2}\int_{-1}^{1}\Phi(\mu_p)\mu_p d\mu_p \qquad (18)$$

There are various methods to solve Eq. (7). Two of the most common methods used for solving ERT are [4] (1) two-flux method, and (2) two discrete ordinate method. These methods can also be used for solving GEPRT. Solution of Eq. (7) for a one-dimensional slab using the two discrete ordinate method in acoustically thick regime is same as EPRT if one modifies the extinction coefficient as [4]

$$K'_e = (1 - w_\omega g)K_e \qquad (19)$$

where K'_e is the effective extinction coefficient, and g is a factor which is equal to $\langle\Phi\rangle$ in the diffusive or the acoustically thick regime. g is equal to $\langle\Phi\rangle$ in the diffusive regime because the two discrete ordinate method is exact in the diffusive regime [4]. Using Eqs. (2) and (10), Eq. 19 can be written as

$$l'_{\text{eff}} = \frac{l_{\text{iso}}}{(1 - w_\omega g)} \qquad (20)$$

where l'_{eff} the effective mean free path and l_{iso} is is the effective isotropic scattering mean free path and is given as

$$l_{\text{iso}} = \frac{l_u l_p}{l_u + l_p} \qquad (21)$$

Equation (20) can also be written as

$$l'_{\text{eff}} = \frac{l_u \dfrac{l_p}{(1-g)}}{l_u + \dfrac{l_p}{(1-g)}} \qquad (22)$$

which means that effective mean free path due to particles (l'_p) is

$$l'_p = \frac{l_p}{(1-g)} \qquad (23)$$

As pointed out earlier, $g = \langle\Phi\rangle$ only for an acoustically thick medium. Two flux method is more appropriate for optically thin regime in ERT [4]. Similarly for GEPRT in the acoustically thin regime it is safe to assume that two flux method is more appropriate as GEPRT and EPRT are same in formulation. For acoustically thin medium with spherical scatterers the recommended value of g based on two flux method is [4]

$$g = 1 - 2B \qquad (24)$$

where B is given by

$$B = \frac{1}{2}\int_0^1\int_{-1}^0\Phi(\mu_i,\mu)d\mu_i d\mu \qquad (25)$$

Combining Eqs. (23)–(25) it can be seen that m.f.p due to particles depends upon the acoustic thickness of the medium. For isotropic scattering or symmetrical scattering such as Rayleigh scattering of EM waves by spherical particles [5] $g = 0$ for both acoustically thin and thick cases because $B = 0.5$ making $g = 0$ (Eq. 24) for acoustically thin case and $\langle\Phi\rangle = 0$, making $g = 0$ for acoustically thick case. Between the acoustically thin and thick case numerical techniques such as multi-flux method [4] or the discrete ordinate method [4] have to be used. It is to be noted that this dependence of m.f.p on the acoustic thickness is in the thickness direction of the medium, i.e., the heat flow is in the thickness direction. If the heat flow is in the transverse direction of an infinitely long thin medium, various researchers [7] have shown that m.f.p gets modified depending on the boundary condition such as diffuse versus specular reflection of phonons from the boundaries. However m.f.p of the phonons is dependent on the acoustic thickness irrespective of the boundary condition if the heat flow is in the thickness direction just due to asymmetric nature of the scattering phase function as shown in this paper.

4 Transport Cross Section [3,9]

It can be shown that GEPRT is completely consistent with transport theory of phonons as described in standard solid state text books [3]. In the transport theory of phonons the transport scattering cross section is different than the total scattering cross section [3,8]. In this section we briefly discuss why the transport cross section is different than the scattering cross section. Most of the material in this section has been taken from Peierls [9] and Ziman [3]. Boltzmann equation in steady state can be written as [3]

$$\nu_k.\nabla F_k + a.\frac{\partial F_k}{\partial \nu_k} = \left(\frac{\partial F_k}{\partial t}\right)_{\text{scatt}} \qquad (26)$$

where F is the distribution function for the carrier, v the velocity, a the acceleration of the carriers, and k is the wave vector. k in the subscript denotes that F is a function of k. Subscript "scatt" denotes the scattering term. For phonons the acceleration term in Eq. (26) can be neglected [1] where as for electrons it has to be there. We will show that transport cross section is different than the scattering cross section for the phonon case, but the conclusions equally hold for the electrons where the acceleration term in Eq. (26) remains [9]. After neglecting a, Eqs. (26) can be written as

$$\nu_k.\frac{\partial F_k}{\partial T}\nabla T = \left(\frac{\partial F_k}{\partial t}\right)_{\text{scatt}} \qquad (27)$$

Right hand side (R.H.S) of Eq. (27) is given by [3,9]

$$\left(\frac{\partial F_k}{\partial t}\right)_{\text{scatt}} = \int d\Omega'\Gamma(\theta_p)\{F_{k'} - F_k\} \qquad (28)$$

where the integration is taken over a sphere of radius k. $d\Omega$ is the element of solid angle, θ_p is the scattering angle. k' is state of the carrier after scattering. θ_p is also the angle between the k' and k. $\Gamma(\theta_p)$ is the differential scattering probability. Under diffusive transport approximation F_k in of Eq. (27) is replaced by F_k^0 [3,9] Therefore Eq. (27) reduces to

$$\nu_k.\frac{\partial F_k^0}{\partial T}\nabla T = \int d\Omega'\Gamma(\theta_p)\{F_{k'} - F_k\} \qquad (29)$$

This equation has an exact solution if k-space is spherical (isotropic), so that v_k and k are both in the same direction [3,9] and the scattering is elastic, such as those by elastic particles [3,9]. This means that left hand side (L.H.S) of Eq. (29) is the scalar product of v_k with a vector which is constant on a spherical surface in k-space. It can be shown that [3,9] with above mentioned conditions Eq. (29) reduces to

$$\nu_k.\frac{\partial F_k^0}{\partial T}\nabla T = \{F_k^0 - F_k\}\left[\int (1 - P_i(\cos\theta_p)d\Omega'\Gamma(\theta_p))\right] \qquad (30)$$

where P is the Legendre function. Equation (30) can be written as

$$\nu_k.\frac{\partial F_k^0}{\partial T}\nabla T = \frac{F_k^0 - F}{\Lambda_i} \qquad (31)$$

where Λ_i is given by

$$\frac{1}{\Lambda_i} = \int (1 - P_i(\cos\theta_p)d\Omega'\Gamma(\theta_p)) \qquad (32)$$

In Eq. (31) L.H.S is a dot product of well defined two vector quantities and are spherical harmonics of first order for isotropic case (energy surfaces in k space are spherical) [9]. Therefore Eq. (32) reduces to

$$\frac{1}{\Lambda_l} = \int (1 - P_1(\cos\theta_p) d\Omega' \Gamma(\theta_p)) \tag{33}$$

where subscript i in Eq. (32) is equal to 1. For $i=1$ Eq. (33) reduces to

$$\frac{1}{\Lambda_l} = \int (1 - \cos\theta_p) d\Omega' \Gamma(\theta_p) \tag{34}$$

Λ_l in Eq. (34) is the "transport scattering time." It is the mean time after which direction of phonon gets lost. If the phonon sets out in a definite direction, transporting a certain energy and thus creating a certain heat current, this will not be lost immediately upon the first collision through a small angle, but will persist for some further time before being dissipated [10]. It is to be noted that even for radiative transport of photons the transport scattering time is different than the scattering time [10]. However note that Eq. (34) is valid only for the diffusive case. Using Eq. (34) a transport cross section (σ_T) for the spherical particles can be defined as [3]

$$\sigma_T = 2\pi \int_0^\pi d\sigma (1 - \cos\theta_p)\sin\theta_p d\theta_p \tag{35}$$

where $d\sigma$ is the differential scattering cross section. Note that Eq. (35) takes this form only under diffusive transport approximation, i.e., for acoustically thick case. This is not valid for the acoustically thin case because F_k can not be replaced by F_k^0 in on the L.H.S in Eq. (27) for the acoustically thin case. It can be shown that Eq. (35) can be reduced to

$$l'_p = \frac{l_p}{(1 - \langle \Phi \rangle)} \tag{36}$$

Φ for acoustic waves can be defined analogous to EM waves [11], as

$$\Phi(\Omega_p) = 4\pi \frac{d\sigma}{\sigma} \tag{37}$$

where $d\sigma$ is the differential scattering cross section. $d\sigma$ is given by

$$d\sigma = \frac{f(\theta_p)}{k^2} \tag{38}$$

where k is the wave vector, and f is the scattering function. σ is given as

$$\sigma = \int_{4\pi} d\sigma d\Omega_p = \frac{1}{k^2} \int_{4\pi} f(\theta_p, \phi_p) d\Omega_p \tag{39}$$

Using Eq. (35), Eqs. (37)–(39) and Eq. (6) σ_T for spherical particle can be reduced to

$$\sigma_T = \sigma - \sigma \frac{1}{2} \int_{-1}^1 \Phi(\theta_p)\mu_p d\mu_p \tag{40}$$

Using (18), Eq. (40) reduces to

$$\sigma_T = \sigma(1 - \langle \Phi \rangle) \tag{41}$$

Equation (41) is same as Eq. (36). This shows that GEPRT is completely consistent with existing transport theory in the acoustically thick regime. However, GEPRT shows that particle m.f.p depends on the acoustic thickness of the medium (Eq. (24)). It is a common practice to assume that m.f.p does not depend on the dimension while calculating the thermal conductivity of small structures such as thin film super lattice and etc. [1]. This is a good assumption only if the scattering is symmetric in the forward and the backward direction such as Rayleigh scattering of EM waves because g is same and for optically thick and thin medium and is equal to zero. For acoustic waves due to mode conversion, analytical solution of the phase function will be a tedious task.

However in simple cases such as geometric scattering of the transverse wave that does not go through mode conversion by a sphere, the acoustic phase function will be exactly same as the optic phase function, which is readily available in radiation literature [12].

5 Mean Free Path of Simple Scatterers

In this section we calculate the m.f.p of two simple types of scatterer: (1) acoustically hard Rayleigh sphere, and (2) geometric scatterer for transverse wave incidence. We also discuss the calculation of m.f.p for the general case in the two scattering regime. Both the cases are for the transverse wave which does not go through mode conversion.

Rayleigh Scattering. An acoustically hard Rayleigh sphere is considered for analysis. Rayleigh scattering is valid in the long wavelength regime or for $kr \ll 1$ where r is the radius of the sphere. It can be shown using the analysis in [13] that for plain wave incidence $f(\theta_p)$ is given by

$$f(\theta_p) = \left(\frac{1}{3} + \frac{1}{2}\cos(\theta_p)\right)^2 (kr)^6 \tag{42}$$

and using Eq. (39) σ is given by

$$\sigma = \frac{7}{9} \pi r^2 (kr)^4 \tag{43}$$

Note Eq. (42) is only valid that transverse wave which does not go through mode conversion. Equation (43) shows that scattering cross section for Rayleigh scatterer varies as the 4th power or the wave vector. Using Eqs. (35), (38), and (42) σ_T for the diffusive regime is given as

$$\sigma_T = \frac{3}{9} \pi r^2 (kr)^4 \tag{44}$$

Equations (43) and (44) clearly show that difference between the transport and scattering cross section can be big depending on the situation. Using definition of Φ from Eq. (37) Φ for an acoustically hard Rayleigh sphere for plane wave incidence can be expressed as

$$\Phi(\mu_p) = \frac{36}{7} \left(\frac{1}{3} + \frac{1}{2}\mu_p\right)^2 \tag{45}$$

Figure 2 shows the polar plot of $\Phi(\mu_p)$. Figure 2 shows that the scattering is highly anisotropic and asymmetrical in forward direction. Therefore the m.f.p for this case will be larger than that calculated by assuming isotropic scattering. Table 1 shows the value of g for both isotropic and anisotropic case. Equation (18) is used to calculate g for the acoustically thick regime. Table 1 also shows the error in the calculation of m.f.p if isotropic scattering is assumed. The error is defined as $(l'_p - l_p)/l_p$ where l'_p is calculated using Eq. (36). Table 1 shows that the error in the m.f.p is 133% if isotropic assumption is assumed.

For the calculation of g in the acoustically thin regime Eq. (24) is used. For the calculation of B in Eq. (25), $\Phi(\mu_i, \mu)$ has to be calculated. $\Phi(\mu_p)$ in Eq. (45) can be written as a summation of Legendre functions in the form expressed in Eq. (15). This enables the calculation of a_i in Eq. (15). Once a_i is known using Eq. (16), $\Phi(\mu_i, \mu)$ can be expressed as

$$\Phi(\mu_i, \mu) = \frac{36}{63} \left(\frac{7}{4} + 3\mu_i\mu + \frac{3}{8}(3\mu_i^2 - 1)(3\mu^2 - 1)\right) \tag{46}$$

Table 1 shows that the value of g is different for the acoustically thin and thick medium. This shows that the m.f.p is different for the acoustically thin and thick medium. The difference in m.f.p between the acoustically thin and thick medium is 25%. This calculation clearly shows that the m.f.p formulation given by transport theory provided in standard solid state textbook is only valid
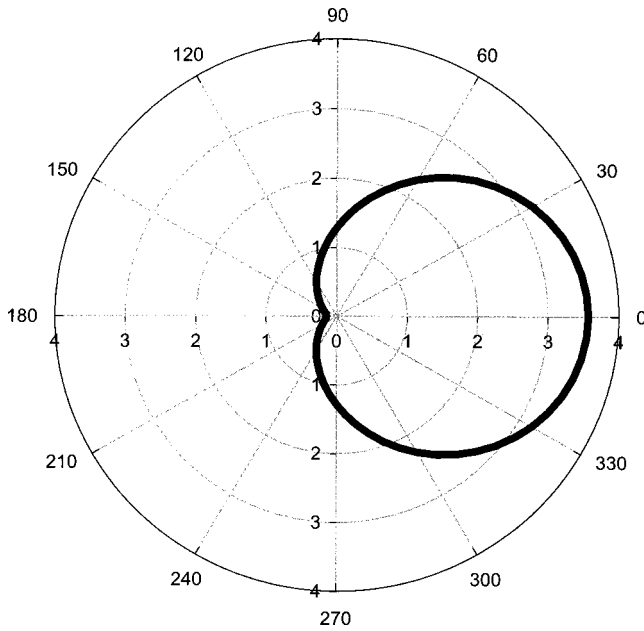
Fig. 2 Polar plot of the phase function of an acoustically hard Rayleigh sphere

Fig. 3 Schematic of the multiple reflection and refraction of acoustic waves by a large sphere

for the diffusive or acoustically thick regime. This also shows that m.f.p due to particle scattering is size dependent.

Calculation of the transport cross section and the phase function for an elastic sphere for longitudinal and in-plane transverse wave will be a tedious task. Various authors have computed the scattering cross section for elastic Rayleigh sphere [14,15] for both longitudinal [14] and for transverse wave incidence [15]. The challenge will be to convert these relation to extract the transport cross section from these analyses for heat transfer problems. De Walton [8] has given the formulation to calculate σ_T for longitudinal wave incidence using the work of Ying and Truell [14] for the diffusive regime.

Geometrical Scattering. Next set of calculations are performed for a large sphere where the scattering is in the geometric acoustic regime, i.e., $kr \gg 1$. Calculations are only performed for that transverse wave which does not go through mode conversion for simplicity [16]. Figure 3 shows the phenomenon of multiple reflection and refraction of plane acoustic waves through a sphere without mode conversion. For a geometrical scatterer $\Phi(\mu_p)$ will be a summation series to account for multiple reflections and refractions as shown in Fig. 3. $\Phi(\mu_p)$ for electromagnetic waves is given in Hottel [12] for the geometrical scattering case. The same formula can be used for the geometrical acoustics without mode conversion except the reflectivity will be the acoustic reflectivity. $\Phi(\mu_p)$ for this case will can be written as [12]

$$\Phi_m(\theta_p) = \frac{4(1-R)^2 R^{m-1} \cos(\tau)\sin(\tau)}{\sin(\theta_p)\left|\dfrac{2m\sin(\tau)}{((c_m/c_p)^2 - \cos^2(\tau))^{1/2}} - 2\right|} \quad (47)$$

Table 1 Mean free path. of an acoustically hard Rayleigh sphere

Type of scattering	g for Acoustically Thick	g for Acoustically Thin
Isotropic	0	0
Anisotropic	0.571	0.429
% error in m.f.p compared to Isotropic scattering	133%	75%
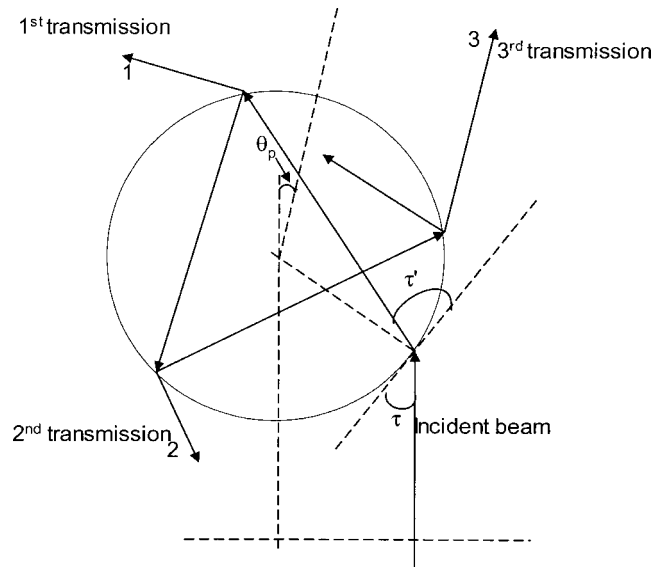
where c_p and c_m are speed of sound in the particle and the host medium respectively, τ is the angle of the incident wave as shown in Fig. 3 and τ' is the angle of refraction as shown in Fig. 3, and R is the reflectivity of the acoustic wave. The subscript m denotes the number of transmissions as shown in Fig. 3. The phase function is obtained by summing the phase function for all m and is given by [12]

$$\Phi(\theta_p) = \frac{R + \sum_{m=1}^{\infty} \Phi_m(\theta_p)}{\int_0^{\pi}\left[R + \sum_{m=1}^{\infty} \Phi_m(\theta_p)\right]\dfrac{\sin(\theta_p)d\theta_p}{2}} \quad (48)$$

For total internal reflection $R=1$ which makes $\Phi=1$ from Eqs. (47) and (48). This shows that for the geometrical scattering case isotropic assumption only holds for total internal reflection.

The series summation of Φ [12] is easy but mathematically cumbersome making the calculation of $\langle\Phi\rangle$ very difficult. Van de Hulst [11] provides an elegant method of calculating $\langle\Phi\rangle$ for geometrical scatterer for electro magnetic waves. The same formula can be used for acoustic waves without mode conversion. $\langle\Phi\rangle$ is given by [11]

$$\langle\Phi\rangle = \int_0^1 \frac{2R^2(1-\cos 2\tau') + (1-R)\cos(2\tau - 2\tau')}{1 - 2R\cos 2\tau' + R^2} d(\cos^2\tau) \quad (49)$$

R for plane wave incidence is given by [17]

$$R(\tau) = \frac{4Z\sin\tau\sqrt{1 - [c\cos\tau]^2}}{[\sin\tau + Z\sqrt{1 - [c\cos\tau]^2}]^2} \quad (50)$$

where Z is the acoustic refractive index ratio of the particle and host medium, and c is the ratio of speed of sound between the particle and the host medium (c_p/c_m). Z is given by $(\rho_p c_p)/(\rho_m c_m)$ where ρ_p and ρ_m are the density of the particle and the host medium respectively. The angles τ and τ' are related to each other by Snell's law as

$$\cos\tau' = c\cos\tau \quad (51)$$

Using Eqs. (49)–(51), $\langle\Phi\rangle$ can be easily calculated for different values of Z and c. Figure (4) shows the plot of g for various values of Z and c. Note that $g = \langle\Phi\rangle$ in the acoustically thick limit. Figure
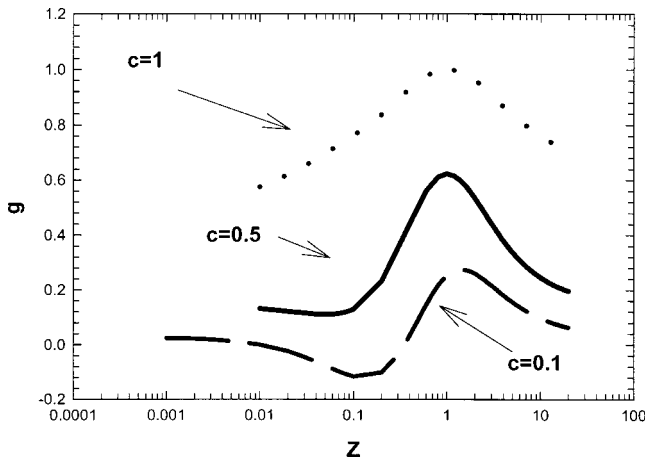
Fig. 4 Values of g for a large sphere acoustically thick regime for various values of Z and c

4 also shows that g can be very different from 1 depending on the values of Z and c. Figure 4 shows that g can be negative or positive. This means that m.f.p can larger or smaller than isotropic m.f.p depending on the value of Z and c. Figure 4 also shows that $g = 1$ for $Z = 1$ and $c = 1$, i.e., for the case where there is no acoustic mismatch between the particle and the host medium. This also means that particles are same as the medium. For this case the particles are not scatterers and therefore m.f.p due to the particle will be infinite. However if one uses the isotropic scattering, i.e., transport cross sections is same as the scattering cross-section to calculate the m.f.p, as proposed by Majumdar [1], m.f.p will be finite leading to wrong conclusions and the interpretations will not be consistent. The formulation proposed in this manuscript removes this discrepancy. The calculations have not been performed for the acoustically thin case for large spheres as it involves the calculation of Φ but is conceptually simple as shown by Eq. (48). The calculations are conceptually very simple for this case and one can utilize the formulation of Φ given in [8]. For longitudinal wave incidence and other transverse wave incidence, the phase function formulation given by Eq. (48) is probably not valid. However, it seems that in the geometrical scattering regime, for the mode conversion case one can use numerical techniques given in [16] and the methodology given in [12] to derive the no-mode conversion case (Eq. (48)), for the calculation of phase function. De Walton [8] has given the formulation for the calculation of transport cross section for longitudinal wave incidence for all values of kr but those formulations are valid only for the diffusive transport regime.

6 Application of GEPRT

The isotropic assumption has been assumed to work well for Rayleigh particles [1]. One of the main reasons that it has been assumed to work well is because most of the work on phonon transport do not deal with predictive modeling of thermal conductivity because the m.f.p of phonon is obtained from the bulk thermal conductivity data by applying kinetic theory [1]. This m.f.p is put back into EPRT for the calculation of thermal conductivity of thin film structures [1]. For pure materials such as Silicon, the atomic impurity scattering due to particle is anisotropic in nature [3] but due to other major uncertainty such as the definition of elastic properties for atomistic impurities it is assumed that the scattering is isotropic [3]. The implications of the anisotropy and asymmetrical scattering might not be serious for atomic scatterer due to other unknowns, but due to the advent of nano technology there will be situations where a proper understanding of the acoustic phase function and anisotropic scattering becomes very important. The general direction of microscale heat transfer is to de-

velop predictive models for thermal conductivity [18] which will require assessing the effect of anisotropic scattering by particles.

There are various situations where the asymmetric nature of scattering will play a big role. Some of the technologies/situations where the GEPRT will be needed to predict and infer the thermal properties are: Nano composites, nanoparticle laden systems such as nano fluids, carbon nanotube/nanofibres laden systems, thin film thermoelectrics at low temperatures etc. Next paragraph provides a brief discussion on usefulness of GEPRT for certain situations.

For example if a composite is made out of ceramic and carbon nanotube [19], then at low temperatures thermal transport in the carbon nanotube will be ballistic. This situation is similar to scattering of EM waves by fibers, which is highly anisotropic and asymmetrical [20]. Similarly for two phase systems containing nano particles or colloidal particles such as nano fluids [21], the transport can be ballistic in the particles at low temperatures. Some times transport properties such as thermal conductivity is also used to estimate the size of nano particles by fitting the theoretical model with experimental data [8]. Understanding of the anisotropy and asymmetry of the scattering by the particles will play an important role in extracting the dimensions of the particles. The usefulness of GEPRT is that these complex situations can be readily analyzed using existing work on radiation for these complex situations. Researchers have also proposed the use of nanowires imbedded in a solid media to reduce the thermal conductivity of composites [22,23]. These composites can be used as thermoelectric devices. Heat transfer in the nanowire will be ballistic at low temperatures and may be even at the room temperature and the scattering will be highly anisotropic and asymmetrical. This paper also shows that m.f.p due to particle scattering depends on the acoustic thickness of the medium where as it is a common practice to assume that m.f.p obtained from bulk thermal conductivity can be used to calculate the thermal conductivity of thin samples [1]. This might lead to wrong conclusions and interpretations.

Finally a phase function can also be defined for electron transport. Following the same approach as phonons, the steady state Boltzmann transport equation under the relaxation time approximation can be written as

$$\nu \cdot \nabla F_\omega + a \cdot \frac{\partial F_\omega}{\partial \nu} = K_u(F_\omega^0 - F_\omega) - K_p F_\omega$$

$$+ \frac{K_p}{4\pi} \int_{4\pi} \Phi(\Omega' \to \Omega) F_\omega(\Omega') d\Omega' \quad (52)$$

Even for electronic transport the transport cross section for spherical scatterer is given by Eq. (35), which essentially means the solution of Eq. (52) in the diffusive regime.

Conclusions

In summary we have extended the equation of phonon radiative transport under the relaxation time approximation for anisotropic scattering by a particulate media. The strength of using the general form is that any complicated situation such as nanotube or nano particle laden two component system can be analyzed using the existing solution techniques from radiation heat transfer literature. GEPRT is totally consistent with EPRT and the existing transport theory. GEPRT also shows that m.f.p due to particles depends on the acoustic thickness of the medium and one needs to make sure that using bulk m.f.p is right or not for the acoustically thin medium depending upon the situation. This paper also provides a simpler method to calculate the m.f.p of a geometrical scatterer.

Nomenclature

a = acceleration of carriers (ms^{-2})
a_i = coefficient in Eq. (15)
B = Parameter in acoustically thin limits (Eq. 25)
c_m = speed of sound in the medium (ms^{-1})
c_p = speed of sound in the particle (ms^{-1})
c = ratio of speed of sound in the particle and the medium
F = distribution function in Boltzmann Equation (Eq. 26 and 52)
f = scattering function
g = factor in Eq. (19)
I = phonon or photon Intensity (Wm^{-2} sr^{-1} s)
k = wave vector (m^{-1})
k' = wave vector after scattering (m^{-1})
K_e = extinction coefficient (m^{-1})
K'_e = effective extinction coefficient (m^{-1})
K_p = scattering coefficient due to particle scattering (m^{-1})
K_u = scattering coefficient due to Umklapp scattering (m^{-1})
l = mean free path (m)
l'_{eff} = effective mean free path (m)
l_p = mean free path due to Particle scattering (m)
l'_p = effective mean free path due to particles (m)
l_u = mean free path due to Umklapp scattering (m)
m = number of reflections
m.f.p = mean free path
n = number of particles per unit volume (m^{-3})
P_i = Legendre polynomial
R = reflectivity of acoustic waves
r = radius of particles (m)
T = temperature (K)
T = time (s)
v = velocity of carriers (ms^{-1})
w = scattering albedo
x = x direction
Z = acoustic refractive index

Greek

$\langle \Phi \rangle$ = asymmetry factor
$d\sigma$ = differential scattering cross section (m^2)
Φ = phase function
Λ_i = transport scattering time (s)
Ω = solid angle (sr)
δ = size parameter (Eq. 9)
μ = direction cosine
ρ = density (kg m^{-3})
σ = scattering cross section (m^2)
σ_T = transport cross section (m^2)
τ = angle of incidence
τ' = angle of reflection
Γ = differential scattering probability (Eq. 28)
ω = angular frequency (s^{-1})

Superscript

0 = equilibrium

Subscript

i = incoming
iso = isotropic scattering
m = medium
p = particle
ω = denoted frequency dependence

References

[1] Majumdar, A., 1993, "Microscale Heat Conduction in Dielectric Thin Films," ASME J. Heat Transfer , **115**, pp. 7–16.
[2] Prasher, R. S., 2003, "Generalized Equation of Phonon Radiative Transport," Appl. Phys. Lett., **83**(1), pp. 48–50.
[3] Ziman, J. M., 1996, *Electrons and Phonons*, Oxford Press, London.
[4] Brewster, M. Q., 1992, *Thermal Radiative Transfer and Properties*, John Wiley & Sons, Inc., New York.
[5] Modest, M. F., 1993, *Radiative Heat Transfer*, McGraw Hill, Inc., New York.
[6] Ozisik, M. N., 1985, *Radiative Transfer and Interactions with Conduction and Convection*, Werbel and Peck, New York.
[7] Chen, G., 1997, "Size and Interface Effects on Thermal Conductivity of Superlattices and Periodic Thin-Film Structures," ASME J. Heat Transfer , **119**, pp. 220–229.
[8] Walton, D., and Lee, E. J., 1967, "Scattering of Phonons by a Square-Well Potential and the Effect of Colloids on the Thermal Conductivity. II. Theoretical," Phys. Rev., **157**(3), pp. 724–729.
[9] Peierls, R. E., 2001, *Quantum Theory of Solids*, Oxford Classic Texts, Oxford
[10] Van Rossum, M. C. W., and Nieuwenhuizen, M. Th., 1999, "Multiple Scattering of Classical Waves: Microscopy, Mesoscopy, and Diffusion," Rev. Mod. Phys., **71**(1), pp. 313–371.
[11] Van De Hulst, H. C., 1981, *Light Scattering by Small Particles*, Dover Publication Inc., New York.
[12] Hottel, H. C., and Sarofim, A. F., 1967, *Radiative Transfer*, McGraw-Hill Book Company, New York.
[13] Bowman, J. J., Senior, T. B. A., and Uslenghi, P. L. E., 1987 *Electromagnetic and Acoustic Scattering by Simple Shapes*, Hemisphere Publishing Corporation, London.
[14] Ying, C. F., and Truell, R., 1956, "Scattering of a Plane Longitudinal Wave by a Spherical Obstacle in an Isotropically Elastic Solid," J. Appl. Phys., **27**(9), pp. 1086–1097.
[15] Einspruch, N. G., Witterholt, E. J., and Truell, R., 1960, "Scattering of a Plane Transverse Wave by a Spherical Obstacle in an Elastic Medium," J. Appl. Phys., **31**(5), pp. 806–818.
[16] Cheek, J. D. N., Ettinger, H., and Hebral, B., 1976, "Analysis of Heat Transfer Between Solids at Low Temperatures," Can. J. Phys., **54**, pp. 1749–1770.
[17] Prasher, R. S., and Phelan, P. E., 2001, "A Scattering Mediated Acoustic Mismatch Model for the Prediction of Thermal Boundary Resistance," ASME J. Heat Transfer , **123**(1), pp. 105–112.
[18] Cahill, D. G., Ford, W. K., Goodson, K. E., Mahan, G. D., Majumdar, A., Maris, H. J., Merlin, R., and Phillpot, S. R., 2003, "Nanoscale Thermal Transport," J. Appl. Phys., **93**(2), pp. 793–818.
[19] Thostenson, E. T., Ren, Z., and Chou, T.-W., 2001, "Advances in the Science and Technology of Carbon Nanotubes and Their Composites: A Review," Compos. Sci. Technol., **61**, pp. 1899–1912.
[20] Yamada, J., and Kurosaki, Y., 2000, "Radiative Characteristics of Fibers with a Large Size Parameter," Int. J. Heat Mass Transfer, **43**, pp. 981–991.
[21] Keblisnki, P., Phillpot, S. R., Choi, S. U. S., and Eastman, J. A., 2002, "Mechanisms of Heat Flow in Suspensions of Nano-sized Particles (Nanofluids)," Int. J. Heat Mass Transfer, **45**, pp. 855–863.
[22] Dresselhaus, G., Dresselhaus, M. S., Sun, X., Zhang, Z., and Chen, G., 1998, *Modeling Thermoelectric Behavior in Bi Nano-Wires*, 17th International Conference on Thermoelectrics, pp. 43–46
[23] Borca-Tasciuc, D-A., Chen, G., Martin-Gonzales, M. S., Prieto, A. L., Stacy, A., Sands, T., Borshchevsky, A., Fleurial, J-P., and Ryan, M. A., 2002, "Thermal Diffusivity Characterization of Bi$_2$Te$_3$ Nanowires Array Inside Amorphous Alumina Template," *Proceedings of ASME International Mechanical Engineering Congress and Exposition*, Paper No. IMECE2002-32774, November 17–22, New Orleans, Lousiana

Seong-Yeon Yoo
e-mail: syyooh@cnu.ac.kr

Jong-Hark Park
e-mail: pjh5250@cnu.ac.kr

Department of Mechanical Design Engineering,
Chungnam National University,
Gungdong, Yusungku, Daejeon, 305-764, Korea

Chang-Hwan Chung
e-mail: cchwan@nanum.kaeri.re.kr

Moon-Ki Chung
e-mail: mkchung@nanum.kaeri.re.kr

Korea Atomic Energy Research Institute,
Dukjindong, Yusungku, Daejeon, 305-353,
Korea

An Experimental Study on Heat/Mass Transfer From a Rectangular Cylinder

Local and average mass transfer rates from a rectangular cylinder having various width to height ratios are measured using naphthalene sublimation technique, and influence of flow characteristics on mass transfer is investigated. The experimental apparatus comprises a wind tunnel, a naphthalene casting facility and a sublimation depth measurement system. Mass transfer data are compared with those of heat transfer which are obtained using thermocouples in the constant heat flux boundary condition, and analogy between heat and mass transfer is examined. The reasons for discrepancy in both transport values are explained in detail.
[DOI: 10.1115/1.1603780]

Keywords: Cylinder, Experimental, Forced Convection, Heat Transfer, Mass Transfer

Introduction

The rectangular cylinder is one of the most interesting bluff bodies in connection with long standing question of heat transfer mechanism in the separating, reattaching and recirculating flow region. The flow approaching to the cylinder stagnates and accelerates on the front face, separates and reattaches on the side faces, and sheds vortices from the rear face. And the aerodynamic characteristics vary drastically as the width to height ratio (c/d) of the cross section of the cylinder increases. Bearman and Trueman [1] measured the base pressure coefficient, drag coefficient and Strouhal number of rectangular cylinders having various width to height ratio, and found a maximum value of drag when $c/d = 0.62$. Igarashi [2] carried out experimental investigations on the characteristics of the flow around rectangular cylinders with $c/d = 0.1 - 4.0$, and found distinct changes of flow patterns at two critical values of $c/d = 0.67$ and 2.8.

It is very important to understand how the complex flow around a rectangular cylinder affect heat transfer. Igarashi [3–5] measured local heat transfer coefficient distribution around a square cylinder and rectangular cylinders using thermocouples, and found that heat transfer coefficients are closely related to the drag coefficients. Ota and Kon [6] conducted heat transfer measurements in the separated, reattached and redeveloped regions of two dimensional air flow over flat plate with blunt leading edge, and found that the separated shear layer play very important role on heat transfer. In this study, naphthalene sublimation technique is employed to measure detailed local mass transfer from a rectangular cylinder, then measured mass transfer data are converted to their counter part of heat transfer process by applying heat/mass transfer analogy. Goldstein et al. [7] and Yoo et al. [8] measured local mass transfer from a square cylinder and its base plate using a naphthalene sublimation technique, and compared mass transfer data with heat transfer data of Igarashi [3,4]. Average values of heat and mass transfer are in good agreement with each other, but local rates of mass transfer are much higher than those of heat transfer when the separated flow reattaches to the side face of the cylinder, which is compensated with the lower values in the rear face [8].

The first purpose of this study is to investigate how flow characteristics influence the distribution of local mass transfer coefficients on each face of rectangular cylinders. The naphthalene sub-

limation technique is applied to obtain local mass transfer rates, and width and height ratio of rectangular cylinder and inlet air velocity are varied. The second purpose is to examine heat and mass transfer analogy in the complex flow conditions. To do this, mass transfer data are compared with those of heat transfer [5] obtained with the same geometries and flow conditions.

Experimental Apparatus and Data Reduction

Experimental Apparatus. The experimental apparatus comprises a wind tunnel, a naphthalene casting facility and an automated sublimation depth measurement system. An open-circuit, blowing-type wind tunnel is used, which has square test section of 300 mm wide×300 mm high. The air speed of the wind tunnel is controlled by an inverter and the free-stream turbulence intensity is less than 0.5 percent over the entire range of speeds. Air velocity is measured by pitot tube, and air temperature is measured by RTD.

The automated sublimation depth measurement system consists of a depth gage along with a signal conditioner, two stepper-motors-driven X-Y traversing table, a hardware unit for motor control, and data acquisition system. The depth gage used to measure the naphthalene surface profile is a linear variable differential transformer (hereafter LVDT), which has ±0.254 mm (±0.01 in) linear range and 25.4 nm (1 μ in) resolution. It is connected to a signal conditioner which supplies current to the LVDT for excitation, converts the AC signal output of the depth gage to a DC voltage. For precise and automatic positioning of the LVDT on the test-piece, LVDT and test-pieces are tightly mounted on an X-Y traverse table, and two stepper motors move the table with 0.0254 mm (0.001 in) per step. The data acquisition system equipped with personal computer controls the movements of stepper-motors and gets the measured data from the signal conditioner.

The test-piece is made of duralumin and machined with 1.5 mm depth and 76 mm length to hold casting naphthalene as shown in Fig. 1. The height of the cross-section of the rectangular cylinder is taken as 20 mm and 30 mm, and width to height ratio (c/d) of the test-pieces varied from 0.33 to 1.5 as described in Fig. 2. The test-piece is installed vertically in the test section of the wind tunnel. Free stream velocity in the test section is varied from 6 to 20 m/s, and corresponding Reynolds number based on d is 7.5 $\times 10^3 < \mathrm{Re} < 3.75 \times 10^4$.

Data Reduction. Using the sublimation depth measurement system, surface profiles are measured on each face of rectangular

---

Fig. 1 Schematic of testpiece

c/d	c - d (mm)
0.33	10 - 30
0.66	20 - 30
1.0	30 - 30
1.33	40 - 30
1.5	30 - 20

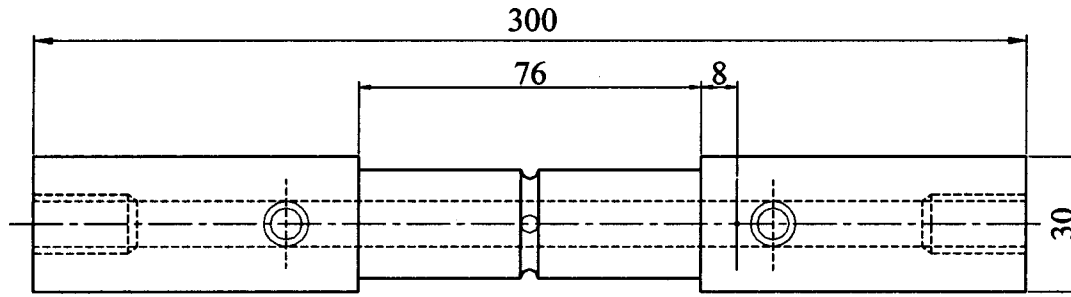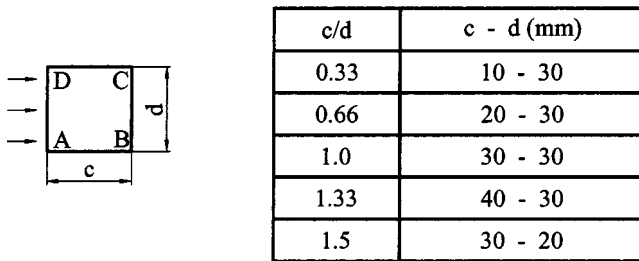**Fig. 2 Geometries of rectangular cylinder**

cylinder before and after the exposure in the wind tunnel. Then, the mass transfer coefficients are determined from the following equation:

$$h_m = \rho_s \Delta t / \rho_{v,w} \Delta \tau \qquad (1)$$

where ρ_s is the density of the solid naphthalene, $\rho_{v,w}$ is the naphthalene vapor density on the surface, Δt is the net sublimation depth, and $\Delta \tau$ is the total exposure time in the wind tunnel. Total naphthalene sublimation depth is calculated from the difference in

naphthalene surface elevations before and after the exposure in the wind tunnel, and the excess sublimation due to natural convection during the sublimation depth measurement period is subtracted from the total sublimation. Approximately 0.05 mm naphthalene is sublimated during an hour run, but geometry change due to sublimation does not affect flow condition. The empirical equation of Ambrose et al. [9] is used to calculate the naphthalene vapor pressure from the naphthalene surface temperature, which equals to air temperature when steady state is reached. Naphthalene vapor density on the surface is then evaluated using the ideal gas law. The measured mass transfer coefficients are presented in the dimensionless form, that is, in terms of Sherwood number, defined as follows:

$$\mathrm{Sh} = h_m d / D_{iff} \qquad (2)$$

The height of the rectangular cylinder, d, is chosen as a characteristic length, and the mass diffusion coefficient of naphthalene in air, D_{iff}, is determined from Cho's correlation [10].

In accordance with uncertainty analysis recommended by Kline and McClintock [11], the estimated error of Sherwood number is determined as follows:

$$\frac{\Delta \mathrm{Sh}}{\mathrm{Sh}} = \sqrt{\left(\frac{\Delta \rho_s}{\rho_s}\right)^2 + \left(\frac{\Delta \Delta t}{\Delta t}\right)^2 + \left(\frac{\Delta \rho_{v,w}}{\rho_{v,w}}\right)^2 + \left(\frac{\Delta \Delta \tau}{\Delta \tau}\right)^2 + \left(\frac{\Delta d}{d}\right)^2 + \left(\frac{\Delta D_{iff}}{D_{iff}}\right)^2}$$
$$= \sqrt{0.011^2 + 0.02985^2 + 0.04266^2 + 0.00278^2 + 0.001^2 + 0.03^2} \qquad (3)$$

Three factors(uncertainties of LVDT, dislocation of measurement point, natural convection of naphthalene during measurement) are considered to estimate the uncertainty of sublimation depth, and their errors are 0.00008/0.03=0.0027, 0.02086/0.7=0.0298, and 0.004, respectively. The uncertainty of naphthalene vapor density is determined from the uncertainties of naphthalene vapor pressure (29.05×0.4/300=0.0386), universal gas constant(ignored) and measured temperature (0.2/(303−293)=0.018). Considering the time to reach steady state in the wind tunnel, $\Delta\Delta\tau/\Delta\tau$ becomes 10/3600. Measured sublimation depth is about 0.02–0.03 mm, so $\Delta d/d$ is 0.03/30. The measurement error for density of solid naphthalene and diffusivity of naphthalene to air is cited from Goldstein and Cho [12]. Therefore, overall uncertainty of Sherwood number is estimated to be 6.11 percent.

Results and Discussion

Mass Transfer Distribution. The distributions of local Sherwood number for the rectangular cylinders with c/d = 0.33, 0.67, 1.0, 1,33 and 1.5 are shown in Fig. 3. Mass transfer coefficients

are measured at 19 (with equal interval which depends on c or d)×11 (with 8 *mm* interval in the spanwise direction) locations on each surface of the rectangular cylinders, and averaged in the spanwise direction. Dramatic variations of mass transfer coefficients are seen on each face of the cylinder, which are closely related to the flow characteristics illustrated in Fig. 4 [4]. On the front face of the cylinder, the local Sherwood number has a minimum at the center of the face, and increases gradually toward the edges regardless of width to height ratio. This trend is in contrast with that of circular cylinder, in which local transfer rates decreases from the stagnation point to separation. Flow in front of a square cylinder stagnates at the center of the front face, and accelerates toward the edges with decreasing boundary layer thickness. On the other hand, flow in front of a circular cylinder accelerates from the front stagnation point with increasing boundary layer thickness. On the side faces, the local Sherwood number has a minimum near the leading edge, and increases rapidly toward the trailing edge due to active turbulent eddy motion which is similar to that seen in the separated flow region of a circular cylinder. The variation of the local Sherwood number is very similar to each other except for c/d=0.33. After the separated flow from the leading edge rolls up, it reattaches on the rear face,
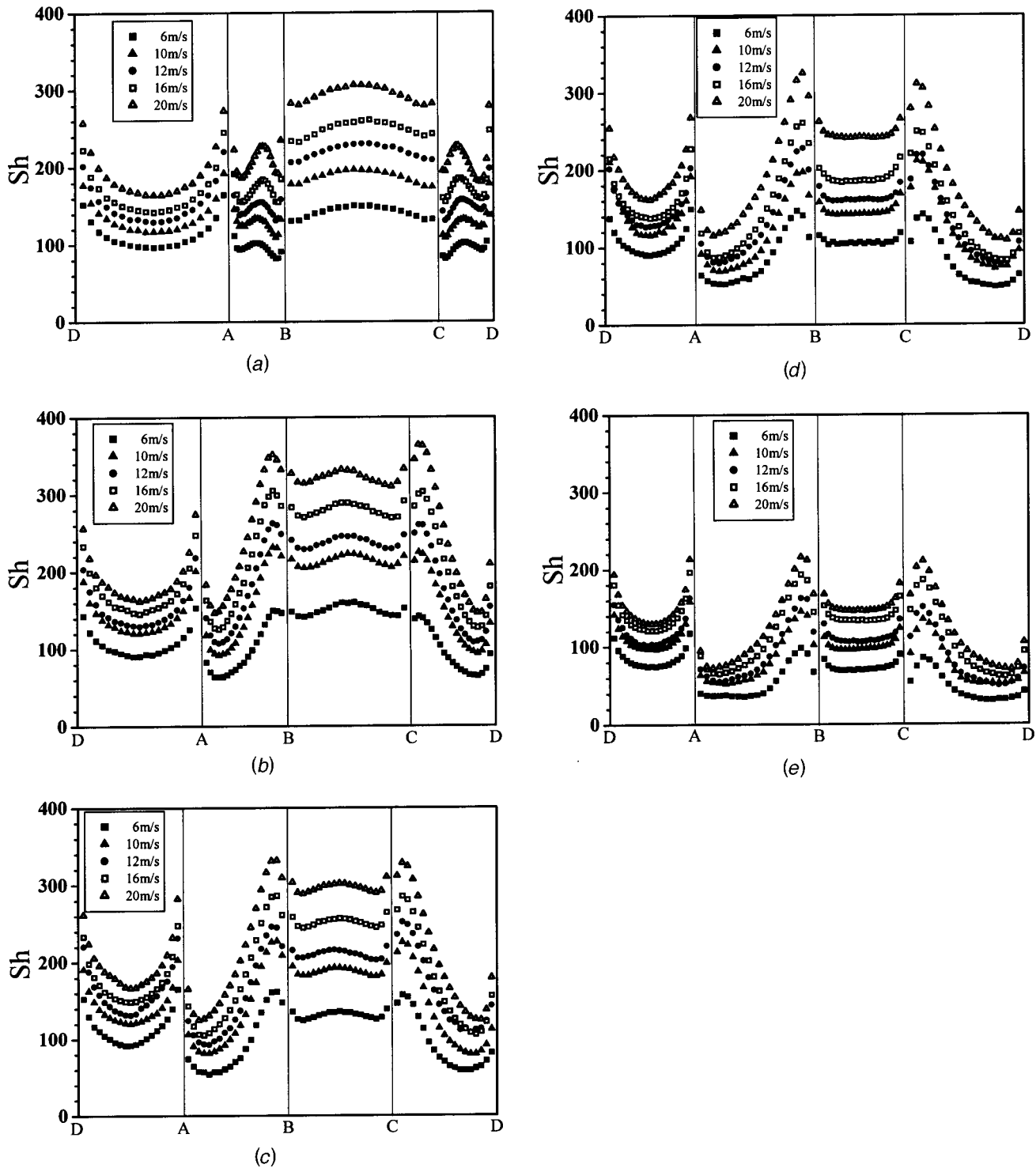
Fig. 3   Distribution of local Sherwood numbers on the rectangular cylinders: (a)c/d**=0.33; (b)**c/d**=0.67; (c)**c/d**=1.0; (d)** c/d**=1.33; and (e)** c/d**=1.5**

passes back around the trailing edge, and then reattaches on the side face [4]. Local maximum in case of $c/d \geq 0.67$ is assumed to be the reattachment point of back flow [13], and mass transfer decrease thereafter. But there is no such a phenomena at c/d $=0.33$, and flow characteristics around the rectangular cylinder seems to be changed drastically at about $c/d=0.67$, On the rear face, the distribution of local Sherwood number looks like convex shape for $c/d=0.33$, "W" shape for $c/d=0.67$ and 1.0, and concave shape for $c/d=1.33$ and 1.5. It is well known that vortices formed in the vicinity of rear face shed alternately from a cylinder.

According to Igarashi [2], the location of vortex formation moves upstream with increasing c/d until $c/d \approx 0.7$, and move downstream afterwards. Nakaguchi et al. [14] also reported that vortex is formed closest to the rear face at about $c/d=0.6$ and 0.7. The change in shape of the local Sherwood number distribution is closely related to the location of vortex formation. Two alternate vortices impinge on the middle of rear face and move away from the surface near the corner. Impingement leads to high mass transfer, and relatively low mass transfer values are seen in the upwash region of vortices. But vortices become less influential as the c/d
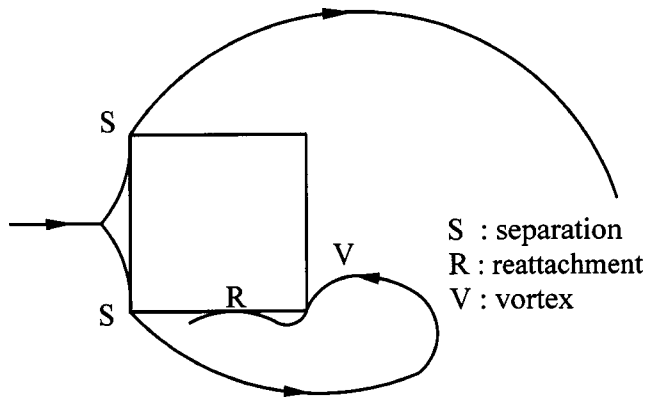
Fig. 4   Sketch of assumed flow structure around a rectangular cylinder

increases, so the distribution of local Sherwood number is almost flat shape in case of $c/d = 1.33$ and 1.5. It is interesting to note that the Sherwood numbers of the rear face are higher than those of front face, and the differences of Sherwood numbers between front and rear face become smaller with increasing c/d.

Figure 5 shows the variations of average Sherwood numbers on each face with Reynolds number. The Sherwood numbers on the front face are correlated well with the relation $\text{Sh} = C\,\text{Re}^{1/2}$ regardless of c/d, which is usually applied to the heat transfer in the laminar boundary layer flow. The Sherwood number on the side face and rear face are agreed well with the relation $\text{Sh} = C\,\text{Re}^{2/3}$ except $c/d = 0.33$. The slope in case of $c/d = 0.33$ is less steep than that of the others, and this is somewhat different from the results of heat transfer measurement in which the exponent n is taken to be 2/3 regardless of c/d [5].

The variation of average Sherwood number with height to width ratio at the freestream velocity of 16 m/s is presented in Fig. 6. On the front face, average Sherwood numbers are almost same except $c/d = 1.5$, in which characteristic length is shorter than the others. On the contrary, distinct change of average Sherwood numbers is seen at $c/d = 0.67$ on the side and rear faces. As explained before, the location of vortex formation is closest at $c/d = 0.67$, and therefore mass transfer values are highest in this case. As the c/d increases, the location of vortex formation moves downstream and the Sherwood number decreases. It is coincident with the fact that fluctuation pressure coefficients peak at $c/d = 0.67$, and decrease rapidly with increasing c/d [1,5,14]. The average Sherwood number on the rear face is much higher than that of side face for all cases, and the reason is considered to be that vortex shedding enhances heat transfer on the rear face.

Heat/Mass Transfer Analogy.   The measured mass transfer coefficients or Sherwood numbers are converted to their counterpart of heat transfer process using the analogy equation. In general, heat transfer data for the forced convective heat transfer process can be expressed as follows:

$$\text{Nu} = C\,\text{Re}^m\text{Pr}^n \tag{3}$$

A similar correlation can be adopted for the forced convective mass transfer process as follows:

$$\text{Sh} = C\,\text{Re}^m\text{Sc}^n \tag{4}$$

Dividing Eq. (3) by Eq. (4) yields following heat and mass transfer analogy relation.

$$\text{Nu}/\text{Sh} = (hd/k)/(h_m d/D_{iff}) = (\text{Pr}/\text{Sc})^n \tag{5}$$

Although exponent n varies depending on geometries and flow conditions, 1/3 is usually used for external flows.

In Fig. 7, mass transfer data are compared with those of heat transfer obtained in the same geometries and flow conditions. In

(a)

(b)

(c)
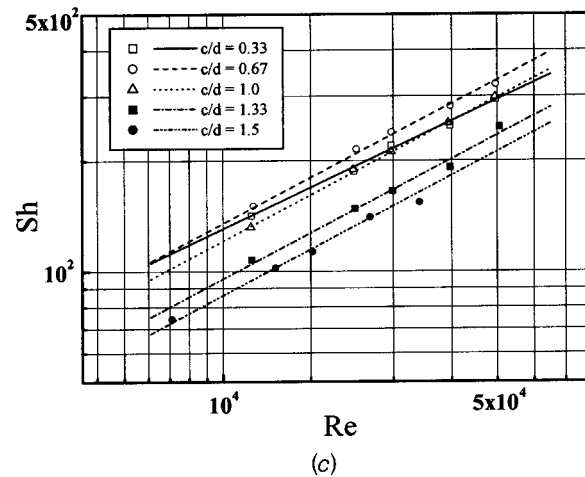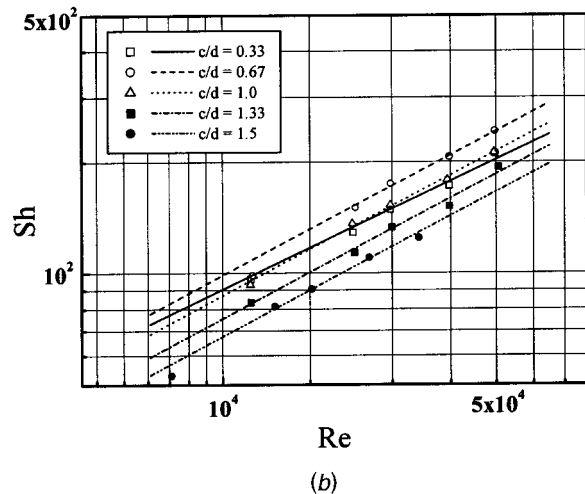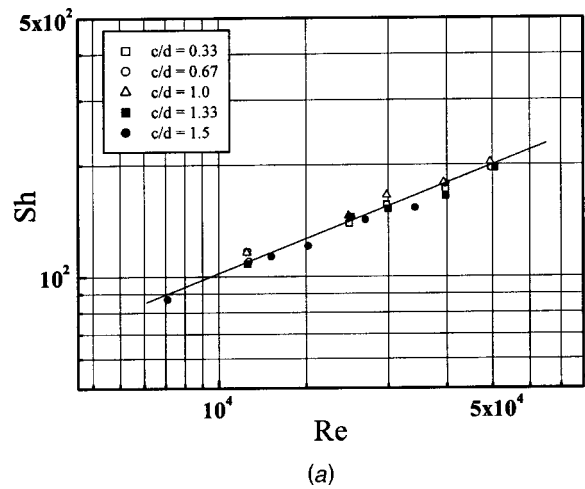
Fig. 5   Variation of average Sherwood number with Reynolds number: (a) front face; (b) side face; and (c) rear face

the heat transfer experiment [5], the whole surface of the test cylinder is covered with a stainless-steel sheet of 0.02 mm thick, and temperatures on each face of a rectangular cylinder are measured using thermocouple under the condition of constant heat flux. The Sherwood numbers obtained in the present study are converted to the dimensionless heat transfer coefficients, Nusselt
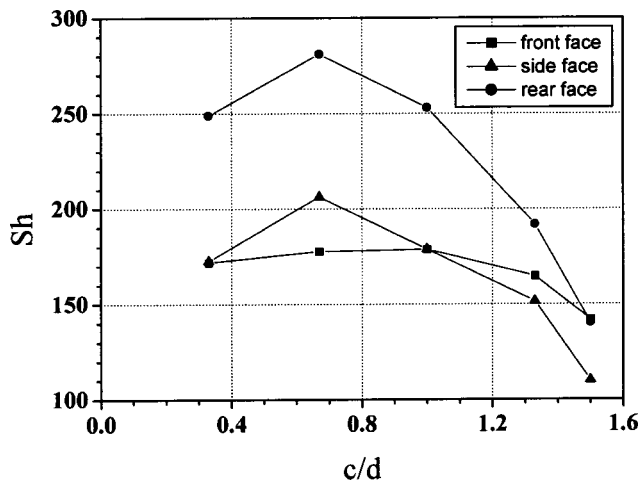
Fig. 6 Comparison of average Sherwood number on each face at U=16 m/s

(a)

(b)

(c)

Fig. 7 Comparison of local mass transfer data with those of heat transfer: (*a*) *c/d*=0.33; (*b*) *c/d*=0.67; and (*c*) *c/d*=1.33

numbers, using heat/mass transfer analogy equation, Eq. (5). The variation trend and values of Nusselt number are similar each other for all cases, but some differences are found if we take a look at detailed distributions more closely. The distributions of Nusselt numbers obtained by mass transfer experiment form parabolic shape on the front face, but those of heat transfer experiment are shown to be rather flat than parabolic. According to Igarashi [5], two cases ($c/d=0.67$ and 1.5) have a flat distribution and the others have a parabolic shape. The parabolic shape distribution seems to be reasonable taking into account flow patterns with stagnation at the center of front face and acceleration toward the corner. Heat transfer data are smoothed out due to conduction error through stainless-steel foil and cylinder block, on the other hand, mass transfer values near the corners seem to be overestimated because casted naphthalene surface can possibly be eroded by shear force of accelerated flow from the center toward the corner. If the conduction effect in the heat transfer experiment and mechanical erosion in the mass transfer measurement are considered, both results become closer [12]. In the rear face, mass transfer distributions at the center have a convex shape due to impingement of counter-rotating vortices as mentioned previously, and become flat as the width to height ratio increase. On the other hand, heat transfer distributions are a nearly flat in most cases or weakly parabolic shape in some cases. Heat transfer values are higher than those of mass transfer, and the difference increases as the velocity increases. Goldstein and Cho [12] report that, in the wake region, heat and mass transfer data match with a lower power of *n* in the analogy equation, which means that the transfer rate is less sensitive to Pr or Sc variation. This may be explained by the fact that the good mixing with the aid of vortex shedding and turbulent eddy motion in the rear face dominates molecular diffusion represented by Pr or Sc. In the side face, quite different distributions are seen between heat transfer and mass transfer at $c/d=0.33$, but variation patterns and values of transfer coefficients become closer as the width to height ratio increase. Relatively slow variations of heat transfer rates may be due to conduction error, and lower values of mass transfer rates can be explained by the small influence of Pr/Sc due to active turbulent eddy motion in the separated region.

Average mass transfer coefficients on each face are also compared with experimental results of heat transfer. As can be seen in Fig. 8, transport coefficients for heat and mass transfer are almost same regardless of c/d in the front face. But in the side and rear faces mass transfer values are smaller than those of heat transfer for all c/d due to those reasons explained above in the comparison of local values. Another reason for the lower values with mass transfer measurement is dissimilarity in the boundary condition.
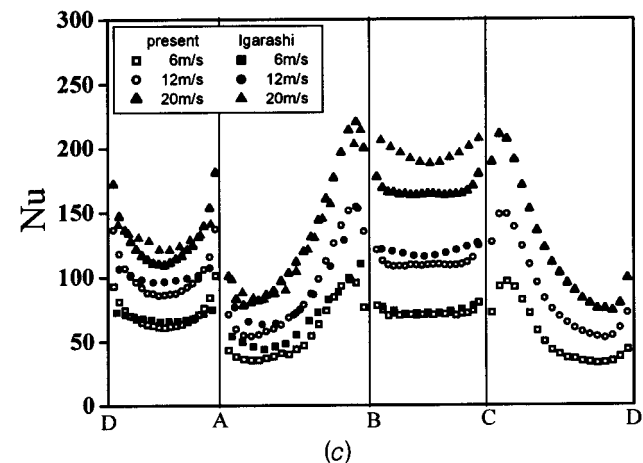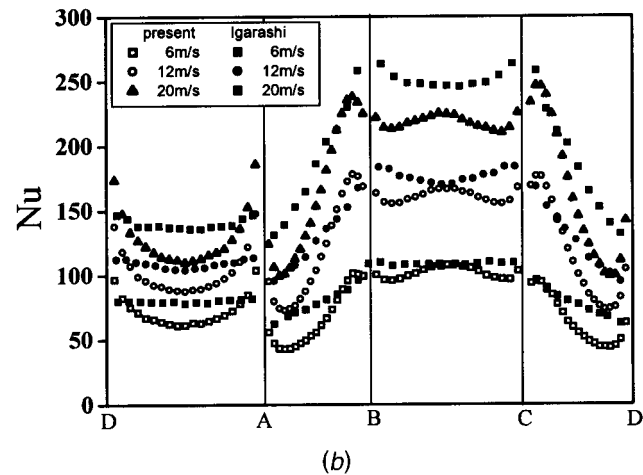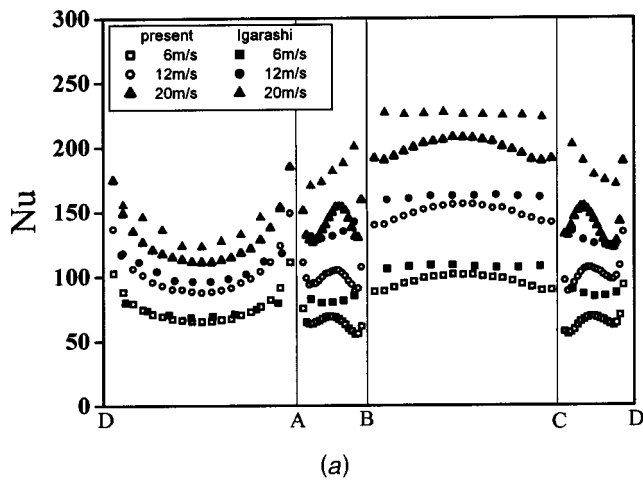
The constant-heat-flux boundary condition is applied for the heat transfer measurement, but that for the mass transfer measurement is a constant-density boundary condition which is equivalent to constant-temperature boundary condition. In general, heat transfer coefficients in the constant heat flux boundary condition are higher than those in the constant temperature boundary condition [15]. Another interesting things to note is that heat transfer correlations for the side face are same for both $c/d=0.33$ and 0.67,

Fig. 8 Comparison of average mass transfer data with those of heat transfer: (*a*) front face; (*b*) side face; and (*c*) rear face

Conclusions

The local and average mass transfer from a rectangular cylinder are investigated, and compared with those of heat transfer to examine heat and mass transfer analogy. A summary of the major results is as follows:

1) Dramatic variations of local mass transfer coefficents are seen on each face of the cylinder, which is closely related to the complex flow phenomena such as stagnation, acceleration, separation, reattachment, recirculation, and vortex shedding.

2) Average Sherwood numbers are correlated quite well with $Re^{1/2}$ on the front face, and $Re^{2/3}$ on the side and rear faces except $c/d = 0.33$.

3) Distinct change of average Sherwood numbers is seen at $c/d = 0.67$ on the side and rear faces, and position of vortex formation seems to affect mass transfer.

4) Variation trends of local heat and mass transfer coefficients are similar each other regardless of width and height ratio, but mass transfer values are somewhat lower than those of heat transfer on the side and rear faces.

5) The discrepancy between heat and mass transfer rates is attributed to the dissimilarity in the boundary condition, the effect of n in the analogy equation, conduction error in the heat transfer measurement, and mechanical erosion in the mass transfer experiment.

6) The heat/mass transfer analogy for a rectangular cylinder is valid in average sense, but careful insight is needed for local values when precision is desired.

Nomenclature

c = width of rectangular cylinder
d = height of rectangular cylinder
D_{iff} = mass diffusion coefficient of naphthalene vapor into air
h = heat transfer coefficient
h_m = mass transfer coefficient
k = thermal conductivity
m = exponent of Reynolds number in the empirical convective heat/mass transfer correlation
n = exponent in the heat/mass transfer analogy equation
Nu = Nusselt number
Pr = Prandtl number
Pr_t = turbulent Prandtl number
Re = Reynolds number
Sc = Schmidt number
Sc_t = turbulent Schmidt number
Sh = Sherwood number
U = free stream velocity in the wind tunnel
ρ_s = density of solid naphthalene
$\rho_{v,w}$ = naphthalene vapor density on the surface
Δt = total exposure time in the wind tunnel
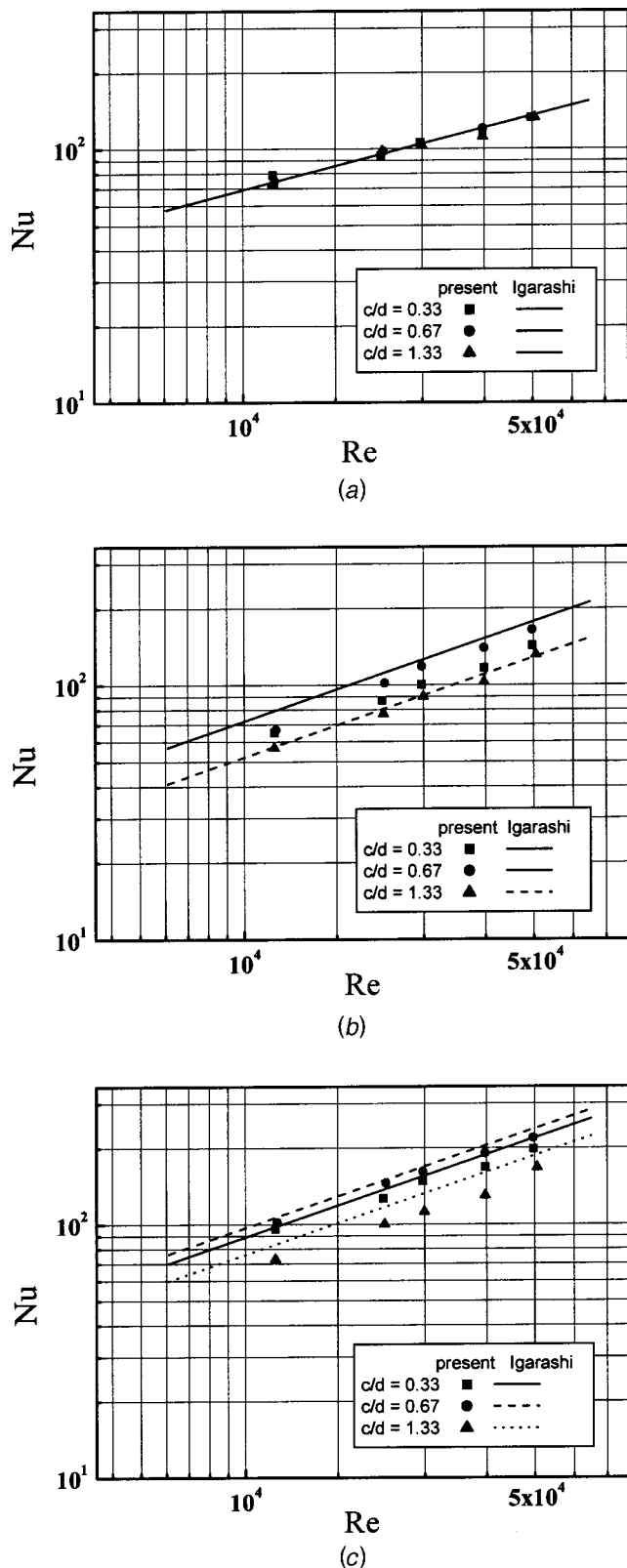$\Delta \tau$ = net sublimation depth of naphthalene

References

[1] Bearman, P. W., and Trueman, D. M., 1972, "An Investigation of the Flow Around Rectangular Cylinders," Aeronaut. Q., **23**, pp. 229–237.
[2] Igarashi, T., 1985, "Characteristics of the Flow Around Rectangular Cylinders (The Case of the Angle of Attack 0 deg)," Bull. JSME, **28**, pp. 1690–1696.
[3] Igarashi, T., 1985, "Heat Transfer from a Square Prism to an Air Stream," Int. J. Heat Mass Transfer, **28**, pp. 175–181.
[4] Igarashi, T., 1986, "Local Heat Transfer from a Square Prism to an Air Stream," Int. J. Heat Mass Transfer, **29**, pp. 774–784.
[5] Igarashi, T., 1987, "Fluid Flow and Heat Transfer Around Rectangular Cylinders (The Case of Width/height Ratio of a Section of 0.33–1.5)," Int. J. Heat Mass Transfer, **30**, pp. 893–901.
[6] Ota, T., and Kon, N., 1979, "Heat Transfer in the Separated and Reattached Flow Over Blunt Flat Plates-Effects of Nose Shape," Int. J. Heat Mass Transfer, **22**, pp. 197–206.
[7] Goldstein, R. J., Yoo, S. Y., and Chung, M. K., 1990, "Convective Mass Transfer from a Square Cylinder and Its Base Plate," Int. J. Heat Mass Transfer, **33**, pp. 9–18.
[8] Yoo, S. Y., Goldstein, R. J., and Chung, M. K., 1993, "Effect of Angle of Attack on Mass Transfer from a Square Cylinder and its Base Plate," Int. J. Heat Mass Transfer, **36**, pp. 371–381.

while much lower values are seen in the case of $c/d = 0.33$ than $c/d = 0.67$ in the mass transfer. Considering different flow patterns between $c/d = 0.33$ and 0.67, it is not expected to have the same heat transfer correlation for both cases.

[9] Ambrose, D., Lawrenson, I. J., and Sparke, C. H., 1975, ''The Vapor Pressure of Naphthalene,'' J. Chem. Thermodyn., **7**, pp. 1173–1176.

[10] Cho, K., 1989, ''Measurement of the Diffusion Coefficient of Naphthalene into Air,'' Ph.D. thesis, Department of Mechanical Engineering, State University of New York.

[11] Kline, S. J., and McClintock, F. A., 1953, ''Describing Uncertainties in Single-Sample Experiments,'' Mech. Eng. (Am. Soc. Mech. Eng.), **75**, pp. 3–8.

[12] Goldstein, R. J., and Cho, H. H., 1995, ''A Review of Mass Transfer Measurements Using Naphthalene Sublimation,'' Exp. Therm. Fluid Sci., **10**, pp. 416–413.

[13] Ota, T., and Nishiyama, H., 1987, ''A Correlation of Maximum Turbulent Heat Transfer Coefficient in Reattachment Flow Region,'' Int. J. Heat Mass Transfer, **30**, pp. 1237–1246.

[14] Nakaguchi, H., Hashimoto, K., and Muto, S., 1968, ''An Experimental Study on Aerodynamic Drag of Rectangular Cylinder,'' J. Japan Soc. Aeronaut. Space Sci., **16**, pp. 1–5.

[15] Zukauskas, A., and Ziugzda, J., 1985, *Heat Transfer of a Cylinder in Crossflow*, Hemisphere Publishing Co.

Thermal Resistance of Particle Laden Polymeric Thermal Interface Materials

Ravi S. Prasher
e-mail: ravi.s.prasher@intel.com

Jim Shipley

Suzana Prstic

Paul Koning

Jin-Lin Wang

Ch5-157, Intel Corporation,
5000 W. Chandler Blvd.,
Chandler, AZ 85226-3699

Particle laden polymers are one of the most prominent thermal interface materials (TIM) used in electronics cooling. Most of the research has primarily dealt with the understanding of the thermal conductivity of these types of TIMs. For thermal design, reduction of the thermal resistance is the end goal. Thermal resistance is not only dependent on the thermal conductivity, but also on the bond line thickness (BLT) of these TIMs. It is not clear which material property(s) of these particle laden TIMs affects the BLT and eventually the thermal resistance. This paper introduces a rheology based semiempirical model for the prediction of the BLT of these TIMs. BLT depends on the yield stress of the particle laden polymer and the applied pressure. The BLT model combined with the thermal conductivity model can be used for modeling the thermal resistance of these TIMs for factors such as particle volume faction, particle shape, base polymer viscosity, etc. This paper shows that there exists an optimal filler volume fraction at which thermal resistance is minimum. Finally this paper develops design rules for the optimization of thermal resistance for particle laden TIMs. [DOI: 10.1115/1.1621893]

Keywords: Contact Resistance, Heat Transfer, Interface, Rheological, Thermophysical

Introduction

Particle-laden polymeric thermal interface materials (TIM) are one of the most commonly used thermal interface materials in microprocessor cooling [1,2]. The thermal conductivity of these particle-laden TIMs is typically enhanced by increasing the volume fraction of the conductive particles in the polymer matrix. Increasing the volume fraction of these particles affects not only the thermal conductivity but also other properties, such as the viscosity and the minimum bond line thickness (BLT) achieved by the TIM [3,4]. Few studies have shown that, like thermal conductivity, BLT also increases with increasing particle volume fraction [5,6]. It has been shown that after certain volume fraction of the particles, the thermal resistance starts to increase in spite of increasing thermal conductivity [4]. Additionally, this may affect the contact resistance between the TIM and the adjoining substrates [6,7].

A common assumption for modeling the thermal resistance of interstitial TIM is that both the substrates touch each other [7,8]. This is a good assumption as long as these TIMs are not filled with particles, as the pure interstitial polymer, such as silicone, or fluid, such as air, will behave like pure fluid and will fill the cavities formed by roughness of the two substrates. However, if the TIMs are loaded with solid particles to increase the thermal conductivity of the polymers, then the two substrates will not touch each other as shown in Fig. 1. This type of model has been recently proposed by Prasher [1], Prasher et al. [5,6], Gwinn and Webb [2], Zhou and Goodson [9] and Campbell et al. [10]. In the past, Fletcher [11] considered a case similar to that shown in Fig. 1 but never made an attempt at separating the bulk resistance from the contact resistance of the TIMs.

The effective thermal resistance, R at the interface after inserting a TIM between the solid surfaces will have two components: the bulk resistance (R_{bulk}) of the TIM arising from its finite thermal conductivity, and contact resistance, R_c between the TIM and the adjoining solids as shown in Fig. 1. R is given by

$$R = \frac{\text{BLT}}{k_{\text{TIM}}} + R_{c_1} + R_{c_2} \tag{1}$$

Equation (1) shows that the thermal resistance is not only dependent on the thermal conductivity, but also on the BLT. Therefore to understand the impact of increasing the particle volume fraction, it is very important to understand its impact on the BLT. Similarly, the contact resistance of the TIM with the adjoining substrate may also be affected by the particle volume fraction, as it is not only dependent on the thermal conductivity, but also on the mechanical response of the material [6] with respect to pressure, which decides the ratio of nominal area of contact and real area of contact of the TIM with the substrate [6].

The BLT of a particle laden TIM should depend on the rheology of the particle laden TIM. The rheology of a polymer system is characterized by various properties such as viscosity, elastic modulus, loss modulus and yield stress [12].

This paper deals with the rheological measurements of particle laden polymers (PLP) which are then used to model the BLT of PLP. Thermal conductivity and the bulk resistance of various PLP TIMs are also measured. Finally, this paper introduces a semi-empirical model for the prediction of the bulk resistance of a PLP TIM. This empirical model is used to define design rules for the formulation of PLP TIMs. This paper does not deal with the modeling of the contact resistance of these types of TIMs. Modeling of the contact resistance of PLP will be discussed briefly in this paper.

Experimental Program

The experimental program consisted of the measurement of the following parameters:
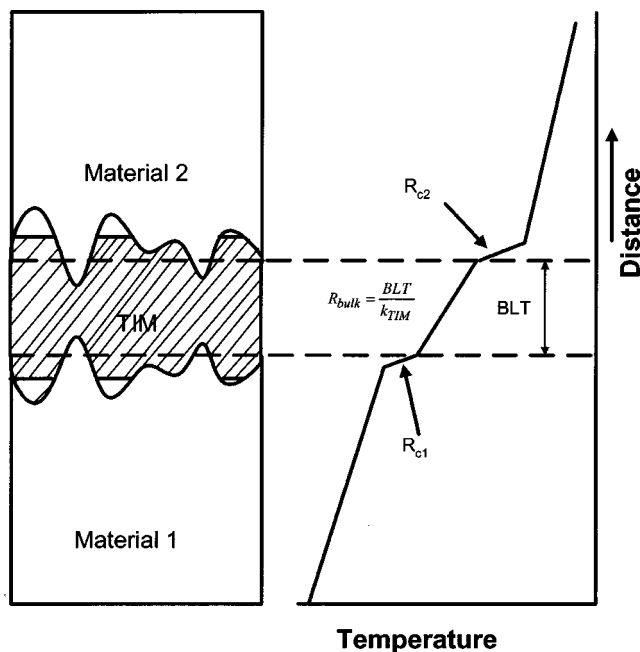
Fig. 1 Schematic of various resistance components of a TIM

Table 1 Experimental plan

TIM	Yield Stress	Viscosity	BLT	Thermal conductivity
Silicone A w/40%, 50%, 60% particle volume fraction	Yes	Yes	Yes	Yes
Silicone B w/40%, 50%, 60% particle volume fraction	Yes	Yes	Only for 60% and 50%	No
Silicone C w/40%, 50%, 60% particle volume fraction	Yes	Yes	Only for 60%	No
PCM	Yes	No	Yes	No
G751	Yes	No	Yes	No

1. Viscosity versus strain rate
2. Yield stress from viscosity versus shear stress data
3. BLT
4. Thermal conductivity
5. Bulk thermal resistance

Nine experimental formulations of silicone based thermal greases by Lord Corp. were used in this study. These nine formulations consisted of three silicone oil polymer matrices with different viscosities; each silicone oil was loaded with three different volume fractions of aluminum particles with 40 percent, 50 percent, and 60 percent volume fraction. Rheological measurements were also performed on commercially available Shin Etsu G751 thermal grease [2] and an olefin phase change material (PCM). Both Shin Etsu G751 and PCM are also PLP. Description of Shin Etshu G751 filler is given in [2]. The PCM used in this study was an olefin based aluminum filled PLP. The experimental program is shown in Table 1. All measurements listed above were not carried out for all the materials, for reasons listed in later sections.

Sample Preparation. Thermally conductive greases are conceptually very simple materials. One takes highly conductive filler and mixes it in an organic fluid at high loading and produces a paste with grease-like consistency. In this work, spherical aluminum was mixed into three different silicone oils. The size distribution of the aluminum fillers was measured by laser light scattering. The average particle size is 7.9 μm. Commercial thermal greases often contain coupling agents and surfactants to aid in the

wetting of the filler, increase the ultimate loading and prevent re-agglomerization of the fillers. The grease suppliers (Lord Corporation) hold the exact nature of these coupling agents and surfactants confidential.

The silicone oil used was polydimethylsiloxane fluid of three viscosities. The three base silicone oils used in this study are referred to as A, B, and C in this manuscript. The shear rate dependence of viscosity of the unfilled silicone oil A is shown in Fig. 2 and can be seen to be Newtonian. Data for the Silicone oil B and C are not shown in this manuscript for brevity.

Compounding of the thermal greases can be accomplished in several styles of mixers. The more common mixer types are the planetary, spiral and double planetary. The thermal greases used in this study were prepared in a lab-scale double planetary mixer manufactured by Charles Ross and Son.

Rheological Measurements

Rheological measurements were performed at 50°C on both strain controlled (Rheometric Scientific RDA II) and stress controlled (Rheometric Scientific SR 5) rheometers. The dynamic viscosity of the materials was measured using the RDA with parallel plate geometry (25 mm diameter and 1.0 mm gap) at 15 percent strain. The frequency was varied from 0.1 to 100 rad s^{-1} in the dynamic viscosity test. The yield stress was measured using the SR 5 with a parallel plate geometry (25 mm diameter and 1.0 mm gap). A stress sweep test was conducted from the stress, which gave about 25 s^{-1} shear rate for each material, down to the stress at which material ceased flow. The stress at which the material stopped flow was taken as the yield stress. It usually happened with a shear rate less than 0.001 s^{-1} for each material.

Figure 2 shows the results on the viscosity of the silicone oil A for various strain rates. It can be seen from Fig. 2 that silicone oil
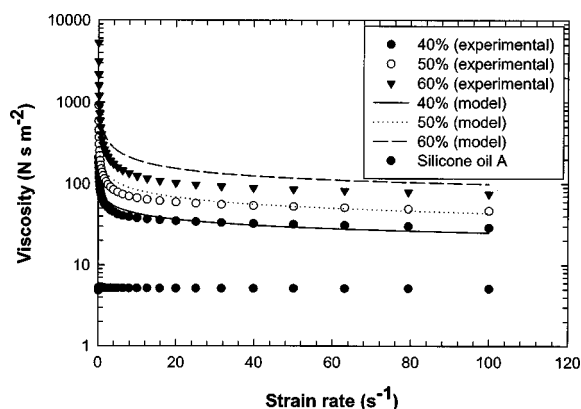

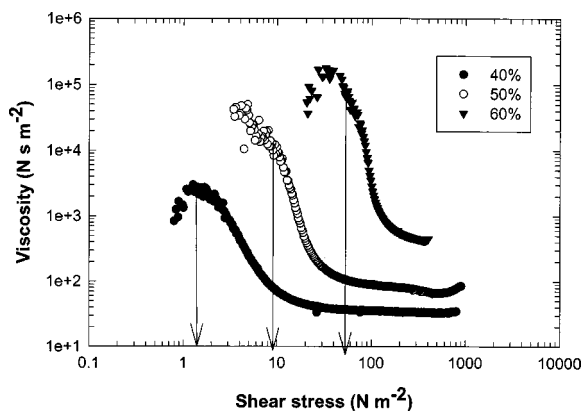**Fig. 2 Viscosity versus strain rate for silicone A**

Fig. 3 Viscosity versus shear stress to obtain yield stress of silicone A

Table 2 Parameters and properties of various TIM formulations

Particle volume fraction	k (Thermal conductivity) ($W\,m^{-1}\,K^{-1}$)	Silicone A ($5.16\ N\,s\,m^{-2}$)			Silicone B ($0.52\ N\,s\,m^{-2}$)			Silicone C ($0.25\ N\,s\,m^{-2}$)		
		K	n	τ_y ($N\,m^{-2}$)	K	n	τ_y ($N\,m^{-2}$)	K	n	τ_y ($N\,m^{-2}$)
40%	0.700	74.10	0.747	1.8	6.10	0.81	0.9	9.70	0.522	0.3
50%	1.100	161.41	0.660	9.9	114.56	0.35	5.9	40.36	0.378	4.1
60%	1.225	444.21	0.496	55.2	453.45	0.20	14.2	305.13	0.213	6.2

is Newtonian, whereas the particle laden silicone oils are all non-Newtonian in behavior. This type of behavior is very common for particle laden polymers [12]. Zhou and Goodson [9] derived a model for the BLT of particle laden systems assuming Newtonian behavior which is probably valid only under very light loading of particles (<10 percent) [12], whereas particle laden TIMs are loaded way above the percolation threshold (>30 percent) [13]. Therefore any model to predict the BLT has to take the highly non-Newtonian behavior of these particles into account. Figure 2 also shows that viscosity increases with increasing particle volume fraction at all strain rates. Data for silicones B and C are not shown for brevity.

Particle laden polymers not only have a strain rate dependent viscosity, but also possess yield stress. Barnes [14] provides a very good review of yield stress of polymers. Yield stress is the stress at which the polymer starts to flow if the polymer is stressed from lower to higher values in a stress sweep test. In this study, these polymers were subjected to higher to lower stress sweep. Yield stress is defined at the stress where the material ceases to flow or alternatively the viscosity reaches a maximum. Figure 3 shows the yield stress measurement for silicon oil A. Data for oils B and C are not shown again for brevity. The presence of yield stress and strain rate dependent viscosity indicates that these particle laden TIMs are non-Newtonian.

Fig. 4 Experimental apparatus for the measurement of BLT and k

Table 2 shows the yield stress for various TIM formulations. Yield stress increases with increasing particle volume fraction. Yield stress also increases with increasing base silicone oil viscosity. Increase of yield stress with particle volume fraction and base polymer viscosity is a very common phenomenon [12]. The yield stress of G751 was 140 Pa and PCM was 89.3 Pa.

BLT and Thermal Measurement

The bond line thickness (BLT) and the thermal conductivity of the material under test was measured using a thermal interface material testing system that is based on the ASTM D 5470 standard. The measurement system is shown in Fig. 4. The system consists of four main components: a mechanical loading fixture, heating block, cooling block, and a laser extensometer to measure the BLT. The mechanical loading fixture allows the user to apply a controllable load using a hydraulic ram. A load cell continuously monitors the applied load and the PID controller adjusts the hydraulic ram force to maintain the desired load set point. During typical operation when the thermal resistance or the thermal conductivity of the material is of interest, a heating block, which incorporates cartridge heaters, applies a heat flux to a cylindrical copper rod. The heat travels through the copper rod, thermal interface material, and into a corresponding cylindrical copper rod which is clamped in a cooling block. A recirculating refrigerated bath pumps fluid through the cooling block to remove the heat from the copper rods. The bath temperature can be adjusted to control the interface material temperature during the test. A laser extensometer measures the BLT of the interface material. The laser extensometer operates by sensing reflections from retro-reflective tape strips applied to the heating and cooling rods. The strips are located 2.5 mm from the end of each rod. These strips function as targets and the laser extensometer, via the scanning laser beam, determines the distance between the selected edges of the targets. The repeatability of the extensometer is $\pm 1\ \mu m$ and has a resolution of 1 μm. The BLT of the material is determined through a two-step process. The first step is to apply a 345 MPa load between the copper rods without an interface material and measure the distance between the targets. This value is deemed the reference BLT. The second step is to remove the load, separate the copper rods, apply the interface material to the surface of the cooling rod, and apply the desired pressure. The laser extensometer once again measures the distance between the two targets to determine the final BLT. The interface material BLT is then calculated by subtracting the reference BLT from the final BLT. The r.m.s roughness of the heating and cooling rods was 1 μm. Figure 5 shows the BLT measurement of silicone A for different pressure. Figure 5 shows that BLT increases with increasing particle volume fraction. BLT was not measured for 40 percent silicone B and 40 percent and 50 percent silicone C. Due to the low yield stress (Table 2) of these materials, BLT was very thin, leading to a greater uncertainty in the experimental data.

Thermal conductivity was measured for silicone A only. This measurement was performed for qualitative validation of the modeling conclusions (to be discussed later). Thermal conductivity of silicone A for various volume fraction is shown in Table 2. For thermal conductivity measurement the system was operated in the BLT control mode so that system attains only specified BLTs.
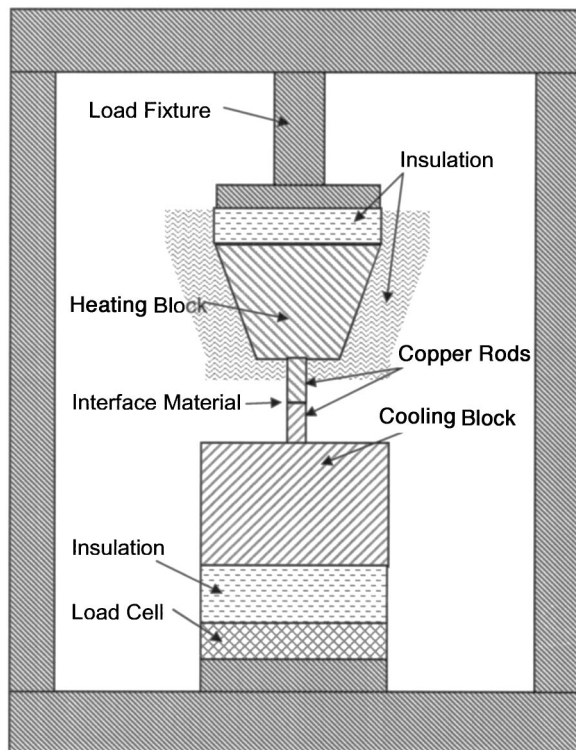
Thermal resistance was measured at three different BLT and thermal conductivity was obtained from the inverse of the slope of the thermal resistance versus BLT measurement. Thermal resistance was also measured for two different pressures (20 and 90 PSI) to validate the modeling conclusions in this paper.

The error in the measurement of the thermal resistance was 7×10^{-7} K m^2 W^{-1}. The details of the error analysis on thermal measurement are given in [5,6]. The error in thermal conductivity measurement is calculated by using Eq. (1). Since thermal con-

ductivity is the slope of the BLT versus thermal resistance curve, which is a straight line, thermal conductivity can be written as

$$k_{\text{TIM}} = \frac{\text{BLT}_1 - \text{BLT}_2}{R_1 - R_2} \qquad (2)$$

where BLT_1 and BLT_2 are successive BLT readings and R_1 and R_2 are successive thermal resistance measurements. Using Eq. (2) error in k_{TIM} is given by [1]

$$\frac{\Delta k_{\text{TIM}}}{k_{\text{TIM}}} = \sqrt{\left(\frac{\Delta \text{BLT}_1}{\text{BLT}_1 - \text{BLT}_2}\right)^2 + \left(\frac{\Delta \text{BLT}_2}{\text{BLT}_1 - \text{BLT}_2}\right)^2 + \left(\frac{R_1}{R_1 - R_2}\right)^2 + \left(\frac{R_2}{R_1 - R_2}\right)^2} \qquad (3)$$

where the symbol Δ represents the error in the respective variables. Since three R versus BLT readings were taken, the error calculation was done by taking pairs out of three readings, i.e., three error assessments were done. For all the three conductivity measurements the worst case error was less than three percent. Note that ΔBLT was taken as 1 μm as mentioned earlier. The error in k_{TIM} is very small because of very small error in BLT measurement.

Rheological Models for Particle Laden Polymers

Careful review of polymer rheology literature reveals [12] that there are primarily four types of constitutive models which are used to explain the rheological behavior of polymers. These models are Newtonian fluid, Power Law fluid, Bingham fluid and Herschel-Bulkley fluid (H-B). The constitutive equations for these different fluids are shown in Table 3. Since all the particle laden

TIMs considered in this study have a well defined yield stress, it can be concluded that neither the Newtonian nor the Power Law fluid model will fit the viscosity versus strain rate data. Therefore the question is whether these fluids behave like Bingham fluids or H-B fluid. Figure 2 shows that the H-B model fits well with the viscosity data, indicating that these fluids behave like H-B fluids. This type of behavior has been seen for other PLP systems [12]. The values of K (consistency index) and n (power law index) for all these TIMs obtained from the curve fit of experimental data are shown in Table 2. Table 2 shows that values of K and τ_y increase with increasing volume fraction for all three silicone oils. This type of behavior is commonly observed for particle laden polymers [12]. Value of n decreases with increasing particle volume fraction. This basically indicates the deviation from Newtonian behavior because for Newtonian fluid with yield stress (Bingham fluid), n is 1. Therefore it is not surprising that increasing particle volume fraction leads to more deviation from the Newtonian behavior.
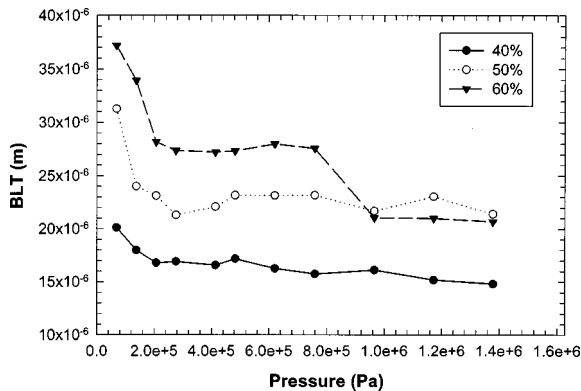
Fig. 5   BLT versus pressure for silicone A

Table 3   Constitutive equation and steady state BLT for various fluids

Types of fluids	Constitutive Equation (viscosity)	Steady State BLT	Notes
Newtonian Fluid	$\eta = cons \tan t$	BLT=0	η = viscosity
Power law fluid	$\eta_p = K(\dot{\gamma})^{n-1}$	BLT=0	K=consistency index, n=power law index, $\dot{\gamma}$ =strain rate, p=power law,
Bingham fluid	$\eta_{BI} = \frac{\tau_y}{\dot{\gamma}} + cons \tan t$	BLT=constant	τ_y=yield stress, BI=Bingham
Herschel-Bulkley fluid	$\eta_{H-B} = \frac{\tau_y}{\dot{\gamma}} + K(\dot{\gamma})^{n-1}$	BLT=constant	H-B=Herschel-Bulkley

Modeling of BLT

Any model which captures the dependence of the BLT on various parameters such as particle volume fraction and pressure has to comprehend the following:

1. BLT of these TIMs changes with time once pressure is applied.
2. BLT reaches a constant value after some time (steady state BLT). This final BLT is different for different pressures.
3. BLT is not the same as the particle size.
   BLT increases with increasing particle volume fraction [5,6].

This paper only focuses on the steady state BLT as it has more practical relevance. Prasher et al. [15] have discussed the modeling of the transient part of the BLT.

The BLT can be modeled for two conditions: (1) constant radius of the TIM (TIM radius is same as substrate radius), i.e., after squeezing the extra TIM flows out (close to actual application); and (2) constant volume, i.e., squeezed TIM radius is smaller than the radius of the substrate. Wherever relevant, we will discuss both cases. Some of the assumptions invoked for the modeling of the BLT are:

1. Lubrication assumption: $h/D \ll 1$; where D is the diameter of the substrate. This is a very reasonable assumption as the thickness of these TIMs are of the order of 50 μm or lower, which is much smaller than the silicon chip size.
2. No-slip boundary condition.
3. Negligible inertial forces.

Newtonian Fluids.   For constant radius, the thickness of the film (h) between the two substrates is given by [16],

$$h = \cfrac{1}{\sqrt{\cfrac{4p}{3\pi\eta r^2}t + \cfrac{1}{h_i^2}}} \qquad (4)$$

where p is the pressure, t the elapsed time, r the radius of the plate, and h_i is the initial thickness of the polymer. Equation (4) clearly shows that the thickness of the film will go to zero after some time, which leads to a zero steady state thickness. This was the model proposed by Zhou and Goodson [9]. They also pointed out that their model will lead to zero thickness, which is physically unrealistic as all particle laden TIMs have well defined constant BLTs for different pressures [2,5]. Zero thickness at steady state from this model is not surprising as it assumes the TIMs to behave like pure liquid.

Power Law Fluid. For constant radius, h is given by [17]

$$h = \left[h_i^{-(l+1/n)} + \left(1 + \cfrac{1}{n}\right)Bt \right]^{(-n/1+n)} \qquad (5)$$

where B is a function of r, p, and n [17]. Equation (5) shows that even for the Power Law fluid steady state thickness, i.e., thickness at large times, will be zero. Therefore, the Power Law fluid model can not be used to model the BLT.

Bingham Fluid. For Bingham fluid, the limiting steady state thickness, h_L, for constant radius is given by [18]

$$h_L = \cfrac{2}{3} r \left(\cfrac{\tau_y}{P} \right) \qquad (6)$$

The Bingham model leads to constant thickness that is only a function of pressure and the yield stress.

The steady-state thickness for the constant volume is given by [18],

$$h_L = \cfrac{2V^{3/5}}{3\pi^{1/5}} \left(\cfrac{\tau_y}{F} \right)^{0.4} \qquad (7)$$

where F is the applied force, and V is the volume of the TIM.

Herschel-Bulkley Fluid. For H-B fluid, the limiting steady state BLT is given by [18]

$$h_L = \cfrac{2}{3} r \left(\cfrac{\tau_y}{p} \right) \qquad (8)$$

Therefore, the steady state thickness of the H-B fluid and Bingham fluid are the same.

Both Bingham and H-B fluid models give a finite steady state thickness of the TIM, which seems more realistic. The steady state BLT is given by Eq. (8). Equation (8) shows that the final steady state BLT only depends on the yield stress of the polymer and the pressure. It does not depend on the viscosity or the power index. The viscosity and the Power Law index are only detrimental in the time required to reach steady state [15]. Therefore for modeling the steady state BLT which is of much greater importance than the time dependent part, one only needs to measure the yield stress.

Figure 6 shows the comparison of the BLT model with the experimental data. Figure 6 clearly shows that the model under predicts the BLT by a huge margin. There are various reasons for the failure of this model. Many research groups, for applications ranging from food science to toothpaste [18,19] and for understanding the behavior of yield stress fluid under squeeze [20], have used Eq. (8) to find out either the yield stress of semi-liquids or the final thickness achieved by the yield-stress fluid for various pressures. A survey of literature dealing with the squeeze of yield stress fluid [18–20] indicates that the pressures applied in these studies were extremely low. Typically these pressures are below 3 psi or 20 k Pa in these studies. In typical electronics cooling
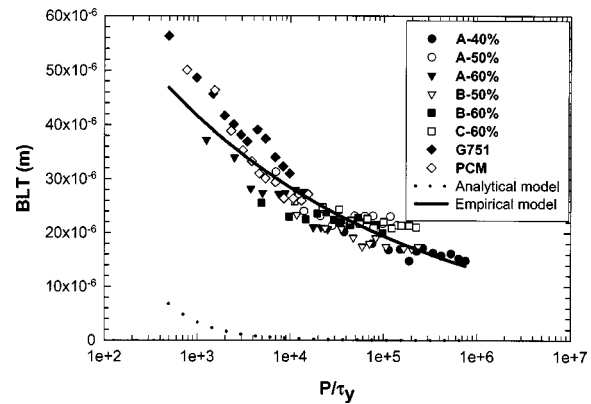

Fig. 6   BLT versus p/τ_y for various TIM

applications, the pressure is of the order of 25 psi (172 k Pa) or more, which is much higher than the pressures under which Eq. (8) has been validated.

For pressures higher than 20 k Pa, experimental data by Meeten [20] showed that thickness does not obey Eq. (8) with respect to force or pressure, but obeys the constant volume type relation as given by Eq. (7). In a very simple model, Meeten [20] assumed that at higher pressures the polymer consisted of well separated regions of high yield stress leading to the failure of Eq. (8), which assumes one continuous phase. Meeten [20] assumed that there are j regions, each with volume v, between the plates. In that case, if V in Eq. (5) is replaced by jv, then h will be given by

$$h_L = \cfrac{2\pi^{1/5}(jv)^{3/5}r^{4/5}}{3} \left(\cfrac{\tau_y}{P} \right)^{0.4} \qquad (9)$$

For highly concentrated suspensions at pressures higher than 20 k Pa, we replace Eq. (7) by

$$h_L = C \left(\cfrac{\tau_y}{P} \right)^m \qquad (10)$$

where C and m are empirical constants. There are various reasons for the failure of the analytical model. For highly concentrated suspension or at high pressure, PLP can not be simply described by assuming a single phase [20,21] due to various reasons such as

1. Flocculation of particles [22]
2. High pressure resulting in plates directly touching the particles [21]
3. Phase migration during squeeze experiments [20]

Therefore Eq. (8) fails to match the experimental data; however the semi-empirical model given by Eq. (10) matches the data very well for all the eight materials considered as shown in Fig. 6. The values of C and m obtained from the experimental fit are 1.31 $\times 10^{-4}$ m and 0.166, respectively. Low value of m clearly indicates that pressure does not have a very pronounced effect on the BLT. Note that in this study the particle volume fraction of the TIMs is always above the percolation threshold, which is around 30 percent [13]. We have performed our experiments in the pressure range varying from 10 psi (68940 Pa) to 200 psi (1378800 pa), which covers the range of pressures for electronics cooling application. Therefore this correlation is strictly valid for particle volume fraction above the percolation threshold and in the pressure range studied in this paper.

Dependence of Bulk Thermal Resistance on Particle Volume Fraction

The bulk thermal resistance of the TIM is given by,

$$R_{\text{bulk}} = \frac{\text{BLT}}{k_{\text{TIM}}} \tag{11}$$

Using Eq. (10) R_{bulk} can be written as

$$R_{\text{bulk}} = \frac{1}{k_{\text{TIM}}} C \left(\frac{\tau_y}{p} \right)^m \tag{12}$$

τ_y depends on particle volume fraction (ϕ) as shown by the experimental data in Table 2. If electrostatic interaction [12] is assumed to be negligible compared to the Van der walls interaction in the particle laden polymer, then τ_y can be expressed as [12]

$$\tau_y = A \left[\frac{1}{(\phi_m/\phi)^{1/3} - 1} \right]^2 \tag{13}$$

where A is constant, and ϕ_m is the maximum particle volume fraction. Equation (13) can also be written as

$$\tau' = \frac{\tau_y}{A} = \left[\frac{1}{(\phi_m/\phi)^{1/3} - 1} \right]^2 \tag{14}$$

where τ' is the dimensionless yield stress. Using τ' Eq. (12) can be written as

$$\frac{R_{\text{bulk}} p^m}{C A^m} = \frac{\tau'^m}{k_{\text{TIM}}} \tag{15}$$

Thermal conductivity of the particle laden system also depends on ϕ. There are various analytical models available in the literature [23]. For spherical particles, one of the most prominent models is the Maxwell model [24]. This model matches the data for spherical particles ϕ up to 30–35 percent [25]. After that, percolation phenomenon takes over [25]. Maxwell's model can not be used to predict the thermal conductivity for higher volume fraction due to the assumptions built into it [24]. Every et al. [26] developed a model which they called modified Bruggeman model to predict the thermal conductivity of two component systems. In this paper we use modified Bruggeman model developed by Every et al. [26] due its ability to predict thermal conductivity from low to high volume fraction and also because it includes the effect of the interface resistance between the filler and the matrix on the effective thermal conductivity of composites. We also make the assumption that $k_f/k_m \gg 1$, where k_f is the filler conductivity and the k_m is the matrix conductivity. This is a very good assumption considering that polymers have very low conductivity and the fillers have very high conductivity (aluminum in this study). Modified Bruggeman model [26] for $k_f/k_m \gg 1$ is given by

$$\frac{k_{\text{TIM}}}{k_m} = \frac{1}{(1-\phi)^{3(1-\alpha)/(1+2\alpha)}} \tag{16}$$

where α is the Biot number and is given as

$$\alpha = \frac{R_b k_m}{d} \tag{17}$$

where R_b is the interface resistance between the filler and the particle, and d is the diameter of the particle. Figure 7 shows the comparison of the model with the thermal conductivity data for Silicon A (Table 2). Thermal conductivity of silicone was assumed to be 0.2 W/mK [5,6]. Figure 7 shows that model matches very well with 40 percent and 50 percent volume fraction with $\alpha = 0.06$ and for 60 percent volume fraction with $\alpha = 0.15$. This suggests that interface resistance for 60 percent sample is higher than 40 percent and 50 percent samples. R_b could arise because of imperfect mixing of the particle with the polymer matrix, or due to
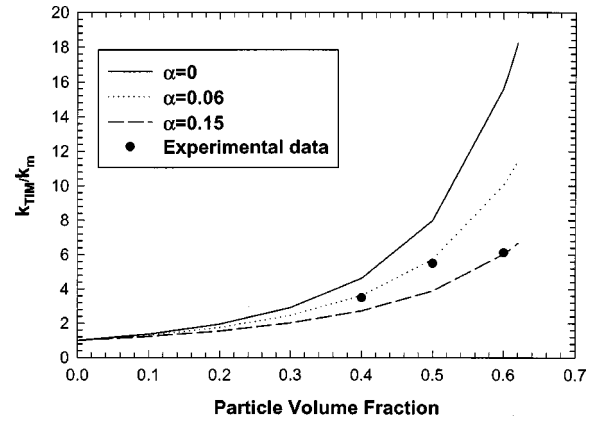
Fig. 7 Thermal conductivity of silicone A sample
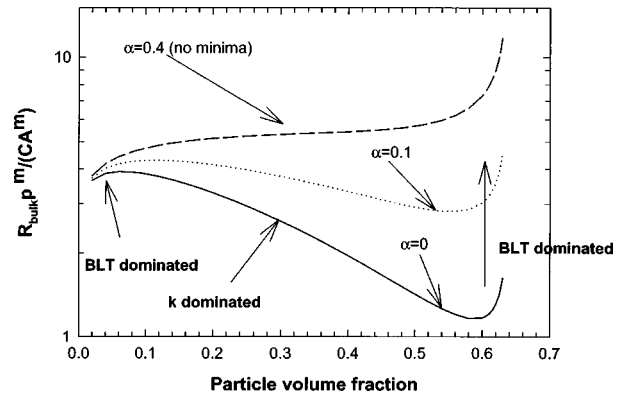
Fig. 8 Modeling results of thermal resistance versus particle volume fraction
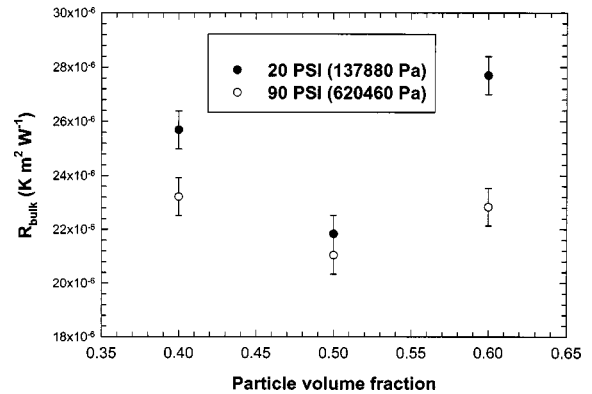
Fig. 9 Experimental results for resistance versus particle volume fraction

phonon acoustic mismatch [27], or a combination of both. Prasher et al. [27] have shown that the contribution due to phonon acoustic mismatch at room temperatures or higher is important only when the thermal conductivity of both the materials is very high. In the present case, it is safe to assume the R_b is arising from imperfect wetting or mixing of the filler particles with the silicon oil, as the thermal conductivity of silicon oil is very low. Therefore the phonon acoustic mismatch component is very low at room temperatures. The reason for higher R_b for 60 percent volume fraction could be due to difficulty in wetting the surface of the particle with the silicone oil as the volume fraction is so high.

Figure 8 shows the plot of Eq. (15) versus different particle

volume fraction for different value of α. Figure 8 shows that R_{bulk} reaches a minima in the high volume fraction range for $\alpha < 0.4$. Therefore there exists an optimal loading after which the thermal resistance will increase in spite of increasing thermal conductivity. Figure 8 also shows that depending on the interface resistance between the particle and the matrix, the location of R_{bulk} minima might shift and after a critical interface resistance there might be no R_{bulk} minima.

Figure 9 shows R_{bulk} for two different pressures for silicone A. Figure 9 shows that R_{bulk} decreases from $\phi = 0.4$ to $\phi = 0.5$ and then increases for $\phi = 0.6$. This validates the modeling conclusion. It is not possible to find out exactly where the minima is, as we did not have a large number of particle volume fractions available between $\phi = 0.5$ and $\phi = 0.6$. This type of behavior of thermal resistance was also observed by Xu et al. [4].

Discussion on the Contact Resistance

Various authors [1,8,9] have modeled the contact resistance of these types of TIMs, assuming them to behave like a pure liquid. Some groups have considered incomplete wetting of the interface between the TIM and the substrate [1,9] and other groups have considered complete wetting of the interface [8]. However this study suggests that a pure liquid model is not good enough for the modeling of the contact resistance of PLP, due to the presence of the yield stress. Intuitively speaking, the area covered by the PLP in the valleys of the interface as shown Fig. 1 will eventually depend on the pressure and yield stress. This relation could be somewhat similar to that obtained for bare metallic contacts where the contact resistance depends on the pressure and the hardness of the softer material. For PLP, TIMs probably hardness will have to be replaced by the yield stress.

Conclusion

This paper introduces a rheology based semi-empirical model for the prediction of the BLT of PLP TIMs. PLP TIMs are non-Newtonian and behave like Herschel-Bulkely fluid. They possess yield stress, which increases with increasing particle volume fraction. BLT is only a function of the pressure and the yield stress. This paper demonstrates both theoretically and experimentally the existence of resistance minima with respect to particle volume fraction. The metric for the comparison of one TIM from another is k_{TIM}/τ_y^m. TIM which gives the maximum value of this parameter is the best TIM.

Acknowledgments

Authors would like to acknowledge the support of Todd Young for helping in the measurement of BLT and k_{TIM}. Authors would also like to acknowledge support of Lord Corporation for supplying the experimental samples.

Nomenclature

A = constant in Eq. (11)
B = function in Eq. (3)
BLT = bondline thickness (m)
C = empirical constant in Eq. (8) (m)
D = particle diameter (m)
h = thickness (m)
h_i = thickness (m)
h_L = steady state thickness (m)
K = consistency index
k = thermal conductivity ($\text{W m}^{-1}\text{K}^{-1}$)
m = empirical constant in Eq. (8)
n = power law index
p = pressure (N m^{-2})
PLP = Particle Laden Polymer
r = radius (m)
R = thermal resistance ($\text{K m}^2\text{W}^{-1}$)
R_{bulk} = bulk thermal resistance ($\text{K m}^2\text{W}^{-1}$)

R_b = thermal interface resistance between the particles and the matrix ($\text{K m}^2\text{W}^{-1}$)
R_c = contact resistance ($\text{K m}^2\text{W}^{-1}$)
t = time (s)
TIM = Thermal Interface Material
V = volume in Eq. (9) (m^3)

Greek

α = Biot number
ϕ = particle volume fraction
ϕ_m = maximum volume fraction
η = viscosity (N s m^{-2})
τ_y = yield stress (N m^{-2})
τ' = dimensionless yield stress

Subscript

1, 2 = side 1 and 2
f = filler
m = matrix
percolation = at percolation threshold

References

[1] Prasher, R. S., 2001, "Surface Chemistry Based Model for the Thermal Contact Resistance of Fluidic Interstitial Thermal Interface Materials," ASME J. Heat Transfer, **123**, pp. 969–975.
[2] Gwinn, J. P., and Webb, R. L., 2002, "Performance and Testing of Thermal Interface Materials," *Thermes 2002*, Y. K. Joshi and S. V. Garimella, eds., Santa Fe, New Mexico, 13–16 January.
[3] Suddith, R. D., 1993, "A Generalized Model to Predict the Viscosity of Solutions With Suspended Particles. 1," J. Appl. Polym. Sci., **48**, pp. 25–36.
[4] Xu, Y., Luo, X., and Chung, D. D. L., 2000, "Sodium Silicate Based Thermal Interface Material for High Thermal Contact Conductance," ASME J. Electron. Packag., **122**, pp. 128–131.
[5] Prasher, R. S., Koning, P., Shipley, J., and Devpura, A., 2001, "Dependence of Thermal Conductivity and Mechanical Rigidity of Particle-Laden Polymeric. Thermal Interface Material on Particle Volume Fraction," Proc. of International Mech. Eng. Cong. and Exp., New York, Nov. 11–16.
[6] Prasher, R. S., Koning, P., Shipley, J., and Devpura, A., 2003, "Dependence of Thermal Conductivity and Mechanical Rigidity of Particle-Laden Polymeric Thermal Interface Material on Particle Volume Fraction," ASME J. Electron. Packag., **125**(3), pp. 386–391.
[7] Madhusudana, C. V., 1996, *Thermal Contact Conductance*, Springer-Verlag, New York.
[8] Das, A. K., and Sadhal, S. S., 1998, "Analytical Solution For Constriction Resistance With Interstitial Fluid," Heat Mass Transfer, **34**, pp. 111–119.
[9] Zhou, P., and Goodson, K. E., 2001, "Modeling and Measurement of Pressure Dependent Junction-Spreader Thermal Resistance for Integrated Circuits," *Proc. of International Mech. Eng. Cong. and Exp.*, ASME, New York.
[10] Campbell, R. C., Smith, S. E., and Dietz, R. L., 1999, "Measurements of Adhesive Bondline Effective Thermal Conductivity and Thermal Resistance Using the Laser Flash Method," *Proceedings of 15th IEEE SEMI-THERM Symposium*, IEEE, Piscataway, NJ, pp. 83–97.
[11] Fletcher, L. S., and Peterson, G. P., 1986, "The Effect of Interstitial Materials on the Thermal Contact Conductance of Metallic Junctions," *Heat Transfer in Systems Seminar-Phase II*, National Cheng University, Tainan, January 13–14.
[12] Shenoy, A. V., 1999, *Rheology of Filled Polymer System*, Kluwer Academic Publishers, MA, pp. 1–390.
[13] Devpura, A., Phelan, P. E., and Prasher, R. S., 2001, "Size Effects on the Thermal Conductivity of Polymers Laden With Highly Conductive Filler Particles," Microscale Thermophys. Eng., **5**(3), pp. 177–189.
[14] Barnes, H. A., 1999, "The Yield Stress—A review or '$\pi\alpha\varpi\tau\alpha\rho\epsilon\lambda$'—Everything Flows," J. Non-Newtonian Fluid Mech., **81**, pp. 133–178.
[15] Prasher, R. S., Shipley, J. C., Prstic, S., Koning, P., and Wang, J., 2002, "Rheological Study of Micro Particle Laden Polymeric Thermal Interface Materials: Experimental (Part 1) and Modeling (Part 2)," *Proc. of International Mechanical Engineering Congress and Exposition*, ASME, New York.
[16] Dienes, G. J., and Klemm, H. F., 1946, "Theory and Application of the Parallel Plate Plastometer," J. Appl. Phys., **17**, pp. 458–471.
[17] Grimm, R. J., 1978, "Squeezing Flows of Polymeric Liquids," AIChE J., **24**(3), pp. 427–439.
[18] Covey, G. H., and Stanmore, B. R., 1981, "Use of the Parallel-Plate Plastometer for the Characterization of Viscous Fluids With a Yield Stress," J. Non-Newtonian Fluid Mech., **8**, pp. 249–260.
[19] Campanella, O. H., and Peleg, M., 1987, "Determination of Yield Stress of Semiliquid Foods From Squeezing Flow Data," J. Food. Sci., **52**(1), pp. 214–217.
[20] Meeten, G. H., 2000, "Yield Stress of Structured Fluids Measured by Squeeze Flow," Rheol. Acta, **39**, pp. 399–408.
[21] Delhaye, N., Poitou, A., and Chaouche, M., 2000, "Squeeze Flow of Highly Concentrated Suspensions of Spheres," J. Non-Newtonian Fluid Mech., **94**, pp. 67–74.

[22] Buscall, R., Mcgown, I. J., Mills, P. D. A., Stewart, R. F., Sutton, D., White, L. R., and Yates, G. E., 1987, "The Rheology of Strongly Flocculated Suspensions," J. Non-Newtonian Fluid Mech., **24**, pp. 183–202.

[23] Progelhof, R. C., Thrones, J. L., and Ruetsch, R. R., 1976, "Methods for Predicting the Thermal Conductivity of Composite Systems: A Review," Polym. Eng. Sci., **16**(9), pp. 615–624.

[24] Hassleman, D. P. H., and Johnson, L. F., 1987, "Effective Thermal Conductivity of Composites With Interfacial Thermal Barrier Resistance," J. Compos. Mater., **21**, pp. 508–515.

[25] Devpura, A, Phelan, P. E., and Prasher, R. S., 1999, "Percolation Theory Applied to the Analysis of Thermal Interface Materials in Flip-Chip Technology," *Proc. of ITHERM*, Las Vegas.

[26] Every, A. G., Tzou, Y., Hassleman, D. P. H., and Raj, R., 1992, "The Effect of Particle Size on the Thermal Conductivity of ZnS/Diamond Composites," Acta Metall. Mater., **40**(1), pp. 123–129.

[27] Prasher, R. S., Alger, O., and Phelan, P. E., 2001, "A Unified Macroscopic and Microscopic Approach to Contact Conduction Heat Transfer," *Proc. of 35th National Heat Transfer Conference*, Anaheim, CA.

An Inverse Determination of Unsteady Heat Fluxes Using a Network Simulation Method

F. Alhama
e-mail: paco.alhama@upct.es
Department of Applied Physics, Technical University of Cartagena, Campus Muralla del Mar. Cartagena 30203, Spain

J. Zueco and C. F. González Fernández
Department of Thermal Engineering and Fluids, Technical University of Cartagena, Campus Muralla del Mar. Cartagena 30203, Spain

This work addresses unsteady heat conduction in a plane wall subjected to a time-variable incident heat flux. Three different types of flux are studied (sinusoidal, triangular and step waveforms) and constant thermal properties are assumed for simplicity. First, the direct heat conduction problem is solved using the Network Simulation Method (NSM) and the collection of temperatures obtained at given instants is modified by introducing a random error. The resulting temperatures act as the input data for the inverse problem, which is also solved by a sequential approach using the NSM in a simple way. The solution is a continuous piece-wise function obtained step by step by minimizing the classical functional that compares the above input data with those obtained from the solution of the inverse problem. No prior information is used for the functional forms of the unknown heat flux. A piece-wise linear stretches of variable slope and length is used for each of the stretches of the solution. The sensitivity of the functional versus the slope of the line, at each step, is acceptable and the complete piece-wise solution is very close to the exact incident heat flux in all of the mentioned waveforms.
[DOI: 10.1115/1.1597614]

Keywords: Heat Transfer, Inverse, Transient

1 Introduction

An important type of inverse heat conduction problem (IHCP) deals with the estimation of the time-variable incident heat flux at the surface of a slab, when the temperature history at a particular location in the slab is known. Since errors are always present in the measured temperatures to some extent, the unsteady heat flux cannot be determined exactly.

The pioneering works on this subject are those of Stolz [1], Shumakov [2], Sparrow et al. [3] and Beck [4], about four decades ago. Beck's paper [4] is an important contribution that emphasises the calculation of surface heat flux. Since then, more than 400 papers have been written on the IHCP to date, or closely related ''ill-posed'' problems. An extensive research bibliography, which includes references to the exact and approximate methods commonly used in this kind of problem, can be found in Beck et al. [5], a book that contains the fundamental concepts of inverse conduction and an extensive survey. Other papers that deal with the heat flux calculations under different assumptions are those written by Kurpisz [6], Huang and Özisik [7] and Park and Chung [8].

The present work addresses the unsteady IHCP in a plane wall with a time-variable incident heat flux. Three types of prescribed flux are studied in addition to constant flux: sinusoidal, triangular and step waveforms. The numerical solution is obtained by means of the Network Simulation Method (NSM). For simplicity, constant thermal properties are assumed.

The NSM has already been successfully used to solve linear and non-linear problems in heat transfer and in other areas of engineering (González-Fernández et al. [9] and Alhama et al. [10]).

The input data for the IHCP are obtained from the solution of the direct heat transfer problem (DHCP), which is also solved numerically by means of the NSM. The solution for the temperature history at a point is recorded from the DHCP. The collection of temperatures at discrete regular times is modified systematically by introducing random errors which are produced by random number generation (Park and Miller [11]).

The inverse heat conduction problem, which is solved by means of the NSM, is a continuous piece-wise function obtained iteratively by minimizing the functional that compares some of the input data with those from the inverse solution.

A straight line segment of variable slope and size is used for each stretch of the piece-wise function. The sensitivity of the functional versus the slope depends on (i) the random error, (ii) the number of terms that form the functional, and (iii) the total number of measurements.

As regards the NSM, three advantages must be mentioned: (i) no mathematical manipulation (inherent to most of the numerical and analytical methods) is required; the computer commercial code used in this work, Pspice [12], does the calculations with sophisticated mathematical algorithms (Nagel [13]); (ii) the parameters of the electrical devices (i.e., the parameters which modify the functional until minimal values are achieved) are varied directly by means of an auxiliary program which manipulates Pspice, makes it run on a PC, and works directly with the results, and (iii) a few programming rules are necessary to elaborate the network file, since the number of different electrical devices involved is very small.

The inclusion of temperature-dependent thermal characteristics as well as the use of other kinds of co-ordinates may be made without special requirements (Alhama [14]).

Copyright © 2003 by ASME

2 Direct Heat Conduction Problem

A long slab of thickness L, density ρ, thermal conductivity k and specific heat c_e, receives an incident heat flux $j(t)$ on one face. An adiabatic condition is imposed on the other face. The mathematical model of the DHCP is defined by the equations

$$\rho c_e \frac{\partial T}{\partial t} = \frac{\partial}{\partial x}\left(k \frac{\partial T}{\partial x}\right), \quad \text{at } 0 < x < L \tag{1}$$

$$j = j_{in}(t) \quad \text{at } x = L \tag{2}$$

$$j = 0 \quad \text{at } x = 0 \tag{3}$$

$$T = T_o \quad \text{at } 0 < x < L, t = 0 \tag{4}$$

Equation (1) is the heat conduction equation for one-dimensional planar geometry; Eqs. (2) and (3) are the boundary conditions (time-variable incident heat flux and adiabatic conditions, respectively) and Eq. (4) is the initial condition. Sinusoidal, triangular and step waveforms are considered for $j_{in}(t)$.

3 Inverse Heat Conduction Problem

The main aim of this work is to estimate the magnitude incident heat flux, starting from the temperature history at a particular location. This set of temperatures (the simulated measurements in the laboratory) emerge from the solution of the DHCP. To make the IHCP amenable to a real experimental environment, normal random errors have to be added to the exact or approximated temperatures from the DHCP.

The temperature field of the DHCP, taken at discrete times $t_j = t_1, t_2, \ldots t_m$, at the particular location of the slab x_f, is used as input data in the IHCP. Naming this set of temperatures $T_{\mathrm{DHCP}}(x_f, t_j)$, with j the time index, a new series of m temperatures, named $T_{\mathrm{IHCP}}(x_f, t_j, \varepsilon_j)$, is generated by adding a random value ε_j to $T_{\mathrm{DHCP}}(x_f, t_j)$. This gives

$$T_{\mathrm{IHCP}}(x_f, t_j, \varepsilon_j) = T_{\mathrm{DHCP}}(x_f, t_j)(1 + \varepsilon_j) \tag{5}$$

where $\varepsilon_j = B u_j$, is the random error percentage (limited within the error percentage interval, $\pm \Delta \varepsilon$), B is a constant which depends on the random error percentage interval, and u_j is the random number produced by a random number generator which is between $[+0.999$ and $-0.999]$.

To make the problem more difficult the distribution of the random error is rectangular, that is, an equal probability is applied to each number from the random number generator.

Mathematically speaking, the formulation of the IHCP involves the original heat conduction Eq. (1), together with the boundary and initial conditions, Eqs. (3) and (4), and the discrete temperature "measurements", Eq. (5). With this information at hand the aim now is to estimate $j(t)$, the incident heat flux at $x = L$, by means of the NSM.

4 Network Simulation Method

The NSM is a hybrid differential-difference method that uses a real continuous time variable in such a way that no time interval needs to be established by the users for the numerical solution. Hence, the immediate advantage of this method is that errors are quantified in terms of the number of control volumes. NSM simulates the behavior of unsteady electric circuits by means of resistors, capacitors and nonlinear devices that seek to resemble thermal systems governed by unsteady linear or non-linear equations. Another advantage of the NSM is that it provides both the temperature and heat flux density fields immediately.

For its application, as regards the spatial co-ordinate, the partial differential equation of the mathematical model is changed into a set of finite-difference equations, one for each control volume.
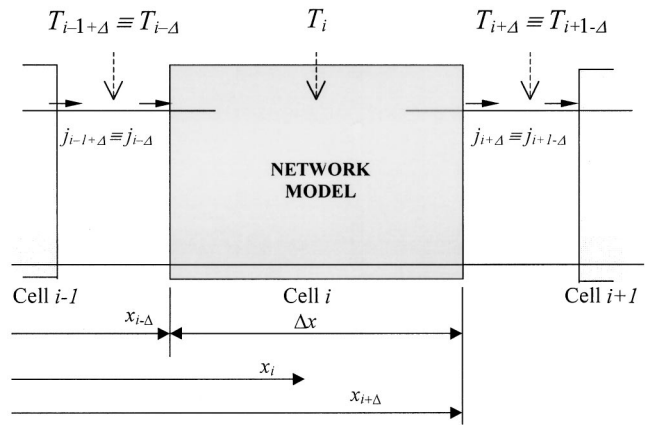

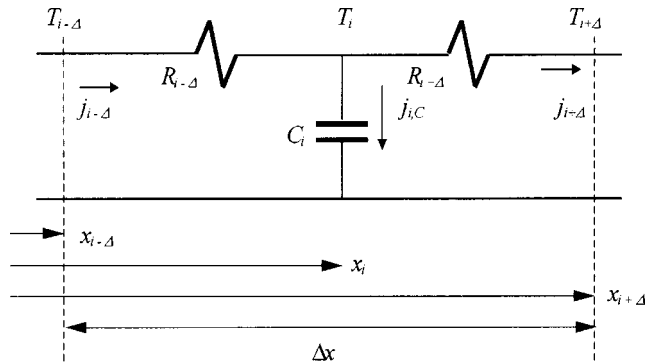**Fig. 1 Nomenclature of temperatures and heat fluxes into the control volume**

Fig. 2 Network model for the control volume

From these equations, and using the equivalence between variables "electric current $(J) \equiv$ heat flux density (j)" and "voltage $(V) \equiv$ temperature (T)", a network model for the control volume (or cell) was designed. In this way, the equations of the circuit are formally equivalent to those of finite differences from the mathematical model; this is the basis of the method. An adequate number of network cells (N) were connected in series and the initial and boundary conditions were easily added to the model. Alhama [14] established the connection between the total number of volume elements and the accuracy of the NSM. For $N = 60$ volume elements, which is the number used in this work for both the IHCP and the DHCP, the error of the method is less than 0.5 percent almost throughout the whole transient period.

According to the nomenclature of Fig. 1 and using the Fourier law, $j_{i \pm \Delta} = \pm k(T_i - T_{i \pm \Delta})/(\Delta x/2)$, where $j_{i-\Delta}$ and $j_{i+\Delta}$ are the entering and leaving heat fluxes, respectively, the finite differences equation is

$$(\Delta x \rho c_e)[dT_i/dt] = (2k/\Delta x)[(T_{i-\Delta} - T_i) - (T_i - T_{i+\Delta})] \tag{6}$$

At this point, each term of the preceding equation is redefined as an electric current. Naming the first term of Eq. (6) $j_{i,C}$, we can write

$$j_{i-\Delta} - j_{i+\Delta} - j_{i,C} = 0 \tag{7}$$

This equation may be interpreted as Kirchhoff's current law in the context of the prevalent equivalence. In this sense, j is a variable that satisfies the energy conservation law and T is a continuous single-valued dependent variable that satisfies Kirchhoff's voltage law. In the light of this brief description, the stage is set to

analyze the time-dependent conduction of heat described by two characteristic variables, T and j, by using an equivalent electric network, whose characteristic variables are the voltage and the electric current.

Within this framework, Eq. (6) envisions the participation of two equal resistors and one capacitor whose resistances and capacitance are $R_{i\pm\Delta}=\Delta x/2k$ and $C_i=\Delta x\rho c_e$, respectively. These passive electrical elements are connected as is shown in Fig. 2. This simple scheme is the network model of the cell. The network for the whole medium is obtained by connecting N circuits in series. The initial condition given by Eq. (4) is satisfied by fixing the initial voltage at the capacitor.

Equation (3), which refers to the adiabatic condition, was implemented in the model by connecting a resistor of infinite value at the input ends of the first cell.

Finally, the inclusion of the boundary condition pertinent to the incident heat flux, Eq. (2), must be studied in detail. In the case of the DHCP, a simple current generator which supports this condition was connected to last cell. With regards to the subject under discussion, an extensive library of source devices permits the direct implementation (one device only) of any time-dependent incident heat flux which may be defined by a mathematical function, sinusoidal, triangular, piece-wise, etc.

5 Inverse Solution

For the solution of the inverse problems, a procedure similar to the sequential function specification method (SFS) was used (see Beck et al. [5] for computational aspects) together with the NSM. While Beck's method uses piece-wise constant stretches to reproduce the incident heat flux, we used successive piece-wise linear stretches of variable slope. To this end a special electric device (stimulus generator) contains in the library of Pspice is used. This source, that simulates the boundary condition, generating a continuous piece-wise (time-dependent) function, is controlled by a simple programming routine (iterative process) which permits the selection of both the length and the slope of each stretch. The change in the slope is continuously varying (increasing or decreasing) until the pre-defined functional reaches a minimum value.

The piece-wise function which is obtained starts at the point $(j_0,0)$ and is defined by the set of points (j_z,t_z), $1\le z\le Z$. The functional to be optimized is of the form

$$F_{(z)}=\Sigma_{(n,n+1,n+2,\dots,n+r)}[T_{inv}(x_f,t_j)$$
$$-T_{\text{IHCP}}(x_f,t_j,\varepsilon_j)]^2_{j=n,n+1,\dots,n+r} \qquad (8)$$

In this equation, $z=1,2,\dots Z$ identifies the stretch (with Z being the total number of stretches of the piece-wise function); $n=1,2,\dots m$ is the value associated to the first temperature within the stretch (m being the total number of temperature measurements), and r the number of temperatures within the functional.
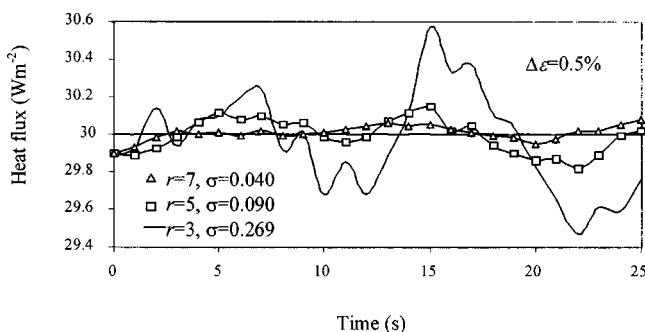
Fig. 3 IHCP solution for constant incident heat flux: $\Delta\varepsilon=0.5$ percent; $r=3$, 5 and 7; $m=25$
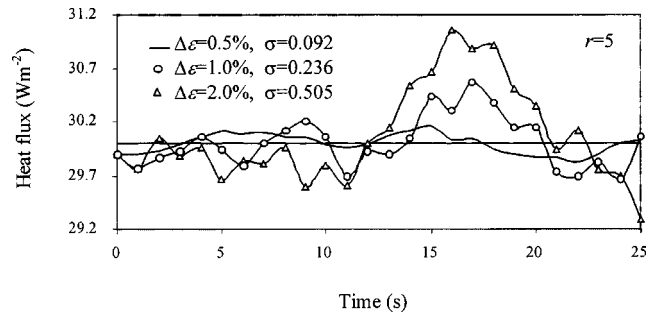
Fig. 4 IHCP solution for a constant incident heat flux: $\Delta\varepsilon=0.5$, 1 and 2 percent; $r=5$; $m=25$

$T_{inv}(x_f,t_j)$ is the temperature solution of the inverse problem at the position x_f and time t_j. The temperatures $T_{\text{IHCP}}(x_f,t_j,\varepsilon_j)$ were already defined in Eq. (5).

Once the slope of the stretch has been optimized, a new stretch of the piece-wise function may be defined. This one goes from the point (j_n,t_n) to one of the points contained in the stretch, (j_{n+1},t_{n+1}), (j_{n+2},t_{n+2}), $\dots$, (j_{n+r},t_{n+r}). The nearer the selected point is to (j_n,t_n), the greater the accuracy of the solution.

Pspice permits the values that specify the linear and nonlinear devices of the network to be defined in a parametric form. In this way, an optimization process may be easily programmed in order to rapidly obtain the minimum value of the functional in this kind of problem. We use simple algorithms to obtain the minimum value of the functional, that is, no optimization commercial code was implemented to shorten the computational time. Nevertheless, this approach may be incorporated in a future work. The principal

(a)

(b)

Fig. 5 IHCP solution for a triangular incident heat flux. $\Delta\varepsilon=2$ percent; $r=3$, 5 and 7; $m=40$: (a) relative error (percent), and (b) heat flux.
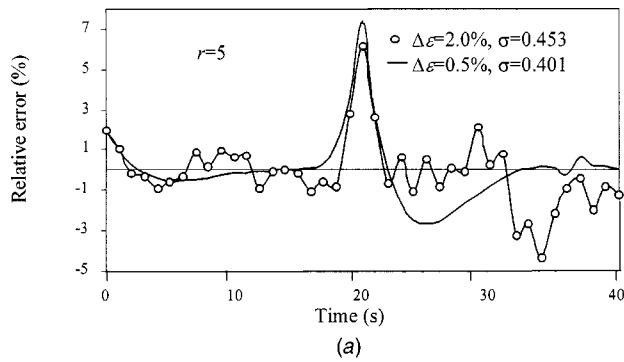
Fig. 6   IHCP solution for a triangular incident heat flux. $\Delta\varepsilon=0.5$ and 2 percent; $r=5$; $m=40$: (a) relative error (percent), and (b) heat flux.

Fig. 8   IHCP solution for a sinusoidal incident heat flux. $\Delta\varepsilon=0$; $r=3$, 5 and 7; $m=40$: (a) relative error (percent), and (b) heat flux.

aim of this paper is to introduce the NSM as a new tool for solving inverse problems, with the emphasis on simplicity.

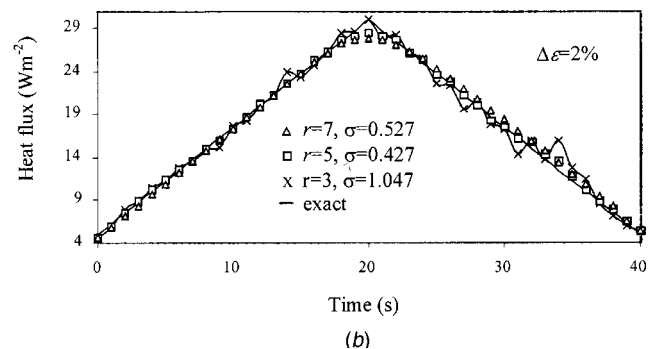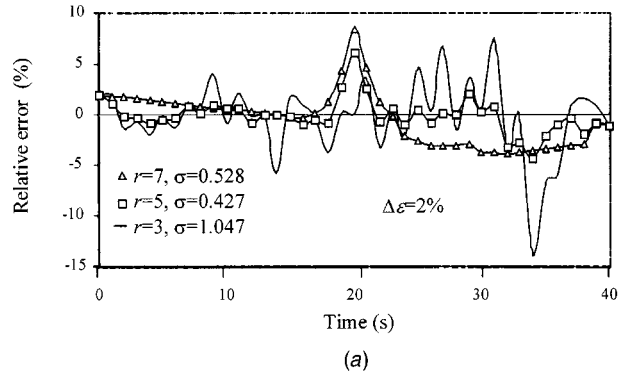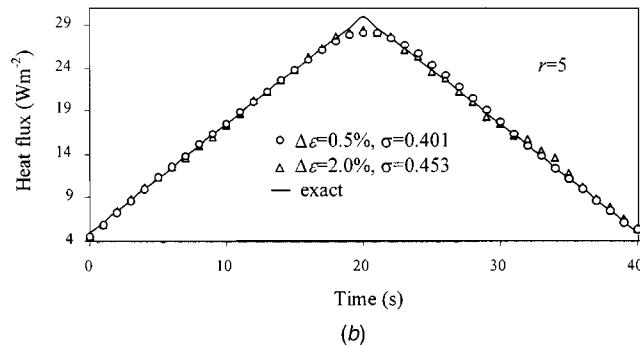The IHCP solution was obtained by simple programming routines that (i) run pspice continuously, (ii) search for the minimum

Fig. 7   IHCP solution for a sinusoidal incident heat flux. $\Delta\varepsilon=0$ and 2 percent; $r=3$; $m=40$ (a) relative error (percent), and (b) heat flux.

value of the functional and (iii) fix the successive stretches of the piece-wise function of $j(L,t)$. The whole network is simulated using standard commercial Ppsice [12] software, run in a Pentium III PC.

6   Results

Four applications were tested: constant, triangular, sinusoidal and step waveforms, which are defined by

$$\text{Constant:} \quad j(L,t)=j_a \tag{9}$$

$$\text{Triangular:} \quad j(L,0<t<t_l)=j_a+[(j_b-j_a)/(t_l)]t \tag{10}$$

$$j(L,t_l<t<2t_l)=j_b-[(j_a-j_b)/t_l](t-t_l)$$

$$\text{Sinusoidal:} \quad j(L,t)=j_a+j_b\sin(\omega t) \tag{11}$$

$$\text{Step waveform:} \quad j(L,0<t<t_l)=j_a \tag{12}$$

$$j(L,t_l<t)=j_b$$

In each of these cases, the solution of the DHCP was first obtained using the NSM. From this solution and using the Eq. (5), the set of data $T_{\text{IHCP}}(x_f,t_j,\varepsilon_j)$ needed for the inverse problem was elaborated. This temperatures depends on (i) the position, x_f, (ii) the time interval between temperature measurements, and (iii) the error, ε_j. The adiabatic surface, $x_f=0$, was selected in all cases for the simulated temperature measurements.

Relative error, e, is defined by means of the equations

$$e=(j_{j,\text{exa}}-j_{j,\text{est}})/(j_{j,\text{max}}-j_{j,\text{min}}) \tag{13}$$

where $j_{j,\text{exa}}$ and $j_{j,\text{est}}$ are the exact and estimated values, respectively, and $j_{j,\text{max}}$ and $j_{j,\text{min}}$ are the extremes of the functions given by Eqs. (9–12). For all cases standard deviation (σ) has been also evaluated.

Fig. 9 IHCP solution for a step incident heat flux. $\Delta\varepsilon=0$; $r=3$, 5 and 7; $m=100$: (a) relative error (percent), and (b) heat flux.
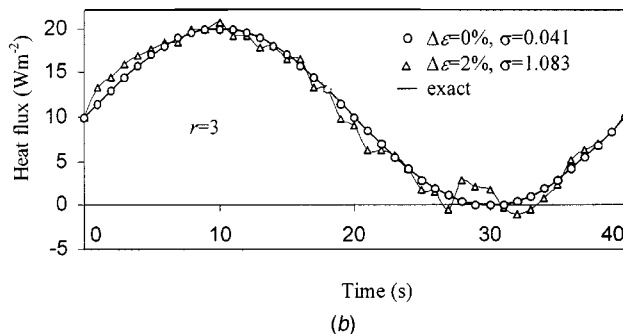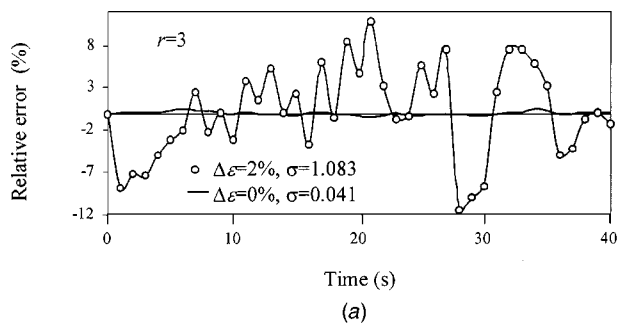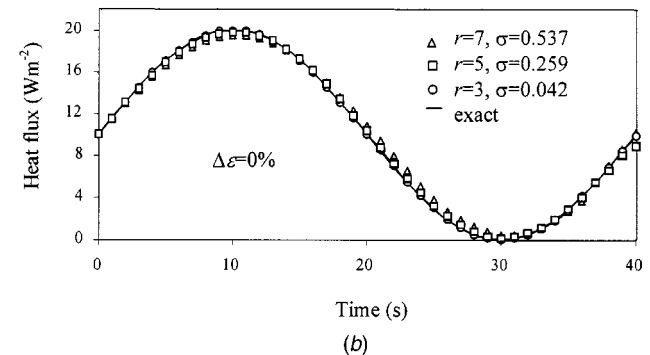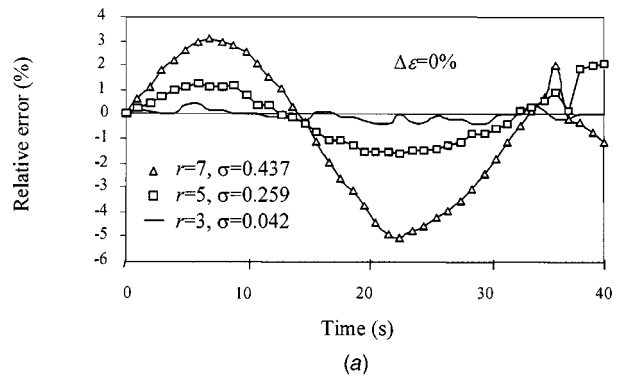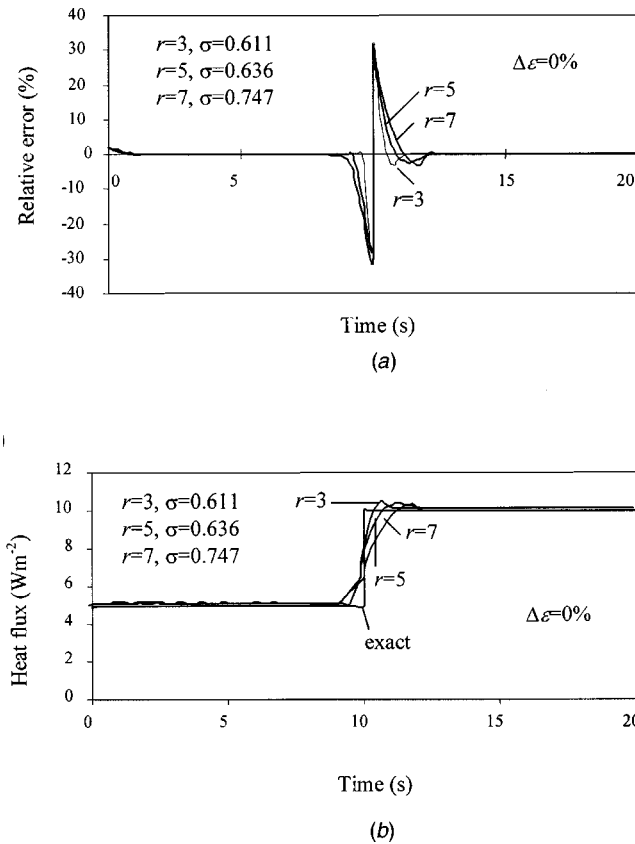
Figures 3 and 4 display the solution for constant incident heat flux. The numerical values are: $L=k=c_e=\rho=1$, $j_a=30$ (S.I. unit). The total number of measurements (m) are 25, and the time interval between measurements 1 s.

The influence of r (number of terms of the functional) may be observed in Fig. 3 for an error of $\Delta\varepsilon=0.5$ percent. The solution of the IHCP becomes more accurate as r increases, and for $r=7$ the inverse solution is very close to the exact value. The influence of the error is shown in Fig. 4 for $r=5$.

Figure 5 shows the influence of r on the solution for the triangular waveform, Eq. (11). In Fig. 5(a) relative error is sketched whereas in Fig. 5(b) refers to heat flux. The numerical values for this application are: $L=k=c_e=\rho=1$, $j_a=5$, $j_b=30$, $\Delta\varepsilon=2$ percent, $t_l=20$ and $m=40$ (time interval between temperature measurements 1 s). The influence of the error in this case can be appreciated in Fig. 6, for $\Delta\varepsilon=0.5$ percent and 2 percent; (a) relative error, and (b) heat flux. As the error decreases the solution for the same value of r becomes more accurate.

The solution for the case of sinusoidal waveform is outlined in Fig. 7 (influence of the error, $\Delta\varepsilon=0$ and 2 percent, for $r=3$) and 8 (influence of the number of functional terms, $r=3$, 5 and 7, for $\Delta\varepsilon=0$); for both figures, (a) relative error (percent), (b) heat flux. The numerical values in this application are: $L=k=c_e=\rho=1$; $\omega=2\pi(0.025)$, $j_a=j_b=10$ and $m=40$. The inverse solutions for $\Delta\varepsilon=0$ percent (Fig. 7) and $r=3$ (Fig. 8) are almost the same as the exact ones.

Finally, the solution of the step waveform is shown in Fig. 9 for measurements with no error and $r=3$, 5 and 7; (a) relative error (percent), (b) heat flux. The numerical values are: $L=k=c_e=\rho=1$; $j_a=5$, $j_b=10$, $t_l=10$ and $m=100$ (time interval between temperature measurements 0.2 s). As r decreases the solution becomes more exact.

Computing time for all the cases is less than 15 minutes in a PC Pentium III (1 Ghz).

7 Conclusions

A variant of the Sequential Function Specification Method has been used together with NSM as the numerical method to solve inverse problems associated with the determination of different kinds of incident heat fluxes. For this, only one network device that generates a piece-wise time-dependent function was required in conjunction with a programming routine. The solution for each case, therefore, takes the form of a piece-wise linear function.

The network model required for the numerical NSM is very simple since very few electrical devices are needed for its implementation and the mathematical manipulations required by the method are made by the circuit resolution code.

To test the potential of the proposed method, several test cases were simulated and solved: (i) constant, (ii) triangular, (iii) sinusoidal and (iv) step waveforms. No prior information was used as regards the functional forms of the unknown heat flux.

The accuracy and effectiveness of the method was illustrated for both exact and error affected input temperatures. The influence of the parameters (random error and number of terms that form the functional) on the results was also studied.

Notation

B = constant
c_e = specific heat, $(\text{kJ kg}^{-1}\,\text{C}^{-1})$
C = capacitor
e = error relative
F = functional defined in Eq. (8)
J = electric current variable (A)
j = heat flux (Wm^{-2})
j_a, j_b = constants
k = thermal conductivity, $(\text{W m}^{-1}\,\text{C}^{-1})$
L = thickness of the slab, (m)
n = first value of temperature within the functional
N = number of volume elements
R = resistor
t = time, s
t_l = constant
T = temperature, (K)
u = random variable
V = voltage (V)
x = spatial co-ordinate (m)
ε = random error value
ρ = density, (kg m^{-3})
σ = standard deviation
ω = angular frequency (s^{-1})
Δx = thickness of the control volume (m)

Subscripts

C = referred to the capacitor
f = referred to particular location at the slab
est = estimated
exa = exact
i = number of the volume element, $1{\leqslant}i{\leqslant}N$
$i{\pm}\Delta$ = right and left ends of the volume element
in = incident
inv = refers to the solution of the inverse problem
j = time index, $j=1,2,\ldots,m$
m = total number of temperature measurements
max = maximum
min = minimum
n = refers to the first temperature within the stretch
o = initial condition
r = number of terms within the functional
z = stretch index of the piece-wise function, $1{\leqslant}z{\leqslant}Z$
Z = number of stretches of the piece-wise function in the IHCP

References

[1] Stolz, G., Jr., 1960, ''Numerical Solution to an Inverse Problem of Heat Conduction for Simple Shape,'' ASME J. Heat Transfer, **82**, pp. 20–26.

[2] Shumakov, N. V., 1957, ''A Method for the Experimental Study of the Process of Heating a Solid Body,'' Soviet-Technical Physics (translated by American Institute of Physics), **2**, p. 771.

[3] Sparrow, E. M., Haji-Sheikh, A., and Lundgren, T. S., 1964, ''The Inverse Problem in Transient Heat Conduction,'' ASME J. Appl. Mech., **86**, pp. 369–375.

[4] Beck, J. V., 1968, ''Surface Heat Flux Determination Using an Integral Method,'' Nucl. Eng. Des., **7**, pp. 170–178.

[5] Beck, J. V., Blackwell, B., and St. Clair, C. R. Jr., 1985, *Inverse Heat Conduction, Ill-Posed Problems*, Wiley-Interscience, New York.

[6] Kurpisz, K., 1991, ''Numerical Solution of One Case Inverse Heat Conduction Problem,'' ASME J. Heat Transfer, **113**, pp. 280–286.

[7] Huang, C. H., and Özisik, M. N., 1992, ''Inverse Problem of Determination Unknown Wall Heat Flux in Laminar Flow Through a Parallel Plate Duct,'' Numer. Heat Transfer, Part A, **21**, pp. 55–70.

[8] Park, H. M., and Chung, O. Y., 1999, ''Inverse Natural Convection Problem of Estimation Wall Heat Flux Using a Moving Source,'' ASME J. Heat Transfer, **121**, pp. 828–836.

[9] González Fernández, C. F., Alhama, F., López Sánchez, J. F., and Horno, J., 1998, ''Application of the Network Method to Heat Conduction Processes With Polynomial and Potential-Exponentially Varying Thermal Properties,'' Numer. Heat Transfer, Part A, **33**, pp. 549–559.

[10] Alhama, F., López Sánchez, J., and González-Fernández, C. F., 1997, ''Heat Conduction Through a Multilayered Wall With Variable Boundary Conditions,'' Energy (Oxford), **22**, pp. 797–803.

[11] Park, S. K., and Miller, K. W., 1988, ''Random Number Generators: Good Ones are Hard to Find,'' Communications ACM, **31**, pp. 1192–1201.

[12] *PSPICE* 6.0, 1994, Microsim Corporation, 20 Fairbanks, Irvine, CA, 92718.

[13] Nagel, L. W., 1977, *SPICE* (A Computer Program to Simulate Semiconductor Circuits), Memo UCB/ERL M520, University of California, Berkeley, CA, Chpts. 4–6.

[14] Alhama, F., 1999, ''Transient Thermal Responses in Nonlinear Heat Conduction Processes Using the Network Simulation Method,'' Ph.D thesis, University of Murcia, Spain.

Design Formulas for Oscillatory Heat Transport in Open-Ended Tubes

Masao Furukawa

Leader, Thermal Engineering Group, NASDA (Japanese Space Agency), Tsukuba Space Center, Tsukuba, Ibaraki 305-8505, Japan

Modified Watson's functions dependent on the Womersley Number, concerning a forced oscillatory pipe flow, are introduced to mathematically simply express the effective thermal conductivity, the tidal displacement, and the tidal work of fluid. Those three are developed into algebraic expressions giving the required electrical oscillating power and the necessary number of capillary tubes. The relative conductivity increase, the specific shaker driving power, and the specific tube bundle size are graphically shown in the figures for several fluids of interest to contribute to designing a heaterless liquid warmer. [DOI: 10.1115/1.1597615]

Keywords: Enhancement, Heat Transfer, Tubes

Introduction

It is well known that sinusoidal fluid oscillations can enhance the mass transfer rate in tubes. Such dispersive phenomena were first examined by Chatwin [1] and then Watson [2] to mathematically find closed-form expressions of the effective longitudinal diffusivity. Regarding a laminar oscillatory flow, Joshi et al. [3]

compared theoretical predictions of Watson with experimental results to show an excellent agreement between the two. Watson's original result was employed by Kurzweg and Jaeger to elucidate the mechanics of high-frequency pulmonary ventilation [4] and was reformulated by them to design a diffusion cell for separating isotopes [5]. Zhang et al. [6] used that expression in calculating the power input of an enhanced mass pump for groundwater reclamation, which may be a practical application of liquid rather than gas dispersion technique.

Then, when describing the heat and mass transfer in a tube, one could find a similarity between the diffusion and conduction equations. Kurzweg and Zhao [7] first recognized it and thereby invented a novel apparatus for enhancing the axial heat conduction. In designing that apparatus, they derived an analytical expression of the effective thermal diffusivity for high-frequency oscillations. Kurzweg [8] also derived that for low-frequency oscillations, basically the same as Watson's expressions in form but replaced the Schmidt number with the Prandtl number. That apparatus [7], called dream pipe, thereafter evolved into an enhanced axial heat transfer (EAHT) device, characteristics of which were numerically simulated by Zhang and Kurzweg [9]. Similar to the EAHT device are a heat exchanger of Kaviany [10,11] and a phase-shifted one of Nishio et al. [12]. They [10,12] also employed Watson's expressions in design/performance calculations. It thus seems that Watson's original or reformulated expressions could apply to almost all types of EAHT devices provided the walls are insulators. His expressions are, however, not so convenient to design purposes because of a little complicated form. Several correlations recently presented by Rocha and Bejan [13] are of use to geometric optimization of open-ended tubes with two reservoirs but do not well conform to design practices of a heaterless liquid warmer proposed for space use. This study has therefore been made to present practical design formulas for such warmers regarded as a kind of EAHT device.

Theoretical Analysis

Figure 1, basically the same plan as drawn by Kurzweg and Zhao [7], shows an EAHT device which could serve as a heat exchanger in a spacecraft environmental control subsystem. It consists of two reservoirs connected to each other by a capillary bundle and its outside surfaces are thermally insulated. One is filled with cold liquid to be warmed up while the other with hot liquid. Heat is axially transported from the hot to the cold reservoir by shaker-caused oscillations without mass transfer. A solenoid valve is appended to each reservoir inlet and those two are synchronously regulated in response to the liquid temperature rise in the cold reservoir. Although not depicted in the figure, the hot reservoir will probably be placed in a high-temperature fluid loop joined with a solar absorber. The cold reservoir can thus have a warmed liquid supply. A way of Watson [2] is also applicable to formulating a problem of present concern. Under cylindrical coordinates taking z and r as the axial and radial distances, momentum/energy equations of a laminar pipe flow are

$$\partial w/\partial t = -(1/\rho)dp/dz + \nu[\partial^2 w/\partial r^2 + (1/r)\partial w/\partial r] \quad (1)$$

$$\partial T/\partial t + w\partial T/\partial z = \kappa[\partial^2 T/\partial r^2 + (1/r)\partial T/\partial r] \quad (2)$$

where t is the time, w the velocity, T the temperature, and p the pressure. Equations (1) and (2) are solved under the condition that the density ρ, the kinematic viscosity ν, and the thermal diffusivity κ are constant as specified. Since the enclosed liquid is subjected to sinusoidal oscillations, the pressure gradient in tube becomes

$$dp/dz = -P\cos\omega t \quad (3)$$

where ω is the angular frequency and P the peak gradient. The axial temperature distribution is then
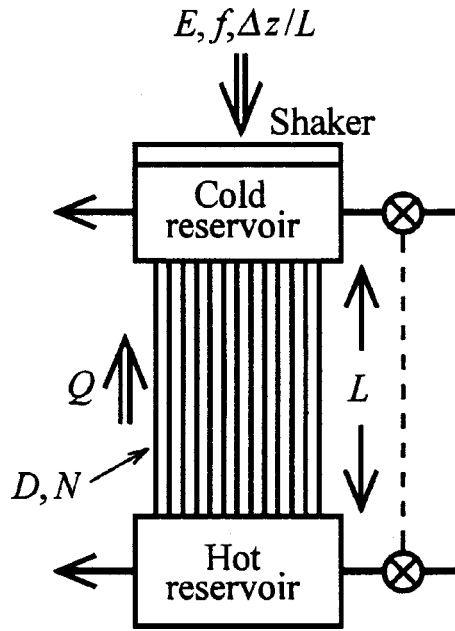
$$T = T_\infty + \gamma(-z + \theta) \quad (4)$$

Fig. 1 Dream pipe used heaterless liquid warming apparatus

where T_∞ is the specified hot temperature, γ the time-averaged temperature gradient, and θ the temperature fluctuation expressed in length. Because of Eqs. (3) and (4), Eqs. (1) and (2) are now written in r and t as independent variables to give w and θ. The separation of variables in Eqs. (1) and (2) results in an analytical solution of the form

$$w = \text{Re}[f(r)\exp(i\omega t)] \tag{5}$$

$$\theta = \text{Re}[g(r)\exp(i\omega t)] \tag{6}$$

Closed-form expressions of $f(r)$ and $g(r)$ are obtained for insulating boundary conditions as $f(a) = f'(a) = 0$ and $g'(0) = g'(a) = 0$, where a is the tube radius. Those two are expressed in Bessel functions of the first kind and the zeroth/first orders to become a same result as already given by Watson [2] and Kurzweg [8].

Once w and θ have thus been found, one can derive the effective thermal diffusivity κ_e, the tidal displacement Δz, and the tidal work per tube, E/N, from

$$\kappa_e = (2/\tau a^2) \int_0^a r\, dr \int_0^\tau (\kappa + w\theta)\, dt \tag{7}$$

$$\Delta z = (2/a^2) \int_0^a r\, dr \int_0^{\tau/2} w\, dt \tag{8}$$

$$E/N = (2\pi\Delta z/\tau) \int_0^a r\, dr \int_0^\tau w(-dp/dz)\, dt \tag{9}$$

where $\tau = 2\pi/\omega$, exactly giving the oscillation period. Equation (7) then reduces to

$$\kappa_e = \kappa(1 + R) \tag{7'}$$

where R shows the relative increase and is obtained by integrating $w\theta$ all over the period and the tube section. A process of the integration in Eqs. (7–9) is quite lengthy but finally leads to

$$R = (\lambda^2/a^2) S_R \tag{10}$$

$$\Delta z = 2\lambda S_z \tag{11}$$

$$E/N = 2\pi\nu P\lambda^2 S_P \tag{12}$$

where λ is the oscillation characteristic length defined in

$$\lambda = P/\rho\omega^2 \tag{13}$$

Factors S_R, S_z, and S_P are dimensionless and depend on the Wormersley number

$$\alpha = a(\omega/\nu)^{1/2} \tag{14}$$

In defining S_R, this number is modified as

$$\tilde{\alpha} = \sigma^{1/2}\alpha = a(\sigma\omega/\nu)^{1/2} \tag{14'}$$

where $\sigma = \nu/\kappa$, thereby expressing the Prandtl number.

Obtained analytical expressions of the above three are

$$S_R = \sigma^2 b_1(\alpha)[1 - b_2(\alpha)/b_2(\tilde{\alpha})]/(\sigma^2 - 1) \quad \text{when } \sigma \neq 1 \tag{15a}$$

$$S_R = \alpha b_1(\alpha) b_2'(\alpha)/4b_2(\alpha) \quad \text{when } \sigma = 1 \tag{15b}$$

$$S_z = 1 - b_3(\alpha)b_1(\alpha)/\alpha^4 \tag{16}$$

$$S_P = b_1(\alpha)S_z \tag{17}$$

Functions $b_1(\alpha)$, $b_2(\alpha)$, and $b_3(\alpha)$, newly introduced in place of $B_1(\alpha)$, $B_2(\alpha)$, and $B_3(\alpha)$ of Watson [2], are

$$b_1(\alpha) = \alpha B'(\alpha)/2B(\alpha) \tag{18}$$

$$b_2(\alpha) = \alpha B''(\alpha)/B'(\alpha) + 1 \tag{19}$$

$$b_3(\alpha) = \alpha^2 B'''(\alpha)/B'(\alpha) + 3\alpha B''(\alpha)/B'(\alpha) + 1 \tag{20}$$

Function $B(\alpha)$ is then expressed in Kelvin ber/bei functions as:

$$B(\alpha) = (\text{ber } \alpha)^2 + (\text{bei } \alpha)^2 \tag{21}$$

The validity of Eqs. (15a,b) and (16) is mathematically demonstrated as follows. One first considers a case where $\alpha = 0$. A result that $S_R = 0$ is obtained from Eqs. (15a,b) because $b_1(0) = 0$. Equations (7') and (10) then make a relation that $\kappa_e = \kappa$ when $\alpha = 0$. This is well consistent with a fact that k_e should approach k as the frequency approaches zero. Since $\lim_{\alpha \to 0} b_3(\alpha)b_1(\alpha)/\alpha^4 = 1$, Eq. (16) becomes such that $S_z = 0$. One then considers a case where $\alpha = \infty$, in which obtained from Eq. (19) are such limit values as $\lim_{\alpha \to \infty} b_2(\alpha)/b_2(\tilde{\alpha}) = 1$ and $\lim_{\alpha \to \infty} b_2'(\alpha) = 0$. These two make Eqs. (15a,b) such that $S_R = 0$. Since $\lim_{\alpha \to \infty} b_3(\alpha)b_1(\alpha)/\alpha^4 = 0$, one has an asymptotical value as $S_z = 1$. Finally, $S_R = S_z = 0$ when $\alpha = 0$ while $S_R = 0$ and $S_z = 1$ when $\alpha = \infty$. If $\alpha = \infty$, Eqs. (5) and (6) will then become such as $w = \lambda\omega \sin \omega t$ and $\theta = -\lambda \cos \omega t$. Since these expressions make $\int_0^\tau w\theta\, dt$ zero, one finds from Eqs. (7) and (7') that $R = 0$ and therefore from Eq. (10) that $S_R = 0$. Calculating Eq. (8) under a velocity profile stated above, one has a maximum displacement value as $\Delta z = 2\lambda$. A relation that $S_z \leqslant 1$ can thus be obtained from Eq. (11).

Equations (10–12) are now used to present practical expressions for the heaterless liquid warmer design. First, for a tube of the length L, Eq. (11) is transformed into

$$\lambda/L = (\Delta z/L)/2S_z \tag{22}$$

where $\Delta z/L$ is the stroke showing an extent of the oscillation amplitude. Although κ_e is calculable from Eq. (7'), the effective thermal conductivity k_e is rather convenient than κ_e for design purposes. Since $\kappa \propto k$ and $R \gg 1$ in cases of concern, Eq. (7') approximately becomes

$$k_e/k \approx R \tag{7''}$$

where k is the thermal conductivity. This relation with Eq. (22) turns into

$$(k_e/k)(D/L)^2 = (\Delta z/L)^2 S_R/S_z^2 \tag{23}$$

where $D=2a$, being the tube diameter. When the hot to cold reservoir temperature difference is ΔT, the enhanced heat transfer rate per tube, Q/N, is estimated at $k_e(\pi a^2/L)\Delta T$. Because of Eqs. (7″) and (10), this estimate results in

$$Q/N = k\pi\lambda^2 S_R(\Delta T/L) \tag{24}$$

It should then be noted that $\Delta T/L$ makes γ in Eq. (4). Dividing Eq. (12) by Eq. (24) makes E/Q. This expression is arranged to give E/QL by using Eqs. (13) and (22). A final expression including neither P nor λ is

$$E/QL = (\Delta z/L)(\mu\omega^2)S_P/kS_R S_z(\Delta T/L) \tag{25}$$

where $\mu=\rho\nu$, being the dynamic viscosity. Applying Eq. (22) to a reciprocal expression of Eq. (24) yields

$$NL^2/Q = 4S_z^2/(\Delta z/L)^2 k\pi S_R(\Delta T/L) \tag{26}$$

The required electrical shaker power E and the required number of tubes, N, can thus be simply calculated from Eqs. (25) and (26) if Q and L are design-specified.

Numerical Results

Equations (15–17) have first been calculated to comprehend how the factors S_R, S_z, and S_P change with the Womersley number α. Results are graphically shown in Figs. 2 and 3, where log α is taken as abscissa and extends over a range from -1.0 to 3.0. A parameter identifying six curves in Fig. 2 is the Prandtl number σ, considered values of which are 0.10, 0.50, 1.0, 5.0, 10.0, and 100.0. It is easily seen from Fig. 2 that all the curves have a peak corresponding to a specified σ value and that S_R becomes almost zero when $\alpha<1$ or $\alpha>100$. Also seen from the figure is that S_R increases with σ but does not gain so much when σ exceeds 10.0. Displayed in Fig. 3 are S_z and S_P, which are respectively put as left ordinate and as right ordinate. It is proved from the figure that S_z and S_P are positive but almost zero when $\alpha<1$. Noted here is that S_z asymptotically goes to 1.0 while S_P to 24.0 when $\alpha>100$. Asymptotical behaviors of S_R and S_z can be explained in a theoretical way. At low α values, viscous effects become important

Fig. 3 Displacement/Power factors versus logarithmic Womersley number

and thereby make both lower. As α gains, S_z increases because viscous resistance becomes smaller. At very high α values, the thermal boundary layer thickness approaches zero. Since no thermal boundary layer causes no thermal diffusion, S_R then becomes zero. A result that $S_R\approx0$ when $\alpha\ll1$ or $\alpha\gg1$ brings a special feature that S_R has a peak value as shown in Fig. 2. The reasonability of the result has then been demonstrated by comparing with several curves found in the literature [3,4,6]. Regarding the effective dispersion coefficient Φ, Zhang et al. [6] present curves of Φ vs α over a range from 10^{-2} to 10^3 with σ as a parameter. There also exists a peak value for Φ at a particular α value corresponding to a specified σ value. Peaks come out in due order of σ and such ones for S_R appear as well in Fig. 2.

Since a general trend of S_R, S_z, and S_P has thus been found, one may safely calculate Eqs. (23), (25), and (26) to present design curves of a heaterless liquid warmer. Calculations have been

Fig. 2 Enhancement factor versus logarithmic Womersley number

Fig. 4 Modified dimensionless effective conductivity versus frequency

Fig. 5 Specific shaker driving power versus frequency

A:ammonia, E:ethanol, M:methanol,
W:water, 1:R134a, 2:R22, 3:RC318

that Eq. (23) has been found under the condition $R \gg 1$. Some obtained numerical results not satisfying that condition are therefore not plotted in the figure. A change of S_R / S_z^2 then acts to form a peak in each curve of Fig. 4 and a bottom in each curve of Fig. 6. Extremely low frequencies, even good at making $(k_e / k) \times (D/L)^2$ larger and NL^2/Q smaller, are generally unsuitable for practical use. An optimal frequency should be selected in a range more than 2.0 Hz so as to maximize the modified dimensionless effective conductivity and to minimize the required number of tubes. Figures 4 and 6 show that there actually exist such optimal frequencies. In this connection, Katsuta et al. [14] offer experimental results on the heat transport coefficient χ of an EAHT device over a frequency range from 0 Hz to 12 Hz to produce a figure of interest. The curves drawn there also indicate the existence of a maximum χ value. This experimentally supports the credibility of the results shown in Fig. 4. A g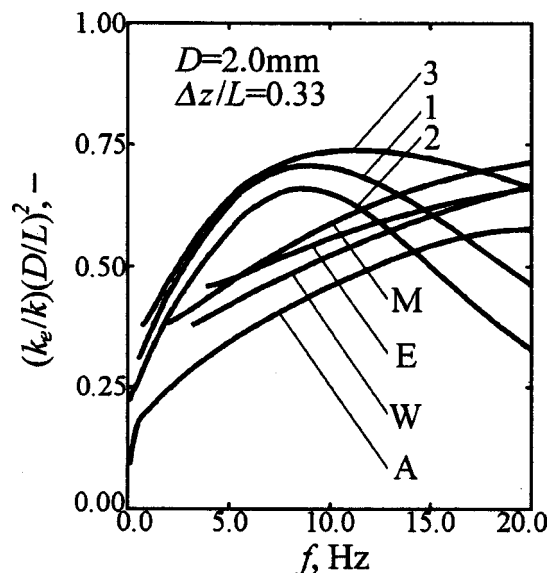raphical trend of curves in Fig. 5 is understandable and tells that the use of ammonia needs less power than the use of the other liquids considered.

Conclusion

The heaterless liquid warmer is an evolved kind of the enhanced axial heat transfer (EAHT) device of Kurzweg and Zhao and has been proposed for space use with practical design formulas. Although an effect of the wall conductivity is left out of account, the formulas can simply specify the modified effective to liquid conductivity ratio, the driving power to transport capability ratio, and the tube bundle size to load ratio. Those ratios, expressed in Eqs. (23), (25), and (26), mainly depend on the enhancement, displacement, and power factors. Those three, newly introduced here and expressed as Eqs. (15–17) in terms of modified Watson's functions, are generally applicable to any type of EAHT device in mathematically describing the thermo-oscillatory characteristics of the tube.

made to give $(k_e / k)(D/L)^2$, E/QL, and NL^2/Q under the condition that all the liquid properties are evaluated at 300 K and the axial temperature gradient $\Delta T/L$ is 0.5 K/m. Considered as the working liquid are ammonia, ethanol, methanol, water, R134a, R22, and RC318. Also taken as design parameters are the tube diameter D, the oscillation stroke $\Delta z/L$, and the oscillation frequency f. Calculated characteristic ratio values have been tabulated to produce a number of curves. Typical of such curves form Figs. 4–6, in which $(k_e / k)(D/L)^2$, E/QL, and NL^2/Q are respectively plotted against f ranging from 0.0 Hz to 20.0 Hz. All the curves marked with A, E, M, W, 1, 2, and 3, corresponding to the liquid nature, in the figures are applicable to design cases where $D = 2.0$ mm and $\Delta z/L = 0.33$. This stroke value comes from experiments of Katsuta et al. [14], who took $\Delta z/L$ to be 1/4, 1/3, or 1/2. It should again be noted that actually calculated is $(\Delta z/L)^2 S_R / S_z^2$ but shown in Fig. 4 as $(k_e / k)(D/L)^2$, and also
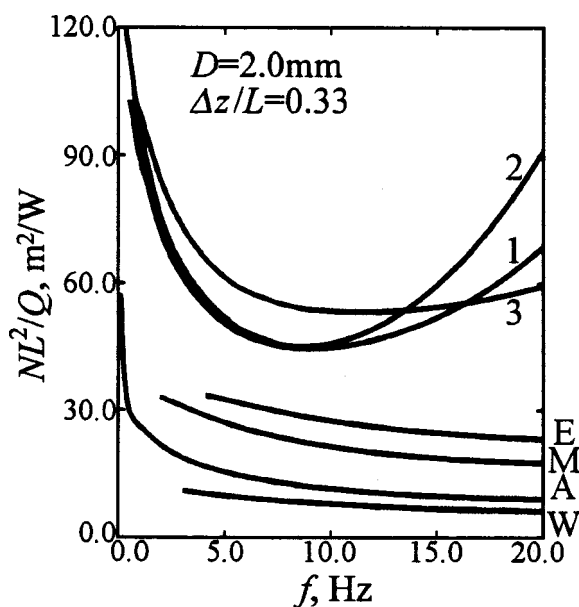
References

[1] Chatwin, P. C., 1975, "On the Longitudinal Dispersion of Passive Contaminant in Oscillating Flows in Tubes," J. Fluid Mech., **71**, pp. 513–527.
[2] Watson, E. J., 1983, "Diffusion in Oscillatory Pipe Flow," J. Fluid Mech., **133**, pp. 233–244.
[3] Joshi, C. H., Kamm, R. D., Drazen, J. M., and Slutsky, A. S., 1983, "An Experimental Study of Gas Exchange in Laminar Oscillatory Flow," J. Fluid Mech., **133**, pp. 245–254.
[4] Kurzweg, U. H., and Jaeger, M. J., 1986, "Tuning Effect in Enhanced Gas Dispersion Under Oscillatory Conditions," Phys. Fluids, **29**(4), pp. 1324–1326.
[5] Kurzweg, U. H., and Jaeger, M. J., 1987, "Diffusional Separation of Gases by Sinusoidal Oscillations," Phys. Fluids, **30**(4), pp. 1023–1025.
[6] Zhang, J. G., Zegel, W. C., and Kurzweg, U. H., 1996, "Enhanced Axial Dispersion in Oscillating Pipe Flow With Different Solute Concentrations at its Ends," ASME J. Fluids Eng., **118**(1), pp. 160–165.
[7] Kurzweg, U. H., and Zhao, L. D., 1984, "Heat Transfer by High-Frequency Oscillations: A New Hydrodynamic Technique for Achieving Large Effective Thermal Conductivities," Phys. Fluids, **27**(11), pp. 2624–2627.
[8] Kurzweg, U. H., 1985, "Enhanced Heat Conduction in Fluids Subjected to Sinusoidal Oscillations," ASME J. Heat Transfer, **107**(2), pp. 459–462.
[9] Zhang, J. G., and Kurzweg, U. H., 1991, "Numerical Simulation of Time-Dependent Heat Transfer in Oscillating Pipe Flow," AIAA J. Thermophysics, **5**(3), pp. 401–406.
[10] Kaviany, M., 1990, "Performance of a Heat Exchanger Based on Enhanced Heat Diffusion in Fluids by Oscillation: Analysis," ASME J. Heat Transfer, **112**(1), pp. 49–55.
[11] Kaviany, M., and Reckker, M., 1990, "Performance of a Heat Exchanger Based on Enhanced Heat Diffusion in Fluids by Oscillation: Experimental," ASME J. Heat Transfer, **112**(1), pp. 56–63.
[12] Nishio, S., Shi, X. H., and Zhang, W. M., 1995, "Oscillation-Induced Heat Transport: Heat Transport Characteristics Along Liquid-Columns of Oscillation-Controlled Heat Transport Tubes," Int. J. Heat Mass Transfer, **38**(13), pp. 2457–2470.
[13] Rocha, L. A. O., and Bejan, A., 2001, "Geometric Optimization of Periodic Flow and Heat Transfer in a Volume Cooled by Parallel Tubes," ASME J. Heat Transfer, **123**(2), pp. 233–239.
[14] Katsuta, M., Nagata, K., Maruyama, Y., and Tsujimori, A., 1991, "Fundamental Characteristics of Heat Conduction Enhancement in Oscillatory Viscous Flow—Dream Pipe," Proc. 3rd ASME/JSME Joint Thermal Engineering Conf., **3**, pp. 69–74.

Fig. 6 Specific tube bundle size versus frequency

A Revision of the Classical Performance Extended Surfaces Assessment: Proposed New Coefficients

M. Alarcón
Thermal Machines and Heat Engines Area, University of Murcia, 30100, Campus, de Espinardo, Murcia, Spain

F. Alhama and C. F. González-Fernández
Department of Applied Physics, Technical University of Cartagena, Campus, Muralla del Mar, 30203 Cartagena, Spain

Keywords: Finned Surfaces, Heat Transfer

1 Introduction

The coefficients most commonly used in the study and design of fins are fin efficiency (Harper and Brown [1]) and fin effectiveness (Gardner [2]). In their definitions, the so-called Murray-Gardner's hypotheses or limiting assumptions are assumed [3]; if these cannot be stated, the assessment of fin system performance is not correct or simply impossible. This occurs when fin-wall systems or unsteady processes are considered; in the last case, the dissipated heat does not instantaneously coincide with the heat rate through the fin base and when the efficiency is calculated using this quantity values greater than unity are obtained in the first few instants of the transient period [4].

The limitations of these parameters to properly reflect the real behavior of finned systems and/or to face *real world* configurations have led to the definition of new coefficients. Among these are *input admittance* (Krause et al. [5]), the *augmentation factor* (Heggs and Stone [6]) and the *enhancement factor*, (Manzoor et al. [7]). The last two parameters refer to fin-wall systems, and consider the fin and the wall to which it is attached as an indissoluble whole.

The suitability of the different coefficients has been discussed for the steady state by Kraus [8] and Wood et al. [9]. Kraus argues that the input admittance is better than efficiency and effectiveness, while Wood et al. conclude that the augmentation factor, *AUG*, is the only parameter that can properly represent the behavior of the fin-wall assembly. Nevertheless, *AUG* is unsuitable for predicting the behavior of the fin-wall assembly subjected to an increase in the heat transfer coefficient h_2, since, while the heat dissipated by the fin-wall assembly increases, *AUG* decreases [9]. This is due to the fact that an increase in h_2 promotes an increase in the heat dissipated by the unfinned wall greater than the increase produced in the fin-wall assembly. In our judgment, then, none of the above coefficients fully satisfies all the requirements that an ideal performance coefficient must fulfil.

After evaluating the aptitude and/or suitability of the five above-mentioned coefficients for studying fin-wall systems, we propose three new performance indicators: "thermal reverse admittance" [4], "specific reverse admittance," and "relative reverse admittance." They are especially suited to representing the performance of fin-wall systems under any hypotheses, including time-dependent processes. This set of indicators can be directly obtained by the Network Simulation Method (NMS), a general-purpose numerical method whose efficacy has been established for different kinds of linear and non-linear problems in the heat transfer domain [10].

2 Conditions That an Ideal Performance Coefficient Must Fulfil

Briefly, an ideal performance coefficient ought to:

1. Be consistent: the higher the value of the parameter the better the performance of the fin, i.e., the dissipated heat; this is not the case with the efficiency [8].
2. Refer to a standard or be weighted by the size of the fin.
3. Provide a maximum value which coincides with the optimum. The optimum of a system occurs when the relationship between the transferred or dissipated heat and the volume or mass of the system is maximum.
4. Serve to compare the relative merits of a given group of finned systems.
5. Have a maximum value of unity, a universal reference in this kind of parameter.
6. Be nondimensional (an interesting, but not essential, characteristic).

3 The New Performance Indicators

3.1 Thermal Reverse Admittance. In the search for a performance coefficient to overcome the difficulties of the coefficients defined to date, the "thermal reverse transfer admittance," or simply "thermal reverse admittance," Y_r, is defined, whose generality means that it is not merely confined to the study of finned systems:

$$Y_r = \frac{J_o}{\theta_i} \tag{1}$$

where J_o is the *output* heat rate dissipated to the surroundings and/or transferred to other elements, depending on the system considered, and θ_i is the excess in the *input section* of the same. This input section is not necessarily a physical surface but may also be an ideal limit which includes boundary conditions. In fin-wall systems (Fig. 1) $\theta_i = \theta_{1\infty}$ is the excess in the fluid that bathes the wall on its naked side, while J_o is the heat dissipated to fluid 2 by the external surface of the fin and the rest of the prime surface.

Y_r refers to the heat that is transferred by the fin or fin-wall assembly, while the Kraus input admittance, Y_i, refers to the heat flux in the input section. The main reason for defining the new coefficient is that in time-dependent systems (transient process, harmonic, etc.) differences in phase exist and there is a damping of the amplitude between the flux in the thermal source and the dissipated flux, both of which depend on the excitation and on the dimensional and thermal characteristics of the system. In time-independent processes $Y_i = Y_r$.

The terms "impedance" and "admittance" are widely identified as quantities of time-dependent processes, both harmonic and non-harmonic. Harmonic processes are of interest in thermal scope (day-night variations, reciprocating compressors, etc.). In these time-dependent processes, thermal admittance is not just the reverse of thermal resistance since it is defined by both modulus and phase, which normally have a marked dependence on frequency. Y_i is really a "conductance," not properly an admittance, since no reference to time-dependence is mentioned. In turn, Y_r has been used with success to obtain the frequency response of fin-wall systems [4].

The definition of thermal reverse admittance is general, and is not restricted to certain hypotheses: multidimensional behavior, variable thermal coefficients and properties, nonlinear boundary conditions, etc. It is defined for instantaneous heat rates and excess and their evaluation is in general made by numerical procedures, NSM being especially suitable.
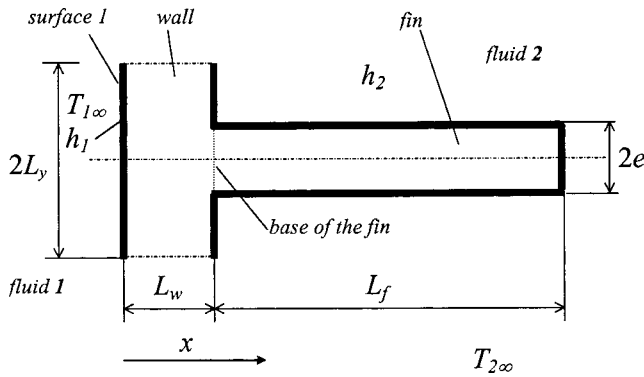
Fig. 1 Fin-wall assembly

This coefficient is indeed useful in the calculation and design of fin systems since, once Y_r, the excess θ_i and the number of fins per unit of length or surface are known, it is possible to calculate the overall heat transferred by the device.

In turn, according to Section 2, thermal reverse admittance is a consistent parameter but cannot be considered as an ideal coefficient, for which reason we have derived new parameters from it.

3.2 The Specific Reverse Admittance. The reverse admittance coefficient refers neither to the quantity of material used nor to an optimum. To overcome this deficiency the "specific reverse admittance," y_r, or the relationship between the thermal reverse admittance, Y_r, and the mass, m, of the fin, has been defined:

$$y_r = \frac{Y_r(W/K)}{m(kg)} = \frac{J_o(W)}{\theta_i(K) \cdot m(kg)} \quad (2)$$

A specific reverse admittance with respect to the volume is also possible. This coefficient fulfils the three first conditions in Section 2:

1. y_r is a consistent parameter, as is Y_r.
2. In Y_r the heat dissipated refers to its own mass, and so the deficiency that a bigger dimension involves a bigger coefficient does not arise.
3. The maximum heat dissipation rate for a given mass and excess θ_i (i.e., the optimum) coincides with the maximum of y_r, because it is the ratio J_o/θ_i that it is usually optimized in the optimization process.

Specific reverse admittance is a universal parameter for comparing the performance of different fin configurations and shapes, taking into account the quantity of material used.

3.3 Relative Reverse Admittance. The above coefficient is dimensional and its maximum value is not unity. In order to overcome these deficiencies and to make more explicit the reference to a standard, relative reverse admittance, y_{rel}, is defined as:

$$y_{rel} = \frac{y_r}{y_{r,opt}} \quad (3)$$

where $y_{r,opt}$ is the specific admittance in the optimum fin for a given type (longitudinal, annular, rectangular, etc.) and/or material. The determination of this coefficient requires the determination of the optimum, which is specific to every fin system.

y_{rel} is a dimensionless coefficient with a maximum value of unity. Thus, it may be considered as an ideal coefficient because it fulfils all the requirements (Section 2). Y_{rel} indicates the margin of enhancement that a fin design can obtain for a given shape. This information is not provided by any of the fin performance indicators defined to date.

Table 1 shows the extent to which the different extended surface performance indicators fulfil the required characteristics. It is clear that only reverse admittances are always consistent and that relative reverse admittance is the coefficient that accomplishes all the characteristics of an ideal indicator.

4 Application of the New Coefficients to a Fin-Wall System

As an example, we shall calculate the reverse admittances (Y_r, y_r, y_{rel}) of the straight fin-wall assembly of rectangular profile of Fig. 1. Classical Murray-Gardner's hypotheses are assumed for simplicity, except that unsteady flux and diabatic extreme of the fin are also considered; θ_b excess is *a priori* unknown.

Fin and wall are of pure aluminum ($k = 229$ W/mK, $\rho = 2700$ kg/m^3, $c = 945$ J/kgK); $\theta_1 = 1$ K and the heat transfer coefficients on both sides of the assembly are $h_1 = 100$ W/m^{2}K, $h_2 = 10$ W/m^{2}K. The dimensions are $L_w = 5 \cdot 10^{-3}$ m, $L_f = 5 \cdot 10^{-2}$ m, $L_y = 10^{-2}$ m, $e = 10^{-3}$ m, $b = 1$ m; the fin with these dimensions is called "initial" fin.

Due to symmetry, only the section between $y = 0$ and $y = L_y$ needs to be analyzed. The mathematical model consists of the following set of equations:

$$0 < x < L_w: \quad \partial j_w/\partial x + \rho c(\partial T/\partial t) = 0; \quad j_w = -k(\partial T/\partial x)$$

$$L_w < x < L_w + L_f:$$

$$\partial j_f/\partial x + \rho c(\partial T/\partial t) + h_2(P/S_f)(T - T_{2\infty}) = 0;$$

$$j_f = -k(\partial T/\partial x)$$

$$x = 0: \quad h_1(T_{1\infty} - T) = -k\,\partial T/\partial x$$

$$x = L_w: \quad -S_w k\,\partial T/\partial x = -S_f k\,\partial T/\partial x + (S_w - S_f)h_2(T - T_{2\infty})$$
$$(4)$$

$$x = L_w + L_f: \quad -k\,\partial T/\partial x = h_2(T_f - T_{2\infty})$$

$$t = 0; \quad 0 < x < L_w + L_f: \quad T = T_0,$$

$$T_{2\infty} = T_0 = 0$$

In the steady state the simulation of the fin-wall system gives values of $Y_r = 0.733$ W/K and $y_r = 1.358$ W/kgK. The efficiency of the fin in these conditions is $\eta = 0.964$. To determine the value

Table 1 Chart of performance coefficient characteristics

| Performance coefficient	Fin-wall system	Transient process	Consistent	Reference to a standard	Maximum occurs in the optimum	Maximum is unity	Dimensionless
Efficiency	No	No	No	Yes	No	No	Yes
Effectiveness	No	No	No	No	No	No	Yes
Input Admittance	No	No	No	No	No	No	No
Augmentation Factor	Yes	Yes	No	No	No	No	Yes
Enhancement	Yes	Yes	No	No	Minimum	No	Yes
Thermal Reverse Admittance	Yes	Yes	Yes	No	No	No	No
Specific Reverse Admittance	Yes	Yes	Yes	No	Yes	No	No
Relative Reverse Admittance	Yes	Yes	Yes	Yes	Yes	Yes	Yes
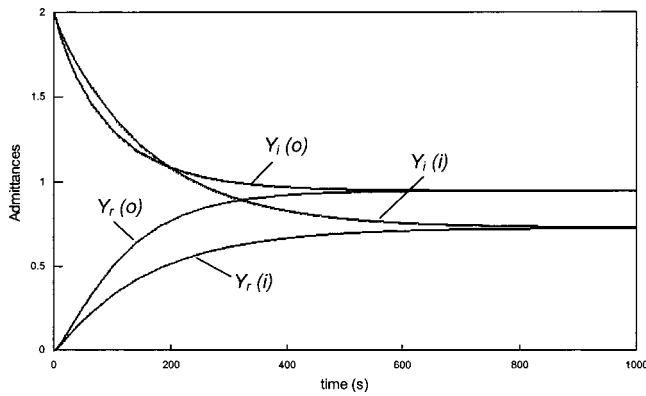
Fig. 2 Reverse admittance, Y_r, and input admittance, Y_i, in a fin-wall assembly under step excitation ((i), initial and (o), optimum)

of the relative admittance y_{rel}, the "optimum" of the system must be found, i.e., the dimensions of the assembly for a given volume (or mass) for which the dissipated heat is *maximum*. If the restrictions of the problem are the volume of the fin $V_f = 10^{-4}$ m^3, $L_y = 0.005$ m, and 0.01 m$< L_f < 0.2$ m, the optimum fin length, $L_{f,opt}$, as determined by means of NSM [11], is 0.13 m, which corresponds to half the fin thickness, $e_{opt} = 3.846 \times 10^{-4}$ m. The coefficients of performance in the optimum are $\eta_{opt} = 0.635$, $Y_{r,opt} = 0.954$ W/K, and $y_{r,opt} = 1.767$ W/kgK. Finally, the relative reverse admittance, y_{rel}, of the initial fin is 0.768, indicating that the fin design can be substantially improved.

As has been demonstrated, efficiency behaves inconsistently and so comparison of the efficiency of the two fins provides confusing information: the efficiency of the initial fin is greater than that of the fin of optimum dimensions. On the other hand, the admittances of the two fin-wall systems reflect the real situation: either the reverse admittance or the specific reverse admittance is bigger in the fin of optimum dimensions and the relative admittance of the studied fin provides a value that points to the distance from the optimum. Figure 2 shows the instantaneous input admittance Y_i and reverse admittance Y_r of the fin-wall assembly of the fin of the initial dimensions (i) and the fin of optimum dimensions (o). The difference between both coefficients is clear. Both values coincide in the steady state but not in the transient time.

Table 2 shows the values of the performance indicators for the initial and optimum fin-wall assemblies. Efficiency, effectiveness, augmentation, and enhancement factors have been computed directly from their definitions [1,2,5,6,7] and NSM simulation results.

5 Conclusions

After a study of the conceptual and application characteristics of currently used extended surfaces indicators, in a general analysis of fin-wall systems, the characteristics that must be fulfilled by an ideal coefficient have been detailed. With these in mind, ther-

mal reverse admittance, specific reverse admittance and relative reverse admittance are proposed as new performance indicators for the analysis of extended surfaces under any hypothesis, especially time-dependent processes. These new coefficients, for their generality and precision, outmatch the currently used performance coefficients; the last two are also linked to the concept of system optimization. Thermal reverse admittance, which allows us to know the dissipated heat once the temperature gradient between fluids is known, is an absolute scaling factor of fin-wall assemblies; specific reverse admittance is a measure of efficient use of material for heat transfer task; and relative reverse admittance provides information as to the margin of improvement in fin design.

Finally, a straight fin-wall system has been analyzed as an example of how the new coefficients can be applied. Their superiority over other coefficients is demonstrated. Network Simulation Method is especially suitable for the direct and accurate numerical determination of the proposed coefficient without using special mathematical developments.

Although initially developed for extended surfaces, the thermal reverse admittance and derived coefficients could be applied to the analysis of other thermal systems.

Nomenclature

AUG = augmentation factor
b = with of the fin (m)
c = specific heat (kJ kg^{-1}K^{-1})
e = half fin thickness (m)
h = heat transfer coefficient (Wm^{-2}K^{-1})
j = heat rate density (Wm^{-2})
J = heat rate (W), $J = j \cdot S$
k = thermal conductivity of the material (Wm^{-1}K^{-1})
L = length (m)
L_y = half fin pitch (m)
m = mass of the fin or fin-wall assembly (kg)
P = perimeter of the fin (m), $P = 2 \ (2e+b)$
S = cross-sectional area, external surface (of the fin) (m^2)
t = time (s)
T = temperature of the material at point x (K)
V = volume of the fin or fin-wall assembly (m^3)
x = space co-ordinate (m)
Y = admittance (W/K)
y = specific admittance (W/kg K)

Greek Symbols

η = fin efficiency
ρ = density (kg m^{-3})
θ = temperature excess, i.e., $T - T_{2\infty}$ (K)

Subscripts

b = base of the fin
f = fin
i = input
o = output
opt = refers to the optimum fin
r = reverse
rel = refers to relative reverse admittance
w = wall
0 = initial condition
1 = refers to the unfinned side of the wall
2 = refers to the finned side of the wall
∞ = refers to the external media far from the surfaces

References

[1] Harper, D. R., and Brown, W. B., 1922, "Mathematical Equations for Heat Conduction in Fins of Air Cooled Engines," NACA Report 158.
[2] Gardner, K. A., 1942, "Heat Exchanger Tube Sheet of Temperatures," Refiner. Nat. Gas. Manuf., **21**, pp. 71–77.
[3] Kern, Q. D., and Kraus, A. J., 1972, *Extended Surface Heat Transfer*, McGraw-Hill, New York.

Table 2 Values of performance coefficients in the application

Performance coefficient	initial ($L_f = 0.05$ m)	optimum ($L_{f,opt} = 0.13$ m)
Efficiency	0.964	0.635
Effectiveness	49.15	215.28
Input admittance	0.733	0.954
Augmentation factor	4.033	5.248
Enhancement factor	0.172	0.108
Thermal reverse admittance	0.733	0.954
Specific reverse admittance	1.358	1.767
Relative reverse admittance	0.768	1

[4] Alarcón, M., Alhama, F. A., and González-Fernández, F. C. F., 2002, "Transient Conduction in a Fin-Wall Assembly With Harmonic Excitation. Network Thermal Admittance," Heat Transfer Eng., **23**, pp. 31–43.

[5] Kraus, A. D., Snider, A. D., and Doty, L. F., 1978, "An Efficient Algorithm for Evaluating Arrays of Extended Surface," ASME J. Heat Transfer, **100**, pp. 288–293.

[6] Heggs, P. J., and Stones, P. R., 1980, "Improved Design Methods for Finned Tube Heat Exchanger," Trans. Inst. Chem. Eng., **58**, pp. 147–154.

[7] Manzoor, M., Ingham, D. B., and Heggs, P. J., 1983, "The One-Dimensional Analysis of Fin Assembly Heat Transfer," ASME J. Heat Transfer, **105**, pp. 646–651.

[8] Kraus, A. D., 1988, "Analysis of Extended Surface," ASME J. Heat Transfer, **110**, pp. 1071–1081.

[9] Wood, A. S., Tupholme, G. E., and Heggs, P. J., 2000, "Steady-State Heat Transfer and Performance Assessment," in *Recent Advances in Analysis of Heat Transfer for Fin Type Surfaces*, B. Sunden and P. J. Heggs, eds., WIT Press, pp. 165–210.

[10] González-Fernández, C. F., and Alhama, F., 2001, "Heat Transfer and the Network Simulation Method," in *Network Simulation Method*, J. Horno, ed., Research Signpost, Trivandrum (India), pp. 33–58.

[11] Alarcón, M., 2001, "Transporte de calor en sistemas con aletas. Coeficientes de rendimiento y red de transferencia," Ph.D. thesis, Universidad Politécnica de Cartagena (Spain).

Determination of Drying Times for Irregular Two and Three-Dimensional Objects

A. Z. Sahin and I. Dincer[1]

Mechanical Engineering Department, KFUPM, Dhahran 31261, Saudi Arabia

This paper deals with development of a new analytical model for determining the drying times of irregular-shaped multi-dimensional objects. Geometrically irregular two and three-dimensional products are approximated by elliptical cylinder and ellipsoidal shapes, respectively. Using experimental drying parameters that are available from the literature, drying times of irregular, multi-dimensional products are determined through the present models. Geometric shape factors for the elliptic cylinder and ellipsoid are employed and based on the reference drying time for an infinite slab. In addition, the present models are verified through comparison with experimental drying times of several food products. The accuracy of the predictions using the present models is then discussed, and a considerably high agreement is obtained between the predictions and experimental data.
[DOI: 10.1115/1.1603778]

Keywords: Drying, Heat Transfer, Mass Transfer, Moisture, Porous Media

1 Introduction

Drying is the process of thermally removing moisture to yield a solid product. Mechanical methods for separating a liquid from a solid are not considered in thermal drying. When a wet solid is subjected to thermal drying, two processes occur simultaneously: (i) transfer of energy (mostly as heat) from the surrounding environment to evaporate the surface moisture, and (ii) transfer of internal moisture to the surface of the solid and its subsequent

[1]Present address: Dr. Ibrahim Dincer, School of Manufacturing Engineering; University of Ontario Institute of Technology, 2000 Simcoe Street North, Oshawa, Ontario L1H 7K4, Canada, Tel: 905-721-3209, Fax: 905-721-3140. E-mail: Ibrahim.Dincer@uoit.ca

evaporation due to the former process. Historically, the thermodynamics of moist-air drying systems was developed only about a century ago. Krischer [1] was one of the first to investigate the role of heat transfer in drying. Whittaker [2] presented the limited theory of drying based on the transport equations. Drying is a complex thermal process in which unsteady heat and moisture transfer occur simultaneously. Heat is transferred by convection from heated air to the product to raise the temperatures of both the solid and moisture that is present. Moisture transfer occurs as the moisture travels to the evaporative surface of the product and then into the circulating air as water vapor. The heat and moisture transfer rates are therefore related to the velocity and temperature of the circulating drying air. Moreover, momentum transfer may take place simultaneously coupled with the heat and moisture transfer. However, it is generally considered negligible for solids drying [1].

The driving force for evaporation during the drying process is the difference between the vapor pressure of the water in the product and the partial pressure of the water vapor in the surrounding atmosphere. Increasing the temperature of a moist solid increases the vapor pressure of the water in the solid, while increasing the temperature of air decreases the partial pressure of water vapor in the air. Moisture will migrate from an area of high vapor pressure to one of low pressure. Therefore, there is a moisture gradient resulting from this migration of moisture from within the heated product, where it has a high vapor pressure, through the micropores to the moisture surface, where it is evaporated into the surrounding atmosphere as water vapor with a lower partial pressure. The drying of solid products/objects is a very broad area and many experimental and theoretical investigations have appeared in the literature, e.g., [3–17]. As indicated recently [4,5], determination of drying process parameters, namely drying coefficient and lag factor; and drying moisture transfer parameters, namely moisture diffusivity and moisture transfer coefficient of solid products subject to air drying is of great practical importance. In the literature, several studies, e.g., [4–8,10–12,14–16] have been undertaken to determine/estimate drying process parameters and drying moisture transfer parameters for solids drying.

Food products that are dried are mostly geometrically irregular. Although, recently Sahin et al. [18] studied the drying of regular multi-dimensional products analytically, and presented some illustrative examples, the primary objective of the present work is to develop a new model for irregular shaped objects. To develop the analytical model for the drying of irregular shaped products, the geometries are approximated by either an elliptical cylinder or ellipsoid, taking into consideration the three-dimensional aspect ratios.

2 Modeling

As highlighted earlier, this work is an extention of previous work [18] on the determination of drying times of regular-shaped multi-dimensional objects. Therefore, modeling of moisture transfer will not be presented here. The assumptions made in the modelling drying process are (i) constant thermophysical properties of the moist object, (ii) negligible shrinkage and/or deformation of the moist object, (iii) negligible heat generation inside the moist object, and (iv) constant drying air temperature.

2.1 Drying Time for Infinite Solid Slab Object. Sahin et al. [18] previously developed the following analytical drying time equations for an infinite slab, within two Biot number ranges:

$$t_{\text{slab}} = -\frac{\sigma}{h_m} \ln \Phi_c \qquad \text{for Bi} < 0.1 \tag{1}$$

$$t_{\text{slab}} = -\frac{L^2}{D\mu_1^2} \ln\left(\frac{\Phi_c}{A_1}\right) \qquad \text{for } 0.1 \leq \text{Bi} \leq 100 \tag{2}$$

where Φ_c is the dimensionless centerline/average moisture content, A_1 is the coefficient containing μ_1 in the unsteady moisture transfer equation as detailed in Ref. [18], and σ is the volume-area ratio (m).

After substituting the lag factor (G) and drying coefficient (S) (so-called: drying process parameters), as introduced earlier [6,7], the drying time becomes:

$$t_{\text{slab}} = -\frac{1}{S} \ln\left(\frac{\Phi_c}{G}\right) \qquad \text{for } 0.1 \leq \text{Bi} \leq 100 \qquad (3)$$

Here, for a drying process of a moist solid object the lag factor shows the internal resistance to moisture diffusivity within the moist object whereas the drying coefficient shows the drying capability of the moist object.

2.2 Drying Time for Irregular Multi-Dimensional Object.

The determination of drying times for various types of objects subject to drying is essential for system design and analysis. It is obvious that one-dimensional analysis may not be accurate enough, therefore, the objective is now to determine the drying times of multi-dimensional objects (two or three-dimensional). This was previously carried out by the authors [18] for regular multi-dimensional objects and it is now extended to include the irregular multi-dimensional objects subject to drying. As is known, in many cases, particularly for the multi-shaped objects, the direct analytical solution may not be obtained. However, this difficulty can be eliminated by introducing a new parameter (i.e., shape factor). In this regard, the shape factor E is the ratio of drying time for a slab object to the drying time for any shape as follows:

$$E = \frac{t_{\text{slab}}}{t_{\text{shape}}} \qquad (4)$$

where E is related to a function of the shape of the object and the Biot number. Once the geometric shape factor, E, is available, then the drying time for the irregular shape product, t_{shape}, can be calculated using Eq. (4) as the drying time for the slab object can readily be calculated from Eqs. (1–3).

2.3 Geometric Shape Factors.

Analytical solutions for the shape factors for the geometrically irregular two or three-dimensional products are not possible. Therefore, these two and three-dimensional products are approximated as elliptical cylinders and ellipsoids, respectively. In all the geometrical shapes considered, L is the characteristic dimension (shortest distance from center to surface) and the parameters a_1 and a_2 are the ratios of the second and third dimensions to the characteristic dimension, respectively.

The analytical expressions for the geometric shape factors were initially discussed by Hossain et al. [19,20] for cooling applications. They provided three semi-analytical models for predicting the shape factors for cooling applications; the variational formula [21], pseudo-ellipse formula [21] and empirical correlation [22]. These were modified for drying processes.

Two-Dimensional Irregular Products. Geometrically irregular two-dimensional products are considered to be represented by an infinite elliptical cylinder of semi-minor axis L and semi-major axis $a_1 L$.

The variational formula for the shape factor in this case is given as

$$E = \frac{1 + \dfrac{\text{Bi}}{2}}{\dfrac{V}{AL} + \dfrac{\text{Bi}}{2}\left(\dfrac{a_1^2}{1 + a_1^2}\right)} \qquad (5)$$

where Bi is the Biot number, V is the volume of an elliptical object (m^3) and A is the surface area of an elliptical cylinder (m^2).

The Pseudo-ellipse formula is derived using the solution of McNabb et al. [21] as follows:

$$E = 1 + \frac{1 + \dfrac{2}{\text{Bi}}}{a_1^2 + \dfrac{2a_1}{\text{Bi}}} \qquad (6)$$

The empirical correlation for irregularly shaped objects is written as

$$E = 1 + \left(\frac{AL}{V} - 1\right)\left[X\left(\frac{3.56}{a_1^{1.77}}\right) + \frac{1 - X\left(\dfrac{3.56}{a_1^{1.77}}\right)}{a_1^{1.47}}\right] \qquad (7)$$

where the function X is given by

$$X(x) = \frac{x}{(2\,\text{Bi})^{1.34} + x}. \qquad (8)$$

The pseudo-ellipse formula is considered the most superior among the three models presented, as also stated by Hossaini et al. [19], and is used in the present study to determine the geometric shape factors.

Three-Dimensional Irregular Products. When the axial (longitudinal) dimension is finite, then the diffusion process becomes three-dimensional. In this case, geometrically irregular three-dimensional products are considered to be represented by ellipsoid having semi-axes of L, $a_1 L$, and $a_2 L$.

The variational formula for this case becomes

$$E = \frac{1 + \dfrac{\text{Bi}}{2}}{\dfrac{V}{AL} + \dfrac{\text{Bi}/2}{1 + 1/a_1^2 + 1/a_2^2}}. \qquad (9)$$

Similarly, the pseudo-ellipse formula becomes

$$E = 1 + \frac{1 + \dfrac{2}{\text{Bi}}}{a_1^2 + \dfrac{2a_1}{\text{Bi}}} + \frac{1 + \dfrac{2}{\text{Bi}}}{a_2^2 + \dfrac{2a_2}{\text{Bi}}} \qquad (10)$$

and the empirical correlation for the case of a prolate spheroid ($a_1 = 1$) is given by

$$E = 2 + \left(\frac{p_2 L}{s_2} - 1\right)\left\{X\left(\frac{3.56}{a_2^{1.77}}\right) + \frac{1 - X\left(\dfrac{3.56}{a_2^{1.77}}\right)}{a_2^{2.75}}\right\} \qquad (11)$$

and for the case of an oblate spheroid ($a_1 = a_2$)

$$E = 1 + \left(\frac{p_1 L}{s_1} - 1\right)\left\{2X\left(\frac{3.56}{a_1^{1.77}}\right) + \left[1 - X\left(\frac{3.56}{a_2^{1.77}}\right)\right]\left(\frac{1}{a_1^{1.47}} + \frac{1}{a_1^{2.75}}\right)\right\}. \qquad (12)$$

where p and s are the perimeter and area of the orthogonal cross-section, respectively, and X is given by Eq. (8).

The pseudo-ellipse formula appears to be the most practical of the three models presented and therefore, is used in the present study to determine the geometric shape factors.

The two special cases are of common interest. Many objects, particularly food products, appear to have these two shapes.

(a) Prolate Spheroid, $a_1 = 1$ (e.g., egg). The geometric shape factor for a prolate spheroid is obtained using Eq. (10):

$$E = 2 + \frac{1 + \dfrac{2}{\text{Bi}}}{a_2^2 + \dfrac{2a_2}{\text{Bi}}} \qquad (13)$$

(b) Oblate Spheroid, $a_1 = a_2 = a$ (e.g., Hamburger). In this case the shape factor from Eq. (10) is

$$E = 1 + 2\,\frac{1 + \dfrac{2}{\text{Bi}}}{a^2 + \dfrac{2a}{\text{Bi}}}. \qquad (14)$$

3 Results and Discussion

The two or three-dimensional irregular shaped objects is approximated such that they can be represented as an elliptical cylinder or ellipsoid, respectively. Geometrically, there are three parameters to consider, namely volume, surface area and the characteristic dimension (i.e., shortest distance from center to surface of the object). The representative model (elliptical cylinder or ellipsoid) can be selected in such a way that two of the three parameters are equal to those of the actual irregular shaped object. There are three possibilities for approximation of the irregular shaped objects: (1) model shape and irregular shaped object have the equal volume and characteristic dimension; (2) model shape and irregular shape have the equal volume and the surface area; and (3) model shape and irregular shape have the equal surface area and characteristic dimension. Of these approaches, the first method appears to be the best for transient processes. In conjunction with this, in the present study the model shape will be determined such that its volume and characteristic dimension are equal to those of the irregular shaped object. In addition, if the irregular product has a flat-plate surface, this will be considered as the symmetry surface, so that the characteristic dimension will be measured from this surface to the other outer surface in a perpendicular direction to the symmetry surface.

As given in Eqs. (13) and (14), drying shape factors appear to be function of Biot number and parameters a_1 and a_2 for multi-dimensional objects. Long irregular shaped objects can be modeled as infinite elliptic cylinders or half elliptic cylinders. As the
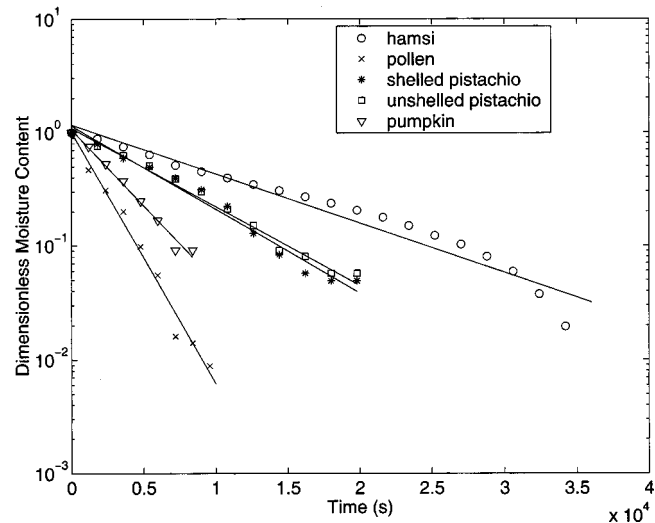

Fig. 1 Experimental drying data and theoretical profiles for the products. The correlations and their correlation coefficients for the products are: $\Phi_c = 1.16554\exp(-0.00010t)$ and 0.95450 for hamsi; $\Phi_c = 1.00870\exp(-0.00051t)$ and 0.98468 for pollen; $\Phi_c = 1.14469\exp(-0.00017t)$ and 0.97813 for shelled pistachio; $\Phi_c = 1.09184\exp(-0.00016t)$ and 0.98725 for unshelled pistachio; and $\Phi_c = 1.06393\exp(-0.00031t)$ and 0.98595 for pumpkin.

length increases, i.e., for large values of a_1, the drying shape factor decreases. The effect of the Biot number is not as significant as for a_1.

Note that the drying shape factor varies as a function of Biot number and a_1 for various fixed values of parameter a_2 for ellipsoid shape products. In general, as a_1 and a_2 increase a decrease in drying shape factor is observed. This indicates that objects subject to drying that are elongated in one or two directions, dry faster. The effect of the Biot number on the drying shape factor is found to be less significant that the geometric factors a_1 and a_2. The extreme case where $a_1 = a_2 = 1$ corresponds to spherical geometry where the drying shape factor is equal to 3. On the other hand, $a_1 = a_2 \rightarrow \infty$ corresponds to the case of a slab, for which the drying shape factor is equal to 1. The drying shape factors in all the cases vary between these two extremes, i.e., between 1 and 3.

3.1 Experimental Data and Model Verification. Midilli [23] conducted a large number of drying experiments on regular and irregular shaped objects and provided drying data for five different irregular shaped products. These included hamsi (a small fish of anchovy type living in the Black Sea), pollen, shelled pistachio, unshelled pistachio and mammouth pumpkin. The experimental drying data for these products are shown in Fig. 1. Expo-

Table 1 Experimental data and theoretical predictions of drying times for several products

Product	Approx. Shape	L (m)	G	S	Bi	D (m²/s)	Φ_c	a_1	a_2	E	t_{pred} (s)	t_{exp} (s)	% error
Hamsi	ellipsoid	0.00425	1.16554	0.0001	3.44	6.1611E-10	0.15	1.588	8.824	1.48	37206	34200	8.79
Pollen	slab	0.00125	1.0087	0.00064	0.07	9.1437E-09	0.054	-	-	1	9645	9576	0.722
Shelled Pistachio	ellipsoid	0.0049	1.14469	0.00023	2.13	2.0667E-09	0.03	-	-	2.5	17754	19800	−10.33
Unshelled Pistachio	cylinder	0.0038	1.09184	0.00022	0.6	1.9375E-09	0.035	-	-	2	20089	19800	1.462
Mammouth Pumpkin	square	0.0025	1.06393	0.00035	0.3	3.804E-09	0.046	-	-	1.5	7600	8388	−9.389

nential drying curves were fitted to obtain lag factor (G) and drying coefficient (S) values, as detailed earlier [4–7]. The resultant equations are shown on the graph. These drying equations provided the lag factor and the drying coefficients for the products considered.

To verify the accuracy of the present model, theoretically predicted drying times were compared with the experimental, as shown in Table 1. Firstly, the closest analytical shapes that would represent the irregular shaped products were determined. Making use of the characteristic length (L), the lag factor (G) and the drying coefficient (S), relevant parameters such as Biot number (Bi), and moisture diffusivity (D) were calculated. The following explicit relations were used for determining the Biot number and drying coefficient [15].

$$\text{Bi} = 0.0576 G^{26.7} \qquad (15)$$

$$D = 0.0004 S^{1.4531} \qquad (16)$$

In Table 1, the experimental drying time (t_{exp}) to achieve a given centerline moisture content (Φ_c) is based on experimental values and is obtained as outlined in previous work [6,16]. The predicted theoretical drying time (t_{pred}) for these products was calculated using the present method and is given for comparison. The discrepancy between the experimental and theoretical drying times is also shown. The agreement is good in general, with the error between the experimental measurement and theoretical prediction being within ±10 percent. This error is due to measurement errors and the assumptions made regarding the shape of the product in the model.

Conclusions

Drying of irregular shaped multi-dimensional objects is very common in practice. This paper has presented a study of an analytical method to determine shape factors and hence, drying times of irregular shaped objects. The shape of the irregular two-and three-dimensional objects considered were approximated by representative elliptical cylinder and ellipsoid shapes, respectively. The present model was verified by comparisons with experimental drying times of several food products, namely hamsi, pollen, shelled pistachio, unshelled pistachio and mammouth pumpkin. The theoretical predictions show that the accuracy of the present model was within the ±10 percent range.

Acknowledgments

Nomenclature

a_1 = ratio of second dimension to the characteristic length
a_2 = ratio of third dimension to the characteristic length
A = area (m²)
A_1 = coefficient involving μ_1 as given in Ref. [18]
Bi = Biot number ($= h_m L / D$)
D = moisture diffusivity (m²/s)
E = shape factor
G = lag factor
h_m = moisture transfer coefficient (m/s)
L = characteristic dimension (m)
p = perimeter of the orthogonal cross-section (m)

s = area of the orthogonal cross-section (m²)
S = drying coefficient (1/s)
t = time (s)
V = volume (m³)
x = parameter in equation (8)
X = function given by equation (8)
Φ_c = dimensionless centerline/average moisture content
μ = root of characteristic equation
σ = volume-area ratio ($= V/A$)(m)

References

[1] Krischer, O., 1963, *Die wissenschaflichen Grundlagen der Trocknungstechnik*, 2nd ed. Springer, Berlin.
[2] Whittaker, S., 1977, "Simultaneous Heat, Mass and Moisture Transfer in Porous Media. A Theory of Drying," in *Advances in Heat Transfer*, J. P. Hartnett and T. F. Irvine, Jr., eds., **13**, Academic, New York, pp. 119–203.
[3] Kudra, T., and Mujumdar, A. S., 1995, "Special Drying Techniques and Novel Dryers," in *Handbook of Industrial Drying*, **2**, A. S. Mujumdar ed., pp. 1087–1149.
[4] Dincer, I., Hussain, M. M., Sahin, A. Z., and Yilbas, B. S., 2002, "Development of a New Moisture Transfer (Bi-Re) Correlation for Food Drying Applications," Int. J. Heat Mass Transfer, **45**(8), pp. 1749–1755.
[5] Dincer, I., Hussain, M. M., Yilbas, B. S., and Sahin, A. Z., 2002, "Development of a New Drying Correlation for Practical Applications," Int. J. Energy Res., **26**(3), pp. 245–251.
[6] Dincer, I., 1998, "Moisture Loss From Wood Products During Drying—Part I: Moisture Diffusivities and Moisture Transfer Coefficients," Energy Sources, **20**, pp. 67–75.
[7] Dincer, I., 1998, "Moisture Loss From Wood Products During Drying—Part II: Surface Moisture Content Distributions," Energy Sources, **20**, pp. 77–83.
[8] Dolinskiy, A. A., Dorfman, A. S. H., and Davydenko, B. V., 1991, "Conjugate Heat and Mass Transfer in Continuous Processes of Convective Drying," Int. J. Heat Mass Transfer, **34**(11), pp. 2883–2889.
[9] Izumi, M., and Hayakawa, K., 1995, "Heat and Moisture Transfer and Hygrostress Crack Formation and Propagation in Cylindrical, Elastoplastic Food," Int. J. Heat Mass Transfer, **38**(6), pp. 1033–1041.
[10] Perre, P., Moser, M., and Martin, M., 1993, "Advances in Transport Phenomena During Convective Drying With Superheated Steam and Moist Air," Int. J. Heat Mass Transfer, **36**(11), pp. 2725–2746.
[11] Ratti, C., and Mujumdar, A. S., 1997, "Solar Drying of Foods: Modeling and Numerical Simulation," Sol. Energy, **60**(3–4), pp. 151–157.
[12] Seyed-Yagoobi, J., Bell, D. O., and Asensio, M. C., 1992, "Heat and Mass Transfer in a Paper Sheet During Drying," ASME J. Heat Transfer, **114**, pp. 538–541.
[13] Sun, S. H., and Marrero, T. R., 1996, "Experimental Study of Simultaneous Heat and Moisture Transfer Around Single Short Porous Cylinders Using Convection Drying by a Psychrometry Method," Int. J. Heat Mass Transfer, **39**(17), pp. 3559–3565.
[14] Jia, C. C., Sun, D. W., and Cao, C. W., 2000, "Mathematical Simulation of Temperature and Moisture Yields Within a Grain Kernel During Drying," Drying Technol., **18**, pp. 1305–1325.
[15] Dincer, I., Sahin, A. Z., Yilbas, B. S., Al-Farayedhi, A. A., and Hussain, M. M., 2000, "Exergy and Energy Analysis of Food Drying Systems," Progress Report 2, KFUPM Project #ME/ENERGY/203.
[16] Dincer, I., and Dost, S., 1996, "A Modeling Study for Moisture Diffusivities and Moisture Transfer Coefficients in Drying of Solid Objects," Int. J. Energy Res., **20**, pp. 531–539.
[17] Akiyama, T., Liu, H., and Hayakawa, K., 1997, "Hygrostress Multicrack Formation and Propagation in Cylindrical Viscoelastic Food Undergoing Heat and Moisture Transfer Processes," Int. J. Heat Mass Transfer, **40**(7), pp. 1601–1609.
[18] Sahin, A. Z., Dincer, I., Yilbas, B. S., and Hussain, M. M., 2002, "Determination of Drying Times for Regular Multi-Dimensional Objects," Int. J. Heat Mass Transfer, **45**, pp. 1757–1766.
[19] Hossain, M. M., Cleland, D. J., and Cleland, A. C., 1992, "Prediction of Freezing and Thawing Times for Foods of Two-Dimensional Irregular Shape by Using a Semi-Analytical Geometric Factor," Int. J. Refrig., **15**, pp. 235–240.
[20] Hossain, M. M., Cleland, D. J., and Cleland, A. C., 1992, "Prediction of Freezing and Thawing Times for Foods of Three-Dimensional Irregular Shape by Using a Semi-Analytical Geometric Factor," Int. J. Refrig., **15**, pp. 241–246.
[21] McNabb, A., Wake, G. C., Hossain, M. M., and Lambourne, R. D., 1990, "Transition Times Between Steady States for Heat Conduction: Part II—Approximate Solutions and Examples," Occas Pubs Maths Stats No. 21, Massey University, New Zealand.
[22] Cleland, D. J., Cleland, A. C., and Earle, R. L., 1987, "Prediction of Freezing and Thawing Times for Multi-Dimensional Shapes by Simple Methods: Part II—Irregular Shapes," Int. J. Refrig., **10**, pp. 234–240.
[23] Midilli, A., 2002, personal communication for experimental drying data, Mechanical Engineering Department, Nigde University.

Turbulent Film Condensation on a Horizontal Elliptical Tube

Cha'o-Kuang Chen

Professor
e-mail: ckchen@mail.ncku.edu.tw

Hai-Ping Hu

Postgraduate Student

Department of Mechanical Engineering,
National Cheng Kung University, Tainan, Taiwan 701,
Republic of China

This is an investigation of turbulent film condensation on a horizontal elliptical tube. The high tangential velocity of the vapor flow at the boundary layer is determined from potential flow theory. The Colburn analogy is used to define the local liquid-vapor interfacial shear which occurs for high velocity vapor flow across an elliptical tube surface. The results developed in this study are compared with those generated by previous theoretical and experimental results. [DOI: 10.1115/1.1603779]

Introduction

Film condensation was conducted by the pioneering investigator, Nusselt, who in 1916 investigated laminar film condensation on vertical plates [1]. Shekriladze et al. [2] analyzed film condensation on horizontal tubes under low velocity vapor flow conditions, and subsequently some literature relating to research into laminar film condensation on horizontal tubes was published, e.g., Refs. [3–5]. Yang and Hsu [6] analyzed the problem of combined free- and forced-convection on a horizontal elliptical tube, with particular reference to the effects of vapor shear and pressure gradient. Although laminar film condensation has been widely discussed in published literature, it is worthwhile developing an understanding of turbulent flow condensation since, according to Michael et al. [7], condensate films may be partially turbulent at high vapor velocities. Sarma et al. [8] assumed that condensate film flow is under turbulent regime in the region away from the upper stagnation point. He carried out theoretical research into turbulent film condensation on a horizontal tube, and found that his results were in good agreement with experimental data. However, other than the research of Sarma et al. there has been relatively little recent investigation of the issues relating to turbulent film condensation on horizontal elliptical tubes. Therefore, the aim of this present study is to investigate turbulent film condensation on an isothermal elliptical tube in terms of the local condensate film thickness and heat transfer characteristics, and to compare the results obtained with previously published theoretical and experimental data.

Description of the Physical Model

Consider a horizontal elliptical tube immersed in a downward flowing, pure vapor. Condensation occurs on the wall of the tube, and a continuous film of the liquid runs downward over the tube. The physical model and the coordinate system adopted in this
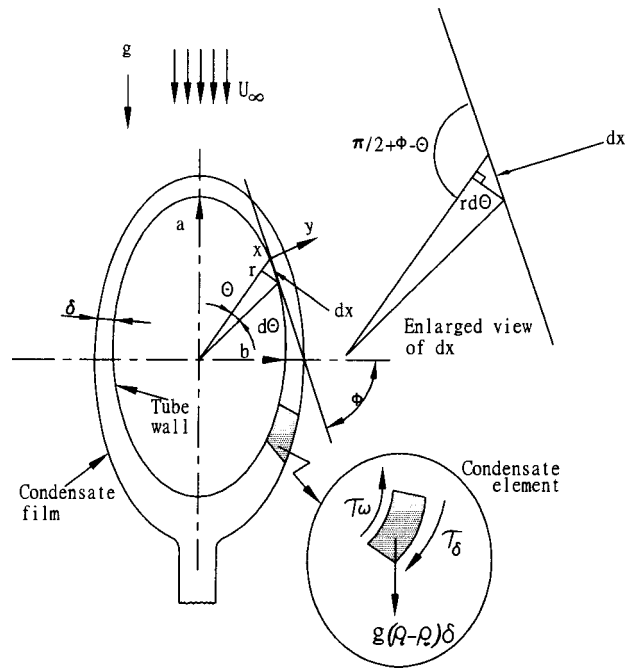
Fig. 1 Physical model and coordinate system

study are shown in Fig. 1. The energy equation, heat balance equation and force balance equation for the turbulent condensate film are described by the following equations:

$$\frac{d}{dy}\left[\left(1+\frac{\varepsilon_m}{\nu}\mathrm{Pr}\right)\frac{dT}{dy}\right]=0 \tag{1}$$

$$\frac{d}{d\phi}\int_0^\delta \rho_l u\,dy=\frac{(1-e^2)K}{(1-e^2\sin^2\phi)^{3/2}h_{fg}}\,a\,\frac{dT}{dy}_{y=0} \tag{2}$$

$$\tau_w-\tau_\delta-g\,\delta(\rho_l-\rho_\nu)\sin\phi=0 \tag{3}$$

where the wall shear stress $\tau_w=\rho(\nu+\varepsilon_m)du/dy_{y=0}$
The boundary conditions are described as

$$(1)\quad \text{at }y=0;\ T=T_w$$

$$(2)\quad \text{at }y=\delta;\ T=T_{\mathrm{sat}} \tag{4}$$

These governing equations are subject to the following assumptions:

1. Turbulent region is far more than laminar region. Thus, laminar region can be neglected.
2. Turbulent conduction across the condensate layer is more significant than the convective term; thus, the convective terms can be neglected.
3. Vapor boundary layer separation is neglected.
4. The eddy diffusivity for momentum ε_M is equal to that for energy ε_H.

In turbulent region the semi-empirical equation which describes heat transfer in the flow parallel to a moderately curved surface may also be used to describe the heat transfer in the flow parallel to an elliptical surface. Jakob [9] proposed the following expression:

$$\mathrm{Nu}=B\,\mathrm{Re}^{0.8}\,\mathrm{Pr}^{1/3} \tag{5}$$

According to Colburn analogy, the heat transfer factor can be represented as follows:

$$\frac{f}{2}=\mathrm{St}\,\mathrm{Pr}^{2/3} \tag{6}$$

Combining Eqs. (5) and (6) gives

$$f_\phi = B \pi \, \text{Re}_\nu^{-0.2} \sin \phi \qquad (7)$$

where the value of constant B is 0.034, $\text{Re}_\nu = u_\infty 2a/\nu_\nu$, $\text{St} = \text{Nu}/\text{Re} \, \text{Pr}$.

The local shear stress is defined by the relationship

$$\tau_\delta = \frac{1}{2} \rho_\nu u_\nu^2 f_\phi \qquad (8)$$

According to potential flow theory, the vapor velocity at the edge of the boundary is given by

$$u_e = u_\infty (1 + \sqrt{1-e^2}) \sin \phi \qquad (9)$$

Incorporating Eqs. (7), (8), and (9) into Eq. (3) to be rewritten in the following form:

$$\tau_w - \frac{(1+\sqrt{1-e^2})^2}{2} \rho_\nu u_\infty^2 B \pi \, \text{Re}_v^{-0.2} \sin^3 \phi - g\delta(\rho_l - \rho_\nu)\sin \phi = 0 \qquad (10)$$

The following dimensionless variables, and equations are now defined:

$$u^* = \sqrt{\tau_w/\rho} \quad u^+ = \frac{u}{u^*} \quad T^+ = \frac{T-T_w}{T_{\text{sat}} - T_w} \quad y^+ = \frac{yu^*}{\nu_l}$$

$$\text{Re}^* = \frac{\text{Re}^+}{\text{Gr}^{1/3}} \quad \text{Re}^+ = \frac{au^*}{\nu_l} \quad \delta^+ = \frac{\delta u^*}{\nu_l} \quad \text{Fr} = \frac{u_\infty^2}{ga}$$

$$\text{Gr} = \frac{ga^3}{\nu_l^2} \frac{\rho_l - \rho_\nu}{\rho_l} \qquad (11)$$

The energy equation yields the following dimensionless energy equation:

$$\frac{d}{dy^+}\left[\left(1 + \frac{\varepsilon_m}{\nu_l}\text{Pr}\right)\frac{dT^+}{dy^+}\right] = 0 \qquad (12)$$

Substitution of Eq. (11) into Eq. (2) and into Eq. (10) respectively gives

$$\frac{d}{d\phi}\int_0^{\delta^+} u^+ dy^+$$

$$= \frac{1-e^2}{(1-e^2\sin^2\phi)}\left[\frac{Cp(T_s-T_w)}{h_{fg}\text{Pr}}\right]\text{Gr}^{1/3}\,\text{Re}^*\frac{dT^+}{dy^+}\bigg|_{y^+=0} \qquad (13)$$

$$\text{Re}^{*3} = \text{Re}^* \frac{(1+\sqrt{1-e^2})^2}{4}$$

$$\times \frac{(1-e^2)^{-0.2}}{(1-e^2\sin^2\phi)^{-0.3}} 2^{0.8}\pi B \frac{\rho_\nu}{\rho_l}\left(\frac{\nu_l}{\nu_\nu}\right)^{-0.2}$$

$$\times \text{Gr}^{1.4/6}\text{Fr}^{0.9}\sin^3\phi + \delta^+\sin\phi \qquad (14)$$

where sub cooling parameter $S = Cp(T_s - T_w)/h_{fg}\text{Pr}$, interfacial shear parameter $\psi = 2^{0.8}\pi B \rho_\nu/\rho_l(\nu_l/\nu_\nu)^{-0.2}\text{Gr}^{1.4/6}$.

The dimensionless boundary conditions of Eq. (12) are as follows:
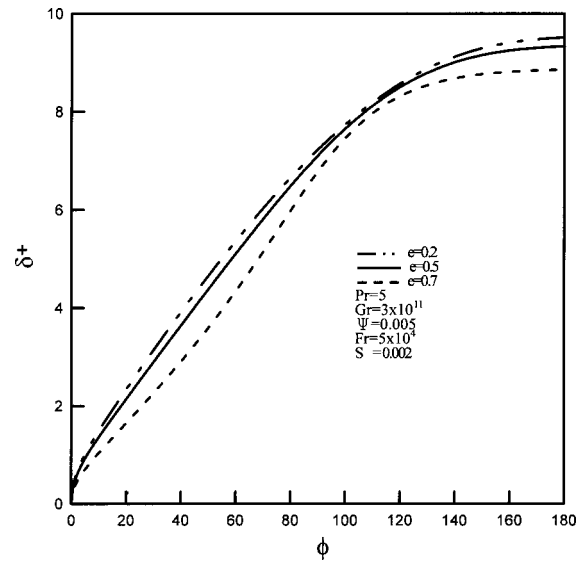
$$(1) \text{ at } y^+ = 0; \quad T^+ = 0$$

Fig. 2 Effect of eccentricity on local film thickness

$$(2) \text{ at } y^+ = \delta^+; \quad T^+ = 1 \qquad (15)$$

Further, the velocity profile of Eq. (13) can be obtained from the following expression [8]:

$$\left(1 + \frac{\varepsilon_m}{\nu}\right)\frac{du^+}{dy^+} = 1 \qquad (16)$$

The boundary condition is

$$u^+ = 0 \quad \text{at} \quad y^+ = 0$$

The eddy diffusivity distribution of Eq. (16), which was presented by Kato et al. [10] is given by following equation:

$$\frac{\varepsilon_m}{\nu} = 0.4y^+[1 - \exp(-0.0017y^{+2})] \qquad (17)$$

Considering the condensation heat transfer, the heat transfer coefficient is expressed as

$$K_l \frac{\partial T}{\partial y}\bigg|_{y=0} = h(T_s - T_w) \qquad (18)$$

Obviously, the local Nusselt number can also be expressed as follows:

$$\frac{\text{Nu}}{\text{Re}^{1/2}} = \frac{\text{Gr}^{1/12}}{\text{Fr}^{1/4}}\text{Re}^*\frac{dT^+}{dy^+}\bigg|_{y=0} \qquad (19)$$

Further, the mean Nusselt number can be written as follows:

$$\frac{\text{Nu}_m}{\text{Re}^{1/2}} = \frac{1}{\pi}\int_0^{\delta^+}\frac{\text{Nu}}{\text{Re}^{1/2}}d\phi \qquad (20)$$

The dimensionless governing Eqs. (12–14), subject to the relevant boundary conditions, can be used to estimate δ^+, Re^*, and Nusselt.
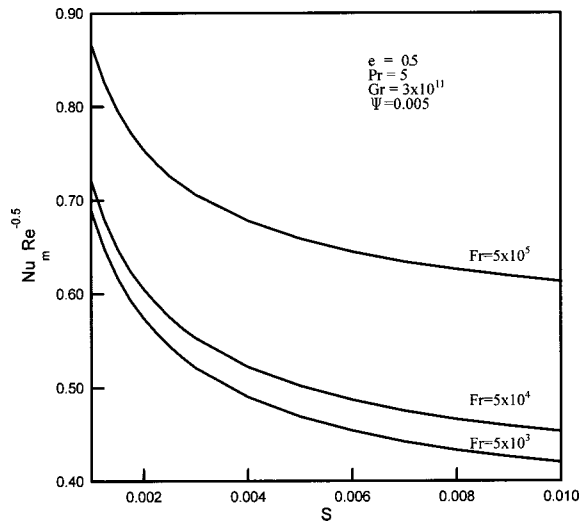
Fig. 3 Effect of sub cooling parameter on average heat transfer

Results and Discussion

Figure 2 presents the relationship between the dimensionless film thickness and different degrees of horizontal elliptical tube eccentricity. When the semi-major axis remains a constant, it is noted that the dimensionless film thickness increases as the eccentricity decreases. Figure 3 presents the relationship between the average heat transfer coefficient of the horizontal elliptical tube and the sub-cooling parameter for different Froude values. The eccentricity of the tube in question is 0.5. For any particular Froude value, it will be seen that the mean Nusselt number decreases as the value of the sub-cooling parameter, S, increases. However, for a constant value of S, the mean Nusselt number is dependent upon the Froude value, and will increase as the Froude value increases.

Figure 4 provides a comparison between the present results and earlier experimental and theoretical data for a horizontal elliptical tube (eccentricity $e=0$, $e=0.5$). Observation of Fig. 4 shows that the theoretical mean Nusselt Number calculated in the present study is broadly similar to the results generated by Fujii, Mandelzwing, Nobbs and Lee [3,11–13] in all range of vapor velocity
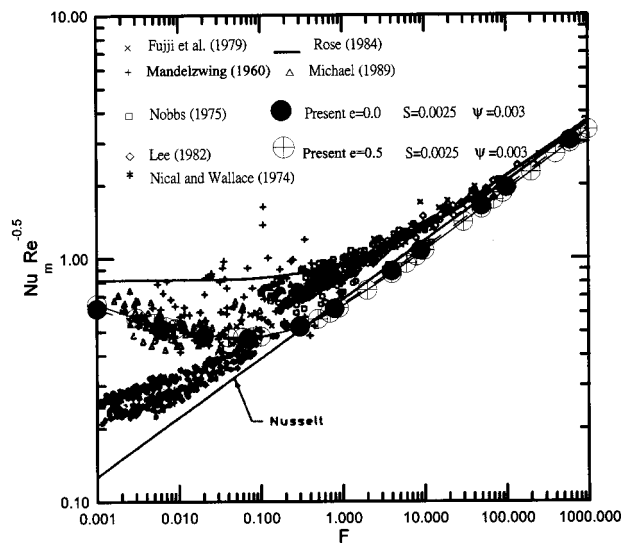

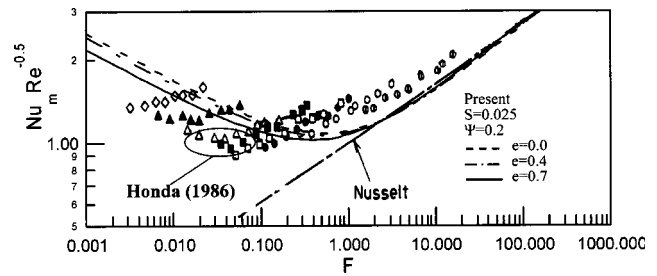**Fig. 4 Comparison of present results with other data, $F=2/(SFr)$**

Fig. 5 Comparison of present results with other data

(i.e., $0.001 < F < 1000$). However, it should be noted that the experimental data generated by Nicol and Wallace [14] is lower than the present results in the case of high velocity vapor flow (values of F below 0.01). Figure 5 shows the variation in the theoretical results of the Nusselt Number with vapor velocity for an elliptical tube with differing degrees of eccentricity. It is noted that mean Nusselt Number increases as eccentricity increases at low velocities ($0.1 < F < 100$). This result is in good agreement with the results published by Yang [6]. However, at high velocity ($F < 0.1$), an increase in eccentricity leads to a decrease in the Nusselt Number. Therefore, under high vapor velocity conditions, the actual velocity of the vapor is one of the most important factors in determining the value of the average heat transfer coefficient. Horizontal elliptical tubes with lower eccentricity have higher average vapor velocity, and as a result the heat transfer coefficient is higher. Figure 5 also presents Honda's [4] experimental results for comparison purposes. It can be seen that there is a broad similarity between the two sets of results at both low and high vapor velocities.

Concluding Remarks

From the theory developed, the following conclusions can be arrived at:

1. In the case of a horizontal elliptical tube with a vertical semi-major axis immersed in a low velocity vapor flow, the Nusselt Number is found to be principally affected by increasing eccentricity, rather than by the vapor velocity. Increasing eccentricity results in higher Nusselt Numbers. However, in the case of high vapor velocity flow, the actual velocity of the flow is key in determining the value of the average heat transfer coefficient. When the length of the semi-major axis is maintained at a constant value and when the horizontal elliptical tube has a lower degree of eccentricity, higher average vapor velocities result in an increase in the Nusselt Number.
2. The present results confirm that Colburn's analogy may be used successfully to estimate the liquid-vapor interfacial shear at the interface for high velocity vapors condensing on an elliptical tube.
3. The present results confirm Jakob's theory that the semi-empirical equation describes the heat transfer in a flow parallel to a plane or to a moderately curved surface may also be used to describe the heat transfer in a flow parallel to an elliptical surface in the turbulent region.

Nomenclature

a, b = length of semi-major, semi-minor axis of ellipse (m)
Cp = specific heat of condensate at constant pressure (J/Kg.K)
e = eccentricity of ellipse, $\sqrt{1-(b/a)^2}$
Fr = Froude number
Gr = Grashof number
g = acceleration due to gravity (m/s^2)
h_{fg} = latent heat (J/kg)

k = thermal conductivity, (W/m.k)
Nu = Nusselt number
Nu_m = mean Nusselt number
Pr = Prandtl number
Re = Reynolds number
S = sub-cooling parameter
T = temperature (K)
T^+ = dimensionless temperature
u_e = velocity component in x-direction (m/s)
u_∞ = the vapor velocity of the free stream (m/s)
u^+ = dimensionless velocity
x = coordinate measured distance along circumference (m)
y = coordinate measured distance normal to the elliptic surface (m)
y+ = dimensionless distance

Greek Symbols

δ = condensate film thickness (m)
δ^+ = dimensionless film thickness
ψ = shear parameter
ν = kinematic viscosity (m^2/s)
ρ = density (Kg/m^3)
τ = shear stress (N/m^2)
θ = angle measured from top of tube
ϕ = angle between tangent to tube surface and normal to direction of gravity

Subscripts

l = liquid
sat = saturation
ν = vapor
w = tube wall
δ = vapor-liquid interface

References

[1] Nusselt, W., 1916, "Die Oberflachen Kondensation Des Wasserdampers," Zeitsehrift des vereines deutsher ingenieure, **60**, pp. 541–546.
[2] Shekriladze, I. G., and Gomelauri, V. I., 1966, "Thepretical Study of Laminar Film Condensation of Flowing Vapor," Int. J. Heat Mass Transfer, **9**, pp. 581–591.
[3] Fujii, T., Honda, H., and Oda, K., 1979, "Condensation of Steam on a Horizontal Tube—The Influence of Oncoming Velocity and Thermal Condition at the Tube Wall," *Condensation Heat Transfer*, 18th Nat. Heat Transf. Conf., San Diego, CA, pp. 35–43.
[4] Honda, H., Zozu, S., Uchima, B., and Fujii, T., 1986, "Effect of Vapor Velocity on Film Condensation of R-113 on Horizontal Tubes in Across Flow," Int. J. Heat Mass Transfer, **29**(3), pp. 429–438.
[5] Rose, J. W., 1984, "Forced Convection Film Condensation on a Horizontal Tube-Effect of Pressure Variation in the Condensate Film," Int. J. Heat Mass Transfer, **27**, pp. 39–47.
[6] Yang, S. A., and Hsu, C. H., 1997, "Free and Forced-Convection Film Condensation from a Horizontal Elliptic Tube with a Vertical Plate and Horizontal Tube as Special Cases," Int. J. Heat Fluid Flow, **18**, pp. 567–574.
[7] Michael, A. G., Rose, J. W., and Daniels, L. C., 1989, "Forced Convection Condensation on a Horizontal Tube-Experiments with Vertical Downflow of Steam," ASME J. Heat Transfer , **111**, pp. 792–797.
[8] Sarma, P. K., Vijayalakshmi, B., Mayinger, F., and Kakac, S., 1998, "Turbulent Film Condensation on a Horizontal Tube with External Flow of Pure Vapors," Int. J. Heat Mass Transfer, **41**(3), pp. 537–545.
[9] Jakob M., 1949, *Heat Transfer*, John Wiley & Sons, New York.
[10] Kato, H., Shiwaki, N. N., and Hirota, M., 1968, "On the Turbulent Heat Transfer by Free Convection from a Vertical Plate," Int. J. Heat Mass Transfer, **11**, pp. 1117–1125.
[11] Mandelzwing, S. I., 1960, "The Effect of Vertically Downward Velocity on the Heat Transfer from a Steam-Nitrogen Mixture Condensation on a Horizontal Cylinder," M.Sc. thesis, Queen Mary College, University of London, United Kingdom.
[12] Nobbs, D. W., and Mayhew, Y. R., 1976, "Effect of Downward Vapor Velocity and Inundation Rates on Horizontal Tubes and Tube Banks," Symp. on Steam Turbine Condensers, NEL Report No. 619, pp. 39–52.
[13] Lee, W. C., and Rose, 1982, "Film Condensation on a Horizontal Tube-Effect of Vapor Velocity," *Proc. 7th Int. Heat Transfer Conf.*, Munich, pp. 101–106.
[14] Nical, A. A., and Wallace, D. J., 1974, "The Influence of Vapor Shear Force on Condensation on a Cylinder," Inst. Chem. Eng. Symp. Ser., **38**, pp. 1–19.

A Maximum Entropy Solution for a Two-Dimensional Inverse Heat Conduction Problem

Sun Kyoung Kim[1]

Woo Il Lee
e-mail: wilee@snu.ac.kr
Mem. ASME

Department of Mechanical Engineering, Seoul National University, Seoul 151-742, Korea

A solution scheme based on the maximum entropy method (MEM) for the solution of two-dimensional inverse heat conduction problems is established. MEM finds the solution which maximizes the entropy functional under the given temperature measurements. The proposed method converts the inverse problem to a nonlinear constrained optimization problem. The constraint of the optimization problem is the statistical consistency between the measured temperature and the estimated temperature. Successive quadratic programming (SQP) facilitates the numerical estimation of the maximum entropy solution. The characteristic feature of the proposed method is investigated with the sample numerical results. The presented results show considerable enhancement in resolution for stringent cases in comparison with a conventional method. [DOI: 10.1115/1.1597613]

Keywords: Conduction, Inverse

1 Introduction

Inverse estimation of unknown conditions has been widely applied to various thermal problems. Such problems are referred to as inverse heat conduction problem (IHCP). Among the various classes of IHCPs, the inverse estimation of unknown boundary conditions is the one investigated most [1–3].

Efforts have been made to overcome the difficulties encountered in obtaining the surface conditions of places in a solid where sensors cannot be located or are even inaccessible. Such difficulties arise frequently in many experimental situations [4]. For example lack of space or environmental conditions can obstruct installation of thermal sensors. Moreover, presence of a thermal sensor disturbs the boundary conditions. In such cases, solutions of IHCPs can be utilized to perform reliable experimental analyses. Recent applications include the re-entry of a space vehicle [5], heat transfer coefficient evaluation [6], quenching of a material process [7] and hyperthermia cancer treatment [8].

As is in other inverse problems, the difficulties in IHCP are due to its extreme sensitivity to measurement errors, which incurs instability of inverse solutions. In order to overcome such instability and to obtain a reliable inverse solution, a few numerical techniques have been proposed. These include the regularization method (RM) [3,9], the sequential function specification method (SFM) [3], the space marching methods [10–12], the conjugate gradient method (CGM) utilizing the adjoint problem [2,13,14], and the mode reduction method based on filtering technique [15–17]. A number of modifications for these methods have been made in order to enhance accuracy and stability of inverse estimation.

For example, the function specification method has been combined with the regularization method [3,18], CGM incorporating sequential schemes has been investigated [19–21], and the mode reduction method has been also combined with a sequential scheme [22]. Despite such contributions made for better inverse solutions, resolution improvement is limited with the existing methods [23]. Especially for a case with abrupt changes in heat flux, the conventional methods are not satisfactory in terms of resolution. Thus, in order to achieve better inverse solution for IHCP, the current study employs the maximum entropy method (MEM), which has shown distinguished resolution for many inverse problems [24–26].

MEM aims to obtain maximum possible information from measurement data with limited accuracy [24]. That is, if an inverse solution is maximum entropy (ME) one, it is the most probabilistically likely one among the candidates of many inverse solutions, which are consistent with the measurement data. The entropy functional that the current method desires to maximize takes a logarithmic form and the constraint has a quadratic form. Consequently, the solution procedure requires a nonlinear constrained optimization. Such non-linearity gives rise to computational difficulty.

Not many works about IHCP methods are based on ME principle and it is still a maturing method. Ramos and Giovannini applied ME principle to detect defects by estimating thermal conductance using tomographic technique [27]. Lair et al. estimated heat flux in die forging using MEM [28]. Muniz et al. solved a retrospective IHCP [2], whose unknown is an initial condition, using MEM and Tikhonov regularization method. They compared the results by both methods [29]. The ME solutions in that study do not show noticeable improvement. The aforementioned three works do not reveal any characteristic features of MEM such as super-resolution or entropy concentration. Those works do not address the procedure in determining the total sum of unknown components that should be provided as an observed value for ME estimation [25]. Furthermore, performing simply bounded unconstrained optimization with a fixed regularization parameter makes them fail to obtain a true ME solution. That is, by such a method, maximum state of the information entropy cannot be attained. Recently, Kim and Lee proposed a ME-based solution method for one-dimensional IHCPs with unknown heat flux [30]. In the referenced work, several generic features of MEM including remarkable resolution improvement were found.

In this study, a two-dimensional IHCP is solved using MEM. MEM seeks an inverse solution that simultaneously achieves maximum state of the information entropy and consistency with temperature readings. The successive quadratic programming (SQP) is employed as a solution method for the optimization problem [31]. SQP is a general and powerful method for gradient-based constrained optimization problems. SQP has already been applied to MEM in other fields successfully [32,33]. In order to investigate solution behavior in two-dimensional IHCPs, reconstruction of a space- and time-varying heat flux is carried out for different measurement error levels and heat flux forms. The results obtained by the proposed method are compared with the results by a conventional method.

2 Problem Statement

Direct Problem. The problem in the study considers Fourier heat conduction inside an arbitrary isotropic solid domain, R, as illustrated in Fig. 1. The governing equation for temperature $T(\mathbf{r},t)$ where $\mathbf{r}$ is a position vector over the domain R, and t is time ($0 \leq t \leq t_f$), is describes as

$$C \frac{\partial T}{\partial t} - \nabla \cdot \lambda \nabla T = 0, \quad \text{in } R. \qquad (1a)$$

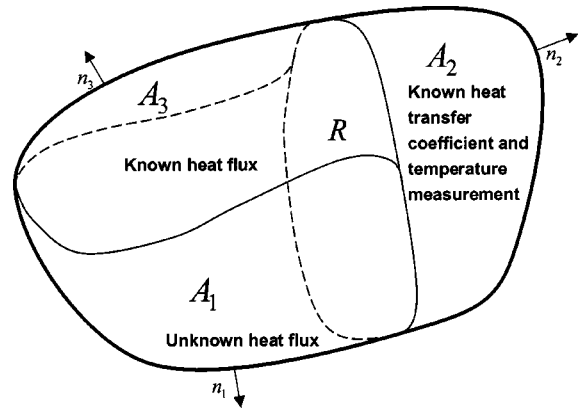Here, C and λ are the volumetric heat capacity and the thermal

Fig. 1 Overview of the considered inverse problem

conductivity, respectively. The corresponding conditions for the top, left, bottom, and right boundaries A_1, A_2, and A_3, respectively are specified as follows:

$$\lambda \frac{\partial T}{\partial n_1} = f(\mathbf{r},t), \quad \text{on } A_1, \qquad (1b)$$

$$\lambda \frac{\partial T}{\partial n_2} = h[T_\infty - T(\mathbf{r},t)], \quad \text{on } A_2, \qquad (1c)$$

$$\lambda \frac{\partial T}{\partial n_3} = q''(\mathbf{r},t), \quad \text{on } A_3, \qquad (1d)$$

where h, T_∞, and q'' denote the heat transfer coefficient and the ambient temperature, respectively, for the lower surface. The heat transfer coefficient is well known in many engineering situations as a result of accumulated research for the last several decades [34]. In addition, initially the domain is maintained at a uniform temperature that

$$T(\mathbf{r},0) = T_o, \quad \text{in } R. \qquad (1e)$$

A direct solution of the problem gives temperature as a function of location and time for given initial and boundary conditions assuming the surface heat flux $f(\mathbf{r},t)$ known. Thus, temperature estimated for a particular function $f(\mathbf{r},t)$ can be denoted as $T(\mathbf{r},t;f)$.

Inverse Problem. Through inverse analysis, the unknown condition which is consistent with temperature observation can be estimated. Usually, multi-dimensional inverse problems with inside measurements employing many sensors are not very practical. Embedding sensors inside a solid body is not an easy task. Besides, sensor itself can affect the heat conduction. Thus, this study assumes measurement on the boundary only. Thanks to remarkable advances in the thermal imaging technique, accurate temperature distribution on a solid surface can be acquired as a continuous function [35]. This non-contact non-destructive thermometry technique has been used widely for remote measurements of the temperatures of both static and moving surfaces, and can perform a lot of tasks that standard sensors such as thermocouples and resistance temperature detectors (RTD) cannot. In heat transfer experiments, the infrared thermo-graphic technology [36] and the liquid crystal image method [37] have been employed. Especially, the infrared thermo-graphic technology facilitates simple instrumentation and sensitive measurement (up to 0.05°C). Its detail about instrumentation and application is described in [38]. An inverse estimation method utilizing such a measurement technique has been already applied to a real-world problem [39]. A comprehensive review of the thermal imaging technique in the heat transfer research can be found elsewhere [40].

The temperature measured on the lower surface can be expressed as a continuous function $Y(\mathbf{r},t)$. If no error is included in the measured temperature, the inverse solution can be obtained by

$$\text{find } f(\mathbf{r},t) \text{ such that } T(\mathbf{r},t;f) = Y(\mathbf{r},t) \text{ on } A_2 \qquad (2)$$

However, measured data in actual experiments involve errors to a certain degree. The above statement may not determine the unknown heat flux in a stable manner due to the ill-posed nature of inverse problems [2,3]. Thus, as widely used, consistency between measured and computed temperatures is represented by the following residual functional [2,14].

$$J(f) = \int_0^{t_f} \sum_{k=1}^{P} [T(\mathbf{r}_k,t;f) - Y(\mathbf{r}_k,t)]^2 dt \qquad (3)$$

where $\mathbf{r}_k$ is the kth measurement location on A_2 and P is the number of measurements for a given time. If a constant error level throughout the measurement is assumed, the following expression is admissible [13,14].

$$T(\mathbf{r}_k,t;f) - Y(\mathbf{r}_k,t) \cong \sigma, \quad \text{on } A_2 \qquad (4)$$

where σ is the standard deviation of the temperature measurement. Then, the target value of the residual becomes

$$J = \sigma^2 t_f P \qquad (5)$$

Practical inverse methods for IHCP accept $f(\mathbf{r},t)$ approximately satisfying Eq. (5) as an inverse solution. Let us refer to such a solution as a feasible solution and refer to the above equality (Eq. (5)) as a feasibility condition. A feasible solution is regarded as a solution that is statistically consistent with the measurement data. Most conventional methods such as RM, SFM, and CGM can achieve a feasible solution without difficulty.

Even with the identical temperature readings, the achieved solution can vary according to the selection of the method. In other words, the solution is not unique but is just one of the feasible solutions. The conventional methods can provide similar but different solutions for the identical IHCP. However, in terms of accuracy, the solution that is closer to the exact solution is preferred to other feasible solutions. A postulation can be made such that a unique solution exists among the feasible solutions which is most probabilistically likely under given measurement data. Therefore, it is required to reformulate the inverse problem to seek such a solution. This study introduces the maximum entropy method (MEM) to IHCP in order to obtain such solution. The way that MEM achieves the most probabilistically likely solution and the manner in which MEM is implemented for IHCP are presented in the following section.

3 Maximum Entropy Method

As previously stated, the inverse problem is reformulated to seek the most likely solution using MEM. Here, the maximum entropy principle is introduced, and the inverse problem is stated in the form of a nonlinear constrained optimization. Conventional methods for IHCP such as CGM can be regarded as unconstrained optimizations, which aim to achieve the feasibility condition (or discrepancy principle [2]) only. On the other hand, the current optimization problem considers the entropy functional as an objective function and the feasibility condition given by Eq. (5) becomes a constraint. This feature enforces IHCP to be reformulated into a nonlinear constrained optimization problem.

Maximum Entropy Principle. The present inverse problem considers the determination of M equivalent heat flux components using P temperature readings per single time step during N time steps. A total of $U \equiv P \times N$ measurement data are utilized for estimation of $W \equiv M \times N$, heat flux components.

Consider W identical partitions. In the ith partition, a number of quantized heat flux, f_i, is stored. It is known that the maximum state of the likelihood based on the probability of quanta distribution is achievable by [41]

$$\text{maximize } H(\mathbf{f}) \equiv -\sum_{i=1}^{W} f_i \ln \frac{f_i}{F}, \qquad (6)$$

where $\mathbf{f} = \{f_1, f_2, \ldots, f_W\}$ and the total number of heat flux quanta F is given by

$$F = \sum_{i=1}^{W} f_i \qquad (7)$$

Here, H is called the information entropy [42]. Generally, the entropy in an isolated system never decreases, i.e., spontaneously tends towards the maximum value possible. In other words, since MEM reflects such property of nature, it searches the most natural solution rather than the smoothest solution. As a result, MEM enables us to minimize additional assumptions and information. Above all, the most notable merit of MEM is that the enhancement of resolution and the suppression of noise are achieved at the same time. A detailed and comprehensive review of the characteristics of MEM can be found elsewhere [24].

Optimization Problem. Generally, a nonlinear equality constraint like Eq. (5) is difficult to satisfy. Hence, it is replaced by a more tolerable criterion as follows:

$$|J - U\sigma^2 \Delta t| \leq \delta \qquad (8)$$

where time step Δt is given by $\Delta t = t_f / N$. Here, δ is selected by assuming constant sampling intervals in time and space considering the total number of temperature readings, U [43].

$$\delta = \sqrt{2U} \sigma^2 \Delta t \qquad (9)$$

This value makes Eq. (8) equivalent to the similar expressions used in previous studies [2,3]. The optimization problem for desired ME solution for the prescribed IHCP is as follows:

maximize the objective function $H(\mathbf{f})$
subject to nonlinear equality constraint

$$C_1(\mathbf{f}) \equiv J - U\sigma^2 \Delta t = 0 \qquad (10)$$

with the maximum violation of δ
linear equality constraint

$$C_2(\mathbf{f}) \equiv \sum_{i=1}^{W} f_i - F = 0 \qquad (11)$$

Bounds

$$0 < f_i \leq F \qquad (12)$$

Here, the inequality constraint given by Eq. (8) is treated as an equality constraint of the optimization problem by setting δ as the maximum violation of the equality constraint. The corresponding Lagrangian function can be written as

$$L = H - \Lambda_n C_n, \quad n = 1,2 \qquad (13)$$

where C_n denotes the constraints, and Λ_n is the Lagrange multipliers corresponding to each constraint. It is noted that the total sum F and the standard deviation σ are to be known prior to the above optimization. In summary, MEM in this study aims to seek a unique profile of heat flux under the assumption that the maximum state of likelihood is obtained via maximizing the entropy functional H. In order to obtain a reliable ME solution, a suitable optimization method, which can handle nonlinearity of H and J, is essential. Detailed solution strategy is described in the following section.

4 Solution Procedure

The current approach requires more computational efforts compared to the conventional methods due to the requirement of the constrained optimization. Furthermore, the evaluation of the entropy functional requires the total sum F of the heat flux components f_i to be known a priori. In most cases, it is impractical to acquire the total sum in advance as provided data. In order to evaluate the total sum and give an initial guess for ME estimation, the conjugate gradient method (CGM) is utilized. CGM is based on the adjoint formulation, which facilitates the evaluation of the gradient in an efficient manner by solving the adjoint problem [2]. The solution of the adjoint problem also provides the gradient required during ME estimation.

In summary, the current approach is comprised of two computational phases. The first phase achieves a feasible solution by CGM. The second phase starts with the result of the first phase as an initial guess. In the present study, the successive quadratic programming (SQP) is adopted to perform the optimization for the second phase. Both phases require the numerical evaluation of temperature $T(\mathbf{r},t;f)$. This work employs the finite volume method with Crank-Nicolson scheme for numerical discretization of the governing equation [44].

First Phase. A preliminary analysis is performed to provide the total sum and a proper initial guess for ME estimation. Thanks to the energy conservation the conventional inverse estimators for IHCP are capable of evaluating the total of the heat flux components ($F=\Sigma_{i=1}^{W}f_i$) with acceptable accuracy despite some local biases [45]. As stated earlier, CGM is employed for the first phase. CGM utilizes the adjoint formulation of which essence is that the gradient is evaluated by solving the adjoint problem and the step size along the conjugate direction is determined utilizing the solution of the sensitivity problem without having to perform exhaustive line search. The adjoint formulation for multidimensional IHCPs has already been derived in complete and sound form by Jarny et al. [14]. Kim et al. have showed a complete ME based formulation using CGM for a one-dimensional IHCP [46]. Thus, the adjoint formulation is not repeated here.

Second Phase. In order to perform the prescribed nonlinear constrained optimization, the successive quadratic programming (SQP) is utilized [31]. SQP searches the desired optimum by repeating the following three steps consecutively: (i) approximation of the Lagrangian function in the quadratic form and the constraints in the linear form; (ii) determination of the search direction; and (iii) control of the step length along the search direction with a proper penalty. SQP requires evaluation of the Hessian matrix and the gradient vector of H and J. As noted, the gradient vector of J can be obtained by solving the adjoint problem. However, the Hessian matrix of J is not easy to evaluate. Sometimes, it is an impractical task. In such cases, the Hessian matrix of J is approximated by the Broyden-Fletcher-Goldfarb-Shanno (BFGS) update formula [31]. It ensures the positive definiteness of the Hessian matrix and the convergence of the solution procedure. On the other hand, the evaluation of gradient vector and the Hessian matrix of H are rather straightforward.

$$\nabla H = -\left(\ln\frac{f_i}{F}+1\right), \quad i=1,\ldots,W \tag{14}$$

$$\nabla\nabla H = -\frac{1}{f_i}\delta_{ij}, \quad i=1,\ldots,W, \quad j=1,\ldots,W \tag{15}$$

where δ_{ij} is Kronecker delta. Since the Hessian matrix is diagonal and negative-definite as shown above, a uniform convergence can be achieved. Convergence is checked by the following criterion.
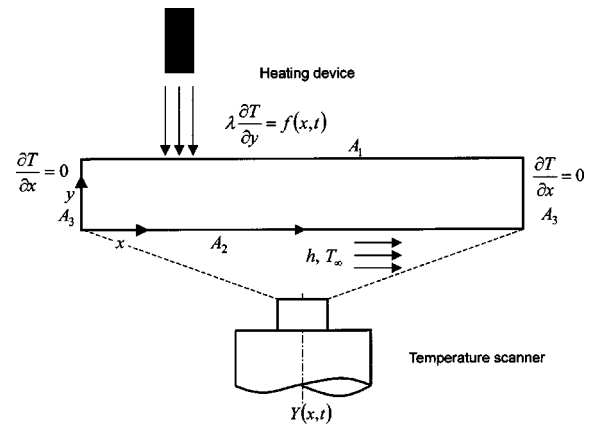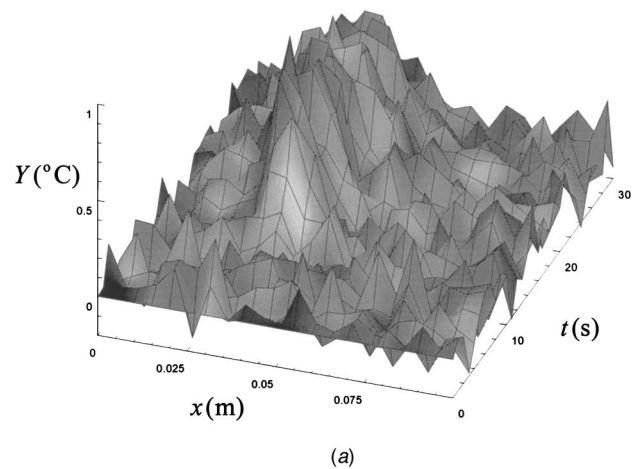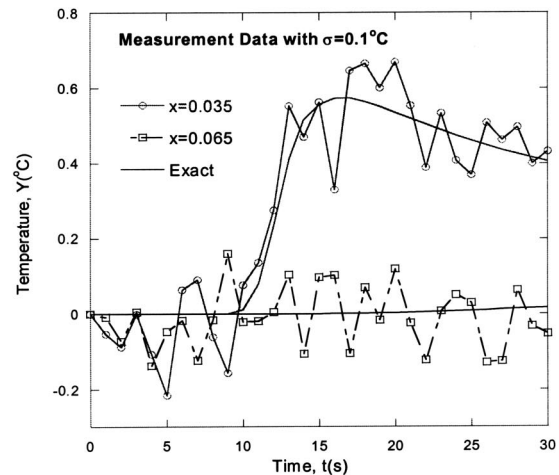
$$\frac{H^{k+1}-H^k}{H^k}<\varepsilon \tag{16}$$

Fig. 2 Overview of the inverse problem in the test cases

where k indicates the number of iterations and ε is chosen to be 10^{-3}. In this study, SQP is implemented by an existing computer code, CFSQP [47]. It is slightly modified to allow $\nabla\nabla H$ to be evaluated by Eq. (15) and to accommodate the above convergence criterion.

(a)

(b)

Fig. 3 Noisy measurement data ($\sigma=0.1°C$) for single impulse heat flux: (a) over time and space domain; (b) time-varying measurement data at $x=0.35$ and $x=0.65$
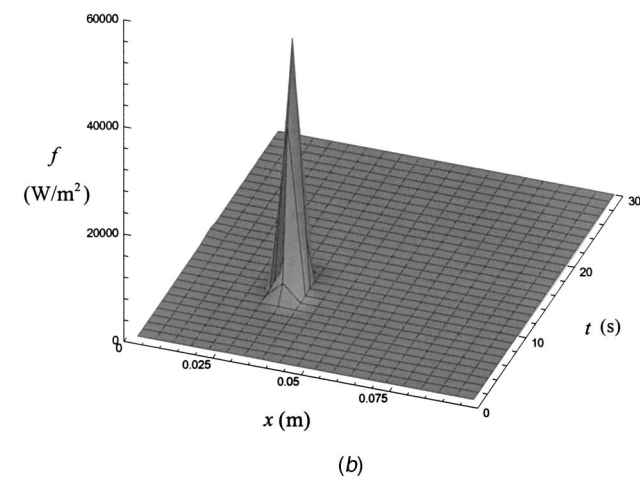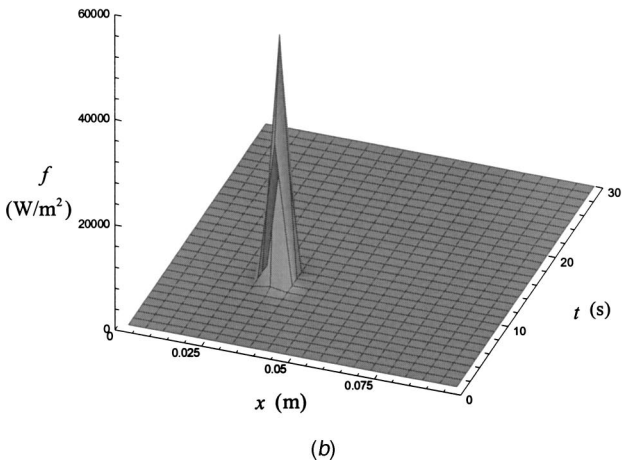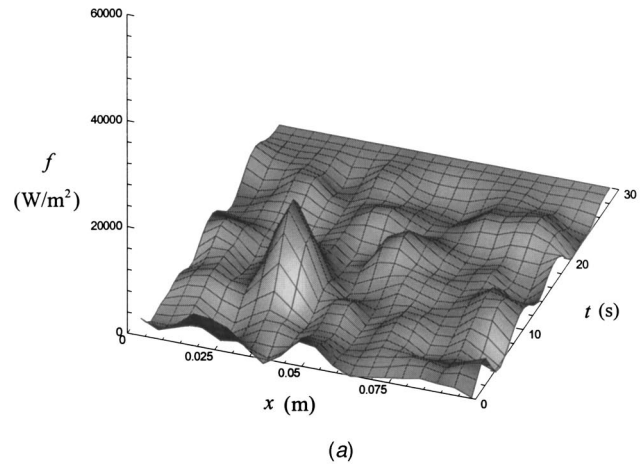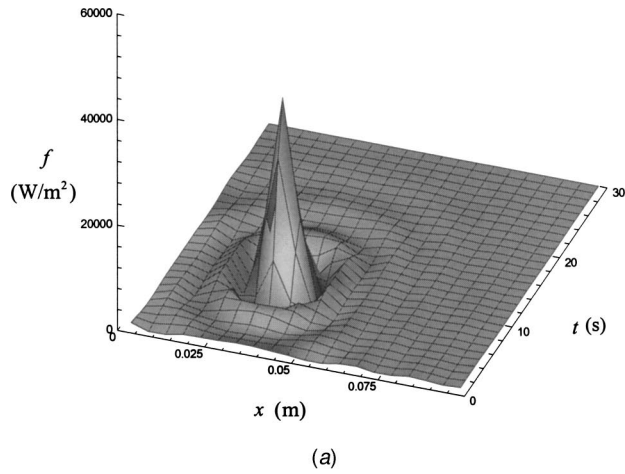
Fig. 4 Heat fluxes estimated with (*a*) CGM and (*b*) MEM using exact measurement data for single impulse heat flux

Fig. 5 Heat fluxes estimated with (*a*) CGM and (*b*) MEM using noisy measurement data ($\sigma=0.1°$C) for single impulse heat flux

5 Result and Discussion

A few test cases are presented to verify the stability and accuracy of the proposed method. The prescribed two-dimensional IHCP is investigated with computational results. The heat fluxes estimated with MEM are compared with the heat flux estimated using CGM. First, the impulse tests are performed for single impulse and multiple impulses. Second, the method is tested for rectangular heat flux. Finally, the sinusoidal heat flux case is investigated.

Problem Specification for Test Cases. The domain of interest in the test cases is a $a \times b$ two-dimensional slab, which is shown in Fig. 2. The position vector **r** is given by $\mathbf{r} \equiv \{x,y\}$ where x ($0 \leq x \leq a$) and y ($0 \leq y \leq b$). As a result, the temperature reading $Y(\mathbf{r},t)$ and the unknown heat flux $f(\mathbf{r},t)$ become functions of x, $Y(x,t)$ and $f(x,t)$, respectively. The space domain is discretized by uniform $P \times P$ equi-spaced nodes and the time domain is discretized by a constant step Δt. The upper surface (A_1) is subject to unknown time-varying heat flux while the lower surface (A_2) is under convective heat exchange. At the same time, temperature scanning is conducted to obtain the surface temperature over the lower surface. The unknown heat flux is to be estimated from the scanned temperature. Other sides (A_3) are thermally insulated. If not specified, the values used in the test cases are given as $a=0.1$ m, $b=0.01$ m, $\Delta t=1$ s, $h=10$ W/m^2°C, $T_\infty=0°$C, $T_o=0°$C, $q''=0$ W/m^2, $M=20$, and $P=21$. The case study considers homogeneous isotropic slab made of AISI-304 steel with constant thermophysical properties ($\lambda=14.311$ W/m°C and C

$=3.56732 \times 10^6$ J/m^3°C). The heat flux components are estimated on the line connecting two adjacent surface nodes in order to treat each heat flux component equivalently in the information entropy formulation.

Measurement Data Generation. Test cases have been conducted using artificially generated measurement data with and without errors. The measured temperature for k^{th} nodal point on the lower surface and m^{th} time step with artificially embedded errors is expressed as follows.

$$Y_m^k = T(x_k,0,t_m;f^e) + \sigma r_m^k \tag{17}$$

where r_m^k is a normally distributed random variable with zero mean and unit standard deviation. The random variable is gener-

Table 1 Estimated deterministic biases, D_1 and D_2

Case	D_1 MEM	D_1 CGM	D_2 MEM (W/m^2)	D_2 CGM (W/m^2)
Impulse Case (1)	0.527	0.657	2618.2	3271.5
Impulse Case (2)	0.538	0.813	2660.4	4864.8
Impulse Case (3)	...	...	5307.5	9423.2
Impulse Case (4)	0.845	0.949	3616.5	4019.2
Rectangular Case	...	...	13723.3	17621.6
Sinusoidal Case	...	...	2420.5	983.6
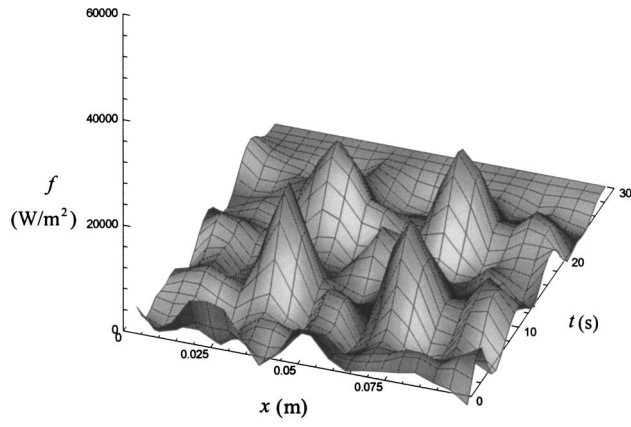
(a)
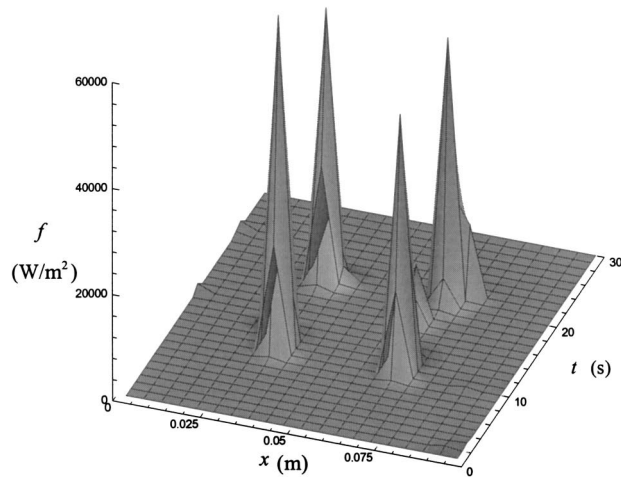
(b)

Fig. 6 Heat fluxes estimated with (a) CGM and (b) MEM using noisy measurement data ($\sigma=0.1°C$) for multiple impulse heat fluxes

(a)

(b)

Fig. 7 Heat fluxes estimated with (a) CGM and (b) MEM using noisy measurement data ($\sigma=0.1°C$) for single impulse heat flux. Underdetermined case with fewer sensors ($P=11$ and $M=20$).

ated by the IMSL® C function random_normal [48]. The exact data are obtained by numerical computation when the exact heat flux f^e is applied.

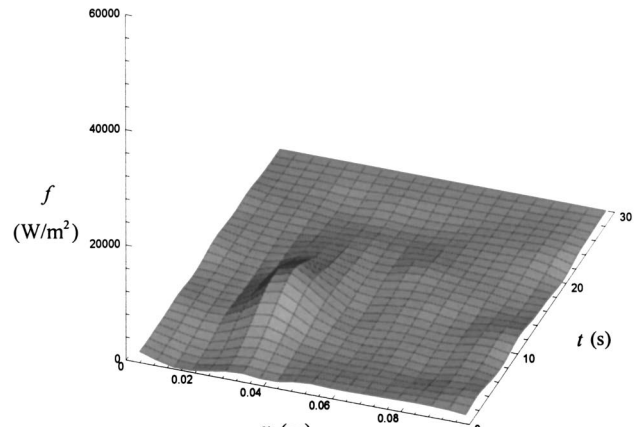**Deterministic Bias Measure.** Accuracy of an inverse method can be evaluated by the deterministic biases, which is calculated by [19,45]

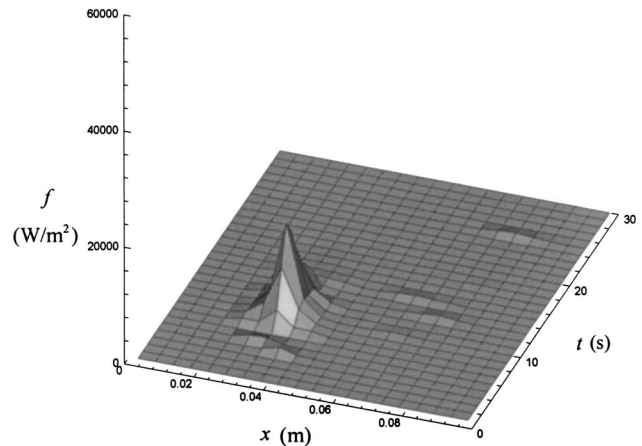$$D_1 = \frac{1 - \bar{f}_o}{f_o} \quad (18a)$$

$$D_2 = \sqrt{\frac{1}{M(N-1)} \sum_{i=1}^{N} \sum_{j=1}^{M} [f(x_i, t_j) - f_e(x_i, t_j)]^2} \quad (18b)$$

where $\bar{f}_o$ is the estimated impulse magnitude, and x_i and t_j are discrete point and time of each heat flux component, respectively. Sum of squares of errors in measured and estimated temperature on A_2 is not calculated since the feasibility condition is always enforced.

Note that the variance test [45] cannot be carried out using MEM since it can be only applied to a positive information recovery [30]. This is evident in the logarithms involved in the entropy representation. The sign of the estimated heat flux for single non-zero temperature reading will change somewhere in the domain.

Heat Flux With Impulses. When the heat flux on the top surface is concentrated within narrow interval in the space and time domains, such heat flux can be regarded as a thermal impulse. This case provides important insights into the deterministic nature for an inverse estimator [45]. The impulse heat flux is expressed as follows:

$$f(x,t) = \begin{cases} f_o & \bar{x}_r - w/2 \leq x \leq \bar{x}_r + w/2, \ \bar{t}_r - p/2 \leq t \leq \bar{t}_r + p/2 \\ & \quad \text{for} \quad r = 1, \ldots, N_r \\ 0 & \text{elsewhere} \end{cases}$$

$$(19)$$

where $f_o = 10^5$ W/m^2, $w = 0.005$ m, $t_f = 30$ s, and $p = 1$ s. The spot and time of the impulse are denoted by $\bar{x}_r$ and $\bar{t}_r$, respectively. The impulse test includes three different numerical experiments: (1) single impulse test with exact measurement ($N_r = 1$, $\bar{x}_1 = 0.0325$ m, $\bar{t}_1 = 10$ s, $\sigma = 0°C$); (2) single impulse test with noisy measurement ($N_r = 1$, $\bar{x}_1 = 0.0325$ m, $\bar{t}_1 = 10$ s, $\sigma = 0.1°C$); and (3) multiple impulses test with noisy measurement ($N_r = 4$, $\bar{x}_1 = \bar{x}_2 = 0.0325$ m, $\bar{t}_1 = \bar{t}_2 = 10$ s, $\bar{x}_3 = \bar{x}_4 = 0.0675$ m, $\bar{t}_3 = \bar{t}_4 = 20$ s, $\sigma = 0.1°C$). The measurement data for case (2) is shown in Fig. 3(a). Severe impairment in measurement data can be observed. Figure 3(b) shows the exact and noisy measurement data at $x = 0.35$ and $x = 0.65$. As can be seen, the measurement error level given by $\sigma = 0.1°C$ poses a stringent case because the ap-
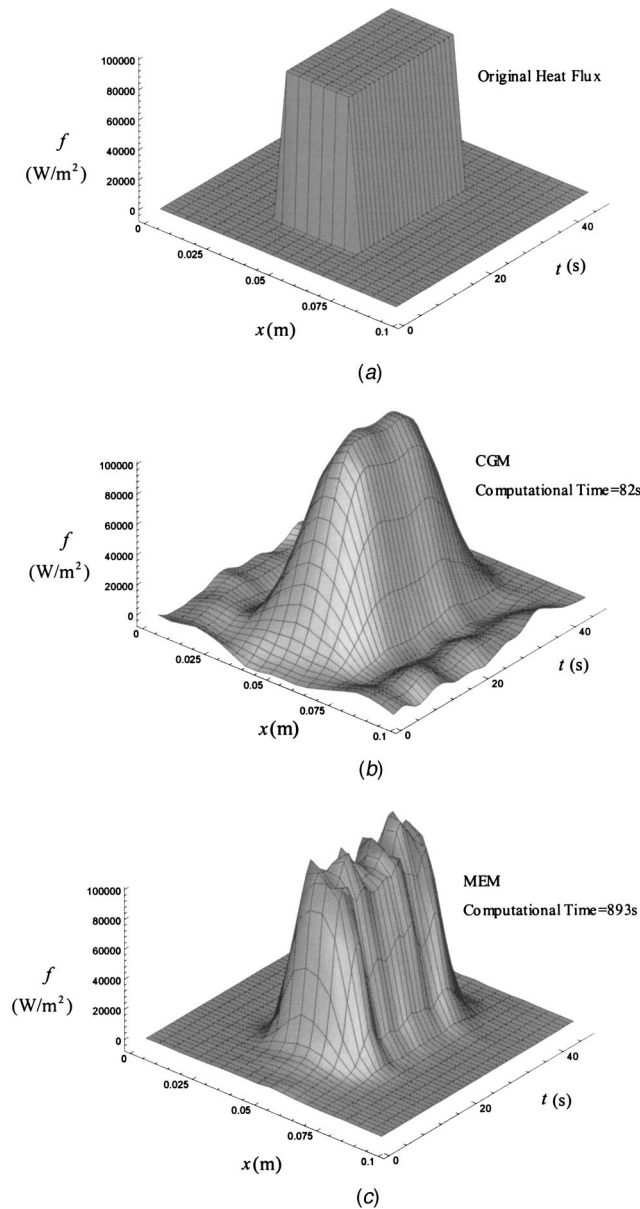
(a)

(b)

(c)

Fig. 8 (a) **Heat fluxes estimated with** (b) **CGM and** (c) **MEM using noisy measurement data** ($\sigma=0.1°C$) **for rectangular heat flux**

(a)

(b)

(c)

Fig. 9   Heat fluxes estimated with (a) **CGM and** (b) **MEM using noisy measurement data** ($\sigma=0.1°C$) **for sinusoidal heat flux**

proximate temperature rise is 0.6°C. Figure 4 display the comparison between the results of CGM and MEM for the first case. Both cases fail to recover the original impulse exactly. However, MEM achieves obviously better solution as shown. Such a trend is clearly evidenced by the result of the second case as can be seen in Fig. 5 and Table 1. The results by MEM with exact and noisy data are nearly indistinguishable while the results by CGM are noticeably different. Such remarkable resolution of MEM is termed as super-resolution, which is known to be one of the characteristic features of MEM [24]. Another result can be seen in Fig. 6, which presents the recovery of multiple impulses. Similar trend is observed in this result.

Figure 7 show results for an underdetermined case with 11 temperature readings and 20 unknown heat flux components. All other conditions are remained same as in case (2). The result for MEM provides better resolution as shown in the figure and Table 1. It is

well known that MEM is excellent for incomplete data recovery, especially in the case of image reconstruction [24,25]. Such excellence is proven also for IHCP here.

Rectangular Heat Flux. The developed method is tested for rectangular heat flux of the form

$$f(x,t) = \begin{cases} f_o & 0.035 \text{ m} \leq x \leq 0.065 \text{ m}, \quad 10 \text{ s} \leq t \leq 35 \text{ s} \\ 0 & \text{elsewhere} \end{cases}$$

(20)

where $f_o = 10^5 \text{ W/m}^2$ and $t_f = 45$ s. Figures 8($a-c$) shows the exact heat flux, which is estimated by MEM and CGM. Noticeable resolution improvement is observed for the result with MEM. However, the enhancement in resolution is not so apparent as in the impulse test. The presented ME estimation is achieved at the expense of more than twenty times the computational cost of the compared estimation as specified in the figure. Computations are performed on a PC equipped with an Intel Pentium II® CPU. This higher computational cost is due to the nonlinear constrained optimization. Hence, some trade-off between resolution and computational cost should be made according to situations encountered.

Sinusoidal Heat Flux. This case considers estimation of a sinusoidal heat flux form, which can be regarded as a representative form with smooth heat flux variation. The exact heat flux for this case is of the form

$$f(x,t) = 0.25f_o[\sin(2\pi x/a - 0.5\pi) + 1][\sin(2\pi t/t_f - 0.5\pi) + 1] \tag{21}$$

where $f_o = 10^5$ W/m^2 and $t_f = 45$ s. Figure 9 shows the exact heat flux and estimated heat fluxes by MEM and CGM. As displayed, CGM depicts the original heat flux more accurately. This is due to the smooth functional form of the original heat flux. The ME estimation performs over-resolving in this case by losing opportunity of suitable smoothing, which is a negative aspect of super-resolution. CGM seems to be appropriate for reconstructing the object with mild curvature overall. Thus, a rough inference that MEM is more effective for heat flux form with sharp changes and impulses can be made. Why MEM shows such nature is well explained by Donoho et al. [49]. They have explained this nature with the nearly blackness theory that MEM is worth applying to recovery of nearly black objects. Here, nearly black means that the values to estimate are mostly zero over the domain except for some locations. As shown in the presented results, the nearly blackness theory is considered applicable to an IHCP.

6 Conclusion

The maximum entropy method (MEM), which seeks the most likely solution among the feasible inverse solutions, is investigated for a two-dimensional inverse heat conduction problem. The inverse heat conduction problem is reformulated for MEM and the solution method using the successive quadratic programming (SQP) is proposed. The result is remarkably improved for impulse heat flux compared with the result by CGM. The result for rectangular heat flux also presents considerable improvement. Sharp edges are well represented using MEM. The maximum entropy estimation for sinusoidal heat flux shows no enhancement despite higher computational cost. In summary, the maximum entropy method is verified effectual in improving inversion accuracy for heat fluxes with impulses or sharp edges. This result is well explained by an existing theory called nearly blackness theory.

Acknowledgments

References

[1] Ozisik, M. N., and Orlande, H. R. B., 2000, *Inverse Heat Transfer: Fundamentals and Applications*, Taylor & Francis, New York.
[2] Alifanov, O. M., 1994, *Inverse Heat Transfer Problems*, International Series in Heat and Mass Transfer, Springer-Verlag, New York.
[3] Beck, J. V., Blackwell, B., and St. Clair, C. R., 1985, *Inverse Heat Conduction: Ill-Posed Problems*, Wiley, New York.
[4] Beck, J. V., and Woodbury, K. A., 1998, "Inverse Problems and Parameter Estimation: Integration of Measurements and Analysis," Meas. Sci. Technol., **9**(6), pp. 839–847.
[5] Alifanov, O. M., 1997, "Mathematical and Experimental Simulation in Aerospace System Verification," Acta Astronaut., **41**(1), pp. 43–52.
[6] Kim, S. K., Koo, B. Y., and Lee, W. I., 2000, "The Evaluation of the Heat Transfer Coefficient During Hot-Jet Impingement Using an Inverse Method With Regularization Parameter Optimization," International Journal of Transport Phenomena, **2**(3), pp. 173–186.
[7] Huang, X. C., Bartsch, G., and Schroederrichter, D., 1994, "Quenching Experiments With a Circular Test Section of Medium Thermal Capacity Under Forced-Convection of Water," Int. J. Heat Mass Transfer, **37**(5), pp. 803–818.
[8] Liauh, C. T., Hills, R. G., and Roemer, R. B., 1993, "Comparison of the Adjoint and Influence Coefficient Methods for Solving the Inverse Hyperthermia Problem," ASME J. Biomech. Eng., **115**(1), pp. 63–71.
[9] Tikhonov, A. N., and Arsenin, V. I. A., 1977, *Solutions of Ill-Posed Problems*, Scripta Series in Mathematics, Washington, Winston, New York, distributed solely by Halsted Press.
[10] D'Souza, N., 1976, "Numerical-Solution of One-Dimensional Inverse Transient Heat-Conduction by Finite-Difference Method," Mech. Eng. (Am. Soc. Mech. Eng.), **98**(5), p. 105.
[11] Raynaud, M., and Bransier, J., 1986, "A New Finite-Difference Method for the Nonlinear Inverse Heat-Conduction Problem," Numer. Heat Transfer, **9**(1), pp. 27–42.
[12] Weber, C. F., 1981, "Analysis and Solution of the Ill-Posed Inverse Heat-Conduction Problem," Int. J. Heat Mass Transfer, **24**(11), pp. 1783–1792.
[13] Neto, A. J. S., and Ozisik, M. N., 1992, "2-Dimensional Inverse Heat-Conduction Problem of Estimating the Time-Varying Strength of a Line Heat-Source," J. Appl. Phys., **71**(11), pp. 5357–5362.
[14] Jarny, Y., Ozisik, M. N., and Bardon, J. P., 1991, "A General Optimization Method Using Adjoint Equation for Solving Multidimensional Inverse Heat-Conduction," Int. J. Heat Mass Transfer, **34**(11), pp. 2911–2919.
[15] Scarpa, F., and Milano, G., 1995, "Kalman Smoothing Technique Applied to the Inverse Heat-Conduction Problem," Numer. Heat Transfer, Part B, **28**(1), pp. 79–96.
[16] Park, H. M., and Lee, J. H., 1998, "A Method of Solving Inverse Convection Problems by Means of Mode Reduction," Chem. Eng. Sci., **53**(9), pp. 1731–1744.
[17] Battaglia, J. L., 2002, "A Modal Approach to Solve Inverse Heat Conduction Problems," Inverse Probl. Eng., **10**(1), pp. 41–63.
[18] Beck, J. V., and Murio, D. A., 1986, "Combined Function Specification-Regularization Procedure for Solution of Inverse Heat-Conduction Problem," AIAA J., **24**(1), pp. 180–185.
[19] Dowding, K. J., and Beck, J. V., 1999, "A Sequential Gradient Method for the Inverse Heat Conduction Problem (Ihcp)," ASME J. Heat Transfer, **121**(2), pp. 300–306.
[20] Reinhart, H. J., and Hao, N. H., 1996, "A Sequential Conjugate Gradient Method for the Stable Numerical Solution to Inverse Heat Conduction Problems," Inverse Probl. Eng., **2**, pp. 263–272.
[21] Kim, S. K., Lee, W. I., and Lee, J. S., 2002, "Solving a Nonlinear Inverse Convection Problem Using the Sequential Gradient Method," KSME International Journal, **16**(5), pp. 710–719.
[22] Park, H. M., and Jung, W. S., 2001, "On the Solution of Multidimensional Inverse Heat Conduction Problems Using an Efficient Sequential Method," ASME J. Heat Transfer, **123**(6), pp. 1021–1029.
[23] Beck, J. V., Blackwell, B., and HajiSheikh, A., 1996, "Comparison of Some Inverse Heat Conduction Methods Using Experimental Data," Int. J. Heat Mass Transfer, **39**(17), pp. 3649–3657.
[24] Wu, N., 1997, *The Maximum Entropy Method*, Springer Series in Information Sciences, 32, Springer, New York.
[25] Skilling, J., and Bryan, R. K., 1984, "Maximum-Entropy Image-Reconstruction—General Algorithm," Mon. Not. R. Astron. Soc., **211**(1), p. 111.
[26] Golan, A., Judge, G., and Robinson, S., 1994, "Recovering Information From Incomplete or Partial Multisectoral Economic Data," Rev. Econ. Stat., **76**(3), pp. 541–549.
[27] Ramos, F. M., and Giovannini, A., 1995, "Solution of a Multidimensional Heat-Conduction Inverse Problem Using the Finite Analytic Method and the Principle of Maximum-Entropy," Int. J. Heat Mass Transfer, **38**(1), pp. 101–111.
[28] Lair, P., Dumoulin, J., and Millan, P., 1998, "Inverse Method for Flux Characterization Using Infrared Thermography in Die Forging," Numer. Heat Transfer, Part A, **33**(3), pp. 267–277.
[29] Muniz, W. B., Ramos, F. M., and Velho, H. F. D., 2000, "Entropy and Tikhonov-Based Regularization Techniques Applied to the Backwards Heat Equation," Computers & Mathematics with Applications, **40**(8–9), pp. 1071–1084.
[30] Kim, S. K., and Lee, W. I., 2002, "Solution of Inverse Heat Conduction Problems Using Maximum Entropy Method," Int. J. Heat Mass Transfer, **45**(2), pp. 381–391.
[31] Reklaitis, G. V., Ravindran, A., and Ragsdell, K. M., 1983, *Engineering Optimization: Methods and Applications*, Wiley, New York.
[32] Tan, Y., and Deng, C., 2000, "Solving for a Quadratic Programming With a Quadratic Constraint Based on a Neural Network Frame," Neurocomputing, **30**(1–4), pp. 117–128.
[33] McIntyre, N. S., Pratt, A. R., Piao, H., Maybury, D., and Splinter, S. J., 1999, "Resolution Enhancement of X-Ray Photoelectron Spectra by Maximum Entropy Deconvolution," Appl. Surf. Sci., **145**, pp. 156–160.
[34] Rohsenow, W. M., Hartnett, J. P., and Cho, Y. I., 1998, *Handbook of Heat Transfer*, 3rd ed., Mcgraw-Hill Handbooks, McGraw-Hill, New York.
[35] Lloyd, J. M., 1975, *Thermal Imaging System*, Plenum Press, New York.
[36] Mayer, R., Henkes, R., and Van Ingen, J. L., 1998, "Quantitative Infrared-Thermography for Wall-Shear Stress Measurement in Laminar Flow," Int. J. Heat Mass Transfer, **41**(15), pp. 2347–2360.
[37] Ekkad, S. V., and Han, J. C., 1996, "Heat Transfer Inside and Downstream of Cavities Using Transient Liquid Crystal Method," J. Thermophys. Heat Transfer, **10**(3), pp. 511–516.
[38] Allison, S. W., and Gillies, G. T., 1997, "Remote Thermometry With Thermographic Phosphors: Instrumentation and Applications," Rev. Sci. Instrum., **68**(7), pp. 2615–2650.
[39] Kwon, P., Schiemann, T., and Kountanya, R., 2001, "An Inverse Estimation Scheme to Measure Steady-State Tool-Chip Interface Temperatures Using an Infrared Camera," Int. J. Mach. Tools Manuf., **41**(7), pp. 1015–1030.
[40] Valvano, J. W., 1992, "Temperature Measurements," Adv. Heat Transfer, **23**, pp. 359–436.
[41] Jaynes, E. T., 1957, "Information Theory and Statistical Mechanics," Phys. Rev., **106**, pp. 620–630.
[42] Shannon, C. E., 1948, "A Mathematical Theory of Communication," Bell Syst. Tech. J., **27**, pp. 379–423.

[43] Graham, N. Y., 1983, "Smoothing With Periodic Cubic-Splines," Bell Syst. Tech. J., **62**(1), pp. 101–110.

[44] Patankar, S. V., 1980, *Numerical Heat Transfer and Fluid Flow*, Series in Computational Methods in Mechanics and Thermal Sciences, Hemisphere Pub. Corp., New York.

[45] Raynaud, M., and Beck, J. V., 1988, "Methodology for Comparison of Inverse Heat-Conduction Methods," ASME J. Heat Transfer, **110**(1), pp. 30–37.

[46] Kim, S. K., Jung, B. S., Lee, J. S., and Lee, W. I., 2002, "An Inverse Estimation of Surface Temperature Using the Maximum Entropy Method," in *Pro-ceedings of the Twelfth International Heat Transfer Conference*, Elsevier SAS.

[47] Lawrence, C., Zhou, Z. L., and Tits, A. L., 1997, *User's Guide for Cfsqp Version 2.5*, Electrical Engineering Dept. and Institute for System Research, University of Maryland, College Park, MD.

[48] *IMSL Math/Library User's Guide*, 1994, Visual Numerics, http://vni.com

[49] Donoho, D. L., Johnstone, I. M., Hoch, J. C., and Stern, A. S., 1992, "Maximum-Entropy and the Nearly Black Object," J. R. Stat. Soc. Ser. B. Methodol., **54**(1), pp. 41–81.

Discussion: "Commentary on Correlations for Convective Vaporization in Tubes," (Webb, Ralph. L., 2003, ASME J. of Heat Transfer, 125(1), pp. 184−185.)

John R. Thome[1]

Introduction

This discussion responds to the recently published commentary presented by Webb [1] in this journal. Several simple, but important misrepresentations were made in his commentary about the flow pattern/flow structure flow boiling model of Kattan et al. [2–4] and all *four* other prediction methods [5–8] he discusses, creating confusion in the state-of-the-art and perpetuating his misconceptions about these flow boiling models. In fact, it is quite surprising that his comments about the paper by Kattan et al. [2–4] survived a peer review, given that they received the ASME 1998 Heat Transfer Division Best Paper Award for their work. While it is essential to expose new methods to critical and objective examination, on the other hand purposely incorrect or uninformed comments are not appropriate and hence that is what I would like to set straight below for the heat transfer community.

Correct Heat Flux to be Used in Flow Boiling Correlations

Regarding [1], Webb's thesis is that in a flow boiling model describing intube evaporation, the nucleate boiling contribution (through the nucleate boiling heat transfer coefficient) should be calculated in a nucleate boiling correlation using the residual heat flux, that is the total heat flux at the wall minus that taken away by the two-phase convection or the so called convective boiling heat flux. He refers to several published sets of flow boiling data measured under nucleate boiling dominated conditions and under convective boiling dominated conditions as his proof for this thesis. Clearly, for nucleate boiling dominated test conditions, the nucleate boiling mechanism dominates and hence the total heat flux can be used for calculating the nucleate boiling heat transfer coefficient since the convective boiling heat flux is negligible. Furthermore, it is self evident that for convective boiling dominated test conditions, it does not make much difference what heat flux is used to calculate the nucleate boiling heat transfer coefficient, since it is in any case negligible. Between these two extremes, neither mechanism is dominant. Following the asymptotic approach widely and successfully employed by Churchill and others in numerous single and two-phase processes, each heat transfer coefficient of the contending mechanisms is calculated separately at the local conditions (that is, at the local total heat flux in the present case for nucleate boiling) and are then combined together using an asymptotic law with a selected exponent. It should be noted that the asymptotic approach is itself empirically based and experience shows that it works well.

This asymptotic approach is in fact what Steiner and Taborek [8] applied so nicely in the flow boiling method they presented for vertical tubes, evaluating a very large, diversified database and finding the best exponent for their asymptotic model to be 3. However, they did not calculate their nucleate boiling heat transfer

coefficient based on $(T_w$-$T_{sat})$ nor based on the residual heat flux, which is what Webb claims to support his thesis. In fact, Steiner and Taborek used the total heat flux just like in the other methods [4–8] enounced by Webb. This fact is evident by simply referring to their example calculation presented in [8] where the local design heat flux of 60 kW/m^2 is directly input to their nucleate boiling correlation or to their Eq. (3a), defining their flow boiling heat transfer coefficient obtained from their asymptotic equation. Secondly, Steiner and Taborek did not use the Gorenflo [9] nucleate pool boiling correlation as Webb incorrectly claims. In fact, they used a Gorenflo-like nucleate pool boiling correlation of their own, something they stated quite clearly to avoid confusion, that used different standard reference conditions, different standard heat transfer coefficients and an additional residual correction factor based on the molecular weight of the fluid; refer to Chapters 4 and 7 (and Tables 4.3 and 7.5) in Collier and Thome [10] to see the two different sets of tabular values, conditions and methods. Hence, Webb misrepresents simple facts in the literature to try to support his residual heat flux thesis.

Proceeding to a physical view point of the situation at flow boiling conditions with significant contributions of both nucleate boiling and convective boiling, the surface of the tube must be covered by a layer of closely packed growing and departing bubbles. Hence, all the heat flux must first pass from the heated wall through this "nucleate boiling layer" of bubbles attached to the heated wall, where some of it is converted to latent heat, and the remaining heat flux flows out towards the vapor-liquid interface where convective evaporation converts liquid into vapor. Hence, the nucleate boiling process sees the total heat flux, not the *residual* heat flux. It is not physically clear how the convective boiling heat flux could circumvent the nucleate boiling layer on the wall packed with bubbles, which is Webb's thesis, without first being made available to the nucleate boiling process. This physical situation is also similar to the nucleate pool boiling process taking place in an otherwise stagnant pool, where only a fraction of the heat is absorbed by the bubbles at the surface and the rest departs in the rising superheated liquid; here, again, the total heat flux is used to calculate the local nucleate boiling heat transfer coefficient, not the residual latent heat flux. In contrast, Webb presented no physical interpretation of this process to support his thesis.

Literature Ignored in Commentary

In an additional attempt to support his thesis and discredit a flow boiling model counter to it, Webb states that "the Kattan et al. correlation was based on a small refrigerant data base." In their original three-part publication, 702 flow pattern observation data points were obtained in [2] while 1141 flow boiling heat transfer coefficients were reported in [3] and used in the Kattan et al. heat transfer model in [4]. Their database covered five refrigerants (R-134a, R-123, R-502, R-402A, and R-404A) and a wide range of mass velocities (100–500 kg/m^{2}s), pressures (1–9 bar) and vapor qualities (0.15–0.98), in particular with numerous data at high vapor qualities and in stratified-wavy flow that are the most difficult to predict. In citing this work for an award, the ASME Heat Transfer Division must have considered this to be an exemplary database. Relative to state-of-the-art in 2002 when writing his comments, Webb also ignored numerous new additions to the database, appearing after peer review in widely cited journals. For example, in 1998 in [11] the database was extended to include R-407C with its mixture effects, additional R-134a data, and even to refrigerant-oil mixtures up to 50 percent wt percent oil (achieved by only introducing the local liquid viscosity of the refrigerant-oil mixture into the model without any changes to the heat transfer equations). In 1999 in the *J. Heat Transfer*, Zürcher et al. [12] presented a large new heat transfer database for evaporation of ammonia in a stainless steel tube at numerous mass velocities and showed the same heat transfer model still worked without change, only making minor fixes to the flow pattern map

[1]Professor, Laboratory of Heat and Mass Transfer, Faculty of Engineering Science and Technology, Swiss Federal Institute of Technology Lausanne, CH-1015 Lausanne, Switzerland. E-mail: john.thome@epfl.ch

Copyright © 2003 by ASME

using the new database that went to very low mass velocities (down to 20 kg/m^2 s), along with a largely successful comparison to an older, independent ammonia database. In 2000, Zürcher et al. [13] presented a new general version of the Steiner-Taborek onset of nucleate boiling criterion to use in their model to distinguish the heat flux threshold at which nucleate boiling ceases to occur, extending the ammonia heat transfer database to 11 mass velocities to look also at the flow transition effects. In an independent study in 2001 in another widely read journal, Kabelec and de Buhr [14] found that their ammonia flow boiling data agreed quite well with the Kattan et al. heat transfer model. In early 2002, Zürcher et al. [15,16] presented new developments on the flow pattern map and heat transfer model. Hence, the original ''small refrigerant database'' that by the year 1999 included seven fluids plus refrigerant-oil mixtures is actually a huge database, all gone missing in his commentary in 2002. It is true, and we have stated this, that for the most part we have avoided including other flow boiling data measured using electrically heated tubes, which we do not think are appropriate for stratified types of flows.

More recently, R-22 and R-410A have also been added to the database behind this method in [17] and also the maverick fluid CO$_2$ over a very wide range of reduced pressures [18], i.e., currently a total of 10 fluids plus oil mixtures. We have also recently submitted for review a two-part paper in which we compare the void fraction model we use in our heat transfer model and flow pattern map to about 250 time-averaged void fraction measurements (very good results) based on processing 227,000 dynamic void fraction images using a new measurement technique, images now being newly processed to provide experimental data on the dry angle around the upper tube perimeter in stratified-wavy flows. Furthermore, our sister method for in tube condensation, based on the same basic approach used in our flow boiling model, has recently been completed, covering a database of 15 fluids from 9 independent laboratories [19,20], and captures 85 percent of the heat transfer data to within $\pm$20 percent.

In summary, this two-phase flow pattern, simplified two-phase flow structure approach has shown promise over the years and, being realistic, has the potential to continue to evolve and improve to attain higher accuracies and reliability as we and others learn more about the influence of two-phase flows on flow boiling heat transfer. This flow pattern/flow structure type of heat transfer model so far appears to be a sound, unified approach to predict local two-phase heat transfer coefficients for both evaporation and condensation that also correctly captures the trends in the data quite well too. Notably, our two-phase flow pattern, simplified two-phase flow structure papers reflect an attentive reading and referencing of the state-of-the-art in heat transfer and two-phase flow published by others.

References

[1] Webb, R. L., 2003, ''Commentary on Correlations for Convective Vaporization in Tubes,'' J. Heat Transfer,, **125**, pp. 184–185.

[2] Kattan, N., Thome, J. R., and Favrat, D., 1998, ''Flow Boiling in Horizontal Tubes. Part 1: Development of a Diabatic Two-Phase Flow Pattern Map,'' J. Heat Transfer, **120**, pp. 140–147.

[3] Kattan, N., Thome, J. R., and Favrat, D., 1998, ''Flow Boiling in Horizontal Tubes. Part 2: New Heat Transfer Data for Five Refrigerants,'' J. Heat Transfer, **120**, pp. 148–155.

[4] Kattan, N., Thome, J. R., and Favrat, D., 1998, ''Flow Boiling in Horizontal Tubes. Part 3: Development of a New Heat Transfer Model Based on Flow Patterns,'' J. Heat Transfer, **120**, pp. 156–165.

[5] Gungor, K. E., and Winterton, R. H. S., 1986, ''A General Correlation for Flow Boiling in Tubes and Annuli,'' Int. J. Heat Mass Transfer, **29**(3), pp. 351–358.

[6] Gungor, K. E., and Winterton, R. H. S., 1987, ''Simplified General Correlation for Saturated Flow Boiling and Comparisons of Correlations with Data,'' Chem. Eng. Res. Des., **65**, pp. 148–156.

[7] Liu, Z., and Winterton, R. H. S., 1988, ''Wet Wall Flow Boiling Correlation with Explicit Nucleate Boiling Term,'' *Multiphase Transport and Particulate Phenomena*, T. Nejat Veziroglu, ed., Hemisphere Publishing Co., New York, **1**, pp. 419–432.

[8] Steiner, D., and Taborek, J., 1992, ''Flow Boiling Heat Transfer in Vertical Tubes Correlated by an Asymptotic Model,'' Heat Transfer Eng., **13**(2), pp. 43–69.

[9] Gorenflo, D., 1992, *VDI Wärmeatlas*, Section Ha, VDI Verlag, Düsseldorf, (English ed.).

[10] Collier, J. G., and Thome, J. R., 1994, *Convective Boiling and Condensation*, Oxford University Press, Oxford, England.

[11] Zürcher, O., Thome, J. R., and Favrat, D., 1998, ''Intube Flow Boiling of R-407C and R-407C/Oil Mixtures Part II: Plain Tube Results and Predictions,'' HVAC&R Res., **4**(4), pp. 373–399.

[12] Zürcher, O., Thome, J. R., and Favrat, D., 1999, ''Evaporation of Ammonia in a Smooth Horizontal Tube: Heat Transfer Measurements and Predictions,'' J. Heat Transfer, **121**, pp. 89–101.

[13] Zürcher, O., Thome, J. R., and Favrat, D., 2000, ''An Onset of Nucleate Boiling Criterion for Horizontal Flow Boiling,'' Int. J. Therm. Sci., **39**(9), pp. 909–918.

[14] Kabelac, S., and de Buhr, H. J., 2001, ''Flow Boiling of Ammonia in a Plain and a Low Finned Horizontal Tube,'' Int. J. Refrig., **24**, pp. 41–50.

[15] Zürcher, O., Favrat, D., and Thome, J. R., 2002, ''Development of a Diabatic Two-Phase Flow Pattern Map for Horizontal Flow Boiling,'' Int. J. Heat Mass Transfer, **45**, pp. 291–303.

[16] Zürcher, O., Favrat, D., and Thome, J. R., 2002, ''Evaporation of Refrigerants in a Horizontal Tube: An Improved Flow Pattern Dependent Heat Transfer Model Compared to Ammonia Data,'' Int. J. Heat Mass Transfer, **45**, pp. 303–317.

[17] Wojtan, L., and Thome, J. R., 2003, ''Flow Boiling in Horizontal Tubes: New Results for R-410a and R-134a Compared to R-22,'' *Int. Congress of Refrigeration*, Washington, D.C., August.

[18] Thome, J. R., and El Hajal, J., 2003, ''Flow Boiling Heat Transfer to Carbon Dioxide: General Prediction Method,'' Int. J. Refrig., **26** in press.

[19] El Hajal, J., Thome, J. R., and Cavallini, A., 2003, ''Condensation in Horizontal Tubes, Part 1: Two-Phase Flow Pattern Map,'' Int. J. Heat Mass Transfer, **46** pp. 3349–3363.

[20] Thome, J. R., El Hajal, J., and Cavallini, A., 2003, ''Condensation in Horizontal Tubes, Part 2: New Heat Transfer Model Based on Flow Regimes,'' Int. J. Heat Mass Transfer, **46**, pp. 3365–3387.

Closure to "Discussion: 'Commentary on Correlations for Convective Vaporization in Tubes,' (Webb, Ralph. L., 2003, ASME J. of Heat Transfer, 124(1), pp. 184−185.)"

Ralph L. Webb
e-mail: r5w@psu.edu
The Pennsylvania State University, Department of
Mechanical Engineering, University Park, PA 16802

There was no attempt on my part to discredit any of the cited models. Rather, the intent was to focus on two key points:

1. That the foundation of the flow boiling model originally proposed by Chen (1966) and extensively used later by other correlation developers, clearly states that the F-Factor should be dependent only on "hydrodynamic" parameters and should be independent of heat flux. Hence, the nucleate boiling contribution should be calculated from an appropriate pool boiling correlation at the system $(T_{wall}-T_{sat})$—not at the total system heat flux.

2. The four cited correlations do not follow the basic model structure proposed by Chen. Hence, the reader should be very careful in using the cited correlations. For the cited correlations, the nucleate boiling contribution **must** be calculated at the total system heat flux. Otherwise errors will result.

After reading Prof. Thome's discussion, I stand on the commentary made in my Technical Note. My reference to the generic Chen model is not limited to the "superposition model" which he published in 1966. As stated in my Technical Note the generic Chen model is meant to be a class of models, for which the F-factor is independent of heat flux and the exponent "n" is chosen to best fit the data. I believe that the concept of an F-factor that depends only on hydrodynamic parameters and is independent of heat flux is a sound and rationally based concept, which has been applied by a many correlation developers. As stated in my Technical Note, there is very strong support for the Chen proposal that the F-factor is independent of heat flux, as shown in data reported by Kenning and Cooper (1989), Wadekar (1990), and Cornwell and Scoones (1988) and Cornwell and Scoones (*Proc. 2nd UK Heat Transfer Conf., V-1, 21–32*, 1988). The second group of models, as cited in the Webb Technical Note and amplified in the Thome discussion teach in opposition to the Chen concept. Further, I believe that a flow boiling model that calculates the nucleate boiling contribution at the total system heat flux lacks a rational basis and is inconsistent with the experimental findings of Kenning and Cooper (1989), Wadekar (1990), and Cornwell and Scoones (*Proc. 2nd UK Heat Transfer Conf., V-1, 21–32*, 1988). Interested readers may wish to read the Webb and Gupte (1992) survey paper, which provides a detailed discussion of the foundation of convective boiling models that existed up to 1992.

The key purpose of my Technical Note was to emphasize that the four cited correlations fall within a different class of models than the concept proposed by Chen. We felt it important that the reader (and user of such correlations) clearly understand that a different "rule" is used to calculate the nucleate boiling component for the four cited correlations. Without strict specification and clear understanding of how to calculate the nucleate boiling component for each of the two "classes" of models, mistakes in application of the correlations will exist.

My comment concerning the size of the data base used in the Katten et al. correlation were not intended to be critical. We simply stated what is reported in Katten et al. (1998) that the database is for five refrigerants and contains 702 data points. The size of their database is small, relative to those used by Steiner and Taborek or Liu and Winterton. The Steiner and Taborek data base had 10,152 points for water, plus 2362 data points for four refrigerants, seven hydrocarbons, NH_3, N_2, H_2, and He. The Liu and Winterton database has 5549 data points for eight fluids (including four refrigerants).

Prof. Thome has argued that the one should calculate the h_{nb} in the Steiner and Taborek correlation at the total system heat flux. I disagree with this interpretation. He refers to the example problem in the Steiner and Taborek paper. The example states that a constant heat flux of 60 kW/m^2 is applied to the tube wall. The nucleate boiling coefficient is evaluated at 20 kW/m^2, which is the "normalized heat flux" for the nucleate boiling correlation. Actually, an iterative procedure is required to fully work the example. This would involve assuming q_{nb} [or (T_w-T_{sat})] and iterating until the assumed and calculated values agree. The example merely illustrated the calculation steps.

I believe that the subject addressed in my Technical Note can lead to considerable confusion (and error) on the part of correlation users, unless it is clearly specified how the correlations are to be applied. Commentary to avoid such confusion was the sole purpose of writing the Technical Note. I have high respect for Prof. Thome both personally and professionally.

Erratum: "Measuring Thermal and Thermoelectric Properties of One-Dimensional Nanostructures Using a Microfabricated Device" [Journal of Heat Transfer, 2003, 125(5), pp. 881−888]

**Li Shi, Deyu Li, Choongho Yu, Wanyoung Jang, Dohyung Kim, Zhen Yao, Philip Kim,
and Arunava Majumdar**

The correct affiliation for Wanyoung Jang and Zhen Yao is as follows: Department of Physics, Center for Nano and Molecular Science and Technology, University of Texas at Austin, Austin, TX 78712